Transactions of the ASME®

Technical Editor, **LEWIS T. WHEELER (1997)**

Department of Mechanical Engineering,
University of Houston,
Houston, TX 77204-4792

Transactions of the ASME, Journal of Applied Mechanics (ISSN 0021-8936) is published quarterly (Mar., June, Sept., Dec.) for $210.00 per year by The American Society of Mechanical Engineers, 345 East 47th Street, New York, NY 10017.

Periodicals postage paid at New York, NY and additional mailing office. POSTMASTER: Send address changes to Transactions of the ASME, Journal of Applied Mechanics, c/o THE AMERICAN SOCIETY OF MECHANICAL ENGINEERS, 22 Law Drive, Box 2300, Fairfield, NJ 07007-2300.

CHANGES OF ADDRESS must be received at Society headquarters seven weeks before they are to be effective. Please send old label and new address. **PRICES:** To members, $40.00, annually: to nonmembers, $210.00. Add $30.00 for postage to countries outside the United States and Canada.

Journal of Applied Mechanics

Published Quarterly by The American Society of Mechanical Engineers

VOLUME 63 • NUMBER 4 • DECEMBER 1996

(Contents continued on Outside Back Cover)

CONTENTS (CONTINUED)

BRIEF NOTES

DISCUSSION

BOOK REVIEWS

ANNOUNCEMENTS AND SPECIAL NOTES

Effect of the Interphase Zone on the Bulk Modulus of a Particulate Composite

M. P. Lutz
Department of Civil Engineering,
University of California,
Berkeley, CA 94720

R. W. Zimmerman[1]
Earth Sciences Division,
Lawrence Berkeley Laboratory,
University of California,
Berkeley, CA 94720
Assoc. Mem. ASME

An exact solution is found for the problem of hydrostatic compression of an infinite body containing a spherical inclusion, with the elastic moduli varying with radius outside of the inclusion. This may represent an interphase zone in a composite, or the transition zone around an aggregate particle in concrete, for example. Both the shear and the bulk moduli are assumed to be equal to a constant term plus a power-law term that decays away from the inclusion. The method of Frobenius series is used to generate an exact solution for the displacements and stresses. The solution is then used to estimate the effective bulk modulus of a material containing a random dispersion of these inclusions. The results demonstrate the manner in which a localized interphase zone around an inclusion may markedly affect both the stress concentrations at the interface, and the overall bulk modulus of the material.

1 Introduction

The behavior of many composite materials is known to be greatly affected by the interface between the matrix and the inclusions. The earliest analyses of the mechanical behavior of composites assumed that the two components are both homogeneous, and that the components are perfectly bonded across a sharp and distinct interface (Eshelby, 1957; Hashin and Shtrikman, 1961). Later models considered the effect of sliding across the interface (Aboudi, 1989; Jasiuk et al., 1992), debonding between the inclusion and matrix (Benveniste, 1984), and other effects. In some materials, the components are well bonded to each other, but the interface is not sharp. In polymer-fiber composites, for example, as well as in some metal-matrix composites, diffusion of material between the matrix and fiber may create an elastic moduli profile that smoothly varies from that of the fiber to that of the matrix (Theocaris, 1992). In some polymer composites, a binding agent is applied to the fibers to promote adhesion between the fiber and the matrix (Drzal et al., 1983). This binding agent may diffuse into the matrix during the curing process, leading to a gradient in resin concentration. This gradient, in turn, leads to a gradient in the elastic moduli.

In other cases, such as the transition zone around concrete (Mehta and Monteiro, 1992), the moduli of the matrix varies as the inclusion particle is approached, but the interface with the inclusion is still distinct, since the inhomogeneous region is restricted to the matrix phase. Nonuniformities in the hydration process, caused by adhesion of water films to the aggregate (inclusion) particles, leads to a "transition zone" that is characterized by an increase in porosity near the inclusions, along with other microstructural differences. Although little quantitative analysis has been done to study the elastic moduli in this zone, it seems clear that one effect will be to cause the elastic moduli of the cement paste to decrease near the inclusions, as compared to their values in pure cement paste.

The types of materials described above cannot be adequately modeled without accounting for the variation of elastic moduli with radial distance from the center of the inclusion. This is particularly true with regard to localized phenomena such as stress concentrations. In this paper, we solve the problem of hydrostatic compression of a body containing a spherical inclusion, with a radially symmetric elastic moduli profile outside of the inclusion. This solution is then used to estimate the effective bulk modulus of a body containing a random dispersion of such inclusions.

2 Previous Models of Interphase Zones

Recognition of the importance of modeling the "interphase zone" in composite materials has existed for some time. Hashin and Rosen (1964) developed a model for composites in which a thin layer existed outside of each inclusion. The elastic moduli were uniform within this layer, but different from those in the matrix or inclusions. Use of this model for a material with an inhomogeneous interphase will be problematic, however, as it is not clear how one would choose a single pair of effective elastic moduli to represent the entire interphase region. And whereas this model may be useful in predicting the overall moduli of a composite with an inhomogeneous interphase, it is incapable of properly estimating the effect that the property gradient has on stress concentrations (see Jayaraman and Reifsnider, 1992, Fig. 5, for example).

A number of researchers have attempted to account for variations of the moduli within the interphase zone. Jayaraman and Reifsnider (1992) considered a transition zone outside of a cylindrical inclusion, and allowed the moduli to vary according as r^{β}, where β is some constant. As this variation would lead to the moduli vanishing (or blowing up) far from the inclusion, it was necessary to assume that the interphase zone terminated at some specified distance from the inclusion, beyond which lay the "undamaged" matrix material. In this approach, solutions valid in the interphase region and exterior to the interphase must be joined together by matching up the tractions and displacements at the interphase/matrix boundary. This model is more general than the three-shell model of Hashin and Rosen (1964), in that it allows the moduli to vary within the interphase zone. Our model is similar to that used by Jayaraman and Reifsnider (1992), except that the moduli will vary continuously throughout the entire region outside of the inclusion. Furthermore, we will be considering particulate composites with spheri-

[1] Current address: ERE Department, Imperial College, London SW7 2BP, U.K.

Contributed by the Applied Mechanics Division of THE AMERICAN SOCIETY OF MECHANICAL ENGINEERS for publication in the ASME JOURNAL OF APPLIED MECHANICS.

Discussion on this paper should be addressed to the Technical Editor, Professor Lewis T. Wheeler, Department of Mechanical Engineering, University of Houston, Houston, TX 77204-4792, and will be accepted until four months after final publication of the paper itself in the ASME JOURNAL OF APPLIED MECHANICS.

Manuscript received by the ASME Applied Mechanics Division, Apr. 25, 1995; final revision, Apr. 3, 1996. Associate Technical Editor: I. M. Daniel.

cal inclusions, rather than fiber composites with cylindrical inclusions.

3 Governing Equations for Radially Symmetric Deformations

The derivation of the governing equation for radially symmetric elastic deformation of a body whose moduli vary with radius have been given by Herve and Zaoui (1993), Lutz and Ferrari (1993), and others, and will be reviewed here briefly; an analogous derivation for axisymmetric deformations in cylindrical coordinates has been given by Kwon et al. (1994). The displacement vector will have only one nonzero component, u_r, which will vary only with the r coordinate. Since there is only one nonzero displacement component, the subscript r can be dropped, and the displacement vector can be written as

$$\mathbf{u} = [u_r(r, \theta, \phi), u_\theta(r, \theta, \phi), u_\phi(r, \theta, \phi)] \Rightarrow [u(r), 0, 0]. \tag{1}$$

The only nonzero components of the strain are (Sokolnikoff, 1956, p. 184):

$$\epsilon_{rr} = \frac{du}{dr}, \quad \epsilon_{\theta\theta} = \epsilon_{\phi\phi} = \frac{u}{r}, \tag{2}$$

where total derivatives can be used, since u does not depend on θ or ϕ. Two of the three equations of stress equilibrium are identically satisfied; the third takes the form (Sokolnikoff, 1956, p. 184)

$$\frac{d\tau_{rr}}{dr} + \frac{2\tau_{rr} - \tau_{\theta\theta} - \tau_{\phi\phi}}{r} = 0. \tag{3}$$

The stress-strain equations take the usual form for an isotropic material:

$$\tau_{rr} = \lambda(\epsilon_{rr} + \epsilon_{\theta\theta} + \epsilon_{\phi\phi}) + 2\mu\epsilon_{rr}, \tag{4a}$$

$$\tau_{\theta\theta} = \lambda(\epsilon_{rr} + \epsilon_{\theta\theta} + \epsilon_{\phi\phi}) + 2\mu\epsilon_{\theta\theta}, \tag{4b}$$

$$\tau_{\phi\phi} = \lambda(\epsilon_{rr} + \epsilon_{\theta\theta} + \epsilon_{\phi\phi}) + 2\mu\epsilon_{\phi\phi}. \tag{4c}$$

These stress-strain relations remain valid even if the moduli vary with position.

The stress-displacement relations are found by eliminating the strains from Eqs. (2) and (4):

$$\tau_{rr} = (\lambda + 2\mu)\frac{du}{dr} + 2\lambda\frac{u}{r}, \tag{5a}$$

$$\tau_{\theta\theta} = \tau_{\phi\phi} = \lambda\frac{du}{dr} + 2(\lambda + \mu)\frac{u}{r}. \tag{5b}$$

Finally, we substitute the expressions for the stresses given by Eq. (5) into the equilibrium Eq. (3), and allow the moduli λ and μ to vary with r. This leads to the following equation that governs radially symmetric deformations:

$$\frac{d}{dr}\left[(\lambda + 2\mu)\frac{du}{dr} + 2\lambda\frac{u}{r}\right] + \frac{4\mu}{r}\left[\frac{du}{dr} - \frac{u}{r}\right] = 0, \tag{6}$$

which can also be written as

$$[\lambda(r) + 2\mu(r)]\left[\frac{d^2u}{dr^2} + \frac{2}{r}\frac{du}{dr} - \frac{2}{r^2}u\right] + [\lambda'(r) + 2\mu'(r)]\frac{du}{dr} + 2\lambda'(r)\frac{u}{r} = 0, \tag{7}$$

where the prime ($'$) denotes differentiation with respect to r. If both λ and μ were uniform, only the term inside the large brackets would remain; this is the classical equation for radially symmetric deformations that was solved by Lamé in 1859 (see Rekach, 1979, pp. 50–51).

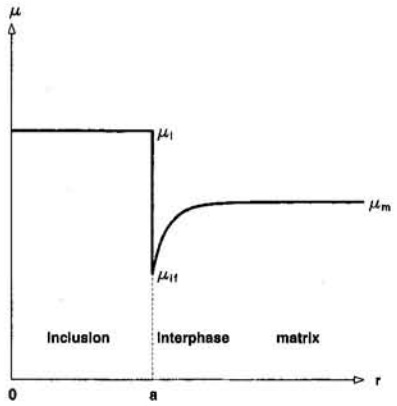

Fig. 1 Schematic diagram of the moduli variation described by Eq. (8). In this figure the interphase zone is a *damage zone* in which the moduli are less than in the pure matrix material.

In the problem at hand, the moduli in the matrix vary smoothly with radius, and approach those of the "pure matrix" component as $r \to \infty$. In general, the precise variation of the moduli will not be known, although some measurements suggest a power-law behavior (Theocaris, 1986, 1992). The main requirements of the assumed modulus variation are that it decay away from the interface, and asymptotically level off to some constant value. Furthermore, we would like the values of the moduli at the interface and at infinity to be controllable parameters, and would also like to be able to control the extent of the interphase zone. Finally, it will be convenient if the moduli vary in such a way that the governing equation is of the form that can be solved by the method of Frobenius, as done by Lutz and Ferrari (1993) for the problem of a radially inhomogeneous sphere. Bearing these factors in mind, we assume that the moduli vary according to (see Fig. 1)

$$\lambda(r) = \lambda_m + (\lambda_{if} - \lambda_m)(r/a)^{-\beta}, \tag{8a}$$

$$\mu(r) = \mu_m + (\mu_{if} - \mu_m)(r/a)^{-\beta}, \tag{8b}$$

where a is the radius of the inclusion, the subscript m refers to the pure matrix component, and the subscript if refers to the interface with the inclusion. The parameter β controls the rate at which the moduli decay away from the inclusion; larger values of β correspond to interphase zones that are more localized. It will be seen below that β must be an integer in order for the Frobenius theory to apply. As the moduli variations are never known precisely, restricting β to integer values poses no serious limitation, in practice. Note that as $\{\lambda_m, \lambda_{if}, \mu_m, \mu_{if}\}$ are all independently variable, the Poisson ratio of the interphase zone is not restricted to be constant, as it has been in some previous models. For notational convenience, we now rewrite Eq. (8) as

$$\lambda(r) = \lambda_m + \bar{\lambda}r^{-\beta}, \tag{9a}$$

$$\mu(r) = \mu_m + \bar{\mu}r^{-\beta}, \tag{9b}$$

where $\bar{\lambda} = (\lambda_{if} - \lambda_m)a^\beta$, and $\bar{\mu} = (\mu_{if} - \mu_m)a^\beta$.

4 Solution of Governing Equation for an Inhomogeneous Matrix

An analytical solution to Eq. (7) can be found using the classical method of Frobenius series. This method has previously been used by Lutz and Ferrari (1993) to solve the problem of an inhomogeneous sphere under hydrostatic loading, and by Mikata (1994) to find the thermal stresses in a fiber composite with an inhomogeneous interphase zone. If we substi-

tute Eq. (9) into Eq. (7), and then multiply through by r^β, the result is a second-order, linear ODE with variable coefficients, which can be written in standard form (Boyce and DiPrima, 1969, p. 177) as

$$P(r)\frac{d^2u}{dr^2} + Q(r)\frac{du}{dr} + R(r)u = 0, \tag{10a}$$

$$P(r) = (\bar{\lambda} + 2\bar{\mu}) + (\lambda_m + 2\mu_m)r^\beta, \tag{10b}$$

$$Q(r) = 2P(r)r^{-1} - \beta(\bar{\lambda} + 2\bar{\mu})r^{-1}, \tag{10c}$$

$$R(r) = -2P(r)r^{-2} - 2\beta\bar{\lambda}r^{-2}. \tag{10d}$$

For physically realistic values of the various moduli parameters, this equation will have a *regular singular point* at $r = 0$, since $P(r)$ is analytic at the origin, $Q(r)$ has a pole of order one, and $R(r)$ has a pole of order two. Hence, the equation could be solved by a Frobenius series expansion about $r = 0$. However, as the matrix occupies the region $r > a$, it seems more natural to expand the solution about $r = \infty$, which is also a regular singular point of Eq. (10). By expanding about $r = \infty$, a solution can be found that is in a sense a perturbation of the known solution for a homogeneous matrix.

We therefore first let $t = 1/r$, which has the effect of transforming the singular point at $r = \infty$ to the origin $t = 0$ (Coddington, 1961, pp. 180–181). The coefficients $P(r)$, $Q(r)$, and $R(r)$ in Eq. (10) transform by simply replacing r with $1/t$, whereas the derivatives of $u(r)$ transform according to the chain rule, as follows:

$$\frac{du}{dr} = \frac{d\hat{u}}{dt}\frac{dt}{dr} = \frac{-1}{r^2}\frac{d\hat{u}}{dt} = -t^2\frac{d\hat{u}}{dt}, \tag{11}$$

$$\frac{d^2u}{dr^2} = -t^2\frac{d}{dt}\left[-t^2\frac{d\hat{u}}{dt}\right] = t^4\frac{d^2\hat{u}}{dt^2} + 2t^3\frac{d\hat{u}}{dt}, \tag{12}$$

where we distinguish between the two functions $u(r)$ and $\hat{u}(t) \equiv u(1/r)$. The resulting differential equation for $\hat{u}(t)$ is

$$\hat{P}(t)\frac{d^2\hat{u}}{dt^2} + \hat{Q}(t)\frac{d\hat{u}}{dt} + \hat{R}(t)\hat{u} = 0, \tag{13a}$$

$$\hat{P}(t) = (\lambda_m + 2\mu_m) + (\bar{\lambda} + 2\bar{\mu})t^\beta, \tag{13b}$$

$$\hat{Q}(t) = \beta(\bar{\lambda} + 2\bar{\mu})t^{\beta-1}, \tag{13c}$$

$$\hat{R}(t) = -2(\lambda_m + 2\mu_m)t^{-2} - 2[\bar{\lambda}(\beta + 1) + 2\bar{\mu}]t^{\beta-2}. \tag{13d}$$

If β is a non-negative integer, Eq. (13) will have a regular singular point at $t = 0$, in which case we look for general solutions of the form

$$\hat{u}(t) = \sum_{n=0}^{\infty} C_n t^{n+m}, \tag{14}$$

where the C_n are constants, and m is a parameter that is a priori unknown. We now substitute the series given by Eq. (14) into Eq. (13), multiply out all the terms, and group together terms that are multiplied by the same power of t, to arrive at

$$\sum_{n=0}^{\infty}(\lambda_m + 2\mu_m)[(n + m - 1)(n + m) - 2]C_n t^{n+m-2} + \sum_{n=0}^{\infty}\{[(\bar{\lambda} + 2\bar{\mu})(n + m - 1)(n + m) + \beta(n + m) - 2] - 2\beta\bar{\lambda}\}C_n t^{n+m+\beta-2} = 0. \tag{15}$$

In order for a power series to sum to zero, the coefficient of each power of t must vanish identically. Since $\beta > 0$, the lowest-order term appearing anywhere in Eq. (15) is t^{m-2}, which occurs in the first sum when $n = 0$. Setting the coefficient of this term equal to zero leads to the *indicial* equation

$$(m - 1)m - 2 = 0. \tag{16}$$

The two roots of the indicial equation are $m_1 = -1$ and $m_2 = 2$. Usually, each of the two roots leads to a different power series solution. The case where the two roots differ by an integer, however, is a special case that usually causes one of the two linearly independent solutions to have a logarithmic dependence (see, for example, Mikata, 1994). However, it so happens that our problem is a special subcase again, in which two independent power-series solutions do exist. When this occurs (see Butkov, 1968, p. 147), both solutions can be found by using the smaller of the two indices, which is -1. It is difficult to see a priori that this special subcase will occur, other than by attempting to find the logarithmic solution, and determining that it vanishes. In order to present the solutions in as succinct a manner as possible, we will derive both solutions using the index $m_1 = -1$.

With $m = -1$, Eq. (15) takes the form

$$\sum_{n=0}^{\infty}(\lambda_m + 2\mu_m)n(n - 3)C_n t^{n-3} + \sum_{n=\beta}^{\infty}\{(\bar{\lambda} + 2\bar{\mu})[n^2 - (3 + \beta)n + 2\beta] - 2\beta\bar{\lambda}\}C_{n-\beta}t^{n-3} = 0, \tag{17}$$

where we have rewritten the second sum in terms of t^{n-3}, in order for it to be of the same form as the first. We now set the coefficient of each power of t equal to zero, starting with the lowest power, which occurs when $n = 0$. In order to avoid discussing special cases, we now limit our treatment to values of $\beta > (m_2 - m_1) = 3$. This restriction causes no real loss of generality, since relevant values of β are probably very large. For example, Theocaris (1986) fitted power-law-type curves to elastic moduli in an interphase zone in a set of E-glass fiber-epoxy resin composites, and found values of β on the order of 100. Values of $\beta \leq 3$ would correspond to interphase zones whose thicknesses are larger than the inclusion radius.

For all values of n from 0 to $\beta - 1$, only the first summation contributes a t^{n-3} term. Because of the appearance of $n(n - 3)$ in the first summation, we see that C_0 and C_3 can be arbitrary; all other values of C_n, for $n \leq \beta - 1$, must vanish. For $n \geq \beta$, setting the coefficient of t^{n-3} equal to zero in Eq. (17) yields a recursion relation between C_n and $C_{n-\beta}$:

$$C_n = \frac{-\{(\bar{\lambda} + 2\bar{\mu})[n^2 - (3 + \beta)n + 2\beta] - 2\beta\bar{\lambda}\}C_{n-\beta}}{n(n - 3)(\lambda_m + 2\mu_m)}, \tag{18}$$

which can also be written as

$$C_{n+\beta} = \frac{-\{(\bar{\lambda} + 2\bar{\mu})[n^2 + (\beta - 3)n - \beta] - 2\beta\bar{\lambda}\}C_n}{(n + \beta)(n + \beta - 3)(\lambda_m + 2\mu_m)}. \tag{19}$$

Equation (19) shows that the arbitrary constant C_0 will generate nonzero constants C_β, $C_{2\beta}$, etc., whereas the arbitrary constant C_3 generates $C_{\beta+3}$, $C_{2\beta+3}$, etc. Hence we have two linearly independent solutions of the forms

$$\hat{u}_1(t) = t^{-1}\sum_{n=0}^{\infty} C_{n\beta}t^{n\beta}, \tag{20}$$

$$\hat{u}_2(t) = t^{-1}\sum_{n=0}^{\infty} C_{n\beta+3}t^{n\beta+3}. \tag{21}$$

In order to simplify subsequent calculations, we note from Eqs. (9), (18) that since all the moduli with overbars actually contain a factor a^β, a factor of a^n can be factored out of each C_n; hence, we define $\Gamma_n = C_n a^{-n}$. Next, we revert back to the

physical variable r, by substituting $t = 1/r$ in Eqs. (20), (21), in which case the two independent solutions can be written as

$$u_1(r) = r \sum_{n=0}^{\infty} \Gamma_{n\beta}(a/r)^{n\beta}, \tag{22}$$

$$u_2(r) = r \sum_{n=0}^{\infty} \Gamma_{n\beta+3}(a/r)^{n\beta+3}, \tag{23}$$

where the Γ_n are found from the recursion formula (18), with $\bar{\lambda}$ replaced by $\lambda_{if} - \lambda_m$, $\bar{\mu}$ replaced by $\mu_{if} - \mu_m$, and $\Gamma_0 = \Gamma_3 = 1$. The general solution outside of the inclusion is therefore given by

$$u(r) = A_1 u_1(r) + A_2 u_2(r), \tag{24}$$

where the two constants A_1 and A_2 will be chosen so as to satisfy the boundary conditions. Before doing this, however, we briefly discuss the convergence of the two series solutions.

5 Convergence of the Solutions

To test the convergence of the series solutions, the ratio test can be applied to pairs of successive nonzero terms. For each of the two solutions, Eqs. (9), (18), (22), (23) can be used to show that the limit of the absolute value of the ratio of two successive nonzero terms is given by

$$\lim_{n\to\infty} \left| \frac{\Gamma_{n+\beta}(a/r)^{n+m+\beta}}{\Gamma_n(a/r)^{n+m}} \right| = \frac{|(\lambda_{if} + 2\mu_{if}) - (\lambda_m + 2\mu_m)|}{|\lambda_m + 2\mu_m|} (a/r)^{\beta}. \tag{25}$$

In order for the series to converge for all $r \geq a$, which is to say for the entire region outside of the inclusion, we need

$$\frac{|(\lambda_{if} + 2\mu_{if}) - (\lambda_m + 2\mu_m)|}{|(\lambda_m + 2\mu_m)|} < 1. \tag{26}$$

But $\lambda + 2\mu = K + 4\mu/3$, where K is the bulk modulus, and as all stable solids have positive values of K and μ, it is expected that $\lambda_m + 2\mu_m > 0$. Hence, Eq. (26) is equivalent to the condition

$$0 < (\lambda_{if} + 2\mu_{if}) < 2(\lambda_m + 2\mu_m). \tag{27}$$

The combination $M = \lambda + 2\mu$ is the elastic modulus that governs the velocity of compressional waves. The condition that M be non-negative throughout a body is sufficient to guarantee the existence of solutions to certain elastostatic boundary value problems (Gurtin, 1972, pp. 102–110). Hence it is plausible that a nonpositive value of the compressional wave modulus at the interface between the matrix and the inclusion will prevent the series solution from converging. However, as mentioned above, it is expected that the condition $\lambda_{if} + 2\mu_{if} > 0$ will always be satisfied. As all the moduli $\{\lambda, \mu, K, M, \text{etc.}\}$ are assumed to have the same $r^{-\beta}$ dependence, we see that the series will converge for all cases where the elastic moduli are lower in the interphase zone than in the undisturbed matrix material.

Equation (27) also implies, however, that the series will not converge if the modulus M_{if} is more than twice as large as the compressional wave modulus of the pure matrix. As there is nothing physically unrealistic about having $M_{if} > 2M_m$, we would expect a solution to exist in these cases. The reason that the series fail to converge is related to the fact that, for large n, the series essentially behaves as power series in the parameter $(M_{if} - M_m)/M_m$; this can be seen from Eq. (18). Since power series always converge inside some disk in the complex plane, and diverge outside of that disk, the existence of a physical singularity at $(M_{if} - M_m)/M_m = -1$ causes the series to diverge when $(M_{if} - M_m)/M_m > +1$. A similar situation arose in the solution of the problem of compression of a radially inhomogeneous sphere (Lutz and Ferrari, 1993). The difficulty can be circumvented by subjecting the series solution to an Euler transformation (Hinch, 1991; Lutz and Ferrari, 1993), which transforms the divergent series into a convergent one. The method, although cumbersome, is straightforward, and for computational purposes is readily implemented on a computer. For illustrative purposes, therefore, only cases for which $M_{if} < 2M_m$ will be considered, in which case the Euler transformation is not needed.

6 Spherical Inclusion in an Inhomogeneous Matrix

Using the general solution for the displacements in the matrix region $r > a$, we now solve the problem of a homogeneous spherical inclusion inside a radially inhomogeneous matrix whose moduli vary according to Eq. (9), subjected to uniform hydrostatic pressure of magnitude P at infinity. The subscript i will be used to denote the elastic properties of the inclusion. In the matrix region $r > a$, the solution will be of the form given by Eq. (24), with appropriate choices for the constants A_1 and A_2. In the inclusion, the solution will have the form appropriate for radially symmetric deformations of a *homogeneous* material (Rekach, 1979):

$$u(r) = B_1 r + B_2 r^{-2}. \tag{28}$$

Four boundary conditions are needed to determine the four constants $\{A_1, A_2, B_1, B_2\}$. These conditions are that $\tau_{rr}(r) \to P$ as $r \to \infty$, $\tau_{rr}(r)$ and $u(r)$ must be continuous at $r = a$, and $u(r)$ must be finite as $r \to 0$.

The condition at $r = 0$ shows that $B_2 = 0$. To apply the condition $\tau_{rr}(r) \to P$ as $r \to \infty$, we need expressions for the stresses $\tau^1_{rr}(r)$ and $\tau^2_{rr}(r)$ that are associated with the displacements $u_1(r)$ and $u_2(r)$. From Eq. (5a) and Eqs. (22), (23), we find

$$\tau^1_{rr}(r) = [3\lambda(r) + 2\mu(r)] \sum_{n=0}^{\infty} \Gamma_{n\beta}(a/r)^{n\beta} - [\lambda(r) + 2\mu(r)] \sum_{n=0}^{\infty} n\beta\Gamma_{n\beta}(a/r)^{n\beta}, \tag{29}$$

$$\tau^2_{rr}(r) = [3\lambda(r) + 2\mu(r)] \sum_{n=0}^{\infty} \Gamma_{n\beta+3}(a/r)^{n\beta+3} - [\lambda(r) + 2\mu(r)] \sum_{n=0}^{\infty} (n\beta + 3)\Gamma_{n\beta+3}(a/r)^{n\beta+3}, \tag{30}$$

where $\lambda(r)$ and $\mu(r)$ are given by Eq. (9). Now as $r \to \infty$, $\lambda(r) \to \lambda_m$ and $\mu \to \mu_m$, so we see from Eqs. (29), (30) that $\tau^1_{rr}(r) \to (3\lambda_m + 2\mu_m) = 3K_m$, whereas $\tau^2_{rr}(r) \to 0$. Hence we must have $3K_m A_1 + 0A_2 = P$, which implies

$$A_1 = \frac{P}{3K_m}. \tag{31}$$

Now consider the continuity conditions at $r = a$. The displacement field inside the inclusion is given by $u(r) = B_1 r$, so that in the inclusion, $u(a) = B_1 a$. Equating this value to the displacement in the matrix at $r = a$, using Eqs. (22)–(24), (31), gives

$$B_1 = \frac{P}{3K_m} \sum_{n=0}^{\infty} \Gamma_{n\beta} + A_2 \sum_{n=0}^{\infty} \Gamma_{n\beta+3}. \tag{32}$$

The final equation needed in order to solve for the remaining constant A_2 is found by considering continuity of the normal traction τ_{rr} at $r = a$. Equations (5a) and (28) show that inside the inclusion, $\tau_{rr}(a) = 3K_i B_1$. Using Eqs. (28)–(30) to find $\tau_{rr}(a)$ outside of the inclusion, and equating it to $\tau_{rr}(a)$ inside the inclusion, leads to the condition

$$3K_i B_1 = \frac{P}{3K_m}\left[(3\lambda_{if} + 2\mu_{if})\sum_{n=0}^{\infty}\Gamma_{n\beta} - (\lambda_{if} + 2\mu_{if})\sum_{n=0}^{\infty} n\beta\Gamma_{n\beta}\right] + A_2\left[(3\lambda_{if} + 2\mu_{if})\sum_{n=0}^{\infty}\Gamma_{n\beta+3} - (\lambda_{if} + 2\mu_{if})\sum_{n=0}^{\infty}(n\beta + 3)\Gamma_{n\beta+3}\right]. \quad (33)$$

Simultaneous solution of Eqs. (32), (33) yields

$$A_2 = \frac{-P}{3K_m}\frac{3(K_i - K_{if})\sum_{n=0}^{\infty}\Gamma_{n\beta} + (\lambda_{if} + 2\mu_{if})\sum_{n=0}^{\infty} n\beta\Gamma_{n\beta}}{3(K_i - K_{if})\sum_{n=0}^{\infty}\Gamma_{n\beta+3} + (\lambda_{if} + 2\mu_{if})\sum_{n=0}^{\infty}(n\beta + 3)\Gamma_{n\beta+3}}. \quad (34)$$

This completes the solution, with the displacements given by Eqs. (22)–(24), (28), A_1 given by Eq. (31), A_2 given by Eq. (34), B_1 given by Eq. (32), and $B_2 = 0$.

7 Stresses in the Matrix and Inclusion

To illustrate the effect that the interphase has on the stresses, consider a composite for which $\mu_i = \lambda_i = 5\mu_m = 5\lambda_m$, which implies $\nu_i = \nu_m = 0.25$. As the variation in Poisson ratio is of lesser importance than are the variations in the moduli themselves (cf., Jasiuk and Kouider, 1993), we will also take $\nu = 0.25$ throughout the interphase. (Note, however, that our solution is valid for arbitrary Poisson ratios, including cases where ν varies throughout the interphase zone). The parameter β is taken to be 10, corresponding to an interphase zone whose thickness is about $0.25a$. The degree of inhomogeneity will be quantified by a local damage parameter, defined by $D = (M_m - M_{if})/M_m$. We will consider the cases in which the interface is either 50 percent stiffer than, or 50 percent less stiff than, the pure matrix component, i.e., $D = \pm 0.5$. The radial stress $\tau_{rr}(r)$ is found from the linear combination $A_1\tau^1_{rr}(r) + A_2\tau^2_{rr}(r)$, where $\tau^i_{rr}(r)$ are given in Eqs. (29), (30), the A_i are given by Eqs. (31), (34), and the moduli are given by Eqs. (8a, b). The hoop stresses are found from the same equations, after replacing $(\lambda + 2\mu)$ by λ, and replacing λ by $(\lambda + \mu)$, as indicated by Eq. (5). The radial stress, τ_{rr}, and the hoop stresses, $\tau_{\phi\phi} = \tau_{\theta\theta}$, are shown in Figs. 2 and 3. Also shown in each figure are the stresses that would be found in the absence of an interphase zone, which corresponds to taking $D = 0$. The altered moduli of the interphase zone are seen to alter the local stresses both within the interphase zone *and* inside the inclusion. The region outside of the inclusion in which the stresses are perturbed is essentially confined to the interphase region, as can be seen by comparing Figs. 2 and 3 to Fig. 1, which is drawn to a scale that corresponds to the present case of $\beta = 10$.

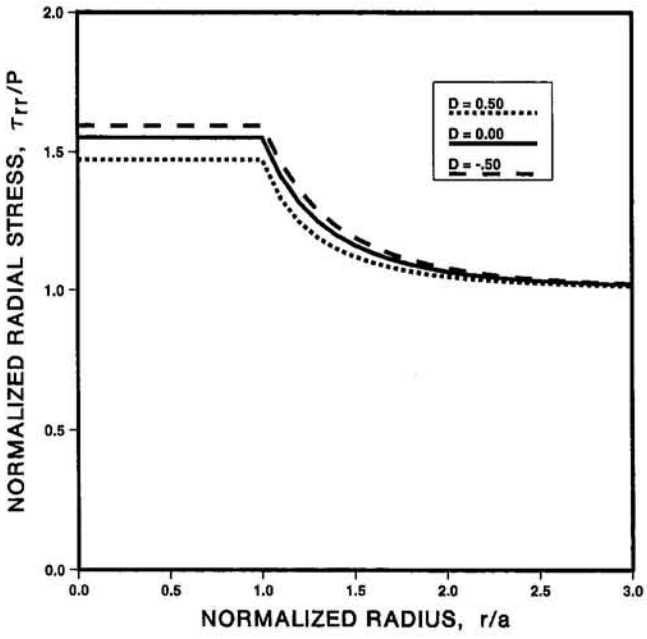

Fig. 2 Radial stress τ_{rr} for the case of hydrostatic compression of a body containing a single spherical inclusion surrounded by an interphase zone. Positive values of D correspond to a damaged interphase zone, as shown in Fig. 1, whereas negative values correspond to an interphase that is stiffer than the pure matrix material. See text for the moduli values used in the calculations.

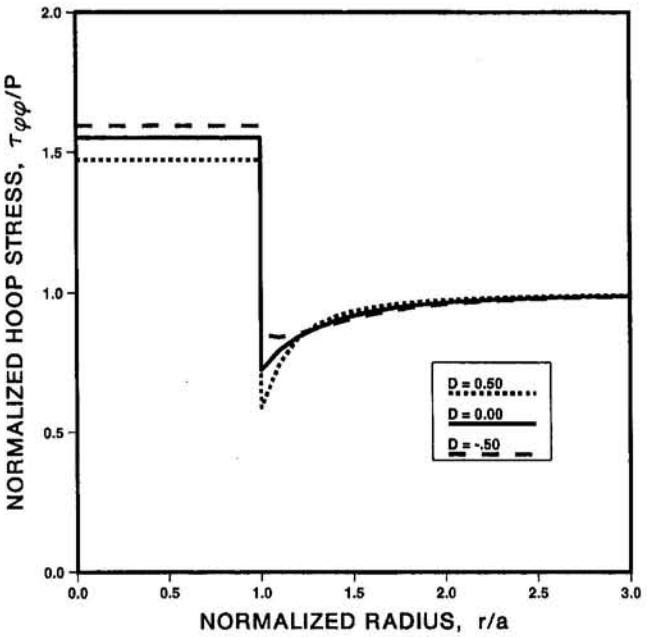

Fig. 3 Hoop stresses $\tau_{\theta\theta} = \tau_{\phi\phi}$ for the situation shown in Fig. 2. Note that, unlike the radial stress, the hoop stress need not be continuous at the interface between the inclusion and matrix.

8 Effective Bulk Modulus

The solution derived above for the stresses and displacements is an exact solution to the problem of a single inclusion embedded in an infinite matrix, with an interphase zone described by a power-law variation in moduli. We will now use this solution to estimate the effective bulk modulus of a material that contains a dispersion of such inclusions. In general, effective moduli of materials consisting of discrete inclusions in a matrix can be found rigorously only to first order in the inclusion concentration. Although various approximate methods have been used to estimate effective moduli at higher concentrations, there is as yet no agreed-upon method for doing so; see Christensen (1990), Zimmerman (1991), and Ferrari (1994) for critical discussions of some of the existing methods. Nevertheless, methods exist that are known to be reasonably accurate for materials with isotropic spherical inclusions. With this in mind, we will use a method for estimating the effective bulk modulus that is correct to first order in concentration, and which, in the case when the matrix becomes homogeneous, reduces to the result found by Mori and Tanaka (1973), Christensen (1979), Ferrari (1994) and others, which is known to be reasonably accurate for moderate values of the inclusion concentration.

The effective bulk modulus K_{eff} of an inhomogeneous body can be found (Willis, 1981, pp. 7–13) by subjecting the body to hydrostatic loading of magnitude P, and then comparing the strain energy stored in the body to that which would be stored in

an identically shaped homogeneous body. Consider a spherical region of radius b, centered on a single inclusion. The strain energy stored in this region can be computed from (Sokolnikoff, 1956, p. 86)

$$U = \tfrac{1}{2}\int_{\Omega} f_i u_i \, dV + \tfrac{1}{2}\int_{\partial\Omega} T_i u_i \, dA, \tag{35}$$

where Ω is the spherical region $r \leq b$, $\partial\Omega$ is the boundary $r = b$, f_i are the components of the body force vector, and T_i are the components of the surface traction vector. In the present problem, the body force is zero, the only nonzero component of the displacement vector on $\partial\Omega$ is u_r, and the traction vector is τ_{rr}. (For clarity, we henceforth will write u_r instead of u.) Due to the radial symmetry of the problem, both u_r and τ_{rr} are uniform on $\partial\Omega$. Hence,

$$U = \tfrac{1}{2}\int_{\partial\Omega} \tau_{rr} u_r dA = \tfrac{1}{2}[\tau_{rr}(b)u_r(b)](4\pi b^2)$$
$$= 2\pi b^2 \tau_{rr}(b) u_r(b). \tag{36}$$

For the hypothetical homogeneous body, the radial displacement would be given by $u_r(r) = \tau_{rr}(b) r / 3K_{\text{eff}}$ (Rekach, 1979), so that

$$U = 2\pi b^2 \tau_{rr}(b) \frac{\tau_{rr}(b) b}{3K_{\text{eff}}} = \frac{2\pi b^3}{3K_{\text{eff}}} [\tau_{rr}(b)]^2. \tag{37}$$

We now equate the strain energy stored in the actual inhomogeneous body, as given by Eq. (36), to that stored in the homogeneous body, as given by Eq. (37), and solve for

$$K_{\text{eff}} = \frac{b\tau_{rr}(b)}{3u_r(b)} = \frac{\tau_{rr}(b)}{3u_r(b)/b}, \tag{38}$$

where we move the b term to the denominator in order that both numerator and denominator have finite values as $b \to \infty$. In order to utilize the solution for a single inclusion in an infinite body, we let $b \to \infty$, in which case we arrive at

$$K_{\text{eff}} = \lim_{b\to\infty}\left\{\frac{\tau_{rr}(b)}{3u_r(b)/b}\right\} = \frac{\lim_{b\to\infty} \tau_{rr}(b)}{3 \lim_{b\to\infty} [u_r(b)/b]}. \tag{39}$$

If we were to evaluate the limits in Eq. (39) by fixing a and letting $b \to \infty$, the effect of the inhomogeneity would be lost. Instead, we first recognize that $(a/b)^3 = c$, the volume fraction of the inclusions, and then renormalize by putting $(a/b)^3 = c > 0$ before taking the limit. Furthermore, we ignore all powers higher than c that appear; this is justified by noting that these powers will be of the form $c^{\beta/3}$, $c^{2\beta/3}$, etc., and we expect, as mentioned above, that $\beta \gg 1$. Using Eqs. (22)–(24) we find that

$$\lim_{b\to\infty} [u_r(b)/b] = A_1 + A_2 c, \tag{40}$$

and using Eqs. (24), (29), (30) we find that

$$\lim_{b\to\infty} \tau_{rr}(b) = 3K_m A_1 - 4\mu_m A_2 c. \tag{41}$$

Equations (39)–(41) can then be solved for

$$\frac{K_{\text{eff}}}{K_m} = \frac{1 + \dfrac{4\mu_m}{3K_m} fc}{1 - fc}, \tag{42a}$$

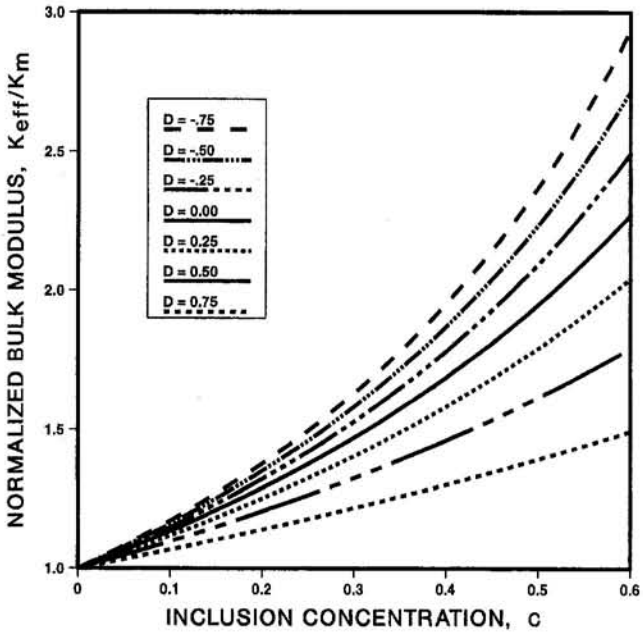

Fig. 4 Effective bulk modulus of a material containing a volume fraction c of inclusions, each surrounded by an interphase zone. The bulk modulus is calculated from Eq. (42), using the moduli parameters that are listed in the text.

where

$$f = \frac{-A_2}{A_1}$$
$$= \frac{3(K_i - K_{if}) \sum_{n=0}^{\infty} \Gamma_{n\beta} + (\lambda_{if} + 2\mu_{if}) \sum_{n=0}^{\infty} n\beta\Gamma_{n\beta}}{3(K_i - K_{if}) \sum_{n=0}^{\infty} \Gamma_{n\beta+3} + (\lambda_{if} + 2\mu_{if}) \sum_{n=0}^{\infty} (n\beta + 3)\Gamma_{n\beta+3}}. \tag{42b}$$

In the limiting case where the interphase zone is homogeneous, $\Gamma_0 = \Gamma_3 = 1$, all other $\Gamma_n = 0$, $K_{if} \to K_m$, etc., so $f \to 3(K_i - K_m)/(3K_i + 4\mu_m)$, and Eq. (42) reduces precisely to the result that has been found by Mori and Tanaka (1973), Christensen (1979), and others. As that expression is known to be accurate for small to moderate values of c, it seems reasonable that Eq. (42) will have similar accuracy when the interphase is inhomogeneous; in any event, Eq. (42) is exact to first order in c.

To study the effect that the inhomogeneous interphase zone has on the overall effective bulk modulus, we again utilize the local damage parameter $D = (M_m - M_{if})/M_m$. In order to focus on the effect of the variation in stiffness, we again take $\nu_i = \nu_m = \nu_{if} = 0.25$, in which case D can also be expressed as $(K_m - K_{if})/K_m$. Figure 4 shows the effective bulk modulus as a function of the inclusion concentration, for the case $\beta = 10$, and various values of D. The curve for $D = 0$ coincides with the Mori-Tanaka prediction, as well as with the Hashin-Shtrikman lower bound (see Christensen, 1979). As the moduli at the interface decrease, the damage parameter D increases, and the effective moduli decrease, as expected. Negative values of D, on the other hand, correspond to an interphase zone that is *stiffer* than the pure matrix; this can occur in a metal-matrix composite, for example, if the inclusion material diffuses into the matrix. In these cases, the interphase zone causes an increase in the effective bulk modulus.

9 Summary and Discussion

An exact closed-form solution has been found for the hydrostatic compression of a body containing a spherical inclusion

that is surrounded by an inhomogeneous interphase zone. The elastic moduli outside of the inclusion are assumed to be described by a constant term, plus a term that decays like $r^{-\beta}$, where β is an integer greater than 3. This model is similar to those used by Theocaris (1986), Jayaraman and Reifsnider (1992), Jasiuk and Kouider (1993) and others, with the exception that the moduli are allowed to smoothly vary from the interface out into the matrix. This may be advantageous for applications to composites whose moduli vary continuously outside of the inclusions, as opposed to those in which the interphase is a distinct region formed by, say, application of a fiber coating. Furthermore, this smooth variation of the moduli permits a closed-form solution to be found, without requiring different solutions to be pieced together at the interphase/matrix "interface".

The presence of the interphase zone was found to have an effect on the stress concentrations around and within the inclusion. The stress within a stiff spherical inclusion is in general greater than the applied far-field stress. This effect is mitigated by the presence of a damage zone outside of the inclusion. One way to see why this occurs is to realize that in the limiting case as $D \to 1$, the elastic moduli at the inclusion matrix boundary will vanish, and the inclusion becomes "uncoupled" from the matrix, in which case no stress can be transmitted to it.

The solution was then used to estimate the effective bulk modulus of a material that contains a random dispersion of such inclusions. In the limiting case of a homogeneous matrix, the expression found for the effective bulk modulus agrees with the result found by Mori and Tanaka (1973), Christensen (1979), Ferrari (1994), and others. The presence of a weakened interphase zone leads to a lowering of the effective moduli, whereas an interphase zone that is stiffer than the pure matrix phase causes an increase in the effective bulk modulus.

Acknowledgments

The work of M. Lutz was supported by California Legislative Grant Account No. 442402-19900, and by National Science Foundation Graduate Engineering Education for Women and Minorities Fellowship No. EID-9018414. The authors thank Mauro Ferrari of UC Berkeley for reviewing this paper.

References

Aboudi, J., 1989, "Micromechanical analysis of fibrous composites with Coulomb frictional slippage between the phases," *Mech. Mater.*, Vol. 8, pp. 103–115.

Benveniste, Y., 1984, "On the effect of debonding on the overall behavior of composite materials," *Mech. Mater.*, Vol. 3, pp. 349–358.

Butkov, E., 1968, *Mathematical Physics,* Addison-Wesley, Reading, MA.

Boyce, W. E., and DiPrima, R. C., 1969, *Elementary Differential Equations and Boundary Value Problems,* John Wiley and Sons, New York.

Christensen, R. M., 1979, *Mechanics of Composite Materials,* John Wiley and Sons, New York.

Christensen, R. M., 1990, "A critical evaluation for a class of micromechanics models," *J. Mech. Phys. Solids,* Vol. 38, pp. 379–404.

Coddington, E. A., 1961, *An Introduction to Ordinary Differential Equations,* Prentice-Hall, Englewood Cliffs, NJ.

Drzal, L. T., Rich, M. J., Koenig, M. F., and Lloyd, P. F., 1983, "Adhesion of graphite fibers to epoxy matrices: II. The effect of fiber finish," *J. Adhesion,* Vol. 16, pp. 133–152.

Ferrari, M., 1994, "Composite homogenization via the equivalent poly-inclusion approach," *Compos. Eng.,* Vol. 4, pp. 37–45.

Gurtin, M. E., 1972, "The linear theory of elasticity," *Handbuch der Physik,* Vol. VIa/2, S. Flugge, ed., Springer-Verlag, Berlin, pp. 1–295.

Hashin, Z., and Rosen, B. W., 1964, "The Elastic Moduli of Fiber-Reinforced Materials," ASME JOURNAL OF APPLIED MECHANICS, Vol. 31, pp. 223–228.

Hashin, Z., and Shtrikman, S., 1961, "Note on a variational approach to the theory of composite elastic materials," *J. Franklin Inst.*, Vol. 271, pp. 336–341.

Herve, E., and Zaoui, A., 1993, "N-layered inclusion-based micromechanical modelling," *Int. J. Eng. Sci.,* Vol. 31, pp. 1–10.

Hinch, E. J., 1991, *Perturbation Methods,* Cambridge University Press, New York.

Jasiuk, I., Chen, J., and Thorpe, M. F., 1992, "Elastic moduli of composites with rigid sliding inclusions," *J. Mech. Phys. Solids,* Vol. 40, pp. 373–391.

Jasiuk, I., and Kouider, M. W., 1993, "The effect of an inhomogeneous interphase on the elastic constants of transversely isotropic composites," *Mech. Mater.,* Vol. 15, pp. 53–63.

Jayaraman, K., and Reifsnider, K. L., 1992, "Residual stresses in a composite with continuously varying Young's modulus in the fiber/matrix interphase," *J. Compos. Maters.,* Vol. 26, pp. 770–791.

Kwon, P., Dharan, C. K. H., and Ferrari, M., 1994, "Macroscopic Analysis of Axisymmetric Functionally Gradient Materials Under Thermal Loading," ASME *Journal of Energy Resources Technology,* Vol. 116, pp. 115–120.

Lutz, M. P., and Ferrari, M., 1993, "Compression of a sphere with radially-varying elastic moduli," *Compos. Eng.,* Vol. 3, pp. 873–884.

Mikata, Y., 1994, "Stress Fields in a Continuous Fiber Composite With a Variable Interphase Under Thermo-Mechanical Loadings," ASME *Journal of Engineering Materials and Technology,* Vol. 116, pp. 367–377.

Mori, T., and Tanaka, K., 1973, "Average stress in matrix and average elastic energy of materials with misfitting inclusions," *Acta Metall.,* Vol. 21, pp. 571–574.

Rekach, V. G., 1979, *Manual of the Theory of Elasticity,* Mir, Moscow.

Sokolnikoff, I. S., 1956, *Mathematical Theory of Elasticity,* 2nd. Ed., McGraw-Hill, New York.

Theocaris, P. S., 1986, "The concept and properties of mesophase in composites," *Composite Interfaces,* H. Ishida and J. L. Koenig, eds., North-Holland, Amsterdam, pp. 329–349.

Theocaris, P. S., 1992, "The elastic moduli of the mesophase as defined by diffusion processes," *J. Reinf. Plastics and Comps.,* Vol. 11, pp. 537–551.

Willis, J. R., 1981, "Variational and related methods for the overall properties of composites," *Adv. Appl. Mech.,* Vol. 21, pp. 1–78.

Zimmerman, R. W., 1991, "Elastic moduli of a solid containing spherical inclusions," *Mech. Mater.,* Vol. 12, pp. 17–24.

A Pressure Projection Method for Nearly Incompressible Rubber Hyperelasticity, Part I: Theory

Jiun-Shyan Chen
Assistant Professor,
Mem. ASME.

Chunhui Pan
Research Assistant.

Department of Mechanical Engineering
and Center for Computer-Aided Design,
The University of Iowa,
2133 Engineering Building,
Iowa City, IA 52242-1527

A least-squares-based pressure projection method is proposed for the nonlinear analysis of nearly incompressible hyperelastic materials. The strain energy density function is separated into distortional and dilatational parts by the use of Penn's invariants such that the hydrostatic pressure is solely determined from the dilatational strain energy density. The hydrostatic pressure and hydrostatic pressure increment calculated from displacements are projected onto appropriate pressure fields through the least-squares method. The method is applicable to lower and higher order elements and the projection procedures can be implemented into the displacement based nonlinear finite element program. By the use of certain pressure interpolation functions and reduced integration rules in the pressure projection equations, this method can be degenerated to a nonlinear version of the selective reduced integration method.

1 Introduction

The use of rubber materials for engineering applications is very broad, including engine mounts, bushings, building and bridge bearings, vehicle door seals, tires, solid rocket motor flexseals, o-rings, off-shore structure flexjoints, and gaskets. These applications utilize the uniqueness of rubber being soft, highly extensible, and highly elastic. To date, laboratory testing and simple equations based on small strain theory are still the primary methods used in the design of rubber products. The main cause of this design process is due to the level of difficulty in performing nonlinear finite element analysis of rubber components which usually experience very large deformation under normal service conditions. The nearly incompressible nature of rubber also adds additional difficulties to the numerical treatment of volume conservation. Therefore, an effective finite element formulation that can handle material incompressibility under large deformation is highly desirable for the analysis of rubber components. Further, strain energy density functions applicable to highly nonlinear and complex deformation problems are also essential to the success of finite element prediction.

Problems arising from the numerical treatment of the incompressibility constraint were first addressed by Herrmann (1965). Mixed formulations have been used successfully for incompressible and nearly incompressible media. In linear elasticity, the Herrmann principle (Herrmann, 1965) was the first effective method to handle the incompressibility constraint and is regarded as a reduced form of the Hellinger-Reissner variational principle. The extension to orthotropic materials was later made by Taylor et al. (1968). A modified Hellinger-Reissner principle was proposed by Key (1969) for incompressible and nearly incompressible anisotropic linear elasticity. Tong (1969), Scharnhorst and Pian (1978), and Murakawa and Atluri (1979) introduced hybrid stress formulations for nonlinear incompressible materials. Belytschko and Bachrach (1986) and Bachrach and Belytschko (1986) used the Hu-Washizu variational principle in conjunction with the γ-operator to develop a bending/incompressible element. The extension to nonlinear incompressible problems was later developed by Liu, Belytschko, and Chen (1988). Perturbed Lagrange multiplier methods were used by Cescotto et al. (1979), Bercovier (1978), Sussman and Bathe (1987), Simo et al. (1985), and, recently by Chang and Saleeb et al. (1991).

Alternatively, the penalty method in conjunction with the reduced integration has been successfully used in incompressible problems. Fried (1974) suggested that the selective reduced integration can cure the failure of the displacement approach. Oden and Kikuchi (1982) discussed the necessary conditions on the order of reduced integration rules to produce stable and convergent schemes. Hughes, Liu, and Brooks (1979) reviewed penalty methods and selective reduced integration of incompressible viscous flows. Malkus and Hughes (1978) and Malkus (1980) proved and unified the equivalence of mixed formulations and selective reduced integration techniques. The B-bar method, generalized from the selective reduced integration method, was later introduced by Hughes (1980). This B-bar method can be treated as a projection method for linear elasticity. Simo et al. (1985) showed that the B-bar method can be derived from a Hu-Washizu principle and then developed a nonlinear tangent matrix for this formulation. Other displacement-based methods are hourglass control on under integrated elements by Belytschko et al. (1984), an explicit incompressible plane strain element using Taylor series expansion developed by Liu et al. (1986), and a volumetric strain projection method for nonlinear hyperelasticity by Chen et al. (1994).

In the B-bar formulation, the discrete gradient matrix B is separated into deviatoric and dilatational parts, and the dilatational B-matrix is projected onto a lower order space to resolve volumetric locking. Our present work is motivated by the simplicity and effectiveness of the B-bar formulation. In order to introduce the projection method within the framework of hyperelasticity, we first separate the strain energy density into distortional and dilatational parts and then project the hydrostatic pressure, which is solely determined from dilatational strain energy density, onto an appropriate pressure field. The projection is performed by imposing a constraint condition between

Contributed by the Applied Mechanics Division of THE AMERICAN SOCIETY OF MECHANICAL ENGINEERS for publication in the ASME JOURNAL OF APPLIED MECHANICS.

Discussion on this paper should be addressed to the Technical Editor, Professor Lewis T. Wheeler, Department of Mechanical Engineering, University of Houston, Houston, TX 77204-4792, and will be accepted until four months after final publication of the paper itself in the ASME JOURNAL OF APPLIED MECHANICS.

Manuscript received by the ASME Applied Mechanics Division, May 8, 1995; final revision, Nov. 28, 1995. Associate Technical Editor: W. K. Liu.

displacement calculated hydrostatic pressure and hydrostatic pressure obtained from pressure interpolation functions in a least-squares sense. The hydrostatic pressure increment is also projected in a consistent manner to preserve the consistency between tangent stiffness and internal force. If particular projection procedures are carried out, this pressure projection method also provides a nonlinear version of the selective reduced integration method. Although the proposed method is applicable to lower and higher order elements, we employ linear pressure in conjunction with biquadratic/triquadratic displacement fields that satisfy Babuska-Brezi (Babuska, 1973, Brezzi, 1974) conditions in numerical examples.

In the present approach, since hydrostatic pressure originally calculated from displacements has been modified through the projection procedures, this method is found to be restricted to materials with a linear pressure-strain relation (constant bulk modulus). This condition is equivalent to the "material restraint" discussed by Sussman and Bathe (1987) where they proved that a linear pressure-strain relation is required for the u/p formulation. For nearly incompressible materials, volumetric strain is expected to be small, and therefore a constant bulk modulus material model is appropriate.

In the next section, the basic equations of hyperelasticity and several rubber strain energy density functions are reviewed. In this section, the Penn's invariants are introduced to decompose the distortional and dilatational deformations and the corresponding strain energy density functions. The relation between hydrostatic pressure and the dilatational strain energy density is established. In Section 3, the decomposed variational principle and the associated finite element formulation is presented. The projection of hydrostatic pressure and hydrostatic pressure increment are introduced through the least-squares methods. The stress, material response, and initial stress tensors are calculated according to the projected hydrostatic pressure. The derivations of the internal force and tangent stiffness are also given. The degeneration to volumetric strain projection method and the nonlinear version of the selective reduced integration method is discussed in Section 4. Further degeneration to selective reduced integration in linear elasticity is provided in Appendix A.

2 Basic Equations

Consider a body which occupies a region Ω_X at the initial stage. The motion of the body can be described by a mapping function Θ such that the image of Ω_X at time t is denoted by Ω_x, and the image of $\mathbf{X} \in \Omega_X$ is defined by $\mathbf{x}$, i.e.,

$$\mathbf{x} = \Theta(\mathbf{X}, t) = \mathbf{X} + \mathbf{u}(\mathbf{X}, t) \tag{2.1}$$

where $\mathbf{X}$ is the material coordinate, $\mathbf{x}$ is the spatial coordinate, $\mathbf{u}$ is displacement, and t is time. Rubber is classified as a hyperelastic material in which the strain energy density function, W, can be defined and the stress-strain relation is given by

$$S_{ij} = \frac{\partial W}{\partial E_{ij}}, \tag{2.2}$$

where S_{ij} is the second Piola-Kirchhoff stress and E_{ij} is the Green-Lagrangian strain which is defined as

$$E_{ij} = \tfrac{1}{2}(G_{ij} - \delta_{ij}), \tag{2.3}$$

$$G_{ij} = F_{ki}F_{kj}, \tag{2.4}$$

$$F_{ij} = \frac{\partial x_i}{\partial X_j}, \tag{2.5}$$

where F_{ij} is the deformation gradient, G_{ij} is the Green deformation tensor, and δ_{ij} is the Kronecker delta. The Cauchy stress σ_{ij} can be obtained by

$$\sigma_{ij} = \frac{1}{J} F_{ik}S_{kl}F_{jl}, \tag{2.6}$$

$$J = \det(\mathbf{F}). \tag{2.7}$$

According to Mooney (1940) and later extended by Rivlin (1956), the strain energy density function of elastic medium can be expressed in terms of the three invariants of the Green deformation tensor: I_1, I_2, I_3 such that

$$W(I_1, I_2, I_3) = \sum_{m+n+l=1}^{\infty} A_{mnl}(I_1 - 3)^m(I_2 - 3)^n(I_3 - 1)^l \tag{2.8}$$

where

$$I_1 = \text{tr}(\mathbf{G}), \quad I_2 = \tfrac{1}{2}[(\text{tr}\,\mathbf{G})^2 - \text{tr}(\mathbf{G}^2)], \quad I_3 = \det(\mathbf{G}). \tag{2.9}$$

The second Piola-Kirchhoff stress can be obtained from W by

$$S_{ij} = \frac{\partial W}{\partial I_n}\frac{\partial I_n}{\partial E_{ij}} = 2[K_1\delta_{ij} + K_2(I_1\delta_{ij} - G_{ij}) + K_3I_3G_{ij}^{-1}] \tag{2.10}$$

where

$$K_n = \frac{\partial W}{\partial I_n}. \tag{2.11}$$

If the behavior of the elastic medium is incompressible, then $I_3 = 1$, and the power series strain energy density function proposed by Rivlin (1956) reduces to

$$\bar{W}(I_1, I_2) = \sum_{m+n=1}^{\infty} A_{mn}(I_1 - 3)^m(I_2 - 3)^n. \tag{2.12}$$

Rivlin's strain energy density function expressed by an infinite power series is normally truncated to neo-Hookean or Mooney-Rivlin forms. However, the material constants in these two functions obtained from tensile data are not adequate in other deformation modes, in addition to the poor fitting in large strain. Yeoh (1990) proposed a cubic strain energy density function:

$$\bar{W} = A_{10}(I_1 - 3) + A_{20}(I_1 - 3)^2 + A_{30}(I_1 - 3)^3, \tag{2.13}$$

and a modified cubic strain energy density function (Yeoh, 1993):

$$\bar{W} = \frac{\alpha}{\beta}[1 - e^{-\beta(I_1-3)}] + A_{10}(I_1 - 3) + A_{20}(I_1 - 3)^2 + A_{30}(I_1 - 3)^3. \tag{2.14}$$

For incompressible materials, a volume conservation constraint needs to be imposed and therefore the strain energy density is modified either by the use of the Lagrangian multiplier method or a penalty method. Additional strain energy density which is a function of $(I_3 - 1)$ and/or hydrostatic pressure is added to the incompressible strain energy density. For nearly incompressible materials, this additional strain energy density can be treated as the dilatational strain energy density resulting from the small volume change of the material. The modified strain energy density function for nearly incompressible materials can be expressed as

$$W(I_1, I_2, I_3) = \bar{W}(I_1, I_2) + \tilde{W}(I_3). \tag{2.15}$$

Since $I_3 = J^2$ and $J - 1$ is a measure of volumetric deformation, $\tilde{W}(I_3)$ represents the part of strain energy density due to volume change. However, for nearly incompressible materials, invariants I_1 and I_2 are not measures of pure distortion (iso-

choric). This can be easily understood by considering a pure dilatational state with $\lambda_1 = \lambda_2 = \lambda_3 = \lambda$, then

$$I_1 = 3\lambda^2, \quad I_2 = 3\lambda^4, \tag{2.16}$$

and

$$\bar{W}(I_1, I_2) = \sum_{m+n=1}^{\infty} A_{mn} 3^{m+n} (\lambda^2 - 1)^m (\lambda^4 - 1)^n \neq 0. \tag{2.17}$$

In other words, $\bar{W}(I_1, I_2)$ contains a certain amount of dilatational energy. Penn (1970) proposed the following invariants to separate the distortional and dilatational deformation:

$$\bar{I}_1 = I_1 I_3^{-1/3}, \quad \bar{I}_2 = I_2 I_3^{-2/3}. \tag{2.18}$$

Clearly, under pure dilation, $\bar{I}_1$ and $\bar{I}_2$ are constants and $\bar{W}(\bar{I}_1, \bar{I}_2) = 0$ and this indicates that $\bar{W}(\bar{I}_1, \bar{I}_2)$ contains only distortional energy. It was observed by Wood and Martin (1964) that the compressibility of rubber is very small even under hundreds of atmospheric pressure. Penn (1970) took a further step and suggested that $\partial W/\partial I_3$ might be independent of $\bar{I}_1$ and $\bar{I}_2$ so that in any deformation W could be separated as a sum of two functions

$$W(\bar{I}_1, \bar{I}_2, I_3) = \bar{W}(\bar{I}_1, \bar{I}_2) + \tilde{W}(I_3). \tag{2.19}$$

The hydrostatic pressure, defined as $\sigma_{mm}/3$, can be related to $\tilde{W}(I_3)$ by using Eqs. (2.2) and (2.6)

$$P = \sigma_{mm}/3 = \frac{1}{3J} G_{kl} \left(\frac{\partial W}{\partial \bar{I}_n} \frac{\partial \bar{I}_n}{\partial E_{kl}} + \frac{\partial W}{\partial J} \frac{\partial J}{\partial E_{kl}} \right);$$

$$n = 1, 2. \tag{2.20}$$

As have been shown by Chang et al. (1991), Penn's invariants satisfy the following conditions:

$$G_{kl} \frac{\partial \bar{I}_n}{\partial E_{kl}} = 0; \quad n = 1, 2. \tag{2.21}$$

Equation (2.20) can be simplified to

$$P = \frac{\partial W}{\partial J} = \frac{\partial \tilde{W}}{\partial J} \tag{2.22}$$

and the second Piola-Kirchhoff stress becomes

$$S_{ij} = 2[\bar{K}_1 I_3^{-1/3} (\delta_{ij} - \tfrac{1}{3} I_1 G_{ij}^{-1}) + \bar{K}_2 I_3^{-2/3} (I_1 \delta_{ij} - G_{ij} - \tfrac{2}{3} I_2 G_{ij}^{-1})] + PJG_{ij}^{-1} \tag{2.23}$$

where

$$\bar{K}_n = \frac{\partial \bar{W}}{\partial \bar{I}_n}. \tag{2.24}$$

It is worth noting that if $\tilde{W}(I_3)$ is expressed as the power series of $I_3 - 1$, the first-order term must be eliminated to satisfy the initial condition of P. The explicit expressions of $\bar{K}_n$'s for various material models can be found in Chen et al. (1994).

3 Pressure Projection Method

3.1 Decomposed Variational Principle and Finite Element Formulation. In the current study, the original configuration is selected as the reference configuration, and the conjugate pair, the second Piola-Kirchhoff stress, S_{ij}, and the Green-Lagrangian strain, E_{ij}, are employed in the total Lagrangian formulation

$$\Pi = \int_{\Omega_X} \bar{W}(\bar{I}_1, \bar{I}_2) d\Omega + \int_{\Omega_X} \tilde{W}(I_3) d\Omega - W^{\text{ext}} \tag{3.1}$$

where Π is the potential energy, W^{ext} is the external work, and Ω_X is the domain of the original configuration of the structure. The equilibrium equation can be obtained from the stationary condition of the potential energy, i.e., to satisfy

$$\delta\Pi = \int_{\Omega_X} \delta E_{ij} \bar{S}_{ij} d\Omega + \int_{\Omega_X} \delta E_{ij} \tilde{S}_{ij} d\Omega - \delta W^{\text{ext}} = 0 \tag{3.2}$$

where

$$\bar{S}_{ij} = \frac{\partial \bar{W}}{\partial E_{ij}} = 2 \left[\bar{K}_1 I_3^{-1/3} \left(\delta_{ij} - \frac{1}{3} I_1 G_{ij}^{-1} \right) + \bar{K}_2 I_3^{-2/3} \left(I_1 \delta_{ij} - G_{ij} - \frac{2}{3} I_2 G_{ij}^{-1} \right) \right], \tag{3.3}$$

$$\tilde{S}_{ij} = \frac{\partial \tilde{W}}{\partial E_{ij}} = \frac{\partial \tilde{W}}{\partial J} \frac{\partial J}{\partial E_{ij}} = PJG_{ij}^{-1}. \tag{3.4}$$

The linearization of Eq. (3.2) leads to

$$\Delta\delta\Pi = \int_{\Omega_X} \frac{\partial \delta u_i}{\partial X_j} (\bar{T}_{ijkl} + \tilde{T}_{ijkl}) \frac{\partial \Delta u_k}{\partial X_l} d\Omega + \int_{\Omega_X} \left[\frac{1}{2} \left(F_{pi} \frac{\partial \delta u_p}{\partial X_j} + F_{pj} \frac{\partial \delta u_p}{\partial X_i} \right) \right] (\bar{C}_{ijkl} + \tilde{C}_{ijkl}) \times \left[\frac{1}{2} \left(F_{qk} \frac{\partial \Delta u_q}{\partial X_l} + F_{ql} \frac{\partial \Delta u_q}{\partial X_k} \right) \right] d\Omega - \Delta\delta W^{\text{ext}} \tag{3.5}$$

where

$$\bar{T}_{ijkl} = \delta_{ik} \bar{S}_{jl}, \tag{3.6}$$

$$\tilde{T}_{ijkl} = \delta_{ik} \tilde{S}_{jl}, \tag{3.7}$$

$$\bar{C}_{ijkl} = \frac{\partial^2 \bar{W}}{\partial E_{ij} \partial E_{kl}}, \tag{3.8}$$

$$\tilde{C}_{ijkl} = \frac{\partial^2 \tilde{W}}{\partial E_{ij} \partial E_{kl}} \equiv \tilde{C}^1_{ijkl} + \tilde{C}^2_{ijkl} \tag{3.9}$$

and

$$\tilde{C}^1_{ijkl} = \frac{\partial (JG_{ij}^{-1})}{\partial E_{kl}} P = JP(G_{ij}^{-1} G_{kl}^{-1} - G_{ik}^{-1} G_{jl}^{-1} - G_{il}^{-1} G_{jk}^{-1}), \tag{3.10}$$

$$\tilde{C}^2_{ijkl} = JG_{ij}^{-1} \frac{\partial P}{\partial E_{kl}}, \tag{3.11}$$

$$\bar{H}_{ij} = \frac{\partial^2 \bar{W}(\bar{I}_1, \bar{I}_2)}{\partial \bar{I}_i \partial \bar{I}_j}. \tag{3.12}$$

For the purpose of introducing the pressure projection method, it is more convenient to convert Eq. (3.5) to the following form:

$$\Delta\delta\Pi = \int_{\Omega_X} \frac{\partial \delta u_i}{\partial X_j} (\bar{T}_{ijkl} + \tilde{T}_{ijkl}) \frac{\partial \Delta u_k}{\partial X_l} d\Omega + \int_{\Omega_X} \left[\frac{1}{2} \left(F_{pi} \frac{\partial \delta u_p}{\partial X_j} + F_{pj} \frac{\partial \delta u_p}{\partial X_i} \right) \right] (\bar{C}_{ijkl} + \tilde{C}^1_{ijkl}) \times \left[\frac{1}{2} \left(F_{qk} \frac{\partial \Delta u_q}{\partial X_l} + F_{ql} \frac{\partial \Delta u_q}{\partial X_k} \right) \right] d\Omega + \int_{\Omega_X} \left[\frac{1}{2} \left(F_{pi} \frac{\partial \delta u_p}{\partial X_j} + F_{pj} \frac{\partial \delta u_p}{\partial X_i} \right) \right] \times JG_{ij}^{-1} \Delta P d\Omega - \Delta\delta W^{\text{ext}}. \tag{3.13}$$

By introducing displacement shape functions and domain discretization, the equilibrium matrix equation can be obtained from Eq. (3.2)

$$\delta\Pi = \delta\mathbf{d}^T \int_{\Omega_X} \mathbf{B}_E^T(\bar{\mathbf{Z}} + \tilde{\mathbf{Z}})d\Omega - \delta\mathbf{d}^T\mathbf{f}^{\text{ext}} = 0, \quad (3.14)$$

and this leads to the equilibrium equation

$$\mathbf{f}^{\text{int}} = \mathbf{f}^{\text{ext}} \quad (3.15)$$

where

$$\mathbf{f}^{\text{int}} = \int_{\Omega_X} \mathbf{B}_E^T(\bar{\mathbf{Z}} + \tilde{\mathbf{Z}})d\Omega \equiv \bar{f}^{\text{int}} + \tilde{f}^{\text{int}}, \quad (3.16)$$

$$\bar{\mathbf{f}}^{\text{int}} = \int_{\Omega_X} \mathbf{B}_E^T\bar{\mathbf{Z}}d\Omega, \quad (3.17)$$

$$\tilde{\mathbf{f}}^{\text{int}} = \int_{\Omega_X} \mathbf{B}_E^T\tilde{\mathbf{Z}}d\Omega, \quad (3.18)$$

and $\bar{\mathbf{Z}}$ and $\tilde{\mathbf{Z}}$ are vector forms of $\bar{S}_{ij}$ and $\tilde{S}_{ij}$, respectively. $\mathbf{B}_E\delta\mathbf{d}$ is the matrix form of δE_{ij}, and $\mathbf{f}^{\text{int}}$ and $\mathbf{f}^{\text{ext}}$ are internal and external force vectors, respectively.

3.2 Pressure Projection. Many displacement-based finite element formulations derived from single field variational principle failed in incompressible and nearly incompressibility problems. In linear elasticity, Hughes (1980) proposed a B-bar formulation to resolve locking for nearly incompressible materials. The gradient B matrix was separated into deviatoric and dilatational parts. The dilatational B matrix was then projected onto a trial space a priori and replaced the original dilatational B matrix. This B-bar formulation was generalized from the earlier work by Malkus and Hughes (1978) in which they proved the equivalence between the mixed formulation and selective reduced integration. In nonlinear hyperelasticity, separation of the B matrix is difficult. Instead, an alternative approach is taken by the segregation of the strain energy density. In Section 2, the strain energy density was separated into pure distortional (isochoric) and pure dilatational parts and, consequently, the hydrostatic pressure is only related to the dilatational energy. To attain the accuracy of the mixed formulation, we deliberately carry out the projection of the element hydrostatic pressure, P^e, and the element hydrostatic pressure increment, ΔP^e (originally calculated from displacements), onto selected pressure function space.

Consider a problem of approximating a square integrable function $P^e(x)$ at the element level, in a least-squares sense, by a linear combination of a sequence of functions $\{Q_1(x), Q_2(x), \ldots, Q_n(x)\}$ in $L_2(\Omega_X^e)$. That is, choose $\mathbf{p}^e = [p_1^e, p_2^e, \ldots, p_n^e]^T$ to minimize

$$\Phi(\mathbf{p}^e) = \|P^e - \mathbf{Q}\mathbf{p}^e\|^2_{L_2(\Omega_X^e)} \quad (3.19)$$

where $\|\cdot\|_{L_2(\Omega_X^e)}$ is the L_2 norm in the element domain Ω_X^e and

$$\mathbf{Q}(x) = [Q_1(x), Q_2(x), \ldots, Q_n(x)]. \quad (3.20)$$

The minimization of $\Phi(\mathbf{p}^e)$ leads to

$$\mathbf{M}^e\mathbf{p}^e = \mathbf{F}^e \quad (3.21)$$

where

$$\mathbf{M}^e = \int_{\Omega_X^e} \mathbf{Q}^T\mathbf{Q}d\Omega, \quad (3.22)$$

$$\mathbf{F}^e = \int_{\Omega_X^e} \mathbf{Q}^T Pd\Omega = \int_{\Omega_X^e} \mathbf{Q}^T \frac{\partial\tilde{W}}{\partial J} d\Omega, \quad (3.23)$$

and the projected hydrostatic pressure, P^{e*}, is

$$P^{e*} \equiv \mathbf{Q}\mathbf{p}^e = \mathbf{Q}\mathbf{M}^{e^{-1}}\mathbf{F}^e. \quad (3.24)$$

Consequently, the internal force vector is modified as

$$\mathbf{f}^{\text{int}} = \bar{\mathbf{f}}^{\text{int}} + \tilde{\mathbf{f}}^{*\text{int}} \quad (3.25)$$

where

$$\tilde{\mathbf{f}}^{*\text{int}} = \int_{\Omega_X} \mathbf{B}_E^T\tilde{\mathbf{Z}}^* d\Omega \quad (3.26)$$

and $\tilde{\mathbf{f}}^{*\text{int}}$ and $\tilde{\mathbf{Z}}^*$ are the modified vectors of $\tilde{\mathbf{f}}^{\text{int}}$ and $\tilde{\mathbf{Z}}$, respectively, due to the pressure projection.

In the present work, the selection of pressure interpolation functions follows Babuska-Brezzi (BB) conditions in which a linear pressure interpolation function is used for the nine-node Lagrangian element

$$\mathbf{Q} = [1, x, y] \quad (3.27)$$

and similarly for a three-dimensional 27-node element

$$\mathbf{Q} = [1, x, y, z]. \quad (3.28)$$

Obviously, there are other alternatives of selecting pressure interpolation functions that do not satisfy the BB condition and will be discussed in the next section.

3.3 Incremental Equation and Solution Procedures. For the nonlinear analysis of rubber deformation, the incremental equation is employed for nonlinear iteration and therefore the hydrostatic pressure increment needs to be calculated in a consistent manner. Similarly, we consider a least-squares approximation of the hydrostatic pressure increment by a linear combination of a sequence of functions $\{\tilde{Q}_1(x), \tilde{Q}_2(x), \ldots, \tilde{Q}_n(x)\}$ in $L_2(\Omega_X^e)$. Determine $\tilde{\mathbf{p}}^e = [\tilde{p}_1^e, \tilde{p}_2^e, \ldots, \tilde{p}_n^e]^T$ to minimize

$$\Psi(\tilde{\mathbf{p}}^e) = \|\Delta P^e - \tilde{\mathbf{Q}}\tilde{\mathbf{p}}^e\|^2_{L_2(\Omega_X^e)} \quad (3.29)$$

where

$$\Delta P^e = \frac{\partial^2\tilde{W}}{\partial J^2} JG_{kl}^{-1}\Delta E_{kl} \quad (3.30)$$

and

$$\tilde{\mathbf{Q}}(x) = [\tilde{Q}_1(x), \tilde{Q}_2(x), \ldots, \tilde{Q}_n(x)]. \quad (3.31)$$

The minimization of $\Psi(\tilde{\mathbf{p}}^e)$ leads to

$$\tilde{\mathbf{p}}^e = \tilde{\mathbf{M}}^{e^{-1}}\tilde{\mathbf{L}}^e\Delta\mathbf{d}^e \quad (3.32)$$

where

$$\tilde{\mathbf{M}}^e = \int_{\Omega_X^e} \tilde{\mathbf{Q}}^T\tilde{\mathbf{Q}}d\Omega, \quad (3.33)$$

$$\tilde{\mathbf{L}}^e = \int_{\Omega_X^e} \frac{\partial^2\tilde{W}}{\partial J^2} \tilde{\mathbf{Q}}^T\mathbf{g}\mathbf{B}_E d\Omega, \quad (3.34)$$

with $\mathbf{g}$ the row vector form of JG_{ij}^{-1} and $\mathbf{B}_E$ the gradient matrix of Green-Lagrangian strain. The projected hydrostatic pressure increment, ΔP^{e*}, is obtained by

$$\Delta P^{e*} \equiv \tilde{\mathbf{Q}}\tilde{\mathbf{p}}^e = \tilde{\mathbf{Q}}\tilde{\mathbf{M}}^{e^{-1}}\tilde{\mathbf{L}}^e\Delta\mathbf{d}^e. \quad (3.35)$$

The newly calculated hydrostatic pressure, P^{e*}, and hydrostatic pressure increment, ΔP^{e*}, will replace P^e and ΔP^e respectively, in the equilibrium and linearized equilibrium equations (Eqs. (3.5)–(3.13)).

By substituting Eq. (3.35) into Eq. (3.13) and introducing shape functions and domain discretization, the tangent stiffness can be obtained in the following form:

$$\Delta\delta\prod = \delta\mathbf{d}^T(\bar{\mathbf{K}} + \tilde{\mathbf{K}}^* + \tilde{\mathbf{K}}^{**})\Delta\mathbf{d} \tag{3.36}$$

where the element matrices of $\bar{\mathbf{K}}$, $\tilde{\mathbf{K}}^*$ and $\tilde{\mathbf{K}}^{**}$, denoted by $\bar{\mathbf{K}}^e$, $\tilde{\mathbf{K}}^{e*}$, and $\tilde{\mathbf{K}}^{e**}$, are

$$\bar{\mathbf{K}}^e = \bar{\mathbf{K}}^e_G + \bar{\mathbf{K}}^e_M, \tag{3.37}$$

$$\tilde{\mathbf{K}}^{e*} = \tilde{\mathbf{K}}^{e*}_G + \tilde{\mathbf{K}}^{e*}_M, \tag{3.38}$$

$$\tilde{\mathbf{K}}^{e**} = \int_{\Omega^e_X} \mathbf{B}_E^T \mathbf{g}^T \tilde{\mathbf{Q}} d\Omega\, \tilde{\mathbf{M}}^{e^{-1}} \tilde{\mathbf{L}}^e \tag{3.39}$$

with

$$\bar{\mathbf{K}}^e_G = \int_{\Omega^e_X} \mathbf{B}_F^T \bar{\mathbf{T}} \mathbf{B}_F d\Omega, \tag{3.40}$$

$$\bar{\mathbf{K}}^e_M = \int_{\Omega^e_X} \mathbf{B}_E^T \bar{\mathbf{C}} \mathbf{B}_E d\Omega, \tag{3.41}$$

$$\tilde{\mathbf{K}}^{e*}_G = \int_{\Omega^e_X} \mathbf{B}_F^T \tilde{\mathbf{T}}^* \mathbf{B}_F d\Omega, \tag{3.42}$$

$$\tilde{\mathbf{K}}^{e*}_M = \int_{\Omega^e_X} \mathbf{B}_E^T \tilde{\mathbf{C}}^{1*} \mathbf{B}_E d\Omega. \tag{3.43}$$

The terms with subscript "*" contain the projected hydrostatic pressure and $\tilde{\mathbf{K}}^{e**}$ results from projection of the hydrostatic pressure increment. The matrices $\bar{\mathbf{T}}$, $\tilde{\mathbf{T}}^*$, $\bar{\mathbf{C}}$, $\tilde{\mathbf{C}}^{1*}$ and $\mathbf{B}_F\delta\mathbf{d}$ are the matrix forms of $\delta_{ik}\bar{S}_{jl}$, $\delta_{ik}\tilde{S}^*_{jl}$, $\bar{C}_{ijkl}$, $\tilde{C}^{1*}_{ijkl}$, and δF_{ij}, respectively, and $\delta_{ik}\tilde{S}^*_{jl}$ and $\tilde{C}^{1*}_{ijkl}$ have been modified due to the hydrostatic pressure projection. Equation (3.39) can be further manipulated as

$$\tilde{\mathbf{K}}^{e**} = \int_{\Omega^e_X} \mathbf{B}_E^T \mathbf{g}^T \tilde{\mathbf{Q}} d\Omega \tilde{\mathbf{M}}^{e^{-1}} \tilde{\mathbf{L}}^e = \tilde{\mathbf{R}}^{e^T} \tilde{\mathbf{M}}^{e^{-1}} \tilde{\mathbf{L}}^e \tag{3.44}$$

where

$$\tilde{\mathbf{R}}^e = \int_{\Omega^e_X} \tilde{\mathbf{Q}}^T \mathbf{g} \mathbf{B}_E d\Omega. \tag{3.45}$$

As can be seen, Eq. (3.44) will lead to an asymmetric tangent stiffness matrix unless the following condition is imposed:

$$\frac{\partial^2 \tilde{W}}{\partial J^2} = k. \tag{3.46}$$

Since $\tilde{W}$ is a function of J, by integrating Eq. (3.46) in conjunction with Eq. (2.22) and imposing a pressure-free initial condition, one can obtain

$$\tilde{W} = \frac{k}{2}(J-1)^2. \tag{3.47}$$

The physical interpretation of k is the bulk modulus and Eq. (3.47) represents a linear hydrostatic pressure-volumetric strain relation. Equation (3.47) is a necessary condition in this development using the pressure projection method. This necessary condition is consistent with the "material constraint condition" discussed by Sussman and Bathe (1987). They proved that a linear pressure-volumetric strain relation must hold when a *u/p* formulation is used for nearly incompressible materials. If Eq. (3.47) is imposed, $\tilde{\mathbf{K}}^{e**}$ becomes a symmetric matrix:

$$\tilde{\mathbf{K}}^{e**} = k\tilde{\mathbf{R}}^{e^T} \tilde{\mathbf{M}}^{e^{-1}} \tilde{\mathbf{R}}^e. \tag{3.48}$$

The final incremental equilibrium equation is

$$(\bar{\mathbf{K}} + \tilde{\mathbf{K}}^* + \tilde{\mathbf{K}}^{**})^{v+1}_{n+1}\Delta\mathbf{d} = (\mathbf{f}^{\text{ext}})_{n+1} - (\bar{\mathbf{f}}^{\text{int}} + \tilde{\mathbf{f}}^{*\text{int}})^v_{n+1} \tag{3.49}$$

where n is the load step counter and v is the iteration counter. Here, $\bar{\mathbf{K}}$ and $\bar{\mathbf{f}}^{\text{int}}$ are related to the distortional energy. Matrices $\tilde{\mathbf{K}}^*$ and $\tilde{\mathbf{f}}^{*\text{int}}$ are related to dilatational energy with hydrostatic pressure calculated from the projection equation. $\tilde{\mathbf{K}}^{**}$ arises due to the projection of the hydrostatic pressure increment.

4 Degeneration to Some Existing Formulations

By the appropriate selection of pressure interpolation functions and integration rules in the projection procedures, this projection method can be degenerated to some existing formulations. For example, choose $\mathbf{Q}$ to be

$$\mathbf{Q} = [\hat{N}_1(\boldsymbol{\xi}), \hat{N}_2(\boldsymbol{\xi}), \ldots, \hat{N}_{NR}(\boldsymbol{\xi})] \tag{4.1}$$

where NR is the number of reduced integration points and $\hat{N}_I(\boldsymbol{\xi})$ is the shape function defined at reduced integration point I, i.e.,

$$\hat{N}_I(\hat{\boldsymbol{\xi}}_J) = \delta_{IJ} \tag{4.2}$$

and $\hat{\boldsymbol{\xi}}_J \equiv (\hat{r}_J, \hat{s}_J, \hat{t}_J)$ is the natural coordinate at reduced integration point J.

For simplicity, the superscript "e" for element matrices is dropped in this section. By performing reduced integration on $\mathbf{M}$ and $\mathbf{F}$ in the pressure projection equation, Eq. (3.24), one can obtain

$$\mathbf{M} = \sum_{I=1}^{NR} \mathbf{Q}^T(\hat{\boldsymbol{\xi}}_I)\mathbf{Q}(\hat{\boldsymbol{\xi}}_I)\hat{J}(\hat{\boldsymbol{\xi}}_I)w_I = \begin{bmatrix} \hat{J}(\hat{\boldsymbol{\xi}}_1)w_1 & 0 & \cdots & 0 \\ 0 & \hat{J}(\hat{\boldsymbol{\xi}}_2)w_2 & \cdots & 0 \\ \vdots & & & \vdots \\ 0 & 0 & \cdots & \hat{J}(\hat{\boldsymbol{\xi}}_{NR})w_{NR} \end{bmatrix}, \tag{4.3}$$

$$\mathbf{F} = \sum_{I=1}^{NR} \mathbf{Q}^T(\hat{\boldsymbol{\xi}}_I)P(\hat{\boldsymbol{\xi}}_I)\hat{J}(\hat{\boldsymbol{\xi}}_I)w_I = \begin{bmatrix} P(\hat{\boldsymbol{\xi}}_I)\hat{J}(\hat{\boldsymbol{\xi}}_I)w_I \\ P(\hat{\boldsymbol{\xi}}_2)\hat{J}(\hat{\boldsymbol{\xi}}_2)w_2 \\ \vdots \\ P(\hat{\boldsymbol{\xi}}_{NR})\hat{J}(\hat{\boldsymbol{\xi}}_{NR})w_{NR} \end{bmatrix} \tag{4.4}$$

where $\hat{J} = \det(\partial X_i/\partial\xi_j)$ and the projected hydrostatic pressure is reduced to a simple form

$$P^*(\boldsymbol{\xi}) = \mathbf{Q}\mathbf{M}^{-1}\mathbf{F} = \sum_{I=1}^{NR} \hat{N}_I(\boldsymbol{\xi})P(\hat{\boldsymbol{\xi}}_I). \tag{4.5}$$

The internal force vector is formed based on this projected hydrostatic pressure. Since hydrostatic pressure is proportional to the volumetric strain, this reduced form is identical to the volumetric strain projection method proposed by Chen et al. (1994).

Similarly, if $\tilde{\mathbf{Q}} = \mathbf{Q}$ is chosen and reduced integration is used in the projection of the hydrostatic pressure increment (Eq. (3.35)), then

$$\tilde{\mathbf{R}} = \sum_{I=1}^{NR} \mathbf{Q}^T(\hat{\boldsymbol{\xi}}_I)\mathbf{g}(\hat{\boldsymbol{\xi}}_I)\mathbf{B}_E(\hat{\boldsymbol{\xi}}_I)\hat{J}(\hat{\boldsymbol{\xi}}_I)w_I = \begin{bmatrix} \hat{J}(\hat{\boldsymbol{\xi}}_1)w_1 & 0 & \cdots & 0 \\ 0 & \hat{J}(\hat{\boldsymbol{\xi}}_2)w_2 & & 0 \\ \vdots & & \ddots & \vdots \\ 0 & 0 & \cdots & \hat{J}(\hat{\boldsymbol{\xi}}_{NR})w_{NR} \end{bmatrix} \times \begin{bmatrix} \mathbf{g}(\hat{\boldsymbol{\xi}}_1)\mathbf{B}_E(\hat{\boldsymbol{\xi}}_1) \\ \mathbf{g}(\hat{\boldsymbol{\xi}}_2)\mathbf{B}_E(\hat{\boldsymbol{\xi}}_2) \\ \vdots \\ \mathbf{g}(\hat{\boldsymbol{\xi}}_{NR})\mathbf{B}_E(\hat{\boldsymbol{\xi}}_{NR}) \end{bmatrix}. \tag{4.6}$$

Using Eqs. (3.35) and (3.30), one can obtain a reduced form of the hydrostatic pressure increment

$$\Delta P^*(\boldsymbol{\xi}) = [\sum_{I=1}^{NR} \hat{N}_I(\boldsymbol{\xi})\mathbf{g}(\hat{\boldsymbol{\xi}}_I)\mathbf{B}_E(\hat{\boldsymbol{\xi}}_I)]\Delta\mathbf{d} = \sum_{I=1}^{NR} \hat{N}_I(\boldsymbol{\xi})\Delta P(\hat{\boldsymbol{\xi}}_I). \quad (4.7)$$

Finally the tangent stiffness matrix is simplified to

$$\mathbf{K} = \int_{\Omega_X^e} \mathbf{B}_F^T(\bar{\mathbf{T}} + \tilde{\mathbf{T}}^*)\mathbf{B}_F d\Omega + \int_{\Omega_X^e} \mathbf{B}_E^T(\bar{\mathbf{C}} + \tilde{\mathbf{C}}^{1*})\mathbf{B}_E d\Omega + k\tilde{\mathbf{R}}^T\tilde{\mathbf{M}}^{-1}\tilde{\mathbf{R}}$$
$$= \int_{\Omega_X^e} \mathbf{B}_F^T(\bar{\mathbf{T}} + \tilde{\mathbf{T}}^*)\mathbf{B}_F d\Omega + \int_{\Omega_X^e} \mathbf{B}_E^T(\bar{\mathbf{C}} + \tilde{\mathbf{C}}^{1*})\mathbf{B}_E d\Omega + k[\sum_{I=1}^{NR} (\mathbf{B}_E^T(\hat{\boldsymbol{\xi}}_I)\mathbf{g}^T(\hat{\boldsymbol{\xi}}_I)\mathbf{g}(\hat{\boldsymbol{\xi}}_I)\mathbf{B}_E(\hat{\boldsymbol{\xi}}_I)\hat{J}(\hat{\boldsymbol{\xi}}_I)w_I]. \quad (4.8)$$

Equation (4.8) provides a nonlinear version of the selective reduced integration method. Further reducing the problem to linear elasticity, this tangent stiffness is identical to that of the selectively reduced integration method and consequently, the B-bar formulation. The detailed derivation is given in the Appendix.

5 Conclusions

This paper focuses on the treatment of hydrostatic pressure for nearly incompressible materials. Although the emphasis is on rubber, the proposed method is applicable to general nearly incompressible hyperelastic materials. By the use of Penn's invariants, the strain energy density is decomposed into distortional and dilatational parts. The hydrostatic pressure, which is the key variable in incompressible problems, is then purely related to the dilatational energy. Unlike the mixed formulation where the hydrostatic pressure is introduced through a multifield variational principle, this method projects the displacement calculated hydrostatic pressure onto the pressure trial space through a least-squares technique. Projection of hydrostatic pressure onto a lower order space is, in concept, consistent with the selective reduced integration method.

Since the projection equation is separatly constructed from the variational equilibrium equation through least-squares method, independent numerical treatment can be introduced to the pressure projection equation to provide flexibility of degenerating this formulation to other forms. For example, as discussed in Section 4, selecting pressure interpolation functions as the shape functions defined at the reduced integration points and employing reduced integration rules in the calculation of L_2 norm, the degenerated pressure projection equation is identical to the volumetric strain projection equation. Further, the resulting tangent stiffness matrix possesses the form of "selective reduced integration."

The present method provides a straightforward approach for the nonlinear analysis of nearly incompressible materials. The implementation of this method into a displacement based nonlinear finite element program will be discussed together with several numerical examples in the second part of this paper.

Acknowledgment

The support of this research by the Automotive Research Center, sponsored by the U.S. Army TARDEC to the University of Iowa is greatly acknowledged.

References

Babuska, I., 1973, "The Finite Element Method with Lagrangian Multipliers," *Numerical Mathematics,* Vol. 20, pp. 179–192.

Bachrach, W. E. and Belytschko, T., 1986, "Axisymmetric Elements With High Coarse-Mesh Accuracy," *Computers & Structures,* Vol. 23, pp. 323–331.

Belytschko, T., and Bachrach, W. E., 1986, "Efficient Implementation of Quadrilaterals with High Coarse-Mesh Accuracy," *Computer Methods in Applied Mechanics and Engineering,* Vol. 54, pp. 279–301.

Belytschko, T., Ong, J. S.-J., Liu, W. K., and Kennedy, J. M., 1984, "Hourglass Control in Linear and Nonlinear Problems," *Computer Methods in Applied Mechanics and Engineering,* Vol. 43, pp. 251–276.

Bercovier, M., 1978, "Perturbation of Mixed Variational Problems, Application to Mixed Finite Element Methods," *R.A.I.R.O. Numerical Analysis,* Vol. 12, pp. 211–236.

Brezzi, F., 1974, "On the Existence, Uniqueness and Approximation of Saddle-Point Problems Arising from Lagrangian Multipliers," *R.A.I.R.O. Numerical Analysis,* Vol. 8, pp. 129–151.

Cescotto, S., and Fonder, G., 1979, "A Finite Element Approach for Large Strains of Nearly Incompressible Rubber-like Materials," *International Journal of Solids and Structures,* Vol. 15, pp. 589–605.

Chang, T. Y. P., Saleeb, A. F., and Li, G., 1991, "Large Strain Analysis of Rubber-like Materials Based on a Perturbed Lagrangian Variational Principle," *Computational Mechanics,* Vol. 8, pp. 221–233.

Chen, J. S., Satyamurthy, K. S., and Hirschfelt, L. R., 1994, "Consistent Finite Element Procedures for Nonlinear Rubber Elasticity with a Higher Order Strain Energy Function," *Computers & Structures,* Vol. 50, pp. 715–727.

Fried, I., 1974, "Finite Element Analysis of Incompressible Material by Residual Energy Balance," *International Journal of Solids and Structures,* Vol. 10, pp. 993–1002.

Herrmann, L. R., 1965, "Elasticity Equations for Incompressible and Nearly Incompressible Materials by a Variational Theorem," *AIAA Journal,* Vol. 3, pp. 1896–1900.

Hughes, T. J. R., 1980, "Generalization of Selective Integration Procedures to Anisotropic and Nonlinear Media," *International Journal for Numerical Methods in Engineering,* Vol. 15, pp. 1413–1418.

Hughes, T. J. R., Liu, W. K., and Brooks, A., 1979, "Review of Finite Element Analysis of Incompressible Viscous Flows by the Penalty Function Formulation," *Journal of Computational Physics,* Vol. 30, pp. 1–60.

Key, S. W., 1969, "A Variational Principle for Incompressible and Nearly Incompressible Anisotropic Elasticity," *International Journal of Solids and Structures,* Vol. 5, pp. 951–964.

Liu, W. K., Belytschko, T., and Chen, J. S., 1988, "Nonlinear Versions of Flexurally Superconvergent Elements," *Computer Methods in Applied Mechanics and Engineering,* Vol. 71, pp. 241–256.

Liu, W. K., Ong, J. S.-J., and Uras, R. A., 1986, "Finite Element Stabilization Matrices–A Unification Approach," *Computer Methods in Applied Mechanics and Engineering,* Vol. 53, pp. 13–46.

Malkus, D. S., 1980, "Finite Elements With Penalties in Nonlinear Elasticity," *International Journal for Numerical Methods in Engineering,* Vol. 16, pp. 121–136.

Malkus, D. S., and Hughes, T. J. R., 1978, "Mixed Finite Element Methods-Reduced and Selective Integration Techniques: A Unification of Concepts," *Computer Methods in Applied Mechanics and Engineering,* Vol. 15, pp. 63–81.

Mooney, M., 1940, "A Theory of Large Elastic Deformation," *Journal of Applied Physics,* Vol. 11, pp. 582–592.

Murakawa, H., and Atluri, S. N., 1979, "Finite Elasticity Solutions Using Hybrid Finite Elements Based on a Complementary Energy Principle, Part 2. Incompressible Materials," ASME JOURNAL OF APPLIED MECHANICS, Vol. 46, pp. 71–77.

Oden, T. J., and Kikuchi, N., 1982, "Finite Element Methods for Constrained Problems in Elasticity," *International Journal for Numerical Methods in Engineering,* Vol. 18, pp. 701–725.

Penn, R. W., 1970, "Volume Changes Accompanying the Extension of Rubber," *Transactions of the Society of Rheology,* Vol. 14:4, pp. 509–517.

Rivlin, R. S., 1956, *Rheology Theory and Applications,* F. R. Eirich, ed., Academic Press, New York, Vol. 1, Chapter 10, pp. 351–385.

Scharnhorst, T., and Pian, T. H. H., 1978, "Finite Element Analysis of Rubber-like Materials by a Mixed Model," *International Journal for Numerical Methods in Engineering,* Vol. 12, pp. 665–676.

Simo, J. C., Taylor, R. L., and Pister, K. S., 1985, "Variational and Projection Methods for Volume Constraint in Finite Deformation Elasto-Plasticity," *Computer Methods in Applied Mechanics and Engineering,* Vol. 51, pp. 177–208.

Sussman, T. S., and Bathe, K. J., 1987, "A Finite Element Formulation for Incompressible Elastic and Inelastic Analysis," *Computers & Structures,* Vol. 26, pp. 357–409.

Taylor, R. L., Pister, K. S., and Herrmann, L. R., 1968, "On a Variational Theorem for Incompressible and Nearly Incompressible Orthotropic Elasticity," *International Journal of Solids and Structures,* Vol. 4, pp. 875–883.

Tong, P., 1969, "An Assumed Stress Hybrid Finite Element Method for an Incompressible and Nearly-incompressible Material," *International Journal of Solids and Structures,* Vol. 5, pp. 455–461.

Wood, L. A. and Martin, G. M., 1964, *Journal of Research of the National Bureau of Standards,* p. 259.

Yeoh, O. H., 1990, "Characterization of Elastic Properties of Carbon Black Filled Rubber Vulcanizates," *Rubber Chemistry and Technology,* Vol. 63, pp. 792–805.

Yeoh, O. H., 1993, "Some Forms of the Strain Energy Function for Rubber," *Rubber Chemistry and Technology,* Vol. 66, pp. 754–771.

APPENDIX

Degeneration to Linear Elasticity

In linear elasticity, $\bar{\mathbf{T}} = \tilde{\mathbf{T}}^* = \tilde{\mathbf{C}}^{1*} = 0$, $\mathbf{B}_E = \mathbf{B}$ and the tangent stiffness matrix (Eq. (4.8)) degenerates to

$$\mathbf{K}^e = \int_{\Omega_X^e} \mathbf{B}^T \bar{\mathbf{C}} \mathbf{B} d\Omega + k\{\sum_{I=1}^{NR} [\mathbf{B}^T(\hat{\xi}_I)\mathbf{g}^T(\hat{\xi}_I)\mathbf{g}(\hat{\xi}_I)\mathbf{B}(\hat{\xi}_I)\hat{J}(\hat{\xi}_I)w_I]\}. \quad (A.1)$$

Further, $\bar{C}_{ijkl}$ and JG_{ij}^{-1} degenerate to

$$\bar{C}_{ijkl} = \tfrac{2}{3}(A_{10} + A_{01})[3(\delta_{ik}\delta_{jl} + \delta_{il}\delta_{jk}) - 2\delta_{ij}\delta_{kl}] \quad (A.2)$$

$$JG_{ij}^{-1} = \delta_{ij}. \quad (A.3)$$

In linear elasticity, the shear modulus can be obtained by

$$\mu = 2\left(\frac{\partial W}{\partial I_1} + \frac{\partial W}{\partial I_2}\right)\Big|_{I_1=I_2=3} = 2(A_{10} + A_{01}) \quad (A.4)$$

and therefore Eq. (A.2) can be rewritten as

$$\bar{C}_{ijkl} = \mu[(\delta_{ik}\delta_{jl} + \delta_{il}\delta_{jk}) - \tfrac{2}{3}\delta_{ij}\delta_{kl}], \quad (A.5)$$

and the matrix forms of the linear $\bar{C}_{ijkl}$ and JG_{ij}^{-1} are

$$\bar{\mathbf{C}} = \frac{2}{3}\mu \begin{bmatrix} 2 & -1 & -1 & 0 & 0 & 0 \\ -1 & 2 & -1 & 0 & 0 & 0 \\ -1 & -1 & 2 & 0 & 0 & 0 \\ 0 & 0 & 0 & \frac{3}{2} & 0 & 0 \\ 0 & 0 & 0 & 0 & \frac{3}{2} & 0 \\ 0 & 0 & 0 & 0 & 0 & \frac{3}{2} \end{bmatrix} \quad (A.6)$$

$$\mathbf{g} = [1, 1, 1, 0, 0, 0]. \quad (A.7)$$

Taking the bulk modulus $k = \lambda + 2/3\mu$, in conjunction with Eq. (A.7), Eq. (A.1) can be simplified to

$$\mathbf{K}^e = \int_{\Omega_X^e} \mathbf{B}^T \bar{\mathbf{C}} \mathbf{B} d\Omega + [\lambda + \tfrac{2}{3}\mu]\{\sum_{I=1}^{NR} [\mathbf{b}^T(\hat{\xi}_I)\mathbf{b}(\hat{\xi}_I)\hat{J}(\hat{\xi}_I)w_I]\} \quad (A.8)$$

where

$$\mathbf{b}_I = [N_{I,X}, N_{I,Y}, N_{I,Z}]. \quad (A.9)$$

Using the orthogonal condition between the deviatoric and dilatational parts of the $\mathbf{B}$ matrix, it can be easily recognized that Eq. (A.8) is identical to the selective reduced integration method in linear elasticity.

A Pressure Projection Method for Nearly Incompressible Rubber Hyperelasticity, Part II: Applications

Jiun-Shyan Chen
Assistant Professor,
Mem. ASME.

Cheng-Tang Wu
Research Assistant.

Chunhui Pan
Research Assistant.

Department of Mechanical Engineering
and Center for Computer-Aided Design,
The University of Iowa,
2133 Engineering Building,
Iowa City, IA 52242-1527

In the first part of this paper a pressure projection method was presented for the nonlinear analysis of structures made of nearly incompressible hyperelastic materials. The main focus of the second part of the paper is to demonstrate the performance of the present method and to address some of the issues related to the analysis of engineering elastomers including the proper selection of strain energy density functions. The numerical procedures and the implementation to nonlinear finite element programs are presented. Mooney-Rivlin, Cubic, and Modified Cubic strain energy density functions are used in the numerical examples. Several classical finite elasticity problems as well as some practical engineering elastomer problems are analyzed. The need to account for the slight compressibility of rubber (finite bulk modulus) in the finite element formulation is demonstrated in the study of apparent Young's modulus of bonded thin rubber units. The combined shear-bending deformation that commonly exists in rubber mounting systems is also analyzed and discussed.

1 Introduction

In most engineering elastomeric applications, rubber components experience strains in the order of several hundred percent. The amount of computation involved in the finite element analysis is tremendous and therefore an accurate and efficient finite element formulation is highly desirable. In Part I of this paper, a least-squares-based pressure projection method was introduced. The formulation was developed in a general framework such that it provides flexibility for the degeneration to other existing formulations. As a result, the expression of the resulting tangent stiffness matrix is rather complex. In this paper, condensed numerical procedures for code implementation are presented so that some of the separately integrated tangent stiffness matrices and force vectors are formed at once to provide better computational efficiency.

In addition to a reliable finite element formulation, an appropriate strain energy density function capable of describing rubber behavior under large strain is essential to the success of nonlinear finite element analysis. Although Mooney-Rivlin strain energy function has been widely used in many finite element formulations such as those in Scharnhorst and Pian (1978), Liu et al. (1988) and Chang et al. (1991), the study by Tschoegl (1971) and James et al. (1975a, b) suggested that the popular Mooney-Rivlin model is not adequate to describe rubber behavior under very large and complex deformations. Yeoh (1993) proposed a Cubic strain energy density function as a correction of the Mooney-Rivlin function to capture the nonlinear shear behavior of rubber at large strain. This function was later modified by adding an additional exponential term (Yeoh, 1993) to improve low strain accuracy.

In the applications to bridge/building bearings, solid rocket motor flexseals and off-shore structure flexjoints, rubber components are highly confined and the deformation is essentially bulk deformation. The work by Payne (1957), Gent and Lindley (1959), and Gent and Meinecke (1970) indicated that the mechanical behavior of highly confined rubber components is strongly affected by the magnitude of rubber bulk modulus, and therefore the "nearly incompressible" nature of rubber plays an important role in these applications. Finite element formulation that can accurately account for bulk deformation is critical to the analysis of this type of problems. Surely, pure incompressible finite element formulation is not applicable. Rubber under combined bending-shear deformation is also common in rubber mounting systems such as engine mounts and bushings. Varying the aspect ratio of rubber components changes the relative contributions of shear and bending to the overall deformation (Rivlin and Saunders, 1949) and thereby changes the structural stiffness. In this paper, the applicability of the present finite element method to these typical elastomeric problems is verified.

In the following, the numerical procedures of the pressure projection method are first presented in Section 2. The fundamental laboratory test problems, uniaxial tension-compression and simple shear, are analyzed in Section 3. These analyses also show how the Mooney-Rivlin model fails under large defamation. Two more incompressible finite elasticity problems, inflation and torsion problems, are analyzed in Section 4 to further illustrate the effectiveness of the proposed method. Some practical elastomeric applications such as bonded rubber units under tension and compression, and combined shear-bending example, together with an engine mount problem, are analyzed and compared to approximate solutions in Section 5.

2 Numerical Procedures

The pressure projection procedures and the corresponding nonlinear finite element formulation for nearly incompressible rubber-like materials were discussed in Part I (Chen et al., 1996). Recall the final incremental equilibrium equation

$$(\bar{\mathbf{K}} + \tilde{\mathbf{K}}^* + \tilde{\mathbf{K}}^{**})^{v+1}_{n+1}\Delta\mathbf{d} = \mathbf{f}^{\text{ext}}_{n+1} - (\bar{\mathbf{f}}^{\text{int}} + \tilde{\mathbf{f}}^{*\text{int}})^{v}_{n+1} \quad (2.1)$$

where n and v are load step and iteration counters, respectively.

Contributed by the Applied Mechanics Division of THE AMERICAN SOCIETY OF MECHANICAL ENGINEERS for publication in the ASME JOURNAL OF APPLIED MECHANICS.

Discussion on this paper should be addressed to the Technical Editor, Professor Lewis T. Wheeler, Department of Mechanical Engineering, University of Houston, Houston, TX 77204-4792, and will be accepted until four months after final publication of the paper itself in the ASME JOURNAL OF APPLIED MECHANICS.

Manuscript received by the ASME Applied Mechanics Division, May 8, 1995; final revision, Nov. 28, 1995. Associate Technical Editor: W. K. Liu.

The matrices $\bar{\mathbf{K}}$ and $\bar{\mathbf{f}}^{\text{int}}$ are associated with the distortional energy density $\bar{W}(\bar{I}_1, \bar{I}_2)$ and are independent of pressure projection. The matrices with superscript "*", $\tilde{\mathbf{K}}*$ and $\tilde{\mathbf{f}}^{*\text{int}}$, are associated with the dilatational energy density $\tilde{W}(I_3)$ and therefore contain projected hydrostatic pressure quantity. The term $\tilde{\mathbf{K}}**$ is resulting from the projection of hydrostatic pressure increment. The explicit expressions of the material response stiffness and geometric response stiffness in each of $\bar{\mathbf{K}}$ and $\tilde{\mathbf{K}}*$ are given in Eqs. (3.40)–(3.43) in Part I.

Equation (2.1) is arranged for clarity and is computational inefficient if those matrices are formed separately. More efficient computational procedures are given below as follows:

1 Initialization.

2 Currently at the beginning of $(n + 1)$th load step and $(v + 1)$th iteration: d^v_{n+1} is known.

3 Compute kinematic variables: $(F_{ij})^v_{n+1}$, $(E_{ij})^v_{n+1}$, $(G^{-1}_{ij})^v_{n+1}$, $(\bar{I}_1)^v_{n+1}$, $(\bar{I}_2)^v_{n+1}$, $(I_3)^v_{n+1}$.

4 Compute the displacement calculated pressure $\partial\tilde{W}/\partial J$.

5 Form $(\mathbf{M}^e)^v_{n+1}$ and $(\mathbf{F}^e)^v_{n+1}$ (Eqs. (3.22) and (3.23) in Part I, respectively) and perform projection on hydrostatic pressure to obtain $(P^{e*})^v_{n+1}$ (Eq. (3.24) in Part I).

6 Compute $(\tilde{S}_{ij})^v_{n+1}$ (Eq. (3.4) in Part I) by replacing the displacement calculated hydrostatic pressure by $(P^{e*})^v_{n+1}$.

7 Compute $(\bar{S}_{ij})^v_{n+1}$ using Eq. (3.3) in Part I, and the total second Piola-Kirchhoff stress is

$$(S_{ij})^v_{n+1} = (\bar{S}_{ij})^v_{n+1} + (\tilde{S}_{ij})^v_{n+1}. \tag{2.2}$$

8 Form internal force vector $(\mathbf{f}^{\text{int}})^v_{n+1}$ by

$$(\mathbf{f}^{\text{int}})^v_{n+1} = \int_{\Omega^e_X} (\mathbf{B}^T_E \mathbf{Z})^v_{n+1} d\Omega \tag{2.3}$$

where $(\mathbf{Z})^v_{n+1}$ is the vector form of $(S_{ij})^v_{n+1}$.

9 Compute $(\tilde{T}_{ijkl})^v_{n+1}$ and $(\tilde{C}^1_{ijkl})^v_{n+1}$ (Eqs. (3.7) and (3.9) in Part I) using $(\tilde{S}_{ij})^v_{n+1}$ and the projected hydrostatic pressure $(P^{e*})^v_{n+1}$).

10 Calculate $(T_{ijkl})^v_{n+1}$ and $(C^1_{ijkl})^v_{n+1}$ by

$$(T_{ijkl})^v_{n+1} = (\bar{T}_{ijkl})^v_{n+1} + (\tilde{T}_{ijkl})^v_{n+1}, \tag{2.4}$$

$$(C^1_{ijkl})^v_{n+1} = (\bar{C}_{ijkl})^v_{n+1} + (\tilde{C}^1_{ijkl})^v_{n+1}. \tag{2.5}$$

where the explicit expressions of $(\bar{T}_{ijkl})^v_{n+1}$ and $(\bar{C}_{ijkl})^v_{n+1}$ are given in Eqs. (3.6) and (3.8) in Part I, respectively.

11 Form $(\tilde{\mathbf{R}}^e)^v_{n+1}$ and $(\tilde{\mathbf{M}}^e)^v_{n+1}$ (Eqs. (3.33) and (3.45) in Part I, respectively) and construct element stiffness matrix

$$(\mathbf{K}^e)^v_{n+1} = \int_{\Omega^e_X} (\mathbf{B}^T_F \mathbf{T} \mathbf{B}_F)^v_{n+1} d\Omega + \int_{\Omega^e_X} (\mathbf{B}^T_E \mathbf{C}^1 \mathbf{B}_E)^v_{n+1} d\Omega + k(\tilde{\mathbf{R}}^{eT})^v_{n+1} (\tilde{\mathbf{M}}^{e^{-1}})^v_{n+1} (\tilde{\mathbf{R}}^e)^v_{n+1}. \tag{2.6}$$

12 Solve global incremental equation:

$$(\mathbf{K})^v_{n+1} \Delta\mathbf{d} = (\mathbf{f}^{\text{ext}})_{n+1} - (\mathbf{f}^{\text{int}})^v_{n+1}. \tag{2.7}$$

13 Update displacement $\mathbf{d}^{v+1}_{n+1} = \mathbf{d}^v_{n+1} + \Delta\mathbf{d}$.

14 Convergence check.

In the present study, linear pressure fields, $\mathbf{Q} = \tilde{\mathbf{Q}} = [1, x, y]$ and $\mathbf{Q} = \tilde{\mathbf{Q}} = [1, x, y, z]$ are used in 9-node two-dimensional and 27-node three-dimensional Lagrangian elements, respectively.

3 Fundamental Test Problems

Three rubber models are used in this section: Mooney-Rivlin, Cubic, and Modified Cubic. The material constants fitted from uniaxial tensile data (Yeoh, 1990) are

(1) Mooney-Rivlin: $A_{10} = 0.2599$ Mpa, $A_{01} = 0.1608$ Mpa

(2) Cubic: $A_{10} = 0.373$ Mpa, $A_{20} = -0.031$ Mpa, $A_{30} = 0.005$ Mpa

(3) Modified Cubic: $A_{10} = 0.363$ Mpa, $A_{20} = -0.028$ Mpa, $A_{30} = 0.005$ Mpa, $\alpha = 0.123$ Mpa, $\beta = 10.1$.

For carbon black filled rubber, the bulk modulus to shear modulus ratio is around $10^4 \sim 10^5$ and therefore bulk modulus $k = 10^5$ Mpa is used in each material model. Nine-node and 27-node elements are used in two-dimensional and three-dimensional problems, respectively.

In this section, analyses and results are compared against analytical solutions and experimental data obtained from (Yeoh, 1990, 1993, 1994).

3.1 Uniaxial Tension-Compression. Since the stress-strain relation of uniaxial tension-compression is independent of cross-sectional geometry, a rubber block with dimension 1 cm × 1 cm × 4 cm is modeled by only one 27-node element in this analysis. The analytical solution can be found in Rivlin and Saunders (1951) as

$$\frac{t}{\lambda - \lambda^{-2}} = 2\left(\frac{\partial W}{\partial I_1} + \frac{1}{\lambda}\frac{\partial W}{\partial I_2}\right) \tag{3.1}$$

where t is the axial force divided by undeformed cross-sectional area, λ is the axial stretch ratio, and $t/(\lambda - \lambda^{-2})$ is called the reduced stress. In this problem, the rubber block is stretched up to 400 percent in axial tension and compressed down to 50 percent in axial compression. The finite element results calculated using different rubber models have excellent agreement with analytical solutions as shown in Fig. 1.

By the comparison with experimental data, one can observe that the Mooney-Rivlin model, which represents a linear relation between reduced stress and λ^{-1} in uniaxial deformation (as described in Eq. (3.1)), is not capable of capturing the upturn in the small strain region, and the nonlinearity beyond ~200 percent tension and ~20 percent compression. The finite element results obtained using the Cubic strain energy density function, on the other hand, agree quite well with experimental data in both large tension and compression but misses a certain amount of accuracy in the small strain region. The Modified Cubic function with an additional exponential term further improves small strain accuracy as shown in Fig. 1.

3.2 Shear of Rubber Component. A double-sandwich shear test problem is described in Fig. 2. When the width-to-thickness ratio (w/h) of the test specimen approaches infinity, rubber deforms in simple shear. The specimen used (Yeoh, 1990) has a width to thickness ratio of 4 and therefore only generates a "nearly" simple shear deformation. The analytical solution of simple shear can be found in Rivlin (1956) as

$$t = 2\left(\frac{\partial W}{\partial I_1} + \frac{\partial W}{\partial I_2}\right)\gamma \tag{3.2}$$

where t is shear stress and γ is shear strain. Note that Eq. (3.2) only provides an appropriate solution for this problem. Figure 2 indicates that the Mooney-Rivlin model, which contains only leading terms in I_1 and I_2, represents a linear shear stress-strain behavior as described in Eq. (3.2). The higher order models, such as the Cubic and Modified Cubic models, are more capable of characterizing the nonlinear shear stress-strain relation as shown in Fig. 2. Similar to the uniaxial deformation, the Modified Cubic strain energy density function further enhances the small strain accuracy when compared against experimental data.

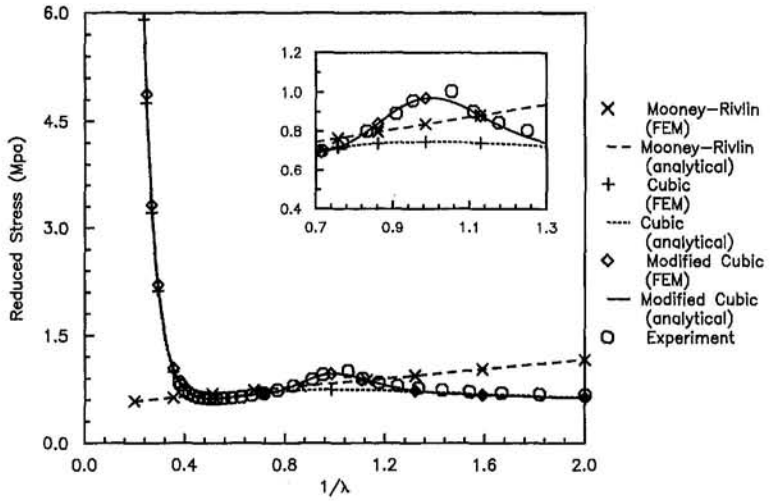

Fig. 1 Rubber block under uniaxial tension-compression: comparison of Mooney-Rivlin, Cubic, and modified Cubic strain energy density functions

The deformed shape at 200 percent shear strain is also plotted in Fig. 2. Due to the geometry of the test specimen, some small amount of bending deformation is observed near the edges.

4 Rubber Elasticity Problems

Since Modified Cubic strain energy density function differs from Cubic function simply at low strain as discussed in Section 3, only Mooney-Rivlin and Cubic strain energy density functions are used in this study.

4.1 Inflation of a Rubber Tube. Inflation is a good test problem for (nearly) incompressible finite element formulations because the pressure-displacement behavior is highly nonlinear and the hydrostatic pressure plays a significant role in this problem.

As described in Fig. 3, an infinitely long rubber cylinder, with inner radius of 6 cm and outer radius of 8 cm, is subjected to an internal pressure, p. The analytical solution of this problem can be derived from Rivlin (1949). For convenience, the analytical solution (considering only Mooney-Rivlin and Cubic strain energy density functions) is summarized as follows:

$$p(\rho) = (A_{10} + A_{01})[H_1(\rho, a_2) - H_1(\rho, a_1)] + A_{20}[H_2(\rho, a_2) - H_2(\rho, a_1)] + A_{30}[H_3(\rho, a_2) - H_3(\rho, a_1)] \quad (4.1)$$

where

$$H_1(\rho, a) = \ln\left(\frac{a^2}{a^2 + K(\rho)}\right) - \frac{K(\rho)}{a^2 + K(\rho)} \quad (4.2)$$

$$H_2(\rho, a) = -2\ln\left(\frac{a^2}{a^2 + K(\rho)}\right) + \left(\frac{K(\rho)}{a^2 + K(\rho)}\right)^2 - 2\frac{K(\rho)}{a^2} \quad (4.3)$$

$$H_3(\rho, a) = 6\ln\left(\frac{a^2}{a^2 + K(\rho)}\right) - \left(\frac{K(\rho)}{a^2 + K(\rho)}\right)^3 - \frac{3}{2}\left(\frac{K(\rho)}{a^2 + K(\rho)}\right)^2 - \frac{3}{2}\left(\frac{K(\rho)}{a^2}\right)^2 + 6\frac{K(\rho)}{a^2} \quad (4.4)$$

$$K(\rho) = \rho^2 - a_2^2 \quad (4.5)$$

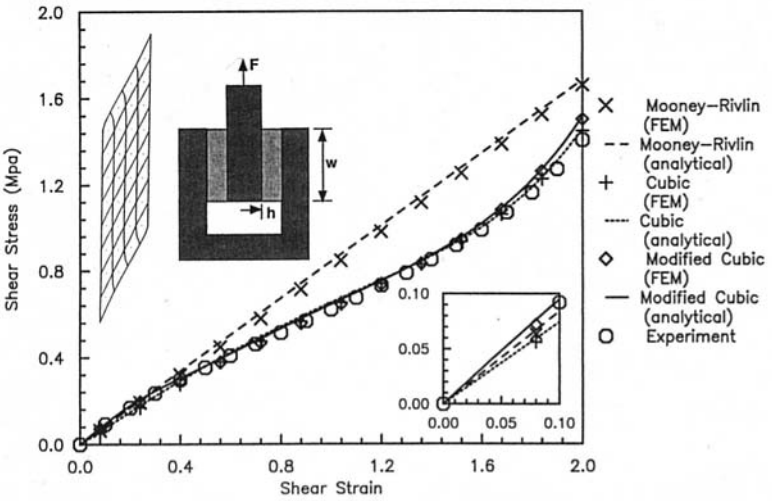

Fig. 2 Rubber block under simple shear deformation: comparison of Mooney-Rivlin, Cubic, and modified Cubic strain energy density functions

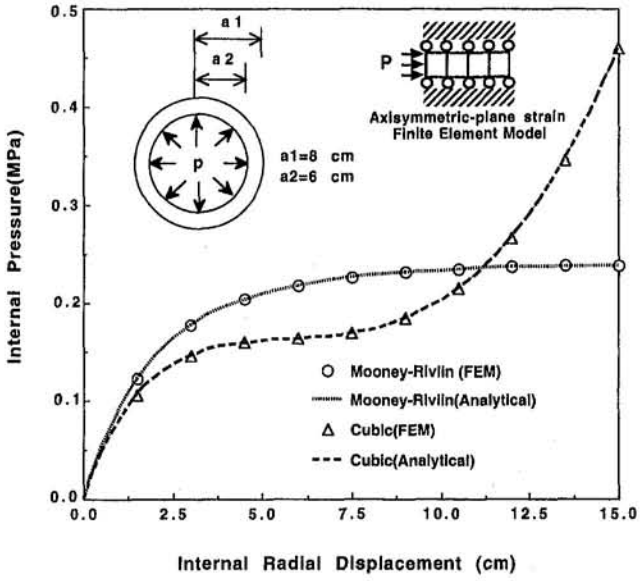

Fig. 3 Rubber cylinder subjected to internal pressure: comparison of load-displacement response using Mooney-Rivlin and Cubic models

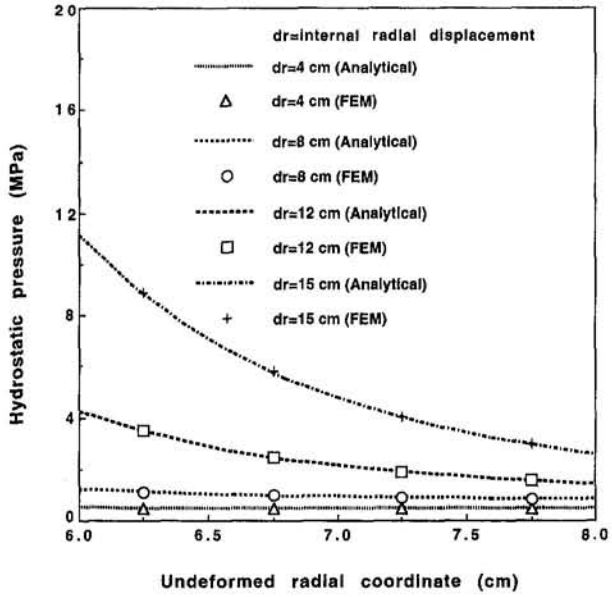

Fig. 4 Rubber cylinder subjected to internal pressure: comparison of hydrostatic pressure calculated from finite element and analytical solution using Cubic rubber model

and a_1 and a_2 are the outer and inner radius of the undeformed cylinder, respectively, ρ is the inner radius of the deformed cylinder, and p is the internal pressure.

This problem is modeled by four axisymmetric 9-node elements with restraints in the axial direction to reflect the plane-strain condition in the axial direction, as shown in Fig. 3. As described in Eqs. (4.1)–(4.5), a limit pressure exists if the Mooney-Rivlin model is used, i.e.,

$$P(\rho)|_{\rho\to\infty} = 2(A_{10} + A_{01}) \ln \frac{a_2}{a_1} = 0.2405 \text{ Mpa}. \quad (4.6)$$

Displacement control is used in this analysis and a total of ten steps are used to inflate the inner radius of the tube from 6 cm to 21 cm. The finite element and analytical pressure-displacement curves obtained using a Mooney-Rivlin material are compared in Fig. 3. The corresponding internal pressure at the final deformed stage is 0.23919 Mpa which is equivalent to 99.5 percent of the limit pressure. The error of finite element solution is 0.014 percent at the final deformed stage. The Cubic material model, compared to Mooney-Rivlin, demonstrates a different load-deflection characteristic, as shown in Fig. 3, due to the contribution of the higher order terms in the strain energy density function. In this analysis, 0.3 percent error is generated by the present finite element solution at the final deformed stage. The hydrostatic pressure distributions at various deformation states are plotted in Fig. 4 and results are satisfactory.

4.2 Simple Torsion of a Solid Rubber Cylinder. A simple torsion is generated by rotating the two end surfaces of a solid cylinder in their own planes about the axis of the cylinder without axial motion. This problem discusses the amount of axial force needed to be applied to the twisted rubber cylinder in order to maintain it in simple torsion. The solution of this problem has been discussed by Rivlin (1949) where the resulting force N acting along the axis of the cylinder is given by

$$N = \pi\phi^2 \int_0^a 2r^3 \left(\frac{\partial W}{\partial I_1} + 2\frac{\partial W}{\partial I_2} \right) dr \quad (4.7)$$

where ϕ is the amount of torsional angle per unit length and a is the radius of the cylinder. The dimension of this problem is described in Fig. 5. Since the twisted angle per unit axial length in simple torsion is constant, only one layer of elements is used in the axial direction. A total of 48 27-node elements, as shown in Fig. 5, are used in this problem.

The axial forces calculated by finite element using Mooney-Rivlin and Cubic strain energy density functions are compared against analytical solutions in Fig. 5. The agreement between finite element and analytical solutions is good. The axial stress distributions at various deformed states calculated using the Cubic model are plotted in Fig. 6 and the results are satisfactory. In this problem, as can be understood from Eq. (4.7), that the initial slope of the $N - \theta$ curve is proportional to $C_{10} + 2C_{01}$. Hence, the Mooney-Rivlin model demonstrates a stiffer response compared to that of the Cubic model, as shown in Fig. 5.

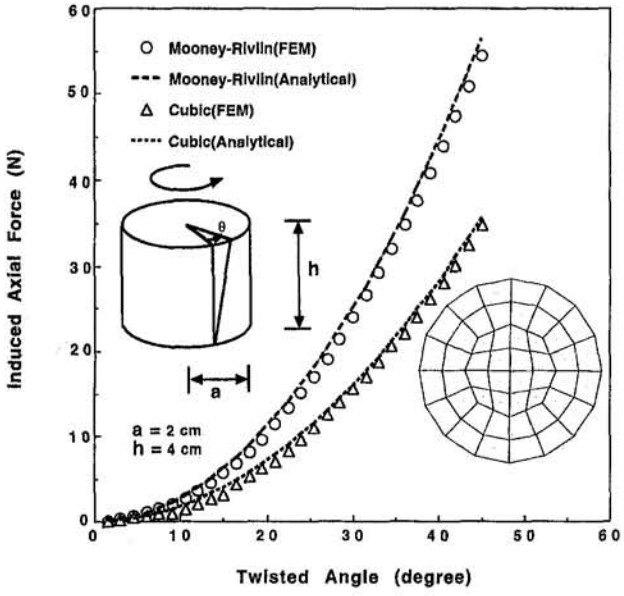

Fig. 5 Rubber solid cylinder subjected to simple torsion: comparison of induced axial force versus twisted angle using Mooney-Rivlin and Cubic models

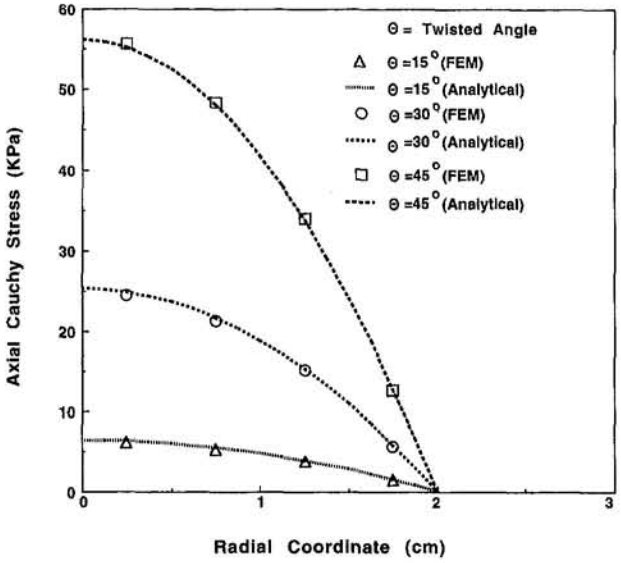

Fig. 6 Rubber solid cylinder subjected to simple torsion: comparison of axial stress distribution calculated from finite element and analytical solution using Cubic model

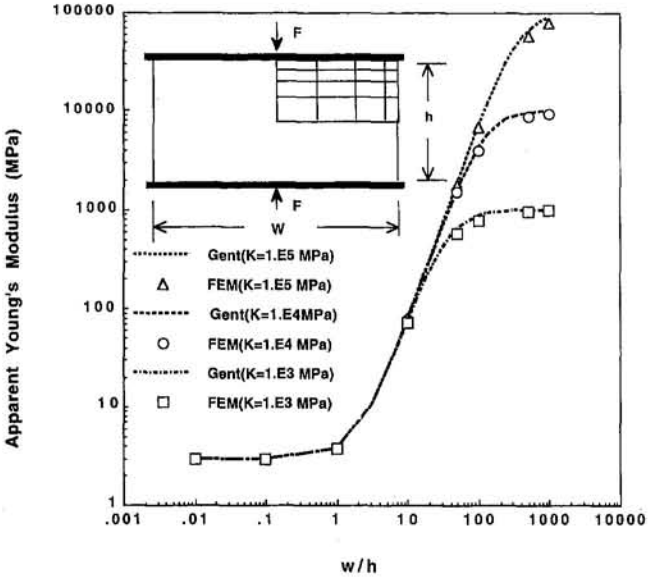

Fig. 8 Plane-strain bonded rubber unit under compression: effect of width/height ratio on the apparent Young's modulus

5 Application to Engineering Elastomers

The study in Section 3 indicates that the Cubic strain energy density is more appropriate for large and complex deformation problems. Only Cubic strain energy density function is considered in problems 5.1 and 5.2. The problem definition of example 5.3 is taken from Tseng et al. (1987) where material constants were characterized using the Mooney-Rivlin model.

5.1 Bulk Deformation of Bonded Rubber. The mechanical behavior of bonded rubber under compression has been studied since the 1950s by Payne (1957), Gent and Lindley (1959), Gent and Meinecke (1970), and others by using the concept of "apparent Young's modulus." In their work, the apparent Young's modulus for a bonded rubber unit was estimated from the Young's modulus of an unbonded rubber unit in conjunction with the shape effect. Based on small deformation assumption, the force-displacement relation of a bonded rubber unit can be described by

$$F = E_a A_0 e \tag{5.1}$$

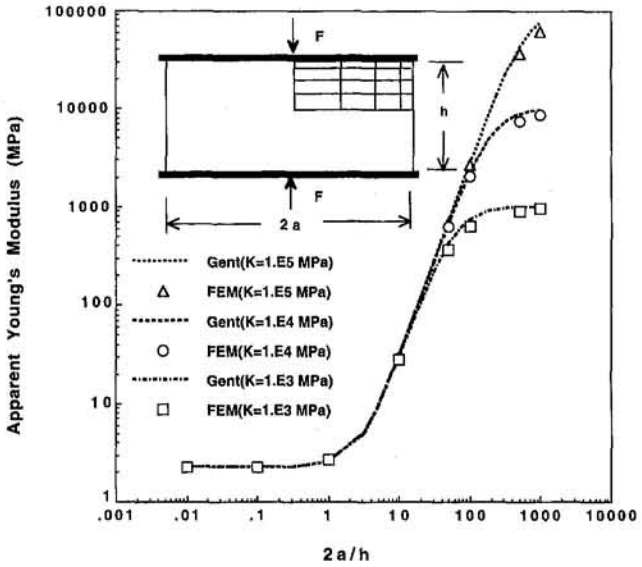

Fig. 7 Axisymmetric bonded rubber unit under compression: effect of width/height ratio on the apparent Young's modulus

and

$$E_a = E_u(1 + \beta S^2) \tag{5.2}$$

where A_0 is the undeformed cross sectional area, e is the compressive (tensile) axial strain, $\beta = 2$ for axisymmetric case and $\beta = 1$ for plane-strain case, S is the shape factor defined by the ratio of loaded area to unloaded area, E_a is called the apparent Young's modulus and E_u is the Young's modulus of unbonded rubber components:

$$E_u = \alpha\left(\frac{\partial W}{\partial I_1} + \frac{\partial W}{\partial I_2}\lambda^{-1}\right)\Bigg|_{I_1=I_2=3}, \tag{5.3}$$

where $\alpha = 6$ for axisymmetric case and $\alpha = 8$ for plane-strain case with λ^{-1} dropped. Gent also mentioned that rubber is not fully incompressible and the bulk modulus, k, should be considered in the deformation of rubber, especially when the rubber unit is very thin and bonded. The apparent Young's modulus E_a in Eq. (5.1) should be replaced by $E_{a'}$ in the following form:

$$\frac{1}{E_{a'}} = \frac{1}{E_a} + \frac{1}{k}. \tag{5.4}$$

The finite element method is used to study this problem. For

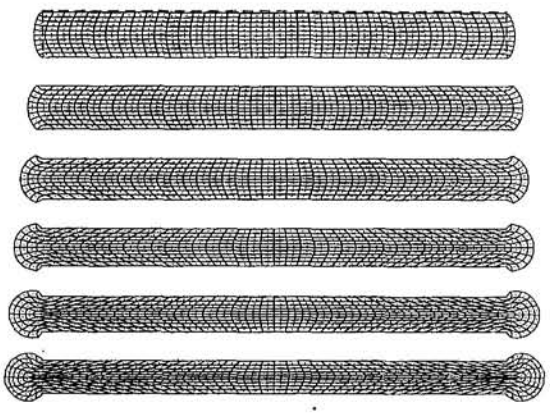

Fig. 9 Deformed geometries of axisymmetric bonded rubber unit under compression

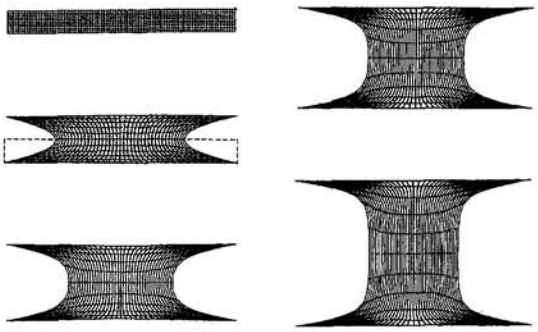

Fig. 10 Deformed geometries of axisymmetric bonded rubber unit under tension

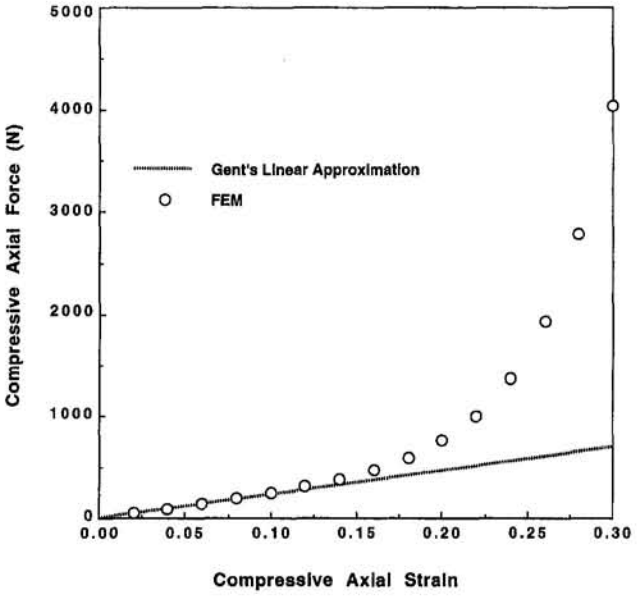

Fig. 11(*a*) Load-deflection curve of axisymmetric rubber unit under compression: comparison of finite element solution and Gent's linear approximation

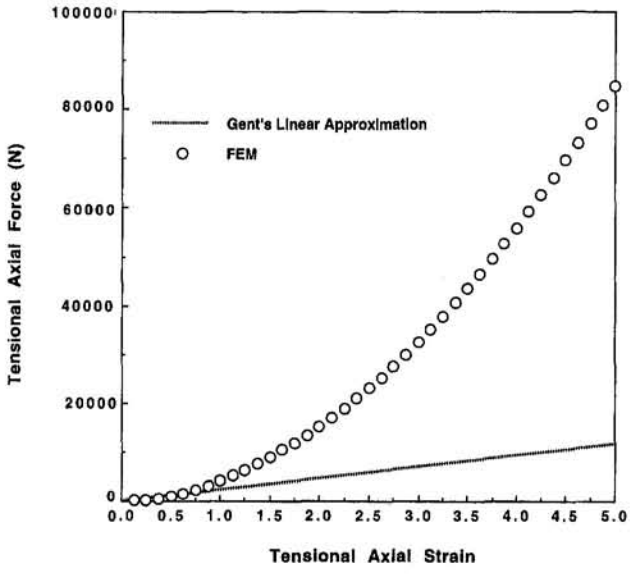

Fig. 11(*b*) Load-deflection curve of axisymmetric rubber unit under tension: comparison of finite element solution and Gent's linear approximation

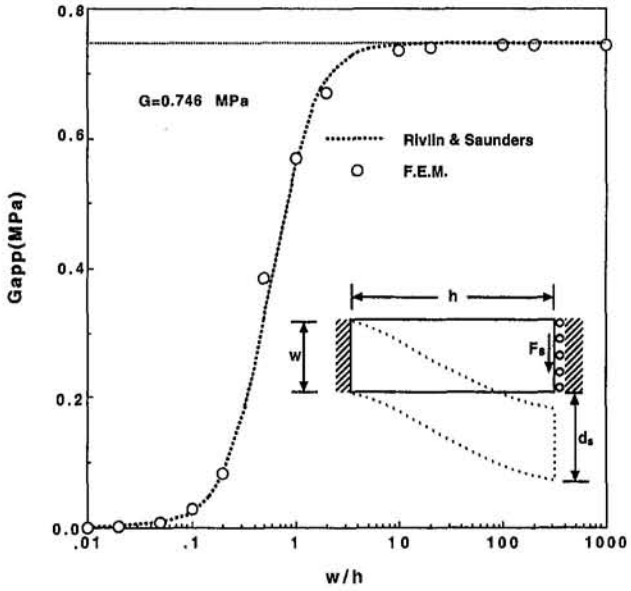

Fig. 12 Plane-strain rubber component under shear and bending deformation: effect of structural geometry on the apparent shear modulus

the comparison with Gent's approximation, linear analysis is first performed. In this problem, rubber behavior is described by the Cubic strain energy density function and a mesh of 4 × 4 nine-node elements, as shown in Fig. 7, are used in the finite element analysis. Three arbitrarily selected bulk moduli, 1×10^3, 1×10^4, 1×10^5 Mpa (representing bulk modulus to shear modulus ratios of 1.34×10^3, 1.34×10^4, 1.34×10^5, respectively) are used to study the effect of bulk modulus on the structural stiffness. In this study, the width/height ratio of the rubber units varies from 0.01 to 1000. The finite element results are compared against Gent's approximation in Figs. 7–8 for axisymmetric and plane-strain cases, respectively, and very good agreement is observed. In the small width/height range, the apparent Young's modulus approaches that of the unbonded case. As the width/height ratio becomes very large, the apparent Young's modulus approaches to bulk modulus and this deformation is called bulk compression (tension).

Large deformation analysis of bonded rubber with $k = 10^4$ Mpa under tension and compression are also performed. An axisymmetric rubber unit with diameter to height ratio of 10 is used in the analysis. Five and 20 elements in the axial and radial directions, respectively, are used to model one quarter of the structure. In the compression analysis, rubber squeezes out at the edges as shown in Fig. 9 and the analysis terminated when the rubber is compressed more than 30 percent of the original thickness, due to excessive mesh entanglement. In the tension analysis, rubber is stretched up to five times the original thickness and the deformed geometries are plotted in Fig. 10. The nonlinear finite element load-displacement curves are also compared against Gent's linear approximate solution in Figs. 11(*a*) and 11(*b*) for compression and tension, respectively. The highly nonlinearities predicted by finite element suggested that Gent's solution is applicable only at around 50 percent strain in tension and around 15 percent strain in compression in this problem.

This problem also demonstrates the need of using a nearly incompressible formulation for rubber that is not purely incompressible. As indicated in Figs. 7–8, the magnitude of bulk modulus determines the structural stiffness in bonded thin rubber components. The finite element formulation that can accurately captures bulk deformation is essential to the success in the analysis of highly confined engineering elastomers. The present formulation decouples the distortional and dilatational

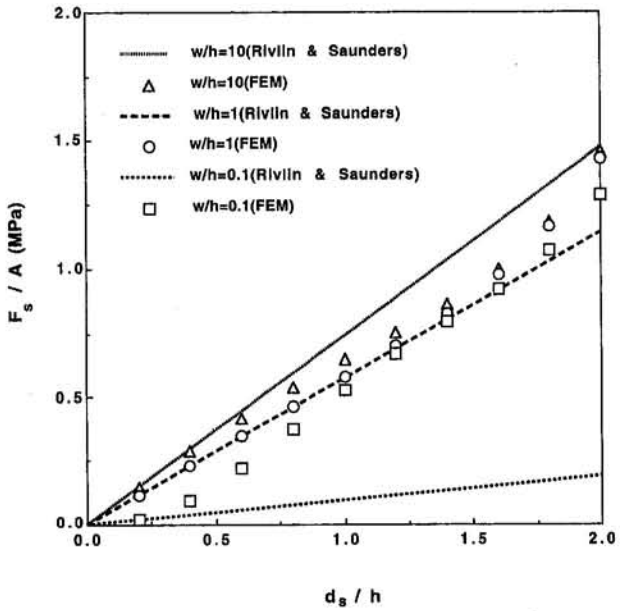

Fig. 13 Load-deflection curves of plane strain rubber component under shear and bending deformation: comparison of finite element solution and linear approximation by Rivlin and Saunders

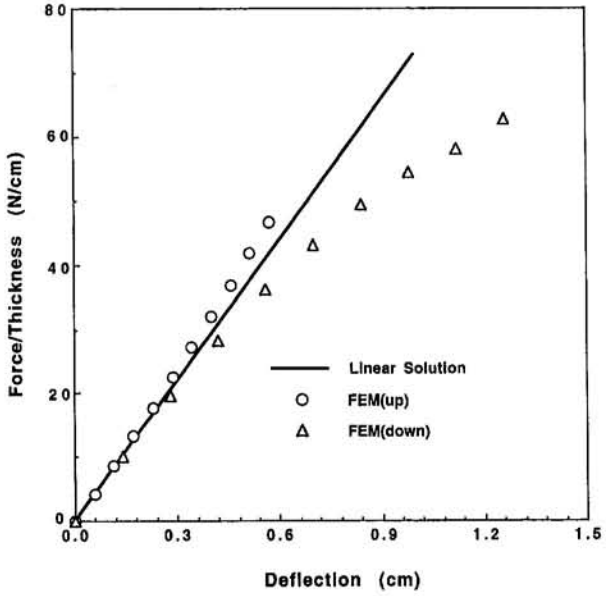

Fig. 15 Load-deflection characteristics of engine mount under vertical load: comparison of finite element results and linear approximation

strain energy and therefore performs quite well in this analysis as shown in Figs. 7–8.

5.2 Combined Shear and Bending of Rubber Components. Rivlin and Saunders (1951) considered the deformation to result from the sum of a simple shear deformation and a bending deformation based on small deformation theory, and proposed an apparent shear modulus given by

$$G_{\text{app}} = G/\left(1 + \frac{h^2}{36K^2}\right) \tag{5.5}$$

$$G = 2\left(\frac{\partial W}{\partial I_1} + \frac{\partial W}{\partial I_2}\right)\Big|_{I_1=I_2=3} \tag{5.6}$$

where K is the radius of gyration, G is the shear modulus, and h is defined in Fig. 12 where the problem definition is given. The finite element nodes on the left end are totally fixed and those on the right end are restrained in the horizontal direction and are forced to move with the same amount of vertical displacement. Plane-strain rubber components with w/h ranging from 0.01 to 1000 (w is fixed as 1 cm) are included in the analysis. Total of 20 × 6 9-node elements are used in the analysis. The finite element apparent shear modulus is calculated by

$$G_{\text{app}} = \frac{F_s h}{A d_s} = (F_s/A)/(d_s/h) \tag{5.7}$$

where F_s and d_s are defined in Fig. 12 and A is the rubber cross-sectional area. The finite element results agree well with

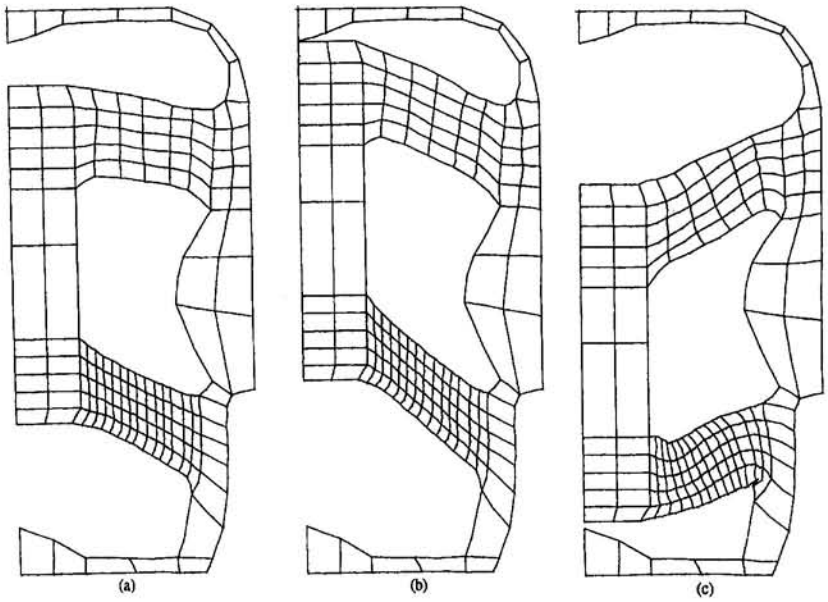

Fig. 14 Undeformed and deformed geometries of engine mount under vertical upward and downward loading

solutions provided by Rivlin and Saunders shown in Fig. 12. When w/h is small, the deformation is primarily in bending and therefore the apparent shear modulus is low. On the other hand, a thin rubber unit with very high w/h value deforms essentially in shear and hence the apparent shear modulus approaches to the shear modulus of rubber.

The nonlinear shear-bending behavior of the rubber unit with $w = 1$ cm and w/h equal to 0.1, 1, 10 is also studied. The nonlinear load-deflection curves predicted by finite element are compared against the linear approximation obtained from Eq. (5.5) in Fig. 13. As indicated in Fig. 13, when deflection is small, rubber unit with $w/h = 0.1$ deforms primarily in bending and the corresponding apparent shear modulus is much lower than that of the other two units. While at large deflection, due to the boundary conditions imposed on the right end of the structure, all three rubber units deform primarily in shear and therefore exhibit similar apparent shear moduli at large strain.

5.3 Analysis of Engine Mount. This engine mount problem is taken from Tseng et al. (1987) (shown in Fig. 14(a)) where rubber was characterized using the Mooney-Rivlin model with $A_{10} = 0.145$ Mpa and $A_{01} = 0.062$ Mpa. Since only limited raw stress-strain data were provided, we did not to recharacterize rubber properties using the Cubic model.

The outer metal box of the engine mount is connected to the car body, therefore the outer metal/rubber interface is totally fixed in the finite element model. The inner metal piece is attached to the engine and, hence, the external load is applied to the inner metal. In this example, the vertical load-deflection characteristic of the engine mount is analyzed.

When vertical load is applied to the inner metal, only half of the structure is modeled, due to symmetry. With a longer travel distance in the downward motion than in the upward motion, the lower rubber leg is expected to undergo large and complicated deformation; and, therefore, a finer mesh is used to model the lower rubber leg. Figure 14 shows that the rubber legs are under a combination of compression (tension), shear and bending deformation. Some localized buckling occurs near the lower right corner of the lower rubber leg. The finite element load-deflection curves are compared against the linear solution obtained from Eqs. (5.1)–(5.7) in Fig. 15. The finite element solution correlates well with the linear approximation at small deformations. The nonlinear load-deflection behavior is due to the severe bending and shear in the rubber components as have discussed in the previous examples.

6 Conclusions

The purpose of this paper is to demonstrate the performance of the present method and to study some of the typical structural characteristics of engineering elastomers using the present method in conjunction with several strain energy density functions. Numerical procedures of the projection method that can be implemented into displacement based finite element programs is presented. A series of numerical examples demonstrate the performance of the present method.

The comparison of finite element analysis results with experimental data in tension-compression and shear suggests that the higher order strain energy density functions are required to capture stress-strain nonlinearities. In the problems with strong boundary constraints, the structural stiffness is largely depending on the magnitude of rubber bulk modulus. This type of analysis requires a finite element formulation that is capable of capturing the bulk deformation of rubber. With the decomposition of the strain energy density function and the use of pressure projection method, the present formulation performs effectively in these classical finite elasticity problems as well as bulk deformation problems.

References

Chang, T. Y. P., Saleeb, A. F., and Li, G., 1991, "Large Strain Analysis of Rubber-like Materials Based on a Perturbed Lagrangian Variational Principle," *Computational Mechanics,* Vol. 8, pp. 221–233.

Chen, J. S., and Pan, C., 1996, "A Pressure Projection Method for Nearly Incompressible Rubber Hyperelasticity, Part I: Theory," ASME JOURNAL OF APPLIED MECHANICS, Vol. 63, pp. 862–868.

Gent, A. N., and Lindley, P. B., 1959, "The Compression of Bonded Rubber Blocks," *Proceedings of the Institution of Mechanical Engineers,* Vol. 173, pp. 111–122.

Gent, A. N., and Meinecke, E. A., 1970, "Compression, Bending and Shear of Bonded Rubber Blocks," *Polymer Engineering and Science,* Vol. 10, pp. 48–53.

James, A. G., Green, A., and Simpson, G. M., 1975a, "Strain Energy Functions of Rubber. I. Characterization of Gum Rubber," *Journal of Applied Polymer Science,* Vol. 19, pp. 2033–2058.

James, A. G., and Green, A., 1975b, "Strain Energy Functions of Rubber. II. The Characterization of Filled Vulcanizates," *Journal of Applied Ploymer Science,* Vol. 19, pp. 2319–2330.

Liu, W. K., Belytschko, T., and Chen, J. S., 1988, "Nonlinear Versions of Flexurally Superconvergent Elements," *Computer Methods in Applied Mechanics and Engineering,* Vol. 71, pp. 241–256.

Payne, A. R., 1957, "Dynamic Properties of Vulcanized Rubber: 5. Shape Factors and Functions in Rubber Engineering," *Research Association of British Rubber Manufactures,* Research Report No. 84, Shawbury.

Rivlin, R. S., 1949, "Large Elastic Deformation of Isotropic Materials, Part VI, Further Results in the Theory of Torsion, Shear and Flexure," *Philosophical Transactions of the Royal Society of London,* Vol. A242, pp. 173–195.

Rivlin, R. S., 1956, "Rheology Theory and Applications," F. R. Eirich, ed., Academic Press, New York, Vol. 1, Chapter 10, pp. 351–385.

Rivlin, R. S., and Saunders, D. W., 1951, "Large Elastic Deformation of Isotropic Materials. Part 7, Experiments on the Deformation of Rubber," *Philosophical Transactions of the Royal Society of London,* Vol. A243, pp. 251–288.

Rivlin, R. S., and Saunders, D. W., 1949, "Cylindrical Shear Mountings," *Transactions, I.R.I.,* Vol. 24, p. 296.

Scharnhorst, T., and Pian, T. H. H., 1978, "Finite Element Analysis of Rubber-like Materials by a Mixed Model," *International Journal for Numerical Methods in Engineering,* Vol. 12, pp. 665–676.

Tschoegl, N. W., 1971, "Constitutive Equations for Elastomers," *Journal of Applied Ploymer Science,* Vol. A1, pp. 1959–1970.

Tseng, N. T., Satyamurthy, K., and Chang, J. P., 1987, "Nonlinear Finite Element Analysis of Rubber Based Products," The 131st Meeting of the Rubber Division, American Chemical Society, Montreal, Quebec, Canada, May 26–29.

Yeoh, O. H., 1990, "Characterization of Elastic Properties of Carbon Black Filled Rubber Vulcanizates," *Rubber Chemistry and Technology,* Vol. 63, pp. 792–805.

Yeoh, O. H., 1993, "Some Forms of the Strain Energy Function for Rubber," *Rubber Chemistry and Technology,* Vol. 66, pp. 754–771.

Yeoh, O. H., 1994, personal communication.

On the Eigenstrain Problem of a Spherical Inclusion With an Imperfectly Bonded Interface

Z. Zhong
Department of Engineering Mechanics and Technology, Tongji University, Shanghai 200092, P. R. China

S. A. Meguid
Engineering Mechanics and Design Laboratory, Department of Mechanical Engineering, University of Toronto, Ontario M5S 1A4, Canada
Mem. ASME.

This article provides a comprehensive theoretical treatment of the eigenstrain problem of a spherical inclusion with an imperfectly bonded interface. Both tangential and normal discontinuities at the interface are considered and a linear interfacial condition, which assumes that the tangential and the normal displacement jumps are proportional to the associated tractions, is adopted. The solution to the corresponding eigenstrain problem is obtained by combining Eshelby's solution for a perfectly bonded inclusion with Volterra's solution for an equivalent Somigliana dislocation field which models the interfacial sliding and normal separation. For isotropic materials, the Burger's vector of the equivalent Somigliana dislocation is exactly determined; the solution is explicitly presented and its uniqueness demonstrated. It is found that the stresses inside the inclusion are not uniform, except for some special cases.

1 Introduction

Since Eshelby (1957) published his celebrated paper on the transformation of ellipsoidal inclusion, eigenstrain problems of inclusion have been successfully employed in predicting the mechanical behavior of heterogeneous materials, such as composites and polycrystals. The importance of eigenstrain is manifested by its presence in broad applications encompassing real nonelastic strains, such as thermal expansion strains, phase transformation strains, initial strains, plastic strains, and misfit strains. Alternatively, equivalent imaginary eigenstrains can also be introduced to model the inhomogeneities of heterogeneous materials.

In view of the above, the inclusion problem has received considerable attention; as evidenced by the work of Willis (1964, 1965), Walpole (1967), Asaro and Barnett (1975), Mura (1987, 1988), Nemat-Nasser and Hori (1993), and others. However, most of the available solutions concerning the inclusion problem assume perfect bonding at the interface between the matrix and the inclusion; i.e., the displacement and the interfacial traction are continuous across the interface. This condition is sometimes violated and consequently, the resulting formulations become inadequate in describing the mechanical behavior of the inclusion problem for situations involving the debonding of fibers in composites and the grain boundary sliding in polycrystalline materials.

The imperfect bonding of the interface has an important influence on the mechanical behavior of composite solids. But the interfacial region is so complex that some simplified interfacial conditions must be introduced to enable the formulation of the problem. One of the most useful interfacial conditions is the assumption that the normal and the tangential displacement discontinuities at the interface are directly proportional to the corresponding traction components which are continuous for reason of equilibrium. This kind of linear interfacial condition has been employed by many researchers (e.g., Ghahremani, 1980; Benveniste, 1985; Achenbach and Zhu, 1989; Gosz et al., 1991; Hashin, 1991; Qu, 1993). Hashin (1991) gave a physical explanation of it and correlated the interface parameters to the interphase elastic moduli.

For the eigenstrain problem of inclusion with an imperfectly bonded interface, Mura and his collaborators obtained several pioneering results (e.g., Mura and Furuhashi, 1984; Mura et al., 1985; Jasiuk et al., 1987). However, they only considered the free sliding interfacial conditions, with vanishing normal displacement discontinuity and shear traction at the interface. For more realistic interfacial conditions, no conclusive results have been reported, except for that of Huang et al. (1993) who treated the interfacial sliding condition in an average sense and that of Qu (1993) who approximated the solution using the first term of a series expansion.

In the present paper, both normal and tangential interfacial displacement discontinuities are considered. The basic equations are obtained for the eigenstrain problem of a spherical inclusion with an imperfectly bonded interface described by a linear interfacial condition. The solution is decomposed into two parts: Eshelby's solution for a perfectly bonded inclusion and Volterra's solution for an equivalent Somigliana dislocation field which models the interfacial sliding and normal separation. For elastically isotropic materials, the Burger's vector of the equivalent Somigliana dislocation is exactly determined and the solution is explicitly presented.

2 Problem Formulation

Consider an infinitely extended elastic medium D containing a uniform eigenstrain ϵ_{ij}^* in a spherical inclusion Ω with an imperfectly bonded interface $\partial\Omega$, as depicted in Fig. 1.

If we consider infinitesimal deformation, the total strain ϵ_{ij} can then be written as the sum of the elastic strain ϵ_{ij}^e and the eigenstrain ϵ_{ij}^*,

$$\epsilon_{ij} = \epsilon_{ij}^e + \epsilon_{ij}^*. \tag{1}$$

Since the total strain must be compatible, then

$$\epsilon_{ij} = (u_{i,j} + u_{j,i})/2 \tag{2}$$

where $u_{i,j} = \partial u_i / \partial x_j$, u_i is the displacement and x_j the Cartesian coordinate of point $\mathbf{x}$. The stress σ_{ij} is related to the strain ϵ_{ij} by Hooke's law, such that

Contributed by the Applied Mechanics Division of THE AMERICAN SOCIETY OF MECHANICAL ENGINEERS for publication in the ASME JOURNAL OF APPLIED MECHANICS.

Discussion on this paper should be addressed to the Technical Editor, Professor Lewis T. Wheeler, Department of Mechanical Engineering, University of Houston, Houston, TX 77204-4792, and will be accepted until four months after final publication of the paper itself in the ASME JOURNAL OF APPLIED MECHANICS.

Manuscript received by the ASME Applied Mechanics Division, July 12, 1995; final revision, Oct. 17, 1995. Associate Technical Editor: D. M. Barnett.

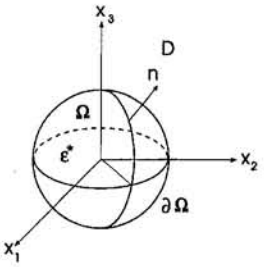

Fig. 1 A schematic of the spherical inclusion problem

$$\sigma_{ij} = C_{ijkl}(\epsilon_{kl} - \epsilon^*_{kl}) \quad \text{in} \quad \Omega \tag{3}$$

$$\sigma_{ij} = C_{ijkl}\epsilon_{kl} \quad \text{in} \quad D - \Omega \tag{4}$$

where C_{ijkl} is the elastic modulus tensor, and the repeated indices imply summation. The equations of equilibrium for stress are

$$\sigma_{ij,j} = 0 \quad \text{in} \quad D. \tag{5}$$

For an imperfectly bonded interface, the interfacial traction remains continuous, while both the normal and the tangential displacements experience a jump across the interface. Accordingly, the interfacial conditions can be written as

$$[\sigma_{ij}]n_j = 0 \tag{6}$$

$$[u_i](\delta_{ik} - n_i n_k) = f(T_k) \tag{7}$$

$$[u_i]n_i n_k = g(N_k) \tag{8}$$

where $[\cdot] = (\text{out}) - (\text{in})$, n_i is the outward unit normal on the interface, and $T_i = \sigma_{kj}n_j(\delta_{ik} - n_i n_k)$ and $N_i = \sigma_{kj}n_k n_j n_i$ represent the shear and the normal traction at the interface, respectively. δ_{ik} denotes the Kronecker δ, f and g are functions. If we consider the case of elastic isotropy and assume that f and g are linear functions such that the tangential and normal displacement discontinuities at the interface are directly proportional to their corresponding interfacial tractions, then the interfacial conditions (7) and (8) reduce to

$$[u_i](\delta_{ik} - n_i n_k) = \alpha T_k \tag{9}$$

$$[u_i]n_i n_k = \beta N_k \tag{10}$$

where α and β denote the compliance in the tangential and the normal directions of the interface, respectively. According to our definition of $[u_i]$, α and β should be positive. It can be seen that α and β characterize the interfacial behavior. For example, the case where $\alpha = 0$ and $\beta = 0$ corresponds to a perfectly bonded interface. When $\beta = 0$ and $\alpha \neq 0$, only interfacial sliding takes place with normal contact remaining intact. Furthermore, the case where $\beta = 0$ and $\alpha \to \infty$ represents the free sliding interface. This kind of linear interfacial condition, in essence, corresponds to modeling the imperfectly bonded interface by a linear spring-layer of vanishing thickness.

The solution of Eqs. (2)–(6), (9), (10) completely determines the eigenstrain problem of an inclusion with a linear imperfectly bonded interface.

Let we now examine the uniqueness of the solution of the current problem. Assume that there are two solutions for displacements, u_i^1 and u_i^2, with σ_{ij}^1 and σ_{ij}^2 being the corresponding stresses. Assuming that $\Delta u_i = u_i^1 - u_i^2$ and $\Delta\sigma_{ij} = \sigma_{ij}^1 - \sigma_{ij}^2$, then

$$\Delta\sigma_{ij,j} = 0 \quad \text{in} \quad D \tag{11}$$

$$\Delta\sigma_{ij} = C_{ijkl}\Delta u_{k,l} \quad \text{in} \quad D \tag{12}$$

$$[\Delta\sigma_{ij}]n_j = 0 \quad \text{on} \quad \partial\Omega \tag{13}$$

$$[\Delta u_i](\delta_{ik} - n_i n_k) = \alpha(\Delta T_k) \quad \text{on} \quad \partial\Omega \tag{14}$$

$$[\Delta u_i]n_i n_k = \beta(\Delta N_k) \quad \text{on} \quad \partial\Omega \tag{15}$$

and $\Delta u_i = 0$ at infinity. Let us introduce a positive-definite quantity such that

$$I = \int_\Omega \Delta\sigma_{ij}\Delta u_{i,j}dV + \int_{D-\Omega} \Delta\sigma_{ij}\Delta u_{i,j}dV \geq 0 \tag{16}$$

If I is transformed using Gauss' theorem to surface integrals together with Eqs. (14) and (15), we can show that

$$I = -\int_{\partial\Omega} [\alpha(\Delta T_i)(\Delta T_i) + \beta(\Delta N_i)(\Delta N_i)]dS \leq 0 \tag{17}$$

since $\alpha \geq 0$ and $\beta \geq 0$. Combining (16) and (17), we have $I = 0$, and conclude that $\sigma_{ij}^1 = \sigma_{ij}^2$. Moreover, if the impotent terms related to the rigid-body translation and rotation are excluded, we also have $u_i^1 = u_i^2$.

3 Solution

The solution of the above problem can be divided into two main parts:

(1) The solution of the eigenstrain problem of inclusion with perfectly bonded interface. This is the well-known Eshelby's solution, which has the following general form for the displacement, strain, and stress fields,

$$u_i^E(\mathbf{x}) = -\int_\Omega C_{mnkl}\epsilon^*_{kl}(\mathbf{x})G_{im,n}(\mathbf{x} - \mathbf{x}')dV' \tag{18}$$

$$\epsilon_{ij}^E(\mathbf{x}) = -\frac{1}{2}\int_\Omega C_{mnkl}\epsilon^*_{kl}(\mathbf{x}')[G_{im,nj}(\mathbf{x} - \mathbf{x}') + G_{jm,ni}(\mathbf{x} - \mathbf{x}')]dV' \tag{19}$$

$$\sigma_{ij}^E(\mathbf{x}) = -C_{ijmn}\left[\int_\Omega C_{pqkl}\epsilon^*_{kl}(\mathbf{x}')G_{mp,qn}(\mathbf{x} - \mathbf{x}')dV' + \epsilon^*_{mn}(\mathbf{x})\right] \tag{20}$$

where $dV' = dx_1'dx_2'dx_3'$, and $G_{ij}(\mathbf{x})$ is the Green's function of elasticity for infinite medium.

(2) The displacement field caused by the interfacial sliding and normal separation can be modeled by an equivalent Somigliana dislocation field whose Burger's vector is defined as

$$b_i = -[u_i]. \tag{21}$$

This dislocation field is given by Volterra's solution as being

$$u_i^V(\mathbf{x}) = \int_{\partial\Omega} C_{mnkl}b_l(\mathbf{x}')n_k(\mathbf{x}')G_{im,n}(\mathbf{x} - \mathbf{x}')dS'. \tag{22}$$

Following Asaro (1975), b_n is extended to the interior of Ω and we can express (22) in another form using Gauss' theorem; i.e.,

$$u_i^V(\mathbf{x}) = -\int_\Omega C_{mnkl}\epsilon^{**}_{kl}(\mathbf{x}')G_{im,n}(\mathbf{x} - \mathbf{x}')dV' + b_i(\mathbf{x}) \tag{23}$$

$$\epsilon^{**}_{kl} = -(b_{k,l} + b_{l,k})/2 \tag{24}$$

where $b_i(\mathbf{x})$ is only defined for $\mathbf{x}$ inside Ω; if $\mathbf{x}$ is outside Ω, $b_i(\mathbf{x})$ is taken as zero.

The corresponding strains and stresses are

$$\epsilon_{ij}^V(\mathbf{x}) = -\frac{1}{2}\int_\Omega C_{mnkl}\epsilon^{**}_{kl}(\mathbf{x}')[G_{im,nj}(\mathbf{x} - \mathbf{x}') + G_{jm,ni}(\mathbf{x} - \mathbf{x}')]dV' - \epsilon^{**}_{ij}(\mathbf{x}) \tag{25}$$

$$\sigma_{ij}^V = -C_{ijmn}\left[\int_\Omega C_{pqkl}\epsilon_{kl}^{**}(\mathbf{x}') G_{mp,qn}(\mathbf{x}-\mathbf{x}')dV' + \epsilon_{mn}^{**}(\mathbf{x})\right] \quad (26)$$

where $\epsilon_{ij}^{**}(\mathbf{x})$ is taken as zero except when $\mathbf{x}$ is inside Ω.

Therefore, the solution of the eigenstrain problem of a spherical inclusion with the linear interfacial condition can be expressed as

$$u_i = u_i^E + u_i^V \quad (27)$$

$$\epsilon_{ij} = \epsilon_{ij}^E + \epsilon_{ij}^V \quad (28)$$

$$\sigma_{ij} = \sigma_{ij}^E + \sigma_{ij}^V. \quad (29)$$

The interfacial traction continuity condition (6) is satisfied automatically, since it is satisfied by Eshelby's solution and Volterra's solution respectively, whereas the Burgers' vector b_i needs to satisfy the interfacial conditions (9) and (10).

The exact solution for this problem has not been obtained before, except for the free sliding case ($\alpha \to \infty$ and $\beta = 0$) solved originally by Mura and Furuhashi (1984) and corrected later by Furuhashi et al. (1991). In this case, Eshelby's solution (1957) for the uniform eigenstrain problem of spherical inclusion with a perfectly bonded interface gives

$$\sigma_{ij}^E = -\frac{2\mu}{45(1-\nu)}[10(1+\nu)\epsilon_{ll}^*\delta_{ij} + 3(7-5\nu)e_{ij}^*] \quad (30)$$

for point $\mathbf{x}$ inside Ω, where μ is the shear modulus, ν Poisson's ratio, and e_{ij}^* is the deviatoric part of ϵ_{ij}^*. Accordingly, the shear and the normal tractions at the interface resulting from Eshelby's solution can be expressed as

$$T_i^E = -\frac{2\mu(7-5\nu)}{15(1-\nu)a^3}(a^2 e_{ij}^* x_j - e_{kl}^* x_k x_l x_i) \quad (31)$$

$$N_i^E = -\frac{4\mu(1+\nu)}{9(1-\nu)a}\epsilon_{ll}^* x_i - \frac{2\mu(7-5\nu)}{15(1-\nu)a^3}e_{kl}^* x_k x_l x_i \quad (32)$$

where a is the radius of the spherical inclusion Ω defined by $x_i x_i \le a^2$ for which $n_i = x_i/a$.

The Burgers' vector can be assumed to have the form

$$b_i = a^2\lambda x_i + a^2 A_{ij}x_j + B_{kl}x_k x_l x_i \quad (33)$$

where λ is a scalar, A_{ij} and B_{ij} are symmetric deviatoric tensors with the requirement that $A_{ll} = B_{ll} = 0$. λ, A_{ij}, and B_{ij} need to be determined using (9) and (10). Hence, the tangential and the normal displacement discontinuities at the interface can be written as

$$[u_i](\delta_{ik} - n_i n_k) = -a^2 A_{ik}x_i + A_{ij}x_i x_j x_k \quad (34)$$

$$[u_i]n_i n_k = -a^2\lambda x_k - (A_{ij} + B_{ij})x_i x_j x_k. \quad (35)$$

The stress inside the inclusion caused by Somigliana dislocation (detailed derivation of the stress field inside and outside the inclusion is provided in the Appendix) is

$$\sigma_{ij}^V = \frac{4\mu(1+\nu)}{3(1-\nu)}a^2\lambda\delta_{ij} + \frac{2\mu(7-5\nu)}{15(1-\nu)}a^2 A_{ij} + \frac{24\mu\nu}{5(1-\nu)}B_{kl}x_k x_l\delta_{ij} - \frac{4\mu}{35(1-\nu)} \times [2(7-4\nu)B_{ij}|x|^2 + 12\nu B_{il}x_l x_j + 12\nu B_{jl}x_l x_i - 2(7-10\nu)B_{kl}x_k x_l\delta_{ij} - \tfrac{7}{3}(5-\nu)a^2 B_{ij}]. \quad (36)$$

In this case, the shear and the normal tractions at the interface corresponding to Volterra's solution are

$$T_i^V = \frac{2\mu(7-5\nu)}{15(1-\nu)a}(a^2 A_{ij}x_j - A_{kl}x_k x_l x_i) - \frac{4\mu(7+19\nu)}{105(1-\nu)a}(a^2 B_{ij}x_j - B_{kl}x_k x_l x_i) \quad (37)$$

$$N_i^V = \frac{4\mu(1+\nu)}{3(1-\nu)}a\lambda x_i + \frac{2\mu(7-5\nu)}{15(1-\nu)a}A_{kl}x_k x_l x_i + \frac{4\mu(35+11\nu)}{105(1-\nu)a}B_{kl}x_k x_l x_i. \quad (38)$$

Therefore, the total shear and normal tractions at the interface are

$$T_i = T_i^E + T_i^V \quad (39)$$

$$N_i = N_i^E + N_i^V. \quad (40)$$

Substituting (31), (32), (34), (35), and (37)–(40) into (9) and (10), and comparing the corresponding terms of the polynomial, one can deduce that

$$\lambda = \frac{\beta_0 k_1}{3(1+\beta_0 k_1)}\left(\frac{\epsilon_{ll}^*}{a^2}\right) \quad (41)$$

$$A_{ij} = \frac{\alpha_0 k_2 + \alpha_0\beta_0 k_2(k_3+k_4)}{1+\alpha_0(k_2+k_3)+\beta_0 k_4+\alpha_0\beta_0 k_2(k_3+k_4)}\left(\frac{e_{ij}^*}{a^2}\right) \quad (42)$$

$$B_{ij} = \frac{(\beta_0-\alpha_0)k_2}{1+\alpha_0(k_2+k_3)+\beta_0 k_4+\alpha_0\beta_0 k_2(k_3+k_4)}\left(\frac{e_{ij}^*}{a^2}\right) \quad (43)$$

with

$$\alpha_0 = \frac{\mu\alpha}{a} \quad \beta_0 = \frac{\mu\beta}{a}$$

$$k_1 = \frac{4(1+\nu)}{3(1-\nu)} \quad k_2 = \frac{2(7-5\nu)}{15(1-\nu)}$$

$$k_3 = \frac{4(7+19\nu)}{105(1-\nu)} \quad k_4 = \frac{4(35+11\nu)}{105(1-\nu)}.$$

It is noted that A_{ij} and B_{ij} satisfy the requirement that $A_{ll} = B_{ll} = 0$, since $e_{ll}^* = 0$. Once λ, A_{ij}, and B_{ij} are determined, the displacement, strain, and stress fields inside and outside the inclusion can be calculated using (27)–(29).

Although the interfacial tractions at the imperfectly bonded interface remain continuous, as in the perfectly bonded case, the stress discontinuity across the interface is not the same. This discontinuity at the interface can be obtained by a slight modification of the methods developed earlier by Hill (1961) and Walpole (1978) as summarized below.

The displacement gradient $u_{i,j}$ has a jump across the interface which can be expressed as

$$[u_{i,j}] = -b_{i,j} + c_i n_j \quad (44)$$

such that it satisfies the relation

$$[u_{i,j}]dx_j = -b_{i,j}dx_j \quad (45)$$

where dx_j is a line element on the interface and c_i is an unknown vector to be determined. The stress discontinuity can be written as

$$[\sigma_{ij}] = C_{ijkl}([u_{k,l}] - [\epsilon^*_{kl}]) \tag{46}$$

where $[\epsilon^*_{kl}] = \epsilon^*_{ij}(\text{out}) - \epsilon^*_{ij}(\text{in})$, $\epsilon^*_{kl}(\text{out}) = 0$ and $\epsilon^*_{kl}(\text{in}) = -\epsilon^*_{kl}$. By means of (48) and (50) we obtain

$$[\sigma_{ij}]n_j = C_{ijkl}(-b_{k,l} + c_k n_l + \epsilon^*_{ij})n_j = 0 \tag{47}$$

where n_i is the outward unit normal on the interface. The solution for c_i can thus be obtained such that

$$c_i = C_{jkmn}(b_{m,n} - \epsilon^*_{ij})n_k N_{ij}(\mathbf{n})/D(\mathbf{n}) \tag{48}$$

where $N_{ij}(\mathbf{n})$ and $D(\mathbf{n})$ are the respective co-factor and determinant of the matrix $C_{ikjl}n_k n_l$ (known as the acoustical tensor for the direction $\mathbf{n}$). For isotropic materials,

$$D(\mathbf{n}) = \mu^2(\lambda + 2\mu)n^6 \tag{49}$$

$$N_{ij}(\mathbf{n}) = \mu n^2[(\lambda + 2\mu)\delta_{ij}n^2 - (\lambda + \mu)n_i n_j] \tag{50}$$

where λ and μ are Lamé constants, and $n = (n_i n_i)^{1/2}$. Thus, the stress discontinuity at the interface can be expressed as

$$[\sigma_{ij}] = C_{ijkl}[C_{pqmn}(b_{m,n} - \epsilon^*_{mn})n_q n_l N_{kp}(\mathbf{n})/D(\mathbf{n}) - (b_{k,l} - \epsilon^*_{kl})]. \tag{51}$$

The above expression has been derived earlier by Huang et al. (1993) for the case of pure sliding without normal separation.

Let us now examine the elastic strain energy stored in body D which contains an imperfectly bonded inclusion Ω. In this case, the total elastic strain energy W can be described as

$$W = W^E + W^V \tag{52}$$

with

$$W^E = -\tfrac{1}{2}\int_\Omega \sigma^E_{ij}\epsilon^*_{ij}\,dV \tag{53}$$

and

$$W^V = -\tfrac{1}{2}\int_\Omega \sigma^V_{ij}\epsilon^*_{ij}\,dV. \tag{54}$$

In the above expressions, W^E represents the elastic strain energy for the perfectly bonded inclusion model of Eshelby, while W^V is the elastic strain energy induced by the imperfectly bonded interface. When ϵ^*_{ij} is uniform inside Ω, W^E and W^V can be simplified to

$$W^E = -\tfrac{1}{2}V\sigma^E_{ij}\epsilon^*_{ij} \tag{55}$$

$$W^V = -\tfrac{1}{2}V\bar{\sigma}^V_{ij}\epsilon^*_{ij} \tag{56}$$

where σ^E_{ij} is the uniform stress inside the perfectly bonded inclusion given by (30), $\bar{\sigma}^V_{ij}$ is the average of the stress σ^V_{ij} over the inclusion Ω, and V is the volume of Ω.

4 Discussion

Let us now examine some aspects of the solution. When $\alpha = \beta = 0$, we have $\lambda = A_{ij} = B_{ij} = 0$ which means that there exist no displacement discontinuities at the interface, and the solution reduces to Eshelby's solution for spherical inclusion with a perfectly bonded interface. For the case of pure sliding without normal separation across the interface, we have $\beta = 0$, leading to $\lambda = 0$, and

$$A_{ij} = -B_{ij} = \frac{\alpha_0 k_2}{1 + \alpha_0(k_2 + k_3)}\left(\frac{e^*_{ij}}{a^2}\right) = \frac{14\alpha_0(7 - 5\nu)}{6\alpha_0(21 + \nu) + 105(1 - \nu)}\left(\frac{e^*_{ij}}{a^2}\right). \tag{57}$$

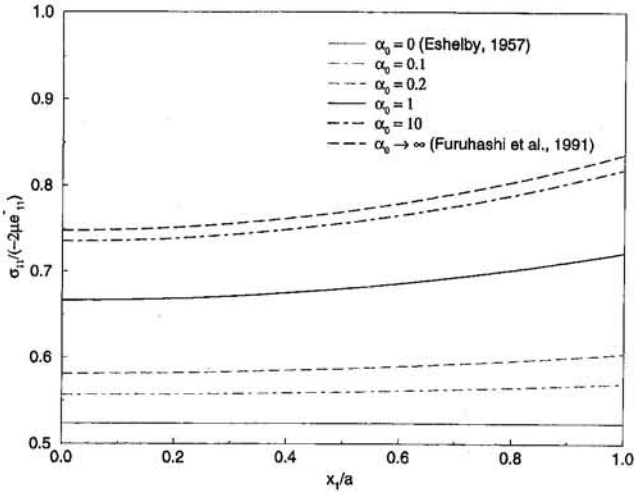

Fig. 2 Variation of the normal stress $\sigma_{11}/(-2\mu e^*_{11})$ versus x_1/a ($x_2 = x_3 = 0$) in the case of pure sliding ($\beta_0 = 0$) with only $e^*_{11} \neq 0$

Furthermore,

$$A_{ij} = -B_{ij} = \frac{7(7 - 5\nu)}{3(21 + \nu)}\left(\frac{e^*_{ij}}{a^2}\right) \tag{58}$$

for the case where $\alpha \to \infty$, which corresponds to the free sliding interface. This solution is identical to the result of Furuhashi et al. (1991). If $\alpha = 0$ and $\beta \neq 0$, only normal separation without sliding occurs at the interface. In this case, $A_{ij} = 0$ and

$$\lambda = \frac{\beta_0 k_1}{3(1 + \beta_0 k_1)}\left(\frac{\epsilon^*_{ll}}{a^2}\right) \tag{59}$$

$$B_{ij} = \frac{\beta_0 k_2}{1 + \beta_0 k_4}\left(\frac{e^*_{ij}}{a^2}\right). \tag{60}$$

If $e^*_{ij} = 0$ and $\epsilon^*_{ll} \neq 0$, then according to Eqs. (41)–(43), we have $A_{ij} = B_{ij} = 0$ and $\lambda \neq 0$. This means that volumetric-type eigenstrains only cause normal separation (no sliding) and the stress inside the inclusion is uniform. Nevertheless, if $\epsilon^*_{ll} = 0$ and at least one component of e^*_{ij} is not vanishing, say $e^*_{12} \neq 0$, accordingly, $A_{12} \neq 0$, $B_{12} \neq 0$, $\lambda = 0$, which implies that the deviatoric component of the eigenstrain results in normal separation as well as sliding at the interface.

Unlike the perfectly bonded interface, our solution indicates that the stresses inside the inclusion of an imperfectly bonded interface are not uniform, except for two special cases. The first case is that where $e^*_{ij} = 0$ and $\epsilon^*_{ll} \neq 0$, which has already been discussed. In the second case where $\alpha = \beta \neq 0$, we can find that uniform stresses do appear inside the inclusion, since $B_{ij} = 0$.

Figure 2 shows the variation of the normal stress $\sigma_{11}/(-2\mu e^*_{11})$ along the x_1-axis ($0 \leq x_1/a \leq 1$, $x_2 = x_3 = 0$), when $e^*_{11} \neq 0$ and other components of the eigenstrain are nonexistent. In this case, we set $\beta_0 = 0$ (pure sliding) and α_0 is allowed to vary from 0 to ∞, with $\nu = 0.3$. This figure demonstrates the nonuniform distribution of the stress inside the inclusion. Only for the case where $\alpha_0 = 0$ (Eshelby's solution) does the stress distribution become uniform. The figure also shows the case where $\alpha_0 \to \infty$, which corresponds to the earlier attempt made by Furuhashi et al. (1991). The results reveal that the nonuniformity of the stress σ_{11} increases with the increase of α_0.

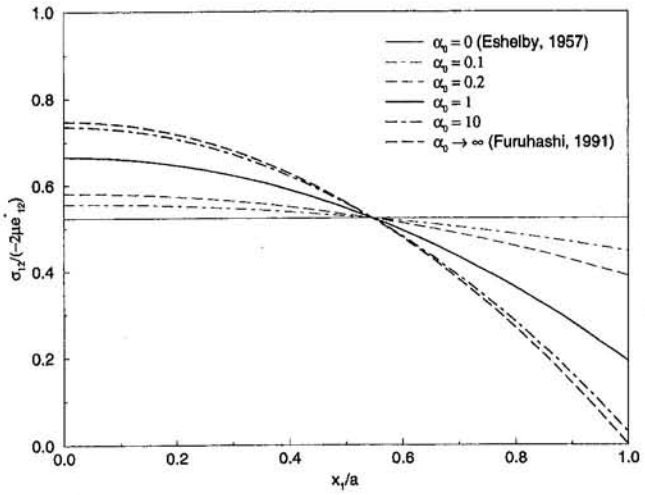

Fig. 3 Variation of the shear stress $\sigma_{12}/(-2\mu e^*_{12})$ versus x_1/a ($x_2 = x_3 = 0$) in the case of pure sliding ($\beta_0 = 0$) with only $e^*_{12} \neq 0$

Figure 3 shows the variation of the shear stress $\sigma_{12}/(-2\mu e^*_{12})$ along the x_1-axis when $e^*_{12} \neq 0$ and other components of the eigenstrain are zero. In this case, when the interface is perfectly bonded ($\alpha_0 = 0$), no variation in the shear stress $\sigma_{12}/(-2\mu e^*_{12})$ distribution along x_1/a is observed. However, for $\alpha_0 > 0$, the shear stress decreases with an increase in x_1/a. When α_0 approaches ∞, this decrease in the shear stress becomes rather rapid, indicative of the large variation in the stress field in the inclusion.

Figure 4 gives the variation of the elastic strain energy W/W^E versus the interfacial sliding compliance α_0, when $e^*_{11} \neq 0$ and other components of the eigenstrain are nonexistent, with $\beta_0 = 0$ and $\nu = 0.3$. The results indicate that the elastic strain energy decreases rapidly with an increase in α_0 for small values of α_0 ($\alpha_0 \leq 1$). For greater values of α_0, W/W^E decreases asymptotically to approach the free sliding interface case ($\alpha_0 \to \infty$).

5 Concluding Remarks

A new solution is obtained for the eigenstrain problem of spherical inclusion with an imperfectly bonded interface. The interface is modeled by a linear spring-layer of vanishing thickness. Both the tangential and the normal displacement discontinuities are taken into account. The formulations are obtained using Eshelby's solution of the eigenstrain problem for perfectly bonded inclusion and Volterra's solution for an equivalent Somigliana dislocation field to model the interfacial sliding and normal separation. For isotropic materials, the Burger's vector of the equivalent Somigliana dislocation is determined exactly and the resulting solution is explicitly presented. Unlike the case of a perfectly bonded interface, the stresses inside the imperfectly bonded inclusion are not uniform, except for some special cases.

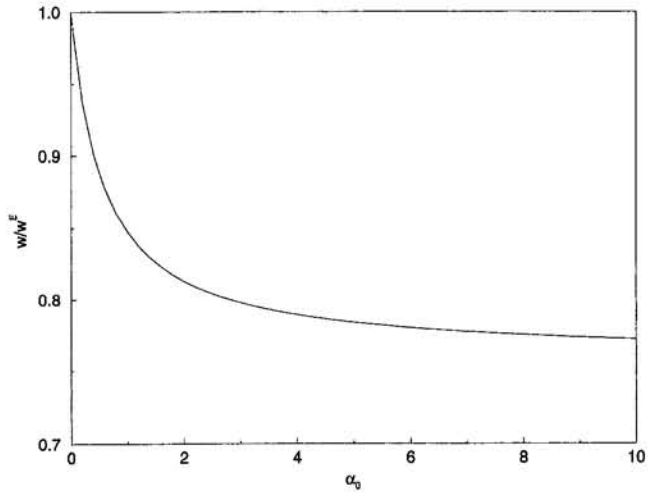

Fig. 4 Variation of the elastic strain energy W/W^E versus the interfacial compliance α_0

Acknowledgments

This work was supported by the Natural Sciences and Engineering Research Council of Canada (NSERC) and ALCOA Foundation of USA. Partial support of Dr. Z. Zhong has also been provided by the National Natural Science Foundation of China. Finally, the authors wish to thank Professor D. M. Barnett for his helpful comments.

References

Achenbach, J. D., and Zhu, H., 1989, "Effect of Interfacial Zone on Mechanical Behavior and Failure of Fiber-Reinforced Composites," *J. Mech. Phys. Solids*, Vol. 37, pp. 381–393.

Asaro, R. J., 1975, "Somigliana Dislocations and Internal Stresses; with Application to Second Phase Hardening," *Int. J. Engng. Sci.*, Vol. 13, pp. 271–286.

Asaro, R. J., and Barnett, D. M., 1975, "The Non-uniform Transformation Strain Problem for an Anisotropic Ellipsoidal Inclusion," *J. Mech. Phys. Solids*, Vol. 23, pp. 77–83.

Benveniste, Y., 1985, "The Effect Mechanical Behavior of Composite Materials with Imperfect Contact between the Consitituents," *Mechanics of Materials*, Vol. 4, pp. 197–208.

Eshelby, J. D., 1957, "The Determination of the Elastic Field of an Ellipsoidal Inclusion and Related Problems," *Proc. Roy. Soc.*, Vol. A241, pp. 376–396.

Furuhashi, R., Mori, T., and Mura, T., 1991, "On Stress Field inside the Spherical Sliding Inclusions," *Research Report of Meiji University*, No. 4(60), pp. 39–43.

Ghahremani, F., 1980, "Effect of Grain Boundary Sliding on Anelasticity of Polycrystals," *Int. J. Solids Struc.*, Vol. 16, pp. 825–845.

Gosz, M., Moran, B., and Achenbach, J. D., 1991, "Effect of a Viscoelastic Interface on the Transverse Behavior of Fiber-reinforced Composites," *Int. J. Solids Struct.*, Vol. 27, pp. 1757–1771.

Hashin, Z., 1990, "Thermoelastic Properties of Fiber Composites with Imperfect Interface," *Mechanics of Materials*, Vol. 8, pp. 333–348.

Hashin, Z., 1991, "The Spherical Inclusion with Imperfect Interface," ASME JOURNAL OF APPLIED MECHANICS, Vol. 58, pp. 444–449.

Hill, R., 1961, "Discontinuity Relations in Mechanics of Solids," *Progress in Solid Mechanics*, Vol. 2, North-Holland, Amsterdam, p. 245.

Huang, J. H., Furuhashi, R., and Mura, T., 1993, "Frictional Sliding Inclusions," *J. Mech. Phys. Solids*, Vol. 41, pp. 247–265.

Jasiuk, I., Tsuchida, E., and Mura, T., 1987, "The Sliding Inclusion under Shear," *Int. J. Solids Struc.*, Vol. 23, pp. 1373–1385.

Mura, T., and Furuhashi, R., 1984, "The Elastic Inclusion With a Sliding Interface," ASME JOURNAL OF APPLIED MECHANICS, Vol. 51, pp. 308–310.

Mura, T., Jasiuk, I., and Tsuchida, B., 1985, "The Stress Field of a Sliding Inclusion," *Int. J. Solids Struc.*, Vol. 21, pp. 1165–1179.

Mura, T., 1987, *Micromechanics of Defects in Solids*, 2nd rev. ed., Martinus Nijhoff.

Mura, T., 1988, "Inclusion Problems," ASME *Appl. Mech. Rev.*, Vol. 41, No. 1, pp. 15–19.

Nemat-Nasser, S., and Hori, M., 1993, *Micromechanics: Overall Properties of Heterogeneous Materials*, North-Holland, Amsterdam.

Qu, J., 1993, "The Effect of Slightly Weakened Interfaces on the Overall Elastic Properties of Composite Materials," *Mechanics of Materials*, Vol. 14, pp. 269–281.

Walpole, L. J., 1967, "The Elastic Field of an Inclusion in an Anisotropic Medium," *Proc. Roy. Soc.*, Vol. A300, pp. 235–251.

Walpole, L. J., 1978, "A Coated Inclusion in an Elastic Medium," *Math. Proc. Camb. Phil. Soc.*, Vol. 83, pp. 495–506.

Willis, J. R., 1964, "Anisotropic Elastic Inclusion Problems," *Q. J. Mech. Appl. Math.*, Vol. 17, pp. 157–174.

Willis, J. R., 1965, "Dislocations and Inclusions," *J. Mech. Phys. Solids*, Vol. 13, pp. 377–395.

APPENDIX

Derivation of u_i^V and σ_{ij}^V

Substituting Green's function for isotropic elastic medium

$$G_{ij}(\mathbf{x} - \mathbf{x}') = \frac{\delta_{ij}}{4\pi\mu|\mathbf{x} - \mathbf{x}'|} - \frac{1}{16\pi\mu(1-\nu)} \frac{\partial^2}{\partial x_i \partial x_j} |\mathbf{x} - \mathbf{x}'| \quad \text{(A1)}$$

into (23), we have

$$u_i^V = \frac{1}{8\pi(1-\nu)}[\psi_{kl,kli} - 2\nu\phi_{ll,i} - 4(1-\nu)\phi_{il,l}] + b_i \quad \text{(A2)}$$

$$\phi_{ij} = \int_\Omega \frac{\epsilon_{ij}^{**}(\mathbf{x}')dV'}{|\mathbf{x}-\mathbf{x}'|} \quad \text{(A3)}$$

$$\psi_{ij} = \int_\Omega \epsilon_{ij}^{**}(\mathbf{x}')|\mathbf{x}-\mathbf{x}'|\,dV' \quad \text{(A4)}$$

where b_i is given by (33) for point $\mathbf{x}$ inside Ω and $b_i = 0$ for point $\mathbf{x}$ outside Ω, and ϵ_{ij}^{**} is given in (24).

Substituting (33) into (24) leads to

$$\epsilon_{ij}^{**} = -a^2(\lambda\delta_{ij} + A_{ij}) - B_{il}x_l x_j - B_{jl}x_l x_i - B_{kl}x_k x_l \delta_{ij}. \quad \text{(A5)}$$

Introducing the following integrals

$$I_1 = \int_\Omega \frac{dV'}{|\mathbf{x}-\mathbf{x}'|} \quad \text{(A6)}$$

$$J_1 = \int_\Omega |\mathbf{x}-\mathbf{x}'|\,dV' \quad \text{(A7)}$$

$$I_{ij} = \int_\Omega \frac{x_i' x_j' dV'}{|\mathbf{x}-\mathbf{x}'|} \quad \text{(A8)}$$

$$J_{ij} = \int_\Omega x_i' x_j' |\mathbf{x}-\mathbf{x}'|\,dV', \quad \text{(A9)}$$

we obtain the following expressions for ϕ_{ij} and ψ_{ij}:

$$\phi_{ij} = -a^2(\lambda\delta_{ij} + A_{ij})I_1 - B_{il}I_{lj} - B_{jl}I_{li} - B_{kl}I_{kl}\delta_{ij} \quad \text{(A10)}$$

$$\psi_{ij} = -a^2(\lambda\delta_{ij} + A_{ij})J_1 - B_{il}J_{lj} - B_{jl}J_{li} - B_{kl}J_{kl}\delta_{ij}. \quad \text{(A11)}$$

IF Ω is a spherical domain, it can be shown that

$$I_1 = 2\pi\left(a^2 - \frac{|\mathbf{x}|^2}{3}\right) \quad \text{(A12)}$$

$$J_1 = \frac{2\pi}{3}\left(\frac{3a^4}{2} + a^2|\mathbf{x}|^2 - \frac{|\mathbf{x}|^4}{10}\right) \quad \text{(A13)}$$

$$I_{ij} = \pi\left(\frac{|\mathbf{x}|^4}{35} - \frac{2a^2|\mathbf{x}|^2}{15} + \frac{a^4}{3}\right)\delta_{ij} - 2\pi\left(\frac{|\mathbf{x}|^2}{7} - \frac{a^2}{5}\right)x_i x_j \quad \text{(A14)}$$

$$J_{ij} = \frac{2\pi}{9}\left(\frac{|\mathbf{x}|^6}{105} - \frac{3a^2|\mathbf{x}|^4}{35} + \frac{3a^4|\mathbf{x}|^2}{5} + a^6\right)\delta_{ij} - \pi\left(\frac{|\mathbf{x}|^4}{63} - \frac{2a^2|\mathbf{x}|^2}{35} + \frac{a^4}{15}\right)x_i x_j \quad \text{(A15)}$$

for point $\mathbf{x}$ inside Ω, and

$$I_1 = \frac{4\pi a^3}{3|\mathbf{x}|} \quad \text{(A16)}$$

$$J_1 = \frac{4\pi a^3}{3}\left(|\mathbf{x}| + \frac{a^2}{5|\mathbf{x}|}\right) \quad \text{(A17)}$$

$$I_{ij} = \frac{4\pi a^5}{15}\left(\frac{1}{|\mathbf{x}|} - \frac{a^2}{7|\mathbf{x}|^3}\right)\delta_{ij} + \frac{4\pi a^7}{35|\mathbf{x}|^5}x_i x_j \quad \text{(A18)}$$

$$J_{ij} = \frac{4\pi a^5}{105}\left(7|\mathbf{x}| + \frac{2a^2}{|\mathbf{x}|} - \frac{a^4}{9|\mathbf{x}|^3}\right)\delta_{ij} - \frac{4\pi a^7}{105}\left(\frac{1}{|\mathbf{x}|^3} - \frac{a^2}{3|\mathbf{x}|^5}\right)x_i x_j \quad \text{(A19)}$$

for point $\mathbf{x}$ outside Ω.

In this case, u_i^V can be obtained by using (A2)–(A5), (A10)–(A19),

$$u_i^V = \frac{2(1-2\nu)}{3(1-\nu)}a^2\lambda x_i + \frac{7-5\nu}{15(1-\nu)}a^2 A_{il}x_l + \frac{4(7-10\nu)}{35(1-\nu)}B_{kl}x_k x_l x_i - \left[\frac{4(7-4\nu)}{35(1-\nu)}|\mathbf{x}|^2 - \frac{2(5-\nu)}{15(1-\nu)}a^2\right]B_{il}x_l \quad \text{(A20)}$$

for point $\mathbf{x}$ inside Ω, and

$$u_i^V = -\frac{(1+\nu)a^5}{3(1-\nu)}\lambda x_i\frac{1}{|\mathbf{x}|^3} + \frac{a^5}{6(1-\nu)}\left[3a^2A_{kl}x_k x_l x_i\frac{1}{|\mathbf{x}|^7} - 3A_{kl}x_k x_l x_i\frac{1}{|\mathbf{x}|^5} - \frac{6a^2}{5}A_{il}x_l\frac{1}{|\mathbf{x}|^5} - 2(1-2\nu)A_{il}x_l\frac{1}{|\mathbf{x}|^3}\right] - \frac{a^5}{30(1-\nu)}\left[\frac{30\nu a^2}{7}B_{kl}x_k x_l x_i\frac{1}{|\mathbf{x}|^7} + 6B_{kl}x_k x_l x_i\frac{1}{|\mathbf{x}|^5} - \frac{12\nu a^2}{7}B_{il}x_l\frac{1}{|\mathbf{x}|^5} + 4(1-2\nu)B_{il}x_l\frac{1}{|\mathbf{x}|^3}\right] \quad \text{(A21)}$$

for point $\mathbf{x}$ outside Ω.

The stress caused by Somigliana dislocation can be obtained using $\sigma_{ij}^V = C_{ijkl}u_{k,l}^V$, such that

$$\sigma_{ij}^V = \frac{4\mu(1+\nu)}{3(1-\nu)}a^2\lambda\delta_{ij} + \frac{2\mu(7-5\nu)}{15(1-\nu)}a^2A_{ij} + \frac{24\mu\nu}{5(1-\nu)}B_{kl}x_k x_l\delta_{ij} - \frac{4\mu}{35(1-\nu)} \times \left[2(7-4\nu)B_{ij}|x|^2 + 12\nu B_{il}x_l x_j + 12\nu B_{jl}x_l x_i - 2(7-10\nu)B_{kl}x_k x_l\delta_{ij} - \frac{7}{3}(5-\nu)a^2B_{ij}\right] \quad \text{(A22)}$$

for point $\mathbf{x}$ inside Ω, and

$$\sigma_{ij}^V = -\frac{2\mu(1+\nu)a^5}{3(1-\nu)}\lambda\left(\frac{\delta_{ij}}{|\mathbf{x}|^3} - \frac{3x_i x_j}{|\mathbf{x}|^5}\right) + \frac{\mu a^7}{1-\nu}\left[A_{kl}\frac{x_k x_l}{|\mathbf{x}|^7}\delta_{ij} + (A_{il}x_l x_j + A_{jl}x_l x_i)\frac{1}{|\mathbf{x}|^7} - 7A_{kl}\frac{x_k x_l x_i x_j}{|\mathbf{x}|^9}\right] - \frac{\mu a^5}{1-\nu}\left[(1-2\nu)A_{kl}\frac{x_k x_l}{|\mathbf{x}|^5}\delta_{ij}\right.$$

$$+(A_{il}x_lx_j+A_{jl}x_lx_i)\frac{1}{|\mathbf{x}|^5}-5A_{kl}\frac{x_kx_lx_ix_j}{|\mathbf{x}|^7}\Bigg]$$

$$-\frac{2\mu a^7}{5(1-\nu)}\left[A_{ij}\frac{1}{|\mathbf{x}|^5}-\frac{5}{2}(A_{il}x_lx_j+A_{jl}x_lx_i)\frac{1}{|\mathbf{x}|^7}\right]$$

$$-\frac{2\mu(1-2\nu)a^5}{3(1-\nu)}\left[A_{ij}\frac{1}{|\mathbf{x}|^3}-\frac{3}{2}(A_{il}x_lx_j+A_{jl}x_lx_i)\frac{1}{|\mathbf{x}|^5}\right]$$

$$-\frac{2\mu\nu a^7}{7(1-\nu)}\left[B_{kl}\frac{x_kx_l}{|\mathbf{x}|^7}\delta_{ij}+(B_{il}x_lx_j+B_{jl}x_lx_i)\frac{1}{|\mathbf{x}|^7}\right.$$

$$\left.-7B_{kl}\frac{x_kx_lx_ix_j}{|\mathbf{x}|^9}\right]-\frac{2\mu a^5}{5(1-\nu)}\left[(1-2\nu)B_{kl}\frac{x_kx_l}{|\mathbf{x}|^5}\delta_{ij}\right.$$

$$+(B_{il}x_lx_j+B_{jl}x_lx_i)\frac{1}{|\mathbf{x}|^5}-5B_{kl}\frac{x_kx_lx_ix_j}{|\mathbf{x}|^7}$$

$$\left.-5B_{kl}\frac{x_kx_lx_ix_j}{|\mathbf{x}|^7}\right]+\frac{4\mu\nu a^7}{35(1-\nu)}$$

$$\times\left[B_{ij}\frac{1}{|\mathbf{x}|^5}-\frac{5}{2}(B_{il}x_lx_j+B_{jl}x_lx_i)\frac{1}{|\mathbf{x}|^7}\right]$$

$$-\frac{4\mu(1-2\nu)a^5}{15(1-\nu)}\left[B_{ij}\frac{1}{|\mathbf{x}|^3}-\frac{3}{2}(B_{il}x_lx_j+B_{jl}x_lx_i)\frac{1}{|\mathbf{x}|^5}\right] \tag{A23}$$

for point $\mathbf{x}$ outside Ω.

Thermally Induced Instability of Laminated Beams and Plates

A. Tylikowski[1]
Visiting Professor.

R. B. Hetnarski
James E. Gleason Professor,
Fellow ASME.

Department of Mechanical Engineering,
Rochester Institute of Technology,
Rochester, NY 14623

A theoretical investigation of dynamic stability for linear elastic structures due to non-uniform, time and space-dependent stochastic temperature fields is presented. The study is based on the reformulation of stochastic stability problems as a stability of Itô type equations in some appropriate Hilbert space and is adopted for stability problems of structures with time and space-dependent stochastic coefficients. Uniform stochastic stability criteria of the structure equilibrium are derived using the Liapunov direct method. The energy-like functional and the generalized Itô lemma are used to derive the sufficient stability conditions of the equilibrium state. A symmetrically laminated cross-ply plate subjected to the wide-band Gaussian temperature distribution and a laminated beam subjected to local short-time heatings are analysed in detail.

1 Introduction

Thermal buckling problems of laminated structures have been considered in the literature for the last ten years. Most papers were concerned with time-independent temperature field in the structure and a static approach was applied (cf., Boley and Weiner, 1960; Chen and Chen, 1987; Tauchert, 1987a). More recently, the problem of thermally induced vibrations of plates was investigated by Tauchert (1987b). Based on the dynamic equation of laminated plates some more general thermally induced vibration problem can be solved. The temperature in the plate is treated as a time and space-dependent stochastic field. It can be decomposed into a sum of two terms of which the first is constant in time and the second is time dependent. The temperature variations have a significant effect on the dynamic behavior and the static component of buckling load. As a result, the time-dependent components of temperature field can destabilize the unperturbed state of the structure.

The present paper examines thermal buckling of thin laminated plates due to a nonuniform, time and space-dependent stochastic temperature field. The structures are described by partial differential equations including transverse inertia terms, a dissipation of energy, and both force and moment thermal resultants. The study is based on the reformulation of stochastic stability problems as a stability of Itô-type equations in some appropriate Hilbert space and is adopted for stability problems of structures governed by partial differential equations with time and space-dependent stochastic coefficients. The uniform stochastic stability criteria of the structure equilibrium are derived using the Liapunov direct method. The method is applied without earlier finite dimensional or modal approximations. The energy-like functional is proposed; its positiveness is equivalent to the condition in which static buckling does not occur. To estimate deviations of solutions from the equilibrium state (the distance between a solution with nontrivial initial conditions and the trivial solution) a scalar measure of distance equal to the square root of the functional is introduced. The generalized Itô lemma is used to show a supermartingale property of the functional and, in consequence, to derive sufficient stability conditions of the equilibrium state. From the mathematical point of view the temperature fields are described by a wide-band Gaussian process with an arbitrary space correlation function and a sequence of local rapid increments randomly distributed over the length of the beam, having independent increments and arriving in time according to the Poisson probability distribution.

Two particular problems are analyzed in detail. The first is devoted to stability analysis of a symmetrically cross-ply laminated rectangular plate subjected to a space and time-dependent Gaussian wide-band temperature field. Assuming the symmetric temperature distribution, the thermal moment resultants vanish and there exists the undeflected state of equilibrium. For the statistically homogeneous temperature field the uniform stability condition is reduced to the static thermal buckling problem with modified plate bending stiffnesses.

The second example is devoted to a laminated beam subjected to local short-time heatings described by the Poisson measure. The explicit criterion for the uniform stochastic stability is expressed in terms of the damping coefficient, the mean arrival rate of thermal pulses, the mean square value of temperature changes, and the beam parameters.

2 Assumptions, Definitions, and Basic Equations

Consider a thin rectangular plate a by b of constant thickness h composed of layers of the same thickness of orthotropic materials bonded together. It is assumed that each layer is orthotropic and elastic. The plate thickness is small compared to its length and width. The Kirchhoff hypothesis on nondeformable normal element to the middle surface is used and the rotary and coupling inertias are neglected. The energy of general three-dimensional motion is dissipated only in the transverse motion by viscous damping with a constant proportionality coefficient β. Temperature variations change expansional strains in the plate according to the Duhamel-Neumann equation. An elastic-thermal coupling is neglected and the thermal stresses approach is used. The temperature field in the plate is assumed to be known and it can be decomposed into a time-independent and time and space-dependent components.

With the stated assumptions, thermal force and thermal moment resultants in the laminated plate are given in the form (Whitney, 1987)

[1] On leave from Warsaw University of Technology, Warsaw, Poland.

Contributed by the Applied Mechanics Division of THE AMERICAN SOCIETY OF MECHANICAL ENGINEERS for presentation at the International Mechanical Engineering Congress and Exposition, the Winter Annual Meeting of The ASME, Atlanta, GA, Nov. 17–22, 1996.

Discussion on this paper should be addressed to the Technical Editor, Professor Lewis T. Wheeler, Department of Mechanical Engineering, University of Houston, Houston, TX 77204-4792, and will be accepted until four months after final publication of the paper itself in the ASME JOURNAL OF APPLIED MECHANICS.

Manuscript received by the ASME Applied Mechanics Division, Dec. 6, 1993; final revision, Apr. 12, 1996. Associate Technical Editor: M. Taya.

Paper No. 96-WA/APM-4.

$$\begin{bmatrix} N_x^T \\ N_y^T \\ N_{xy}^T \end{bmatrix} = \int_{-h/2}^{h/2} \begin{bmatrix} \bar{Q}_{11} & \bar{Q}_{12} & \bar{Q}_{16} \\ \bar{Q}_{12} & \bar{Q}_{22} & \bar{Q}_{26} \\ \bar{Q}_{16} & \bar{Q}_{26} & \bar{Q}_{66} \end{bmatrix} \begin{bmatrix} \bar{\epsilon}_1 \\ \bar{\epsilon}_2 \\ \bar{\epsilon}_6 \end{bmatrix} dz \quad (1)$$

$$\begin{bmatrix} M_x^T \\ M_y^T \\ M_{xy}^T \end{bmatrix} = \int_{-h/2}^{h/2} \begin{bmatrix} \bar{Q}_{11} & \bar{Q}_{12} & \bar{Q}_{16} \\ \bar{Q}_{12} & \bar{Q}_{22} & \bar{Q}_{26} \\ \bar{Q}_{16} & \bar{Q}_{26} & \bar{Q}_{66} \end{bmatrix} \begin{bmatrix} \bar{\epsilon}_1 \\ \bar{\epsilon}_2 \\ \bar{\epsilon}_6 \end{bmatrix} z dz \quad (2)$$

where $\bar{\epsilon}_1$, $\bar{\epsilon}_2$, $\bar{\epsilon}_6$ are thermal expansional strains, and $\bar{Q}_{ij}$ are in-plane reduced stiffnesses of lamina.

The laminate constitutive relations, from which in-plane force N_x^i, N_y^i, N_{xy}^i and moment resultants M_x^i, M_y^i, M_{xy}^i can be calculated, are given by

$$\begin{bmatrix} N_x^i \\ N_y^i \\ N_{xy}^i \\ M_x^i \\ M_y^i \\ M_{xy}^i \end{bmatrix} = \begin{bmatrix} A_{11} & A_{12} & A_{16} & B_{11} & B_{12} & B_{16} \\ A_{12} & A_{22} & A_{26} & B_{12} & B_{22} & B_{26} \\ A_{16} & A_{26} & A_{66} & B_{16} & B_{26} & B_{66} \\ B_{11} & B_{12} & B_{16} & D_{11} & D_{12} & D_{16} \\ B_{12} & B_{22} & B_{26} & D_{12} & D_{22} & D_{26} \\ B_{16} & B_{26} & B_{66} & D_{16} & D_{26} & D_{66} \end{bmatrix} \begin{bmatrix} \epsilon_x^0 \\ \epsilon_y^0 \\ \epsilon_{xy}^0 \\ \kappa_x \\ \kappa_y \\ \kappa_{xy} \end{bmatrix} - \begin{bmatrix} N_x^T \\ N_y^T \\ N_{xy}^T \\ M_x^T \\ M_y^T \\ M_{xy}^T \end{bmatrix} \quad (3)$$

where A_{ij}, B_{ij}, D_{ij} are extensional, coupling, and bending stiffnesses, respectively. Using constitutive relations (3) and expressing the strains by the displacement state w the linear equation of motion can be derived with the trivial solution $w = w_{,t} = 0$ corresponding to the plane (undisturbed) state.

The main purpose of the paper is to examine a uniform stochastic stability of the equilibrium state. The trivial solution is called uniformly stochastically stable if the following logic sentence is true:

$$\bigwedge_{\epsilon \geq 0} \bigwedge_{\delta \geq 0} \bigvee_{r \geq 0} \|w(., 0)\| \leq r \Rightarrow P(\sup_{t \geq 0} \|w(., t)\| \geq \epsilon) \leq \delta \quad (4)$$

where $\|w(., t)\|$ is a measure of disturbed solution w from the equilibrium state. In the present analysis the direct Liapunov method is proposed to establish criteria for the uniform stability. The crucial point of the method is a construction of a suitable Liapunov functional (Tylikowski, 1986), which is positive for any motion of the analyzed system. It follows that the measure of distance can be chosen as the square root of Liapunov functional $\|w(., t)\| = V^{1/2}$.

3 Symmetrical Cross-ply Laminated Rectangular Plate due to a Space and Time-Dependent Gaussian Wide-Band Temperature Field

Consider a thin elastic cross-ply symmetrically laminated plate consisting of an odd number of orthotropic layers. Due to the geometrical and thermal orthotropy of layers the thermal expansional strains are given by

$$\begin{bmatrix} \bar{\epsilon}_1 \\ \bar{\epsilon}_2 \\ \bar{\epsilon}_6 \end{bmatrix} = \begin{bmatrix} \alpha_L \\ \alpha_T \\ 0 \end{bmatrix} T(x, y, z, t) \quad (5)$$

where α_L and α_T are linear coefficients of thermal expansion parallel and transverse to the principal material axis, and $T(x, y, z, t)$ is a temperature field. Therefore, from the material symmetry follows that $B_{ij} = 0$, $A_{16} = A_{26} = 0$.

Assume that the temperature distribution has a product form and is symmetric with respect to $z = 0$,

$$T(x, y, z, t) \equiv T^*(x, y, t) T_1(z) = T^*(x, y, t) T_1(-z). \quad (6)$$

Due to the cross-ply arrangement of layers the thermal forces can be calculated from Eqs. (1) and (5),

$$\begin{bmatrix} N_x^T \\ N_y^T \\ N_{xy}^T \end{bmatrix} = T^*(x, y, t) \int_{-h/2}^{h/2} \begin{bmatrix} Q_{11}Q_{12}\ 0 \\ Q_{12}Q_{22}\ 0 \\ 0\ \ 0\ Q_{66} \end{bmatrix} \begin{bmatrix} \alpha_L \\ \alpha_T \\ 0 \end{bmatrix} T_1(z) dz. \quad (7)$$

The thermal forces are assumed to be stochastic fields proportional to $T^*(x, y, t)$

$$\begin{bmatrix} N_x^T \\ N_y^T \\ N_{xy}^T \end{bmatrix} = T^*(x, y, t) \int_{-h/2}^{h/2} \begin{bmatrix} Q_{11}\alpha_L + Q_{12}\alpha_T \\ Q_{12}\alpha_L + Q_{22}\alpha_T \\ 0 \end{bmatrix} T_1(z) dz = T^*(x, y, t) \begin{bmatrix} k_x \\ k_y \\ 0 \end{bmatrix}. \quad (8)$$

Due to the thermal, material, and geometrical symmetry the thermal moments are equal to zero $M_x^T = M_y^T = M_{xy}^T = 0$.

Assuming that the plate in a prebuckling state is undeformed, i.e., $\kappa_x = \kappa_y = \kappa_{xy} = 0$, and using Eq. (3), we notice that the in-plane moment resultants are also equal to zero $M_x^i = M_y^i = M_{xy}^i = 0$. Relations between in-plane force resultants and thermal force resultants can be found since for the simply supported edges the midplane strains vanish. Therefore, substituting $\epsilon_x^0 = \epsilon_y^0 = \epsilon_{xy}^0 = 0$ into the first three rows of Eq. (3) the in-plane force resultants are equal to the negatives of the thermal forces

$$\begin{bmatrix} N_x^i \\ N_y^i \\ N_{xy}^i \end{bmatrix} = - \begin{bmatrix} N_x^T \\ N_y^T \\ 0 \end{bmatrix} \quad (9)$$

The plate is heated, and it is assumed that a time and space-dependent temperature field with known statistic characteristics can be calculated. With these conditions, the dynamic equation of transverse plate motion is given in the form (cf., Whitney, 1987)

$$D_{11}w_{,xxxx} + 2(D_{12} + 2D_{66})w_{,xxyy} + D_{22}w_{,yyyy} + N_x^i w_{,xx} + N_y^i w_{,yy} + \rho h w_{,tt} + 2\rho h \beta w_{,t} = 0 \quad (x, y) \in \Omega \equiv (0, a) \times (0, b). \quad (10)$$

Consider a simply supported plate with its edges immovable in the plane of the plate, i.e.,

$$w = 0, \quad M_x = 0 \quad \text{for} \quad x = 0, a \quad (11)$$

$$w = 0, \quad M_y = 0 \quad \text{for} \quad y = 0, b. \quad (12)$$

Let us divide the dynamic Eq. (10) by ρh, denote $d_{ij} = D_{ij}/\rho h$, $n = N/\rho h$, and introduce the notations

$$\Box w = d_{11}w_{,xxxx} + 2(d_{12} + 2d_{66})w_{,xxyy} + d_{22}w_{,yyyy} \quad (13)$$

$$\triangle_n w = n_{x0}^T w_{,xx} + n_{y0}^T w_{,yy} \quad \triangle_k w = k_x w_{,xx} + k_y w_{,yy}. \quad (14)$$

Assuming that the temperature is equal to the sum of a mean time-independent component T_0 and a variable component $T^*(x, y, t)$ equal to the difference of temperature from the mean. For a temporarily wide-band Gaussian process with an arbitrary space correlation function $Q_T(x_1, x_2, y_1, y_2)$, we can

rewrite the dynamic Eq. (10) as the Itô differential equation in Hilbert space X with the inner product $\langle ., . \rangle$ over a probability space

$$dw = w_{,t}dt \tag{15}$$

$$dw_{,t} = -[\Box w + \Delta_n w + 2\beta w_{,t}]dt + \Delta_k w dW \tag{16}$$

with $(x, y) \in \Omega$. Here, W is a Wiener process with values in Hilbert space Y with a mean zero and a nuclear covariance operator Q, $A:X \supset \mathcal{D}(A) \to X$, $B:X \to \mathcal{L}(Y, X)$. The operator $\Box$ corresponds to the biharmonic operator for isotropic plates. Introducing the operator notation we describe the plate vibrations as an equation in Hilbert space X

$$d\mathcal{U} = A\mathcal{U}dt + [B\mathcal{U}]dW \tag{17}$$

where $\mathcal{U} = \text{col}\,(w, w_{,t})$

$$A = \begin{bmatrix} 0 & 1 \\ -\Box - \Delta_n & -2\beta \end{bmatrix}, \quad B = \begin{bmatrix} 0 & 0 \\ \Delta_k & 0 \end{bmatrix}. \tag{18}$$

In order to examine the uniform stochastic stability of the plate equilibrium (the trivial solution $\mathcal{U} = 0$) we choose the Liapunov functional in the form

$$V = \int_\Omega \mathcal{G}(\mathcal{U}, \mathcal{U}_{,x}, \mathcal{U}_{,xx})d\Omega \tag{19}$$

where the integrand function $\mathcal{G}$ is given by

$$\mathcal{G} = w_{,t}^2 + 4\beta w_{,t}w + 4\beta^2 w^2 + d_{11}w_{,xx}^2 + 2d_{12}w_{,xx}w_{,yy} + 4d_{66}w_{,xy}^2 + d_{22}w_{,yy}^2 - n_{x0}^T w_{,x}^2 - n_{y0}^T w_{,y}^2. \tag{20}$$

According to the generalized Itô lemma in infinite dimensional spaces (cf., Curtain and Falb, 1970) the differential of functional V is equal to

$$dV = \langle V'_{\mathcal{U}}, A\mathcal{U}\rangle dt + \tfrac{1}{2}Tr([B\mathcal{U}]^* V''_{\mathcal{U}\mathcal{U}}[B\mathcal{U}]Q)dt + \langle V'_{\mathcal{U}}, [B\mathcal{U}]dW\rangle \tag{21}$$

where $Tr(.)$ denotes the trace of the operator, and $V'_{\mathcal{U}}$ and $V''_{\mathcal{U}\mathcal{U}}$ denote the first and the second Frechet derivatives of functional V, respectively,

$$\frac{\partial \mathcal{G}}{\partial \mathcal{U}} = \begin{bmatrix} 4\beta w_{,t} + 8\beta^2 w \\ 2w_{,t} + 4\beta w \end{bmatrix}, \quad \frac{\partial^2 \mathcal{G}}{\partial \mathcal{U}^2} = \begin{bmatrix} 8\beta^2 & 4\beta \\ 4\beta & 2 \end{bmatrix}. \tag{22}$$

Substituting the operator A in the first part of differential (21), and integrating by parts, we have

$$\langle V'_{\mathcal{U}}, A\mathcal{U}\rangle = -4\beta \int_\Omega [d_{11}w_{,xx}^2 + 2d_{12}w_{,xx}w_{,yy} + 4d_{66}w_{,xy}^2 + d_{22}w_{,yy}^2 - n_{x0}^T w_{,x}^2 - n_{y0}^T w_{,y}^2]d\Omega \tag{23}$$

By definition, the trace part (in Eq. (21)) is given by the formula

$$dV_{Tr} = \tfrac{1}{2}\sum_{i=1}^{\infty} \lambda_i \langle [B\mathcal{U}]e_i, V''_{\mathcal{U}\mathcal{U}}[B\mathcal{U}]e_i\rangle dt \tag{24}$$

where $\{e_i\}$ is an orthonormal basis in the space Y. Substituting the operator B and the Hessian matrix of $\mathcal{G}$ we obtain the trace part of the functional differential in the form

$$dV_{Tr} = Q_T(x, x, y, y)\Delta_k^2 w. \tag{25}$$

Proceeding similarly as in the proof of the Chebyshev inequality we may show that the equilibrium state of the plate with the time and space-dependent temperature field is uniformly stochastically stable if the following inequality is valid

$$\mathcal{B} = \int_\Omega [4\beta(d_{11}w_{,xx}^2 + 2d_{12}w_{,xx}w_{,yy} + 4d_{66}w_{,xy}^2 + d_{22}w_{,yy}^2 - n_{x0}^T w_{,x}^2 - n_{y0}^T w_{,y}^2) - Q_T(x, x, y, y)(k_x w_{,xx} + k_y w_{,yy})^2]d\Omega \geq 0. \tag{26}$$

As inequality (26) depends on all parameters of the plate and the temperature field the sufficient stability condition (26) describes the balance between the energy added to the plate by the changing temperature field and the energy extracted from the system by the damping.

The inequality (26) holds for every function w satisfying the boundary conditions (11)–(12). The functional $\mathcal{B}$ is quadratic and can be rewritten in the form

$$\mathcal{B} = \int_\Omega [(d_{11} - Q_T(x, x, y, y)k_x^2/4\beta)w_{,xx}^2 + 2(d_{12} - Q_T(x, x, y, y)k_x k_y/4\beta)w_{,xx}w_{,yy} + (d_{22} - Q_T(x, x, y, y)k_y^2/4\beta)w_{,yy}^2 + 4d_{66}w_{,xy}^2 - n_{x0}^T w_{,x}^2 - n_{y0}^T w_{,y}^2]dxdy \tag{27}$$

It constitutes the variational problem $\delta\mathcal{B} = 0$. Using the theorem on the minimum of a quadratic functional (Rektorys, 1975) the functional $\mathcal{B}$ assumes its minimum value for function satisfying the associated partial differential equation

$$\Box^* w + n_{x0}^T w_{,xx} + n_{y0}^T w_{,yy} = 0 \tag{28}$$

where the operator $\Box^*$ is defined in the following way

$$\Box^* w = [(d_{11} - Q_T(x, x, y, y)k_x^2/4\beta)w_{,xx}]_{,xx} + [(d_{12} - Q_T(x, x, y, y)k_x k_y/4\beta)w_{,yy}]_{,xx} + [(d_{12} - Q_T(x, x, y, y)k_x k_y/4\beta)w_{,xx}]_{,yy} + [(d_{22} - Q_T(x, x, y, y)k_y^2/4\beta)w_{,yy}]_{,yy} + 4d_{66}w_{,xxyy} \tag{29}$$

The problem is self-adjoint as for every pair of elements u and w satisfying the boundary conditions (11)–(12) we have

$$\int_0^a \int_0^b w\Box^* u dxdy = \int_0^a \int_0^b u\Box^* w dxdy \tag{30}$$

Therefore the sufficient dynamic stability condition for the thermally induced vibration is reduced to the self-adjoint eigenvalue problem described by the fourth-order partial differential operator $\Box^*$ with the space-dependent coefficients.

Equations (26) and (28) represent the main results of this section. They allow to perform specific calculations.

Example. Consider a square plate composed of a large number of orthotropic layers with a thermal field having the same properties in x and y direction, i.e., $n_{x0}^T = n_{y0}^T$, $k_x = k_y$. The temperature distribution has the space correlation function of the form

$$Q_T(x, x, y, y) = Q_T \sin\frac{\pi x}{a} \sin\frac{\pi y}{a} \tag{31}$$

Due to the thermal symmetry, Eq. (26) reduces to

$$\Box^* w + \Delta_n w = 0. \tag{32}$$

The estimation of the first eigenvalue is obtained by means of the Schwartz iterative method (Collatz, 1963). Assuming the first-order approximation in the form

$$w_1 = \sin\frac{\pi x}{a}\sin\frac{\pi y}{a} \tag{33}$$

the zero-order approximation given by the equation $\Delta_n w_o = -\Box^* w_1$ has the form

$$w_o = \gamma_1 \sin\frac{\pi x}{a}\sin\frac{\pi y}{a} - \gamma_2 \sin^2\frac{\pi x}{a}\sin^2\frac{\pi y}{a} \tag{34}$$

where

$$\gamma_1 = \left(\frac{\pi}{a}\right)^2 d/n_{x0}^T \quad \gamma_2 = Q_T k_x^2 \left(\frac{\pi}{a}\right)^2 /2\beta n_{x0}^T \tag{35}$$

$$d = (d_{11} + 2(d_{12} + 2d_{66}) + d_{22})/2. \tag{36}$$

The Schwartz constants (Collatz, 1963) are equal to

$$a_o = \int_0^a \int_0^b w_0(-\Delta_n w_0)\,dxdy = \frac{\pi^2}{2}\left[(\gamma_1 - 64\gamma_2/9\pi^2)^2 + 0.2308\gamma_2^2\right] \tag{37}$$

$$a_1 = \int_0^a \int_0^b w_1(-\Delta_n w_o)\,dxdy = 2\pi^2(\gamma_1/4 - 16\gamma_2/9\pi^2) \tag{38}$$

$$a_2 = \int_0^a \int_0^b w_1(-\Delta_n w_1)\,dxdy = \pi^2/2 \tag{39}$$

Using the Schwartz constants we calculate the Schwartz ratios μ_1 and μ_2,

$$\mu_1 = \frac{a_0}{a_1} = \gamma_1 - \frac{64}{9\pi^2}\gamma_2 + 0.2308\gamma_2^2 \Big/ \left(\gamma_1 - \frac{64}{9\pi^2}\gamma_2\right) \tag{40}$$

$$\mu_2 = \frac{a_1}{a_2} = \gamma_1 - \frac{64}{9\pi^2}\gamma_2. \tag{41}$$

In order to obtain the two-sided estimate of the first eigenvalue λ_1, the lower estimate of the second eigenvalue λ_2 is needed. It can be found by comparison of the considered eigenvalue problem with some simpler problem and by application of the minimax principle. This simpler problem can be defined, by substituting the minimal values of coefficients in functional (27).

$$\mathcal{B} \geq \int_\Omega [(d_{11} - Q_T k_x^2/4\beta)w_{,xx}^2 + 2(d_{12} - Q_T k_x^2/4\beta)w_{,xx}w_{,yy} + (d_{22} - Q_T k_x^2/4\beta)w_{,yy}^2 + 4d_{66}w_{,xy}^2 - n_{x0}^T(w_{,x}^2 + w_{,y}^2)]\,dxdy \geq 0 \tag{42}$$

Thus the lower estimate of the second eigenvalue is given by $l_2 = 4(\gamma_1 - \gamma_2)$.

If $l_2 < \mu_2$ the estimate $\mu_2 - (\mu_1 - \mu_2)/(l_2/\mu_2 - 1) \leq \lambda_1 \leq \mu_2$ holds and if $l_2 \geq \mu_2$ the lower estimate of the first eigenvalue is calculated for the simplified problem (42)

$$\lambda_1 \geq \gamma_1 \max\left\{1 - \frac{\gamma_2}{\gamma_1}, 1 - 0.72\frac{\gamma_2}{\gamma_1} - \frac{0.2308(\gamma_2/\gamma_1)^2}{3 - 3.28\gamma_2/\gamma_1}\right\}. \tag{43}$$

Therefore, the constant inplane force n_{x0}^T corresponding to the constant temperature $(T_0)_{cr}$ cannot be greater than the lower estimation of the first eigenvalue λ_1

$$T_0\frac{h}{2}[(Q_{11} + Q_{12})\alpha_L + (Q_{12} + Q_{22})\alpha_T] \leq \lambda_1. \tag{44}$$

Finally, the dynamic thermal buckling condition obtained from Eq. (44), determining the critical value of constant temperature component $(T_0)_{cr}$, has the form

$$\alpha_m(T_0)_{cr}\left(\frac{a}{h}\right)^2 = \frac{\pi^2}{12}(F+1)\frac{1 + 2\dfrac{\nu_{12}F}{F+1} + 4\dfrac{G_{12}}{(F+1)E_1} - \dfrac{Q_T(0,0)k_x^2}{2\beta D_{11}\rho h}}{\dfrac{\alpha_L}{\alpha_m}(1 + \nu_{12}F) + F\dfrac{\alpha_T}{\alpha_m}(1 + \nu_{12})} \times \max\left\{1 - \frac{Q_T k_x^2}{2\beta d}, 1 - 0.72\frac{Q_T k_x^2}{2\beta d} - 0.2308\left(\frac{Q_T k_x^2}{2\beta d}\right)^2 \Big/ \left[3 - 3.28\frac{Q_T k_x^2}{2\beta d}\right]\right\}. \tag{45}$$

Equation (45) describes the line bounding stability region. In Eq. (45) F is the ratio of principal lamina stiffnesses ($F = E_2/E_1$), where E_1 and E_2 are Young's moduli in longitudinal and transverse directions, respectively, G_{12} denotes the shear modulus of the lamina, and ν_{12} is the Poisson's ratio for transverse strain in direction 2 when the stress is applied in direction 1. In addition, α_m stands for the linear thermal expansion coefficient of the lamina matrix. Stability domains calculated for the glass-epoxy, the graphite-epoxy and aluminum plate according to Eq. (45) are shown in Fig. 1. The Schwartz iterative method has increased the stability domains in comparison with those obtained for the simplified problem (42). The stability domains in the simplified approach are bounded by straight lines, shown in part as dotted lines. The areas between the continuous lines and dotted lines represent the increase of the stability domains. The mechanical properties of those materials are given in Table 1.

4 Laminated Beam due to Local Short-Time Heatings

In numerous applications, for example in electronic elements, aircraft panels (e.g., White, 1985) and in thin-walled aerospace structures, intense short-time local heatings often occur. They may destabilize initially plane shape of elements. In order to evaluate the effect of such phenomena and calculate critical temperature we consider a laminated beam of rectangular cross section of the length l, width g, and total thickness h. Equations of symmetrically laminated beams may be derived by considering the beam as a special case of a laminated plate. Beams have a high length-to-width ratio. Therefore, the transverse displacement is a function of the variable x only, $w = w(x)$. The symmetry of laminate and stress-free conditions for lateral surfaces imply

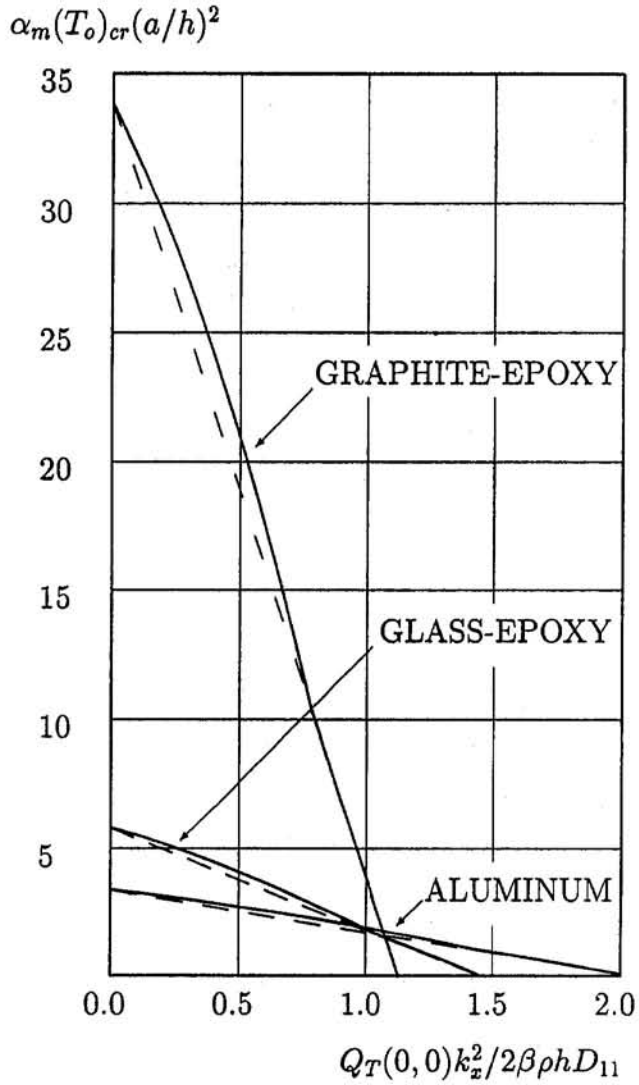

Fig. 1 Dynamic thermal buckling regions

$$M_y^i = M_{xy}^i = 0, \quad N_y^i = N_{xy}^i = 0. \tag{46}$$

The only one nonzero moment may be expressed by the transverse displacement in the classic form

$$M_x = -\frac{g}{(D^{-1})_{11}} w_{,xx}. \tag{47}$$

In the case of beam compressed by an axial force, equation of the plane motion has the form

$$\rho A w_{,tt} + 2\rho A\beta w_{,t} + \frac{g}{(D^{-1})_{11}} w_{,xxxx} + gN_x^i w_{,xx} = -gM_{y,xx}^T \qquad x \in (0, l) \tag{48}$$

where N_x^i is the inplane force resultant.

The beam is assumed to be simply supported,

$$w(t, 0) = w(t, l) = 0, \quad w_{,xx}(t, 0) = w_{,xx}(t, l) = 0, \tag{49}$$

and with immovable ends $\epsilon_x(0) = \epsilon_x(l) = 0$.

For the beam geometry in the absence of axial motion we have $\epsilon_x^0 = 0$.

Substituting ϵ_x^0 into the first three rows of Eq. (3) and eliminating ϵ_{xy}^0 and ϵ_y^0 we can write the axial force in the form

$$N_x^i = -\frac{A_{22}N_x^T - A_{12}N_y^T}{A_{22}}. \tag{50}$$

Dividing Eq. (48) by ρA, substituting $e = 1/[(D^{-1})_{11}\rho h]$, $n_0 = N_0/\rho h$, $n(t) = N(t)/\rho h$, and assuming the uniform temperature distribution over the beam cross section $T(x, y, z, t) = T(x, t)$, the thermal moment in Eq. (48) vanishes and we have the following homogeneous equation of motion:

$$w_{,tt} + 2\beta w_{,t} + ew_{,xxxx} + (n^0 + n(t))w_{,xx} = 0, \qquad x \in (0, l) \tag{51}$$

where n^0 and $n(t)$ are constant and time-dependent components of the inplane force resultant n^i, respectively.

Since the axial motion is neglected, the axial forces n^0 and $n(t)$ are substituted by their mean values calculated over the beam length

$$(\bar{n}_0, \bar{n}(t)) = \frac{1}{l}\int_0^l (n^0, n(t))d\xi. \tag{52}$$

To calculate n^0 and $n(t)$ we may observe that for an angle-ply symmetrically laminated beam thermal force resultants calculated from Eq. (1) are expressed in the following way:

$$\begin{bmatrix} N_x^T \\ N_y^T \end{bmatrix} = T^*(x, t) \times \int_{-h/2}^{h/2} \begin{bmatrix} \bar{Q}_{11} & \bar{Q}_{12} & \bar{Q}_{16} \\ \bar{Q}_{12} & \bar{Q}_{22} & \bar{Q}_{26} \end{bmatrix} \begin{bmatrix} \alpha_L \cos^2\Theta + \alpha_T \sin^2\Theta \\ \alpha_L \sin^2\Theta + \alpha_T \cos^2\Theta \\ (\alpha_L - \alpha_T)\sin(2\theta) \end{bmatrix} dz \tag{53}$$

where Θ is the lamination angle. Integration of Eq. (53) leads to the expression for the thermal force resultants in the shortened form

$$(N_x^T, N_y^T) = (I_x, I_y)T^*(x, t) = h\bar{Q}_{11}\alpha_m(S_x, S_y) \tag{54}$$

where S_x and S_y are known dimensionless constants.

Finally, the components of axial forces have the form

$$(\bar{n}^0, \bar{n}(t)) = C\int_0^l (T_0(\xi), (T(\xi, t) - T_0(\xi)))d\xi \tag{55}$$

where $T_0(x)$ is the time mean value of the temperature field and $C = (A_{22}I_x - A_{22}I_y)/\rho h l A_{22}$.

The force discontinuity is related to the temperature increament dT in the following way (similar to Eq. (55)):

$$dn = C\int_0^l dT(\xi, t)d\xi. \tag{56}$$

If the beam is subjected to a sequence of random heatings causing temperature variations randomly distributed over the beam, having independent increments and arriving in time according to the Poisson distribution, the equation of motion (51) can be rewritten as the Itô partial differential equation of the form

$$dw = vdt \tag{57}$$

$$dv = -(2\beta v + ew_{,xxxx} + n_0 w_{,xx})dt - \epsilon w_{,xx}\int_{-\infty}^{\infty} u\nu(du, dt), \quad x \in (0, l) \tag{58}$$

Table 1 Mechanical properties of single orthotropic lamina

	glass-epoxy	graphite-epoxy	aluminum
F	0.22	0.0458	1
G_{12}/E_1	0.08	0.0271	0.4
ν_{12}	0.26	0.26	0.25
α_L/α_m	0.088	-0.013	0.375
α_T/α_m	0.5	0.76	0.375

where ϵ is a constant containing information on the space distribution $f(x)$ of the temperature field $\epsilon = C\int_0^l f(\xi)d\xi$, and the Poisson measure $\nu(dt, S)$ denotes a random number of temperature changes belonging to the domain S in the time interval $(t, t + dt)$; its distribution has the known form

$$P\{\nu([t_1, t_2], S) = n\} = \frac{1}{n!}\left(\int_{t_1}^{t_2} \lambda\Pi(dt, S)\right)^n \exp\left(\int_{t_1}^{t_2} \lambda\Pi(dt, S)\right). \quad (59)$$

The mean value of the Poisson measure ν equals to the ordinary measure Π of (dt, S) multiplied by a mean arrival rate λ of the temperature pulses

$$\mathbf{E}\nu(dt, S) = \lambda(t)\Pi(dt, S). \quad (60)$$

In the steady-state condition the mean arrival rate λ is constant and

$$\mathbf{E}\nu(dt, S) = \lambda\Pi(S)dt. \quad (61)$$

We introduce an energy-like Liapunov functional of the form

$$V = \int_0^l (v^2 + 4\beta vw + 4\beta^2 w^2 + ew_{,xx}^2 - n_0 w_{,x}^2)dx. \quad (62)$$

The functional is positive definite if a constant component n_0 of axial temperature force satisfies the classic buckling condition. Then we can choose a measure of motion disturbances as a square root of functional $\|w\| = V^{1/2}$. In order to calculate the differential of functional it is necessary to apply the generalized Itô formula (Gikhman and Dorogovtsev, 1965), which yields

$$dV = \int_0^l [2vdv + 4\beta wdv + 4\beta vdw + 8\beta^2 wdw + 2ew_{,xx}dw_{,xx} - 2n_0 w_{,x}dw_{,x}]dx + \int_0^l \int_{-\infty}^{\infty} [(v + u\epsilon w_{,xx})^2 + 4\beta w(v + u\epsilon w_{,xx}) - v^2 - 4\beta wv]\nu(dt, du)dx. \quad (63)$$

Substituting dw from Eq. (57) and dv from Eq. (58), integrating by parts, and using boundary conditions, we obtain

$$dV = -\int_0^l [4\beta ew_{,xx}^2 - 4\beta n_0 w_{,x}^2 - \lambda\epsilon^2\mathbf{E}(\Delta T^2)w_{,xx}^2]dxdt + -\int_0^l (2v + 4\beta w)\epsilon w_{,xx}dx \int_{-\infty}^{\infty} u\nu(dt, du) \quad (64)$$

where $\mathbf{E}(\Delta T^2)$ is a mean square value of the temperature increments. Applying the Gikhman and Skorokhod (1972) stability theorem we can write the uniform stability condition in the form

$$\int_0^l [4\beta ew_{,xx}^2 - 4\beta n_0 w_{,x}^2 - \lambda\epsilon^2\mathbf{E}(\Delta T^2)w_{,xx}^2]dx > 0 \quad (65)$$

As functions satisfying boundary conditions (49) satisfy the following inequality,

$$\int_0^l w_{,xx}^2 dx \geq \left(\frac{\pi}{l}\right)^2 \int_0^l w_{,x}^2 dx, \quad (66)$$

we can rewrite the stability condition (65) in the form

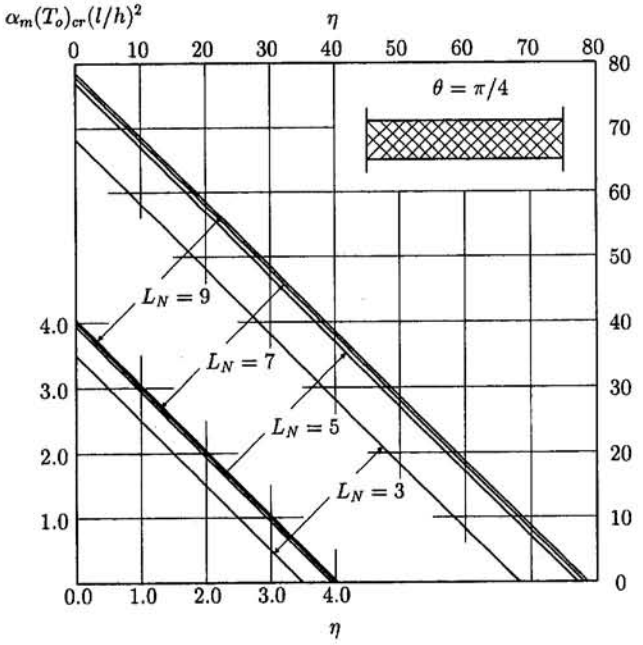

Fig. 2 Dynamic thermal buckling regions for a beam

$$\int_0^l \left[(4\beta e - \lambda\epsilon^2\mathbf{E}(\Delta T^2))\left(\frac{\pi}{l}\right)^2 - 4\beta n_0\right]w_{,x}^2 dx > 0. \quad (67)$$

Therefore, the beam subjected to a sequence of local short-term heatings is uniformly stochastically stable if the following condition imposed on the beam parameters and the temperature fields is satisfied:

$$\frac{\lambda\mathbf{E}(\Delta T^2)\epsilon^2}{4\beta} < \left[e - n_0\left(\frac{l}{\pi}\right)^2\right]. \quad (68)$$

Using the inverse matrix D^{-1} and the relation between the axial force n_0 and the constant mean temperature T_0 Eq. (68) can be written in the form

$$\frac{h^3}{12\rho h}\bar{Q}_{11}\left[1 + \frac{2p_{12}p_{16}p_{26}\phi^2(L_N) - p_{22}p_{16}^2\phi^2(L_N) - p_{66}p_{12}^2}{p_{22}p_{66} - p_{26}^2\phi^2(L_N)}\right] + -\frac{1}{\rho}\bar{Q}_{11}\alpha_m(S_x - S_y\bar{Q}_{12}/\bar{Q}_{22})T_0\left(\frac{a}{\pi}\right)^2 - \frac{\lambda\mathbf{E}(\Delta T^2)\epsilon^2}{4\beta} > 0 \quad (69)$$

$$p_{ij} = \frac{\bar{Q}_{ij}}{\bar{Q}_{11}}$$

$$\phi(L_N) = \frac{3L_N^2 - 3}{L_N^3}.$$

Finally, the thermal buckling condition in dimensionless variables has the form

$$\alpha_m(T_0)_{cr}\left(\frac{l}{h}\right)^2 \leq k_1 - \eta \quad (70)$$

where k_1 is a known coefficient depending on the material and geometrical parameters and the number of layers L_N

$$k_1 = \frac{\pi^2}{12}\left[1 + \frac{2p_{12}p_{16}p_{26}\phi^2(L_N) - p_{22}p_{16}^2\phi^2(L_N) - p_{66}p_{12}^2}{p_{22}p_{66} - p_{26}^2\phi^2(L_N)}\right]\Big/(S_x - S_y\bar{Q}_{12}/\bar{Q}_{22}) \quad (71)$$

and the independent variable η in Eq. (70) depends on the thermal characteristics of temperature field and the dissipative properties of the beam

$$\eta = \frac{\lambda \mathbf{E}(\Delta T)^2 \alpha_m^2 \pi^2 \bar{Q}_{11}}{4\beta\rho h^2} \times \left(\frac{1}{l}\int_0^l f(\xi)d\xi\right)^2 \left(S_x - S_y \frac{\bar{Q}_{12}}{\bar{Q}_{22}}\right). \quad (72)$$

Stability domains for graphite-epoxy and glass-epoxy beams with the lamination angle $\theta = \pi/4$ and for various numbers of layers are shown in Fig. 2. As anticipated, because of the negative value of α_L/α_m, the graphite-epoxy composites (upper right lines) exhibit increased stability domains compared to those of glass-epoxy laminate (lower left lines) which display positive thermal expansion coefficients.

Stability boundaries are seen to tend to a limit with an increasing number of layers. The limit case $L_N \to \infty$ corresponding to the specially orthotropic plates (as $D_{16} = D_{26} \to 0$) overestimates the critical value of $\alpha_m(T_0)_{cr}(l/h)^2$. The presence of bending-torsional coupling terms (D_{16}, D_{26}) decreases the stability domains for both the glass-epoxy and the graphite-epoxy beams.

5 Conclusions

A method has been presented for analyzing the thermally induced instability of elastic laminated plates subjected to time and space-varying temperature fields. The major conclusion is that the Liapunov method is an effective tool of solving the stability problem of laminated plates. The explicit criteria developed in the paper define stability regions in terms of the intensity of excitation process and the physical characteristics of the plate. The analytical formulas defining the stability regions are derived using the calculus of variations. Stability regions depend essentially on the constant temperature and the plate material.

Acknowledgment

A financial support for the first author (AT) by the International Research and Exchange Board and by the Polish State Committee for Scientific Research is gratefully acknowledged.

References

Boley, B. A., and Weiner, J. H., 1960, *Theory of Thermal Stresses,* John Wiley, and Sons, New York.

Collatz, L., 1963, *Eigenwertaufgaben mit technische Anwendungen,* Akademische Verlagsgesellschaft Geest & Portig, Leipzig.

Curtain, R. H., and Falb, P. L., 1970, "Itô's lemma in Infinite Dimensions," *J. Math. Anal. Appl.,* Vol. 31, pp. 352–369.

Gikhman, I. I., and Dorogovtsev, A. J., 1965, "Stability of Differential Equations with Impulse Coefficients," *Ukrainian Mathematical Journal,* Vol. 17, pp. 3–21, in Russian.

Gikhman, I. I., and Skorokhod, A. V., 1972, *Stochastic Differential Equations,* Springer-Verlag, New York.

Khasminski, R. Z., 1969, *Stochastic Stability of Differential Equations,* Nauka, Moscow, in Russian.

Lien-Wen Chen, and Lei-Yi Chen, 1987, "Thermal Buckling of Laminated Composite Plates," *Journal of Thermal Stresses,* Vol. 10, pp. 345–356.

Rektorys, K., 1977, *Variational Methods in Mathematics, Science and Engineering,* D. Reidel, Boston, MA.

Tauchert, T. R., 1987, "Thermal Buckling of Thick Antisymmetric Angle-Ply Laminates," *Journal of Thermal Stresses,* Vol. 10, pp. 113–124.

Tauchert, T. R., 1987, "Thermal Stresses in Plates—Dynamical Problems," *Thermal Stresses II,* R. B. Hetnarski, ed., North Holland, Amsterdam.

Tylikowski, A., 1984, "Stochastic Stability of Beams with Impulse Parametric Excitations," *The 9th International Conference on Nonlinear Oscillations,* Vol. 1, Y. A. Mitropolskii ed., Naukova Dumka, Kiev, pp. 367–369.

Tylikowski, A., 1986, "Dynamic Stability of Viscoelastic Continuous Systems Under Time-Dependent Loadings," *Mechanika Teoretyczna i Stosowana,* Vol. 24, pp. 127–137.

White, R. G., 1985, "Some Influence of Material Properties on the Dynamic Response of CFPR Structures," *Composite Structures 3, Proceedings of the International Conference on Composite Structures,* Elsevier Applied Science, London, pp. 434–443.

Whitney, J. M., 1987, *Structural Analysis of Laminated Anisotropic Plates,* Technomic Publishing, Lancaster.

An Integral-Equation Formulation for Anisotropic Elastostatics

M. M. Perez[1]
Reseacher,
Wessex Institute of Technology,
Ashurst Lodge,
Ashurst, Southampton SO4 2AA, U.K.

L. C. Wrobel
Brunel University,
Department of Mechanical Engineering,
Uxbridge UB8 3PH, Middlesex, U.K.

In this paper a conceptually simple integral-equation formulation for homogeneous anisotropic linear elastostatics is presented. The basic idea of the approach proposed here is to rewrite the system of differential equations of the anisotropic problem to enable the use of the isotropic fundamental solution. This procedure leads to an extended form of Somigliana's identity where a domain term occurs as a result of the anisotropy of the material. A supplementary integral equation is then established to cope with the resulting domain unknowns. Although the solution of these integral equations requires discretization of the contour of the structural component into boundary elements and its domain into internal cells, the numerical scheme presented here depends only on the boundary variables of the problem. Once the boundary solution is obtained it is possible to compute the unknowns within the domain, if required. The main objective of the present work is to develop an alternative integral-equation formulation that could be used to reduce the time needed to compute three-dimensional solutions for linear homogeneous anisotropic problems. Another possible advantage of the proposed formulation is its generality, which enables its direct extension to include dynamic and plastic effects in the analysis. Encouraging results are presented for four examples where structural elements are submitted to tension and shear effects.

1 Introduction

To solve current technological problems that occur in industry, the use of composite materials or directionally solidified alloys is sometimes essential. Further, as plastic deformation is physically anisotropic (Fung, 1965), many fabrication processes such as cold-pressing, forging, or spinning, usually destroy any initial isotropy which may have been present, leaving as a result an anisotropic material.

As the treatment of anisotropic problems is generally regarded as difficult, the increasing number of industrial applications of anisotropic materials has attracted the attention of many researchers concerned with computational modeling. However, despite the importance that computational modeling has assumed in providing answers to realistic industrial problems, it seems that the progress achieved in the analysis of orthotropic and anisotropic problems has been relatively slow, when compared with the significant developments in numerical modeling made in the last decades.

This paper is concerned with the development of an alternative integral-equation formulation for the numerical analysis of homogeneous anisotropic linear elastic problems. The approach presented here consists of rewriting the generalized form of Hooke's law in a slightly different way to enable the use of Kelvin's fundamental solutions for elastostatics. This procedure leads to an extended form of Somigliana's identity which includes a domain term that accounts for the anisotropy of the material. The first primary integral equation of the method is obtained by taking the limiting form of this equation as the interior point approaches the boundary. In order to cope with the domain unknowns arising from this formulation, a supplementary integral equation is derived from the extended form of Somigliana's identity. This supplementary integral equation is then regarded as the second primary integral equation of the proposed method.

To solve the system formed by the two integral equations it is necessary to discretize the contour of the mechanical or structural element under consideration into boundary elements and its interior into domain cells. Two coupled systems of linear algebraic equations are then obtained. The solution of these simultaneous systems of linear equations is done using a technique equivalent to the FEM condensation of internal degrees of freedom (Desai and Abel, 1972), leading to a final solution that is dependent exclusively on the boundary variables of the problem.

The purpose of the present work is to investigate whether the use of the isotropic fundamental solutions for linear elastostatics constitutes or not a reliable alternative for the analysis of anisotropic problems. Once the formulation proposed here is verified for two-dimensional problems there are no conceptual difficulties in including dynamic and nonlinear (e.g., elastoplasticity) effects in the formulation. Most importantly, it can be directly extended to obtain a general integral equation formulation for three-dimensional homogeneous anisotropic problems.

As regards BEM, Rizzo and Shippy (1970) (and Benjumea and Sikarskie, 1972) used the two-dimensional anisotropic fundamental solution presented by Green (1943) in a real-variable direct boundary integral equation formulation. One year later, Cruse and Swedlow (1971) issued a report where a complex-variable anisotropic fundamental solution was used for plane elasticity. A more recent complex-variable approach for two-dimensional anisotropic elastic problems was presented by Lee and Mal (1990), where the integral equations are discretized in the complex plane.

It is important to mention that although two-dimensional complex fundamental solutions for anisotropic elasticity present no particular difficulty in their implementation (see, for instance, Cruse and Swedlow, 1971), the evaluation of the contour integrals for the three-dimensional case is regarded complicated, especially for the fundamental tractions (Vogel and Rizzo, 1973), and too time-consuming for routine numerical use by Wilson and Cruse (1978). An alternative approach to

[1] On leave from Departamento de Engenharia Mecânica, Universidade Federal de Uberlândia, 38400-902 Uberlândia, MG, Brazil.

Contributed by the Applied Mechanics Division of THE AMERICAN SOCIETY OF MECHANICAL ENGINEERS for publication in the ASME JOURNAL OF APPLIED MECHANICS.

Discussion on this paper should be addressed to the Technical Editor, Professor Lewis T. Wheeler, Department of Mechanical Engineering, University of Houston, Houston, TX 77204-4792, and will be accepted until four months after final publication of the paper itself in the ASME JOURNAL OF APPLIED MECHANICS.

Manuscript received by the ASME Applied Mechanics Division, Nov. 10, 1993; final revision, Aug. 19, 1996. Associate Technical Editor: L. T. Wheeler.

the problem has been presented by Mura and Kinoshita (1971). However, the need to compute series expansions for the fundamental displacements and tractions at each integration point makes this formulation also unsuitable for extensive computation.

Barnett (1972) developed a simple numerical scheme for evaluating the derivatives of the anisotropic elastic Green's function for three-dimensional problems by using Fourier transform method. This procedure was reviewed by Mura (1987), together with other analytical and approximate expressions for the three-dimensional anisotropic Green's function. Recently, Voorhees et al. (1992) presented a boundary integral technique for a system with cubic elastic anisotropy which requires integrating the derivatives of the three-dimensional Green's function. In this approach an analytical form for the Green's function described in the review paper of Bacon et al. (1979) was used.

The inspiration for the formulation proposed here was drawn from the tentative approach proposed by Brebbia and Dominguez (1989) for anisotropic elasticity; from the work of Shi (1990), where a supplementary integral equation for the solution of bending and eigenvalue problems of anisotropic plates was derived from the integral equation for the displacements within the domain; and from the work of Telles and Brebbia (1979), where the complete integral formulation for plasticity was first presented. Moreover, the method proposed here is a direct extension of the formulation proposed by Perez and Wrobel (1992, 1993) for the analysis of homogeneous anisotropic problems in potential theory.

2 Integral-Equation Formulation

The governing differential equation for linear anisotropic elasticity—Navier equation—is expressed by (Balaš et al., 1989):

$$D_{ijkl}u_{k,jl} + b_i = 0 \tag{1}$$

where D_{ijkl} represents the fourth-order tensor of elastic properties; u_k denotes the components of the displacement vector, and b_i is the body force vector. This equation is sufficient to completely describe the elastic behavior of the material once boundary conditions are defined. As only homogeneous materials are considered in this paper, the components of the elasticity tensor are regarded as constant throughout the domain.

To enable the use of isotropic fundamental solutions, the elasticity tensor was divided into two components, namely:

$$D_{ijkl} = D^0_{ijkl} + \hat{D}_{ijkl}. \tag{2}$$

In this equation, D^0_{ijkl} stands for an isotropic reference tensor while $\hat{D}_{ijkl}$ denotes the difference between the actual tensor of elastic constants of the anisotropic material and the isotropic reference tensor. This reference isotropic tensor is defined by averaging the elastic constants of the anisotropic material (Brebbia and Dominguez, 1989).

Taking Eq. (2) into consideration, the weighted residual statement to the anisotropic problem analysed here can then be written as

$$\int_\Omega u^*_{ij}(\xi, \chi)(D^0_{jklm} + \hat{D}_{jklm})u_{l,km}(\chi)d\Omega(\chi) + \int_\Omega u^*_{ij}(\xi, \chi)b_j(\chi)d\Omega(\chi) = \int_{\Gamma_2} u^*_{ij}(\xi, \chi)[p_j(\chi) - \bar{p}_j(\chi)]d\Gamma(\chi) + \int_{\Gamma_1} p^*_{ij}(\xi, \chi)[\bar{u}_j(\chi) - u_j(\chi)]d\Gamma(\chi) \tag{3}$$

where ξ and χ are the load and field points, respectively; $u^*_{ij}(\xi, \chi)$ denotes the isotropic fundamental displacements; $p^*_{ij}(\xi, \chi)$ denotes the fundamental tractions; $u_j(\chi)$ and $p_j(\chi)$ stand for displacements and tractions, respectively, while the superimposed bar denotes prescribed values ($\bar{u}_j(\chi)$ on Γ_1 and $\bar{p}_j(\chi)$ on Γ_2); $\Gamma_1 + \Gamma_2 = \Gamma$ constitutes the boundary of the structural component being analyzed, and Ω denotes the region enclosed by Γ.

The appropriate expressions for the reference isotropic fundamental displacements and tractions for two-dimensional plane-strain problems are given (Brebbia et al., 1984) by

$$u^*_{ij}(\xi, \chi) = \frac{-1}{8\pi(1-\nu)G}[(3 - 4\nu)\ln(r)\delta_{ij} - r_{,i}r_{,j}] \tag{4}$$

$$p^*_{ij}(\xi, \chi) = \frac{-1}{4\pi(1-\nu)r}\left\{[(1-2\nu)\delta_{ij} + 2r_{,i}r_{,j}]\frac{\partial r}{\partial n} - (1-2\nu)(r_{,i}n_j - r_{,j}n_i)\right\} \tag{5}$$

where δ_{ij} is the Kronecker delta; G is the shear modulus; ν is the Poisson's ratio; $r = r(\xi, \chi)$ denotes the distance between ξ and χ; $r_{,i}$ represents the derivatives of r with respect to the coordinates of the field point, i.e., $r_{,i} = \partial r/\partial x_i(\chi) = r_i/r$; n is the outward unit vector normal to the boundary at χ, while n_i denotes its direction cosines. The case of plane stress can be analyzed through the use of an effective Poisson's ratio (Brebbia and Dominguez, 1989).

Integrating by parts the first term on the left-hand side of Eq. (3) yields

$$-\int_\Omega \epsilon^*_{jki}(\xi, \chi)(D^0_{jklm} + \hat{D}_{jklm})\epsilon_{lm}(\chi)d\Omega(\chi) + \int_\Omega u^*_{ij}(\xi, \chi)b_j(\chi)d\Omega(\chi) = -\int_{\Gamma_2} u^*_{ij}(\xi, \chi)\bar{p}_j(\chi)d\Gamma(\chi) - \int_{\Gamma_1} u^*_{ij}(\xi, \chi)p_j(\chi)d\Gamma(\chi) + \int_{\Gamma_1} p^*_{ij}(\xi, \chi)[\bar{u}_j(\chi) - u_j(\chi)]d\Gamma(\chi) \tag{6}$$

where $\epsilon^*_{jki}(\xi, \chi)$ represents the isotropic fundamental strain tensor and $\epsilon_{lm}(\chi)$ the actual strain field. The fundamental strains ϵ^*_{jki} at any point χ, due to a unit point load applied at ξ in the direction i, can be written as (Brebbia et al., 1984):

$$\epsilon^*_{jki}(\xi, \chi) = \frac{-1}{8\pi(1-\nu)Gr} \times [(1-2\nu)(r_{,k}\delta_{ij} + r_{,j}\delta_{ik}) - r_{,i}\delta_{jk} + 2r_{,i}r_{,j}r_{,k}]. \tag{7}$$

The constitutive equation relating stresses and strains for a linearly elastic material (generalized Hooke's law) is used along with Eq. (2) to write

$$(D^0_{jklm} + \hat{D}_{jklm})\epsilon_{lm} = \sigma^0_{jk} + \hat{\sigma}_{jk} \tag{8}$$

where σ^0_{jk} is the isotropic component of the actual stress tensor while $\hat{\sigma}_{jk}$ is the residual one. Applying Eq. (8) to the first term on the left-hand side in Eq. (6) yields

$$-\int_\Omega \epsilon^*_{jki}(\xi, \chi)\sigma^0_{jk}(\chi)d\Omega(\chi) - \int_\Omega \epsilon^*_{jki}(\xi, \chi)\hat{\sigma}_{jk}(\chi)d\Omega(\chi) + \int_\Omega u^*_{ij}(\xi, \chi)b_j(\chi)d\Omega(\chi) = -\int_{\Gamma_2} u^*_{ij}(\xi, \chi)\bar{p}_j(\chi)d\Gamma(\chi) - \int_{\Gamma_1} u^*_{ij}(\xi, \chi)p_j(\chi)d\Gamma(\chi) + \int_{\Gamma_1} p^*_{ij}(\xi, \chi)[\bar{u}_j(\chi) - u_j(\chi)]d\Gamma(\chi). \tag{9}$$

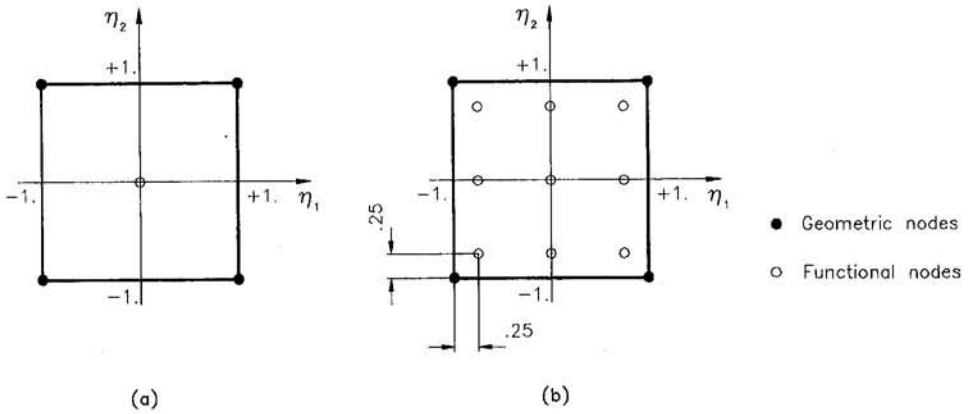

Fig. 1 Constant (*a*), and subparametric discontinuous (*b*), parent internal cells

Recalling that the isotropic fundamental tensors comply with $\sigma^*_{jki} = D^0_{jklm}\epsilon^*_{lmi}$ and, from Eq. (8), that $\sigma^0_{jk} = D^0_{jklm}\epsilon_{lm}$, it is possible to rewrite the first term in Eq. (9) in the form

$$\int_\Omega \epsilon^*_{jki}(\xi, \chi)\sigma^0_{jk}(\chi)d\Omega(\chi) = \int_\Omega \sigma^*_{jki}(\xi, \chi)\epsilon_{jk}(\chi)d\Omega(\chi). \quad (10)$$

Integrating by parts the right-hand side term in Eq. (10) and substituting the result into Eq. (9) leads to

$$\int_\Omega \sigma^*_{jki,k}(\xi, \chi)u_j(\chi)d\Omega(\chi) - \int_\Omega \epsilon^*_{jki}(\xi, \chi)\hat{\sigma}_{jk}(\chi)d\Omega(\chi) + \int_\Omega u^*_{ij}(\xi, \chi)b_j(\chi)d\Omega(\chi) = -\int_\Gamma u^*_{ij}(\xi, \chi)p_j(\chi)d\Gamma(\chi) + \int_\Gamma p^*_{ij}(\xi, \chi)u_j(\chi)d\Gamma(\chi) \quad (11)$$

where the first term on the left-hand side can be shown to reduce to the displacement vector at point ξ (Brebbia et al., 1984) and the dash through the integration symbols denotes integrals that are to be interpreted in the Cauchy principal value sense. Equation (11) can then be written as

$$u_i(\xi) = \int_\Gamma u^*_{ij}(\xi, \chi)p_j(\chi)d\Gamma(\chi) - \int_\Gamma p^*_{ij}(\xi, \chi)u_j(\chi)d\Gamma(\chi) - \int_\Omega \epsilon^*_{jki}(\xi, \chi)\hat{\sigma}_{jk}(\chi)d\Omega(\chi) - \int_\Omega u^*_{ij}(\xi, \chi)b_j(\chi)d\Omega(\chi). \quad (12)$$

This equation can be seen as Somigliana's identity with an additional domain term which takes into account the anisotropy of the material. This additional domain term introduces a set of domain variables represented by the residual stress field $\hat{\sigma}_{jk}(\chi)$.

An integral equation for load points on the boundary is obtained by a limiting process, taking the load point ξ from within the domain to the contour Γ. The resulting integral equation is expressed by

$$c_{ij}(\xi)u_j(\xi) + \int_\Gamma p^*_{ij}(\xi, \chi)u_j(\chi)d\Gamma(\chi) - \int_\Gamma u^*_{ij}(\xi, \chi)p_j(\chi)d\Gamma(\chi) = -\int_\Omega \epsilon^*_{jki}(\xi, \chi)\hat{\sigma}_{jk}(\chi)d\Omega(\chi) - \int_\Omega u^*_{ij}(\xi, \chi)b_j(\chi)d\Omega(\chi) \quad (13)$$

where the elements of the tensor $c_{ij}(\xi)$ are functions of the internal angle of the boundary at point ξ.

Whereas Eq. (13) provides the first primary integral equation of the proposed formulation, another integral equation is still required to provide, after discretization, the necessary number of linear equations to solve the problem numerically. This supplementary integral equation is obtained by differentiating Eq. (12) with respect to the coordinates of the load point ξ, as expressed by

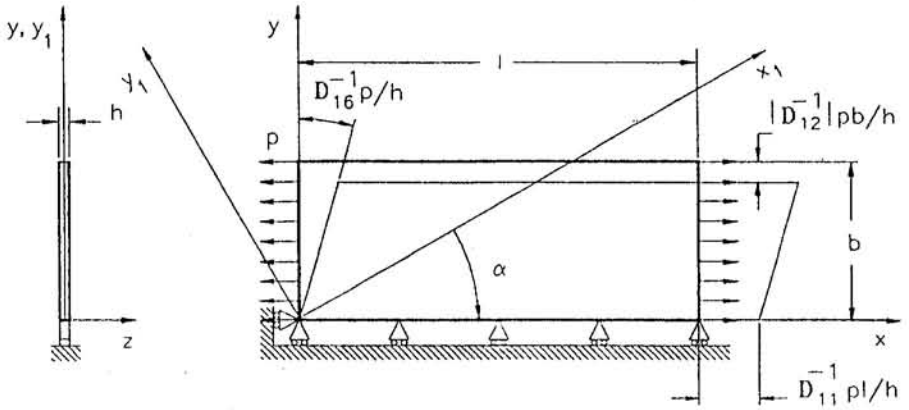

Fig. 2 Rectangular plate subjected to uniform tension

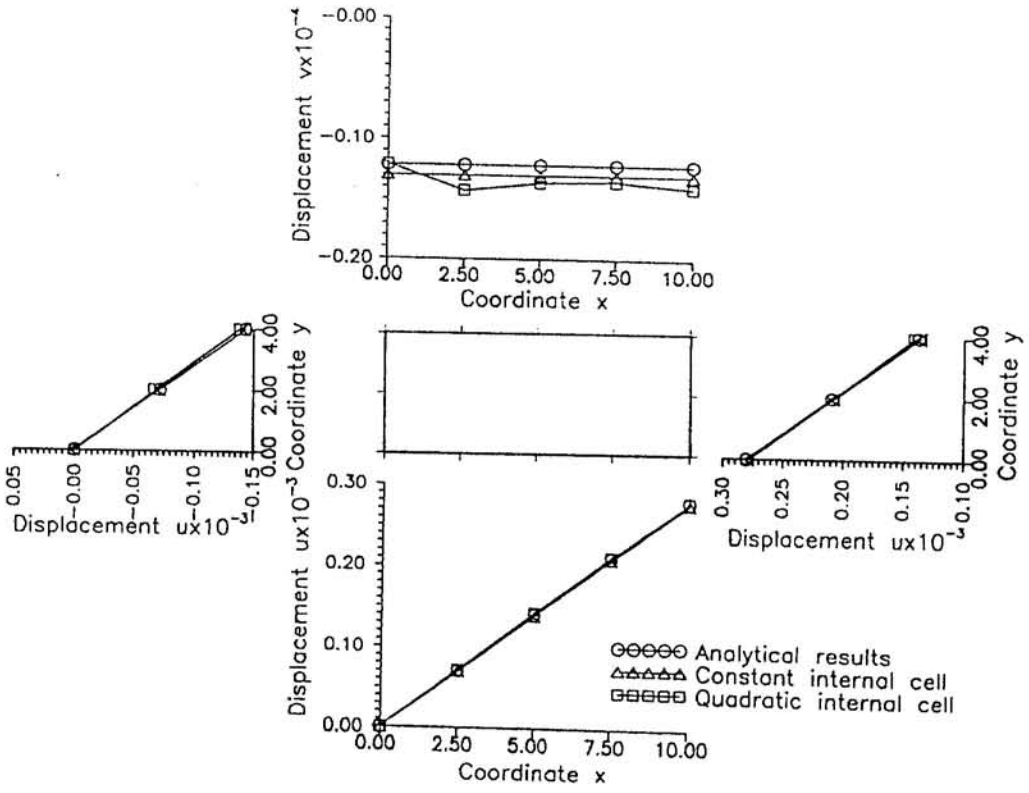

Fig. 3 Results obtained for plate under simple tension. Displacements in *m*.

$$\frac{\partial u_i(\xi)}{\partial x_l(\xi)} = \frac{\partial}{\partial x_l(\xi)} \int_\Gamma u^*_{ij}(\xi, \chi) p_j(\chi) d\Gamma(\chi)$$

$$- \frac{\partial}{\partial x_l(\xi)} \int_\Gamma p^*_{ij}(\xi, \chi) u_j(\chi) d\Gamma(\chi)$$

$$- \frac{\partial}{\partial x_l(\xi)} \int_\Omega \epsilon^*_{jki}(\xi, \chi) \hat{\sigma}_{jk}(\chi) d\Omega(\chi)$$

$$- \frac{\partial}{\partial x_l(\xi)} \int_\Omega u^*_{ij}(\xi, \chi) b_j(\chi) d\Omega(\chi) \quad (14)$$

and then combining these derivatives to obtain the strain tensor $\epsilon_{ij}(\chi)$. This strain tensor is then related to the residual stress tensor $\hat{\sigma}_{ij}(\xi)$ using the generalized Hooke's law, leading to the second primary integral equation of the method, that is

$$\hat{D}_{ijmn} \frac{1}{2} \left[\frac{\partial u_m(\xi)}{\partial x_n(\xi)} + \frac{\partial u_n(\xi)}{\partial x_m(\xi)} \right]$$

$$+ \hat{D}_{ijmn} \frac{1}{2} \left[\frac{\partial}{\partial x_n(\xi)} \int_\Gamma p^*_{mk}(\xi, \chi) u_k(\chi) d\Gamma(\chi) \right.$$

$$\left. + \frac{\partial}{\partial x_m(\xi)} \int_\Gamma p^*_{nk}(\xi, \chi) u_k(\chi) d\Gamma(\chi) \right]$$

$$= \hat{D}_{ijmn} \frac{1}{2} \left[\frac{\partial}{\partial x_n(\xi)} \int_\Gamma u^*_{mk}(\xi, \chi) p_k(\chi) d\Gamma(\chi) \right.$$

$$\left. + \frac{\partial}{\partial x_m(\xi)} \int_\Gamma u^*_{nk}(\xi, \chi) p_k(\chi) d\Gamma(\chi) \right]$$

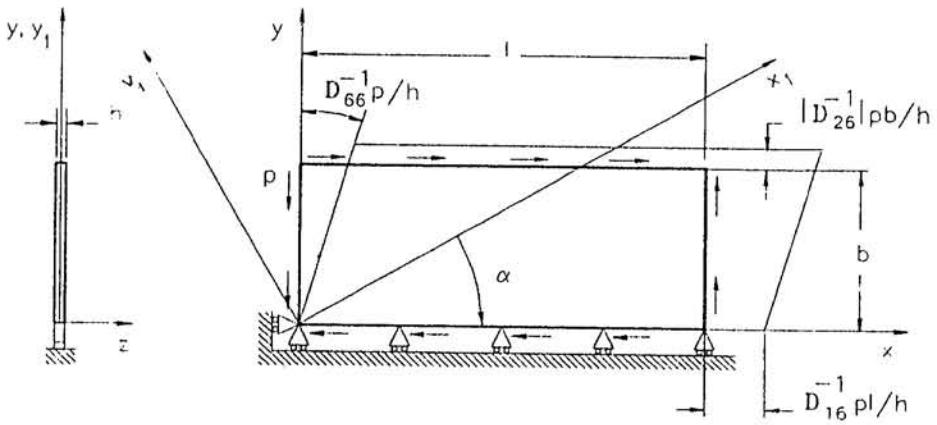

Fig. 4 Rectangular plate subjected to shear loading

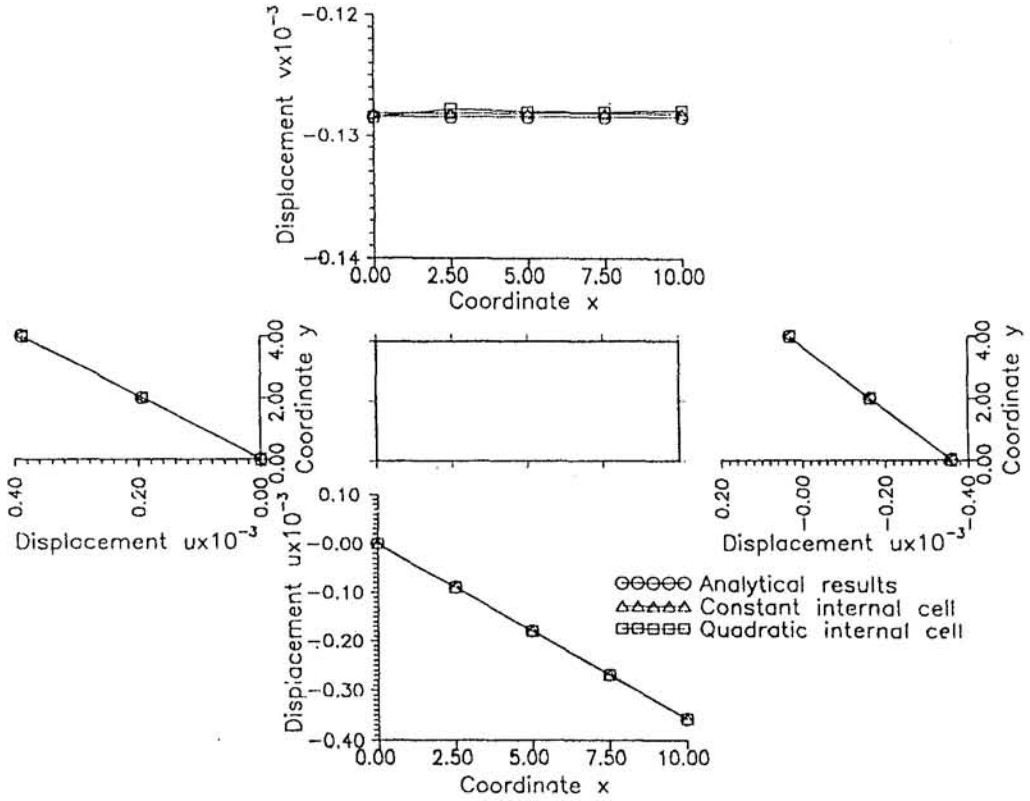

Fig. 5 Results obtained for plate under shear loading. Displacements in m.

$$
\begin{aligned}
&- \hat{D}_{ijmn}\frac{1}{2}\left[\frac{\partial}{\partial x_n(\xi)}\int_{\Omega}\epsilon^*_{mkl}(\xi,\chi)\hat{\sigma}_{kl}(\chi)d\Omega(\chi)\right.\\
&\left.+\frac{\partial}{\partial x_m(\xi)}\int_{\Omega}\epsilon^*_{nkl}(\xi,\chi)\hat{\sigma}_{kl}(\chi)d\Omega(\chi)\right]\\
&- \hat{D}_{ijmn}\frac{1}{2}\left[\frac{\partial}{\partial x_n(\xi)}\int_{\Omega}u^*_{mk}(\xi,\chi)b_k(\chi)d\Omega(\chi)\right.\\
&\left.+\frac{\partial}{\partial x_m(\xi)}\int_{\Omega}u^*_{nk}(\xi,\chi)b_k(\chi)d\Omega(\chi)\right] \quad (15)
\end{aligned}
$$

where the first term on the left-hand side is equal to $\hat{\sigma}_{ij}(\xi)$.

As the load point ξ is considered within the domain in Eq. (15), it is possible to apply the differentiation directly to the kernel of the boundary integrals. Recalling the identity

$$\frac{\partial r(\xi,\chi)}{\partial x_i(\chi)} = r_{,i} = -\frac{\partial r(\xi,\chi)}{\partial x_i(\xi)}, \quad (16)$$

the following tensors are obtained:

$$\frac{1}{2}\left[\frac{\partial u^*_{mk}(\xi,\chi)}{\partial x_n(\xi)}+\frac{\partial u^*_{nk}(\xi,\chi)}{\partial x_m(\xi)}\right] = -\epsilon^*_{mnk}(\xi,\chi) \quad (17)$$

and

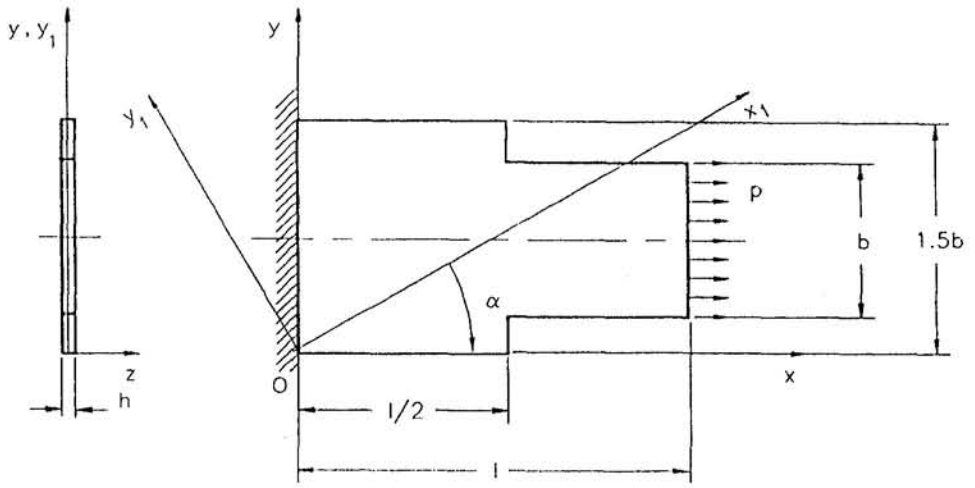

Fig. 6 Filleted plate in tension

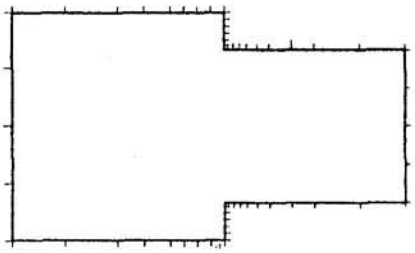

(a)

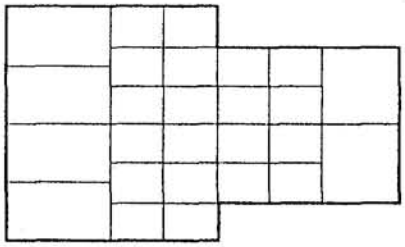

(b)

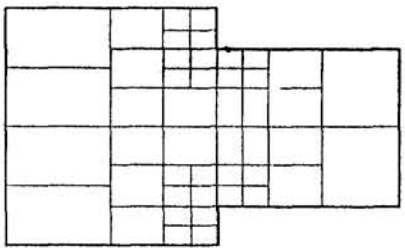

(c)

Fig. 7 Boundary discretization (*a*), and internal meshes with 26 (*b*), and 44 (*c*) internal cells

$$\frac{1}{2}\left[\frac{\partial p^*_{mk}(\xi,\chi)}{\partial x_n(\xi)}+\frac{\partial p^*_{nk}(\xi,\chi)}{\partial x_m(\xi)}\right]=-p^*_{mnk}(\xi,\chi) \quad (18)$$

where $\epsilon^*_{mnk}(\xi,\chi)$ is given by Eq. (7), while $p^*_{mnk}(\xi,\chi)$ is given by

$$p^*_{mnk}(\xi,\chi)=\frac{1}{4\pi(1-\nu)r^2}$$

$$\times\left\{(1-2\nu)(\delta_{mn}n_k-\delta_{mk}n_n-\delta_{nk}n_m-2r_{,m}r_{,n}n_k)\right.$$

$$-2\nu(r_{,m}r_{,k}n_n+r_{,n}r_{,k}n_m)-\frac{\partial r}{\partial n}[2\nu(r_{,m}\delta_{nk}+r_{,n}\delta_{mk})$$

$$\left.+2r_{,k}\delta_{mn}-8r_{,m}r_{,n}r_{,k}]\right\}. \quad (19)$$

However, differentiation of the domain integrals needs further attention due to their singular kernel.

2.1 Differentiation of the Singular Domain Integrals.

In order to obtain the final form of the integral equation for the residual stresses $\hat{\sigma}_{ij}(\xi)$ expressed by Eq. (15) it is necessary to differentiate the extended form of Somigliana's identity, Eq. (12), with respect to the coordinates of the load point. This differentiation can be directly applied to the fundamental solution tensors for the boundary integrals. However, the same procedure cannot be applied to differentiate the domain integrals as the concept of differentiation of singular integrals does not follow the classical rule (Mikhlin, 1962, 1970). The correct differentiation of these integrals yields additional terms, which can be determined analytically through the use of Leibnitz' rule (Brebbia et al., 1984; Perez and Wrobel, 1992, 1993).

According to Telles and Brebbia (1979), where the problem of differentiation of similar domain terms in a BEM formulation for plasticity is presented in detail, the derivative of the domain integrals can be written as

$$\frac{\partial}{\partial x_n(\xi)}\int_\Omega \epsilon^*_{mkl}(\xi,\chi)\hat{\sigma}_{kl}(\chi)d\Omega(\chi)$$

$$=\int_\Omega \frac{\partial \epsilon^*_{mkl}(\xi,\chi)}{\partial x_n(\xi)}\hat{\sigma}_{kl}(\chi)d\Omega(\chi)$$

$$+\hat{\sigma}_{kl}(\xi)\int_{\Gamma'_1}\epsilon^*_{mkl}(\xi,\chi)\frac{\partial r}{\partial x_n(\xi)}d\Gamma(\chi) \quad (20)$$

where Γ'_1 defines a circle of unit radius centered at the load point and $\hat{\sigma}_{kl}(\xi)$ corresponds to the first term on the left-hand side of Eq. (15).

The expression for the derivatives of the domain integral obtained in Eq. (20) can be substituted into the second term on the right-hand side of Eq. (15). This term then assumes the form

$$\frac{1}{2}\left[\frac{\partial}{\partial x_n(\xi)}\int_\Omega \epsilon^*_{mkl}(\xi,\chi)\hat{\sigma}_{kl}(\chi)d\Omega(\chi)\right.$$

$$\left.+\frac{\partial}{\partial x_m(\xi)}\int_\Omega \epsilon^*_{nkl}(\xi,\chi)\hat{\sigma}_{kl}(\chi)d\Omega(\chi)\right]$$

$$=\frac{1}{2}\left[\int_\Omega \frac{\partial \epsilon^*_{mkl}(\xi,\chi)}{\partial x_n(\xi)}\hat{\sigma}_{kl}(\chi)d\Omega(\chi)\right.$$

$$+\hat{\sigma}_{kl}(\xi)\int_{\Gamma'_1}\epsilon^*_{mkl}(\xi,\chi)\frac{\partial r}{\partial x_n(\xi)}d\Gamma(\chi)$$

$$+\int_\Omega \frac{\partial \epsilon^*_{nkl}(\xi,\chi)}{\partial x_m(\xi)}\hat{\sigma}_{kl}(\chi)d\Omega(\chi)$$

$$\left.+\hat{\sigma}_{kl}(\xi)\int_{\Gamma'_1}\epsilon^*_{nkl}(\xi,\chi)\frac{\partial r}{\partial x_m(\xi)}d\Gamma(\chi)\right]. \quad (21)$$

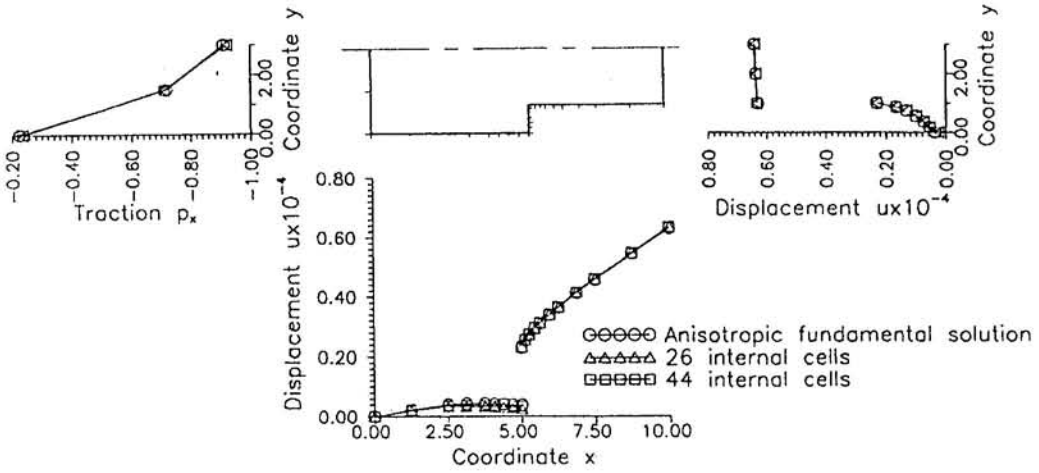

(a)

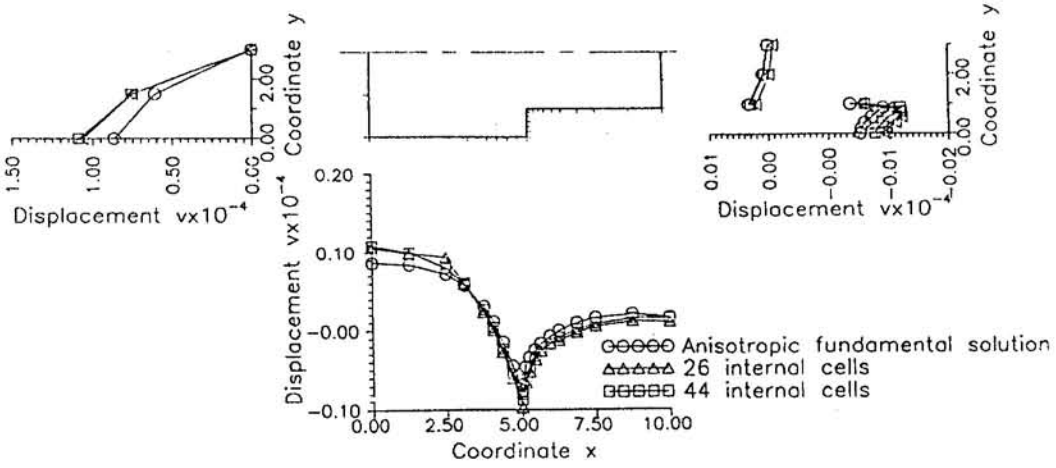

(b)

Fig. 8 Results obtained for $\alpha = 0$ deg. Variables in the x direction (a), and vertical displacements (b). Displacements given in m and tractions in MPa.

Combining the domain integrals in Eq. (21) yields

$$\frac{1}{2}\left[\int_\Omega \frac{\partial \epsilon^*_{mkl}(\xi,\chi)}{\partial x_n(\xi)}\hat{\sigma}_{kl}(\chi)d\Omega(\chi) + \int_\Omega \frac{\partial \epsilon^*_{nkl}(\xi,\chi)}{\partial x_m(\xi)}\hat{\sigma}_{kl}(\chi)d\Omega(\chi)\right] = -\int_\Omega \epsilon^*_{mnkl}(\xi,\chi)\hat{\sigma}_{kl}(\chi)d\Omega(\chi) \quad (22)$$

where

$$\epsilon^*_{mnkl}(\xi,\chi) = \frac{1}{8\pi(1-\nu)Gr^2}[(1-2\nu)(\delta_{nk}\delta_{ml}+\delta_{mk}\delta_{nl}) + 2\nu(\delta_{nl}r_{,m}r_{,k}+\delta_{ml}r_{,n}r_{,k}+\delta_{nk}r_{,m}r_{,l}+\delta_{mk}r_{,n}r_{,l}) - \delta_{mn}\delta_{kl} + 2\delta_{mn}r_{,k}r_{,l}+\delta_{kl}r_{,m}r_{,n} - 8r_{,m}r_{,n}r_{,k}r_{,l}]. \quad (23)$$

Further, combining the integrals over Γ'_i together, it is possible to express the additional term resulting from the differentiation process in the form

$$\hat{\sigma}_{kl}(\xi)\frac{1}{2}\left[\int_{\Gamma'_i}\epsilon^*_{mkl}(\xi,\chi)\frac{\partial r}{\partial x_n(\xi)}d\Gamma(\chi) + \int_{\Gamma'_i}\epsilon^*_{nkl}(\xi,\chi)\frac{\partial r}{\partial x_m(\xi)}d\Gamma(\chi)\right] = -\frac{1}{16(1-\nu)G}[(6-8\nu)\hat{\sigma}_{kl}(\xi)-\hat{\sigma}_{jj}(\xi)\delta_{kl}]. \quad (24)$$

Finally, Eq. (15) can be rewritten as

$$-\hat{\sigma}_{ij}(\xi) + \hat{D}_{ijmn}\int_\Gamma p^*_{mnk}(\xi,\chi)u_k(\chi)d\Gamma(\chi) = \hat{D}_{ijmn}\int_\Gamma \epsilon^*_{mnk}(\xi,\chi)p_k(\chi)d\Gamma(\chi)$$

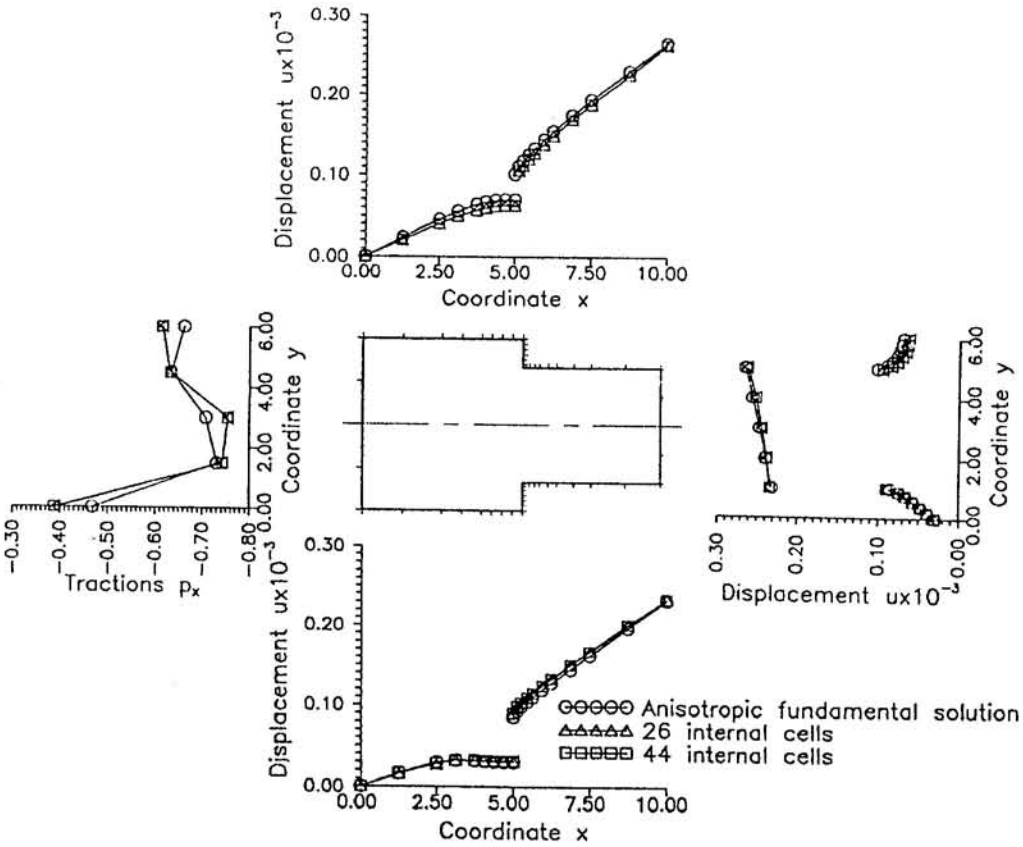

Fig. 9 Variables in the *x* direction for α = 30 deg. Displacements given in *m* and tractions in MPa.

$$- \hat{D}_{ijmn}\left\{\int_{\Omega} \epsilon^*_{mnkl}(\xi, \chi)\hat{\sigma}_{kl}(\chi)d\Omega(\chi) + \frac{1}{16(1-\nu)G}[(6-8\nu)\hat{\sigma}_{ij}(\xi) - \hat{\sigma}_{ll}(\xi)\delta_{ij}]\right\} - \hat{D}_{ijmn}\int_{\Omega} \epsilon^*_{mnk}(\xi, \chi)b_k(\chi)d\Omega(\chi). \quad (25)$$

Equations (13) and (25), together with appropriate boundary conditions, provide the necessary integral relations for the numerical solution of the problem.

3 Matrix Formulation

Following the approach used by Perez and Wrobel (1992, 1993) for anisotropic problems of potential theory, the numerical solution of the system formed by Eqs. (13) and (25) is obtained by discretizing the contour Γ into boundary elements and the domain Ω into internal cells. Then, by applying the discrete version of Eq. (13) at each boundary node, the first set of linear equations is obtained in the form

$$\mathbf{HU} - \mathbf{GP} = \mathbf{ES} - \mathbf{VB} \quad (26)$$

where $\mathbf{H}$ and $\mathbf{G}$ are the conventional BEM influence matrices; $\mathbf{U}$ and $\mathbf{P}$ denote nodal boundary displacement and nodal boundary traction vectors, respectively; $\mathbf{E}$ is the matrix resulting from the domain integration of ϵ^*_{jki}; $\mathbf{S}$ represents the vector of domain unknowns $\hat{\sigma}_{ij}$ at the internal collocation points; $\mathbf{V}$ is the matrix resulting from the domain integration of u^*_{ij}; and $\mathbf{B}$ is the actual body force vector.

The supplementary set of linear equations can similarly be obtained by applying the discretized version of Eq. (25) at the internal collocation points. This procedure leads to

$$\bar{\mathbf{H}}\mathbf{U} - \bar{\mathbf{G}}\mathbf{P} = \bar{\mathbf{E}}\mathbf{S} - \bar{\mathbf{V}}\mathbf{B} \quad (27)$$

where $\bar{\mathbf{H}}$ and $\bar{\mathbf{G}}$ are matrices concerned with boundary integrals; $\bar{\mathbf{E}}$ is a square matrix resulting from the domain integration of ϵ^*_{ijkl}; and $\bar{\mathbf{V}}$ is the matrix resulting from the domain integration of ϵ^*_{jki}.

To avoid the computation of the residual stresses $\hat{\sigma}_{ij}$ at interior points, the coupling of the two equations is done by eliminating the domain unknown vector $\mathbf{S}$. With this purpose Eq. (27) is written in the form

$$\mathbf{S} = \bar{\mathbf{E}}^{-1}(\bar{\mathbf{H}}\mathbf{U} - \bar{\mathbf{G}}\mathbf{P} + \bar{\mathbf{V}}\mathbf{B}). \quad (28)$$

The expression for vector $\mathbf{S}$ in Eq. (28) is then substituted into Eq. (26), resulting in

$$(\mathbf{H} - \mathbf{E}\bar{\mathbf{E}}^{-1}\bar{\mathbf{H}})\mathbf{U} = (\mathbf{G} - \mathbf{E}\bar{\mathbf{E}}^{-1}\bar{\mathbf{G}})\mathbf{P} - (\mathbf{V} - \mathbf{E}\bar{\mathbf{E}}^{-1}\bar{\mathbf{V}})\mathbf{B}. \quad (29)$$

This procedure is equivalent to the FEM condensation of internal degrees-of-freedom (Desai and Abel, 1972).

The final system of linear equations can be obtained by substituting the boundary conditions and rearranging Eq. (29) in order to obtain an expression of the form

$$\mathbf{AX} = \mathbf{F} \quad (30)$$

from which the boundary unknowns $\mathbf{X}$ of the problem are computed. Once this solution is obtained, the domain unknowns can be computed, if required, by referring to Eq. (5).

The algorithm recently proposed by Guiggiani and Gigante (1990) for evaluation of multidimensional Cauchy principal value integrals was used to determine the components of matrix

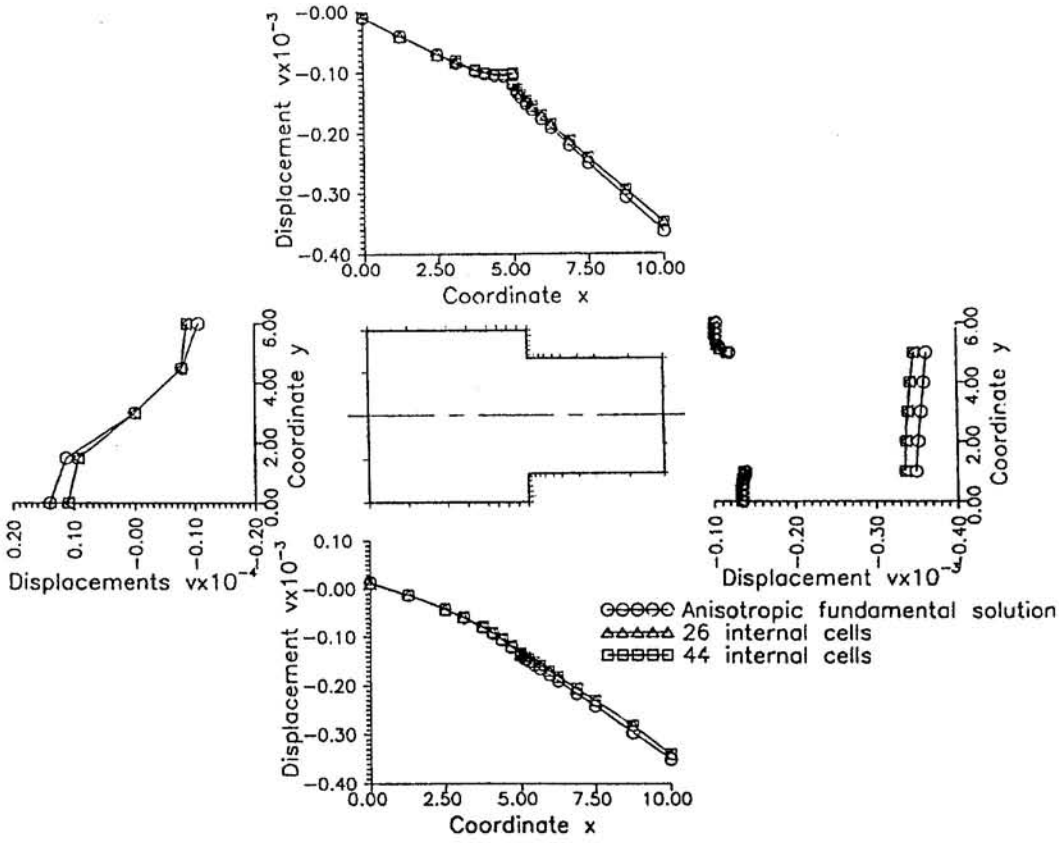

Fig. 10 Vertical displacements for α = 30 deg. Units in *m*.

$\bar{\mathbf{E}}$ when the integration is performed over the cell that contains the load point. Standard Gaussian numerical integration was used otherwise.

In this work quadratic boundary elements were used for the discretization of the contour Γ, while rectangular discontinuous internal cells were used for discretization of the domain Ω. For the latter, either constant or Lagrangian quadratic interpolation functions were used to approximate the unknowns $\hat{\sigma}_{ij}$ within each cell (Fig. 1).

4 Numerical Examples

Four examples are presented in this paper. In these examples the loading is applied on the middle plane of the cross section of the plate, thus causing a state of generalized plane stress (Lekhnitskii, 1968; Ashton et al., 1969).

In all examples the xy-axes are the reference axes of analysis, x_1y_1 are the principal directions of elasticity of the material (Lekhnitskii, 1968), and α denotes the angle between them. It should be noted that the angle α is to be measured as indicated in Fig. 2, i.e., from the principal axes of orthotropy to the reference geometrical axes (Ashton et al., 1969).

The isotropic reference elastic constants were computed in the xy-axes $E_0 = (E_{xx} + E_{yy})/2$, $\nu_0 = (\nu_{xy} + \nu_{yx})/2$ and $G_0 = E_0/[2(1 + \nu_0)]$.

Example 1. Plate stretching. Figure 2 depicts a rectangular plate subjected to tension by normal forces distributed along its two side edges. The D_{ij}^{-1} terms are coefficients of deformation (components of the inverse of the elasticity matrix) (Lekhnitskii, 1963). The length of the plate is l = 10 m, its height b = 4 m, and its thickness h = 0.25 m. The load intensity per unit length p was taken as 0.25 MN/m. The angle α was made equal to 30 deg.

The elastic properties of the material on the principal axes of elasticity were taken as $E_{x_1x_1}$ = 144.789 GPa, $E_{y_1y_1}$ = 11.721 GPa, $G_{x_1y_1}$ = 9.653 GPa and $\nu_{x_1y_1}$ = 0.21, representative of a fiber-reinforced graphite epoxy (Snyder and Cruse, 1975).

Six quadratic boundary elements were used for discretizing the contour of the plate while both constant and quadratic discontinuous internal cells were used for domain discretization. The results obtained using one constant internal cell and one subparametric quadratic internal cell are presented in Fig. 3, along with the analytical solution to the problem (Lekhnitskii, 1968). In this figure it is important to notice that the magnitude of the results presented for the top side of the plate, 10^{-4}, is one order smaller than the order for the other sides, 10^{-3}.

Example 2. Shear loading. In this example, the load intensity per unit length p is tangentially distributed along all edges of the rectangular plate (Fig. 4). This loading causes the anisotropic plate to be subjected to both shear on plane xy, which is determined by D_{66}^{-1}, and either elongation or shortening of its sides, depending on the signs of D_{16}^{-1} and D_{26}^{-1} (Lekhnitskii, 1968; Pagano and Chou, 1969). The results obtained using one constant and one subparametric quadratic internal cell are presented in Fig. 5, along with the analytical solution to the problem (Lekhnitskii, 1968). The angle α is kept equal to 30 deg.

Example 3. Filleted plate in tension. A rectangular filleted plate of fiber-reinforced graphite epoxy is submitted to uniform tensile loading (Fig. 6). The dimensions of the plate are l = 10 m, b = 4 m, and h = 0.25 m, while p was taken as 0.25 MN/m.

The contour was discretized using 28 quadratic boundary elements, Fig. 7(a), while 26 (Fig. 7(b)) and 44 (Fig. 7(c)) quadratic internal cells were used for the domain discretization.

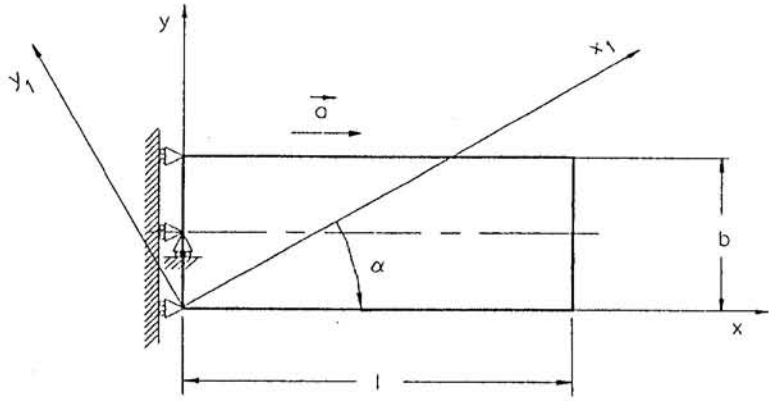

Fig. 11 Rectangular plate under inertial loading

Results for the case where the principal directions of elasticity x_1y_1 are aligned with the reference axes xy ($\alpha = 0$ deg) are presented in Fig. 8(a) for variables in the x direction and in Fig. 8(b) for variables in the y direction. Similarly, results for $\alpha = 30$ deg are presented in Fig. 9 for variables in the x direction and in Fig. 10 for variables in the y direction.

It can be seen from Figs. 8–10 that the results obtained using the formulation proposed here converge to the solution obtained using the anisotropic fundamental solution (Cruse and Swedlow, 1971). The influence of refining the internal discretization can be noted in the graph on the right hand side of Fig. 8(b).

Example 4. Inertial load. A rectangular plate of mahogany, which is considered here as a plane homogeneous orthotropic material, is analysed under inertial loading due to an acceleration $a = 9.81$ m/s^2 (Fig. 11). The axis x_1 coincides with the fiber axis of the wood whilst the axis y_1 coincides with the transversal axis of orthotropy. The elastic properties of mahogany (13 percent moisture content) are $E_{x_1x_1} = 12.397$ GPa, $E_{y_1y_1} = 0.483$ GPa, $G_{x_1y_1} = 0.469$ GPa and $\nu_{x_1y_1} = 0.55$, while its density is 530 Kg/m^3 (Bodig and Goodman, 1973). The dimensions of the plate are $l = 1$ m, $b = 0.2$ m and unit thickness.

Six quadratic boundary elements and one quadratic internal cell were used for modeling the problem. Results obtained using the formulation presented in this paper were plotted along with results obtained using the anisotropic fundamental solution and particular integrals (Deb and Banerjee, 1990). These results are presented in Fig. 12 and Fig. 13 for variables in the x and y directions, respectively. The maximum difference for displacements in the x direction, computed using the two different approaches to the problem, is around four percent for the displacement u at the corner $x = 1$ m, $y = 0.2$ m.

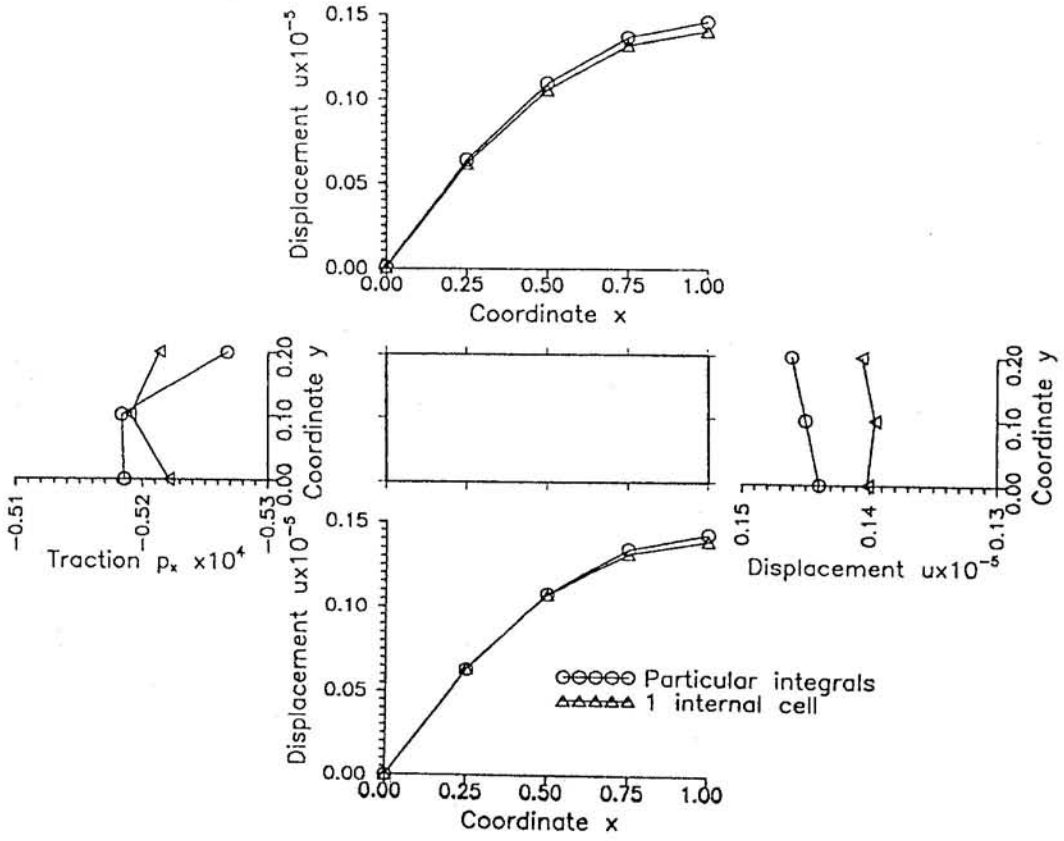

Fig. 12 Variables in the x direction for $\alpha = 30$ deg. Displacements given in m and tractions in Pa.

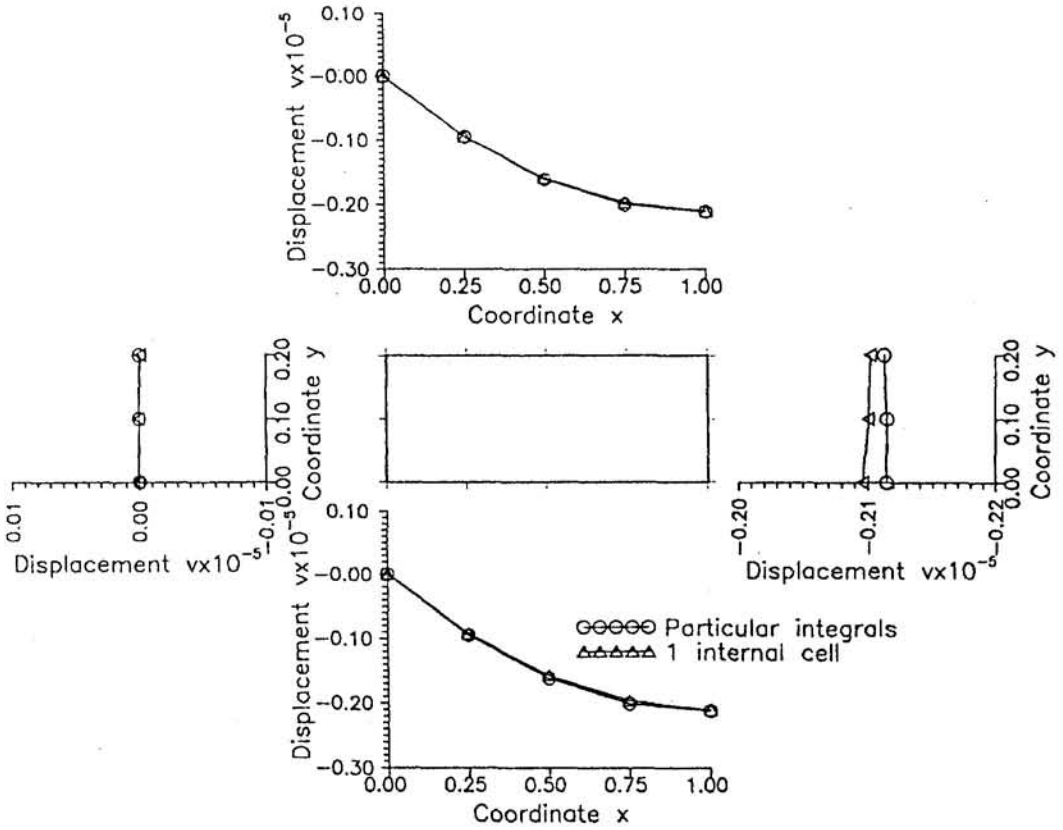

Fig. 13 Vertical displacements for α = 30 deg. Units in m.

5 Concluding Remarks

In this paper, an alternative boundary integral-equation formulation in which Kelvin's fundamental solutions for isotropic elastostatics are used for solving homogeneous anisotropic problems of the elasticity theory is presented. The proposed approach can also be used for any nonlinear or transient problems by considering the nonlinear term or the time derivative as a body force type term. Therefore, it is expected that this generalization will extend the range of application of boundary integral-equation methods in anisotropy to many problems where the fundamental solution is not known nor ever likely to be known.

The body force term, as defined in the Navier equation, Eq. (1), represents the domain loading caused, for instance, by gravitational or centrifugal forces (Brebbia et al., 1984). In the classical boundary element approach to anisotropic problems, this body force term results in domain integrals that have to be evaluated numerically. However, in contrast to isotropic problems, no Galerkin tensor corresponding to the anisotropic fundamental solution is found in the literature to make it possible to transform these domain integrals into equivalent boundary ones. Therefore, alternative techniques, such as the one presented here, or the one presented by Deb and Banerjee (1990), which introduces particular integrals to account for the specific cases of inertial and centrifugal loads, have to be used to compute the influence of body forces into the analysis.

Although the need for discretizing the domain might be seen as a practical disadvantage of the formulation proposed here, current mesh generators can greatly mitigate this possible disadvantage. Moreover, apart from using the anisotropic fundamental solution, there is no reliable alternative integral-equation formulation for the analysis of anisotropic materials that completely avoids the need to define any sort of internal nodes; for instance, no reference has been found in the literature where the solution of bending problems of homogeneous anisotropic materials was obtained using any sort of alternative integral-equation formulation.

Acknowledgments

The authors are grateful to Dr. Paulo Sollero, from Universidade Estadual de Campinas, Brazil, for the results using the anisotropic fundamental solution presented in Example 3. The first author would also like to acknowledge the financial support received from the Conselho Nacional de Desenvolvimento Científico e Technológico, CNPq, of the Ministry for Science and Technology of Brazil.

References

Ashton, J. E., Halpin, J. C., and Petit, P. H., 1969, *Primer on Composite Materials: Analysis,* Technomic Publishing Company, Stanford, CT.

Bacon, D. J., Barnett, D. M., and Scattergood, R. O., 1979, "Anisotropic Continuum Theory of Lattice Defects," *Progress in Materials Science,* Vol. 23, pp. 251–262.

Balaš, J., Sládek, J., and Sládek, V., 1989, *Stress Analysis by Boundary Element Methods,* (Studies in Applied Mechanics 23), Elsevier, New York.

Barnett, D. M., 1972, "The Precise Evaluation of Derivatives of the Anisotropic Elastic Green's Functions," *Phys. Stat. Sol.,* Vol. 49b, pp. 741–748.

Benjumea, R., and Sikarskie, D. L., 1972, "On the Solution of Plane, Orthotropic Elasticity Problems by an Integral Method," ASME JOURNAL OF APPLIED MECHANICS, Vol. 39, pp. 801–808.

Bodig, J., and Goodman, J. R., 1963, "Prediction of Elastic Parameters for Wood," *Wood Science,* Vol. 5, No. 4, pp. 249–264.

Brebbia, C. A., Telles, J. C. F., and Wrobel, L. C., 1984, *Boundary Element Techniques: Theory and Applications in Engineering,* Springer-Verlag, Berlin.

Brebbia, C. A., and Dominguez, J., 1989, *Boundary Elements: An Introductory Course,* Computational Mechanics Publications, Southampton, U.K., and McGraw-Hill, New York.

Cruse, T. A., and Swedlow, J. L., 1971, "Interactive Program for Analysis and Design Problems in Advanced Composites Technology," Report AFML-TR-71-268, Department of Mechanical Engineering, Carnegie Institute of Technology, Carnegie-Mellon University, Pittsburgh, PA.

Deb, A., and Banerjee, P. K., 1990, "BEM for General Anisotropic 2D Elasticity Using Particular Integrals," *Communications in Applied Numerical Methods,* Vol. 6, pp. 111–119.

Desai, C. S., and Abel, J. F., 1972, *Introduction to the Finite Element Method,* Van Nostrand Reinhold Company.

Fung, Y. C., 1965, *Foundations of Solid Mechanics,* Prentice-Hall, Englewood Cliffs, NJ.

Green, A. E., 1943, "A Note on Stress Systems in Aelotropic Materials—1," *Philosophical Magazine,* Vol. 34, pp. 416–418.

Guiggiani, M., and Gigante, A., 1990, "A General Algorithm for Multidimensional Cauchy Principal Value Integrals in the Boundary Element Method," ASME JOURNAL OF APPLIED MECHANICS, Vol. 57, pp. 906–915.

Lee, K. J., and Mal, A. K., 1990, "A Boundary Element Method for Plane Anisotropic Elastic Media," ASME JOURNAL OF APPLIED MECHANICS, Vol. 57, pp. 600–606.

Lekhnitskii, S. G., 1963, *Theory of Elasticity of an Anisotropic Elastic Body,* Holden-Day, San Francisco, CA.

Lekhnitskii, S. G., 1968, *Anisotropic Plates,* Gordon and Breach, New York.

Mikhlin, S. G., 1962, "Singular Integral Equations," *American Mathematical Society Transactions,* Series 1, Vol. 4, pp. 84–197.

Mikhlin, S. G., 1970, *Mathematical Physics, an Advanced Course* (North-Holland Series in Applied Mathematics and Mechanics), Vol. 11, North-Holland, Amsterdam.

Mura, T., 1987, *Micromechanics of Defects in Solids,* 2nd rev. ed., Martinus Nijhoff.

Mura, T., and Kinoshita, N., 1971, "Green's Functions for Anisotropic Elasticity," *Phys. Stat. Sol. (b),* Vol. 47, pp. 607–618.

Pagano, N. J., and Chou, P. C., 1969, "The Importance of Signs of Shear Stress and Shear Strain in Composites," *Journal of Composite Materials,* Vol. 3, pp. 166–173.

Perez, M. M., and Wrobel, L. C., 1992, "A General Integral Equation Formulation for Homogeneous Orthotropic Potential Problems," *Engineering Analysis with Boundary Elements,* Vol. 10, pp. 323–332.

Perez, M. M., and Wrobel, L. C., 1993, Use of Isotropic Fundamental Solutions for Heat Conduction in Anisotropic Media, *International Journal of Numerical Methods for Heat and Fluid Flow,* Vol. 3, pp. 49–62.

Rizo, F. J., and Shippy, D. J., 1970, "A Method for Stress Determination in Plane Anisotropic Elastic Bodies," *Journal of Composite Materials,* Vol. 4, pp. 36–61.

Shi, G., 1990, "Boundary Element Method in Bending and Eigenvalue Problems of Anisotropic Plates," *Boundary Elements in Mechanical and Electrical Engineering,* Computational Mechanics Publications, Southampton, U.K.

Snyder, M. D., and Cruse, T. A., 1975, "Boundary-Integral Equation Analysis of Cracked Anisotropic Plates," *International Journal of Fracture,* Vol. 11, No. 2.

Swedlow, J. L., and Cruse, T. A., 1971, "Formulation of Boundary Integral Equations for Three-Dimensional Elasto-Plastic Flow," *International Journal of Solids and Structures,* Vol. 7, pp. 1673–1683.

Telles, J. C. F., and Brebbia, C. A., 1979, "On the Application of the Boundary Element Method to Plasticity," research note, *Applied Mathematical Modelling,* Vol. 3, pp. 466–470.

Vogel, S. M., and Rizzo, F. J., 1973, "An Integral Equation Formulation of Three Dimensional Anisotropic Elastostatic Boundary Value Problems," *Journal of Elasticity,* Vol. 3, No. 3, pp. 203–216.

Voorhees, P. W., McFadden, G. B., and Johnson, W. C., 1992, "On the Morphological Development of Second Phase Particles in Elastically-Stressed Solids," *Acta Metallurgica et Materiala,* Vol. 40, No. 11, pp. 2979–2992.

Wilson, R. B., and Cruse, T. A., 1978, "Efficient Implementation of Anisotropic Three Dimensional Boundary-Integral Equation Stress Analysis," *International Journal for Numerical Methods in Engineering,* Vol. 12, pp. 1383–1397.

Exact Solutions for Laminated Piezoelectric Plates in Cylindrical Bending

P. Heyliger

S. Brooks

Department of Civil Engineering,
Colorado State University,
Fort Collins, CO 80523

Exact solutions are presented for the problem of piezoelectric laminates in cylindrical bending under an applied surface traction or potential. An arbitrary number of elastic or piezoelectric layers can be considered in this analysis. Example problems are considered for several representative cases, with resulting displacement, potential, stress, and electric displacement distributions shown to demonstrate the effects of the electroelastic coupling.

1 Introduction

The foundations and governing equations for linear piezoelectricity are well established and have been documented by a number of authors, including Cady (1964) and Nye (1972). Tiersten (1969) also presented extensive development of this theory as it applied to the linear vibrations of piezoelectric plates. Piezoelectric laminates have seen extensive experimental study but somewhat limited theoretical development. Ray and co-workers (1992, 1993) studied a single layer of piezoelectric material in cylindrical bending and a laminate with surface piezoelectric layers. In the latter case, the piezoelectric coefficient e_{33} was set equal to zero. Heyliger (1994) considered a similar problem in which this coefficient was nonzero, resulting in a different form of the solution of the elastic and electric field variables.

Most of the studies that have appeared to date such as the work of Tzou and co-workers (1989) and Lee (1989, 1990) on piezoelectric laminates have incorporated a number of simplifying assumptions regarding the nature of the elastic and electric field quantities. This includes the assumptions related to the distribution of the displacement and electrostatic potential through the thickness of the laminate.

In the present study, exact solutions are presented for piezoelectric laminates in the two-dimensional configuration of cylindrical bending. This extends the work of Pagano (1969, 1970b) for elastic laminates. The expressions for the displacements, stresses, potential, and electric displacement are presented for several representative laminates. These results should provide a means of comparison for simpler and more computationally efficient piezoelectric plate theories while also providing information regarding the behavior of these increasingly important laminates.

2 Exact Solution

Governing Equations. The geometry of the laminate is such that the thickness dimension of the laminate coincides with the z-direction, with the length of the plate in the y-direction denoted as L and the total thickness denoted as H. Each layer of the laminate is of thickness h_i and can be purely elastic or piezoelectric. The general problem considered in this study is to determine the behavior of the elastic and electric field components throughout the laminate under an applied mechanical or electrical loading. The forcing function is introduced through either an applied surface displacement, traction, potential, or electric charge. It is also possible to consider internally applied quantities in this formulation.

A single piezoelectric layer has the constitutive equations given in contracted notation by (Tiersten 1969)

$$\sigma_i = C_{ij}S_j - e_{ki}E_k$$
$$D_k = e_{kj}S_j + \epsilon_{kl}E_l. \tag{1}$$

Here σ_i are the components of the stress tensor, C_{ij} are the elastic stiffness components, S_j are the components of infinitesimal strain, e_{ki} are the piezoelectric coefficients, E_k are the components of the electric field, D_k are the components of the electric displacement, and ϵ_{kl} are the dielectric constants. For these equations only, the indices i and j range from 1 to 6, and k and l range from 1 to 3. The poling direction is coincident with the x_3 or z-axis. In cylindrical bending, all variables are assumed to be independent of the $x_1 = x$-axis.

The displacement components u_i, where $u_1 = u$, $u_2 = v$, and $u_3 = w$, are related to the strains S_{ij} through

$$S_{ij} = \frac{1}{2}\left(\frac{\partial u_i}{\partial x_j} + \frac{\partial u_j}{\partial x_i}\right). \tag{2}$$

To be consistent with Eq. (1), the conventional notation for the strain indices has been used, i.e., $S_{11} = S_1$, $S_{23} = S_4$, etc. The electric field components can be related to the electrostatic potential ϕ using the relation

$$E_i = -\frac{\partial \phi}{\partial x_i}. \tag{3}$$

The materials used in this study are originally orthotropic, with a rotation about the z-axis then allowed. It is assumed that the nonzero components of the rotated piezoelectric tensor e_{ij} are e_{31}, e_{32}, e_{33}, e_{24}, e_{25}, and e_{36}. The rotated elastic stiffnesses C_{ij} are those of a monoclinic material, and the necessary dielectric constants are given by ϵ_{22} and ϵ_{33}.

The equilibrium equations in the absence of body forces are given by

$$\sigma_{ij,j} = 0 \tag{4}$$

and the charge equation of electrostatics is given as

$$D_{i,i} = 0. \tag{5}$$

Substituting in the constitutive relations, the stress-strain relations, and the field-potential relations gives the governing equa-

Contributed by the Applied Mechanics Division of THE AMERICAN SOCIETY OF MECHANICAL ENGINEERS for publication in the ASME JOURNAL OF APPLIED MECHANICS.

Discussion on this paper should be addressed to the Technical Editor, Professor Lewis T. Wheeler, Department of Mechanical Engineering, University of Houston, Houston, TX 77204-4792, and will be accepted until four months after final publication of the paper itself in the ASME JOURNAL OF APPLIED MECHANICS.

Manuscript received by the ASME Applied Mechanics Division, May 27, 1993; final revision, June 19, 1995. Associate Technical Editor: X. Markenscoff.

tions of the problem in terms of the displacement components u, v, and w and the electrostatic potential ϕ as

$$C_{26}\frac{\partial^2 v}{\partial y^2} + C_{36}\frac{\partial^2 w}{\partial y \partial z} + C_{66}\frac{\partial^2 u}{\partial y^2} + e_{36}\frac{\partial^2 \phi}{\partial y \partial z} + C_{45}\left(\frac{\partial^2 w}{\partial y \partial z} + \frac{\partial^2 v}{\partial z^2}\right) + C_{55}\frac{\partial^2 u}{\partial z^2} + e_{25}\frac{\partial^2 \phi}{\partial y \partial z} = 0 \quad (6)$$

$$C_{22}\frac{\partial^2 v}{\partial y^2} + C_{23}\frac{\partial^2 w}{\partial y \partial z} + C_{26}\frac{\partial^2 u}{\partial y^2} + e_{32}\frac{\partial^2 \phi}{\partial y \partial z} + C_{44}\left(\frac{\partial^2 w}{\partial y \partial z} + \frac{\partial^2 v}{\partial z^2}\right) + C_{45}\frac{\partial^2 u}{\partial z^2} + e_{24}\frac{\partial^2 \phi}{\partial y \partial z} = 0 \quad (7)$$

$$C_{44}\left(\frac{\partial^2 v}{\partial y \partial z} + \frac{\partial^2 w}{\partial y^2}\right) + C_{45}\frac{\partial^2 u}{\partial y \partial z} + e_{24}\frac{\partial^2 \phi}{\partial y^2} + C_{23}\frac{\partial^2 v}{\partial y \partial z} + C_{33}\frac{\partial^2 w}{\partial z^2} + C_{36}\frac{\partial^2 u}{\partial y \partial z} + e_{33}\frac{\partial^2 \phi}{\partial z^2} = 0 \quad (8)$$

$$e_{24}\left(\frac{\partial^2 v}{\partial y \partial z} + \frac{\partial^2 w}{\partial y^2}\right) + e_{25}\frac{\partial^2 u}{\partial y \partial z} - \epsilon_{22}\frac{\partial^2 \phi}{\partial y^2} + e_{32}\frac{\partial^2 v}{\partial y \partial z} + e_{33}\frac{\partial^2 w}{\partial z^2} + e_{36}\frac{\partial^2 u}{\partial y \partial z} - \epsilon_{33}\frac{\partial^2 \phi}{\partial z^2} = 0. \quad (9)$$

These represent the governing equation for a single piezoelectric layer. For a layer with no piezoelectric effects, these equations reduce to the three-dimensional equations of elasticity and, assuming $\epsilon_{11} = \epsilon_{22} = \epsilon_{33}$, the Laplace equation for electrostatics.

For the problems considered in this study, an arbitrary number of laminae are assumed to be perfectly bonded together. At the top and bottom surface of the laminate, a specified load, displacement, potential, or charge can be imposed. Of primary interest here are the cases in which either a known normal traction or potential are imposed on the top and/or bottom surfaces. These are the cases considered in this study, with the shear tractions specified to be zero on the top and bottom surfaces. The laminate is assumed to be simply supported, and the vertical edges of the laminate are assumed to be grounded. Hence along a vertical plate edge, the normal stress σ_y, transverse displacement w, and electrostatic potential ϕ are specified to be zero.

Both the applied load and potential can be expressed in the form of a Fourier series. These functions are represented in the form

$$q(y) = q_o \sin py \quad (10)$$

$$\hat{\phi}(y) = \hat{\phi}_o \sin py \quad (11)$$

where

$$p = p(n) = \frac{n\pi}{L} \quad (12)$$

and n is an integer. These expressions can be used either for the top or bottom of the laminate.

At each interface between layers, continuity conditions of displacement, traction, potential, and electric displacement must be enforced. Using an indexing scheme, the conditions for the ith layer can be expressed as, for example,

$$u^i\left(y, \frac{-h_i}{2}\right) = u^{i+1}\left(y, \frac{h_{i+1}}{2}\right). \quad (13)$$

Here i represents the layer number, with $i = 1$ the top layer, and each layer has an individual coordinate system with the origin at the left end in the center of the layer. Similar interface conditions exist for v, w, ϕ, σ_z, σ_{xz}, σ_{yz}, and D_z.

Method of Solution. There are two types of solution presented here corresponding to laminae with the principal material directions unaligned or coincident with the x or y-axes.

Off-Axis Laminae. Solutions for the displacement components and the electrostatic potential are sought in the form

$$u(x, y, z) = U(z)\cos py = \bar{U}\exp(psz)\cos py$$
$$v(x, y, z) = V(z)\cos py = \bar{V}\exp(psz)\cos py$$
$$w(x, y, z) = W(z)\sin py = \bar{W}\exp(psz)\sin py$$
$$\phi(x, y, z) = \Phi(z)\sin py = \bar{\Phi}\exp(psz)\sin py. \quad (14)$$

Here the overbarred terms are constants and s is an unknown number. Substitution of these expressions into the equilibrium and charge equations results in the system of equations

$$\begin{bmatrix} C_{55}s^2 + A_{11} & C_{45}s^2 + A_{12} & A_{13}s & A_{14}s \\ C_{45}s^2 + A_{12} & C_{44}s^2 + A_{22} & A_{23}s & A_{24}s \\ -A_{13}s & -A_{23}s & C_{33}s^2 + A_{33} & e_{33}s^2 + A_{34} \\ -A_{14}s & -A_{24}s & e_{33}s^2 + A_{34} & A_{44} - \epsilon_{33}s^2 \end{bmatrix} \times \begin{Bmatrix} \bar{U} \\ \bar{V} \\ \bar{W} \\ \bar{\Phi} \end{Bmatrix} = \begin{Bmatrix} 0 \\ 0 \\ 0 \\ 0 \end{Bmatrix} \quad (15)$$

The elements A_{ij} are given by

$$A_{11} = -C_{66} \quad A_{12} = -C_{26} \quad A_{13} = C_{36} + C_{45} \quad A_{14} = e_{25} + e_{36}$$
$$A_{22} = -C_{22} \quad A_{23} = C_{23} + C_{44} \quad A_{24} = e_{32} + e_{24}$$
$$A_{33} = -C_{44} \quad A_{34} = -e_{24} \quad A_{44} = \epsilon_{22}. \quad (16)$$

Setting the determinant of this matrix to zero results in the characteristic equation

$$As^8 + Bs^6 + Cs^4 + Ds^2 + E = 0. \quad (17)$$

Expressions for the coefficients of this polynomial are lengthy and are not given here. This equation can be written as the fourth-order equation

$$r^4 + cr^3 + dr^2 + er + f = 0 \quad (18)$$

where

$$r = s^2 \quad (19)$$

$$c = \frac{B}{A} \quad d = \frac{C}{A} \quad e = \frac{D}{A} \quad f = \frac{E}{A}. \quad (20)$$

The roots of Eq. (18) are a function of the material properties and the form of the applied load or potential as represented by p. They can be real, imaginary, or complex. Regardless of the nature of the roots, the solutions for $V(z)$, $W(z)$, and $\Phi(z)$ corresponding to a given root s are based on an initial construction of the solution for $U(z)$. The remaining components can then be computed using Eq. (15), which is rearranged as

$$\begin{bmatrix} C_{44}s^2 + A_{22} & A_{23}s & A_{24}s \\ -A_{23}s & C_{33}s^2 + A_{33} & e_{33}s^2 + A_{34} \\ -A_{24}s & e_{33}s^2 + A_{34} & A_{44} - \epsilon_{33}s^2 \end{bmatrix} \begin{Bmatrix} \bar{V} \\ \bar{W} \\ \bar{\Phi} \end{Bmatrix} = \bar{U}\begin{Bmatrix} -C_{45}s^2 - A_{12} \\ A_{13}s \\ A_{14}s \end{Bmatrix}. \quad (21)$$

General expressions for the constants $\bar{V}$, $\bar{W}$, and $\bar{\Phi}$ can be

constructed as a function of the real, imaginary, or complex roots. These are

$$\tilde{V}(s) = \frac{f_{11}s^6 + f_{12}s^4 + f_{13}s^2 + f_{14}}{\tilde{\Delta}(s)} \tag{22}$$

$$\tilde{W}(s) = \frac{s(f_{21}s^4 + f_{22}s^2 + f_{23})}{\tilde{\Delta}(s)} \tag{23}$$

$$\tilde{\Phi}(s) = \frac{s(f_{31}s^4 + f_{32}s^2 + f_{33})}{\tilde{\Delta}(s)} \tag{24}$$

$$\tilde{\Delta}(s) = d_1s^6 + d_2s^4 + d_3s^2 + d_4. \tag{25}$$

The constants d_i and f_{ij} are lengthy and are not given here. The solutions for the elastic and electric field components corresponding to each type of root are developed separately below.

Case 1: Real Roots for r. Given n real roots for r, the $2n$ roots for s can be obtained using Eq. (19). These roots are either real or imaginary depending on the sign of r. Following the nomenclature used in Pagano (1970), the solution for the displacement components and electrostatic potential corresponding to the these roots can in either case be written as

$$U(z) = \sum_{j=1}^{n} U_j(z) \quad V(z) = \sum_{j=1}^{n} L_jU_j(z)$$

$$W(z) = \sum_{j=1}^{n} M_jW_j(z) \quad \Phi(z) = \sum_{j=1}^{n} N_jW_j(z) \tag{26}$$

where

$$U_j(z) = F_jC_j(z) + G_jS_j(z)$$

$$W_j(z) = G_jC_j(z) + \alpha_jF_jS_j(z). \tag{27}$$

Here F_j and G_j are real constants, there is no sum on j, and the functions C and S are defined as

$$C_j = \cosh(pm_jz) \quad S_j(z) = \sinh(pm_jz) \quad \alpha_j = 1 \ (r > 0) \tag{28}$$

$$C_j = \cos(pm_jz) \quad S_j(z) = \sin(pm_jz) \quad \alpha_j = -1 \ (r < 0) \tag{29}$$

with $m_j = |s_j|$. The coefficients L_j, M_j, and N_j are more specific representations of the parameters given in Eqs. (22)–(25) and are given in this case as

$$L_j = \frac{1}{\Delta_j}(f_{11}\alpha_jm_j^6 + f_{12}m_j^4 + f_{13}\alpha_jm_j^2 + f_{14}) \tag{30}$$

$$M_j = \frac{m_j}{\Delta_j}(f_{21}m_j^4 + f_{22}\alpha_jm_j^2 + f_{23}) \tag{31}$$

$$N_j = \frac{m_j}{\Delta_j}(f_{31}m_j^4 + f_{32}\alpha_jm_j^2 + f_{33}) \tag{32}$$

where the determinant Δ_j is given by

$$\Delta_j = d_1\alpha_jm_j^6 + d_2m_j^4 + d_3\alpha_jm_j^2 + d_4. \tag{33}$$

Using the constitutive equations in (1), the corresponding expressions for the stress and electric displacement can be computed as

$$\sigma_i = \sin py \sum_{j=1}^{n} [-C_{i2}L_j - C_{i6} + C_{i3}\alpha_j\frac{m_j^2}{D_j}(f_{21}m_j^4 + f_{22}m_j^2\alpha_j + f_{23}) + e_{3i}\alpha_j\frac{m_j^2}{D_j}(f_{31}m_j^4 + f_{32}m_j^2\alpha_j + f_{33})]pU_j(z) \tag{34}$$

$$\sigma_{yz} = \cos py \sum_{j=1}^{n} [C_{44}(L_jm_j + M_j) + e_{24}N_j + C_{45}m_j]pW_j(z) \tag{35}$$

$$\sigma_{xz} = \cos py \sum_{j=1}^{n} [C_{45}(L_jm_j + M_j) + e_{25}N_j + C_{55}m_j]pW_j(z) \tag{36}$$

$$\sigma_{xy} = \sin py \sum_{j=1}^{n} [-C_{26}L_j - C_{66} + C_{36}\alpha_j\frac{m_j^2}{D_j}(f_{21}m_j^4 + f_{22}m_j^2\alpha_j + f_{23}) + e_{36}\alpha_j\frac{m_j^2}{D_j}(f_{31}m_j^4 + f_{32}m_j^2\alpha_j + f_{33})]pU_j(z) \tag{37}$$

$$D_y = \cos py \sum_{j=1}^{n} [e_{24}(L_jm_j + M_j) + e_{25}m_j - \epsilon_{22}N_j]pW_j(z) \tag{38}$$

$$D_z = \sin py \sum_{j=1}^{n} [-e_{32}L_j - e_{36} + e_{33}\alpha_j\frac{m_j^2}{D_j}(f_{21}m_j^4 + f_{22}m_j^2\alpha_j + f_{23}) - \epsilon_{33}\alpha_j\frac{m_j^2}{D_j}(f_{31}m_j^4 + f_{32}m_j^2\alpha_j + f_{33})]pU_j(z) \tag{39}$$

Here $i = 1, 2, 3$ correspond to x, y, and z for the normal stress components.

Case 2: Complex Roots for r. The elastic, electric, and geometric properties for some laminae yield complex roots. These occur in conjugate pairs, which result in the final roots for s in the form $\pm(a \pm ib)$, where $i = \sqrt{-1}$ and a and b are positive constants. The solution for $U(z)$ in this case can be expressed as

$$U(z) = c_1e^{az}\cos bz + c_2e^{az}\sin bz + c_3e^{-az}\cos bz + c_4e^{-az}\sin bz \tag{40}$$

where c_1–c_4 are real constants. Following some algebraic manipulations and using Eqs. (21)–(25), the solution for $V(z)$ can be expressed as

$$V(z) = c_1e^{az}(\Gamma_1\cos bz - \Omega_1\sin bz) + c_2e^{az}(\Omega_1\cos bz + \Gamma_1\sin bz) + c_3e^{-az}(\Gamma_1\cos bz + \Omega_1\sin bz) + c_4e^{-az}(-\Omega_1\cos bz + \Gamma_1\sin bz). \tag{41}$$

Here $\Gamma_1 = \Re[\tilde{V}(a + ib)]$ and $\Omega_1 = \Im[\tilde{V}(a + ib)]$. Similarly, the final expression for $W(z)$ can be expressed as

$$W(z) = c_1e^{az}[(a\Gamma_2 - b\Omega_2)\cos bz + (-b\Gamma_2 - a\Omega_2)\sin bz] + c_2e^{az}[(b\Gamma_2 + a\Omega_2)\cos bz + (a\Gamma_2 - b\Omega_2)\sin bz] + c_3e^{-az}[(b\Omega_2 - a\Gamma_2)\cos bz + (-b\Gamma_2 - a\Omega_2)\sin bz] + c_4e^{-az}[(b\Gamma_2 + a\Omega_2)\cos bz + (-a\Gamma_2 + b\Omega_2)\sin bz] \tag{42}$$

where $\Gamma_2 = \Re[\tilde{W}(a + ib)]$ and $\Omega_2 = \Im[\tilde{W}(a + ib)]$. The final expression for Φ is identical to that of $W(z)$ except the subscript on Γ and Ω changes from 2 to 3, with $\Gamma_3 = \Re[\tilde{\Phi}(a + ib)]$ and $\Omega_3 = \Im[\tilde{\Phi}(a + ib)]$.

The expressions for the stress and electric displacement components can be obtained by the appropriate differentiation and

Table 1 Elastic, piezoelectric, and dialectric properties of piezoelectric materials

Property	PZT-4	PVDF	$(Pb_{.88}Ca_{.12})((CO_{.5}W_{.5})_{.04}Ti_{.96})O_3$
E_1 (GPa)	81.3	237.	127.
E_2	81.3	23.2	127.
E_3	64.5	10.5	119.
ν_{12}	0.329	0.154	0.199
ν_{13}	0.432	0.178	0.174
ν_{23}	0.432	0.177	0.174
G_{23}	25.6	2.15	53.5
G_{13}	25.6	4.40	53.5
G_{12}	30.6	6.43	53.0
e_{24} (C/m^2)	12.72	-.01	2.96
e_{31}	-5.20	-.13	0.80
e_{32}	-5.20	-.14	0.80
e_{33}	15.08	-.28	6.88
$\frac{\epsilon_{33}}{\epsilon_0}$	1300	11.98	181
$\frac{\epsilon_{22}}{\epsilon_0}$	1475	11.98	202

combination with the constitutive equations as given in Eq. (1). These expressions are omitted here for brevity.

On-Axis Laminae. If the material axes of the lamina coincide with the x or y-axes, the material constants $C_{26} = C_{36} = C_{45} = e_{25} = e_{36} = 0$ and the displacement in the x-direction uncouples from the other displacements and the electrostatic potential. A procedure similar to that of the previous section is used with the matrix Eq. (15) modified such that the first row and column are eliminated and the exponential arguments of the fields are taken as (sz) instead of (psz) in Eq. (14). Two of the roots are computed as $\pm p\sqrt{C_{66}/C_{55}}$, with the remaining six roots found from the characteristic equation

$$-As^6 + Bs^4 + Cs^2 + D = 0 \tag{43}$$

where the constants A, B, C, and D are easily determined. This can be expressed as the third-order equation

$$g^3 + dg + f = 0. \tag{44}$$

The nature of the subsequent solution depends on the magnitude of the parameter κ, which is given by the value

$$\kappa = \frac{d^3}{27} + \frac{f^2}{4}. \tag{45}$$

If $\kappa < 0$, then the three roots for g are real and distinct. For $\kappa = 0$, there will be three real roots, at least two of which are equal. For $\kappa > 0$, there will be one real root and two conjugate complex roots. The case $\kappa = 0$ was not found for any of the materials considered in this study. Only the remaining two cases are considered.

Case 1: $\kappa < 0$. Given three real roots for g, the roots of the original sixth-order equation can be determined by considering

$$\gamma = s^2 = g + \frac{B}{3A}. \tag{46}$$

This will lead to six roots for m, which can are either real or imaginary depending on the sign of γ. The solution for V, W, and Φ can be cast in the same form as for the off-axis lamina in Eq. (26) with $n = 3$ and, for the expressions that follow, the argument of the trigonometric and hyperbolic functions in Eqs. (28)–(29) are $(m_j z)$ rather than $(pm_j z)$. Additionally,

$$m_j = \left| g_j + \frac{B}{3A} \right|^{1/2}. \tag{47}$$

The values for the coefficients in Eq. (26) now take the form

$$L_j = \frac{pm_j}{J_j}\left[(\alpha_j m_j^2 \epsilon_{33} - p^2\epsilon_{22})(C_{23} + C_{44}) + (\alpha_j m_j^2 e_{33} - e_{24}p^2)(e_{24} + e_{32})\right] \tag{48}$$

$$R_j = \frac{pm_j}{J_j}\left[(\alpha_j m_j^2 e_{33} - e_{24}p^2)(C_{44} + C_{23}) + (C_{44}p^2 - \alpha_j m_j^2 C_{33})(e_{24} + e_{32})\right] \tag{49}$$

$$J_j = (\alpha_j m_j^2 \epsilon_{33} - p^2\epsilon_{22})(\alpha_j m_j^2 C_{33} - p^2 C_{44}) + m_j^4 e_{33}^2 - 2\alpha_j m_j^2 p^2 e_{33} e_{24} + e_{24}^2 p^4. \tag{50}$$

The stresses and electric displacement components can be computed with little difficulty.

If the layer is nonpiezoelectric, the coefficients $e_{ij} = 0$ and the elastic and electric fields uncouple within a given layer. The elastic solutions have been given by Pagano (1970a, b) for the on-axis and off-axis laminates and are not repeated here. The two roots corresponding to the potential can be computed as

$$n_{1,2} = \pm p\sqrt{\frac{\epsilon_{22}}{\epsilon_{33}}}. \tag{51}$$

The electrostatic potential within the elastic layer is therefore given by

$$\Phi(z) = \sin py \sum_{j=1}^{2} B_j \exp(n_j z) \tag{52}$$

where B_j are constants. The components of electric displacement for these layers are given by

$$D_y = -\epsilon_{22} p \cos py \sum_{j=1}^{2} B_j \exp(n_j z) \tag{53}$$

$$D_z = -\epsilon_{33} \sin py \sum_{j=1}^{2} B_j n_j \exp(n_j z). \tag{54}$$

Case 2: $\kappa > 0$. When $\kappa > 0$, there will be one real root for g and two roots that are complex conjugate. The case of real roots for g has been discussed in the previous section, and the focus here is on the remaining two roots. When γ is complex, the two complex conjugate roots of g can be used to express the final roots of m as $\pm(a \pm ib)$, where $i = \sqrt{-1}$ and a and b are positive constants. The general solution for V in this case can be expressed as

$$V(z) = e^{az}(c_1 \cos bz + c_2 \sin bz) + e^{-az}(c_3 \cos bz + c_4 \sin bz) \tag{55}$$

where $c_1 - c_4$ are real constants. The corresponding solution for W can be written as

$$W(z) = e^{az}[(c_1\beta_1 + c_2\beta_2)\cos bz + (-c_1\beta_2 + c_2\beta_1)\sin bz] + e^{-az}[(-c_3\beta_1 + c_4\beta_2)\cos bz + (-c_3\beta_2 - c_4\beta_1)\sin bz]. \tag{56}$$

Here the parameters β_1 and β_1 are defined to be

$$\beta_1 = a\Gamma_1 - b\Omega_1 \quad \beta_2 = b\Gamma_1 + a\Omega_1 \tag{57}$$

where

$$\Gamma_1 = \frac{\xi_1\xi_3 + \xi_2\xi_4}{\xi_3^2 + \xi_4^2} \tag{58}$$

$$\Omega_1 = \frac{\xi_2\xi_3 - \xi_1\xi_4}{\xi_3^2 + \xi_4^2} \tag{59}$$

where $\xi_1 = \Re(pF_1)$, $\xi_2 = \Im(pF_1)$, $\xi_3 = \Re(pF_2)$, $\xi_4 = \Im(pF_2)$. The functions F_1 and F_2 given by

Table 2 Thickness distributions for two-layer piezoceramic

	Applied Load			Applied Potential		
z x 10^3	V x 10^{13}	W x 10^{10}	Φ x 10^4	V x 10^{11}	W x 10^{10}	Φ
5.0	-170.406	1.05609	0.0	-17.2277	2.21625	1.0
3.75	-129.322	1.05896	6.17969	-14.4289	2.29892	.967338
2.5	-88.8804	1.06105	10.5763	-11.6676	2.37336	.935611
1.25	-48.8826	1.06236	13.2037	-8.93234	2.43971	.904762
0.0	-9.13120	1.06291	14.0706	-6.21137	2.49809	.874736
-1.25	31.5361	1.06292	11.3823	-5.03124	2.62086	.655129
-2.5	72.3126	1.06263	8.14620	-3.85882	2.74217	.436359
-3.75	113.341	1.06203	4.35533	-2.69006	2.86221	.218094
-5.0	154.765	1.06112	0.0	-1.52091	2.98116	0.0

a. Displacements and potential.

	Applied Load				Applied Potential			
z x 10^3	σ_y	σ_z	σ_{yz}	D_z x 10^{10}	σ_y	σ_z x 10^2	σ_{yz}	D_z x 10^7
5.0	57.8914	1.0	0.0	-2.21625	98.0706	0.0	0.0	-4.38016
3.75	43.9608	.958954	1.99926	-2.34277	29.3552	-5.79244	2.50035	-4.14535
2.5	30.1904	.850095	3.45477	-2.67988	-38.9872	-16.1166	2.31044	-3.91847
1.25	16.5305	.694665	4.37185	-3.16447	-107.217	-20.4299	-.560217	-3.69876
0.0	2.93185	.513734	4.75387	-3.73402	-175.593	-8.20718	-6.11227	-3.48550
0.0	3.77076	.513734	4.75387	-3.73402	135.710	-8.20718	-6.11227	-3.48550
-1.25	-13.1944	.328502	4.56889	-3.80575	87.2734	6.57771	-1.73460	-3.46700
-2.5	-30.2007	.163623	3.71705	-3.87336	38.9426	7.90257	.743546	-3.45386
-3.75	-47.3021	.045329	2.19569	-3.92364	-9.43411	3.22258	1.32334	-3.44601
-5.0	-64.5526	0.0	0.0	-3.94337	-58.0090	0.0	0.0	-3.44340

b. Stresses and electric displacement.

Table 3 Thickness distributions for two-layer angle ply

	Applied Load				Applied Potential			
z x 10^3	U x 10^{10}	V x 10^{10}	W x 10^9	Φ x 10^2	U x 10^{12}	V x 10^{11}	W x 10^{12}	Φ
5.0	-.206992	-.495662	.346564	0.0	-.764064	-.468075	15.6059	1.0
3.75	-.206070	-.364412	.346799	.134270	-.755342	-.424885	12.2777	.871884
2.5	-.204588	-.240359	.346939	.230526	-.639752	-.389956	8.97940	.745014
1.25	-.204392	-.119897	.346995	.289030	-.420367	-.362492	5.70691	.619210
0.0	-.207306	.000495	.346968	.310144	-.096538	-.342085	2.45603	.494292
-1.25	-.204461	.120891	.346877	.289005	.269690	-.356217	-.77633	.370085
-2.5	-.204705	.241306	.346704	.230483	.529472	-.377512	-3.99341	.246419
-3.75	-.206214	.365260	.346446	.134230	.686048	-.406159	-7.19927	.123116
-5.0	-.207145	.496354	.346093	0.0	.738964	-.442736	-10.3979	0.0

a. Displacements and potential.

	Applied Load			Applied Potential		
z x 10^3	σ_x	σ_y	σ_{xy}	σ_x	σ_y	σ_{xy}
5.0	59.7588	79.7839	-42.1976	-.724839	1.16623	-6.72581
3.75	34.9072	49.6298	-20.2912	-1.44536	.271217	-6.01241
2.5	11.5045	21.2152	.293333	-1.84070	-.265246	-5.65146
1.25	-11.4374	-6.59348	20.5300	-1.93095	-.466448	-5.62344
0.0	-34.8876	-34.9076	41.3746	-1.72257	-.340519	-5.92280
0.0	34.8919	34.8719	41.2207	-1.39763	-.015570	6.30743
-1.25	11.4529	6.56881	20.3894	-1.70438	-.265235	5.81390
-2.5	-11.4720	-21.2210	.170115	-1.70708	-.181898	5.65351
-3.75	-34.8512	-49.6081	-20.3923	-1.40754	.233379	5.82299
-5.0	-59.6717	-79.7249	-42.2709	-.794152	.994541	6.33291

b. Intralaminar stresses.

	Applied Load				Applied Potential			
z x 10^3	σ_z	σ_{xz}	σ_{yz}	D_z x 10^{10}	σ_z x 10^2	σ_{xz}	σ_{yz} x 10^2	D_z x 10^7
5.0	1.0	0.0	0.0	-.156059	0.0	0.0	0.0	-.116937
3.75	.946384	-1.22100	2.53343	-.153601	-.064501	-.248914	2.69964	-.115712
2.5	.816009	-1.61094	3.92066	-.147352	-.175424	-.476821	2.59877	-.114655
1.25	.652840	-1.20250	4.20759	-.138952	-.249742	-.697131	1.05460	-.113762
0.0	.499904	.009427	3.39620	-.130007	-.256322	-.922764	-.637134	-.113034
-1.25	.346993	1.21556	4.20638	-.121071	-.221507	-.685872	-1.29919	-.112469
-2.5	.183886	1.61881	3.91882	-.112677	-.150059	-.461787	-2.28504	-.112065
-3.75	.053581	1.22444	2.53188	-.106434	-.054817	-.237534	-2.29396	-.111823
-5.0	0.0	0.0	0.0	-.103979	0.0	0.0	0.0	-.111743

c. Interlaminar stresses and electric displacement.

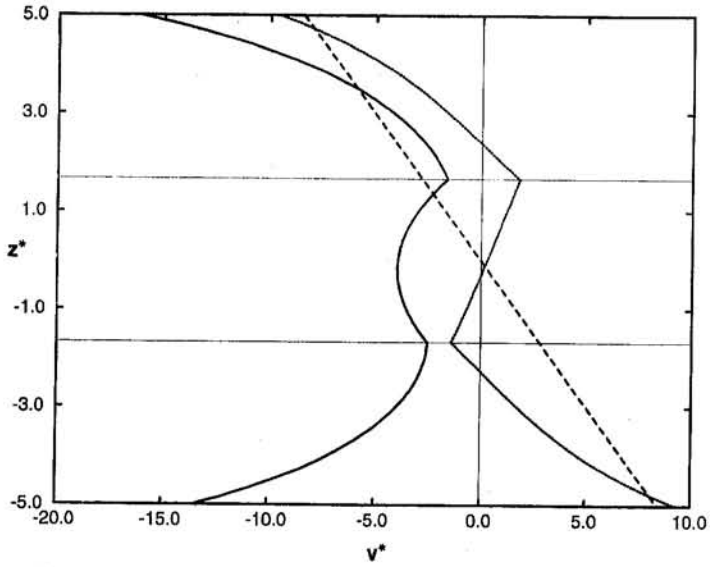

Fig. 1(*a*) Displacement in *y*-direction

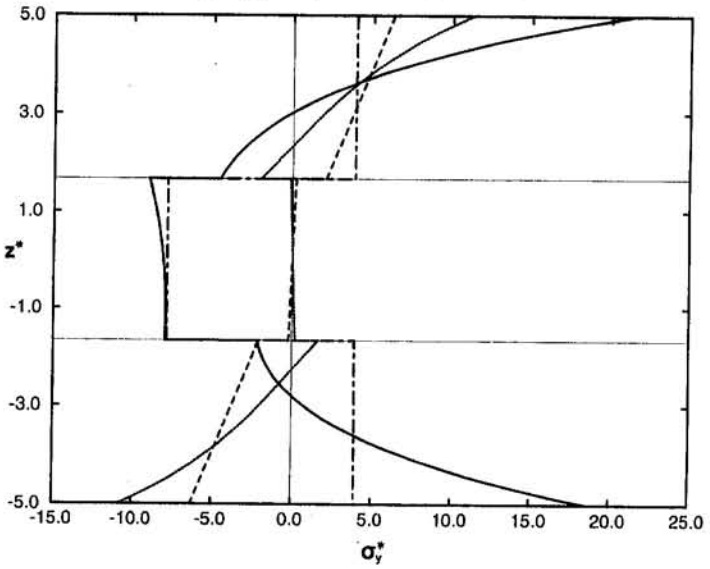

Fig. 1(*b*) Normal stress σ_y

Fig. 1 Through-thickness distributions for PVDF cross-ply under applied traction (case 1) and potential (case 2)

$$F_1 = [\epsilon_{33}(a^2 - b^2 + 2iab) - \epsilon_{22}p^2](C_{44} + C_{23}) + [e_{33}(a^2 - b^2 + 2iab) - e_{24}p^2](e_{24} + e_{32}) \quad (60)$$

$$F_2 = (e_{33}^2 + C_{33}\epsilon_{33})[(a^2 - b^2)^2 - 4a^2b^2 + 4iab(a^2 - b^2)] + p^2(a^2 - b^2 + 2iab)(-C_{33}\epsilon_{22} - C_{44}\epsilon_{33} - 2e_{33}e_{24}) + p^4(C_{44}\epsilon_{22} + e_{24}^2). \quad (61)$$

Using similar steps, the final solution for Φ can be written as

$$\Phi(z) = e^{az}[(c_1\beta_3 + c_2\beta_4)\cos bz + (-c_1\beta_4 + c_2\beta_3)\sin bz] + e^{-az}[(-c_3\beta_3 + c_4\beta_4)\cos bz + (-c_3\beta_4 - c_4\beta_3)\sin bz] \quad (62)$$

where in this case

$$\beta_3 = a\Gamma_2 - b\Omega_2 \quad \beta_4 = b\Gamma_2 + a\Omega_2. \quad (63)$$

Here the parameters Γ_2 and Ω_2 are defined to be

$$\Gamma_2 = \frac{\eta_1\xi_3 + \eta_2\xi_4}{\xi_3^2 + \xi_4^2} \quad (64)$$

$$\Omega_2 = \frac{\eta_2\xi_3 - \eta_1\xi_4}{\xi_3^2 + \xi_4^2} \quad (65)$$

where $\eta_1 = \mathrm{R}(pF_3)$ and $\eta_2 = \mathrm{I}(pF_3)$, with

$$F_3 = [e_{33}(a^2 - b^2 + 2iab) - e_{24}p^2](C_{44} + C_{23}) + [-C_{33}(a^2 - b^2 + 2iab) + C_{44}p^2](e_{24} + e_{32}). \quad (66)$$

Solution for the Laminate. The form of the solution within each layer is given for the displacement components U, V, and W, the stresses σ_y, σ_z, σ_{xz}, σ_{yz}, and σ_{xy}, the electrostatic potential Φ, and the electric displacement components D_y and D_z. In general, these solutions are a function of eight constants that must be computed using the boundary and interface conditions for the complete laminate.

To evaluate these constants, the boundary conditions at the top and bottom surfaces of the laminate and the interface condi-

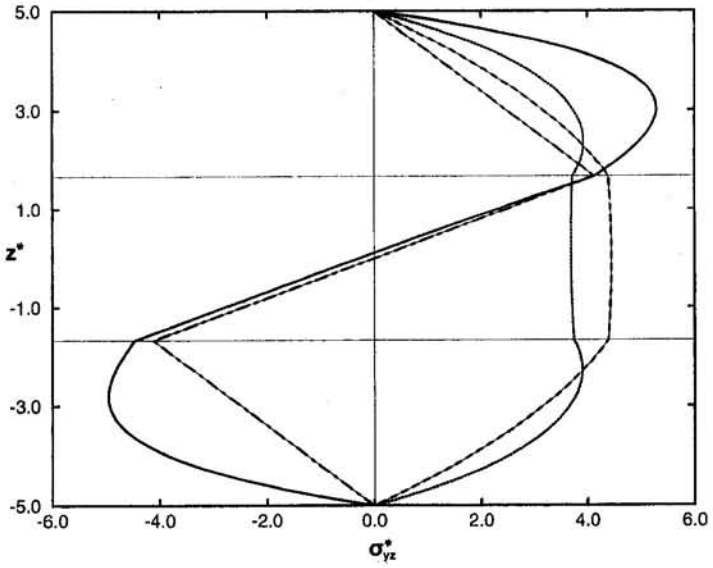

Fig. 1(*c*) Shear stress σ_{yz}

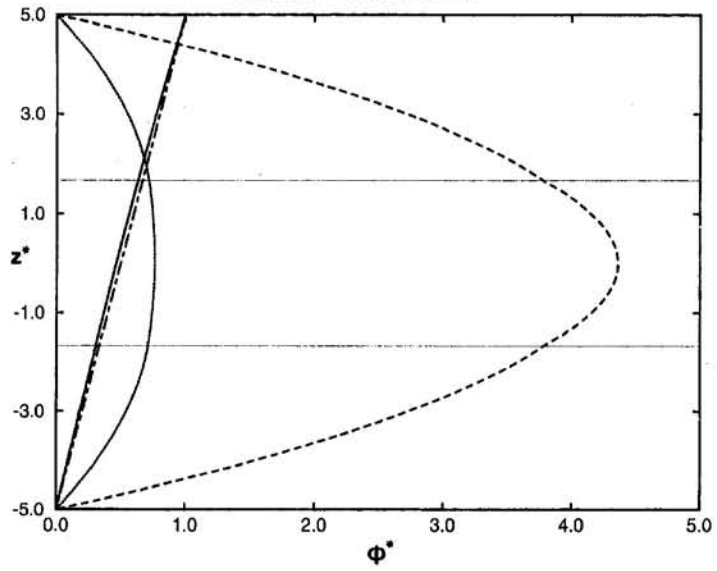

Fig. 1(*d*) Electrostatic potential

tions between the dissimilar plies are imposed. For n layers, this results in four conditions on both the top and bottom surfaces and eight continuity conditions at each of the $(n - 1)$ interfaces. This results in a system of $8n$ equations with $8n$ unknowns. Once the constants are evaluated, final expressions for the elastic and electric field variables can be computed at any location within the laminate.

3 Numerical Examples

In this section, the solution methodology is applied to three basic geometries. These are (1) a two-ply laminate of dissimilar piezoceramics, (2) a two-layer angle ply constructed of the piezopolymer PVDF, and (3) a three-layer cross-ply constructed of PVDF. The material properties for all of the materials considered in these examples are given in Table 1. The properties for PZT-4 are taken from Berlincourt and co-workers (1964), those for $(Pb_{.88}Ca_{.12})((CO_{.5}W_{.5})_{.04}Ti_{.96})O_3$ from Yamashita and co-workers (1981), and from Tashiro and co-workers (1981) for the PVDF. The latter values were for a single crystal, and were used because this is one of the few complete sets of constants available for this material. These geometries were considered only to demonstrate the solution and give representative behavior for the computed field quantities. No extensive effort was made to assess the influence of any of the geometric or material parameters in this initial study. The resulting displacements, stresses, and potential are given in meters, Newtons/meter^2, and volts, respectively.

Two-Ply Laminates. Two separate laminates are studied in this section. The dimensions are $L = 0.1$ m and $H = 0.01$ m. A two-ply laminate composed of $[\text{PZT-4}/(Pb_{.88}Ca_{.12})((CO_{.5} \times W_{.5})_{.04}Ti_{.96})O_3]$ with equal thickness layers is considered first. For these material properties the u-displacement uncouples from the remaining displacements; hence only the in-plane fields are considered for this example. There are two loading conditions. First, a transverse normal stress was applied along the top with $q_0 = 1$ and the potential and shear stresses at the top and bottom surfaces specified to be zero. The second loading condition considers a layer under a sinusoidal $(n = 1)$ potential at the top surface with the bottom surface held at zero potential. The top and bottom surfaces of the laminate are traction-free. The maximum magnitudes of the through-thickness distributions for both cases are given at several locations of z for the

elastic and electric fields in Table 2. For this and the next example, two values are given at the material interface if there is a discontinuity in the stress components. Integrating the shear stress over the end of the laminate yields a normalized value of exactly half the applied resultant load for the applied load case, and a value of zero for the applied potential case.

The piezopolymer polyvinlidene flouride (PVDF) has seen significant application in piezoelectric laminates. It is of interest because it possesses differing properties in the 1 and 2 directions. A two-layer angle-ply $[-45/+45]$ is constructed with the same load conditions as in the previous case. The thicknesses of each layer are $h_{1,2} = 0.005$ m. The maximum value distributions are listed in Table 3.

The trends of all results are dominated by the difference in material properties. In the first example, the displacements in the upper layer are slightly larger and the stress σ_y is smaller than the lower layer because of the lower modulus in the PZT-4. Likewise, the potential gradient in the upper layer is smaller than that of the lower layer in part because of the much larger dielectric constant. For the angle-ply, there is a mild antisymmetry of the results because of the location of the forcing function on the upper surface. This behavior increases as the length/thickness ratio of the laminate is decreased.

The Three-Layer Cross-Ply. In this example, a three-layer [90/0/90] laminate is constructed with $H = 0.01$ m with the 90-deg plies parallel to the y-axis. The cases of applied surface traction and applied surface potential are considered separately. Two L/H ratios are considered: 4 and 100. In all plots the dotted ($L/H = 4$) and dashed ($L/H = 100$) lines denote the applied load case, with the solid ($L/H = 4$) and chain-dashed ($L/H = 100$) lines denoting the case of applied potential. The maximum values of v, σ_y, σ_{yz}, and ϕ through the laminate thickness are displayed graphically in Figures 1(a)-(d). In these figures, the functions are plotted against the parameter $\bar{z} = z \times 10^3$. The scaled functions are defined for the applied load case (termed case 1) as $v^* = v \times 10^{13}$ ($L/H = 4$) and $v^* = v \times 10^9$ ($L/H = 100$), $\sigma_y^* = \sigma_y/1000\ L^2$, $\sigma_{yz}^* = \sigma_{yz}/10\ L$, and $\phi^* = \phi/0.01\ L$. The results for the applied potential (case 2) are also shown in the same figures, with the exception of the v displacement for $L/H = 100$. This distribution is nearly constant at -1.5×10^{-11} m and is not plotted. The scaled field quantities are given as $v^* = v \times 10^{13}$, $\sigma_y^* = \sigma_y$, $\sigma_{yz}^* = \sigma_{yz} \times 100\ L$, and $\phi^* = \phi$. As the aspect ratio increases, the quantities approach piecewise linear behavior through the thickness of the individual laminae. There are significant differences in behavior between thick and thin laminates, demonstrating the need to use adequate levels of approximation when modeling these laminates.

4 Closure

The field distributions in the examples considered here demonstrate the limitations of some simplified theories in making approximations regarding the nature of assumed elastic and electric fields through the thickness of the laminate. Common assumptions made regarding the displacement and potential distributions can have possibly significant effects on the resulting approximations for the remaining field quantities. The solutions and results provided here should provide a means of comparison to assess relative accuracies, advantages, and disadvantages of more computationally efficient and general plate theories for piezoelectric laminates.

References

Berlincourt, D. A., Curran, D. R., and Jaffe, H., 1964, "Piezoelectric and Piezomagnetic Materials and Their Function in Transducers," *Physical Acoustics,* W. P. Mason, ed., Vol. 1, pp. 169–270.

Cady, W. G., 1964, *Piezoelectricity,* rev. ed., Vols. I and II, Dover Publications, New York.

Heyliger, P. R., 1994, "Static Behavior of Laminated Elastic/Piezoelectric Plates," *AIAA Journal,* Vol. 32, pp. 2481–2484.

Lee, C.-K., and Moon, F. C., 1989, "Laminated Piezopolymer Plates for Torsion and Bending Sensors and Actuators," *Journal of the Acoustical Society of America,* Vol. 85, pp. 2432–2439.

Lee, C.-K., 1990, "Theory of Laminated Piezoelectric Plates for the Design of Distributed Sensors/Actuators. Part I: Governing Equations and Reciprocal Relationships," *Journal of the Acoustical Society of America,* Vol. 87, pp. 1144–1158.

Nye, N. Y., 1972, *Physical Properties of Crystals: Their Representation by Tensors and Matrices,* Oxford University Press, Oxford, UK.

Pagano, N. J., 1969, "Exact Solutions for Composites in Cylindrical Bending," *Journal of Composite Materials,* Vol. 3, July, pp. 398–411.

Pagano, N. J., 1970a, "Exact Solutions for Rectangular Bidirectional Composites and Sandwich Plates," *Journal of Composite Materials,* Vol. 4, Jan., pp. 20–34.

Pagano, N. J., 1970b, "Influence of Shear Coupling in Cylindrical Bending of Anisotropic Laminates," *Journal of Composite Materials,* Vol. 4, July, pp. 330–343.

Ray, M. C., Rao, K. M., and Samanta, B., 1992, "Exact Analysis of Coupled Electroelastic Behavior of a Piezoelectric Plate Under Cylindrical Bending," *Computers and Structures,* Vol. 45, pp. 667–677.

Ray, M. C., Bhattacharya, R., and Samanta, B., 1993, "Exact Solutions for Static Analysis of Intelligent Structures," *AIAA Journal,* Vol. 31, pp. 1684–1691.

Tiersten, H. F., 1969, *Linear Piezoelectric Plate Vibrations,* Plenum, New York.

Tashiro, K., Tadokoro, H., and Kobayashi, M., 1981, "Structure and Piezoelectricity of Poly(Vinylidene Flouride)," *Ferroelectrics,* Vol. 32, pp. 167–175.

Tzou, H. S., and Gadre, M., 1989, "Theoretical Analysis of a Multi-Layered Thin Shell Coupled with Piezoelectric Shell Actuators for Distributed Vibration Controls," *Journal of Sound and Vibration,* Vol. 132, pp. 433–450.

Yamashita, Yokoyama, and Honda, 1981, "(Pb, Ca)($(Co_{1/2}W_{1/2})$, TiO_3 Piezoelectric Ceramics and Their Applications," Proceedings of the 3rd Meeting on Ferroelectric Materials and Their Applications, *Japanese Journal of Applied Physics,* Vol. 20, Supplement 20-4, pp. 183–187.

A Generalized Method of Rotational Superposition for Problems With Elliptical Distribution of Boundary Values[1]

Gwolong Lai
Associate Professor,
Department of Construction Engineering,
National Yunlin Institute of Technology,
Yunlin, Taiwan 640, R.O.C.

A. R. Robinson
Professor Emeritus,
Department of Civil Engineering,
University of Illinois at Urbana-Champaign,
Urbana, IL 61801
Mem. ASME

An extension of the usual rotational superposition is developed from geometrical considerations. This approach relates the solution of any dynamic or static elasticity problem which corresponds to boundary values on a circular area to the solution of the problem in which the same boundary values are "stretched" in one direction. From the two-dimensional problems that correspond by rotational superposition to the circular case, new two-dimensional problems are formulated which, when superposed properly, result in the solution for the elliptical boundary distribution. This new technique is first presented for stretching the boundary values of axially symmetric problems, and then extended to others, including the elliptical shear dislocation problem.

1 Introduction

In general, it is a very difficult task to find the analytical solution for most three-dimensional static or dynamic elasticity problems. By contrast, several analytical techniques are available for solving two-dimensional problems. For some special three-dimensional problems, however, there exists a one-to-one correspondence between a three-dimensional problem and certain two-dimensional problems that can be constructed. Rotational superposition is an effective approach to expressing a three-dimensional problem in terms of the corresponding fictitious two-dimensional problems (Aleksandrov, 1961).

The method of rotational superposition, which was first developed for the solution of axially symmetric problems, can be traced back to Smirnov and Sobolev (1933) for dynamic problems, but is usually ascribed to Weber (1940) for static problems. Later, Kostrov (1964a) employed this technique to solve an axisymmetric dynamic problem of a tension crack propagating in an unbound medium and extended the application to the problem of an expanding shear crack over a circular region (Kostrov, 1964b). The rotational superposition technique has also been used to solve static elasticity problems involving solids of revolution (Alexandrov, 1968).

In this paper, a brief review is first given of the usual rotational superposition for dynamic elasticity problems in a half-space where nonzero boundary values are specified on an expanding circular area of the boundary plane. The surface boundary values are then imagined to be "stretched" in one direction so that the circular area becomes an elliptical one. The main thrust of the analysis is then to use the geometrical relationships between the ellipse and the generating circle to obtain a set of new two-dimensional problems and a new superposition rule that lead to the solution of the "stretched" three-dimensional problem. The new technique that results then permits solution of dynamic boundary value problems over an expanding elliptical region if the boundary values are obtainable from those of the corresponding problem for a circular region by merely stretching the *boundary values* in one direction. It should be clear that in dynamic problems only the boundary values undergo a simple stretching, not the entire field. In general, this is also true for a static problem.

As illustrative examples, the new superposition method is first applied to stretching the boundary values of axially symmetric problems. Then the new approach is extended to find the solution of an elliptical shear dislocation problem in an elastic unbounded medium.

2 The Rotational Superposition Technique for the Circular Case

Consider a linearly elastic half space $y \geq 0$. A plane-strain field $(u_{x2}, u_{y2}, 0)$ and an antiplane field $(0, 0, u_{z2})$ that are functions of x_2, y_2, t and satisfy the three-dimensional equations of motion are applied at an angle ω_1 with the x-axis, as shown in Fig. 1. If these plane-strain and antiplane displacement fields are multiplied respectively by weighting functions $w_p(\omega_1)$ and $w_a(\omega_1)$ and their effects superposed for ω_1 from 0 to π, the three-dimensional field generated is clearly a solution of the three-dimensional dynamic elasticity equations. This resulting displacement field is expressed as follows (Johnson and Robinson, 1972):

$$u_\rho = \int_0^\pi u_{x2}(\rho \cos(\omega_1 - \omega), y, t) \cos(\omega_1 - \omega) w_p(\omega_1) d\omega_1 - \int_0^\pi u_{z2}(\rho \cos(\omega_1 - \omega), y, t) \sin(\omega_1 - \omega) w_a(\omega_1) d\omega_1$$

$$u_\omega = \int_0^\pi u_{x2}(\rho \cos(\omega_1 - \omega), y, t) \sin(\omega_1 - \omega) w_p(\omega_1) d\omega_1 + \int_0^\pi u_{z2}(\rho \cos(\omega_1 - \omega), y, t) \cos(\omega_1 - \omega) w_a(\omega_1) d\omega_1$$

$$u_y = \int_0^\pi u_{y2}(\rho \cos(\omega_1 - \omega), y, t) w_p(\omega_1) d\omega_1 \qquad (1)$$

where (ρ, ω, y) are the cylindrical coordinates of Fig. 1.

[1] This paper contains a portion of the dissertation submitted by the first author to the Graduate College of the University of Illinois at Urbana-Champaign in partial fulfillment of the requirements for the degree of Doctor of Philisophy.

Contributed by the Applied Mechanics Division of THE AMERICAN SOCIETY OF MECHANICAL ENGINEERS for publication in the ASME JOURNAL OF APPLIED MECHANICS.

Discussion on this paper should be addressed to the Technical Editor, Professor Lewis T. Wheeler, Department of Mechanical Engineering, University of Houston, Houston, TX 77204-4792, and will be accepted until four months after final publication of the paper itself in the ASME JOURNAL OF APPLIED MECHANICS.

Manuscript received by the ASME Applied Mechanics Division, May 11, 1994; final revision, Mar. 21, 1996. Associate Technical Editor: X. Markenscoff.

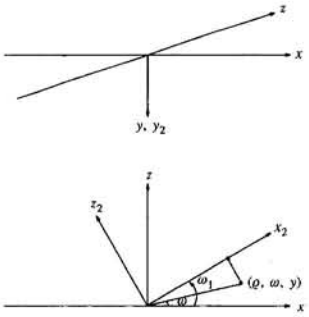

Fig. 1 The geometry of rotational superposition

If the three-dimensional problem is axially symmetric, a plane-strain problem (with $w_p(\omega_1) = 1$) can be found that when superposed rotationally as above gives rise to the specified axisymmetric problem. The antiplane problem is absent here. If the plane-strain problem is taken to be symmetric, i.e.,

$$u_{x2}(-x_2, y_2, t) = -u_{x2}(x_2, y_2, t)$$
$$u_{y2}(-x_2, y_2, t) = u_{y2}(x_2, y_2, t), \tag{2}$$

then the plane-strain problem is unique and the following simplified expressions can be obtained (Thompson and Robinson, 1969):

$$u_\rho = \int_0^\pi u_{x2}(\rho \cos \eta, y, t) \cos \eta d\eta$$
$$u_\omega = 0$$
$$u_y = \int_0^\pi u_{y2}(\rho \cos \eta, y, t) d\eta. \tag{3}$$

The expressions for the stresses are

$$\sigma_\rho = \int_0^\pi [\sigma_{x2} - 2\mu\epsilon_{x2} \sin^2 \eta] d\eta$$
$$\sigma_\omega = \int_0^\pi [\sigma_{x2} - 2\mu\epsilon_{x2} \cos^2 \eta] d\eta$$
$$\sigma_y = \int_0^\pi \sigma_{y2} d\eta$$
$$\tau_{y\rho} = \int_0^\pi \tau_{xy2} \cos \eta d\eta$$
$$\tau_{y\omega} = \tau_{\rho\omega} = 0. \tag{4}$$

The task of finding the fictitious plane problem, i.e. its boundary and initial conditions, that corresponds to an axisymmetric problem is usually done by solving a set of Abel integral equations (Aleksandrov, 1961). For example, assume that the boundary and initial conditions for the axisymmetric problem are specified functions of σ_y and $\tau_{y\rho}$, then the first and fourth of Eqs. (4) can be solved to determine the corresponding quantities for the plane strain problem. The result is

$$\sigma_{y2}(x_2, y, t) = \frac{1}{\pi} \frac{\partial}{\partial x_2} \left\{ \int_0^{x_2} \sigma_y(r, y, t) \frac{r}{\sqrt{x_2^2 - r^2}} dr \right\}$$
$$\tau_{xy2}(x_2, y, t) = \frac{1}{\pi x_2} \frac{\partial}{\partial x_2} \left\{ \int_0^{x_2} \tau_{y\rho}(r, y, t) \frac{r^2}{\sqrt{x_2^2 - r^2}} dr \right\}. \tag{5}$$

For the axisymmetric problem in which the normal and tangential tractions are specified on the boundary $y = 0$, Eqs. (5) for $y = 0$ give the boundary tractions for the corresponding plane-strain problem. The plane problem can then be solved directly (Smirnov, 1964; Thompson and Robinson, 1969; Eringen and Suhubi, 1975). The results when superposed in accordance with Eqs. (3) and (4) yield the solution of the axisymmetric problem.

A more general type of rotational superposition that is often useful results in nonaxially symmetric distribution of boundary tractions or displacements. One very useful example of this is a case in which a displacement or a traction in one direction, say x, is applied to an expanding circular area on the boundary plane (Kostrov, 1964b; Johnson and Robinson, 1972). Corresponding to this kind of problem, a fictitious antiplane problem as well as a fictitious plane-strain problem is now necessary and the weighting functions in Eqs. (1) are taken in the following form:

$$w_p(\omega_1) = \cos \omega_1 \quad w_a(\omega_1) = \sin \omega_1. \tag{6}$$

To guarantee uniqueness, the plane-strain problem is taken as antisymmetric with respect to the y-axis and the antiplane problem as symmetric, i.e.,

$$u_{x2}(-x_2, y_2, t) = u_{x2}(x_2, y_2, t)$$
$$u_{y2}(-x_2, y_2, t) = -u_{y2}(x_2, y_2, t)$$
$$u_{z2}(-x_2, y_2, t) = u_{z2}(x_2, y_2, t). \tag{7}$$

With these assumptions, the following simplified expressions can be obtained by a change of variable ($\eta = \omega_1 - \omega$) in Eqs. (1):

$$u_\rho = \left\{ \int_0^\pi u_{x2}(\rho \cos \eta, y, t) \cos^2 \eta d\eta - \int_0^\pi u_{z2}(\rho \cos \eta, y, t) \sin^2 \eta d\eta \right\} \cos \omega$$
$$u_\omega = \left\{ -\int_0^\pi u_{x2}(\rho \cos \eta, y, t) \sin^2 \eta d\eta + \int_0^\pi u_{z2}(\rho \cos \eta, y, t) \cos^2 \eta d\eta \right\} \sin \omega$$
$$u_y = \left\{ \int_0^\pi u_{y2}(\rho \cos \eta, y, t) \cos \eta d\eta \right\} \cos \omega. \tag{8}$$

Similar expressions for the stresses can be found in Johnson and Robinson (1972).

Depending on the given boundary values, the fictitious plane problems can then be determined in a way very similar to the axisymmetric case. For instance, consider the dynamic problem of an expanding circular shear dislocation nucleated from the origin on the $y = 0$ plane in an unbounded medium. The boundary conditions on the dislocation plane are given by the following equations:

$$u_\rho(\rho, \omega, t)|_{y=0^+} = -u_\rho(\rho, \omega, t)|_{y=0^-} = u_x(\rho, t) \cos \omega$$
$$u_\omega(\rho, \omega, t)|_{y=0^+} = -u_\omega(\rho, \omega, t)|_{y=0^-} = -u_x(\rho, t) \sin \omega$$
$$\sigma_y = 0 \quad \text{for} \quad y = 0 \tag{9}$$

where $u_x(\rho, t)$ is the distribution function of the tangential relative displacements in the x-direction. The fact that the $\sigma_y = 0$ everywhere on the $y = 0$ plane follows from the antisymmetric nature of the problem with respect to the plane $y = 0$. To solve this problem, first we can examine the form of the first two of Eqs. (8). It can be observed that if one chooses

$$u_{x2} = -u_{z2} = U(x_2, t) \quad \text{for} \quad y_2 = 0, \tag{10}$$

the three-dimensional motion resulting from superposition will always be in the x direction ($\omega = 0$) on the $y = 0$ plane, as

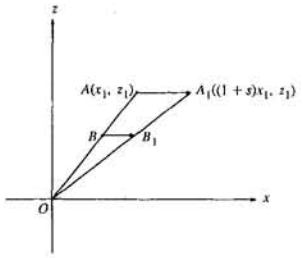

Fig. 2 A simple stretch in the *x*-direction

required by the first two of Eqs. (9). The following equation can then be obtained:

$$\left.\frac{u_\rho}{\cos\omega}\right|_{y=0^+} = -\left.\frac{u_\omega}{\sin\omega}\right|_{y=0^+} = \int_0^\pi U(\rho\cos\eta, t)d\eta = u_x(\rho, t). \quad (11)$$

From this the function $U(x_2, t)$ is then also determined, i.e.,

$$U(x_2, t) = \frac{1}{\pi}\frac{\partial}{\partial x_2}\left\{\int_0^{x_2} u_x(\xi, t)\frac{\xi}{\sqrt{x_2^2 - \xi^2}}d\xi\right\}. \quad (12)$$

Therefore the fictitious plane problems corresponding to the circular shear dislocation problem are determined uniquely and their boundary conditions for $y_2 = 0^+$ are as defined below.

(1) The plane-strain problem:

$$u_{x2}(x_2, t) = U(x_2, t)$$
$$\sigma_{y2} = 0. \quad (13)$$

(2) The antiplane problem:

$$u_{z2}(x_2, t) = -U(x_2, t). \quad (14)$$

3 The Geometry of a Stretch in the *x*-Direction

Up to this point, known results have been summarized for dealing with three-dimensional problems with boundary values over a circular region. In order to develop the new rotational superposition with a stretching effect, some necessary geometrical relationships will first be established in this section. Consider a line $\overline{OA}$ on the xz-plane as shown in Fig. 2. The point $A(x_1, z_1)$ will move to the point $A_1((1 + s)x_1, z_1)$ if the whole surface is stretched $(1 + s)$ times in the x-direction. Then a point B on the line $\overline{OA}$ will move to a point B_1 on the line $\overline{OA_1}$ also. Because $\overline{AA_1}$ is parallel to $\overline{BB_1}$, it is apparent that the triangle OAA_1 is similar to the smaller triangle OBB_1. Therefore the following geometrical relationship holds:

$$\frac{\overline{OB}}{\overline{OA}} = \frac{\overline{OB_1}}{\overline{OA_1}}. \quad (15)$$

Similarly, any shape on the xz-plane will change when the whole surface is stretched $(1 + s)$ times in the x-direction, e.g., a circle is stretched into an ellipse. The geometrical relationships between a circle with center at the origin and the resulting ellipse after stretching can be easily found. As shown in Fig. 3, A_1, B_1, C_1, and D_1 are the transformed points on the stretched surface corresponding to the points A, B, C, and D on the original surface, respectively. Point A_2 is determined such that line $\overline{A_1A_2}$ is tangent to the ellipse and perpendicular to the line $\overline{OA_2}$. Point B_2 is the intersection of lines $\overline{B_1C_1}$ and $\overline{OA_2}$. In any standard analytic geometry textbook (e.g., Lehmann, 1942, p. 161), it is shown that

$$z = mx + r\sqrt{m^2(1 + s)^2 + 1} \quad (16)$$

is the equation of the tangent $\overline{A_1A_2}$ where

$$m = -\frac{1}{\tan\beta_1}, \quad (17)$$

r is the radius of the circle, and β_1 is the new angle that the line $\overline{OA_2}$ makes with the x-axis. The length $\overline{OA_2}$ is the distance from the origin (0, 0) to the line $\overline{A_1A_2}$. Again from (Lehmann, 1942, p. 72), it is seen that

$$\overline{OA_2} = r\sqrt{(1 + s)^2\cos^2\beta_1 + \sin^2\beta_1}. \quad (18)$$

It will be convenient to set $\overline{OA_2} = r \cdot p(\beta_1)$ with

$$p(\beta_1) = \sqrt{(1 + s)^2\cos^2\beta_1 + \sin^2\beta_1}. \quad (19)$$

In addition, the condition that the tangent $\overline{A_1A_2}$ passes through the point $A_1((1 + s)r\cos\omega_1, r\sin\omega_1)$ leads to the following relationship between ω_1 and β_1:

$$\tan\beta_1 = (1 + s)\tan\omega_1. \quad (20)$$

Taking the differentials of both sides,

$$\sec^2\beta_1 d\beta_1 = (1 + s)\sec^2\omega_1 d\omega_1,$$

we can deduce that

$$d\omega_1 = \frac{1 + s}{(1 + s)^2\cos^2\beta_1 + \sin^2\beta_1}d\beta_1 = \frac{1 + s}{p^2(\beta_1)}d\beta_1. \quad (21)$$

By noticing in Fig. 3 that the triangle OA_1A_2 is similar to the triangle OB_1B_2 and employing Eq. (15), we readily derive a useful equation which relates the segment $\overline{OB}$ to $\overline{OB_2}$ and $\overline{OC}$ to $\overline{OC_1}$:

$$\frac{\overline{OB_2}}{\overline{OA_2}} = \frac{\overline{OB_1}}{\overline{OA_1}} = \frac{\overline{OB}}{\overline{OA}}$$

or

$$\overline{OB_2} = \frac{\overline{OA_2}}{\overline{OA}}\cdot\overline{OB} = \frac{p(\beta_1)\cdot r}{r}\cdot\overline{OB} = p(\beta_1)\cdot\overline{OB},$$

and finally

$$\overline{OC_1}\cdot\cos(\beta_1 - \omega) = p(\beta_1)\cdot\overline{OC}\cdot\cos(\omega_1 - \omega_0). \quad (22)$$

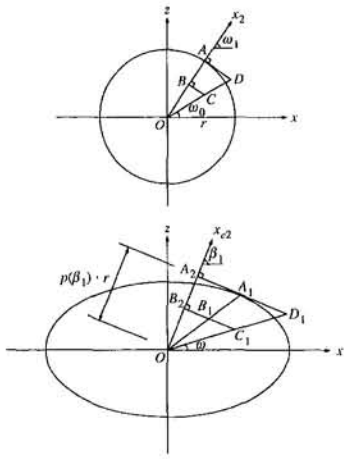

Fig. 3 Geometrical representations of a circle and the resulting ellipse after a stretching in the *x*-direction

4 Rotational Superposition With Stretching on the *xz*-Plane

In Section 2 it has been shown how to solve three-dimensional axisymmetric dynamic problems by finding a corresponding plane-strain problem, solving it, and applying rotational superposition to the two-dimensional results. The solution of the fictitious plane-strain problem is, of course, determined by its boundary values.

Now consider a three-dimensional problem with nonzero boundary values u_y or σ_y on the $y = 0$ surface that can be interpreted as a "stretch" in the x-direction of an axisymmetric distribution on the xz-plane. For convenience, this problem will be called a "stretched boundary value problem." As noted in the Introduction, in general the entire field is not simply stretched in the same way. The analysis of the present section and an example following will show how to obtain modified two-dimensional problems and from these to find the solution for the stretched boundary value problem. After this method is developed, it will be shown in Section 6 that the same stretching process is applicable to problems arising from the stretching of a nonaxisymmetric problem that can be solved by rotational superposition. In that section a shear dislocation over an expanding elliptical region is found by beginning with the corresponding problem for an expanding circular area.

First for an axisymmetric distribution normal to the xz-plane, consider a known plane distribution $f(x_2)$ which is an even function of x_2 along the x_2-axis (see Fig. 3). As before, an axisymmetric distribution on the xz-plane can be constructed readily by defining the value of the distribution F at any point $C(\rho_0, \omega_0)$ as follows:

$$F(C) = F(\rho_0, \omega_0) = \int_0^\pi f(\rho_0 \cos(\omega_1 - \omega_0))d\omega_1$$
$$= \int_0^\pi f(\rho_0 \cos \omega_1)d\omega_1. \quad (23)$$

Here $f(x_2)$ and $F(\rho_0, \omega_0)$ can be the normal component of displacement or traction that enters the boundary conditions. It is apparent that the resulting distribution F is a function of ρ_0 only. If the function $F(\rho_0)$ is known beforehand, the inverse problem of constructing the corresponding distribution $f(x_2)$ can be solved readily. The solution to the inverse problem is, as in Eqs. (5),

$$f(x_2) = \frac{1}{\pi}\frac{\partial}{\partial x_2}\left\{\int_0^{x_2} F(\xi)\frac{\xi}{\sqrt{x_2^2 - \xi^2}}d\xi\right\}. \quad (24)$$

The problem now is to construct a surface distribution which is a stretch in one direction of an axisymmetric distribution on the xz-plane. A new rotational superposition with stretching effect is defined for the value of the distribution F_e at any point $C_1(\rho, \omega)$. A weighting function $w_e(\beta_1)$ for stretching is included in the superposition, as shown in the following equation:

$$F_e(C_1) = F_e(\rho, \omega)$$
$$= \int_0^\pi f_e(\rho \cos(\beta_1 - \omega), \beta_1)w_e(\beta_1)d\beta_1 \quad (25)$$

where the distribution $f_e(x_{e2}, \beta_1)$ is a stretch of the distribution $f(x_2)$ with a stretching ratio as a function of β_1. The function $f_e(x_{e2}, \beta_1)$ is defined in terms of the function $f(x_2)$ by

$$f_e(x_{e2}, \beta_1) = f\left(\frac{x_{e2}}{p(\beta_1)}\right). \quad (26)$$

The weighting function $w_e(\beta_1)$ is derived from the geometrical relationships between ω_1 and β_1, as follows:

$$w_e(\beta_1) = \frac{d\omega_1}{d\beta_1} = \frac{1+s}{(1+s)^2\cos^2\beta_1 + \sin^2\beta_1} = \frac{1+s}{p^2(\beta_1)}. \quad (27)$$

From the geometrical relationships established in the previous section, the following equalities can be easily proved, from which the relationship between the axisymmetric distribution F and the stretched distribution F_e is verified:

$$\rho \cdot \cos(\beta_1 - \omega) = p(\beta_1)\cdot\rho_0\cdot\cos(\omega_1 - \omega_0)$$
$$f_e(\rho\cos(\beta_1 - \omega), \beta_1) = f(\rho_0\cos(\omega_1 - \omega_0))$$
$$w_e(\beta_1)\cdot d\beta_1 = d\omega_1$$

so that

$$F_e(C_1) = F(C). \quad (28)$$

Therefore, the new rotational superposition with the stretching effect defined by Eq. (25) results in a value of the distribution F_e at the stretched point C_1 that is the same value that F has at the original point C. It is now clear that the surface distribution F_e is a stretch of the axisymmetric distribution F in the x-direction.

5 An Expanding Uniformly Distributed Elliptical Normal Load on the Surface of a Half-Space

Consider the problem of a linearly elastic half-space subjected to an expanding elliptical normal traction on the surface. The normal load intensity is assumed to be uniformly distributed of unit magnitude acting downward in an expanding elliptical region on the surface $y = 0$. The boundary conditions are as defined below:

$$\sigma_y(x, z, t) = -1 \quad \text{for} \quad \sqrt{\frac{x^2}{(1+s)^2} + z^2} \le \alpha t$$
$$= 0 \quad \text{for} \quad \sqrt{\frac{x^2}{(1+s)^2} + z^2} > \alpha t$$
$$\tau_{y\rho} = 0 \quad \text{for} \quad y = 0$$
$$\tau_{y\omega} = 0 \quad \text{for} \quad y = 0. \quad (29)$$

5.1 The Corresponding Plane-Strain Problem. The problem for the elliptical distribution is solved by first examining its counterpart, an axisymmetric problem with an expanding circular normal load on the surface. The axisymmetric boundary values on the surface $y = 0$ are given by

$$\sigma_y(\rho, t) = -1 \quad \text{for} \quad \rho \le \alpha t$$
$$= 0 \quad \text{for} \quad \rho > \alpha t$$
$$\tau_{y\rho}(\rho, t) = 0. \quad (30)$$

The fictitious plane-strain problem corresponding to this axisymmetric problem can then be found by substituting the above boundary values into Eqs. (5), which gives the boundary conditions for $y_2 = 0$ of the plane-strain problem as follows:

$$\sigma_{y2}(x_2, t) = -\frac{1}{\pi} \quad \text{for} \quad |x_2| \le \alpha t$$
$$= -\frac{1}{\pi}\left[1 - \frac{|x_2|}{\sqrt{x_2^2 - \alpha^2 t^2}}\right] \quad \text{for} \quad |x_2| > \alpha t$$
$$\tau_{xy2}(x_2, t) = 0. \quad (31)$$

After the plane-strain problem corresponding to the axisymmetric case is found, the plane-strain problem corresponding to the elliptical normal load problem can be determined readily by stretching the boundary values in Eqs. (31) according to Eq. (26). That is, for $y_2 = 0$,

$$\sigma^e_{y2}(x_{e2}, t, \beta_1) = -\frac{1}{\pi} \quad \text{for} \quad |x_{e2}| \le \alpha_{\beta_1} t$$

$$= -\frac{1}{\pi}\left[1 - \frac{|x_{e2}|}{\sqrt{x^2_{e2} - \alpha^2_{\beta_1} t^2}}\right] \quad \text{for} \quad |x_{e2}| > \alpha_{\beta_1} t$$

$$\tau^e_{xy2}(x_{e2}, t, \beta_1) = 0 \tag{32}$$

where

$$\alpha_{\beta_1} = p(\beta_1)\cdot\alpha = \sqrt{(1+s)^2\cos^2\beta_1 + \sin^2\beta_1}\cdot\alpha. \tag{33}$$

Here it should be noted that the stretched plane problem for the elliptical case is a function of β_1.

5.2 Solution to the Stretched Plane-Strain Problem. Since the tractions on the surface $y_2 = 0$ in Eqs. (32) are homogeneous functions of degree zero, the stretched plane-strain problem can be readily solved by using the method of self-similar potentials (Smirnov, 1964; Thompson and Robinson, 1969; Eringen and Suhubi, 1975). The displacement and stress fields for the fictitious plane-strain problem are then determined readily as below:

$$u^e_{x2} = -\int_0^t \mathrm{Re}\left[\int_0^{\theta_1} \theta\Phi'\,d\theta + \int_0^{\theta_2} \sqrt{b^{-2} - \theta^2}\Psi'\,d\theta\right] d\tau$$

$$u^e_{y2} = -\int_0^t \mathrm{Re}\left[\int_0^{\theta_1} \sqrt{a^{-2} - \theta^2}\Phi'\,d\theta - \int_0^{\theta_2} \theta\Psi'\,d\theta\right] d\tau \tag{34}$$

$$\frac{\sigma^e_{x2}}{\mu} = \mathrm{Re}\left[\int_0^{\theta_1} (b^{-2} + 2\theta^2 - 2a^{-2})\Phi'\,d\theta + \int_0^{\theta_2} 2\theta\sqrt{b^{-2} - \theta^2}\Psi'\,d\theta\right]$$

$$\frac{\sigma^e_{y2}}{\mu} = \mathrm{Re}\left[\int_0^{\theta_1} (b^{-2} - 2\theta^2)\Phi'\,d\theta - \int_0^{\theta_2} 2\theta\sqrt{b^{-2} - \theta^2}\Psi'\,d\theta\right]$$

$$\frac{\tau^e_{xy2}}{\mu} = \mathrm{Re}\left[\int_0^{\theta_1} 2\theta\sqrt{a^{-2} - \theta^2}\Phi'\,d\theta + \int_0^{\theta_2} (b^{-2} - 2\theta^2)\Psi'\,d\theta\right] \tag{35}$$

where a and b are the speeds of the P and S waves, μ is shear modulus,

$$\Phi'(\theta, \beta_1) = \frac{\alpha^2_{\beta_1}}{\mu\pi}\frac{\theta(b^{-2} - 2\theta^2)}{R(\theta^2)(1 - \alpha^2_{\beta_1}\theta^2)^{3/2}}$$

$$\Psi'(\theta, \beta_1) = -\frac{\alpha^2_{\beta_1}}{\mu\pi}\frac{2\theta^2\sqrt{a^{-2} - \theta^2}}{R(\theta^2)(1 - \alpha^2_{\beta_1}\theta^2)^{3/2}}$$

in which

$$R(\theta^2) = (b^{-2} - 2\theta^2)^2 + 4\theta^2\sqrt{a^{-2} - \theta^2}\sqrt{b^{-2} - \theta^2}$$

is the Rayleigh function, and θ_1 and θ_2 are the complex functions defined implicitly by

$$t - \theta_1 x_{e2} - y_2\sqrt{a^{-2} - \theta_1^2} = 0$$

$$t - \theta_2 x_{e2} - y_2\sqrt{b^{-2} - \theta_2^2} = 0. \tag{36}$$

5.3 The Displacement and Stress Fields for the Elliptical Load Problem. After the displacement and stress fields for the stretched plane-strain problem are determined, the three-dimensional displacement and stress fields for the elliptical normal load problem can be found by superposing the two-dimensional fields using the rotational superposition with stretching, which results in the following equations:

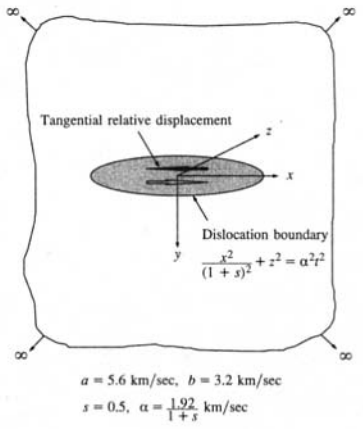

Fig. 4 An expanding elliptical shear dislocation (circular when $s = 0$) on the $y = 0$ plane

$$u_\rho = \int_0^\pi u^e_{x2}(\rho\cos(\beta_1 - \omega), y, t, \beta_1) \times \cos(\beta_1 - \omega) w_e(\beta_1)\,d\beta_1$$

$$u_\omega = \int_0^\pi u^e_{x2}(\rho\cos(\beta_1 - \omega), y, t, \beta_1) \times \sin(\beta_1 - \omega) w_e(\beta_1)\,d\beta_1$$

$$u_y = \int_0^\pi u^e_{y2}(\rho\cos(\beta_1 - \omega), y, t, \beta_1) w_e(\beta_1)\,d\beta_1 \tag{37}$$

$$\sigma_\rho = \int_0^\pi [\sigma^e_{x2} - 2\mu\epsilon^e_{x2}\sin^2(\beta_1 - \omega)] w_e(\beta_1)\,d\beta_1$$

$$\sigma_\omega = \int_0^\pi [\sigma^e_{x2} - 2\mu\epsilon^e_{x2}\cos^2(\beta_1 - \omega)] w_e(\beta_1)\,d\beta_1$$

$$\sigma_y = \int_0^\pi \sigma^e_{y2} w_e(\beta_1)\,d\beta_1$$

$$\tau_{\rho\omega} = \int_0^\pi \mu\epsilon^e_{x2}\sin 2(\beta_1 - \omega) w_e(\beta_1)\,d\beta_1$$

$$\tau_{y\rho} = \int_0^\pi \tau^e_{xy2}\cos(\beta_1 - \omega) w_e(\beta_1)\,d\beta_1$$

$$\tau_{y\omega} = \int_0^\pi \tau^e_{xy2}\sin(\beta_1 - \omega) w_e(\beta_1)\,d\beta_1 \tag{38}$$

where $w_e(\beta_1)$ is the weighting function for stretching as defined in Eq. (27). Because the displacement and stress fields resulting from superposition satisfy the boundary conditions on the surface $y = 0$ as given by Eqs. (29), they are the solution to the elliptical normal load problem being considered.

6 Application to the General Elliptical Shear Dislocation Problem

In addition to the problem of normal tractions or displacements on an elliptical area, the problem with tangential boundary values in one direction over an elliptical region can also be dealt with by a different rotational superposition with a stretching effect. Consider the problem of an expanding elliptical shear dislocation nucleated from the origin on the $y = 0$ plane in an unbounded medium as shown in Fig. 4. The boundary conditions on the $y = 0$ plane are taken as follows:

$$u_\rho(x, z, t)|_{y=0^+} = -u_\rho(x, z, t)|_{y=0^-} = u_x(\rho_b, t)\cos\omega$$

$$u_\omega(x, z, t)|_{y=0^+} = -u_\omega(x, z, t)|_{y=0^-} = -u_x(\rho_b, t)\sin\omega$$

$$\sigma_y = 0 \quad \text{for} \quad y = 0 \tag{39}$$

where

$$\rho_b(x, z) = \sqrt{\frac{x^2}{(1+s)^2} + z^2}. \tag{40}$$

In this problem, the elliptical shear dislocation can be considered as a stretch in the x-direction of the circular dislocation in Section 2. The rotational superposition defined by Eqs. (1) and (6) can now be modified in a similar manner as in Section 4. The new rotational superposition used for the elliptical shear dislocation problem is then defined by the following equations:

$$u_\rho = \int_0^\pi u^e_{x2}(\rho\cos(\beta_1-\omega), y, t, \beta_1)\cos(\beta_1-\omega) \times \cos\beta_1 w_e(\beta_1)d\beta_1 - \int_0^\pi u^e_{z2}(\rho\cos(\beta_1-\omega), y, t, \beta_1) \times \sin(\beta_1-\omega)\sin\beta_1 w_e(\beta_1)d\beta_1$$

$$u_\omega = \int_0^\pi u^e_{x2}(\rho\cos(\beta_1-\omega), y, t, \beta_1)\sin(\beta_1-\omega) \times \cos\beta_1 w_e(\beta_1)d\beta_1 + \int_0^\pi u^e_{z2}(\rho\cos(\beta_1-\omega), y, t, \beta_1) \times \cos(\beta_1-\omega)\sin\beta_1 w_e(\beta_1)d\beta_1$$

$$u_y = \int_0^\pi u^e_{y2}(\rho\cos(\beta_1-\omega), y, t, \beta_1) \times \cos\beta_1 w_e(\beta_1)d\beta_1 \tag{41}$$

where the weighting function $w_e(\beta_1)$ for stretching is as given in Eq. (27).

It will now be verified that the same stretching approach used for the axisymmetric case, Eq. (26) can also be applied to find the plane problems that lead to the superpositions of Eqs. (41). That is, the plane problems corresponding to the elliptical shear dislocation problem are determined readily by stretching the boundary values of the plane problems for the circular case found in Section 2 in accordance with Eq. (26). For $y_2 = 0^+$,

(1) the plane strain problem is determined by

$$u^e_{x2}(x_{e2}, t, \beta_1) = u_{x2}\left(\frac{x_{e2}}{p(\beta_1)}, t\right) = U\left(\frac{x_{e2}}{p(\beta_1)}, t\right)$$

$$\sigma^e_{y2} = 0 \tag{42}$$

and

(2) the antiplane problem is determined by

$$u^e_{z2}(x_{e2}, t, \beta_1) = \mu_{z2}\left(\frac{x_{e2}}{p(\beta_1)}, t\right) = -U\left(\frac{x_{e2}}{p(\beta_1)}, t\right) \tag{43}$$

where $U(x_2, t)$ is as given in Eq. (12).

In order to confirm that the new rotational superposition defined by Eqs. (41) together with the above plane problems give rise to the elliptical shear dislocation problem, the superposed three-dimensional boundary values on the surface $y = 0^+$ are examined, as follows:

$$u_\rho = \int_0^\pi [u^e_{x2}\cos(\beta_1-\omega)\cos\beta_1 - u^e_{z2} \times \sin(\beta_1-\omega)\sin\beta_1]w_e(\beta_1)d\beta_1$$
$$= \int_0^\pi u^e_{x2}[\cos(\beta_1-\omega)\cos\beta_1 + \sin(\beta_1-\omega)\sin\beta_1]w_e(\beta_1)d\beta_1$$
$$= \int_0^\pi u^e_{x2}w_e(\beta_1)d\beta_1 \cdot \cos\omega$$

$$u_\omega = \int_0^\pi u^e_{x2}[\sin(\beta_1-\omega)\cos\beta_1 - \cos(\beta_1-\omega)\sin\beta_1]w_e(\beta_1)d\beta_1$$
$$= -\int_0^\pi u^e_{x2}w_e(\beta_1)d\beta_1 \cdot \sin\omega$$

$$\sigma_y = 0.$$

In addition, the following equality can be verified from the results in Section 4.

$$\int_0^\pi u^e_{x2}(\rho\cos(\beta_1-\omega), t, \beta_1)w_e(\beta_1)d\beta_1 = u_x(\rho_b, t)$$

Therefore, the three-dimensional fields resulting from superposition have the same boundary values on the surface $y = 0^+$ as given by Eqs. (39) for the elliptical shear dislocation problem being considered.

Once the boundary conditions are established as the superposition of two-dimensional fields by the new rotational superposition, any other field quantities can be expressed as

$$\sigma_\rho = \int_0^\pi [\sigma^e_{x2} - 2\mu\epsilon^e_{x2}\sin^2(\beta_1-\omega)]\cos\beta_1 w_e(\beta_1)d\beta_1 - \int_0^\pi \tau^e_{zx2}\sin 2(\beta_1-\omega)\sin\beta_1 w_e(\beta_1)d\beta_1$$

$$\sigma_\omega = \int_0^\pi [\sigma^e_{x2} - 2\mu\epsilon^e_{x2}\cos^2(\beta_1-\omega)]\cos\beta_1 w_e(\beta_1)d\beta_1 + \int_0^\pi \tau^e_{zx2}\sin 2(\beta_1-\omega)\sin\beta_1 w_e(\beta_1)d\beta_1$$

$$\sigma_y = \int_0^\pi \sigma^e_{y2}\cos\beta_1 w_e(\beta_1)d\beta_1$$

$$\tau_{\rho\omega} = \int_0^\pi [\mu\epsilon^e_{x2}\sin 2(\beta_1-\omega)\cos\beta_1 + \tau^e_{zx2}\cos 2(\beta_1-\omega)\sin\beta_1]w_e(\beta_1)d\beta_1$$

$$\tau_{y\rho} = \int_0^\pi [\tau^e_{xy2}\cos(\beta_1-\omega)\cos\beta_1 - \tau^e_{zy2}\sin(\beta_1-\omega)\sin\beta_1]w_e(\beta_1)d\beta_1$$

$$\tau_{y\omega} = \int_0^\pi [\tau^e_{xy2}\sin(\beta_1-\omega)\cos\beta_1 + \tau^e_{zy2}\cos(\beta_1-\omega)\sin\beta_1]w_e(\beta_1)d\beta_1. \tag{44}$$

7 A Specific Spreading Elliptical Shear Dislocation in an Infinite Medium

As a specific application of the general results of Section 6, the problem of an elliptical shear dislocation spreading in an infinite medium is now treated. The relative displacement distribution function $u_x(\rho_b, t)$ that, together with Eqs. (39), defines the boundary conditions on the $y = 0$ plane is taken in the following form:

$$u_x(\rho_b, t) = D\sqrt{\alpha^2 t^2 - \rho_b^2} \quad \text{for} \quad \rho_b \le \alpha t$$
$$= 0 \quad \text{for} \quad \rho_b > \alpha t \tag{45}$$

where D is a constant, α is the speed of propagation of the elliptical dislocation boundary along the minor axis, and the parameter $\rho_b(x, z)$ is as defined in Eqs. (40). It has been shown that Eq. (45) is also the solution form for the crack surface in self-similar problems of an elliptical shear crack propagating in an isotropic medium subjected to a homogeneous shear (Burridge and Willis, 1969). Thus, the results given in this section will correspond to a solution for an elliptical shear crack problem.

To solve this problem, again the corresponding circular shear dislocation problem is examined first. The boundary conditions on the $y = 0$ plane of the circular problem are given by Eqs. (9) together with the following relative displacement distribution:

$$u_x(\rho, t) = D\sqrt{\alpha^2 t^2 - \rho^2} \quad \text{for} \quad \rho \le \alpha t$$
$$= 0 \quad \text{for} \quad \rho > \alpha t. \tag{46}$$

Kostrov (1964b) showed that these boundary conditions actually correspond to the case of an expanding circular shear crack in an infinite elastic solid. From the previous results, the boundary values given by Burridge and Willis (1969), Eqs. (39) and (45), should then be the solution form on the crack plane for an expanding elliptical shear crack. In their paper, Burridge and Willis assumed that this is the case and then verified the solution. The results of this paper show much more simply that their reasonable assumption was indeed correct.

To return to the calculations, the distribution Eq. (46) is substituted into Eqs. (13) and (14) to give the boundary values on $y_2 = 0^+$ for the plane problems corresponding to the circular dislocation problem. The results are

(1) for the plane-strain problem

$$u_{x2}(x_2, t) = \frac{D}{\pi}\left[\alpha t + \frac{|x_2|}{2}\log\left|\frac{\alpha t - |x_2|}{\alpha t + |x_2|}\right|\right]$$
$$\sigma_{y2} = 0 \tag{47}$$

and

(2) for the antiplane problem

$$u_{z2}(x_2, t) = -u_{x2}(x_2, t). \tag{48}$$

The fictitious plane problems for the elliptical shear dislocation problem can then be readily determined from stretching as in Eqs. (42) and (43), which results in the boundary conditions on $y_2 = 0^+$ for the stretched plane problems as follows:

(1) the stretched plane-strain problem

$$u^e_{x2}(x_{e2}, t, \beta_1) = \frac{D}{\pi p(\beta_1)}\left[\alpha_{\beta_1} t + \frac{|x_{e2}|}{2}\log\left|\frac{\alpha_{\beta_1} t - |x_{e2}|}{\alpha_{\beta_1} t + |x_{e_2}|}\right|\right]$$
$$\sigma^e_{y2}(x_{e2}, t, \beta_1) = 0 \tag{49}$$

and

(2) The stretched antiplane problem

$$u^e_{z2}(x_{e2}, t, \beta_1) = -u^e_{x2}(x_{e2}, t, \beta_1) \tag{50}$$

where

$$\alpha_{\beta_1} = p(\beta_1)\cdot\alpha = \sqrt{(1+s)^2\cos^2\beta_1 + \sin^2\beta_1}\cdot\alpha. \tag{33}$$

7.1 Solution to the Stretched Plane Problems. It is apparent that the tangential displacement for $y_2 = 0^+$ in Eqs. (49) is a homogeneous function of degree 1. Thus this stretched plane-strain problem can also be solved straightforwardly by employing the method of self-similar potentials, which gives the following two-dimensional displacement fields:

$$u^e_{x2} = -\frac{2D\alpha^3_{\beta_1} b^2}{\pi p(\beta_1)}\int_0^t \mathrm{Re}\left[\int_0^{\theta_1}\frac{2\theta^3}{(1-\alpha^2_{\beta_1}(\theta^2)^2}\,d\theta + \int_0^{\theta_2}\frac{\theta(b^{-2}-2\theta^2)}{(1-\alpha^2_{\beta_1}\theta^2)^2}\,d\theta\right]d\tau$$

$$u^e_{y2} = -\frac{2D\alpha^3_{\beta_1} b^2}{\pi p(\beta_1)}\int_0^t \mathrm{Re}\left[\int_0^{\theta_1}\frac{2\theta^2\sqrt{a^{-2}-\theta^2}}{(1-\alpha^2_{\beta_1}\theta^2)^2}\,d\theta - \int_0^{\theta_2}\frac{\theta^2(b^{-2}-2\theta^2)}{(1-\alpha^2_{\beta_1}\theta^2)^2\sqrt{b^{-2}-\theta^2}}\,d\theta\right]d\tau. \tag{51}$$

The solution of the antiplane problem can also be found readily by using the method of self-similar potentials (Johnson and Robinson, 1972). The result is

$$u^e_{z2} = \frac{D\alpha^3_{\beta_1}}{\pi p(\beta_1)}\int_0^t \mathrm{Re}\left(\frac{\theta_2^2}{1-\alpha^2_{\beta_1}\theta_2^2}\right)d\tau. \tag{52}$$

7.2 Determination of the Three-Dimensional Fields. Once the stretched plane problems have been solved, the three-dimensional displacement fields for the expanding elliptical shear dislocation problem are completely determined by superposing the two-dimensional fields for the stretched plane problems according to Eqs. (41). The stress fields can be found from the fundamental stress-displacement relationships for plane fields and Eqs. (44) if they are of interest.

A numerical example with properties shown in Fig. 4 has been examined. The calculated displacement responses at some points are illustrated in Fig. 5. By symmetry, the radial and vertical displacements are zero when $\omega = 90$ deg, and the circumferential displacement is zero when $\omega = 0$ deg. In addition, it can be readily seen from the results that the body has not been disturbed until the arrival of the first P-wave front at the point at which the field is calculated.

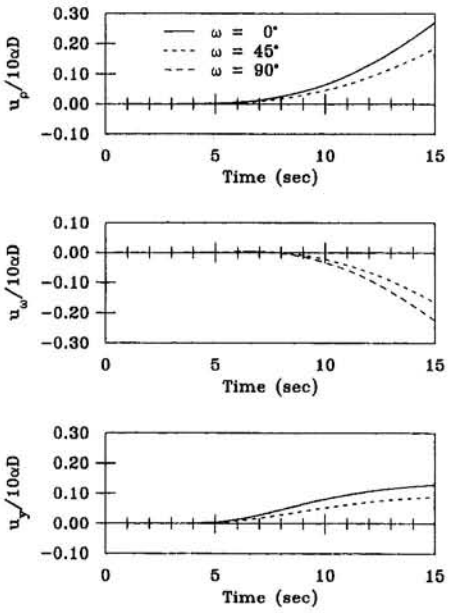

Fig. 5 Response at (ϱ = 10 km, ω, y = 15 km) due to a spreading elliptical shear dislocation (s = 0.5)

8 Conclusion

An extension of the usual rotational superposition to include a stretching in one direction of a boundary value distribution on a plane has been presented. This stretching technique is applicable to three-dimensional boundary value problems whenever the distribution of boundary values can be considered a "stretch" in one direction of a circular surface distribution. By means of the generalizations developed, the rotational superposition technique becomes even more powerful and more versatile. In addition to the two examples given in this paper, this new approach could prove useful in a number of other applications including problems in layered media. In this way, it is possible to increase the small number of unsymmetric three-dimensional static and dynamic elasticity problems that have been solved exactly.

References

Aleksandrov, A. Ia. (Alexandrov, A. Y.), 1961, "Solution of Axisymmetric Problems of the Theory of Elasticity with the Aid of Relations between Axisymmetric and Plane States of Stress," *Journal of Applied Mathematics and Mechanics* (English Translation of *Prikladnaya Matematika i Mekhanika*), Vol. 25, pp. 1361–1375.

Alexandrov, A. Y., 1968, "Solution of Three-Dimensional Problems of the Theory of Elasticity for Solids of Revolution by Means of Analytical Functions," *International Journal of Solids and Structures,* Vol. 4, pp. 701–721.

Burridge, R., and Willis, J. R., 1969, "The Self-Similar Problem of the Expanding Elliptical Crack in an Anisotropic Solid," *Proceedings of the Cambridge Philosophical Society,* Vol. 66, pp. 443–468.

Eringen, A. C., and Suhubi, E. S., 1975, *Elastodynamics, Volume II, Linear Theory,* Academic, New York.

Johnson, J. J., and Robinson, A. R., 1972, "Wave Propagation in a Half Space Due to an Interior Point Load Parallel to the Surface," Civil Engineering Studies, SRS 388, University of Illinois, Urbana, Illinois.

Kostrov, B. V., 1964a, "The Axisymmetric Problem of Propagation of a Tension Cracks," *Journal of Applied Mathematics and Mechanics* (English Translation of *Prikladnaya Matematika i Mekhanika*), Vol. 28, pp. 793–803.

Kostrov, B. V., 1964b, "Self-Similar Problems of Propagation of Shear Cracks," *Journal of Applied Mathematics and Mechanics* (English Translation of *Prikladnaya Matematika i Mekhanika*), Vol. 28, pp. 1077–1087.

Lehmann, C. H., 1942, *Analytic Geometry,* John Wiley and Sons, New York.

Smirnov, V. I., and Sobolev, S. L., 1933, "On the Application of a New Method of Investigation of the Elastic Vibrations in the Space with Axial Symmetry," (In Russian) *Trudy Instituta Seismologii, Akademiya Nauk SSSR,* No. 29.

Smirnov, V. I., 1964, *A Course of Higher Mathematics,* Vol. III, Part 2, Addison-Wesley, Reading, MA.

Thompson, J. C., and Robinson, A. R., 1969, "Exact Solutions of Some Dynamic Problems of Indentation and Transient Loadings of an Elastic Half Space," Civil Engineering Studies, SRS 350, University of Illinois, Urbana, Illinois.

Weber, C., 1940, "Zur Umwandlung von Rotationssymmetrischen Problemen in Zweidimensionale und Umgekehrt," *Zeitschrift für Angewandte Mathematik und Mechanik,* Vol. 20, pp. 117–118.

Subsonic and Intersonic Crack Growth Along a Bimaterial Interface

R. P. Singh
Graduate Aeronautical Labs, 105-50,
California Institute of Technology,
Pasadena, CA 91101
Mem. ASME

A. Shukla
Dynamic Photomechanics Laboratory,
Department of Mechanical Engineering
and Applied Mechanics,
University of Rhode Island,
Kingston, RI 02881
Fellow ASME

An experimental investigation has been conducted to study the dynamic failure of bimaterial interfaces. Interfacial crack growth is observed using dynamic photoelasticity and characterized in terms of crack-tip velocity, complex stress intensity factor, and energy release rate. On the basis of crack-tip velocity two growth regimes are established, viz. the subsonic and transonic regimes. In the latter regime crack-tip velocities up to 1.3 times the shear wave velocity of the more compliant material are observed. This results in the formation of a line of discontinuity in the stress field surrounding the crack tip and also the presence of a pseudo crack tip that travels with the Rayleigh wave velocity (of the more compliant material).

Introduction

In recent years there has been a resurgence of interest in the dynamic failure of bimaterial interfaces. This interest is primarily motivated by the role of interfacial fracture in determining the macroscopic response and failure modes of various multiphase materials. The first experimental study of this phenomenon of dynamic interface fracture was by Tippur and Rosakis (1991). Their investigation demonstrated the possibility of interfacial crack propagation at velocities up to 80 percent of the shear wave velocity of the more compliant material comprising the bimaterial interface. This experimental study motivated several analytical and numerical investigations of the same problem (Yang et al., 1991; Wu, 1991; Nakamura, 1991; and Deng, 1992). A higher order asymptotic stress field for dynamic crack propagation along bimaterial interfaces was provided by Liu et al. (1993). The same paper also presented experimental evidence of the highly dynamic and transient nature of this phenomenon. Most recently, Lambros and Rosakis (1994) demonstrated that dynamic crack propagation along a bimaterial interface can occur at transonic velocities (with respect to the more compliant material). However, experimental data, especially in the transonic regime, is still limited and analytical studies are nearly nonexistent.

This study is motivated by the need to employ experimental techniques to investigate the phenomena of both subsonic and transonic crack propagation along bimaterial interfaces. Thus, dynamic photoelasticity was employed in conjunction with high-speed photography to study the failure of bimaterial interfaces in the subsonic and transonic regimes. Failure was obtained by subjecting the bimaterial specimen to dynamic impact loading. Varying the velocity of the projectile used to impact the bimaterial specimen results in very different crack propagation characteristics. Low-velocity impact leads to subsonic crack propagation, in which the crack-tip velocity is less than the shear wave velocity of the more compliant material. Whereas, high-velocity impact leads to transonic crack propagation, in which the crack-tip velocity is greater than the shear wave velocity but less than the plane wave velocity of the more compliant material. This paper investigates and discusses the various physical phenomena that characterize crack propagation in both the subsonic and transonic regimes.

Experimental Procedure

The experimental setup used to investigate crack propagation along a bimaterial interface subjected to impact loading is shown in Fig. 1. As demonstrated in the figure, the bimaterial specimen is placed on the optical bench of a high-speed Cranz-Schardin spark-gap camera and subjected to impact by a projectile fired from a gas gun. This impact results in a compressive wave that traverses the width of the specimen and reflects as a tensile wave from the opposite free surface. The reflected wave loads the crack tip resulting in crack initiation and subsequent crack growth. The dynamic stress field produced by the propagating crack is observed using dynamic photoelasticity in conjunction with high speed photography. This is made possible by the transparent and photoelastic nature of the compliant half of the bimaterial specimen. The high-speed Cranz-Schardin camera provides a total of twenty images at framing rates of up to one million frames per second. These photographic images represent the full-field isochromatic fringe patterns for the stress field surrounding the propagating interface crack. Note that the isochromatic fringe patterns are observed only in the compliant and transparent half of the specimen.

The bimaterial specimen used to investigate interface fracture is shown in Fig. 2. It consists of a compliant half bonded directly to the stiff half. The compliant half was chosen to be a transparent and photoelastic polyester resin (Homalite-100), while aluminum was chosen as the other half. This combination provides a significant mismatch in the mechanical properties of the two materials comprising the bimaterial interface. The properties of both the materials are listed in Table 1.

The bonding of the two materials comprising the interface is done by a direct-bonding procedure to ensure a "true bimaterial bond." First, the Homalite and aluminum halves of the specimen are machined to size, mechanically abraded by sand-blasting and cleaned. Then, a thin layer of uncured polyester resin, to which a curing agent (Methyl ethyl ketone peroxide) has been added, is applied to the bonding surfaces and the two specimen halves are held together until the resin cures. After room temperature curing for 48 hours the resin achieves the same mechanical and optical properties as Homalite-100 resulting in a true bimaterial bond. This bonding procedure was evaluated by conducting tension tests on two Homalite-100 halves bonded with this technique. The experiment provided a tensile strength of 21 MPa (3000 psi) which compares well

Contributed by the Applied Mechanics Division of THE AMERICAN SOCIETY OF MECHANICAL ENGINEERS for publication in the ASME JOURNAL OF APPLIED MECHANICS.

Discussion on this paper should be addressed to the Technical Editor, Professor Lewis T. Wheeler, Department of Mechanical Engineering, University of Houston, Houston, TX 77204-4792, and will be accepted until four months after final publication of the paper itself in the ASME JOURNAL OF APPLIED MECHANICS.

Manuscript received by the ASME Applied Mechanics Division, Feb. 23, 1995; final revision, Mar. 16, 1996. Associate Technical Editor: W. N. Sharpe, Jr.

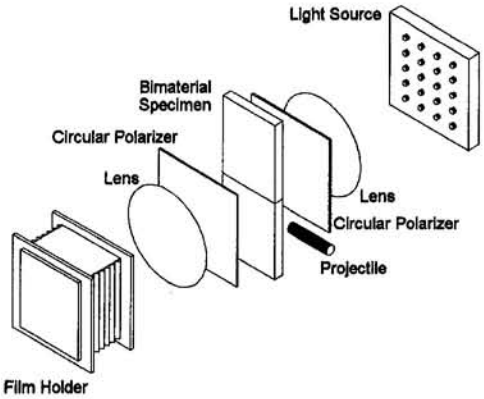

Fig. 1 Experimental setup for investigating the fracture of a bimaterial interface subjected to impact loading by a projectile fired from a gas gun

with the standard value of 28 MPa (4000 psi) for homogeneous Homalite-100. The starter crack along the interface is formed by incorporating a strip of Teflon tape during the bonding procedure.

In this experimental investigation the bimaterial interface specimen was subjected to two different magnitudes and rates of loading, as determined by the velocity of the gas gun fired projectile. The same steel projectile (12.5 mm diameter and 100 mm long) was used for both experiments. The impact velocities used were a "low" velocity of 5 m/s and a "high" velocity of 30 m/s. These projectile velocities correspond to impact energies of 1.25 J and 45.4 J, respectively. The low and high-impact velocities resulted in very different crack-tip propagation histories.

Analysis of Isochromatic Fringe Patterns

Isochromatic fringe patterns obtained from the high-speed camera were analyzed to determine various fracture parameters such as the crack-tip velocity, the complex stress intensity factor, and the energy release rate. This analysis procedure is based on the transient higher order asymptotic stress field equations for a crack propagation along a bimaterial interface (Liu et al., 1993). Consider a crack propagating along a bimaterial interface as shown in Fig. 3. From the higher order asymptotic analysis of Liu et al. (1993) the stress field in vicinity of the crack tip is given as

$$\sigma_{ij}(\xi_1, \xi_2, t) = \sum_{m=0}^{\infty} \epsilon^{p_m} \sigma_{ij}^{(m)}(\eta_1, \eta_2, t) \qquad (1)$$

where $\eta_i = \xi_i/\epsilon$, $i \in \{1, 2\}$, and ϵ is a small arbitrary positive

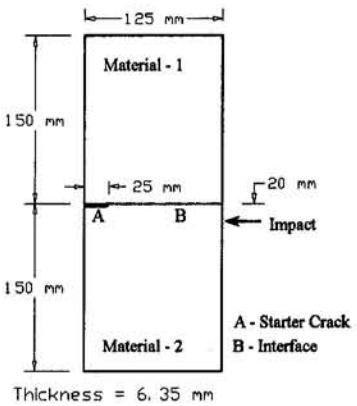

Fig. 2 Schematic of bimaterial interface specimen

Table 1 Material properties of bimaterial system

Property	Homalite-100†	6061 Aluminum
Young's modulus, E, (GPa)	5.3	71
Poisson's ratio, ν	0.35	0.33
Density, ρ, (kg/m3)	1230	2770
P-wave velocity (plane-σ), c_1, (m/s)	2220	5430
S-wave velocity, c_s, (m/s)	1270	3100
Surface wave velocity, c_R, (m/s)	1186	2890
Fracture toughness, K_{Ic}, (MPa$\sqrt{}$m)	0.45	99
Material fringe value, f_σ, (kN/m)	23.7	—

† Maufactured by Homalite, Inc., Delaware, USA.

number. This parameter is used to scale a small region around the crack tip such that the scaled coordinates η_i fill the entire field of observation. Now, $p_0 < p_1 < p_2 < \ldots$, i.e. $\sigma_{ij}^{(0)}$ are the primary terms, $\sigma_{ij}^{(1)}$ are the first-order corrections and so on. The exact form of the stress field equations in terms of positional coordinates, crack-tip velocity, material properties, and various fracture parameters is given by Liu et al. (1993).

The generation of the isochromatic fringe patterns, which are contours of constant maximum shear stress, is governed by the stress optic law,

$$\frac{Nf_\sigma}{2h} = \tau_{\max} = \frac{\sigma_1 - \sigma_2}{2} = \sqrt{\left(\frac{\sigma_x - \sigma_y}{2}\right)^2 + \tau_{xy}^2} \qquad (2)$$

where f_σ is the material fringe value and h is the thickness of the specimen. The stress optic law is coupled with the higher order asymptotic stress field to yield the relation that defines isochromatic fringes in the vicinity of a crack tip propagating dynamically along a bimaterial interface,

$$\begin{aligned}\left(\frac{Nf_\sigma}{2h}\right)^2 &= \mu^2\{[(1+\alpha_1^2)\,\mathrm{Re}F_0''(z_1;t) + 2\alpha_s\,\mathrm{Re}G_0''(z_s;t)]^2 \\ &\quad + [2\alpha_1\,\mathrm{Im}F_0''(z_1;t) + (1+\alpha_s^2)\,\mathrm{Im}G_0''(z_s;t)]^2\} \\ &= \mu^2\{(1+\alpha_1^2)^2\,[\mathrm{Re}F_0''(z_1;t)]^2 \\ &\quad + 4\alpha_s^2[\mathrm{Re}G_0''(z_s;t)]^2 \\ &\quad + 4\alpha_s(1+\alpha_1^2)\,\mathrm{Re}F_0''(z_1;t)\,\mathrm{Re}G_1''(z_s;t) \\ &\quad + 4\alpha_1^2\,[\mathrm{Im}F_0''(z_1;t)]^2 \\ &\quad + (1+\alpha_s^2)^2[\mathrm{Im}G_0''(z_s;t)]^2 \\ &\quad + 4\alpha_1(1+\alpha_s^2)\,\mathrm{Im}F_0''(z_1;t)\,\mathrm{Im}G_1''(z_s;t)\} \qquad (3)\end{aligned}$$

where

$$\alpha_1^2 = 1 - \frac{v^2}{c_1^2}, \quad \alpha_s^2 = 1 - \frac{v^2}{c_s^2} \qquad (4)$$

with v being the crack-tip velocity, and c_1 and c_s the P and S-wave velocities, respectively, of material-1. The modified coordinates z_1 and z_s are defined as $z_1 = \eta_1 + i\alpha_1\eta_2$ and $z_s = \eta_1 + i\alpha_s\eta_2$. The functions F_m'' and G_m'' have been defined by Liu et

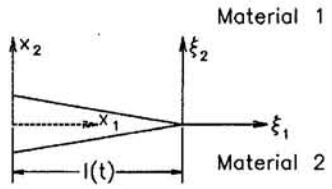

Fig. 3 Schematic of a crack propagating along a bimaterial interface

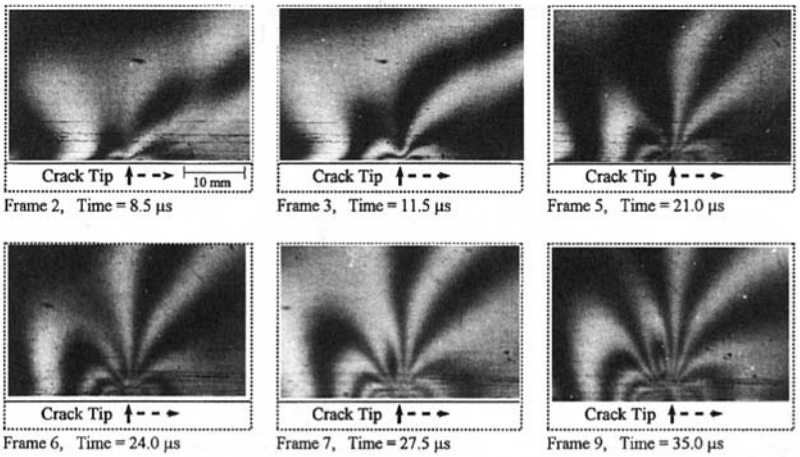

Fig. 4 A typical sequence of isochromatic fringe patterns for the crack propagation along a Homalite/aluminum bimaterial interface subjected to low-velocity impact loading. The fringe pattern is determined on the Homalite half of the specimen.

al. (1993). Equation (3) is used to analyze the experimental isochromatic fringe pattern to determine various fracture parameters, such at the dynamic complex stress intensity factor, the energy release rate, and the nonsingular stress field component. The analysis procedure employs a nonlinear least squares method based on the Newton-Raphson technique.

Results and Discussion

Subsonic Crack Growth. This sections presents and discusses crack propagation along a bimaterial interface resulting from low-velocity (≈5 m/s) impact loading. A typical sequence of isochromatic fringe patterns for crack propagation for such an experiment is shown Fig. 4. The photographs depict the dynamic stress field that surrounds the crack tip as it propagates along the bimaterial interface. Also, the location of the crack tip is indicated in each frame. The crack-tip velocity history corresponding to this experiment was determined from the crack-tip location as a function of time and is plotted in Fig. 5. This plot shows that after initiation the crack-tip velocity increases rapidly to around 80 percent of the shear wave velocity of the more compliant material, c_s^{HOMALITE}. Thereafter, the crack-tip velocity continues to increase, but at a slower rate, and finally reaches the shear wave velocity, c_s^{HOMALITE}.

Broberg (1960) has shown that the crack-tip velocities for unassisted crack growth in homogeneous materials cannot exceed the Rayleigh wave velocity due to energy considerations. However, for bimaterial interfaces the energy to the propagating crack tip is supplied from the stiff half, which has higher wave velocities than the compliant half, and higher crack-tip velocities are possible. Such crack-tip velocities have been observed previously under similar loading conditions but for a different bimaterial system (Tippur and Rosakis, 1991).

For the major duration of the experiment described above the crack-tip velocity was less than the shear wave velocity of the more compliant material ($v < c_s^{\text{HOMALITE}}$). This phenomenon of *subsonic crack growth* was observed typically for all experiments that involved low velocity impact. Moreover, for this crack-tip velocity regime the higher order asymptotic field equations of Liu et al. (1993) are applicable and were used to determine the various fracture parameters. Figure 6 shows the variation of the real and imaginary parts of the complex stress intensity factor, $\mathbf{K}^d$. The magnitudes of both the real and imaginary parts of the stress intensity factor (K_1 and K_2) decrease rapidly to zero with crack propagation. The variation of the energy release rate with crack propagation also shows a decreasing trend and is plotted in Fig. 7. As the crack propagates along the bimaterial interface, the crack-tip velocity increases and the energy required to drive the crack decreases. Yang et al. (1991) have shown that for a crack propagating faster than the Rayleigh wave velocity (but less than the shear wave velocity) of the more compliant material, the energy release rate goes to zero. This accounts for the decreasing trend of the energy release rate as shown in Fig. 7. In actual experiments the energy release rate does not go to zero even after the crack-tip velocity exceeds

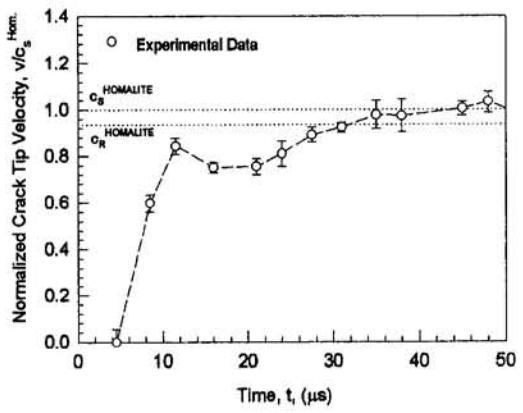

Fig. 5 History of the crack-tip velocity for subsonic crack propagation along a Homalite/aluminum bimaterial interface

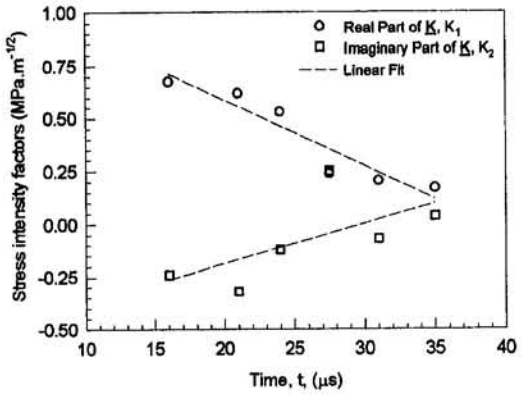

Fig. 6 Variation of the real and imaginary parts of the complex stress intensity factor, K^d, for crack propagation along a Homalite/aluminum bimaterial interface

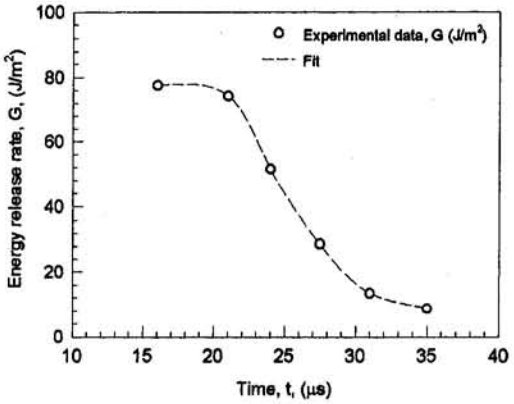

Fig. 7 Variation of the energy release rate, G, for crack propagation along a Homalite/aluminum bimaterial interface

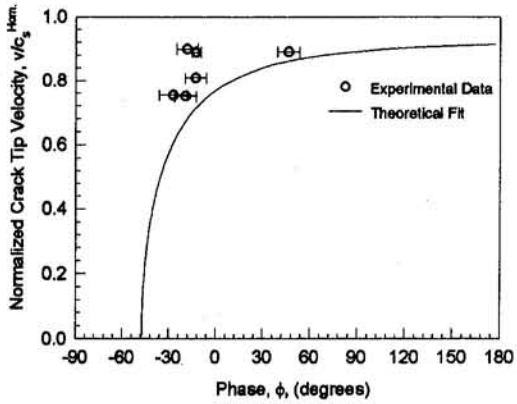

Fig. 9 Fit of constant crack face displacement ratio (Eq. (5)) to experimental data for subsonic crack propagation along a Homalite/aluminum bimaterial interface

the Rayleigh wave velocity of the more compliant material. This is possibly due to the presence of some dissipative mechanism such as crack tip plasticity that is not accounted for in theories based on elastodynamics.

Lambros and Rosakis (1994) have proposed a fracture criterion for crack propagation along bimaterial interfaces at crack-tip velocities less than the shear wave velocity of the more compliant material ($v < c_s^{\text{HOMALITE}}$). This criterion is based on an earlier criterion proposed for quasi-static crack growth along bimaterial interfaces (Liechti and Knauss, 1982). The criterion requires that the ratio of the shearing and opening crack-face displacements at a given point behind the crack tip should remain a constant, i.e.,

$$\left.\frac{\delta_1}{\delta_2}\right|_{r=a} = \frac{1}{\eta}\tan\left[\phi + \epsilon \ln r - \tan^{-1}(2\epsilon)\right] = \text{constant} \quad (5)$$

where δ_1 and δ_2 are the shearing and opening displacements of the crack faces as defined in Fig. 8; η and ϵ are interface parameters that depend on material properties and crack-tip velocity; ϕ is the mode mixity; and $r = a$ is some given point behind the crack tip. Equation (5) is fitted to experimental data for subsonic crack growth along a Homalite/aluminum bimaterial interface as shown in Fig. 9. As shown in the plot the experimental data shows the same trend as the theoretical equation which indicated that for subsonic crack propagation along a Homalite/aluminum bimaterial interface the quantity δ_1/δ_2 is a constant. The fact the quantity δ_1/δ_2 is a constant is employed Lambros and Rosakis (1994) to propose a relation between the energy release rate, G, and the velocity of crack propagation. Figure 10 shows a plot of the normalized energy release rate as a function of crack-tip velocity. The experimental data exhibits the same trend as the fracture criterion proposed by Lambros and Rosakis (1994).

Transonic Crack Growth. When the bimaterial interface is subjected to high velocity impact (≈30 m/s) the resulting fracture phenomenon is different from the earlier case. Typical isochromatic fringe patterns obtained for the fracture of a bimaterial interface subjected to high velocity impact is shown in Fig. 11. The history of the crack-tip velocity for this experiment is plotted in Fig. 12. The crack tip rapidly accelerates directly up to the shear wave velocity of the more compliant material, c_s^{HOMALITE}, and stabilizes around this value for about 20 μs. Thereafter, the crack-tip velocity continues to increase beyond the shear wave velocity of the more compliant material.

The terminal crack-tip velocity observed in these high velocity impact experiments was around 130 percent of the shear wave velocity but less than the plane wave velocity of the more compliant material. This phenomenon of *transonic crack propagation* ($c_s^{\text{HOMALITE}} < v < c_1^{\text{HOMALITE}}$) was observed typically for all high impact velocity experiments. The experimental evidence for transonic crack propagation is still limited (Lambros and Rosakis, 1994, 1995) and theoretical developments are nearly nonexistent. Thus, there is significant speculation as to the nature of the fracture phenomenon under such velocity regimes.

A direct consequence of transonic crack propagation is the formation of a line-of-discontinuity in the stress field surrounding the moving crack tip. The propagating crack tip acts as a source of shear and plane waves which radiate out in to the material and establish the stress field that surrounds the crack tip. If this source (the crack tip) propagates faster than the shear wave velocity then the spreading out of the shear waves is limited and a line-of-discontinuity forms. This line-of-discontinuity represents jumps in the stress and displacement fields and is akin to the formation of shock waves in fluids.

Experimental evidence of the line-of-discontinuity is shown in Fig. 13 in the form of discontinuous isochromatic fringe

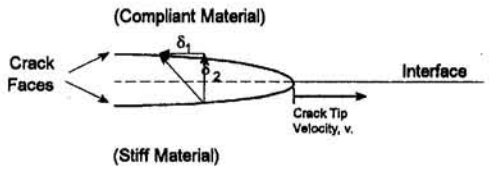

Fig. 8 Opening of crack faces behind the propagating crack tip for subsonic interface fracture

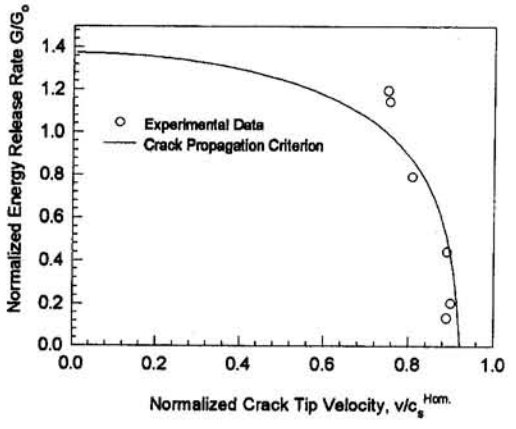

Fig. 10 Comparison of the experimental variation of the energy release rate with the crack growth criterion proposed by Lambros and Rosakis (1994)

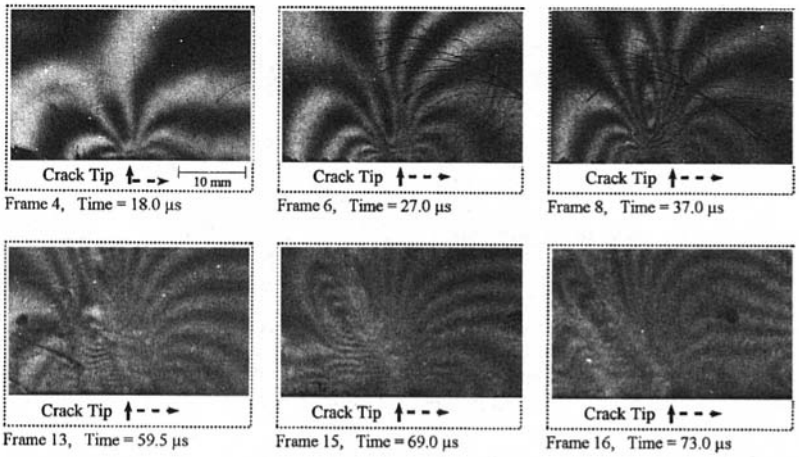

Fig. 11 A typical sequence of isochromatic fringe patterns for the crack propagation along a Homalite/aluminum bimaterial interface subjected to high-velocity impact loading. The fringe pattern is determined on the Homalite half of the specimen.

contours. The line originates at the crack tip and radiates out into the material. The angular orientation of the this line-of-discontinuity can be related to the crack-tip velocity and the shear wave velocity of the material as (Cole and Huth, 1958),

$$\sin \alpha = \frac{c_s}{v} \tag{6}$$

where α denotes the angular orientation of the line-of-discontinuity, c_s is the shear wave velocity of the material, and v is the velocity of the crack tip. The orientations of the line-of-discontinuity determined from the experimental isochromatic fringe patterns were compared with the angles predicted by Eq. (6) and are listed in Table 2. The correspondence between the experimentally observed and theoretically predicted angles is excellent and substantiates the presence of the line-of-discontinuity. Recently, Liu et al. (1995) have considered steady-state transonic crack propagation along an elastic-rigid bimaterial interface. Their asymptotic analysis predicts the presence of the line of discontinuity in the stress field. The angle of orientation of the line of discontinuity as predicted by Liu et al. (1995) is the same as that given by Eq. (6).

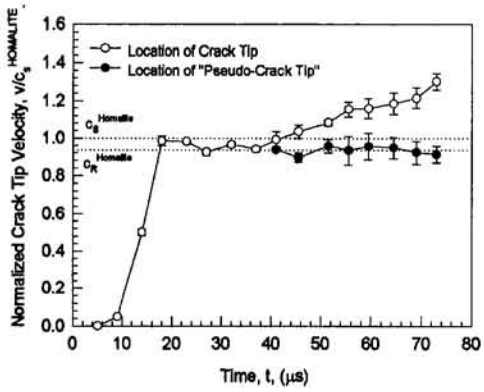

Fig. 12 History of the crack-tip velocity for transonic crack propagation along a Homalite/aluminum bimaterial interface

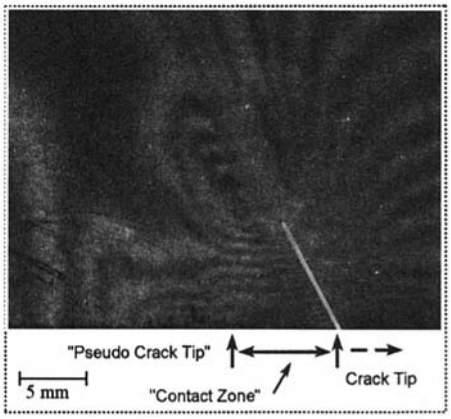

Fig. 13 Discontinuities of isochromatic fringe contours representing the formation of a line-of-discontinuity

The experimental isochromatic fringe patterns also show the presence of a secondary disturbance that trails behind the propagating crack tip. This secondary disturbance, indicated in Fig. 13 as the pseudo-crack tip. This "pseudo-crack tip" propagated along the debonded interface (on the compliant side) at the Rayleigh wave velocity of the more compliant material, c_R^{HOMALITE}. Experimental measurements of the velocity of the "pseudo-crack tip" are plotted in Fig. 12. The disturbance was produced when the crack tip accelerated beyond the Rayleigh wave velocity of the more compliant material, c_R^{HOMALITE}.

An additional phenomenon observed during transonic crack propagation is the presence of a "zone" directly behind the propagating crack tip that is marked by the lack of isochromatic fringe patterns that intersect the interface. This zone is also shown in Fig. 13 and represents large-scale contact occurring behind the dynamically propagating transonic crack tip, as postulated by Liu et al. (1995). The exact nature of this contact zone is yet to be determined. The mechanics of transonic crack propagation are schematically presented in Fig. 14.

Conclusion

An experimental study was conducted to investigate crack propagation along bimaterial interfaces that were subjected to impact loading. The bimaterial specimens were loaded by im-

Table 2 Comparison of experimentally measured and theoretically predicted orientations for the line-of-discontinuity

Frame number	V/c_s^{HOMALITE}	α_{THEORY}	$\alpha_{\text{EXPT.}}$
13	1.16	59.5 deg	63 deg
14	1.19	57.5 deg	55 deg
15	1.21	55.7 deg	53 deg
16	1.30	50.3 deg	48 deg

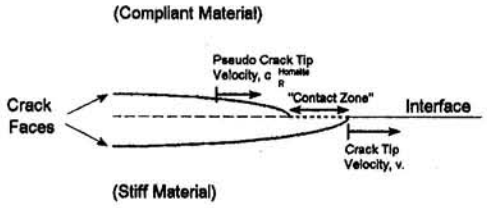

Fig. 14 Opening of crack faces behind the propagating crack tip for transonic interface fracture

pacting them with a projectile fired from a gas gun. This dynamic loading caused the interface crack to initiate and subsequently grow along the interface. The crack propagation phenomenon was observed using dynamic photoelasticity in conjunction with high-speed photography.

Varying the velocity of the projectile used to impact the bimaterial specimen resulted in different crack propagation characteristics. Low-velocity impact led to subsonic crack propagation, in which the crack-tip velocity was less than the shear wave velocity of the more compliant material ($v < c_s^{\text{HOMALITE}}$) whereas high-velocity impact led to transonic crack propagation, in which the crack-tip velocity was greater than the shear wave velocity, but less than the plane wave velocity of the more compliant material ($c_s^{\text{HOMALITE}} < v < c_l^{\text{HOMALITE}}$).

For subsonic crack propagation along the bimaterial interface, the isochromatic fringe pattern surrounding the crack tip was analyzed to determine various fracture parameters. These parameters of interest are, namely, the crack-tip velocity, the complex stress intensity factor, and the energy release rate. After initiation the crack-tip velocity was found to increase rapidly to around 80 percent of the shear wave velocity of the more compliant material, c_s^{HOMALITE}. Thereafter, the crack-tip velocity continued to increase, but at a slower rate, and stayed less than the shear wave velocity of the of the more compliant material, c_s^{HOMALITE}, for the major duration of the experiment. The magnitudes of both the real and imaginary parts of the stress intensity factor (K_1 and K_2) decrease rapidly to zero with crack propagation. The energy release rate also showed a rapidly decreasing trend. Finally, the crack propagation was determined to occur in accordance with the fracture criterion proposed by Lambros and Rosakis (1994).

For the case of transonic crack propagation, the crack-tip velocity was found to increase rapidly to the shear wave velocity of the more compliant material, c_s^{HOMALITE}. Thereafter the crack-tip velocity continued to increase up to 130 percent of the shear wave velocity of the more compliant material, c_s^{HOMALITE}. A direct consequence of this transonic propagation was the formation of a line-of-discontinuity in the stress field surrounding the moving crack tip. This line-of-discontinuity represents jumps in the stress and displacement fields surrounding the crack tip and appeared in the form of discontinuous isochromatic fringe contours. Additionally, transonic crack propagation resulted in large-scale contact of the crack faces behind the propagating crack tip. The stress field also showed the presence of a secondary disturbance, termed the pseudo-crack tip, which propagated and trailed the moving crack-tip at the Rayleigh wave velocity of the more compliant material.

Acknowledgment

The support of the National Science Foundation under grant number CMS 9424114 is gratefully acknowledged.

References

Broberg, K. B., 1960, "The Propagation of a Brittle Crack," *Archiv fur Fysik,* Vol. 18, pp. 159–192.

Cole, J. D., and Huth, J. H., 1958, "Stresses Produced in a Half Plane by Moving Loads," ASME JOURNAL OF APPLIED MECHANICS, Vol. 25, pp. 433–436.

Deng, X., 1992, "Complete Complex Series Expansions of Near-Tip Fields for Steadily Growing Interface Cracks in Dissimilar Isotropic Materials," *Engineering Fracture Mechanics,* Vol. 42, No. 2, pp. 237–242.

Lambros, J., and Rosakis, A. J., 1994, "Dynamic Decohesion of Bimaterials: Experimental Observations and Failure Criteria," To appear in a special volume of the *International Journal of Solids and Structures* devoted to Dynamic Failure of Modern Materials, 1994.

Lambros, J., and Rosakis, A. J., 1995, "Shear Dominated Transonic Crack Growth in Bimaterials, Part I: Experimental Observations," *Journal of Mechanics and Physics of Solids,* Vol. 43, No. 2, pp. 169–188.

Liechti, K. M., and Knauss, W. G., 1982, "Crack Propagation at Material Interfaces: II Experiments on Mode Interaction," *Experimental Mechanics,* Vol. 22, No. 10, pp. 383–391.

Liu, C., Lambros, J., and Rosakis, A. J., 1993, "Highly Transient Elastodynamic Crack Growth in a Bimaterial Interface: Higher Order Asymptotic Analysis and Optical Experiments," *Journal of the Mechanics and Physics of Solids,* Vol. 41, No. 12, pp. 1857–1954.

Liu, C., Huang, Y., and Rosakis, A. J., 1995, "Shear Dominated Transonic Crack Growth in Bimaterials, Part II: Analytical Investigation of Asymptotic Fields and Favorable Velocity Regimes," *Journal of the Mechanics and Physics of Solids,* Vol. 43, No. 2, pp. 189–206.

Nakamura, T., 1991, "Three Dimensional Stress Fields of Elastic Interface Cracks," ASME JOURNAL OF APPLIED MECHANICS, Vol. 58, pp. 939–946.

Tippur, H. V., and Rosakis, A. J., 1991, "Quasi-static and Dynamic Crack Growth Along Bimaterial Interfaces: A Note on Crack-tip Field Measurements Using Coherent Gradient Sensing," *Experimental Mechanics,* Vol. 31, pp. 243–251.

Wu, K. C., 1991, "Explicit Crack-Tip Fields of an Extending Interface Crack in an Anisotropic Bimaterial," *International Journal of Solids and Structures,* Vol. 27, No. 4, pp. 455–466.

Yang, W., Suo, Z., and Shih, C. H., 1991, "Mechanics of Dynamic Debonding," *Proceedings of the Royal Society, London,* Vol. A433, pp. 679–697.

The Elastic Field in a Half-Space With a Circular Cylindrical Inclusion

L. Z. Wu

S. Y. Du

School of Astronautics,
Harbin Institute of Technology,
Harbin 150001, P.R. China

The problem of a circular cylindrical inclusion with uniform eigenstrain in an elastic half-space is studied by using the Green's function technique. Explicit solutions are obtained for the displacement and stress fields. It is shown that the present elastic fields can be expressed as functions of the complete elliptic integrals of the first, second, and third kind. Finally, numerical results are shown for the displacement and stress fields.

1 Introduction

The problem of determining the elastic field in an elastic medium caused by an inclusion with uniform eigenstrain is of interest in engineering. Early work by Eshelby (1957, 1959) showed that an ellipsoidal inclusion with uniform eigenstrain induces a constant stress state within the inclusion. Since then, the inclusion problem has been greatly developed, as pointed out by the extensive reviews of Mura (1987, 1988). A number of techniques have been used to deal with the class of problems. However, many results at present are not expressed in explicit form but are in the form of numerical solutions.

Using the Galerkin vector stress function, Mindlin and Cheng (1950) investigated the thermoelastic stress field in the semi-infinite solid when a uniform dilatational thermal expansion is given inside a spherical region. Youngdahl and Sternberg (1966) analyzed the stress concentration around a cylindrical hole in a semi-infinite medium by using the Papkovich stress functions. Chiu (1978, 1980) obtained the stress field and surface displacement field by superimposing the solution for a half-space under some normal surface stress on the full solution due to two cuboidal domains with initial strains. Utilizing Mindlin's (1953) solution for Green's function in a half-space, Seo and Mura (1979) studied the problem of an ellipsoidal inclusion with uniform eigenstrain. Numerical results are obtained for the stress field. An alternate method for solving the axisymmetric elastic fields in the half-space with an isotropic spheroidal inclusion was proposed by Yu and Sanday (1990). In their study, Eshelby's method for the ellipsoidal inclusion and the Hankel transformation method for the prismatic loop were used. Hasegawa, Lee, and Mura (1993) gave the axisymmetric stresses and displacement fields caused by a solid or hollow circular cylindrical inclusion in the present of uniform eigenstrain in a half-space. Their solutions were obtained from the solution of an infinite body by applying to the boundary plane equal and opposite normal and shear stresses in order to satisfy the traction-free surface condition.

In comparison to the axisymmetric elastic field given by Hasegawa et al. (1993), a general case to a circular cylindrical inclusion with arbitrary uniform eigenstrains in a half-space is considered in the present paper. Analytical solutions for the displacement and stress fields are obtained by using the technique of Green's function. From Wu and Du (1995a, b) and Appendixes B and C it can be found that the displacement and stress fields can be expressed as functions of the complete elliptic integrals of the first, second, and third kind. Finally, numerical results are shown for the displacement and stress fields.

In what follows, the summation convention over repeated Greek and Latin indices is adopted. Greek subscript varies from 1 to 3 and Latin one does from 1 to 2. Furthermore, a comma indicates partial differentiation, thus $f_{,i}$ means $\partial f/\partial x_i$.

2 Statement of the Problem

A semi-infinite domain is defined by $x_3 \geq 0$ as shown in Fig. 1. The surface $x_3 = 0$ is free from external tractions. The present analysis considers a circular cylindrical inclusion Ω with radius a and length $h = h_2 - h_1$ where h_1 and h_2 are the distances from the free surface ($x_3 = 0$) to the upper and lower surfaces of inclusion, respectively. Its objective is to determine the displacement and stress fields when the eigenstrain $\epsilon^*_{\alpha\beta}(\mathbf{x})$ is given. From Wu and Du (1995a), when eigenstrain $\epsilon^*_{\alpha\beta}(\mathbf{x})$ is uniform, the induced displacement field $u_\alpha(\mathbf{x})$ due to $\epsilon^*_{\alpha\beta}$ is given by

$$u_\alpha(\mathbf{x}) = C_{\beta 3\lambda\mu}\epsilon^*_{\lambda\mu}\left[\int_{\Omega_1}\int G_{\alpha\beta}(\mathbf{x}-\mathbf{x}')dx_1'dx_2'\right]\Bigg|_{x_3=h_1}^{h_2} + C_{\beta\gamma\lambda\mu}\epsilon^*_{\lambda\mu}\int_0^{2\pi}\int_{h_1}^{h_2} G_{\alpha\beta}(\mathbf{x}-\mathbf{x}')n_\gamma a d\theta dx_3' \quad (1)$$

where $C_{\beta\gamma\lambda\mu}$ are the elastic moduli, $G_{\alpha\beta}(\mathbf{x}-\mathbf{x}')$ are the elastic Green's functions for the semi-infinite isotropic medium, Ω_1 is the area of the base of circular cylinder, n_γ is the outward unit normal to cylindrical surface, and (r, θ, x_3') are cylindrical coordinates, namely, there are relations $x_1' = a\cos\theta$, $x_2' = a\sin\theta$ on the cylindrical surface.

Following Green's functions in a semi-infinite isotropic medium (see Appendix A) and taking into account the symmetry in directions x_1 and x_2, we only need to solve the following kinds of integrals:

$$T(x_1, x_2, z) = \int_{\Omega_1}\int \frac{dx_1'dx_2'}{R_1}$$

$$T_{\alpha\beta}(x_1, x_2, z) = \int_{\Omega_1}\int \frac{(x_\alpha - x_\alpha')(x_\beta - x_\beta')}{R_1^3}dx_1'dx_2'$$

$$\bar{T}(x_1, x_2, \bar{z}) = \int_{\Omega_1}\int \frac{dx_1'dx_2'}{R_2}$$

Contributed by the Applied Mechanics Division of THE AMERICAN SOCIETY OF MECHANICAL ENGINEERS for presentation at the International Mechanical Engineering Congress and Exposition, the Winter Annual Meeting of The ASME, Atlanta, GA, Nov. 17–22, 1996.

Discussion on this paper should be addressed to the Technical Editor, Professor Lewis T. Wheeler, Department of Mechanical Engineering, University of Houston, Houston, TX 77204-4792, and will be accepted until four months after final publication of the paper itself in the ASME JOURNAL OF APPLIED MECHANICS.

Manuscript received by the ASME Applied Mechanics Division, Mar. 6, 1995; final revision, July 7, 1996. Associate Technical Editor: R. Abeyaratne.

Paper No. 96-WA/APM-8.

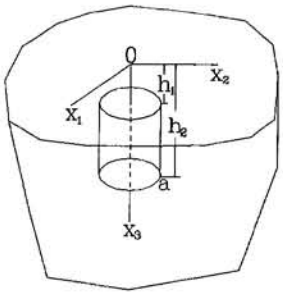

Fig. 1 Cylindrical inclusion in a half-space

$$\bar{T}_{ij}(x_1, x_2, \bar{z}) = \int_{\Omega_1}\int \frac{(x_i - x_i')(x_j - x_j')}{R_2^3}\, dx_1' dx_2'$$

$$\bar{T}_{\alpha 3}(x_1, x_2, z, \bar{z}) = \int_{\Omega_1}\int \frac{(x_\alpha - x_\alpha')(x_3 - x_3')}{R_2^3}\, dx_1' dx_2'$$

$$\bar{T}_3(x_1, x_2, z, \bar{z}) = \int_{\Omega_1}\int \frac{x_3 x_3'}{R_2^3}\, dx_1' dx_2'$$

$$\bar{T}_{ij3}(x_1, x_2, z, \bar{z}) = \int_{\Omega_1}\int \frac{x_3 x_3'(x_i - x_i')(x_j - x_j')}{R_2^5}\, dx_1' dx_2'$$

$$\bar{T}_{i33}(x_1, x_2, z, \bar{z}) = \int_{\Omega_1}\int \frac{x_3 x_3'(x_i - x_i')(x_3 + x_3')}{R_2^5}\, dx_1' dx_2'$$

$$\bar{T}_{333}(x_1, x_2, z, \bar{z}) = \int_{\Omega_1}\int \frac{x_3 x_3'(x_3 + x_3')^2}{R_2^5}\, dx_1' dx_2'$$

$$\tilde{T}_i(x_1, x_2, \bar{z}) = \int_{\Omega_1}\int \frac{x_i - x_i'}{R_2(R_2 + \bar{z})}\, dx_1' dx_2'$$

$$\tilde{T}_{ij}(x_1, x_2, \bar{z}) = \int_{\Omega_1}\int \left[\frac{\delta_{ij}}{R_2 + \bar{z}} - \frac{(x_i - x_i')(x_j - x_j')}{R_2(R_2 + \bar{z})^2}\right] dx_1' dx_2' \quad (2)$$

and

$$Q^1(x_1, x_2, x_3) = a\int_0^{2\pi}\int_{h_1}^{h_2} \frac{\cos\theta\, d\theta dx_3'}{R_1}$$

$$Q^1_{\alpha\beta}(x_1, x_2, x_3) = a\int_0^{2\pi}\int_{h_1}^{h_2} \frac{\cos\theta(x_\alpha - x_\alpha')(x_\beta - x_\beta')}{R_1^3}\, d\theta dx_3'$$

$$\bar{Q}^1(x_1, x_2, x_3) = a\int_0^{2\pi}\int_{h_1}^{h_2} \frac{\cos\theta\, d\theta dx_3'}{R_2}$$

$$\bar{Q}^1_{\alpha\beta}(x_1, x_2, x_3) = a\int_0^{2\pi}\int_{h_1}^{h_2} \frac{\cos\theta(x_\alpha - x_\alpha')(x_\beta - x_\beta')}{R_2^3}\, d\theta dx_3'$$

$$\bar{Q}^1_3(x_1, x_2, x_3) = a\int_0^{2\pi}\int_{h_1}^{h_2} \frac{\cos\theta x_3 x_3'}{R_2^3}\, d\theta dx_3'$$

$$\bar{Q}^1_{ij3}(x_1, x_2. x_3) = a\int_0^{2\pi}\int_{h_1}^{h_2} \frac{\cos\theta x_3 x_3'(x_i - x_i')(x_j - x_j')}{R_2^5}\, d\theta dx_3'$$

$$\bar{Q}^1_{i33}(x_1, x_2, x_3) = a\int_0^{2\pi}\int_{h_1}^{h_2} \frac{\cos\theta x_3 x_3'(x_i - x_i')(x_3 + x_3')}{R_2^5}\, d\theta dx_3'$$

$$\bar{Q}^1_{333}(x_1, x_2, x_3) = a\int_0^{2\pi}\int_{h_1}^{h_2} \frac{\cos\theta x_3 x_3'(x_3 + x_3')^2}{R_2^5}\, d\theta dx_3'$$

$$\tilde{Q}^1_i(x_1, x_2, x_3) = a\int_0^{2\pi}\int_{h_1}^{h_2} \frac{\cos\theta(x_i - x_i')}{R_2(R_2 + \bar{z})}\, d\theta dx_3'$$

$$\tilde{Q}^1_{ij}(x_1, x_2, x_3) = a\int_0^{2\pi}\int_{h_1}^{h_2} \left[\frac{\delta_{ij}}{R_2 + \bar{z}} - \frac{(x_i - x_i')(x_j - x_j')}{R_2(R_2 + \bar{z})^2}\right] \cos\theta d\theta dx_3' \quad (3)$$

where δ_{ij} is the Kronecker delta and

$$z = x_3 - x_3' \quad \bar{z} = x_3 + x_3'$$

$$R_1 = [(x_1 - x_1')^2 + (x_2 - x_2')^2 + z^2]^{1/2}$$

$$R_2 = [(x_1 - x_1')^2 + (x_2 - x_2')^2 + \bar{z}^2]^{1/2}. \quad (4)$$

3 Solution of Eq. (2)

In this paper, we use a similar procedure as in Wu and Du (1995a, b) to solve the integrals of (2) and (3). Since there is no substantive difference in the derivation, some details will be omitted. For this purpose, we shall only give the final expressions below. From Wu and Du (1995a, b), it can be seen that the solution of (2) is related with the position of point $\mathbf{x} = (x_1, x_2, x_3)$, so we shall use some symbols with superscripts i and o to express the corresponding integrals in (2), respectively. When point $\mathbf{x}$ is located within $V_1: x_1^2 + x_2^2 \le a^2$, $-\infty < x_3 < \infty$, superscript i is used. But when $\mathbf{x}$ is located within $V_2: x_1^2 + x_2^2 > a^2$, $-\infty < x_3 < \infty$, we use superscript o.

3.1 When Point x is Located Inside V_1. Following Wu and Du (1995a) and Appendix B, the integrals of (2) can be expressed as

$$T^i(x_1, x_2, z) = I(x_1, x_2, z) \quad T^i_{\alpha\beta}(x_1, x_2, z) = I_{\alpha\beta}(x_1, x_2, z)$$

$$\bar{T}^i(x_1, x_2, \bar{z}) = I(x_1, x_2, \bar{z}) \quad \bar{T}^i_{mn}(x_1, x_2, \bar{z}) = I_{mn}(x_1, x_2, \bar{z})$$

$$\bar{T}^i_{m3}(x_1, x_2, z, \bar{z}) = \frac{z}{\bar{z}} I_{m3}(x_1, x_2, \bar{z})$$

$$\bar{T}^i_{33}(x_1, x_2, z, \bar{z}) = \frac{z^2}{\bar{z}^2} I_{33}(x_1, x_2, \bar{z})$$

$$\bar{T}^i_3(x_1, x_2, z, \bar{z}) = \frac{\bar{z}^2 - z^2}{4\bar{z}^2} I_{33}(x_1, x_2, \bar{z})$$

$$\bar{T}^i_{113}(x_1, x_2, z, \bar{z}) = -\frac{(\bar{z}^2 - z^2)x_2^2}{12(x_1^2 + x_2^2)} U_1(x_1, x_2, \bar{z}) + \frac{(\bar{z}^2 - z^2)(x_1^2 - x_2^2)}{48\bar{z}^2(x_1^2 + x_2^2)^2} U_2(x_1, x_2, \bar{z}) + \frac{(\bar{z}^2 - z^2)\pi}{6\bar{z}}$$

$$\bar{T}^i_{123}(x_1, x_2, z, \bar{z}) = \frac{(\bar{z}^2 - z^2)x_1 x_2}{12(x_1^2 + x_2^2)} U_1(x_1, x_2, \bar{z}) + \frac{(\bar{z}^2 - z^2)x_1 x_2}{24\bar{z}^2(x_1^2 + x_2^2)^2} U_2(x_1, x_2, \bar{z})$$

$$\bar{T}^i_{133}(x_1, x_2, z, \bar{z}) = \frac{(\bar{z}^2 - z^2)x_1}{24(x_1^2 + x_2^2)\bar{z}} [I^1(x_1, x_2, \bar{z}) - \bar{z}^2 I^2(x_1, x_2, \bar{z}) - (a^2 - x_1^2 - x_2^2 + \bar{z}^2) \times (a^2 - x_1^2 - x_2^2 - \bar{z}^2) I^3(x_1, x_2, \bar{z}, -\bar{z}^2)]$$

$$\bar{T}^i_{333}(x_1, x_2, z, \bar{z}) = \frac{\bar{z}^2 - z^2}{12} [(a^2 - x_1^2 - x_2^2 - \bar{z}^2) I^3(x_1, x_2, \bar{z}, -\bar{z}^2)$$

$$- (a^2 - x_2^2 - x_2^2)I^3(x_1, x_2, \bar{z}, 0)] + \frac{(\bar{z}^2 - z^2)\pi}{6\bar{z}}$$

$$\tilde{T}_1^i(x_1, x_2, \bar{z}) = \frac{\bar{z}x_1}{2(x_1^2 + x_2^2)}[I^1(x_1, x_2, \bar{z}) - 2(a^2 + x_1^2 + x_2^2) \times I^2(x_1, x_2, \bar{z}) + (a^2 - x_1^2 - x_2^2)^2 I^3(x_1, x_2, \bar{z}, 0)] + x_1\pi$$

$$\tilde{T}_{11}^i(x_1, x_2, \bar{z}) = \frac{\bar{z}^2 x_2^2}{x_1^2 + x_2^2} U_3(x_1, x_2, \bar{z}) + \frac{x_1^2}{x_1^2 + x_2^2} U_4(x_1, x_2, \bar{z}) + \frac{x_1^2 - x_2^2}{4(x_1^2 + x_2^2)^2} U_5(x_1, x_2, \bar{z}) - \bar{z}\pi$$

$$\tilde{T}_{12}^i(x_1, x_2, \bar{z}) = -\frac{\bar{z}^2 x_1 x_2}{x_1^2 + x_2^2} U_3(x_1, x_2, \bar{z}) + \frac{x_1 x_2}{x_1^2 + x_2^2} U_4(x_1, x_2, \bar{z}) + \frac{x_1 x_2}{2(x_1^2 + x_2^2)^2} U_5(x_1, x_2, \bar{z}) \quad (5)$$

with

$$U_1(x_1, x_2, \bar{z}) = 3I^2(x_1, x_2, \bar{z}) + 2(a^2 - x_1^2 - x_2^2)I^3(x_1, x_2, \bar{z}, 0) + (a^2 - x_1^2 - x_2^2 - \bar{z}^2)I^3(x_1, x_2, \bar{z}, -\bar{z}^2)$$

$$U_2(x_1, x_2, \bar{z}) = -3\bar{z}^2 I^1(x_1, x_2, \bar{z}) + \bar{z}^2[3(a^2 - x_1^2 - x_2^2) + \bar{z}^2]I^2(x_1, x_2, \bar{z}) - (a^2 - x_1^2 - x_2^2)^2(a^2 - x_1^2 - x_2^2 - 2\bar{z}^2)I^3(x_1, x_2, \bar{z}, 0) + (a^2 - x_1^2 - x_2^2 + \bar{z}^2)^2(a^2 - x_1^2 - x_2^2 - \bar{z}^2) \times I^3(x_1, x_2, \bar{z}, -\bar{z}^2) - 2\bar{z}^2(a^2 - x_1^2 - x_2^2)^3 I^4(x_1, x_2, \bar{z})$$

$$U_3(x_1, x_2, \bar{z}) = I^2(x_1, x_2, \bar{z}) - (a^2 - x_1^2 - x_2^2)I^3(x_1, x_2, \bar{z}, 0)$$

$$U_4(x_1, x_2, \bar{z}) = I^1(x_1, x_2, \bar{z}) + (a^2 - x_1^2 - x_2^2)I^2(x_1, x_2, \bar{z}) + 2\bar{z}^2(a^2 - x_1^2 - x_2^2)I^3(x_1, x_2, \bar{z}, 0)$$

$$U_5(x_1, x_2, \bar{z}) = -I^0(x_1, x_2, \bar{z}) + (a^2 - x_1^2 - x_2^2)I^1(x_1, x_2, \bar{z}) + (a^2 - x_1^2 - x_2^2)(a^2 - x_1^2 - x_2^2 - 2\bar{z}^2)I^2(x_1, x_2, \bar{z}) - (a^2 - x_1^2 - x_2^2)^2(a^2 - x_1^2 - x_2^2 - 4\bar{z}^2)I^3(x_1, x_2, \bar{z}, 0) - 2\bar{z}^2(a^2 - x_1^2 - x_2^2)^3 I^4(x_1, x_2, \bar{z}) \quad (6)$$

where $I^k(x_1, x_2, z)(k = 1, 2, 4)$, $I^3(x_1, x_2, z, s)$, $I(x_1, x_2, z)$ and $I_{\alpha\beta}(x_1, x_2, z)$ in (5) and (6) can be found in Wu and Du (1995a) and $I^0(x_1, x_2, z)$ is given in Appendix B.

It should be shown that the remaining components can be obtained by the following formulae:

$$\bar{T}_{223}^i(x_1, x_2, z, \bar{z}) = \bar{T}_{113}^i(x_2, x_1, z, \bar{z})$$
$$\bar{T}_{233}^i(x_1, x_2, z, \bar{z}) = \bar{T}_{133}^i(x_2, x_1, z, \bar{z})$$
$$\tilde{T}_2^i(x_1, x_2, \bar{z}) = \tilde{T}_1^i(x_2, x_1, \bar{z})$$
$$\tilde{T}_{22}^i(x_1, x_2, \bar{z}) = \tilde{T}_{11}^i(x_2, x_1, \bar{z}). \quad (7)$$

3.2 When Point x is Located Inside V_2. Following Wu and Du (1995b), the integrals in (2) can be written as

$$T^o(x_1, x_2, z) = \bar{I}(x_1, x_2, z) \quad T_{\alpha\beta}^o(x_1, x_2, z) = \bar{I}_{\alpha\beta}(x_1, x_2, z)$$
$$\bar{T}^o(x_1, x_2, \bar{z}) = \bar{I}(x_1, x_2, \bar{z}) \quad \bar{T}_{mn}^o(x_1, x_2, \bar{z}) = \bar{I}_{mn}(x_1, x_2, \bar{z})$$

$$\bar{T}_{m3}^o(x_1, x_2, z, \bar{z}) = \frac{z}{\bar{z}}\bar{I}_{m3}(x_1, x_2, \bar{z})$$

$$\bar{T}_{33}^o(x_1, x_2, z, \bar{z}) = \frac{z^2}{\bar{z}^2}\bar{I}_{33}(x_1, x_2, \bar{z})$$

$$\bar{T}_3^o(x_1, x_2, z, \bar{z}) = \frac{\bar{z}^2 - z^2}{4\bar{z}^2}\bar{I}_{33}(x_1, x_2, \bar{z})$$

$$\bar{T}_{113}^o(x_1, x_2, z, \bar{z}) = \bar{T}_{113}^i(x_1, x_2, z, \bar{z}) - \frac{(\bar{z}^2 - z^2)\pi}{6\bar{z}}$$

$$\bar{T}_{123}^o(x_1, x_2, z, \bar{z}) = \bar{T}_{123}^i(x_1, x_2, z, \bar{z})$$

$$\bar{T}_{133}^o(x_1, x_2, z, \bar{z}) = \bar{T}_{133}^i(x_1, x_2, z, \bar{z})$$

$$\bar{T}_{333}^o(x_1, x_2, z, \bar{z}) = \bar{T}_{333}^i(x_1, x_2, z, \bar{z}) - \frac{(\bar{z}^2 - z^2)\pi}{6\bar{z}}$$

$$\tilde{T}_1^o(x_1, x_2, \bar{z}) = \tilde{T}_1^i(x_1, x_2, \bar{z}) + \frac{(a^2 - x_1^2 - x_2^2)x_1\pi}{x_1^2 + x_2^2}$$

$$\tilde{T}_{11}^o(x_1, x_2, \bar{z}) = \tilde{T}_{11}^i(x_1, x_2, \bar{z}) + \frac{a^2(x_1^2 - x_2^2)\bar{z}\pi}{(x_1^2 + x_2^2)^2} + \bar{z}\pi$$

$$\tilde{T}_{12}^o(x_1, x_2, \bar{z}) = \tilde{T}_{12}^i(x_1, x_2, \bar{z}) + \frac{2a^2 x_1 x_2 \bar{z}\pi}{(x_1^2 + x_2^2)^2} \quad (8)$$

where $\bar{I}(x_1, x_2, z)$ and $\bar{I}_{\alpha\beta}(x_1, x_2, z)$ have already been given in Wu and Du (1995b). It should be pointed out that the remaining components can still be obtained by the relations given in (7) but the corresponding superscript i should be replaced by letter o. Thus, we fully determine the integrals of (2). In the next section, we shall solve the integrals of (3). For these integrals, we do not need to consider the position of point **x**.

4 Solution of Eq. (3)

For brevity, let us first introduce functions $\hat{J}^c(x_1, x_2, z)$ and $\hat{J}_{\alpha\beta}^c(x_1, x_2, z)$ which satisfy the following relations:

$$J^c(x_1, x_2, x_3) = \hat{J}^c(x_1, x_2, z)|_{x_3=-h}^{h}$$
$$J_{\alpha\beta}^c(x_1, x_2, x_3) = \hat{J}_{\alpha\beta}^c(x_1, x_2, z)|_{x_3=-h}^{h} \quad (9)$$

where functions $J^c(x_1, x_2, x_3)$ and $J_{\alpha\beta}^c(x_1, x_2, x_3)$ are defined and given in Wu and Du (1995a). Using a similar procedure shown in Wu and Du (1995a), the integrals of (3) can be expressed in the following form:

$$Q^1(x_1, x_2, x_3) = \hat{J}^c(x_1, x_2, z)|_{x_3=h_1}^{h_2}$$
$$Q_{\alpha\beta}^1(x_1, x_2, x_3) = \hat{J}_{\alpha\beta}^c(x_1, x_2, z)|_{x_3=h_1}^{h_2}$$
$$\bar{Q}^1(x_1, x_2, x_3) = -\hat{J}^c(x_1, x_2, \bar{z})|_{x_3=h_1}^{h_2}$$
$$\bar{Q}_{mn}^1(x_1, x_2, x_3) = -\hat{J}_{mn}^c(x_1, x_2, \bar{z})|_{x_3=h_1}^{h_2}$$

$$\bar{Q}_{13}^1(x_1, x_2, x_3) = \frac{8ax_3\bar{z}}{x_1^2 + x_2^2}[-ax_2^2 J^4(x_1, x_2, \bar{z}) + x_1^2\sqrt{x_1^2 + x_2^2}\, J^5(x_1, x_2, \bar{z}) - a(x_1^2 - x_2^2)J^6(x_1, x_2, \bar{z})]|_{x_3=h_1}^{h_2} + \hat{J}_{13}^c(x_1, x_2, \bar{z})|_{x_3=h_1}^{h_2}$$

$$\bar{Q}_{23}^1(x_1, x_2, x_3) = \frac{8ax_1x_2x_3\bar{z}}{x_1^2 + x_2^2}[aJ^4(x_1, x_2, \bar{z}) + \sqrt{x_1^2 + x_2^2}\, J^5(x_1, x_2, \bar{z}) - 2aJ^6(x_1, x_2, \bar{z})]|_{x_3=h_1}^{h_2} + \hat{J}_{23}^c(x_1, x_2, \bar{z})|_{x_3=h_1}^{h_2}$$

$$\bar{Q}_3^1(x_1, x_2, x_3) = -\frac{4ax_1x_3}{\sqrt{x_1^2 + x_2^2}}[J^8(x_1, x_2, \bar{z}) + x_3\bar{z}J^5(x_1, x_2, \bar{z})]|_{x_3=h_1}^{h_2}$$

$$\bar{Q}^1_{33}(x_1, x_2, x_3) = -4\bar{Q}^1_3(x_1, x_2, x_3) - \hat{J}^c_{33}(x_1, x_2, \bar{z})\big|^{h_2}_{x_3'=h_1}$$

$$\bar{Q}^1_{113}(x_1, x_2, x_3)$$
$$= -\frac{4ax_1x_3}{3\bar{z}\sqrt{(x_1^2+x_2^2)^3}}[-2ax_2^2\sqrt{x_1^2+x_2^2}\,V_1(x_1, x_2, x_3, x_3', \bar{z})$$
$$+ (x_1^4 + x_1^2x_2^2 + 3a^2x_2^2)V_2(x_1, x_2, x_3, x_3', \bar{z})$$
$$- 2a(x_1^2 - x_2^2)\sqrt{x_1^2+x_2^2}\,V_3(x_1, x_2, x_3, x_3', \bar{z})$$
$$+ a^2(x_1^2 - 3x_2^2)V_4(x_1, x_2, x_3, x_3', \bar{z})]\big|^{h_2}_{x_3'=h_1}$$

$$\bar{Q}^1_{123}(x_1, x_2, x_3) = -\frac{4ax_2x_3}{3\bar{z}\sqrt{(x_1^2+x_2^2)^3}}$$
$$\times [a(x_1^2 - x_2^2)\sqrt{x_1^2+x_2^2}\,V_1(x_1, x_2, x_3, x_3', \bar{z})$$
$$+ (x_1^4 + x_1^2x_2^2 - 2a^2x_1^2 + a^2x_2^2)V_2(x_1, x_2, x_3, x_3', \bar{z})$$
$$- a(3x_1^2 - x_2^2)\sqrt{x_1^2+x_2^2}\,V_3(x_1, x_2, x_3, x_3', \bar{z})$$
$$+ a^2(3x_1^2 - x_2^2)V_4(x_1, x_2, x_3, x_3', \bar{z})]\big|^{h_2}_{x_3'=h_1}$$

$$\bar{Q}^1_{223}(x_1, x_2, x_3) = -\frac{4ax_1x_3}{3\bar{z}\sqrt{(x_1^2+x_2^2)^3}}$$
$$\times [2ax_2^2\sqrt{x_1^2+x_2^2}\,V_1(x_1, x_2, x_3, x_3', \bar{z})$$
$$+ (x_2^4 + x_1^2x_2^2 + a^2x_1^2 - 2a^2x_2^2)V_2(x_1, x_2, x_3, x_3', \bar{z})$$
$$- 4ax_2^2\sqrt{x_1^2+x_2^2}\,V_3(x_1, x_2, x_3, x_3', \bar{z})$$
$$- a^2(x_1^2 - 3x_2^2)V_4(x_1, x_2, x_3, x_3', \bar{z})]\big|^{h_2}_{x_3'=h_1}$$

$$\bar{Q}^1_{133}(x_1, x_2, x_3) = \frac{4ax_3}{3(x_1^2+x_2^2)}[ax_2^2W_1(x_1, x_2, x_3', \bar{z})$$
$$- x_1^2\sqrt{x_1^2+x_2^2}\,W_2(x_1, x_2, x_3', \bar{z})$$
$$+ a(x_1^2 - x_2^2)W_3(x_1, x_2, x_3', \bar{z})]\big|^{h_2}_{x_3'=h_1}$$

$$\bar{Q}^1_{233}(x_1, x_2, x_3) = \frac{4ax_1x_2x_3}{3(x_1^2+x_2^2)}[-aW_1(x_1, x_2, x_3', \bar{z})$$
$$- \sqrt{x_1^2+x_2^2}\,W_2(x_1, x_2, x_3', \bar{z}) + 2aW_3(x_1, x_2, x_3', \bar{z})]\big|^{h_2}_{x_3'=h_1}$$

$$\bar{Q}^1_{333}(x_1, x_2, x_3) = -\frac{4ax_1x_3}{3\sqrt{x_1^2+x_2^2}}[\bar{z}x_3'J^{11}(x_1, x_2, \bar{z})$$
$$+ \bar{z}x_3J^5(x_1, x_2, \bar{z}) + 2J^8(x_1, x_2, \bar{z})]\big|^{h_2}_{x_3'=h_1}$$

$$\tilde{Q}^1_1(x_1, x_2, x_3)$$
$$= \frac{\pi(h_2 - h_1)}{2(x_1^2+x_2^2)^2}\{a^2(x_2^2 - x_1^2)[\mathrm{sgn}\,(a^2 - x_1^2 - x_2^2) - 1]$$
$$- (x_1^2 + x_2^2)^2[\mathrm{sgn}\,(a^2 - x_1^2 - x_2^2) + 1]\}$$
$$+ \frac{1}{(x_1^2+x_2^2)^2}\{(x_1^2 - x_2^2)J^0(x_1, x_2, \bar{z})$$
$$+ [(x_2^2 - x_1^2)(2a^2 + \bar{z}^2) + 2x_2^2(x_1^2 + x_2^2)]J^1(x_1, x_2, \bar{z})$$
$$+ (a^2 - x_1^2 - x_2^2)[a^2(x_1^2 - x_2^2)$$
$$+ (x_1^2 + x_2^2)^2][J^2(x_1, x_2, \bar{z}) + \bar{z}^2J^4(x_1, x_2, \bar{z})]\}\big|^{h_2}_{x_3'=h_1}$$

$$\tilde{Q}^1_2(x_1, x_2, x_3) = \frac{\pi a^2x_1x_2(h_2 - h_1)}{(x_1^2+x_2^2)^2}[1 - \mathrm{sgn}\,(a^2 - x_1^2 - x_2^2)]$$
$$+ \frac{2x_1x_2}{(x_1^2+x_2^2)^2}\{-J^0(x_1, x_2, \bar{z}) - (2a^2 + x_1^2 + x_2^2 + \bar{z}^2)$$
$$\times J^1(x_1, x_2, \bar{z}) + a^2(a^2 - x_1^2 - x_2^2)$$
$$\times [J^2(x_1, x_2, \bar{z}) + \bar{z}^2J^4(x_1, x_2, \bar{z})]\}\big|^{h_2}_{x_3'=h_1}$$

$$\tilde{Q}^1_{11}(x_1, x_2, x_3) = \frac{x_1\bar{z}^2\pi}{2(x_1^2+x_2^2)^3}[(a^2 - x_1^2 - x_2^2)(x_1^2 + x_2^2)$$
$$- 4a^2x_2^2][\mathrm{sgn}\,(a^2 - x_1^2 - x_2^2) - 1]\big|^{h_2}_{x_3'=h_1}$$
$$+ \frac{x_1}{2(x_1^2+x_2^2)}Y(x_1, x_2, \bar{z})\big|^{h_2}_{x_3'=h_1}$$
$$- \frac{4ax_1\bar{z}}{\sqrt{(x_1^2+x_2^2)^3}}[2ax_2^2\sqrt{x_1^2+x_2^2}Z_1(x_1, x_2, \bar{z})$$
$$- (x_1^4 + x_1^2x_2^2 + 3a^2x_2^2)Z_2(x_1, x_2, \bar{z})$$
$$+ 2a(x_1^2 - x_2^2)\sqrt{x_1^2+x_2^2}Z_3(x_1, x_2, \bar{z})$$
$$+ a^2(x_1^2 - 3x_2^2)Z_4(x_1, x_2, \bar{z})]\big|^{h_2}_{x_3'=h_1}$$

$$\tilde{Q}^1_{12}(x_1, x_2, x_3)$$
$$= \frac{a^2(x_2^2 - 3x_1^2)x_2\bar{z}^2\pi}{2(x_1^2+x_2^2)^3}[\mathrm{sgn}\,(a^2 - x_1^2 - x_2^2) - 1]\big|^{h_2}_{x_3'=h_1}$$
$$+ \frac{4ax_2\bar{z}}{\sqrt{(x_1^2+x_2^2)^3}}[a(x_1^2 - x_2^2)\sqrt{x_1^2+x_2^2}\,Z_1(x_1, x_2, \bar{z})$$
$$+ (x_1^4 + x_1^2x_2^2 + a^2x_2^2 - 2a^2x_1^2)Z_2(x_1, x_2, \bar{z})$$
$$- a(3x_1^2 - x_2^2)\sqrt{x_1^2+x_2^2}\,Z_3(x_1, x_2, \bar{z})$$
$$+ a^2(3x_1^2 - x_2^2)Z_4(x_1, x_2, \bar{z})]\big|^{h_2}_{x_3'=h_1}$$

$$\tilde{Q}^1_{22}(x_1, x_2, x_3) = \frac{x_1\bar{z}^2\pi}{2(x_1^2+x_2^2)^3}[(a^2 + x_1^2 + x_2^2)(x_1^2 + x_2^2)$$
$$- 4a^2x_2^2][\mathrm{sgn}\,(a^2 - x_1^2 - x_2^2) - 1]\big|^{h_2}_{x_3'=h_1}$$
$$+ \frac{x_1}{2(x_1^2+x_2^2)}Y(x_1, x_2, \bar{z})\big|^{h_2}_{x_3'=h_1}$$
$$- \frac{4ax_1\bar{z}}{\sqrt{(x_1^2+x_2^2)^3}}[2ax_2^2\sqrt{x_1^2+x_2^2}\,Z_1(x_1, x_2, \bar{z})$$
$$+ (x_1^2x_2^2 + x_2^4 + a^2x_1^2 - 2a^2x_2^2)Z_2(x_1, x_2, \bar{z})$$
$$- 4ax_2^2\sqrt{x_1^2+x_2^2}\,Z_3(x_1, x_2, \bar{z})$$
$$- a^2(x_1^2 - 3x_2^2)Z_4(x_1, x_2, \bar{z})]\big|^{h_2}_{x_3'=h_1} \quad (10)$$

with

$$V_i(x_1, x_2, x_3, x_3', \bar{z}) = x_3'J^{i+9}(x_1, x_2, \bar{z})$$
$$+ x_3J^{i+3}(x_1, x_2, \bar{z}) + 2x_3\bar{z}^2J^{i+13}(x_1, x_2, \bar{z}) \quad (11)$$

$$W_i(x_1, x_2, x_3', \bar{z}) = x_3'J^{i+9}(x_1, x_2, \bar{z}) - \bar{z}J^{i+3}(x_1, x_2, \bar{z}) \quad (12)$$

$$Y(x_1, x_2, \bar{z}) = -3\bar{z}J^1(x_1, x_2, \bar{z})$$
$$+ [4(a^2 + x_1^2 + x_2^2) + \bar{z}^2]\bar{z}J^2(x_1, x_2, \bar{z})$$
$$+ (a^2 - x_1^2 - x_2^2)(a^2 - x_1^2 - x_2^2 - 2\bar{z}^2)J^3(x_1, x_2, \bar{z}, -\bar{z}^2)$$
$$+ 4(x_1^2 + x_2^2)\bar{z}^3J^4(x_1, x_2, \bar{z}) + \bar{z}^2\pi \quad (13)$$

$$Z_i(x_1, x_2, \bar{z}) = J^{i+3}(x_1, x_2, \bar{z}) + \bar{z}^2J^{i+13}(x_1, x_2, \bar{z})$$
$$(i = 1, 2, 3, 4) \quad (14)$$

where sgn (x) is signum x, $J^i(x_1, x_2, z)$ $(i = 1, 2, 4, \ldots, 9)$ and $J^3(x_1, x_2, z, s)$ have already been given in Appendix B of Wu and Du (1995a) and $J^k(x_1, x_2, z)$ $(k = 10, 11, \ldots, 17)$ are expressed in Appendix C of this paper.

Evidently, if variable cos θ in (3) is replaced by sin θ and the corresponding integrals are expressed by $Q^2(x_1, x_2, x_3)$, $Q^2_{\alpha\beta}(x_1, x_2, x_3)$, $\bar{Q}^2(x_1, x_2, x_3)$, $\bar{Q}^2_{\alpha\beta}(x_1, x_2, x_3)$, $\bar{Q}^2_3(x_1, x_2, x_3)$, $\bar{Q}^2_{\alpha\beta3}(x_1, x_2, x_3)$, $\tilde{Q}^2_m(x_1, x_2, x_3)$ and $\tilde{Q}^2_{mn}(x_1, x_2, x_3)$, all the other components related with the displacement field are given

by exchanging 1 and 2 in the superscripts and subscripts, for example,

$$\bar{Q}^2(x_1, x_2, x_3) = \bar{Q}^1(x_2, x_1, x_3)$$
$$\bar{Q}^2_{11}(x_1, x_2, x_3) = \bar{Q}^1_{22}(x_2, x_1, x_3)$$
$$\bar{Q}^2_{123}(x_1, x_2, x_3) = \bar{Q}^1_{123}(x_2, x_1, x_3)$$
$$\hat{Q}^2_1(x_1, x_2, x_3) = \hat{Q}^1_2(x_2, x_1, x_3)$$
$$\hat{Q}^2_{22}(x_1, x_2, x_3) = \hat{Q}^1_{11}(x_2, x_1, x_3). \quad (15)$$

5 The Displacement and Stress Fields

According to Green's functions in a semi-infinite isotropic medium and (1)–(3), the induced displacement field within the region V_1: $x_1^2 + x_2^2 \le a^2$, $-\infty < x_3 < \infty$ due to uniform eigenstrain $\epsilon^*_{\alpha\beta}$ can be written as

$$u^i_m(\mathbf{x}) = \frac{1}{16\pi\mu(1-\nu)}\{2\mu\epsilon^*_{n3}[(3-4\nu)(T^i(x_1, x_2, z)\delta_{mn} + \bar{T}^i_{mn}(x_1, x_2, \bar{z})) + \bar{T}^i(x_1, x_2, \bar{z})\delta_{mn} + T^i_{mn}(x_1, x_2, z) + 2\bar{T}^i_3(x_1, x_2, z, \bar{z})\delta_{mn} - 6\bar{T}^i_{mn3}(x_1, x_2, z, \bar{z}) + 4(1-\nu)(1-2\nu)\tilde{T}^i_{mn}(x_1, x_2, \bar{z})]|^{h_2}_{x_3=h_1} + (\lambda\epsilon^*_{\alpha\alpha} + 2\mu\epsilon^*_{33})[T^i_{m3}(x_1, x_2, z) + (3-4\nu)\bar{T}^i_{m3}(x_1, x_2, z, \bar{z}) + 6\bar{T}^i_{m33}(x_1, x_2, z, \bar{z}) - 4(1-\nu)(1-2\nu)\tilde{T}^i_m(x_1, x_2, \bar{z})]|^{h}_{x_3=-h} + \sum_{k=1}^{2}(\lambda\delta_{nk}\epsilon^*_{\alpha\alpha} + 2\mu\epsilon^*_{nk})[(3-4\nu)(Q^k(x_1, x_2, x_3)\delta_{mn} + \bar{Q}^k_{mn}(x_1, x_2, x_3)) + \bar{Q}^k(x_1, x_2, x_3)\delta_{mn} + Q^k_{mn}(x_1, x_2, x_3) + 2\bar{Q}^k_3(x_1, x_2, x_3)\delta_{mn} - 6\bar{Q}^k_{mn3}(x_1, x_2, x_3) + 4(1-\nu)(1-2\nu)\tilde{Q}^k_{mn}(x_1, x_2, x_3)] + \sum_{k=1}^{2} 2\mu\epsilon^*_{k3}[Q^k_{m3}(x_1, x_2, x_3) + (3-4\nu)\bar{Q}^k_{m3}(x_1, x_2, x_3) + 6\bar{Q}^k_{m33}(x_1, x_2, x_3) - 4(1-\nu)(1-2\nu)\tilde{Q}^k_m(x_1, x_2, x_3)]\}$$

$$u^i_3(\mathbf{x}) = \frac{1}{16\pi\mu(1-\nu)}\{2\mu\epsilon^*_{m3}[T^i_{m3}(x_1, x_2, z) + (3-4\nu)\bar{T}^i_{m3}(x_1, x_2, z, \bar{z}) - 6\bar{T}^i_{m33}(x_1, x_2, z, \bar{z}) + 4(1-\nu)(1-2\nu)\tilde{T}^i_m(x_1, x_2, \bar{z})]|^{h_2}_{x_3=h_1} + (\lambda\epsilon^*_{\alpha\alpha} + 2\mu\epsilon^*_{33})[(3-4\nu)(T^i(x_1, x_2, z) + \bar{T}^i_{33}(x_1, x_2, z, \bar{z})) + (5-12\nu+8\nu^2)\bar{T}^i(x_1, x_2, \bar{z}) + T^i_{33}(x_1, x_2, z) + 2(5-8\nu)\bar{T}^i_3(x_1, x_2, z, \bar{z}) + 6\bar{T}^i_{333}(x_1, x_2, z, \bar{z})]|^{h_2}_{x_3=h_1} + \sum_{k=1}^{2}(\lambda\delta_{mk}\epsilon^*_{\alpha\alpha} + 2\mu\epsilon^*_{mk})[Q^k_{m3}(x_1, x_2, x_3) + (3-4\nu)\bar{Q}^k_{m3}(x_1, x_2, x_3) - 6\bar{Q}^k_{m33}(x_1, x_2, x_3) + 4(1-\nu)(1-2\nu)\tilde{Q}^k_m(x_1, x_2, x_3)] + \sum_{k=1}^{2} 2\mu\epsilon^*_{k3}[(3-4\nu)(Q^k(x_1, x_2, x_3) + \bar{Q}^k_{33}(x_1, x_2, x_3)) + (5-12\nu+8\nu^2)\bar{Q}^k(x_1, x_2, x_3) + Q^k_{33}(x_1, x_2, x_3) + 2(5-8\nu)\bar{Q}^k_3(x_1, x_2, x_3) + 6\bar{Q}^k_{333}(x_1, x_2, x_3)]\} \quad (16)$$

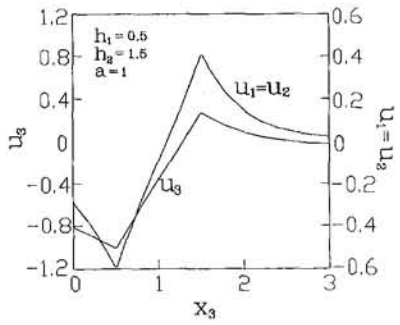

Fig. 2 Variations of the displacement field along the x_3-axis under the conditions $\epsilon^*_{11} = \epsilon^*_{22} = \epsilon^*_{33} = 1$, $\epsilon^*_{12} = \epsilon^*_{13} = \epsilon^*_{23} = 0$ for u_3 and $\epsilon^*_{11} = \epsilon^*_{22} = \epsilon^*_{33} = 0$, $\epsilon^*_{12} = \epsilon^*_{13} = \epsilon^*_{23} = 1$ for $u_1(u_2)$

where λ and μ are the Lame constants and ν is Poisson's ratio. Obviously, the corresponding displacement field within V_2: $x_1^2 + x_2^2 > a$, $-\infty < x_3 < \infty$, can easily be obtained by replacing the superscript i of (16) with letter o.

Following Wu and Du (1995a, b) and Appendixes B and C, it is found that the present displacement field can be expressed as functions of the complete elliptic integrals of the first, second, and third kind. In order to determine the stress field, we only need to solve the first partial derivatives of the three complete elliptic integrals with respect to variable x_i. These three first partial derivatives have been obtained in Wu and Du (1995a) and they are still functions of the complete elliptic integrals of the first, second, and third kind. Thus, according to Hooke's law

$$\sigma_{\alpha\beta}(\mathbf{x}) = \begin{cases} \lambda\delta_{\alpha\beta}[u_{\gamma,\gamma}(\mathbf{x}) - \epsilon^*_{\gamma\gamma}] \\ \quad + \mu[u_{\alpha,\beta}(\mathbf{x}) + u_{\beta,\alpha}(\mathbf{x}) - 2\epsilon^*_{\alpha\beta}] & \mathbf{x} \in \Omega \\ \lambda\delta_{\alpha\beta}u_{\gamma,\gamma}(\mathbf{x}) + \mu[u_{\alpha,\beta}(\mathbf{x}) + u_{\beta,\alpha}(\mathbf{x})] & \mathbf{x} \notin \Omega, \end{cases} \quad (17)$$

we can determine the corresponding stress field. Because of the complexity of stress field, here we will not give its concrete expressions.

6 Results and Discussions

It is seen from the results in Sections 3–5 that the displacement field and stress field caused by a circular cylindrical inclusion with arbitrarily uniform eigenstrain in a half-space can be expressed by functions of the complete elliptic integrals of the first, second, and third kind. Following Appendix D, we can find that the logarithmic singularity caused by eigenstrain $\epsilon^*_{\alpha\beta}$ exists at $x_1^2 + x_2^2 = a^2$, $x_3 = h_1$ or h_2. This conclusion is similar to one given by Hasegawa et al. (1993).

Figures 2–4 show the variations of the displacement field and stress field along the x_3-axis. The figures are sketched in nondimensional form for a constant value of Poisson's ratio $\nu = 0.3$. Figure 2 illustrates the distribution of the displacement field along the x_3-axis under the conditions $\epsilon^*_{11} = \epsilon^*_{22} = \epsilon^*_{33} = 1$, $\epsilon^*_{12} = \epsilon^*_{13} = \epsilon^*_{23} = 0$ for u_3 and $\epsilon^*_{11} = \epsilon^*_{22} = \epsilon^*_{33} = 0$, $\epsilon^*_{12} = \epsilon^*_{13} = \epsilon^*_{23} = 1$ for $u_1(u_2)$. From this figure, it can be seen that the displacement field has the minimums and maximums at $x_3 = h_1$ and h_2, respectively. When x_3 increases, $u_1(u_2)$ and u_3 tend towards zero.

Figure 3 shows the variations of the stress field ($\sigma_{11} = \sigma_{22}$ and σ_{33}) along the x_3-axis under the condition $\epsilon^*_{11} = \epsilon^*_{22} = \epsilon^*_{33} = 1$, $\epsilon^*_{12} = \epsilon^*_{13} = \epsilon^*_{23} = 0$ when radius a equals 0.1, 1 and 5, respectively. From this figure where three continuous changing curves correspond to the stress σ_{33} while other three ones whose variations are discontinuous correspond to $\sigma_{11}(\sigma_{22})$, we can see that the stress $\sigma_{11}(\sigma_{22})$ is positive outside the inclusion while it is negative within the inclusion. Evidently, when the cylindrical inclusion becomes slender (radius a decreases), the stress com-

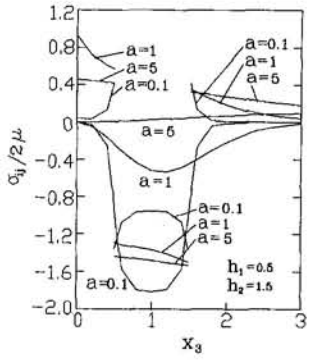

Fig. 3 Variations of the stress components along the x_3-axis under the condition $\epsilon_{11}^* = \epsilon_{22}^* = \epsilon_{33}^* = 1$, $\epsilon_{12}^* = \epsilon_{13}^* = \epsilon_{23}^* = 0$. Here, three continuous changing curves correspond to σ_{33} while other three ones which are discontinuous correspond to $\sigma_{11}(\sigma_{22})$.

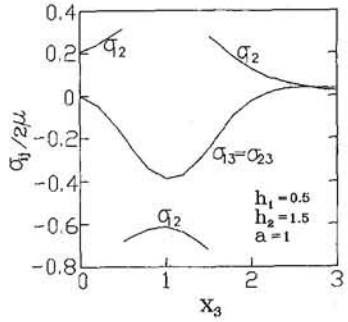

Fig. 4 Variations of the stress components σ_{12} and $\sigma_{13}(\sigma_{23})$ along the x_3-axis under the condition $\epsilon_{11}^* = \epsilon_{22}^* = \epsilon_{33}^* = 0$, $\epsilon_{12}^* = \epsilon_{13}^* = \epsilon_{23}^* = 1$

ponents $\sigma_{11}(\sigma_{22})$ and σ_{33} vary sharply. When $a = 5$, however, the change of the stress field ($\sigma_{11} = \sigma_{22}$ and σ_{33}) is stable. It should be shown that the stress component σ_{33} is continuous at $x_3 = h_1$ and h_2.

Figure 4 illustrates the variations of σ_{12} and $\sigma_{13}(\sigma_{23})$ along the x_3-axis under $\epsilon_{11}^* = \epsilon_{22}^* = \epsilon_{33}^* = 0$, $\epsilon_{12}^* = \epsilon_{13}^* = \epsilon_{23}^* = 1$. From this figure, it can be seen that σ_{12} has a discontinuous change, whereas $\sigma_{13}(\sigma_{23})$ is continuous.

Acknowledgment

This research was supported by National Education Foundation for Doctoral Degrees.

References

Byrd, P. F., and Friedman, M. D., 1971, *Handbook of Elliptic Integrals for Engineers and Scientists,* 2nd ed., Springer-Verlag, New York.

Chiu, Y. P., 1978, "On the Stress Field and Surface Deformation in a Half Space With a Cuboidal Zone in Which Initial Strains Are Uniform," ASME JOURNAL OF APPLIED MECHANICS, Vol. 45, pp. 302–306.

Chiu, Y. P., 1980, "On the Internal Stress in a Half Plane and a Layer Containing Localized Inelastic Strains or Inclusions," ASME JOURNAL OF APPLIED MECHANICS, Vol. 47, pp. 313–318.

Eshelby, J. D., 1957, "The Determination of the Elastic Field of an Ellipsoidal Inclusion and Related Problems," *Proceedings of the Royal Society, London,* Vol. A241, pp. 376–396.

Eshelby, J. D., 1959, "The Elastic Field Outside an Elastic Inclusion," *Proceedings of the Royal Society, London,* Vol. A252, pp. 561–569.

Hasegawa, H., Lee, V. G., and Mura, T., 1993, "Hollow Circular Cylindrical Inclusion at the Surface of a Half-Space," ASME JOURNAL OF APPLIED MECHANICS, Vol. 60, pp. 33–40.

Magnus, W., Oberhettinger, F., and Soni, R. P., 1966, *Formulas and Theorems for the Special Functions of Mathematical Physics,* 3rd ed., Springer-Verlag, New York.

Mindlin, R. D., and Cheng, D. H., 1950, "Thermoelastic Stress in the Semi-Infinite Solid," *Journal of Applied Physics,* Vol. 21, pp. 931–933.

Mindlin, R. D., 1953, "Force at a Point in the Interior of a Semi-Infinite Solid," *Proceedings of First Midwestern Conference on Solid Mechanics,* pp. 55–59.

Mura, T., 1987, *Micromechanics of Defects in Solids,* Martinus Nijhoff, pp. 112–113.

Mura, T., 1988, "Inclusion Problem," ASME *Applied Mechanics Review,* Vol. 41, pp. 15–20.

Seo, K., and Mura, T., 1979, "The Elastic Field in a Half Space Due to Ellipsoidal Inclusions With Uniform Dilatational Eigenstrains," ASME JOURNAL OF APPLIED MECHANICS, Vol. 46, pp. 568–572.

Wu, L. Z., and Du, S. Y., 1995a, "The Elastic Field Caused by a Circular Cylindrical Inclusion—Part 1: Inside the Region $x_1^2 + x_2^2 \le a^2$, $-\infty < x_3 < \infty$ Where the Circular Cylindrical Inclusion Is Expressed by $x_1^2 + x_2^2 \le a^2$, $-h \le x_3 \le h$," ASME JOURNAL OF APPLIED MECHANICS, Vol. 62, pp. 579–584.

Wu, L. Z., and Du, S. Y., 1995b, "The Elastic Field Caused by a Circular Cylindrical Inclusion—Part 2: Inside the Region $x_1^2 + x_2^2 > a^2$, $-\infty < x_3 < \infty$ Where the Circular Cylindrical Inclusion Is Expressed by $x_1^2 + x_2^2 \le a^2$, $-h \le x_3 \le h$," ASME JOURNAL OF APPLIED MECHANICS, Vol. 62, pp. 585–589.

Youngdahl, C. K., and Sternberg, E., 1966, "Three-Dimensional Stress Concentration Around a Cylindrical Hole in a Semi-Infinite Elastic Body," ASME JOURNAL OF APPLIED MECHANICS, Series E, Vol. 33, pp. 855–865.

Yu, H. Y., and Sanday, S. C., 1990, "Axisymmetric Inclusion in a Half Space," ASME JOURNAL OF APPLIED MECHANICS, Vol. 57, pp. 74–77.

APPENDIX A

Following Mura (1987), Green's functions in the semi-infinite isotropic medium can be expressed as

$$G_{ij}(\mathbf{x} - \mathbf{x}') = \frac{1}{16\pi\mu(1-\nu)}\left\{\frac{3-4\nu}{R_1}\delta_{ij} + \frac{1}{R_2}\delta_{ij} + \frac{(x_i - x_i')(x_j - x_j')}{R_1^3} + \frac{(3-4\nu)(x_i - x_i')(x_j - x_j')}{R_2^3} + \frac{2x_3x_3'}{R_2^3}\left[\delta_{ij} - \frac{3(x_i - x_i')(x_j - x_j')}{R_2^2}\right] + \frac{4(1-\nu)(1-2\nu)}{R_2 + x_3 + x_3'}\left[\delta_{ij} - \frac{(x_i - x_i')(x_j - x_j')}{R_2(R_2 + x_3 + x_3')}\right]\right\}$$

$$G_{3j}(\mathbf{x} - \mathbf{x}') = \frac{(x_j - x_j')}{16\pi\mu(1-\nu)}\left\{\frac{x_3 - x_3'}{R_1^3} + \frac{(3-4\nu)(x_3 - x_3')}{R_2^3} - \frac{6x_3x_3'(x_3 + x_3')}{R_2^5} + \frac{4(1-\nu)(1-2\nu)}{R_2(R_2 + x_3 + x_3')}\right\}$$

$$G_{i3}(\mathbf{x} - \mathbf{x}') = \frac{x_i - x_i'}{16\pi\mu(1-\nu)}\left\{\frac{x_3 - x_3'}{R_1^3} + \frac{(3-4\nu)(x_3 - x_3')}{R_2^3} + \frac{6x_3x_3'(x_3 + x_3')}{R_2^5} - \frac{4(1-\nu)(1-2\nu)}{R_2(R_2 + x_3 + x_3')}\right\}$$

$$G_{33}(\mathbf{x} - \mathbf{x}') = \frac{1}{16\pi\mu(1-\nu)}\left\{\frac{3-4\nu}{R_1} + \frac{8(1-\nu)^2 - (3-4\nu)}{R_2} + \frac{(x_3 - x_3')^2}{R_1^3} + \frac{(3-4\nu)(x_3 + x_3')^2 - 2x_3x_3'}{R_2^3} + \frac{6x_3x_3'(x_3 + x_3')^2}{R_2^5}\right\}, \quad (i, j = 1, 2) \quad \text{(A1)}$$

where μ is the shear modulus, ν is Poisson's ratio, and

$$R_1^2 = (x_1 - x_1')^2 + (x_2 - x_2')^2 + (x_3 - x_3')^2 \quad \text{(A2)}$$

$$R_2^2 = (x_1 - x_1')^2 + (x_2 - x_2')^2 + (x_3 + x_3')^2. \quad \text{(A3)}$$

APPENDIX B

According to Wu and Du (1995a) and the formula

$$\int \frac{x^n f(x)dx}{\sqrt{ax^2 + bx + c}} = \frac{x^{n-1}\sqrt{ax^2 + bx + c}}{na} f(x) - \frac{(2n-1)b}{2na} \times \int \frac{x^{n-1} f(x)dx}{\sqrt{ax^2 + bx + c}} - \frac{(n-1)c}{na} \int \frac{x^{n-2} f(x)dx}{\sqrt{ax^2 + bx + c}} - \frac{1}{na} \int x^{n-1}\sqrt{ax^2 + bx + c}\, \frac{df(x)}{dx}\, dx \quad \text{(B1)}$$

we can obtain

$$I^0(x_1, x_2, z) = \int_{t_1}^{t_2} \frac{t^2 dt}{\sqrt{(t + z^2)(t - t_1)(t_2 - t)}}$$

$$= \frac{1}{3}\{(2t_1 + 2t_2 - z^2) I^1(x_1, x_2, z) + [z^4 + (t_1 + t_2)z^2 - t_1 t_2]\, I^2(x_1, x_2, z) - z^2(t_1 + z^2)(t_2 + z^2) I^3(x_1, x_2, z, -z^2)\} \quad \text{(B2)}$$

where $I^1(x_1, x_2, z)$, $I^2(x_1, x_2, z)$ and $I^3(x_1, x_2, z, s)$ are given in Appendix A of Wu and Du (1995a) and

$$t_1 = (a - \sqrt{x_1^2 + x_2^2})^2, \quad t_2 = (a + \sqrt{x_1^2 + x_2^2})^2 \quad \text{(B3)}$$

APPENDIX C

1 Evaluation of the Integrals $J^i(x_1, x_2, z)(i = 10, \ldots, 13)$

Letting $\xi = \sqrt{(t^2 - t_1^2)/(t_2^2 - t_1^2)}\, t_2/t$, we have

$$J^{10}(x_1, x_2, z) = \int_{t_1}^{t_2} \frac{dt}{t^2\sqrt{(t_2^2 - t^2)(t^2 - t_1^2)}} = \frac{1}{t_2 t_1^2} E\left(\frac{\sqrt{t_2^2 - t_1^2}}{t_2}\right) \quad \text{(C1)}$$

$$J^{11}(x_1, x_2, z) = \frac{1}{2a\sqrt{x_1^2 + x_2^2}} \int_{t_1}^{t_2} \frac{a^2 + x_1^2 + x_2^2 + z^2 - t^2}{t^2\sqrt{(t_2^2 - t^2)(t^2 - t_1^2)}}\, dt = \frac{a^2 + x_1^2 + x_2^2 + z^2}{2a\sqrt{x_1^2 + x_2^2}} J^{10}(x_1, x_2, z) - \frac{J^2(x_1, x_2, z)}{2a\sqrt{x_1^2 + x_2^2}} \quad \text{(C2)}$$

$$J^{12}(x_1, x_2, z) = \frac{1}{4a^2(x_1^2 + x_2^2)} \int_{t_1}^{t_2} \frac{(a^2 + x_1^2 + x_2^2 + z^2 - t^2)^2}{t^2\sqrt{(t_2^2 - t^2)(t^2 - t_1^2)}}\, dt = \frac{1}{4a^2(x_1^2 + x_2^2)} [(a^2 + x_1^2 + x_2^2 + z^2)^2 J^{10}(x_1, x_2, z) - 2(a^2 + x_1^2 + x_2^2 + z^2) J^2(x_1, x_2, z) + J^1(x_1, x_2, z)] \quad \text{(C3)}$$

$$J^{13}(x_1, x_2, z) = \frac{1}{8a^3\sqrt{(x_1^2 + x_2^2)^3}} \int_{t_1}^{t_2} \frac{(a^2 + x_1^2 + x_2^2 + z^2 - t^2)^3}{t^2\sqrt{(t_2^2 - t^2)(t^2 - t_1^2)}}\, dt = \frac{1}{8a^3\sqrt{(x_1^2 + x_2^2)^3}} [(a^2 + x_1^2 + x_2^2 + z^2)^3 J^{10}(x_1, x_2, z) - 3(a^2 + x_1^2 + x_2^2 + z^2)^2 J^2(x_1, x_2, z) + 3(a^2 + x_1^2 + x_2^2 + z^2) J^1(x_1, x_2, z) - J^0(x_1, x_2, z)]. \quad \text{(C4)}$$

2 Evaluation of the integrals $J^i(x_1, x_2, z)(i = 14, \ldots, 17)$

Following the formula

$$\int \frac{f(t)d[(t_2^2 - t^2)(t^2 - t_1^2)]}{\sqrt{(t_2^2 - t^2)(t^2 - t_1^2)}} = 2f(t)\sqrt{(t_2^2 - t^2)(t^2 - t_1^2)} - 2\int \sqrt{(t_2^2 - t^2)(t^2 - t_1^2)}\, \frac{df(t)}{dt}\, dt, \quad \text{(C5)}$$

we can obtain

$$J^{14}(x_1, x_2, z) = \int_{t_1}^{t_2} \frac{dt}{(t^2 - z^2)^2\sqrt{(t_2^2 - t^2)(t^2 - t_1^2)}} = \frac{1}{2z^2(t_1^2 - z^2)(t_2^2 - z^2)}\{-z^2 J^2(x_1, x_2, z) - [t_1^2 t_2^2 - 2(t_1^2 + t_2^2)z^2 + 3z^4] J^4(x_1, x_2, z) + t_1^2 t_2^2 J^{10}(x_1, x_2, z)\} \quad \text{(C6)}$$

$$J^{15}(x_1, x_2, z) = \frac{1}{2a\sqrt{x_1^2 + x_2^2}} \times \int_{t_1}^{t_2} \frac{a^2 + x_1^2 + x_2^2 + z^2 - t^2}{(t^2 - z^2)^2\sqrt{(t_2^2 - t^2)(t^2 - t_1^2)}}\, dt = \frac{a^2 + x_1^2 + x_2^2}{2a\sqrt{x_1^2 + x_2^2}} J^{14}(x_1, x_2, z) - \frac{J^4(x_1, x_2, z)}{2a\sqrt{x_1^2 + x_2^2}} \quad \text{(C7)}$$

$$J^{16}(x_1, x_2, z) = \frac{1}{4a^2(x_1^2 + x_2^2)} \times \int_{t_1}^{t_2} \frac{(a^2 + x_1^2 + x_2^2 + z^2 - t^2)^2}{(t^2 - z^2)^2\sqrt{(t_2^2 - t^2)(t^2 - t_1^2)}}\, dt = \frac{1}{4a^2(x_1^2 + x_2^2)} [(a^2 + x_1^2 + x_2^2)^2 J^{14}(x_1, x_2, z) - 2(a^2 + x_1^2 + x_2^2) J^4(x_1, x_2, z) + J^2(x_1, x_2, z)] \quad \text{(C8)}$$

$$J^{17}(x_1, x_2, z) = \frac{1}{8a^3\sqrt{(x_1^2 + x_2^2)^3}} \times \int_{t_1}^{t_2} \frac{(a^2 + x_1^2 + x_2^2 + z^2 - t^2)^3}{(t^2 - z^2)^2\sqrt{(t_2^2 - t^2)(t^2 - t_1^2)}}\, dt = \frac{1}{8a^3\sqrt{(x_1^2 + x_2^2)^3}} \{(a^2 + x_1^2 + x_2^2)^3 J^{14}(x_1, x_2, z) - 3(a^2 + x_1^2 + x_2^2)^2 J^4(x_1, x_2, z) + [3(a^2 + x_1^2 + x_2^2) + z^2] J^2(x_1, x_2, z) - J^1(x_1, x_2, z)\} \quad \text{(C9)}$$

where $J^i(x_1, x_2, z)(i = 0, 1, 2, 4)$ are obtained in Appendix B of Wu and Du (1995a) and

$$t_1 = \sqrt{(a - \sqrt{x_1^2 + x_2^2})^2 + z^2},$$
$$t_2 = \sqrt{(a + \sqrt{x_1^2 + x_2^2})^2 + z^2}. \quad \text{(C10)}$$

APPENDIX D

Following Magnus et al. (1966), the complete elliptic integral of the third kind can be expressed by the elliptic integrals of the first and second kind. From the definitions

$$F(k, \varphi) = \int_0^{\varphi} (1 - k^2 \sin^2 t)^{-1/2} dt$$
$$E(k, \varphi) = \int_0^{\varphi} (1 - k^2 \sin^2 t)^{1/2} dt \quad |k| \leq 1 \quad \text{(D1)}$$

where $F(k, \varphi)$ and $E(k, \varphi)$ are the elliptic integrals of the first and second kind, respectively, it can be seen that only the complete elliptic integral of the first kind has singularity when $k = \pm 1$. Below, we investigate this singularity. According to Magnus et al. (1966), $F(k)$ $(F(k, \pi/2))$ can be expressed as

$$F(k) = Q_{-1/2}(2k^2 - 1) \quad \text{(D2)}$$

where $Q_n(x)$ is a Legendre function of the second kind of order n. For function $Q_n(x)$, Byrd and Friedman (1971) gave the following relation:

$$\lim_{x \to 1} Q_n(x) \to \text{const.} \log (1 - x). \quad (x < 1) \quad \text{(D3)}$$

From Wu and Du (1995a) and the expressions of variable k in $F(k)$, we find that when $\sqrt{x_1^2 + x_2^2} \to a$ and $x_3 \to h_1$ or h_2, $F(k)$ can be expressed as the following form:

$$F(k) = \text{const.} \log [(a - \sqrt{x_1^2 + x_2^2})^2 + (x_3 - x_3')^2]. \quad \text{(D4)}$$

Since x_3' in (D4) is evaluated at $x_3' = h_1$ and h_2, $F(k)$ has the logarithmic singularity when $\sqrt{x_1^2 + x_2^2} \to a$ and $x_3 \to h_1$ or h_2. Performing the detailed examination and manipulation, we can find that each component of eigenstrains $\epsilon_{\alpha\beta}^*$ has some effect on the singularity of the elastic field.

A. Piva
Assistant Professor,
Department of Physics,
University of Bologna,
Via Irnerio, 46,
40126 Bologna, Italy

W. Hasan[1]
Ph.D. Student,
Istituto di Scienza delle Costruzioni,
Università di Bologna,
Viale del Risorgimento, 2,
40136 Bologna, Italy

Effect of Orthotropy on the Intersonic Shear Crack Propagation

Of concern in the present paper is the steady-state elastodynamic problem of a semi-infinite shear crack, propagating in an orthotropic medium. An intersonic regime is assumed which leads to a significant change of the singularity at the crack tip.

1 Introduction

The study of crack propagation in anisotropic media is of great interest in the fracture analysis of a wide class of composite materials and the field of research is particularly motivated by its engineering importance.

Many engineering composites exhibit strong directional elastic effects associated with elastic symmetry with respect to three mutually orthogonal planes, orthotropic materials, and this justifies the increasing interest in the analytical solutions for elastodynamic crack propagation in such materials.

Significant contribution has been made in subsonic regime by Achenbach and Bažant (1975), Kassir and Tse (1983), Arcisz and Sih (1984), Piva (1987), Piva and Viola (1988), and Piva and Radi (1991) among others.

After the pioneering contribution of Winkler et al. (1970) and Curran et al. (1970) in which it was shown that under particular conditions a very rapid crack growth should be possible, some analytical studies concerning super-Rayleigh crack propagation in an isotropic medium were treated by Burridge (1973), Burridge et al. (1979), Freund (1979), Georgiadis and Theocaris (1985), Georgiadis (1986), and more recently by Broberg (1989) among others.

In the above mentioned studies some peculiar features of the intersonic shear crack propagation ($c_s < c < c_l$, where c is the crack velocity, c_s is the shear wave velocity, and c_l is the longitudinal-wave velocity) were put in evidence.

One of these features is the role played by the velocity of the crack as a control parameter which determines stable or unstable growth. In particular, it was found that the stress singularity at the propagating crack tip is influenced by a parameter which is a function of the crack velocity, and is weaker than the inverse square root singularity, unless for $c = \sqrt{2}c_s$.

More recently, a number of significant contributions which extended the subject to interfacial crack propagation have appeared. Particularly noteworthy are the works by Lambros and Rosakis (1995) and Liu et al. (1995) where extensive investigations about the intersonic crack growth along an elastic/rigid bimaterial interface have been presented.

Throughout these works it was given evidence of intersonically stable shear crack propagation in the velocity range $\sqrt{2}c_s < c < c_l$, where c_s and c_l are the shear and longitudinal wave speeds of the elastic material, respectively. It was also shown that for $c_s < c < \sqrt{2}c_s$, crack propagation is still possible but unstable.

A significant feature put in evidence by the above mentioned authors and of particular interest in the present work is that the stress singularity at the propagating crack tip was always weaker than the inverse square root singularity (Liu et al., 1995).

The aim of this paper is to extend, from the analytical point of view, the topic concerning the intersonic regime to the problem of a shear crack propagating through an orthotropic elastic solid. Particular attention is paid to the stress singularity and to its variation as a function of the crack velocity as well as of the material orthotropy.

A semi-infinite shear crack, propagating at constant velocity greater than the shear-wave velocity and less than the longitudinal-wave velocity, is considered. The crack propagates under the action of constant shear stresses applied to a segment of its lips, following the moving crack tip.

The basic analysis is performed by using a complex variable approach, proposed in previous papers by Piva (1987), Piva and Viola (1988), and Piva and Radi (1991) to solve elastodynamic crack problems in orthotropic media. The solution of the problem reveals a significant change of the stress singularity at the crack tip with respect to that in the case of subsonic regime, as well as to that obtained for intersonic crack propagation in an isotropic medium.

The parameter which has a controlling effect on the strength of the singularity at the crack tip is represented as a function of the velocity for various orthotropic materials. It can be seen that the results obtained for a bimaterial interface compare reasonably well with those derived herein.

2 Mathematical Preliminaries

Let an orthtropic elastic medium be referred to a Cartesian coordinate system whose axes X, Y, and Z coincide with the three mutually orthogonal principal directions of the material.

An elastodynamic plane problem concerning a semi-infinite crack propagating at constant velocity c in the X direction, will be studied.

Because in the sequel the motion will be referred to as one in the X-Y plane, it is convenient to introduce the Galilean transformation.

$$x = X - ct, \quad y = Y, \tag{1}$$

where t is time and c is a constant velocity.

The stress-strain relations in the xy-plane are

[1] To whom all correspondence should be addressed.

Contributed by the Applied Mechanics Division of THE AMERICAN SOCIETY OF MECHANICAL ENGINEERS for publication in the ASME JOURNAL OF APPLIED MECHANICS.

Discussion on this paper should be addressed to the Technical Editor, Professor Lewis T. Wheeler, Department of Mechanical Engineering, University of Houston, Houston, TX 77204-4792, and will be accepted until four months after final publication of the paper itself in the ASME JOURNAL OF APPLIED MECHANICS.

Manuscript received by the ASME Applied Mechanics Division, Mar. 30, 1995; final revision, Apr. 9, 1996. Associate Technical Editor: I. M. Daniel.

$$\sigma_{xx} = C_{11}u_x + C_{12}v_y, \tag{2a}$$

$$\sigma_{yy} = C_{12}u_x + C_{22}v_y, \tag{2b}$$

$$\tau_{xy} = C_{66}(u_y + v_x), \tag{2c}$$

in which $u = u(x, y)$, $v = v(x, y)$ are the displacement components in the x and y directions, respectively; and subscripts, except for stress components, indicate partial derivatives with respect to the subscripted variables. The coefficients C_{11}, C_{12}, C_{22}, and C_{66} are four independent elastic moduli of the material.

The system of equations governing the elastodynamic displacement field reduces to

$$u_{xx} + 2\beta v_{xy} + \alpha u_{yy} = 0,$$

$$v_{xx} + 2\beta_1 u_{xy} + \alpha_1 v_{yy} = 0, \tag{3}$$

with

$$\alpha = \frac{C_{66}}{C_{11}(1 - M_1^2)}, \quad 2\beta = \frac{C_{12} + C_{66}}{C_{11}(1 - M_1^2)},$$

$$\alpha_1 = \frac{C_{22}}{C_{66}(1 - M_2^2)}, \quad 2\beta_1 = \frac{C_{12} + C_{66}}{C_{66}(1 - M_2^2)}. \tag{4}$$

The quantities $M_1 = c/c_1$ and $M_2 = c/c_2$ are the Mach numbers with $c_1 = (C_{11}/\rho)^{1/2}$, $c_2 = (C_{66}/\rho)^{1/2}$ and ρ is the mass density.

The system (3) may be rewritten as

$$\boldsymbol{\phi}_x + \mathbf{A}\boldsymbol{\phi}_y = \mathbf{0}, \tag{5}$$

where

$$\boldsymbol{\phi} = (\phi^1, \phi^2, \phi^3, \phi^4)^T \equiv (u_x, u_y, v_x, v_y)^T$$

and $\mathbf{A}$ is a 4×4 constant matrix, given by

$$\mathbf{A} = \begin{pmatrix} 0 & \alpha & 2\beta & 0 \\ -1 & 0 & 0 & 0 \\ 2\beta_1 & 0 & 0 & \alpha_1 \\ 0 & 0 & -1 & 0 \end{pmatrix}. \tag{6}$$

The characteristic equation of (6) is

$$\lambda^4 + 2a_1\lambda^2 + a_2 = 0, \tag{7}$$

where

$$2a_1 = \alpha + \alpha_1 - 4\beta\beta_1, \quad a_2 = \alpha\alpha_1.$$

In the intersonic regime the Mach numbers are

$$M_1 = c/c_1 < 1, \quad M_2 = c/c_2 > 1$$

and Eq. (7) provides the eigenvalues

$$\lambda_1 = p, \quad \lambda_2 = -p, \quad \lambda_3 = iq, \quad \lambda_4 = \bar{\lambda}_3,$$

with

$$p = [(a_1^2 - a_2)^{1/2} - a_1]^{1/2}, \quad q = [(a_1^2 - a_2)^{1/2} + a_1]^{1/2},$$

positive constants.

According to the approach proposed in previous papers (Piva, 1987), Eq. (5) may be transformed to

$$\boldsymbol{\psi}_x + \mathbf{B}\boldsymbol{\psi}_y = \mathbf{0}, \tag{8}$$

where

$$\boldsymbol{\psi} = \mathbf{P}^{-1}\boldsymbol{\phi}, \tag{9}$$

and

$$\mathbf{P} = \begin{pmatrix} -\frac{2\beta p^2}{\alpha + p^2} & -\frac{2\beta p^2}{\alpha + p^2} & 0 & \frac{2\beta q^2}{\alpha - q^2} \\ \frac{2\beta p}{\alpha + p^2} & -\frac{2\beta p}{\alpha + p^2} & \frac{2\beta q}{\alpha - q^2} & 0 \\ -p & p & -q & 0 \\ 1 & 1 & 0 & 1 \end{pmatrix}, \tag{10a}$$

$$\mathbf{B} = \mathbf{P}^{-1}\mathbf{A}\mathbf{P} = \begin{pmatrix} p & 0 & 0 & 0 \\ 0 & -p & 0 & 0 \\ 0 & 0 & 0 & -q \\ 0 & 0 & q & 0 \end{pmatrix}. \tag{10b}$$

Furthermore, the system (8) may be decomposed into the two systems

$$\psi_x^1 + p\psi_y^1 = 0, \tag{11}$$

$$\psi_x^2 - p\psi_y^2 = 0, \tag{12}$$

and

$$\psi_x^3 - q\psi_y^4 = 0 \tag{13}$$

$$\psi_x^4 + q\psi_y^3 = 0. \tag{14}$$

It should be noted that the latter system defines the analytic function

$$\Omega(z) = \psi^3(x, y) + i\psi^4(x, y), \quad z = x + i\gamma y, \quad \gamma = 1/q,$$

whose real and imaginary parts may be obtained using (9) and (10a) as follows:

$$\mathrm{Re}\Omega(z) = \psi^3(x, y) = \frac{k}{q}\left(\phi^2 + \frac{2\beta}{\alpha + p^2}\phi^3\right), \tag{15}$$

$$\mathrm{Im}\Omega(z) = \psi^4(x, y) = \frac{k}{\alpha}\left(\phi^1 + \frac{2\beta p^2}{\alpha + p^2}\phi^4\right), \tag{16}$$

where

$$k = \frac{(\alpha + p^2)(\alpha - q^2)}{2\beta(p^2 + q^2)}.$$

In addition, as the problem of concern is antisymmetric with respect to the x-axis, the following relations hold:

$$\phi^1(x, y) = -\phi^1(x, -y), \quad \phi^2(x, y) = \phi^2(x, -y),$$

$$\phi^3(x, y) = \phi^3(x, -y), \quad \phi^4(x, y) = -\phi^4(x, -y). \tag{17}$$

Hence, applying (17) to (15) and (16) leads to the symmetry condition

$$\Omega(z) = \overline{\Omega(\bar{z})}. \tag{18}$$

Consider now the pair of Eqs. (11) and (12) whose integration yields

$$\psi^1(x, y) = F(x - \delta y),$$

$$\psi^2(x, y) = G(x + \delta y), \quad \delta = 1/p \tag{19}$$

with F and G arbitrary functions of their arguments.

It should be noted that as the Cauchy data for Eqs. (11) and (12) are prescribed on the half-line $y = 0$, $x < 0$, the function $F(x - \delta y)$ represents a signal travelling to the right and wavefronts $x - \delta y = \text{const.}$ invade the half-plane $x > 0$, as y increases. In view of the fracture problem to be studied the above region must be assumed undisturbed and therefore it may be stated that $F(x - \delta y)$ vanishes.

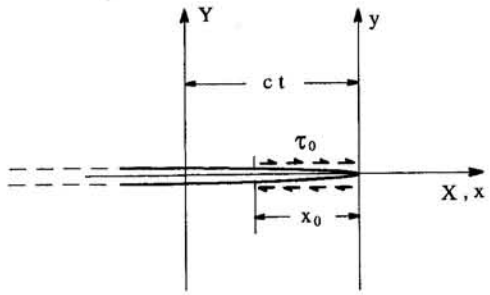

Fig. 1 Moving crack in orthotropic material

On the other hand, the function $G(x + \delta y)$ which represents a backward signal with wavefronts $x + \delta y = \text{const.}$, confined into the half-plane $x < 0$, contributes to the shear field. Therefore, keeping in mind Eqs. (5), (8), (9), and (10), the stress-strain relations (2) may be rewritten as follows:

$$\frac{\sigma_{xx}}{C_{66}} = l_1 \operatorname{Im}\Omega(z) + l_2 G(x + \delta y), \tag{20}$$

$$\frac{\sigma_{yy}}{C_{66}} = l_3 \operatorname{Im}\Omega(z) + l_4 G(x + \delta y), \tag{21}$$

$$\frac{\tau_{xy}}{C_{66}} = l_5 \operatorname{Re}\Omega(z) + l_6 G(x + \delta y), \tag{22}$$

where

$$l_1 = \frac{C_{12}}{C_{66}} + \frac{C_{11}}{C_{66}}\left(\frac{2\beta q^2}{\alpha - q^2}\right), \quad l_2 = \frac{C_{12}}{C_{66}} - \frac{C_{11}}{C_{66}}\left(\frac{2\beta p^2}{\alpha + p^2}\right),$$

$$l_3 = \frac{C_{22}}{C_{66}} + \frac{C_{12}}{C_{66}}\left(\frac{2\beta q^2}{\alpha - q^2}\right), \quad l_4 = \frac{C_{22}}{C_{66}} - \frac{C_{12}}{C_{66}}\left(\frac{2\beta p^2}{\alpha + p^2}\right),$$

$$l_5 = q\left(\frac{2\beta}{\alpha - q^2} - 1\right), \quad l_6 = p\left(1 - \frac{2\beta}{\alpha + q^2}\right).$$

3 Statement and Analysis of the Problem

Consider the antisymmetric problem of a semi-infinite crack situated along the half-line $y = 0$, $x < 0$ and propagating with a constant velocity c in the positive direction of the fixed X-axis. A shear traction τ_0 is applied to a segment x_0 of crack faces and follows the moving crack tip (Fig. 1).

The corresponding boundary value problem is written as follows:

$$\tau_{xy}(x, 0) = -\tau_0, \quad -x_0 < x < 0, \tag{23}$$

$$\tau_{xy}(x, 0) = 0, \quad -\infty < x < -x_0, \tag{24}$$

$$\sigma_{yy}(x, 0) = 0, \quad -\infty < x < \infty, \tag{25}$$

$$v_y(x, 0) = 0, \quad 0 < x < \infty, \tag{26}$$

where the constraint (26) by virtue of (18) is identically fulfilled.

Equation (21) evaluated at $y = 0$ along with condition (25) yields

$$G(x) = -\frac{l_3}{l_4} \operatorname{Im}\Omega(x), \quad -\infty < x < \infty. \tag{27}$$

Furthermore, insertion of (27) into (22) evaluated at $y = 0$ produces

$$\frac{l_4}{C_{66}} \tau_{xy}(x, 0) = l_4 l_5 \operatorname{Re}\Omega(x) - l_3 l_6 \operatorname{Im}\Omega(x), \quad -\infty < x < \infty. \tag{28}$$

Through the position $\tau_{xy}(x, 0) = \tau_{xy}(x, 0^+) \equiv \tau^+(x, y)$ for $-\infty < x < 0$, the boundary conditions (23) and (24) specialize, respectively, to

$$l_4 l_5 \operatorname{Re}\Omega^+(x) - l_3 l_6 \operatorname{Im}\Omega^+(x) = -\frac{l_4 \tau_0}{C_{66}}, \quad -x_0 < x < 0, \tag{29}$$

$$l_4 l_5 \operatorname{Re}\Omega^+(x) - l_3 l_6 \operatorname{Im}\Omega^+(x) = 0, \quad -\infty < x < -x_0, \tag{30}$$

or, because of (18), to the following Riemann-Hilbert problems:

$$\Omega^+(x) - g\Omega^-(x) = f, \quad -x_0 < x < 0, \tag{31}$$

$$\Omega^+(x) - g\Omega^-(x) = 0, \quad -\infty < x < -x_0, \tag{32}$$

where

$$g = \frac{l_3 l_6 + i l_4 l_5}{l_3 l_6 - i l_4 l_5}, \quad f = \frac{2 i l_4}{C_{66}} \frac{(l_3 l_6 + i l_4 l_5)\tau_0}{D^2},$$

and

$$D^2 = (l_4 l_5)^2 + (l_3 l_6)^2. \tag{33}$$

Under the assumptions that stresses vanish at infinity and displacements are one-valued functions, the solution to problem (31) is (Gakhov, 1966)

$$\Omega(z) = \frac{X(z)}{2\pi i} \int_{-x_0}^{0} \frac{f dt}{X(t)(t - z)}, \tag{34}$$

where $X(z)$ is the Plemelj function for the semi-infinite crack obtained as solution to the homogeneous problem of (31) and problem (32). It is found that

$$X(z) = z^r, \tag{35}$$

with

$$r = \frac{\log(g)}{2\pi i} = \frac{1}{\pi} tg^{-1}\left(\frac{l_4 l_5}{l_3 l_6}\right). \tag{36}$$

In the case of isotropic material the elastic moduli C_{ij} may be related to Lamè's coefficients λ and μ as $C_{11} = C_{22} = \lambda + 2\mu$, $C_{12} = \lambda$, $C_{66} = \mu$ so that expression (36) reduces to

$$r = -\frac{1}{\pi} tg^{-1}\left[\frac{4\sqrt{(1 - M_1^2)(M_2^2 - 1)}}{(M_2^2 - 2)^2}\right], \tag{37}$$

which is the result given by Freund (1979) and Georgiadis (1986).

The Cauchy-type integral in Eq. (34) may be evaluated in asymptotic form. When $|\arg z| < \pi$, it is found that

$$\frac{1}{2\pi i}\int_{-x_0}^{0}\frac{dt}{X(t)(t-z)}=\begin{cases}\dfrac{e^{-ir\pi}}{x_0^r}\left[\dfrac{1}{r-1}\left(\dfrac{x_0}{z}\right)+O\left(\dfrac{x_0}{z}\right)^2\right], & |z|>x_0\\[2ex] \dfrac{e^{-ir\pi}}{x_0^r}\left[\dfrac{1}{r}-\dfrac{\pi}{\sin r\pi}\left(\dfrac{x_0}{z}\right)^r-\dfrac{1}{r+1}\left(\dfrac{z}{x_0}\right)+O\left(\dfrac{z}{x_0}\right)^2\right], & |z|<x_0\end{cases}\qquad(38a,b)$$

Thence, by utilizing (38) in (34) one finds the asymptotic behaviour for the potential function $\Omega(z)$ as

$$\Omega(z)=\frac{\tau_0\sin r\pi}{\pi C_{66}l_5}\begin{cases}\dfrac{1}{r-1}\left(\dfrac{x_0}{z}\right)^{1-r}+O\left(\dfrac{x_0}{z}\right)^{2-r}, & |z|>x_0\\[2ex] -\dfrac{\pi}{\sin\alpha\pi}+\dfrac{1}{r}\left(\dfrac{x_0}{z}\right)^{-r}+O\left(\dfrac{x_0}{z}\right)^{r+1}, & |z|<x_0,\end{cases}\qquad(39a,b)$$

from which one recognizes that $\mathrm{Im}\Omega(x)=0$ for $x>0$.

Thus, bearing in mind Eq. (27) and substituting the asymptotic behavior (39*b*) into Eq. (22) leads to the following singular shear stress distribution in the neighbourhood of the crack tip:

$$\tau_{xy}(x,0)\approx\frac{K_2}{\sqrt{2\pi}}x^r,\quad x>0,\qquad(40)$$

where the above expression has been normalized with respect to the Mode II stress intensity factor

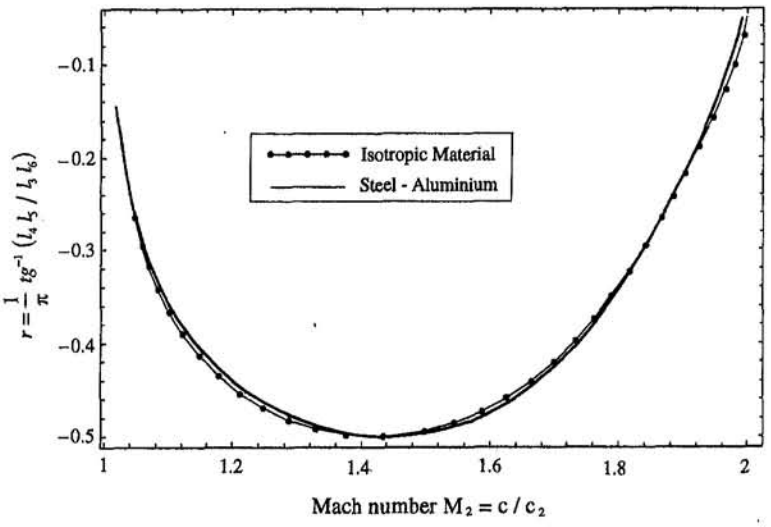

Fig. 2 Exponent r vs M_2 for an Isotropic material and Steel-Aluminium

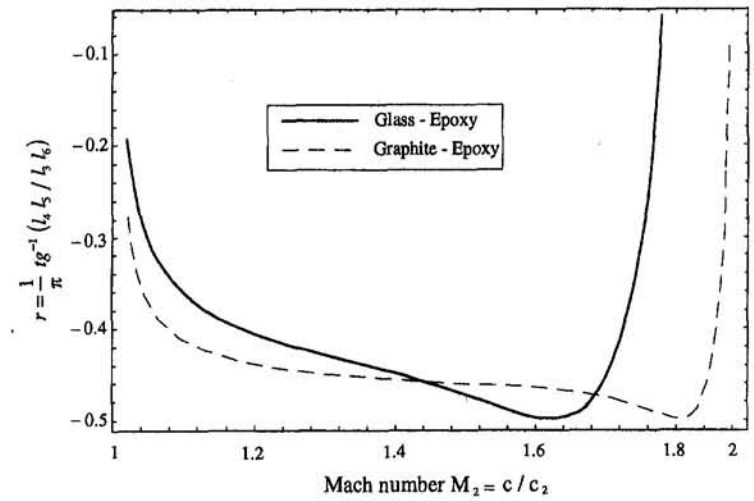

Fig. 3 Exponent r vs M_2 for Graphite-Epoxy and Glass-Epoxy

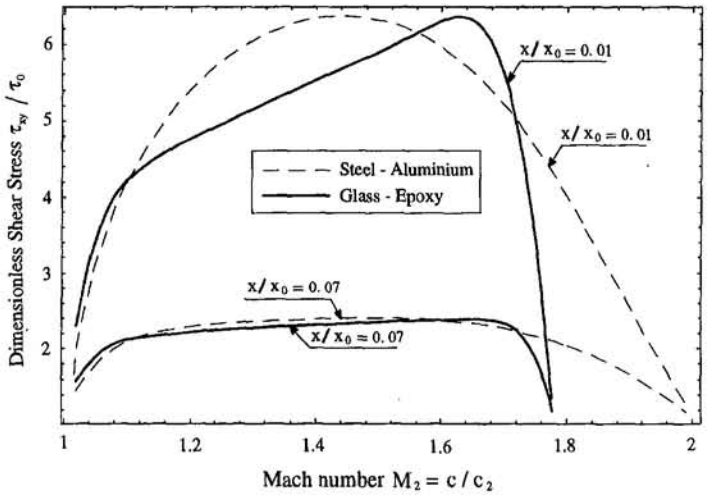

Fig. 4 Variation of τ_{xy}/τ_0 vs M_2 for Steel-Aluminium and Glass-Epoxy

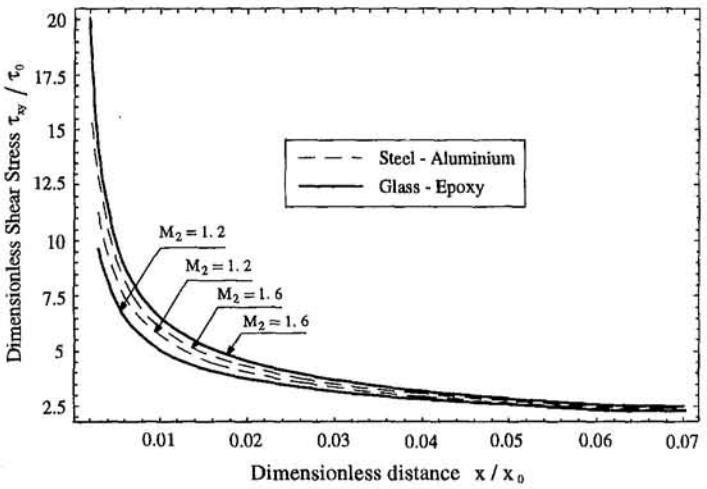

Fig. 5 Variation of τ_{xy}/τ_0 vs x/x_0 for Steel-Aluminium and Glass-Epoxy

$$K_2 = \lim_{x\to 0^+} \sqrt{2\pi}\, x^{-r}\tau_{xy}(x, 0) = \sqrt{2\pi}\,\tau_0\left(\frac{\sin r\pi}{r\pi}\right)x_0^{-r}. \quad (41)$$

4 Discussion of Results

In Figs. 2–3, the order of singularity given by (36) is plotted against the Mach number M_2.

Figure 2 is referred to an isotropic material (dotted line) with Poisson ratio equal to $\frac{1}{3}$ and to a Steel-Aluminium composite (solid line) whose relevant material parameters can be found in Table 1.

Due to the weak anisotropy of the Steel-Aluminium composite the behavior is nearly the same for both materials and corresponds to that obtained from formula (37). The exponent r varies continuously from $r = 0$ at $M_2 = 1$, up to a minimum value $r = -\frac{1}{2}$ at $M_2 = \sqrt{2}$, and back to $r = 0$ at $M_2 = (C_{11}/C_{66})^{1/2} \cong 2$.

Table 1 Material parameters

Composite type	C_{11}/C_{66}	C_{22}/C_{66}	C_{12}/C_{66}
Steel - Aluminium	3.952	4.155	1.959
Glass - Epoxy	3.139	12.190	1.155
Graphite - Epoxy	3.504	29.822	1.723

In Fig. 3 the order of singularity is represented for Graphite-Epoxy (dashed line) and Glass-Epoxy (solid line) composites, which are strongly orthotropic materials (Table 1).

A comparison with Fig. 2 shows that the exponent r varies continuously from 0 to $-\frac{1}{2}$ again, but its minimum moves toward higher values of M_2 and becomes more pronounced as the degree of material orthotropy increases.

It should be noted that there is a close analogy between the trend of profiles shown in Figs. 2, 3 and those provided for a bimaterial interface by Liu et al. (1995). Although they found a stress singularity always weaker than $-\frac{1}{2}$, the two sets of results show a good qualitative agreement. The quantitative discrepancy between the maximum values of the order of singularities is due to the different boundary value problems taken into account.

In Fig. 4 the behavior of the dimensionless shear stress given by (40) is represented as a function of M_2 for Steel-Aluminium (dashed line) and Glass-Epoxy (solid line) composites with (x/x_0) having the values 0.01 and 0.07 for the sake of illustration.

In Fig. 5 the shear stress given by (40) is represented as a function of (x/x_0) for the above mentioned composites and

various values of M_2. In this figure it can be seen that the effect of the degree of material orthotropy is significant in the immediate neighborhood of the crack tip. As the distance from the crack tip increases, in the range of M_2 common to both materials, the shear stress distribution is nearly independent of the degree of material orthotropy as well as of M_2.

Acknowledgments

We are very grateful to the anonymous reviewer for having drawn our attention to the works of Lambros and Rosakis and Liu et al. of which we were unaware.

The financial support by the Italian Ministry of University and Scientific and Technological Research M.U.R.S.T. (40 percent) is also acknowledged.

References

Achenbach, J. D., and Bažant, Z. P., 1975, "Elastodynamic Near-Tip Stress and Displacement Fields for Rapidly Propagating Cracks in Orthotropic Materials," ASME JOURNAL OF APPLIED MECHANICS, Vol. 42, pp. 183–189.

Arcisz, M., and Sih, G. C., 1984, "Effect of Orthotropy on Crack Propagation," *Theoretical and Applied Fracture Mechanics,* Vol. 1, pp. 225–238.

Broberg, K. B., 1989, "The Near-Tip Field at High Crack Velocities," *International Journal of Fracture,* Vol. 39, pp. 1–13.

Burridge, R., 1973, "Admissible Speed for Plane-Strain Shear Cracks with Friction but Lacking Cohesion," *Geophysical Journal of the Royal Astronomical Society,* Vol. 35, pp. 439–455.

Burridge, R., Conn, G., and Freund, L. B., 1979, "The Stability of a Rapid Mode II Shear Crack with Finite Cohesive Traction," *J. Geophysical Research,* Vol. 85, pp. 2210–2222.

Curran, D. R., Shockey, D. A., and Winkler, S., 1970, "Crack Propagation at Supersonic Velocities, II. Theoretical Model," *International Journal of Fracture,* Vol. 6, No. 3, pp. 271–278.

Freund, L. B., 1979, "The Mechanics of Dynamic Shear Crack Propagation," *J. Geophysical Research,* Vol. 84, pp. 2199–2209.

Gakhov, F. D., 1966, *Boundary Value Problems,* Pergamon Press, Oxford, U.K.

Georgiadis, H. G., and Theocaris, P. S., 1985, "On the Solution of Steady-State Elastodynamic Crack Problems by Using Complex Variable Methods," *ZAMP,* Vol. 36, pp. 146–165.

Georgiadis, H. G., 1986, "On the Stress Singularity in Steady-State Transonic Shear Crack Propagation," *International Journal of Fracture,* Vol. 30, pp. 175–180.

Kassir, M. K., and Tse, S., 1983, "Moving Griffith Crack in an Orthotropic Material," *International Journal of Engineering Sciences,* Vol. 21, pp. 315–325.

Lambros, J., and Rosakis, A. J., 1995, "Shear Dominated Transonic Interfacial Crack Growth in a Bimaterial—I. Experimental Observations," *Journal of the Mechanics and Physics of Solids,* Vol. 43, pp. 169–188.

Liu, C., Huang, Y., and Rosakis, A. J., 1995, "Shear Dominated Transonic Interfacial Crack Growth in a Bimaterial—II. Asymptotic Fields and Favorable Velocity Regimes," *Journal of the Mechanics and Physics of Solids,* Vol. 43, pp. 189–206.

Piva, A., 1987, "An Alternative Approach to Elastodynamic Crack Problems in an Orthotropic Medium," *Quarterly Journal of Applied Mathematics,* Vol. 45, pp. 97–104.

Piva, A., and Viola, E., 1988, "Crack Propagation in an Orthotropic Medium," *Engineering Fracture Mechanics,* Vol. 29, pp. 535–548.

Piva, A., and Radi, E., 1991, "Elastodynamic Local Fields for a Crack Running in an Orthotropic Medium," ASME JOURNAL OF APPLIED MECHANICS, Vol. 58, pp. 982–987.

Winkler, S., Shockey, D. A., and Curran, D. R., 1970, "Crack Propagation at Supersonic Velocities—I," *International Journal of Fracture,* Vol. 6, No. 2, pp. 151–152.

On the Analysis and Design of Fiber-Reinforced Composite Shells

A. L. Kalamkarov
Department of Mechanical Engineering,
Technical University of Nova Scotia,
Halifax, Nova Scotia B3J 2X4, Canada
Mem. ASME

A. G. Kolpakov
Russian Academy of Sciences,
Siberian Division,
Novosibirsk, Russia

Closed-form solutions based on a general homogenization composite shell model are obtained for the effective stiffness moduli of the high-stiffness fiber-reinforced angle-ply composite shell. The design problem for the fiber-reinforced shell having the required set of effective stiffnesses is formulated and solved. The set of prescribed stiffnesses for which the design problem is solvable is described, and the effective method of the design parameters calculation based on convex analysis is developed. The minimum number of reinforcing layers required for the design of the fiber-reinforced angle-ply shell with the prescribed stiffnesses is determined. The solution of design problem is generalized on account of minimization of the fiber volume content.

1 Introduction

The large-scale introduction of reinforced composite thin-walled structural members has created a need for further progress in rigorous theoretical modeling capable of predicting both effective characteristics and micro structure of processes occurring under various types of environment.

The mechanical model which allows the prediction of the behavior of multiple inhomogeneities in composite structure is provided by the sets of equations with rapidly varying coefficients which characterize the properties of the individual phases of the composite material. The resulting boundary value problems are rather complex, and it is quite natural, therefore, to seek mechanical models with some averaged coefficients.

Different averaging techniques have been adopted to estimate the effective elastic properties of composites, see e.g., Sendeckyj (1974), Hashin (1983), Weng et al. (1990), Christensen (1991), Tsai (1992), Vasiliev (1993), and Vasiliev and Tarnopol'skii (1990). Analytical averaging schemes were also utilized by Christensen (1990), Milton and Kohn (1988), Vinson and Sierokowski (1986), Vinson (1993), and Nemat-Nasser and Hori (1993) to provide an estimate of the overall elastic properties of inhomogeneous composite structures. The method of optimal design of fiber-reinforced composite shells on account of dynamics and buckling is described in Obraztsov and Vasiliev (1989) (see also Voitkov, 1979).

The effective properties of the composite material of a periodic structure can be calculated by means of the asymptotic homogenization method. The mathematical framework of the asymptotic homogenization technique can be found in Bensoussan et al. (1978), Sanchez-Palencia (1980), Lions (1981), Bakhvalov and Panasenko (1989), and Kalamkarov (1992). This method is mathematically rigorous, and it enables the prediction of both the local and overall averaged properties of the composite solid.

The homogenization model of planarly periodically inhomogeneous plate has been developed by Duvaut (1976). It should be noted, however, that the direct application of the asymptotic homogenization technique to a two-dimensional plate or shell theory will not provide the satisfactory results if the spatial inhomogeneities of the material vary on a scale comparable with the small thickness of the three-dimensional solid under study. A modified approach developed by Caillerie (1984) consists in applying the two-scale asymptotic homogenization formalism to three-dimensional problem for a thin inhomogeneous layer. The similar approach was applied by Kohn and Vogelius (1984) to the problem of bending of a thin homogeneous elastic layer with a rapidly varying thickness (see also Lewinski, 1992).

The rigorous general homogenization composite shell model was developed by Kalamkarov (1987, 1989, 1992, 1993) by applying a modified asymptotic homogenization technique to three-dimensional elastic problem for a thin curvilinear periodically inhomogeneous composite layer with rapidly varying thickness. The application of this general model to the analysis of the fiber-reinforced composite shells provides the accurate analytical determination of their effective stiffnesses as well as the local stress distribution (see Kalamkarov, 1992, 1993).

In the present paper, these results are taken as a basis to formulate and solve a design problem for reinforced composite shell with the required values of effective stiffnesses.

Following this Introduction, Section 2 deals with some basic relations of the general homogenization composite shell model. In Section 3, the fiber-reinforced angle-ply shell is considered, and the analytical formulas for the effective stiffnesses of this shell are provided. Section 4 is devoted to design problem formulation, while in Sections 5 and 6 the effective method of the design parameters calculation based on convex analysis is developed, and the minimum number of reinforcing layers required for the design of the fiber-reinforced angle-ply composite shell with the prescribed effective stiffnesses is determined. Section 7 deals with the generalization of the design problem solution on account of minimization of the fiber volume content. In Section 8, the effectiveness of the developed approach is illustrated by the design examples. Finally, Section 9 concludes the paper.

2 General Homogenization Composite Shell Model

Let us consider a thin three-dimensional composite layer of a periodic structure with the unit cell Ω_δ (see Fig. 1). In this figure, α_1, α_2, and γ are the orthogonal curvilinear coordinates, such that the coordinate lines α_1 and α_2 coincide with the main curvature lines of the midsurface of the carrier layer, and coordinate lines γ are normal to its midsurface ($\gamma = 0$). Thickness

Contributed by the Applied Mechanics Division of THE AMERICAN SOCIETY OF MECHANICAL ENGINEERS for publication in the ASME JOURNAL OF APPLIED MECHANICS.

Discussion on this paper should be addressed to the Technical Editor, Professor Lewis T. Wheeler, Department of Mechanical Engineering, University of Houston, Houston, TX 77204-4792, and will be accepted until four months after final publication of the paper itself in the ASME JOURNAL OF APPLIED MECHANICS.

Manuscript received by the ASME Applied Mechanics Division, May 2, 1995; final revision, Mar. 7, 1996. Associate Technical Editor: J. N. Reddy.

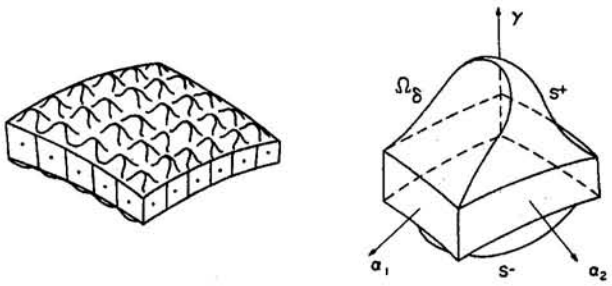

Fig. 1 Curvilinear reinforced composite layer; unit cell Ω_δ

of the layer and scale of the composite material inhomogeneity are assumed to be small as compared with the dimensions of the solid in whole, and characterized by a small parameter δ. The unit cell Ω_δ is determined by the following inequalities:

$$-\delta h_1/2 < \alpha_1 < \delta h_1/2, -\delta h_2/2 < \alpha_2 < \delta h_2/2, \gamma^- < \gamma < \gamma^+, \gamma^\pm = \pm\delta/2 \pm \delta F^\pm(\alpha_1/\delta h_1, \alpha_2/\delta h_2).$$

Here δ is the thickness of the carrier layer, and δh_1, δh_2 are tangential dimensions of the periodicity cell Ω_δ. Functions $F^\pm$ model the shape of the reinforcing elements at the upper (S^+) and lower (S^-) surfaces of the carrier layer, see Fig. 1. These functions are equal to zero in the absence of surface reinforcements, and then δ represents the thickness of the composite layer. The periodic inhomogeneity of the composite material is modeled by the assumption that the stiffness tensor components $a_{klmn}(\alpha_1, \alpha_2, \gamma)$ are piecewise-smooth periodic functions with unit cell Ω_δ.

It is a common practice in performing stress analysis of a composite structural member that the inhomogeneous medium being studied is replaced with a homogeneous anisotropic medium whose response is supposed to be equivalent to that of the actual composite in a certain averaged sense. If the composite material has a periodic structure, the averaged (or effective) properties of the equivalent anisotropic homogeneous material can be estimated by means of the asymptotic homogenization method, which also gives asymptotically correct results for the local stress field in the bulk of the composite solid. This method is based on representation of solution of three-dimensional problem in form of two-scale asymptotic expansion in powers of the small parameter δ. In the previous studies (see Kalamkarov, 1987, 1989, 1992) this approach was adopted in the analysis of composite and reinforced thin-walled structural members. As a result, the general homogenization composite shell model has been developed. It is shown (see Kalamkarov, 1987, 1989) that it is possible to calculate both the effective and local properties of this composite layer by first solving appropriate three-dimensional local problems set on the unit cell, and subsequently solving a two-dimensional boundary value problem for a homogeneous (or quasi-homogeneous) anisotropic shell with the effective stiffness moduli obtained at the first step.

The constitutive relations of the anisotropic homogeneous shell, that is those between the stress resultants N_1, N_2, N_{12} and moment resultants M_1, M_2, M_{12} on one hand, and the midsurface strains ϵ_{11}, ϵ_{22} (elongation), $\epsilon_{12} = \epsilon_{21} = \omega/2$ (shear), τ_{11}, τ_{22} (bending), $\tau_{12} = \tau_{21} = \tau$ (torsion) on the other, can be represented as follows (see Kalamkarov, 1992):

$$\begin{aligned} N_\beta &= \delta\langle b^{\lambda\mu}_{\beta\beta}\rangle\epsilon_{\lambda\mu} + \delta^2\langle c^{\lambda\mu}_{\beta\beta}\rangle\tau_{\lambda\mu}, \\ N_{12} &= \delta\langle b^{\lambda\mu}_{12}\rangle\epsilon_{\lambda\mu} + \delta^2\langle c^{\lambda\mu}_{12}\rangle\tau_{\lambda\mu} \\ M_\beta &= \delta^2\langle z b^{\lambda\mu}_{\beta\beta}\rangle\epsilon_{\lambda\mu} + \delta^3\langle z c^{\lambda\mu}_{\beta\beta}\rangle\tau_{\lambda\mu}, \\ M_{12} &= \delta^2\langle z b^{\lambda\mu}_{12}\rangle\epsilon_{\lambda\mu} + \delta^3\langle z c^{\lambda\mu}_{12}\rangle\tau_{\lambda\mu} \end{aligned} \tag{1}$$

where β assumes the values 1 and 2, and is not summed here; $\lambda, \mu = 1, 2$. The functions $b^{mn}_{kl}(\xi_1, \xi_2, z)$ and $c^{mn}_{kl}(\xi_1, \xi_2, z)$, $k, l, m, n, = 1, 2, 3$, can be calculated from the solution of local problems on the unit cell (Kalamkarov, 1992). Here $\xi_1 = \alpha_1 A_1/(\delta h_1)$, $\xi_2 = \alpha_2 A_2/(\delta h_2)$, $z = \gamma/\delta$, and $A_1(\alpha_1, \alpha_2)$ and $A_2(\alpha_1, \alpha_2)$ are the coefficients of the first quadratic form of the midsurface of the layer. The above functions are determined as follows:

$$\begin{aligned} b^{mn}_{kl} &= \frac{1}{h_\beta} a_{kli\beta} \frac{\partial U^{mn}_i}{\partial \xi_\beta} + a_{kli3} \frac{\partial U^{mn}_i}{\partial z} + a_{klmn} \\ c^{mn}_{kl} &= \frac{1}{h_\beta} a_{kli\beta} \frac{\partial V^{mn}_i}{\partial \xi_\beta} + a_{kli3} \frac{\partial V^{mn}_i}{\partial z} + z a_{klmn} \end{aligned} \tag{2}$$

where functions $U^{mn}_i(\xi_1, \xi_2, z)$ and $V^{mn}_i(\xi_1, \xi_2, z)$ are periodic in variables ξ_1 and ξ_2 with periods A_1 and A_2, respectively. These functions are determined by solving the following set of local problems ($i, j = 1, 2, 3$; $\beta, \lambda, \mu = 1, 2$):

$$\begin{aligned} &\frac{1}{h_\beta}\frac{\partial b^{\lambda\mu}_{i\beta}}{\partial \xi_\beta} + \frac{\partial b^{\lambda\mu}_{i3}}{\partial z} = 0, \quad \frac{1}{h_\beta} n^\pm_\beta b^{\lambda\mu}_{i\beta} + n^\pm_3 b^{\lambda\mu}_{i3} = 0, \quad \text{at} \quad z = z^\pm \\ &\frac{1}{h_\beta}\frac{\partial c^{\lambda\mu}_{i\beta}}{\partial \xi_\beta} + \frac{\partial c^{\lambda\mu}_{i3}}{\partial z} = 0, \\ &\frac{1}{h_\beta} n^\pm_\beta c^{\lambda\mu}_{i\beta} + n^\pm_3 c^{\lambda\mu}_{i3} = 0, \quad \text{at} \quad z = z^\pm \end{aligned} \tag{3}$$

where $n^\pm_i$ are components of the normal to the upper (S^+) and lower (S^-) surfaces of the unit cell, (see Fig. 1) respectively, related to the coordinate system ξ_1, ξ_2, and z.

In the case of perfect bonding at the interface of the composite material, the functions $U^{\lambda\mu}_i$, $V^{\lambda\mu}_i$, as well as the expressions $[(1/h_\beta)n^{(c)}_\beta b^{\lambda\mu}_{i\beta} + n^{(c)}_3 b^{\lambda\mu}_{i3}]$ and $[(1/h_\beta)n^{(c)}_\beta c^{\lambda\mu}_{i\beta} + n^{(c)}_3 c^{\lambda\mu}_{i3})]$ should be continuous at the interface. Here $n^{(c)}_i$ are components of the normal to the interface.

The averaging symbol $\langle \ldots \rangle$ in Eq. (1) denotes the integration over the three-dimensional unit cell of composite layer, as follows:

$$\langle f(\xi_1, \xi_2, z)\rangle = \int_\Omega f(\xi_1, \xi_2, z) d\xi_1 d\xi_2 dz. \tag{4}$$

Local problems, Eqs. (2) and (3), having been solved, the functions $b^{mn}_{kl}(\xi_1, \xi_2, z)$ and $c^{mn}_{kl}(\xi_1, \xi_2, z)$ are averaged by application of Eq. (4), giving the effective stiffnesses of the anisotropic homogeneous shell, $\langle b^{\lambda\mu}_{\alpha\beta}\rangle$, $\langle z b^{\lambda\mu}_{\alpha\beta}\rangle = \langle c^{\lambda\mu}_{\alpha\beta}\rangle$ and $\langle z c^{\lambda\mu}_{\alpha\beta}\rangle$. One may proceed then to solution of the boundary value problem for the homogeneous shell, that can be found in Kalamkarov (1992, p. 141), to calculate the functions $\epsilon_{\lambda\mu}(\alpha_1, \alpha_2)$ and $\tau_{\lambda\mu}(\alpha_1, \alpha_2)$.

It should be noted that the formulas for the coordinates ξ_1 and ξ_2, that are involved in the formulation of local problems, contain metric coefficients $A_1(\alpha_1, \alpha_2)$ and $A_2(\alpha_1, \alpha_2)$. If A_1 and A_2 are not constant (and they can be constant only if the midsurface of the shell is a developable surface), then the effective stiffness moduli will also depend on the tangential coordinates α_1 and α_2. Consequently, the averaged anisotropic shell can be quasi-homogeneous depending on the geometry of the midsurface of the shell.

The notation for the effective stiffnesses used in Eq. (1) are naturally related to the local problem formulation in the general homogenization composite shell model, see Eqs. (2) and (3). There is the following simple correspondence between this notation and the conventional notation for the effective stiffnesses, see e.g., Vinson (1993, p. 316):

$$\begin{aligned} &A_{11} = \delta\langle b^{11}_{11}\rangle, \quad B_{11} = \delta^2\langle z b^{11}_{11}\rangle = \delta^2\langle c^{11}_{11}\rangle, \quad D_{11} = \delta^3\langle z c^{11}_{11}\rangle \\ &A_{12} = \delta\langle b^{22}_{11}\rangle, \quad B_{12} = \delta^2\langle z b^{22}_{11}\rangle = \delta^2\langle c^{22}_{11}\rangle, \quad D_{12} = \delta^3\langle z c^{22}_{11}\rangle \\ &A_{16} = \delta\langle b^{12}_{11}\rangle, \quad B_{16} = \delta^2\langle z b^{12}_{11}\rangle = \delta^2\langle c^{12}_{11}\rangle, \quad D_{16} = \delta^3\langle z c^{12}_{11}\rangle \\ &A_{22} = \delta\langle b^{22}_{22}\rangle, \quad B_{22} = \delta^2\langle z b^{22}_{22}\rangle = \delta^2\langle c^{22}_{22}\rangle, \quad D_{22} = \delta^3\langle z c^{22}_{22}\rangle \end{aligned}$$

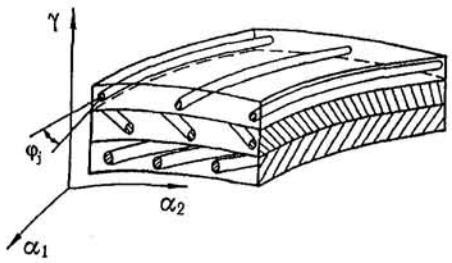

Fig. 2 Fiber-reinforced angle-ply composite shell

$$A_{26} = \delta\langle b_{22}^{12}\rangle, \quad B_{26} = \delta^2\langle zb_{22}^{12}\rangle = \delta^2\langle c_{22}^{12}\rangle, \quad D_{26} = \delta^3\langle zc_{22}^{12}\rangle$$
$$A_{66} = \delta\langle b_{12}^{12}\rangle, \quad B_{66} = \delta^2\langle zb_{12}^{12}\rangle = \delta^2\langle c_{12}^{12}\rangle, \quad D_{66} = \delta^3\langle zc_{12}^{12}\rangle. \tag{5}$$

Both notations related by the Eq. (5) will be used in the sequel.

The general homogenization composite shell model also provides an asymptotic result for the three-dimensional local stress distribution in the composite layer. These stresses can be calculated by means of the following formula ($k, l = 1, 2, 3$; $\mu, \nu = 1, 2$):

$$\sigma_{kl} \approx b_{kl}^{\mu\nu}(\xi_1, \xi_2, z)\epsilon_{\mu\nu}(\alpha_1, \alpha_2) + \delta c_{kl}^{\mu\nu}(\xi_1, \xi_2, z)\tau_{\mu\nu}(\alpha_1, \alpha_2). \tag{6}$$

Analysis of local deformations and stresses was performed earlier by Kalamkarov (1992, 1993). It has been shown, in particular, that the large local shear stresses arise in the matrix material in the case of dense placement of fiber plies. The effect of torsion failure of the matrix material occurs if the fiber volume content exceeds 60 percent. Torsion failure of the matrix causes the delamination of the high-stiffness fiber-reinforced angle-ply shells. It should be noted, however, that the failure of angle-ply composite structures involves many different factors. The experimental results show that the other modes of failure could prevail (see Vasiliev (1993, pp. 130–136) for the details).

The application of the general homogenization composite shell model is limited to the case when thickness of the shell and the scale of periodicity, i.e., parameter δ, is much smaller than the overall dimensions of the solid. This requirement is fulfilled in a large number of applications.

3 Fiber-Reinforced Angle-Ply Composite Shell

The fiber-reinforced angle-ply composite shell is shown in Fig. 2. There are no surface reinforcements in this case. The shell is formed by N layers reinforced by parallel fibers. The fiber within a jth layer, $j = 1, 2, \ldots, N$, makes an angle φ_j with the coordinate line α_1. The thickness of laminate is δ, and the departure of the axis of the fiber of the jth ply from the shell midsurface ($\gamma = 0$) is equal to δa_j. We assume that material of fibers is much stiffer than the matrix material, i.e., $E_F \gg E_M$. This assumption is typical for the polymer matrix fiber-reinforced composites. Local problems (see Eqs. (2) and (3)) are much simplified, on account of the above assumption, by a decoupling in the regions of fibers and matrix.

3.1 Effective Stiffnesses. Local problems of the homogenization composite shell model (see Eqs. (2) and (3)), can be solved analytically for the elliptical cross section of the fibers (see Kalamkarov, 1987). Having solved the local problems, we average the functions $b_{\alpha\beta}^{\lambda\mu}(\xi_1, \xi_2, z)$ and $c_{\alpha\beta}^{\lambda\mu}(\xi_1, \xi_2, z)$ and then sum them up over the all N layers to obtain the following formulas for the effective stiffness moduli of the high-stiffness fiber-reinforced angle-ply shell:

$$\langle b_{\alpha\beta}^{\lambda\mu}\rangle = \sum_{j=1}^{N} E_j B_j^{(\alpha\beta\lambda\mu)}\theta_j, \quad \langle zb_{\alpha\beta}^{\lambda\mu}\rangle = \langle c_{\alpha\beta}^{\lambda\mu}\rangle = \sum_{j=1}^{N} a_j E_j B_j^{(\alpha\beta\lambda\mu)}\theta_j$$
$$\langle zc_{\alpha\beta}^{\lambda\mu}\rangle = \sum_{j=1}^{N} E_j\theta_j[a_j^2 B_j^{(\alpha\beta\lambda\mu)} + C_j^{(\alpha\beta\lambda\mu)}(16(1+\nu_j))^{-1}]. \tag{7}$$

Here E_j and ν_j are Young's modulus and Poisson's ratio of fibers of the jth layer; θ_j is the fiber volume content in the jth layer; and the parameters $B_j^{(\alpha\beta\lambda\mu)}$ and $C_j^{(\alpha\beta\lambda\mu)}$ are determined by the following formulas for each combination of superscripts α, β, λ, $\mu = 1, 2$:

$$B_j^{(1111)} = A_1^4 D_j^{-4}\cos^4\varphi_j,$$
$$B_j^{(1112)} = B_j^{(1211)} = A_1^3 A_2 D_j^{-4}\cos^3\varphi_j\sin\varphi_j$$
$$B_j^{(1122)} = B_j^{(2211)} = B_j^{(1212)} = A_1^2 A_2^2 D_j^{-4}\cos^2\varphi_j\sin^2\varphi_j$$
$$B_j^{(2222)} = A_2^4 D_j^{-4}\sin^4\varphi_j,$$
$$B_j^{(1222)} = B_j^{(2212)} = A_1 A_2^3 D_j^{-4}\cos\varphi_j\sin^3\varphi_j \tag{8}$$

$$C_j^{(1111)} = A_1^4 D_j^{-4}\cos^2\varphi_j \times [2A_2^4\sin^2\varphi_j(1-e_j^2)\Delta_j + \cos^2\varphi_j(1+\nu_j)]$$
$$C_j^{(2222)} = A_2^4 D_j^{-4}\sin^2\varphi_j \times [2A_1^4\cos^2\varphi_j(1-e_j^2)\Delta_j + \sin^2\varphi_j(1+\nu_j)]$$
$$C_j^{(1122)} = C_j^{(2211)} = A_1^2 A_2^2 D_j^{-4}\sin^2\varphi_j\cos^2\varphi_j \times [-2A_1^2A_2^2(1-e_j^2)\Delta_j + (1+\nu_j)]$$
$$C_j^{(1112)} = C_j^{(1211)} = A_1^3 A_2 D_j^{-4}\sin\varphi_j\cos\varphi_j \times [A_2^2(A_2^2\sin^2\varphi_j - A_1^2\cos^2\varphi_j)(1-e_j^2)\Delta_j + \cos^2\varphi_j(1+\nu_j)]$$
$$C_j^{(1222)} = C_j^{(2212)} = A_1 A_2^3 D_j^{-4}\sin\varphi_j\cos\varphi_j \times [A_1^2(A_1^2\cos^2\varphi_j - A_2^2\sin^2\varphi_j)(1-e_j^2)\Delta_j + \sin^2\varphi_j(1+\nu_j)]$$
$$C_j^{(1212)} = 0.5A_1^2A_2^2D_j^{-4} \times [(A_1^2\cos^2\varphi_j - A_2^2\sin^2\varphi_j)^2(1-e_j^2)\Delta_j + 2\sin^2\varphi_j\cos^2\varphi_j(1+\nu_j)] \tag{9}$$

where

$$D_j^2 = A_1^2\cos^2\varphi_j + A_2^2\sin^2\varphi_j,$$
$$\Delta_j = [D_j^2 + A_1^2A_2^2(1-e_j^2)]^{-1} \tag{10}$$

and e_j is the eccentricity of the elliptical cross-section of the fiber of the jth ply. In the case of circular fibers, $e_j = 0$.

It is of interest to compare expressions (7)–(10) for the high-stiffness reinforced shells with the similar results that have been derived in the framework of the semi-empirical approach; see, e.g., Vasiliev (1993). In this procedure, first the averaging the composite material characteristics of individual layers is performed, and then the overall stiffnesses of the composite angle-ply laminate are calculated using the orthotropic effective stiffnesses of laminae and the stacking orientation of each lamina. The comparison shows that the formulas (7) for the moduli $\langle b_{\alpha\beta}^{\lambda\mu}\rangle$ and $\langle zb_{\alpha\beta}^{\lambda\mu}\rangle$ coincide with the corresponding formulas for the effective stiffnesses of a multilayer shell working in a tension-compression, provided that the contribution of the matrix is negligibly small, and that $A_1 = A_2 = 1$. However, the above flexural and torsional stiffnesses, $\langle zc_{\alpha\beta}^{\lambda\mu}\rangle$, do differ from the corresponding results of the semi-empirical approach, and can be converted to these latter by setting $e_j = 1$, $j = 1, 2, \ldots, N$ (which means neglecting the shape of the cross sections of the fibers in all plies), and, in addition to that, by replacing the factor 16 by 12 in the denominator of the last formula (7)

(which means neglecting the correct calculation of the moment of inertia of the fiber cross-section). Apparently, the above Eqs. (7)–(10) derived using the general homogenization composite shell model are more rigorous than the results of the approximate approach, in terms of better accounting the micro structure of the composite material.

3.2 Numerical Example. To obtain an estimate of the magnitude of the correction, consider a three-layer angle-ply composite shell of a thickness δ and with the fiber placement angles $\varphi_1 = \pi/4$, $\varphi_2 = 0$, and $\varphi_3 = -\pi/4$. The fibers in all three layers are made of the similar material with isotropic elastic properties E and ν, and they have the similar circular cross section. We also assume that $\theta_1 = \theta_2 = \theta_3 = \theta_0$, $a_1 = \frac{1}{3}$, $a_2 = 0$, $a_3 = -\frac{1}{3}$, and $A_1 = A_2 = 1$. From the last formula of Eq. (7), the nonzero flexural and torsional moduli of the shell in the conventional notation, see Eq. (5), are given by

$$D_{11} = [0.15 + 0.031(1 + \nu)^{-1}]\delta^3 E\theta_0,$$
$$D_{12} = [0.06 + 0.031\nu(1 + \nu)^{-1}]\delta^3 E\theta_0$$
$$D_{22} = [0.09 + 0.031(1 + \nu)^{-1}]\delta^3 E\theta_0,$$
$$D_{66} = [0.09 + 0.016(1 + \nu)^{-1}]\delta^3 E\theta_0. \quad (11)$$

In order to specify the magnitude of the correction, let us consider the graphite/polyimide angle-ply shell with the following properties of fibers and matrix: $E_F = 300$ GPa, $E_F/E_M = 100$, and $\nu_F = 0.2$. We assume that a lamina thickness is 0.14 mm, and the fiber volume content is 60 percent. The magnitudes of the effective stiffnesses calculated from Eq. (11) are the following: $D_{11} = 2.34$ Nm, $D_{12} = 0.93$ Nm, $D_{22} = 1.55$ Nm, $D_{66} = 1.37$ Nm. The corresponding values resulting from the semi-empirical approach are $D_{11} = 2.4$ Nm, $D_{12} = D_{22} = D_{66} = 1.29$ Nm. The maximum correction of 27 percent is obtained for the effective stiffness D_{12}.

4 Design of the Fiber-Reinforced Composite Shells

In many cases, design of the composite engineering structures is based on some empirical approximate formulas. But it should be understood that a satisfactory design result can be achieved only if the design procedure is based on a rigorous basic theoretical model.

The application of the general homogenization composite shell model to the analysis of the fiber-reinforced composite shell shown in Fig. 2 provides the accurate calculation of its effective stiffness moduli. These results are used in this section for the design of composite shell with the required set of effective stiffnesses. A different approach was developed earlier by Kalamkarov and Kolpakov (1993) for the optimal design of wafer and honeycomb-like reinforced shells.

Suppose, it is required to design the fiber-reinforced composite shell with the prescribed set of effective stiffnesses. Equations (7)–(10) express the effective moduli of the high-stiffness fiber-reinforced composite shell in terms of fiber placement angles φ_j, fiber volume content θ_j, where j is a number of the layer, and some other material properties and geometrical dimensions of the composite shell. Let us assume now that all fibers are of a circular cross section, and that they are made of a similar material with Young's modulus E. We also assume that $A_1 = A_2 = 1$, which is possible for the cylindrical shells or plates, in particular. The set of effective stiffnesses in the tangential directions to the shell surface can be then expressed as follows, cf. Eqs. (5), (7), and (8):

$$A_{11} = \delta\langle b_{11}^{11}\rangle = E\omega Y_1(\gamma, \varphi), \quad A_{22} = \delta\langle b_{22}^{22}\rangle = E\omega Y_2(\gamma, \varphi)$$
$$A_{16} = \delta\langle b_{11}^{12}\rangle = E\omega Y_3(\gamma, \varphi), \quad A_{26} = \delta\langle b_{12}^{22}\rangle = E\omega Y_4(\gamma, \varphi)$$
$$A_{66} = A_{12} = \delta\langle b_{12}^{12}\rangle = \delta\langle b_{11}^{22}\rangle$$
$$= 0.5E\omega[1 - Y_1(\gamma, \varphi) - Y_2(\gamma, \varphi)] \quad (12)$$

where

$$Y_1(\gamma, \varphi) = \sum_{j=1}^{N} \gamma_j \cos^4 \varphi_j, \quad Y_2(\gamma, \varphi) = \sum_{j=1}^{N} \gamma_j \sin^4 \varphi_j$$
$$Y_3(\gamma, \varphi) = \sum_{j=1}^{N} \gamma_j \sin \varphi_j \cos^3 \varphi_j,$$
$$Y_4(\gamma, \varphi) = \sum_{j=1}^{N} \gamma_j \sin^3 \varphi_j \cos \varphi_j. \quad (13)$$

Here $\omega = \sum_{j=1}^{N} \theta_j$, $\gamma = (\gamma_1, \gamma_2, \ldots, \gamma_N)$, and $\gamma_j = \theta_j/\omega$ is the proportion of fiber content within the jth layer, and $\varphi = (\varphi_1, \varphi_2, \ldots, \varphi_N)$. By replacing functionals $Y_1(\gamma, \varphi)$, $Y_2(\gamma, \varphi)$, $Y_3(\gamma, \varphi)$, and $Y_4(\gamma, \varphi)$ by the variables y_1, y_2, y_3, and y_4, and using the conventional notation for the effective stiffnesses, see Eq. (12), we obtain the following algebraic system:

$$A_{11} = E\omega y_1, \quad A_{22} = E\omega y_2, \quad A_{16} = E\omega y_3$$
$$A_{26} = E\omega y_4, \quad A_{66} = A_{12} = 0.5E\omega(1 - y_1 - y_2). \quad (14)$$

If we prescribe values of the effective stiffnesses A_{11}, A_{22}, A_{16}, A_{26}, and $A_{66} = A_{12}$, then Eq. (14) will represent the system for determining $\mathbf{y} = (y_1, y_2, y_3, y_4)$. Since the number of equations in the system (14) exceeds a number of unknowns, the following solvability condition should be fulfilled:

$$A_{66} = A_{12} = 0.5(E\omega - A_{11} - A_{22}). \quad (15)$$

The system (14) can be resolved explicitly, so that

$$y_1 = A_{11}(E\omega)^{-1}, \; y_2 = A_{22}(E\omega)^{-1},$$
$$y_3 = A_{16}(E\omega)^{-1}, \; y_4 = A_{26}(E\omega)^{-1}. \quad (16)$$

The next and major step in the design problem is to determine the fiber volume fractions $\gamma = (\gamma_1, \gamma_2, \ldots, \gamma_N)$ and the fiber placement angles $\varphi = (\varphi_1, \varphi_2, \ldots, \varphi_N)$, such that satisfy equations

$$Y_1(\gamma, \varphi) = y_1, \quad Y_2(\gamma, \varphi) = y_2,$$
$$Y_3(\gamma, \varphi) = y_3, \quad Y_4(\gamma, \varphi) = y_4. \quad (17)$$

The following natural limitations are imposed on the design parameters:

$$\sum_{j=1}^{N} \gamma_j = 1, \quad \gamma_j \geq 0, j = 1, 2, \ldots, N \quad (18)$$

$$\varphi_j \in [0, \pi], j = 1, 2, \ldots, N. \quad (19)$$

The question of a great practical importance here is to determine the minimum number of layers, $N_{\min}$, that is required to design the fiber-reinforced shell with the prescribed effective stiffnesses.

4.1 Design Problem Formulation. Design problem includes the following two questions:

(i) Determine if the system of Eqs. (17) is solvable in the set of variables satisfying conditions (18) and (19).

(ii) If the answer on the question (i) is positive, then find the set of solutions of the system (17) under the conditions (18) and (19).

5 Design Problem Solution

To solve the design problem, we first define a following set of intervals within $[0, \pi]$ that impose the limitations on fiber placement angles φ_j: $\Phi^N = \sum_{i=1}^{N} [a_i, b_i] \subset [0, \pi]$, and consider a set

$$U_\Phi^N = \{\varphi \in \Phi^N, \gamma \in R^N, \gamma \text{ satisfies conditions (18)}\}. \quad (20)$$

Problem (17), (18) is solvable in the set of variables U_Φ^N if and only if the right-hand sides of Eqs. (17), (y_1, y_2, y_3, y_4) belong to an image of the set U_Φ^N under the mapping $\mathbf{Y}$, given by Eqs. (13),

$$\mathbf{Y}: (\gamma, \varphi) \in U_\Phi^N \to (Y_1(\gamma, \varphi), Y_2(\gamma, \varphi), Y_3(\gamma, \varphi), Y_4(\gamma, \varphi)) \in R^4. \quad (21)$$

5.1 Statement 1.

(i) If $N \geq 5$, then image of the set U_Φ^N under the mapping $\mathbf{Y}$, given by Eqs. (13), represents a convex hull (see Rockafellar, 1970) of the following curve Γ:

$$\Gamma = \{\mathbf{y} \in R^4: \mathbf{y} = (\cos^4 \varphi, \sin^4 \varphi, \sin \varphi \cos^3 \varphi, \sin^3 \varphi \cos \varphi), \varphi \in \Phi^N\} \quad (22)$$

(ii) Any point that belongs to the image of the set U_Φ^N under the mapping $\mathbf{Y}$, can be obtained as a value of the function $\mathbf{Y}$ on a vector $(\gamma, \varphi) \in R^5 \times \Phi^5$.

In accordance with the Statement 1, a fiber-reinforced composite shell with any prescribed effective stiffness moduli $\{A_{\alpha\beta}\}$ satisfying the solvability condition (15), can be designed by using not more than five layers of reinforcing fibers.

5.2 Proof of Statement 1. It follows from the condition (18) that the right-hand sides of expressions (13) represent a convex combination of points of curve Γ, see Eq. (22). In the general case, if any set Ω is a subset of R^n, the convex hull of Ω can be obtained by forming all convex combinations of elements of Ω. According to Carathéodory's Theorem, see Rockafellar (1970), it is not really necessary to form combinations involving more than $(n + 1)$ elements at a time. The convex hull of Ω, conv Ω, can be obtained by forming convex combinations involving not more than $(n + 1)$ elements of Ω. In our case, $\Omega = \Gamma$, and $n = 4$. Consequently, we obtain that if $N \geq 5$ then the image of the set U_Φ^N under the mapping $\mathbf{Y}$ will coincide with the whole set conv Γ. That completes the proof.

6 Skew-Symmetric Fiber-Reinforced Shells

Let us consider now a practically important type of the composite shells with the skew-symmetric placement of fibers about the mid-surface of a laminate. In this case, for any layer with the fiber placement angle $+\varphi_j$, there is a symmetric layer with the fiber placement angle $-\varphi_j$, and the fiber volume fraction γ_j is similar in these two layers. In the case of skew-symmetric reinforcement, two last functionals in the Eqs. (13) are identically equal to zero. It is also sufficient in this case to limit the fiber placement angles by the interval $[0, \pi/2]$.

6.1 Design Problem Formulation.

(i) Determine if the equations (cf. Eq. (17))

$$Y_1(\gamma, \varphi) = y_1, \quad Y_2(\gamma, \varphi) = y_2 \quad (23)$$

are solvable in the set of variables (cf. Eq. (20))

$$V_\Phi^N = \{(\gamma, \varphi) \in U_\Phi^N, \gamma_j = \gamma_{N-j}, -\varphi_j = \varphi_{N-j} \in [0, \pi/2], j = 1, 2, \ldots, N/2\}. \quad (24)$$

(ii) If the answer on the question (i) is positive, then find the set of solutions of the system (23) under the conditions (18).

6.2 Statement 2.

(i) If $N \geq 6$, then image of the set V_Φ^N under the mapping $\{Y_1(\gamma, \varphi), Y_2(\gamma, \varphi)\}$, given by two first Eqs. (13), represents a convex hull of a curve

$$\Gamma = \{\mathbf{y} \in R^2: \mathbf{y} = (\cos^4 \varphi, \sin^4 \varphi), \varphi \in \Phi^N\} = \{\mathbf{y} \in R^2: \mathbf{y} = (\eta, (1 - \sqrt{\eta})^2), \eta \in \cos^4 \Phi^N\} \quad (25)$$

where $\cos^4 \Phi$ denotes the image of the set Φ under the mapping $(\cos)^4$.

(ii) Any point that belongs to image of the set V_Φ^N under the mapping $\{Y_1(\gamma, \varphi), Y_2(\gamma, \varphi)\}$, can be obtained as a meaning of the function $\{Y_1(\gamma, \varphi), Y_2(\gamma, \varphi)\}$ on a vector $(\gamma, \varphi) \in U_\Phi^6$.

In accordance with the Statement 2, a skew-symmetric fiber-reinforced composite shell with any prescribed effective stiffness moduli $\{A_{\alpha\beta}\}$ satisfying the solvability condition (15), can be designed by using not more than three pairs of layers of reinforcing fibers with fiber placement angles $+\varphi_j$ and $-\varphi_j$.

6.3 Proof of Statement 2. The proof of Statement 2 is similar to the above proof of Statement 1. Now the dimensionality of space of conv Γ is equal to $n = 2$. According to Carathéordory's Theorem, see Rockafellar (1970), we need not more than $n + 1 = 3$ elements to form the convex hull, conv Γ. The total number of layers of skew-symmetric composite shell should be doubled, and, consequently, we get $N \geq 6$.

7 Minimization of Fiber Content

Let us consider now an optimization of the design problem concerning the minimization of the fiber content ω. We include now the variable ω into the set of independent variables of the system of Eqs. (16), and consider the problem of minimization of ω on account the condition that the composite shell has a given (prescribed) set of effective stiffnesses. Suppose, we already solved the above design problem for some fixed ω value, $\omega = \omega_0$, so that (cf. Eq. (17))

$$Y_i(\gamma, \varphi) = y_i^0, \; i = 1, 2, 3, 4, \quad (26)$$

where $\mathbf{y}^0 = (y_1^0, y_2^0, y_3^0, y_4^0)$ is determined from the expressions (16) with $\omega = \omega_0$. It follows from the formulas (16) that $\mathbf{y} = (\omega_0/\omega)\mathbf{y}^0$ will represent a solution for a given ω value. Moreover, fiber volume fractions γ_i satisfy conditions (18). As a result, we arrive to a problem of searching minimum ω value, such that the point $\mathbf{y}(\omega) = (\omega_0/\omega)\mathbf{y}^0$ belongs to convex set, conv Γ. Curve Γ has been described in Statements 1 and 2. The set

$$L = \{\mathbf{y}(\omega) = (\omega_0/\omega)\mathbf{y}^0, \omega \in (0, \omega_0)\} \quad (27)$$

represents a ray having an origin in the point $\mathbf{y}^0 \in$ conv Γ, and tending to infinity when $\omega \to 0$. Since the set conv Γ is compact (because Γ is compact) the ray L will intersect the boundary of the convex compact set conv Γ when ω equals some certain value, $\omega = \omega^*$, and they will have no other intersections when $\omega < \omega^*$. We formulate this result in form of a Statement 3.

7.1 Statement 3. The above formulated fiber content, ω, minimization problem is solvable if the design problem with the required set of effective stiffnesses and some prescribed ω_0 value is solvable. The ω minimum value is equal to ω^* that corresponds to an intersection of the ray L with the boundary of the set conv Γ. Design project for the composite shell with a minimum fiber content ω^* can be found by solving problem (17), (18) or the problem (23), (18) with a right-hand side equal to $\mathbf{y} = (\omega_0/\omega^*)\mathbf{y}^0$.

8 Design Examples

The developed theory is illustrated by the following two examples of the fiber-reinforced composite shell design.

In the first example, it is required to design a glass/epoxy composite shell with a skew-symmetric placement of the fibers. The shell should have the following effective stiffness moduli: $A_{11} = 25$ GPa, and $A_{22} = 10$ GPa. Young's modulus of fibers

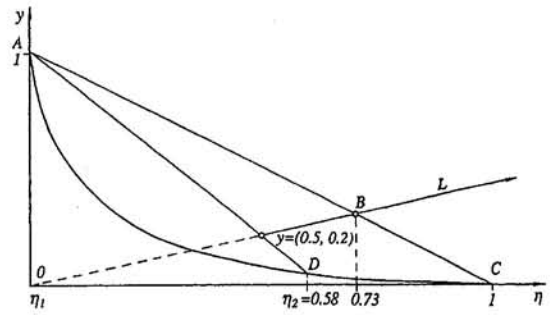

Fig. 3 Curve Γ and the convex hull, conv Γ (area *ABCD*)

is $E = 100$ GPa, and the prescribed fiber volume content is $\omega = 0.5$.

Curve Γ in the considering case is determined as follows (cf. Eq. (25)):

$$\Gamma = \{\mathbf{y} \in R^2: \mathbf{y} = (\eta, (1 - \sqrt{\eta})^2), \quad \eta = \cos^4 \varphi \in [0, 1]\}. \quad (28)$$

Curve Γ and its convex hull (area *ABCD*) are shown in Fig. 3.

The prescribed values $\mathbf{y} = (0.5, 0.2)$ are calculated from the Eqs. (16). It is seen from Fig. 3 that point $\mathbf{y} = (0.5, 0.2)$ belongs to set conv Γ. Consequently, the composite shell with the above prescribed effective stiffnesses can be designed. Let us calculate the design parameters of such composite shell. In fact, the problem (23), (18) can be formulated as a problem of determining the convex combinations of points on curve Γ, that produce a given point $\mathbf{y}$. Apparently, there is an infinite number of points on curve Γ producing given point $\mathbf{y}$. For example, point $\mathbf{y}$ can be obtained as a convex combination of points A and D (see Fig. 3). Introducing subscripts 1 and 2 to coordinates of points A and D, we obtain $\eta_1 = 0$, $\eta_2 = 0.58$. Fiber placement angles φ_1 and φ_2 are expressed in terms of η_1 and η_2 by means of the formula $\varphi_i = \arccos(\eta_i)^{1/4}$, cf. Eq. (25). Using this formula, we obtain $\varphi_1 = 90$ deg and $\varphi_2 \approx 29$ deg. Fiber fractions γ_1 and γ_2 can be also determined from Fig. 3 as follows: $\gamma_1 = |yD|/|AD| \approx 0.14$, and $\gamma_2 = |Ay|/|AD| \approx 0.86$. The resulting four-layer skew-symmetric composite shell design is following: 14 percent reinforcing glass fibers should be placed on angles ±90 deg, and 86 percent of fibers should be placed on angles ±29 deg. Note that the obtained design parameters represent just one of the possible design solutions. However, this is a special design project in the sense that it provides the maximum values of the fiber reinforcing angles. This will simplify significantly the fabrication of the designed composite shell by winding.

8.1 Example on Fiber Volume Content Minimization. In the second example, it is required to design a skew-symmetric composite shell with the effective stiffnesses similar to the above first example, but, unlike of the previous example, it is also required now to minimize the fiber content ω. As it was just shown, the design problem for $\omega = 0.5$ was solvable. Therefore, the design problem including the minimization of ω is solvable as well. Assuming $\omega_0 = 0.5$, and following the above theory, we look for a point of intersection of a ray (cf. Eq. (27))

$$L = \{\mathbf{y}(\omega) = \frac{\omega_0}{\omega}\mathbf{y}^0 = \frac{0.5}{\omega}(0.5, 0.2), \omega \in (0, 0.5)\} \quad (29)$$

with a boundary of the area *ABCD* (see Fig. 3). This point of intersection is denoted by B in Fig. 3, and it has the coordinates (0.73, 0.28). Applying Statement 3 and using Eq. (29), we find that the minimum fiber content is equal to $\omega^* = \omega_0(\mathbf{y}^0/\mathbf{y}) = 0.5(0.5/0.73) \approx 0.34$.

To calculate the design parameters, we should solve the problem (23), (18) with a right-hand side $\mathbf{y}(\omega^*) = (0.73, 0.28)$. It is seen from Fig. 3 that point B can be represented as a convex combination of points of the curve Γ in a unique way, namely, as a convex combination of points A and C. Accordingly, we obtain that $\eta_1 = 0$, $\eta_2 = 1$, and $\varphi_1 = 90$ deg, $\varphi_2 = 0$ deg. The fiber fractions are $\gamma_1 = |BC|/|AC| = 0.27$, and $\gamma_2 = |AB|/|AC| = 0.73$. The resulting design provides the minimum fiber content ($\omega^* = 0.34$) for the above prescribed effective stiffnesses. The designed four-layer symmetric composite shell is formed by two layers with fiber placement angles 90 deg and fiber volume fraction 27 percent, and by two layers with fiber placement angles 0 deg and fiber volume fraction 73 percent.

9 Conclusions

The explicit expressions for the effective stiffness moduli of the high-stiffness fiber-reinforced angle-ply composite shell are obtained. Derivation is based on application of the general homogenization composite shell model. The formulas for the effective stiffnesses provide corrections to the earlier approximate effective moduli results.

The design problem for the fiber-reinforced angle-ply composite shell with the prescribed values of stiffness moduli is formulated and solved using the convex analysis. The set of prescribed effective stiffness values for which the design problem is solvable, is described, and the effective method of the design parameters calculation based on convex analysis is developed. The sufficient number of reinforcing layers required for the design of the fiber-reinforced angle-ply composite shell with the prescribed effective stiffnesses is determined. It is shown in general case that a fiber-reinforced composite shell with any prescribed effective stiffness moduli in the tangential directions to the shell surface that satisfy the solvability condition, can be designed by using not more than five layers of reinforcing fibers. In the case of skew-symmetric fiber-reinforced composite shell, the sufficient number of layers is six, so that a skew-symmetric composite shell with any prescribed effective stiffnesses in the tangential directions that satisfy the solvability condition, can be designed by using not more than three pairs of layers of reinforcing fibers with fiber placement angles $+\varphi_j$ and $-\varphi_j$, $j = 1, 2, 3$.

The design problem is generalized on account of minimization of the fiber content. It is shown that this problem is solvable for any prescribed set of effective stiffnesses for which the design problem is solvable. The effective method of the optimum design parameters calculation is developed.

The effectiveness and advantages of the developed approach are illustrated by the numerical examples.

Acknowledgments

This work has been supported by the Natural Sciences and Engineering Research Council of Canada.

References

Bakhvalov, N. S., and Panasenko, G. P., 1989, *Homogenization: Averaging Processes in Periodic Media,* Kluwer, Dordrecht, The Netherlands.

Bensoussan, A., Lions, J.-L., and Papanicolaou, G., 1978, *Asymptotic Analysis for Periodic Structures,* North-Holland, Amsterdam.

Caillerie, D., 1984, "Thin Elastic and Periodic Plates," *Mathematical Methods in the Applied Sciences,* Vol. 6, pp. 159–191.

Christensen, R. M., 1990, "A Critical Evaluation for a Class of Micromechanics Models," *Journal of the Mechanics and Physics of Solids,* Vol. 38, pp. 379–404.

Christensen, R. M., 1991, *Mechanics of Composite Materials,* Krieger, Malabar, FL.

Duvaut, G., 1976, "Analyse Fonctionnelle et Méchanique des Milieux Continus," *Proceedings of the 14th IUTAM Congress, Delft, 1976,* Amsterdam, pp. 119–132.

Hashin, Z., 1983, "Analysis of Composite Materials—A Survey," ASME JOURNAL OF APPLIED MECHANICS, Vol. 50, pp. 481–505.

Kalamkarov, A. L., 1987, "On the Determination of Effective Characteristics of Cellular Plates and Shells of Periodic Structure," *Mechanics of Solids,* Vol. 22, pp. 175–179.

Kalamkarov, A. L., 1989, "Thermoelastic Problem for Structurally Non-Uniform Shells of Regular Structure," *Journal of Applied Mechanics and Technical Physics,* Vol. 30, pp. 981–988.

Kalamkarov, A. L., 1992, *Composite and Reinforced Elements of Construction,* John Wiley and Sons, New York.

Kalamkarov, A. L., 1993, "Analysis and Design of Thin-Walled Composite Structural Members," *Proceedings of the Second Canadian International Composites Conference,* Canadian Association for Composite Structures and Materials, Montreal, pp. 741–748.

Kalamkarov, A. L., and Kolpakov, A. G., 1993, "Numerical Design of Thin-Walled Structural Members on Account of their Strength," *International Journal for Numerical Methods in Engineering,* Vol. 36, pp. 3441–3449.

Kohn, R. V., and Vogelius, M., 1984, "A New Model for Thin Plates with Rapidly Varying Thickness," *International Journal of Solids and Structures,* Vol. 20, pp. 333–350.

Lewinski, T., 1992, "Homogenizing Stiffnesses of Plates with Periodic Structure," *International Journal of Solids and Structures,* Vol. 29, pp. 309–326.

Lions, J.-L., 1981, *Some Methods in the Mathematical Analysis of Systems and their Control,* Gordon and Breach, New York.

Milton, G. W., and Kohn, R. V., 1988, "Variational Bounds on the Effective Moduli of Anisotropic Composites," *Journal of the Mechanics and Physics of Solids,* Vol. 36, pp. 597–629.

Nemat-Nasser, S., and Hori, M., 1993, *Micromechanics Overall Properties of Heterogeneous Solids,* Elsevier, Amsterdam.

Obraztsov, I. F., and Vasiliev, V. V., 1989, "Optimal Design of Composite Structures," *Handbook of Composites, Vol. 2, Structures and Design,* C. T. Herakovich and Y. M. Tarnopol'skii, eds., North-Holland, Amsterdam, pp. 3–84.

Rockafellar, R. T., 1970, *Convex Analysis,* Princeton University Press, Princeton, NJ.

Sanchez-Palencia, E., 1980, *Non-Homogeneous Media and Vibration Theory,* Springer, Berlin.

Sendeckyj, G. P., 1974, "Elastic Behavior of Composites," *Composite Materials, Vol. 2. Mechanics of Composite Materials,* Academic Press, New York.

Tsai, S. W., 1992, *Theory of Composites Design,* Think Composites, Dayton, OH.

Vasiliev, V. V., 1993, *Mechanics of Composite Structures,* Taylor & Francis, Washington, DC.

Vasiliev, V. V., and Tarnopol'skii, Yu. M., 1990, *Composite Materials,* Mashinostroenie, Moscow (in Russian).

Vinson, J. R., 1993, *The Behavior of Shells Composed of Isotropic and Composite Materials,* Kluwer, Dordrecht.

Vinson, J. R., and Sierokowski, R. L., 1986, *The Behavior of Structures Composed of Composite Materials,* Nijhoff, Dordrecht.

Voitkov, N. I., 1979, "Optimal Design of Composite Plates Under Buckling," *Mechanics of Composite Materials,* Riga Polytechnic Institute, Riga, pp. 86–94 (in Russian).

Weng, G. J., Taya, M., and Abé, H. eds., 1990, *Micromechanics and Inhomogeneity—The T. Mura 65th Anniversary Volume,* Springer, New York.

Random Field Representation and Synthesis Using Wavelet Bases

B. A. Zeldin
Research Associate.

P. D. Spanos
Ryon Chair in Engineering,
Fellow ASME.

George R. Brown School of Engineering,
Department of Mechanical Engineering,
MS 321
Rice University
Houston, TX 77251

The paper addresses the representation and simulation of random fields using wavelet bases. The probabilistic description of the wavelet coefficients involved in the representation of the random field is discussed. It is shown that a broad class of random fields is amenable to a simplified representation. Further, it is shown that a judicious use of the local and multiscale structure of Daubechies wavelets leads to an efficient simulation algorithm. The synthesis of random field samples is based on a wavelet reconstruction algorithm which can be associated with a dynamic system in the scale domain. Implementation aspects are considered and simulation errors are estimated. Examples of simulating random fields encountered in engineering applications are discussed.

1 Introduction

Monte Carlo simulation is a quite powerful, though computationally costly tool for analyzing systems which exhibit randomness. This method is a statistical sampling experiment (Rubinstein, 1981) involving a series of simulations of the random parameters and subsequent evaluation of the system response using deterministic methods. Often the randomness inherent in the problem involves random fields. In this case the implementation of the Monte Carlo procedure requires sequential synthesis of random fields, and to a great extent its appeal depends on the efficiency of the algorithm used for this purpose. The spectral (Shinozuka and Jan 1972) and auto-regressive-moving-average (ARMA) (Samaras et al., 1983; Mignolet and Spanos, 1992; Spanos and Mignolet, 1992) approaches are the commonly used methods in this regard. However, these methods are not well suited for random field simulation using nonuniform meshes. Also, enhancement of local resolution of random field samples can not be readily achieved using these simulation procedures.

Scale-type methods (Fournier et al., 1981; Lewis, 1987; Fenton and Vanmarcke, 1990) were introduced primarily for computer graphics applications; the simulation is based on linear estimation principles. The values of the random field for points within a coarse scale are generated first. Then, the values for the finer scale are estimated based on the generated samples. These methods provide an efficient procedure for simulation of homogeneous and nonhomogeneous fields using nonuniform meshes. However, they lack a solid theoretical foundation for estimating the associated simulation errors.

This paper addresses the problem of random field simulation by using wavelet expansion. Wavelets can be found in several branches of engineering and science and they appeal to scientists and engineers of various backgrounds (Daubechies, 1992). The paper provides a basis for evaluating the error of the scale-type methods and for considering the properties of the generated samples. The scale-type simulation procedure is viewed as a realization of a dynamic system in the scale domain. The proposed algorithm for random field simulation requires only $O(N)$ numerical operations for the generation of a sample of a homogeneous multidimensional random field, where N denotes the size of the field. Numerical examples are given to elucidate the theoretical developments.

Contributed by the Applied Mechanics Division of THE AMERICAN SOCIETY OF MECHANICAL ENGINEERS for publication in the ASME JOURNAL OF APPLIED MECHANICS.

Discussion on this paper should be addressed to the Technical Editor, Professor Lewis T. Wheeler, Department of Mechanical Engineering, University of Houston, Houston, TX 77204-4792, and will be accepted until four months after final publication of the paper itself in the ASME JOURNAL OF APPLIED MECHANICS.

Manuscript received by the ASME Applied Mechanics Division, June 2, 1995; final revision, Apr. 24, 1996. Associate Technical Editor: M. Shinozuka.

2 Background on Deterministic Wavelet Analysis

Orthogonal compactly supported wavelet bases of $L^2(R)$ constructed by Daubechies (1988) are used in this study. Generally, they can be written as

$$\{\psi_{j,n}(x) = 2^{-j/2}\psi(2^{-j}x - n + 1); j, n \in Z\}, \quad (1)$$

where $\psi(x)$ is a wavelet function with support in the segment $[0; 2M - 1]$; M is an integer parameter. Equation (1) shows that the entire wavelet basis is derived from a single function by stretching and shifting. This construction leads to the important concept of a scale. The scale is given by the parameter j and describes the measure of stretching of the wavelet function to capture local signal characteristics.

Also important in wavelet analysis is the scale function $\phi(x)$. In fact, the wavelet function $\psi(x)$ is related to $\phi(x)$ by the equation

$$\psi(x) = \sqrt{2}\sum_{k=0}^{2M-1} g_{k+1}\phi(2x - k), \quad (2)$$

where

$$\phi(x) = \sqrt{2}\sum_{k=0}^{2M-1} h_{k+1}\phi(2x - k), \quad (3)$$

where g_k and h_k are appropriate constants. Closed-form formulae for the functions $\phi(x)$ and $\psi(x)$ are not available, unless $M = 1$. Several algorithms have been proposed in the literature for evaluating these functions numerically. One of them utilizes the frequency domain relationships

$$\hat{\phi}(\omega) = m_0(\omega/2)\hat{\phi}(\omega/2), \quad (4)$$

and

$$\hat{\psi}(\omega) = m_1(\omega/2)\hat{\phi}(\omega/2), \quad (5)$$

between the wavelet and scale functions. Here, the hat denotes a symbol of the Fourier transform

$$\hat{\phi}(\omega) = \frac{1}{\sqrt{2\pi}} \int_{-\infty}^{\infty} \phi(x) e^{-i\omega x} dx, \tag{6}$$

and the 2π-periodic functions $m_0(\omega)$ and $m_f(\omega)$ are defined as

$$m_0(\omega) = \frac{1}{\sqrt{2}} \sum_{k=0}^{2M-1} h_{k+1} e^{-ik\omega}, \tag{7}$$

$$m_1(\omega) = \frac{1}{\sqrt{2}} \sum_{k=1}^{2M-1} g_{k+1} e^{-ik\xi} = e^{-i(M-1)\omega} \overline{m_0(\omega + \pi)}, \tag{8}$$

respectively; the bar denotes complex conjugation. It can be shown that the functions $m_0(\omega)$ of Eq. (7) and $m_1(\omega)$ of Eq. (8) represent the frequency response of a low-pass filter and a high-pass filter, respectively; this makes the wavelet expansion equivalent to a "subband filtering algorithm" (Daubechies, 1992). These filters tend to the ideal low and high pass filters, respectively, as $M \to \infty$. In this case the Daubechies wavelets converge to the Shannon wavelets which relate directly to the sampling theorem (Walter, 1994). The latter wavelets have been also examined by Newland (1993) who defined them as harmonic wavelets.

Wavelets have a number of vanishing moments. That is,

$$\int_{-\infty}^{\infty} x^l \psi(x) dx = 0, \quad \text{for} \quad l = 0, \quad 1, \ldots, m, \tag{9}$$

where $m = M - 1$ for the Daubechies wavelets; this property of the Daubechies wavelets is particularly useful for random field analysis applications since the wavelet coefficients can be associated with the high-frequency components from certain bands. Also, it can be shown, based on Eq. (9), that $d_k^j \sim f^{(M)}(2^{-j}(k-1))$; that is, the wavelet transformation can be viewed as a quasi-differential operator (Belkin, 1993). Note that the scale function satisfies the property

$$\int_{-\infty}^{\infty} \phi(x) dx = 1. \tag{10}$$

That is, the coefficients associated with the scale function capture the averaged characteristics of the signal.

Any function $f(x)$ can be expanded in a wavelet basis in $O(N)$ operations without numerical integration. The wavelet decomposition algorithm can be compared with the fast Fourier transform which requires only $O(N \log N)$ operations to derive an expansion in the basis of trigonometric functions. First, the function $f(x)$ is approximated by its projection into the jth scale of the function $\phi(x)$, where j must be taken sufficiently small to induce a small approximation error. That is,

$$f(x) \approx f_j(x) = \sum_k c_k^j \phi_{j,k}, \tag{11}$$

where $c_k^j = \int_{-\infty}^{\infty} f(x)\phi_{j,k}(x)dx$ are the scale coefficients of the function $f(x)$ associated with the scale j. Then, the function $f_j(x)$ can be decomposed into the components $f_{j+1}(x)$ and $\delta_{j+1}(x)$, which represent the projection of the function $f(x)$ into the coarser scale, and the "details" which are "removed" during this procedure. Subsequently, the following expansion of the function $f(x)$ in terms of the wavelet basis is introduced:

$$f_j(x) = f_{j+1}(x) + \delta_{j+1}(x) = f_{j+l}(x) + \delta_{j+1}(x) + \ldots \delta_{j+l}(x)$$
$$\approx \delta_{j+1}(x) + \ldots \delta_{j+l}(x), \tag{12}$$

where

$$\delta_j = \sum_k d_k^j \psi_{j,k}, \tag{13}$$

and $d_k^j = \int_{-\infty}^{\infty} f(x)\psi_{j,k}(x)dx$ denote the wavelet coefficients of the function $f(x)$. Numerically, the wavelet decomposition algorithm can be represented by the recursive equations

$$c_k^j = \sum_{l=0}^{2M-1} h_{l+1} c_{2k+l-1}^{j-1}, \tag{14}$$

and

$$d_k^j = \sum_{l=0}^{2M-1} g_{l+1} c_{2k+l-1}^{j-1}. \tag{15}$$

Note that this recursive multiscale procedure represents a moving average scheme with the moving averages sampled only at even integers.

The reconstruction algorithm can be expressed as

$$c_k^{j-1} = \langle f_{j-1}, \phi_{j-1,k} \rangle = \langle \sum_l c_l^j \phi_{j,l} + \sum_l d_l^j \psi_{j,l}, \phi_{j-1,k} \rangle$$
$$= \sum_l (c_l^j h_{k-2l+2} + d_l^j g_{k-2l+2}). \tag{16}$$

Equation (16) defines a dynamic relationship between the coefficients on one scale and those on the next finer scale. Indeed, the vector $\mathbf{c}^{j-1}$ is derived by a dynamic system from the initial conditions in the form of the vector $\mathbf{c}^j$ and the "force excitation" $\mathbf{d}^j$. The interpretation of the wavelet reconstruction algorithm as a scale linear system is discussed in Basseville et al. (1992a, b); it is essential to the development of the random fields representation and synthesis algorithm presented in the ensuing sections.

3 Random Field Expansion Using Wavelet Basis

3.1 Random Coefficient Description. In the stochastic case the wavelet coefficients d_k^j in Eq. (13) and the scale coefficients c_k^j in Eq. (11), which are associated with a stochastic process $f(x)$, defined by its auto-correlation function $R_f(x_1, x_2)$, are random variables. In particular, if $f(x)$ is zero mean, the wavelet and scale coefficients are zero mean random variables. Further, the second-order moments of these coefficients can be found from the equations (Walter, 1994; Zeldin and Spanos, 1995)

$$r_{k,l}^{j,i} = E[d_k^j d_l^i]$$
$$= \iint R_f(x_1, x_2)\psi_{j,k}(x_1)\psi_{i,l}(x_2)dx_1 dx_2, \tag{17}$$

$$b_{k,l}^{j,i} = E[c_k^j d_l^i] = \iint R_f(x_1, x_2)\phi_{j,k}(x_1)\psi_{i,l}(x_2)dx_1 dx_2, \tag{18}$$

$$a_{k,l}^{j,i} = E[c_k^j c_l^i] = \iint R_f(x_1, x_2)\phi_{j,k}(x_1)\phi_{i,l}(x_2)dx_1 dx_2, \tag{19}$$

where $E[\ ]$ denotes the operator of mathematical expectation. Note that if $f(x)$ is a stationary random process, the value $r_{k,l}^{j,i}$ depends on the difference in the indices $k - 2^{j-i}l$, only. Similarly, higher-order moments of coefficients d_k^j can be found. If $f(x)$ is a Gaussian random process, d_k^j, $k = \ldots -1, 0, 1, \ldots$ are also Gaussian random variables. In this case d_k^j and c_k^j are completely characterized by their first and second-order moments.

In this context the wavelet decomposition algorithm described in Section 2 is generalized to circumvent the numerical integration involved in Eqs. (17)–(19). Specifically, one can write

$$r_{k,l}^{j,j} = \sum_{n,m=0}^{2M-1} g_{n+1} g_{m+1} a_{2k+n-1,2l+m-1}^{j-1,j-1}, \tag{20}$$

$$b_{k,l}^{j,j} = \sum_{n,m=0}^{2M-1} h_{n+1} g_{m+1} a_{2k+n-1,2l+m-1}^{j-1,j-1}, \tag{21}$$

and

$$a_{k,l}^{j,j} = \sum_{n,m=0}^{2M-1} h_{n+1}h_{m+1}a_{2k+n-1,2l+m-1}^{j-1,j-1}, \quad (22)$$

where the procedure is initiated by evaluating first the correlation parameters $a_{k,l}^{j,j}$ for the finest scale. Similar procedures, in a deterministic setting however, have been previously used to find a representation of mathematical operators in wavelet bases (Belkin et al., 1991). Clearly, this computationally costly scheme requires $O(N^2)$ and $O(N)$ operations for nonstationary and stationary processes, respectively. Alternatively, one can use the quadrature algorithm

$$a_{k,l}^{j,j} = 2^j \sum_{n,m=0}^{q-1} \eta_n\eta_m R_f(2^j n + 2^j(k-1), 2^j m + 2^j(l-1)) + \epsilon, \quad (23)$$

where the coefficients η_n are selected so that ϵ is null if $R_f(x_1, x_2)$ is a polynomial in x_1 and x_2 of order less than q. This implies that $\epsilon \sim O(2^{j(q+1)})$. The coefficients η_n of Eq. (23) can be found from the following system of equations:

$$\sum_{l=0}^{q-1} l^m\eta_l = \Gamma_m, \quad m = 0, \quad 1, \ldots q-1. \quad (24)$$

Here, $\Gamma_m = \int_{-\infty}^{\infty} x^m\phi(x)dx$ are the moments of the scale function; they can be calculated semianalytically as shown in Appendix A. Upon evaluating the parameters $a_{k,l}^{j,j}$ in the neighborhood of the main diagonal of the correlation matrix, $r_{k,l}^{j+1,j+1}$ and $b_{k,l}^{j+1,j+1}$ can be determined by using Eqs. (20)–(22). Note that usually the auto-correlation function $R(x_1, x_2)$ decreases rapidly with the difference $x_2 - x_1$, and only a few coefficients $a_{k,l}^{j,j}$, $r_{k,l}^{j,j}$, and $b_{k,l}^{j,j}$ corresponding to small values of $l - k$ must be evaluated; for more details see Zeldin (1995). The described procedure requires only $O(N)$ and $O(\log N)$ numerical operations for nonstationary and stationary processes, respectively.

3.2 Correlation Properties of Wavelet Coefficients of Random Fields. The correlation of the wavelet coefficients for certain random processes has been previously addressed. Specifically, Flandrin (1989, 1992) has studied an efficient scheme to describe the spectrum of fractional Brownian motions (Keshner, 1982) which constitute a class of nonstationary processes often called $1/f$ noises. It has been found that for a given scale these processes are stationary with well-defined scale invariant spectra. Further, Wornell (1990) has shown that completely uncorrelated wavelet coefficients can be used to model $1/f$ noises. A similar result has been reported by Tewfik and Kim (1992). Using this result Wornell and Oppenheim (1992) have proposed a method of estimating parameters of $1/f$ noises.

This section establishes the correlation properties for a broad class of stochastic processes which are commonly used in engineering applications. As it has been mentioned previously, wavelets behave locally as differential operators. This property simplifies significantly the correlation structure of the wavelet coefficients for a large class of stochastic processes. Thus, the variance of the wavelet coefficients decreases rapidly with the scale of resolution j. In particular, for a sufficiently fine scale one can prove that

$$r_{k,l}^{j,j}/a_{k,l}^{j,j} \sim 2^{jQ}, \quad (25)$$

provided that the auto-correlation function is at least Q times differentiable; $Q \leq M$. Equation (25) indicates that the importance of scales decays exponentially with j. Using this result one can argue that a few scales can provide a reasonably accurate representation of the random field.

In context with the preceding result it is noted that the covariance matrix of the wavelet coefficients is sparse for a large class of random fields. For stationary processes the correlation of the wavelet coefficients from different scales can be evaluated by using the equation

$$r_{k,l}^{j,i} = 2\pi \int_{-\infty}^{\infty} S(\omega)\hat{\psi}_{j,k}(\omega)\overline{\hat{\psi}_{i,l}(\omega)}\,d\omega, \quad (26)$$

where $S(\omega)$ is the spectrum of the stationary process. Since the functions $\hat{\psi}_{j,k}(\omega)$ and $\hat{\psi}_{i,l}(\omega)$ correspond to different frequency bands for $i \neq j$, the correlation of the wavelet coefficients from different scales is small. Thus, by substituting Eqs. (4)–(8) into Eq. (26) one obtains

$$|r_{k,l}^{j,i}| \leq \max(S(\omega)) \int_0^{\pi} \chi_{|j-i|}(\omega)d\omega, \quad (27)$$

where

$$\chi_k(\omega) = 2^{2+(k/2)}|m_0(\omega+\pi)||m_0(2^k\omega+\pi)| \prod_{l=0}^{k-1} |m_0(2^l\omega)|. \quad (28)$$

The function $\chi_k(\omega)$ is plotted in Fig. 2 for wavelets with $M = 1$ and $M = 7$ vanishing moments. Note that the "decorrelation" capacity of wavelets increases with the number of vanishing moments. Germane to this issue is the estimate of the cross-scale correlation of wavelet coefficients presented by Dijkerman and Mazumdar (1994) for Gauss-Markov processes with exponential auto-correlation functions by using a time domain approach.

Relying on the similarity between the auto-correlation function and the kernel of a linear operator, the weakening of the correlation of the wavelet coefficients from the same scale can be determined for some stochastic fields. Specifically, for a

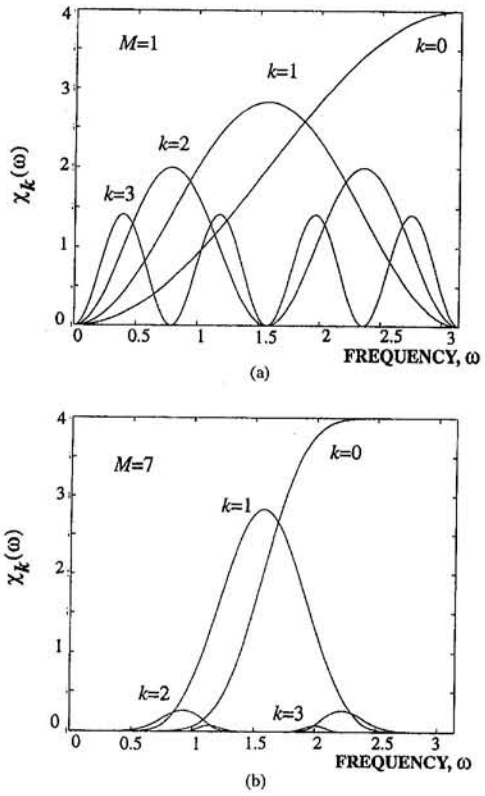

Fig. 1 Function $\chi_k(\omega)$ for wavelets with (a) $M = 1$ vanishing moment, (b) $M = 7$ vanishing moments

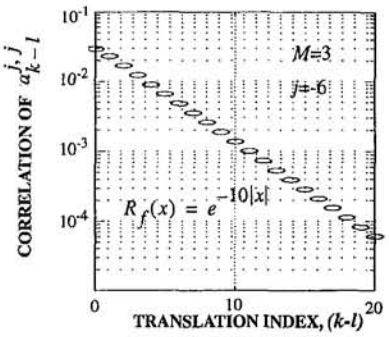

Fig. 2 Correlation parameters a_{k-l} for the scale $j = -6$

stationary random process $f(x)$ having the auto-correlation function

$$R_f(x_1, x_2) \sim |x_1 - x_2|^{-\mu}, \tag{29}$$

and with partial derivatives of order $2Q$

$$\frac{\partial^{2Q}}{\partial x_1^{\nu} \partial x_2^{2Q-\nu}} R_f(x_1, x_2) \sim |x_1 - x_2|^{-\mu-2Q}, \tag{30}$$

where μ and ν are constants, one can show that for wavelets associated with $M \geq Q$

$$a_{k,l}^{j,j} \sim |k - l|^{-\mu} \quad \text{and} \quad r_{k,l}^{j,j} \sim (k - l)^{-\mu-2Q}. \tag{31}$$

These stochastic processes form the so-called Meyer-Belkin class. Equation (31) indicates that the correlation of the scale coefficients decreases faster, especially for large values of M, than the correlation of the scale coefficients. Pertinent numerical examples can be found in Zeldin (1995).

Finally, it has been observed that if the auto-correlation function of a stochastic process has some irregularities along the diagonal $x_1 = x_2$, the covariance matrix of the wavelet coefficients within a scale resembles a diagonally dominant matrix. Thus, wavelets whiten Gauss-Markov processes having auto-correlation functions which are nondifferentiable along the diagonal. In this case wavelets act as semidifferential operators, and point out the diagonal singularity of the auto-correlation function. For the Gauss-Markov process with auto-correlation function

$$R_f(x_2 - x_1) = \exp(|x_2 - x_1|/\theta), \quad \theta = 0.1, \tag{32}$$

the correlation parameters $a_{k,l}^{j,j}$ and $r_{k,l}^{j,j}$ are plotted for $j = -6$ in Fig. 2 and Fig. 3, respectively. The wavelets with $M = 3$ vanishing moments are used. It can be seen that the correlation of the wavelet coefficients is quite weak.

4 One-Dimensional Random Field Simulation

4.1 Mathematical Formulation. Upon developing the random field representation by employing the wavelet basis, numerical simulations can be performed by extending the wavelet reconstruction algorithm described by Eq. (16) to the case of random fields. In this case, assume that the stochastic process $f(x)$ is defined by its auto-correlation function $R_f(x_1, x_2)$ and denote by $f_j(x)$ the projection of $f(x)$ into the scale j of the function $\phi(x)$. This projection is specified by the random vector $\mathbf{c}^j = \{c_1^j, \ldots c_\kappa^j\}$, $\kappa = 2^{-j}$. Note that the number of components of $\mathbf{c}^j$ is quite small for a sufficiently coarse scale. Then, a realization of $\mathbf{c}^j$ can be generated by performing the Cholesky factorization of its covariance matrix. This provides a sample of the projection $f_j(x)$ which is used to initiate the simulation of $f(x)$ for finer scales. Thus, the projection of $f(x)$ into the next $(j - 1)$th scale can be found by simulating the random vector $\mathbf{d}^j = \{d_1^j, \ldots d_\kappa^j\}$; $\mathbf{c}^{j-1}$ can be determined by relying on the wavelet reconstruction algorithm, Eq. (16). Next, the random vector $\mathbf{c}^{j-2}$ can be simulated based on the realization of $\mathbf{c}^{j-1}$ and a simulation of $\mathbf{d}^{j-1}$. This hierarchical procedure generates a sample of the stochastic process $f(x)$.

For a relatively fine scale, the problem of simulating a large dimension random vector with correlated components is rather complex. In this context it is noted that the random variables c_k^j and d_k^j are defined as an average of the stochastic process $f(x)$ over the same domain weighted by the scale and wavelet functions, respectively. It can be shown using the quasi-differential properties of wavelets that $c_k^j \sim f(2^{-j}(k - 1))$ and $d_k^j \sim f^{(M)}(2^{-j}(k - 1))$. Clearly, the derivatives $f^{(M)}(x)$ can be approximated reliably by a finite difference scheme. Thus, one can approximate the coefficient d_k^j by a linear combination of the components of the vector $\mathbf{c}^j$ in the form

$$d_k^j = \sum_l \alpha_{k,l}^j c_l^j + \beta_k^j u_k, \tag{33}$$

where u_k, $k = 1, 2, \ldots$, are uncorrelated zero mean, unit variance random variables which are statistically independent of $\mathbf{c}^j$.

Equation (33) also reflects the assumption that the components of the vector $\mathbf{d}^j$ are statistically independent, given a realization of $\mathbf{c}^j$. Note that this approximation does not imply that the components of $\mathbf{d}^j$ are unconditionally statistically independent, but rather that their dependence is completely reflected by a linear combination of the components of $\mathbf{c}^j$. Equation (33) can be used to simulate efficiently the random vector $\mathbf{d}^j$ based on a realization of $\mathbf{c}^j$. Alternatively, Eq. (33) can be interpreted as reflecting the best linear estimate of the wavelet coefficients in the jth scale by using the scale coefficients in the same scale. This interpretation provides an analog between the proposed method and the scale dynamic linear systems on homogeneous trees (Basseville et al., 1992a, b; Clippingdale and Wilson, 1989; Dijkerman and Mazumdar, 1994; Luettgen et al., 1994).

Note that the summation in Eq. (33) can be confined to adjacent elements, since the correlation of the wavelet coefficients decreases rapidly with the difference $k - l$. The parameters $\alpha_{k,l}^j$ in Eq. (33) can be computed in an optimal way so that the covariance matrices of the wavelet and scale coefficients are well approximated. In particular, the variance of the wavelet coefficients d_k^j and the cross-correlation of the wavelet and the scale coefficients can be equated to the target values. Thus, multiplying Eq. (33) by c_{k+i}^j, $i = -n, \ldots n$ and taking mathematical expectation one finds

$$\sum_{l=-n}^{n} \alpha_{k,l}^j a_{k+l,k+i}^{j,j} = b_{k+i,k}^{j,j}, \; i = -n, \ldots n. \tag{34}$$

The matrix in Eq. (34) is symmetric and positive definite; if the stochastic process is stationary, this is a Toeplitz matrix. This system can be solved without significant computational effort since the number of equations, $2n + 1$, is small. Further,

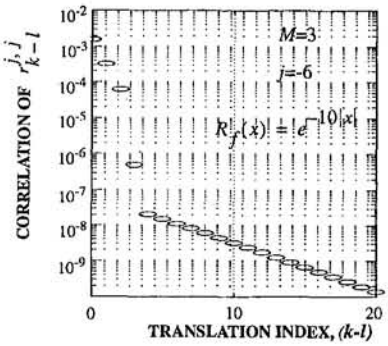

Fig. 3 Correlation parameters r_{k-l} for the scale $j = -6$

the parameter β_k^j can be found by squaring Eq. (33) and taking the mathematical expectation. That is,

$$\beta_k^j = \sqrt{r_{k,k}^j - \sum_{l=-n}^{n} \sum_{i=-n}^{n} \alpha_{k,l}^j \alpha_{k,i}^j a_{k+l,k+i}^j}. \tag{35}$$

Clearly, for the stationary case, Eqs. (34) and (35) must be solved only once for every scale j.

Note that the pyramid structure of the proposed simulation algorithm breaks down in some neighborhood of the boundary. In the present study this problem is addressed by incorporating boundary layers adjoined to the domain of interest. Alternatively, periodic wavelets and functions (Daubechies, 1992) can be used.

Finally, note that the scale-type simulation methods which have been previously introduced in the literature are a rather special case of the proposed approach. Specifically, the Local Average Subdivision method (Fenton and Vanmarcke, 1990; Fenton, 1994) can be reproduced by utilizing the Haar basis ($M = 1$) in the preceding development, whereas the method of Lewis (1987) can be formulated based on the Shannon wavelets ($M = \infty$).

4.2 Error Analysis. The error introduced by Eq. (33) can be assessed numerically in the following manner. Assume that the process is simulated within the jth scale exactly. Also assume that the wavelet coefficients $\mathbf{d}^j$ are found by using the proposed method, Eqs. (33)–(35), and the scale coefficients on the $(j-1)$th scale are determined by relying on the wavelet reconstruction algorithm. Using these assumptions and performing some rather simple mathematical calculations, one can derive the estimated correlation of $\mathbf{d}^j$ and $\mathbf{c}^{j-1}$ which can be compared with the target values. Some numerical results of performing this analysis for $\mathbf{c}^{j-1}$ are shown in Fig. 4. The corresponding auto-correlation function is defined by the equation

$$R(x_1, x_2) = 1/(1 + (x_1 - x_2)^2/\theta^2), \tag{36}$$

where $\theta = 0.1$ is selected, and the Daubechies wavelets with $M = 3$ are utilized. The maximum of the absolute error of estimating the correlation of the scale coefficient normalized by $a_{k,k}^{j,j}$ is plotted as a function of j and n. The error is quite small for fine scales and reaches the maximum value, equal approximately to four percent, for the scale (-2). The mesh size which corresponds to this scale is approximately equal to the scale of fluctuation (Vanmarcke, 1983) of this stochastic process.

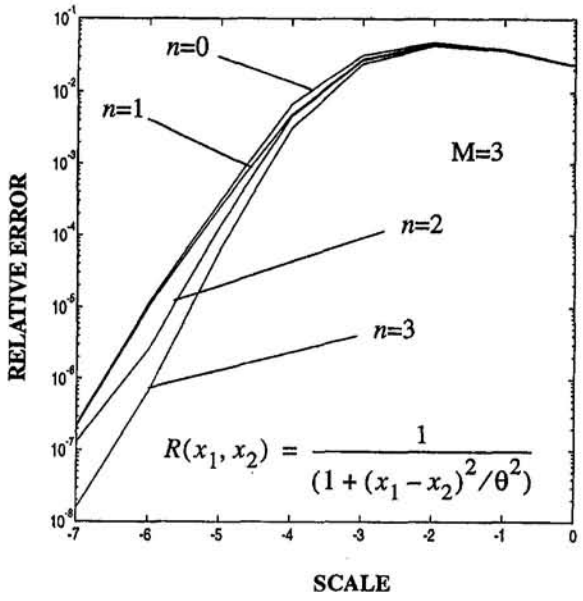

Fig. 4 The maximum of the error of estimation of the scale coefficients

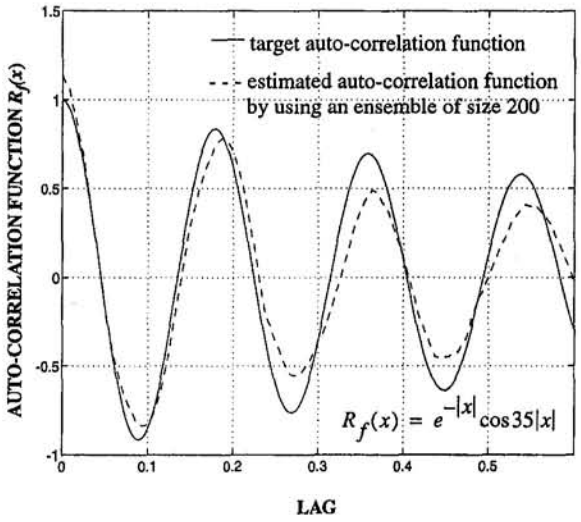

Fig. 5 Auto-correlation function for target and simulated processes

Further, note that the wavelet reconstruction algorithm which is used to determine the wavelet coefficients on the $(j-1)$th scale induces filtering of the wavelet coefficients by a high-pass filter, see Eq. (16). Then, this filter eliminates the low-frequency error and allows only the high frequency error. Further, the high-frequency range for the scale j becomes low frequency for the scale $j-1$. Thus, the error induced by Eq. (33) occurs in different frequency ranges for each scale.

4.3 Algorithm of the Proposed Method. Summarizing the preceding discussion, the proposed algorithm for synthesizing random fields specified by the auto-correlation function $R_f(x)$ can be formulated as follows:

1 Select a wavelet basis; pertinent numerical studies suggest that the Daubechies wavelets with $M = 3$ are quite adequate for forms of $R_f(x)$ encountered in most engineering applications. Note that these wavelets are differentiable functions and the generated field can be readily used in applications necessitating differentiation of the generated field samples.

2 Find the correlation of the wavelet and scale coefficients as discussed in Section 3.

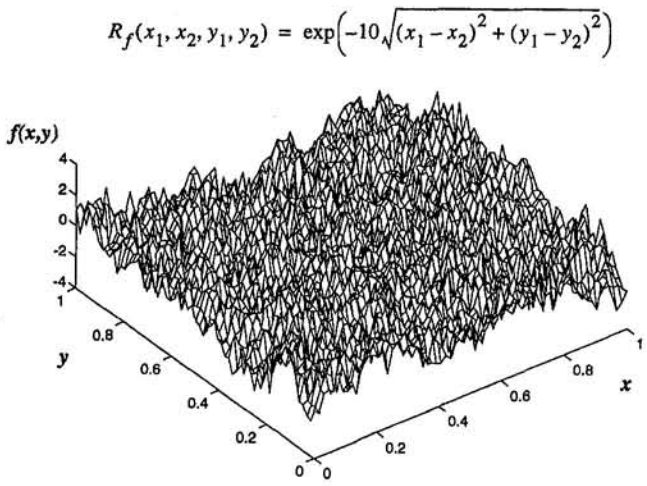

Fig. 6 A synthesized realization of a two-dimensional random field

3 Synthesize a sample of the random process for a relatively coarse scale j by simulating a small-dimensional vector $\mathbf{c}^j$; the Cholesky factorization of the covariance matrix of $\mathbf{c}^j$ is deemed appropriate for this purpose.

4 Generate the vector $\mathbf{d}^j$ by using Eq. (33).

5 Based on the realizations of $\mathbf{c}^j$ and $\mathbf{d}^j$, synthesize a sample of the random process on the next $(j-1)$ scale by using the wavelet reconstruction algorithm of Eq. (16).

6 If the ratio of the variance of the wavelet coefficients to the variance of the scale coefficients is not adequately small, proceed to a refined scale and return to Step 4.

Each step of the proposed algorithm requires, at most, $O(N)$ numerical operations. Moreover, the decorrelation and multiscale properties of wavelets ensure that the requisite number of parameters in Eq. (33) is small.

4.4 Numerical Simulations. Samples of a Gaussian stationary stochastic process with the auto-correlation function

$$R(x_1, x_2) = \exp(-|x_1 - x_2|/\theta) \cos(\lambda|x_1 - x_2|) \quad (37)$$

were generated using the Daubechies wavelets with $M = 3$; the values $\theta = 1$ and $\lambda = 35$ are used. The target auto-correlation function and its estimate involving 200 synthesized samples are plotted in Fig. 5. It is clear that the proposed method approximates the auto-correlation function quite closely.

5 Multidimensional Extension

The proposed random field analysis and synthesis method can be generalized for multidimensional fields by utilizing multidimensional wavelet bases.

There are several methods of constructing multidimensional wavelets (Daubechies, 1992). One of them is based on the tensor product of pertinent one-dimensional multiresolution analyses. In the two-dimensional case it leads to three wavelet functions defined as

$$\Psi^{(1)}(x, y) = \phi(x)\psi(y),$$

$$\Psi^{(2)}(x, y) = \psi(x)\phi(y),$$

and

$$\Psi^{(3)}(x, y) = \psi(x)\psi(y).$$

Note that the set of functions

$$\Psi^{\lambda}_{j;n_1,n_2} = 2^{-j}\Psi^{\lambda}(2^{-j}x - n_1 + 1, 2^{-j}y - n_2 + 1);$$
$$j, n_1, n_2 \in Z, \lambda = 1, 2, 3 \quad (38)$$

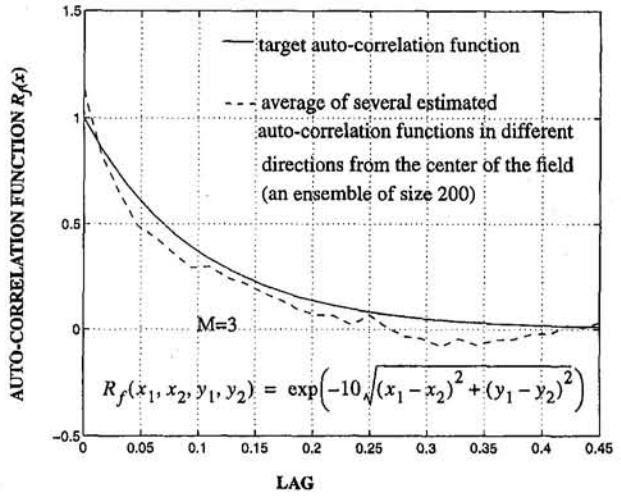

Fig. 7 Auto-correlation function for target and simulated processes

Table 1 The number of floating operations to generate a single random field sample using the proposed algorithms

Type of random fields	Size of random fields	Number of kflops		
		$M = 1$	$M = 2$	$M = 3$
Two-dimensional	32×32	76	150	246
	64×64	222	403	607
	128×128	741	1,269	1,796
	256×256	2,696	4,451	6,077
	512×512	10,272	16,643	22,293

is an orthonormal basis for $L^2(R^2)$. This procedure for constructing two-dimensional wavelets can be generalized, readily, to the n-dimensional case leading to $2^n - 1$ wavelets.

Then, the developments of Sections 3 and 4 can be properly adapted for multidimensional field simulation. This procedure yields a set of equations, similar to Eqs. (17)–(23), (33)–(35), involving multiple integrals and sums. These equations lead to an efficient algorithm for simulating multidimensional random fields. A sample of a two-dimensional field generated by implementing the proposed method in conjunction with the Daubechies wavelets with $M = 3$ is shown in Fig. 6; the auto-correlation function

$$R(x_1, x_2, y_1, y_2) = \exp(-\sqrt{(x_1 - x_2)^2 + (y_1 - y_2)^2}/\theta) \quad (39)$$

with $\theta = 0.1$ was used. The average of several estimates of the auto-correlation function in different directions from the center of the domain of the random field is shown in Fig. 7; the ensemble size in each direction is 200 field samples.

6 Concluding Remarks

The proposed method is computationally efficient due to the reduction of the requisite data storage capacity and the small number of numerical calculations which are necessary for synthesizing a single random field sample.

To perform the synthesis for a given scale, one has to store the scale and wavelet coefficients from the coarser scale. Thus, it is required to store $2N$ elements. Also it is required to store the coefficients of the equations which approximate the wavelet coefficients using the scale coefficients. For the homogeneous case it is further required to store $O(\log N)$ numbers, while for general random fields $O(N)$ additional storage locations are needed.

The number of calculations for a single simulation is determined by the selected implementation scheme of the wavelet reconstruction algorithm, and by the transformation of the scale coefficients into the wavelet coefficients. Efficient procedures for the wavelet reconstruction algorithm are discussed in Herley and Vetterli (1993) which can prove particularly advantageous for large values of M. In any case, the proposed simulation method requires at most $O(N)$ operations for synthesizing a random field sample. Table 1 compares the number of numerical operations needed for the generation of a single sample versus the required resolution level, that is the field size, and the number M. Clearly, the presented method compares quite favorably with alternative methods of random field simulation and merits further investigation.

Acknowledgment

The support of this work by the grant NSF-CMS-9525929 is gratefully acknowledged.

References

Basseville, M., Benveniste, A., Chou, K. C., Goldin, S. A., Nikoukhah, R., and Willsky, A. S., 1992a, "Modeling and Estimation of Multiresolution Stochastic Processes," *IEEE Transaction on Information Theory*, Vol. 38, No. 2, pp. 766–784.

Basseville, M., Benveniste, A., and Willsky, A. S., 1992b, "Multiscale Autoregressive Processes, Part I: Schur-Levinson Parametrizations, Part II: Lattice Structure for Whitening and Modeling," *IEEE Transactions on Signal Processing*, Vol. 40, No. 8, pp. 1915–1953.

Belkin, G., 1993, "On the Representation of Operators in Bases of Compactly Supported Wavelets," *SIAM Journal of Numerical Analysis*, Vol. 6, No. 6, pp. 1716–1740.

Belkin, G., Coifman, R., and Rokhlin, V., 1991, "Fast Wavelet Transform and Numerical Algorithms I," *Communications on Pure and Applied Mathematics*, Vol. 44, pp. 141–183.

Clippingdale, S., and Wilson, R., 1989, "Least-Square Image Estimation on a Multiresolution Pyramid," *IEEE International Conference on Acoustics, Speech and Signal Processing*, Glasgow, pp. 1409–1412.

Daubechies, I., 1988, "Orthogonal Basis of Compactly Supported Wavelets," *Communications on Pure and Applied Mathematics*, Vol. 41, pp. 909–996.

Daubechies, I., 1992, *Ten Lectures on Wavelets*, Society for Industrial and Applied Mathematics, Philadelphia, PA.

Dijkerman, R. W., and Mazumdar, R. R., 1994, "Wavelet Representations of Stochastic Processes and Multiresolution Stochastic Models," *IEEE Transactions on Signal Processing*, Vol. 42, No. 7, pp. 1640–1652.

Fenton, G. A., and Vanmarcke, E. H., 1990, "Simulation of Random Fields via Local Average Subdivision," *Journal of Engineering Mechanics*, Vol. 116, No. 8, pp. 1733–1749.

Fenton, G. A., 1994, "Error Evaluation of Three Random-Field Generators," *Journal of Engineering Mechanics*, Vol. 120, No. 12, pp. 2478–2497.

Flandrin, P., 1989, "On the Spectrum of Fractional Brownian Motions," *IEEE Transactions on Information Theory*, Vol. 35, No. 1, pp. 197–199.

Flandrin, P., 1992, "Wavelet Analysis and Synthesis of Fractional Brownian Motion," *IEEE Transactions on Information Theory*, Vol. 38, No. 2, pp. 910–917.

Fournier, A., Fussel, D., and Carpenter, L., 1982, "Computer Rendering of Stochastic Models," *Communications of the ACM*, Vol. 25, No. 6, pp. 371–384.

Herley, C., and Vetterley, M., 1993, "Wavelets and Recursive Filter Banks," *IEEE Transactions on Signal Processing*, Vol. 41, No. 8, pp. 2536–2556.

Keshner, M. S., 1982, "$1/f$ Noise," *Proceedings of IEEE*, Vol. 70, pp. 212–218.

Lewis, J. P., 1987, "Generalized Stochastic Subdivision," *ACM Transactions on Graphics*, Vol. 6, No. 3, pp. 167–190.

Luettgen, M. R., Karl, W. C., and Willsky, A. S., 1994, "Efficient Multiscale Regularization with Application to the Computation of Optical Flow," *IEEE Transactions on Image Processing*, Vol. 3, No. 1, pp. 41–64.

Mignolet, M. P., and Spanos, P. D., 1992, "Simulation of Homogeneous Two-Dimensional Random Fields: Part I—AR and ARMA Models," ASME JOURNAL OF APPLIED MECHANICS, Vol. 114, pp. 260–269.

Newland, D. E., 1993, *An Introduction to Random Vibrations, Spectral and Wavelet Analysis*, Longman House, Harlow, U.K.

Rubinstein, R. Y., 1981, *Simulation and the Monte Carlo Method*, John Wiley and Sons, New York.

Samaras, E., Shinozuka, M., and Tsurui, A., 1983, "ARMA Representation of Random Processes," *Journal of Engineering Mechanics*, Vol. 111, No. 3, pp. 449–461.

Shinozuka, M., and Jan, C-M., 1972, "Digital Simulation of Random Processes and Its Applications," *Journal of Sound and Vibration*, Vol. 25, No. 1, pp. 111–128.

Spanos, P. D., and Mignolet, M. P., 1992, "Simulation of Homogeneous Two-Dimensional Random Fields: Part II—MA and ARMA Models," ASME JOURNAL OF APPLIED MECHANICS, Vol. 114, 270–277.

Tewfik, A. H., and Kim, 1992, "Correlation Structure of the Discrete Wavelet Coefficients of Fractional Brownian Motion," *IEEE Transactions on Information Theory*, Vol. 38, No. 2, pp. 904–909.

Vanmarcke, E. H., 1983, *Random Fields: Analysis and Synthesis*, MIT Press, Cambridge, MA.

Walter, G. G., 1994, *Wavelets and Other Orthogonal Systems with Applications*, Boca Raton, FL.

Wornell, G. W., 1990, "A Karhunen-Loeve-Like Expansion for $1/f$ Processes via Wavelets," *IEEE Transactions on Information Theory*, Vol. 36, No. 4, pp. 859–861.

Wornell, G. W., and Oppenheim, A. V., 1992, "Estimation of Fractal Signal from Noisy Measurements using Wavelets," *IEEE Transactions on Signal Processing*, Vol. 40, No. 3, pp. 611–623.

Zeldin, B. A., 1995, Ph.D. Dissertation, Rice University, Houston, TX.

Zeldin, B. A., and Spanos, P. D., 1995, "Random Field Simulation Using Wavelet Bases," *Proceedings of the Seventh International Conference on Application of Statistics and Probability in Civil Engineering*, M. Lemare, J.-L. Favre, and A. Mebarki, eds., Balkema, Rotterdam, Paris, France, July 10–13, pp. 1275–1283.

APPENDIX

Determination of Moments of the Scale Function

In this Appendix an efficient method for evaluating the integrals $\Gamma_m = \int x^m \phi(x)\,dx$ appearing in Eq. (24) is presented.

Using the Fourier transform one can obtain

$$\Gamma_m = \int x^m \phi(x)\,dx = \int x^m \phi(x) e^{-ix\omega}\,dx\Big|_{\omega=0}$$

$$= \frac{\sqrt{2\pi}}{(-i)^m}\,\hat{\phi}^{(m)}(0). \tag{A.1}$$

Also, Eq. (10) yields

$$\hat{\phi}(0) = \frac{1}{\sqrt{2\pi}}, \quad \text{and} \quad \Gamma_0 = m_0(0) = 1. \tag{A.2}$$

Further, differentiating Eq. (4) m times yields

$$\hat{\phi}^{(m)}(0) = \left(m_0\left(\frac{\omega}{2}\right)\hat{\phi}\left(\frac{\omega}{2}\right)\right)^{(m)}\Bigg|_{\omega=0}$$

$$= \sum_{k=0}^{m} \frac{1}{2^m}\binom{k}{m} m_0^{(k)}(0)\hat{\phi}^{(m-k)}(0)$$

$$= \frac{1}{2^m - 1}\sum_{k=1}^{m}\binom{k}{m} m_0^{(k)}(0)\hat{\phi}^{(m-k)}(0), \tag{A.3}$$

where the last equality holds because of Eq. (A2). The value $m_0^{(k)}(0)$ can be determined from Eq. (7) as

$$m_0^{(k)}(0) = (-i)^k \kappa_k, \tag{A.4}$$

where

$$\kappa_k = \frac{1}{\sqrt{2}}\sum_{l=0}^{2M-1} l^k h_{l+1}. \tag{A.5}$$

Finally, substituting Eqs. (A3) and (A4) into Eq. (A.1) yields

$$\Gamma_m = \frac{1}{2^m - 1}\sum_{k=1}^{m}\binom{k}{m}\kappa_k \Gamma_{m-k}. \tag{A.6}$$

That is, Eq. (A.6) defines a recursive algorithm for evaluating the moments of the scale function.

Vibration and Coupling Phenomena in Asymmetric Disk-Spindle Systems

R. G. Parker
Department of Mechanical Engineering,
Ohio State University,
Columbus, OH 43210
Mem. ASME

C. J. Mote, Jr.

Vice-Chancellor-University Relations,
FANUC Chair in Mechanical Systems,
Department of Mechanical Engineering,
University of California,
Berkeley, CA 94720
Fellow ASME

This paper analytically treats the free vibration of coupled, asymmetric disk-spindle systems in which both the disk and spindle are continuous and flexible. The disk and spindle are coupled by a rigid clamping collar. The asymmetries derive from geometric shape imperfections and nonuniform clamping stiffness at the disk boundaries. They appear as small perturbations in the disk boundary conditions. The coupled system eigenvalue problem is cast in terms of "extended" eigenfunctions that are vectors of the disk, spindle, and clamp displacements. With this formulation, the eigenvalue problem is self-adjoint and the eigenfunctions are orthogonal. The conciseness and clarity of this formulation are exploited in an eigensolution perturbation analysis. The amplitude of the disk boundary condition asymmetry is the perturbation parameter. Exact eigensolution perturbations are derived through second order. For general boundary asymmetry distributions, simple rules emerge showing how asymmetry couples the eigenfunctions of the axisymmetric system and how the degenerate pairs of axisymmetric system eigenvalues split into distinct eigenvalues. Additionally, properties of the formulation are ideal for use in modal analyses, Ritz-Galerkin discretizations, and extensions to gyroscopic or nonlinear analyses.

Introduction

In circular disk vibration research, the support structure is normally modeled as rigid. In spindle (rotor) analyses, components attached to the flexible spindle are commonly assumed rigid. As mechanical components become lighter and more flexible, however, a growing number of systems are not adequately modeled by either of these idealizations. For instance, a model in which both the disk and spindle deform elastically is required to capture the coupled vibratory response exhibited by computer disk drives and turbomachinery. Disk-spindle coupling allows bearing excitation to drive disk vibration or disk excitation to drive spindle vibration. Uncoupled disk and spindle systems are commonly idealized further as being axisymmetric, though asymmetries may be present in the design and are unavoidably generated by manufacturing imperfection. Two experimental observations expose the asymmetry in computer disk drives (and likely other disk-spindle systems as well):

1 Coupled disk-spindle vibration occurs in disk vibration modes having any number of nodal diameters while the coupled, *axisymmetric* disk-spindle model predicts coupling in only the one nodal diameter disk vibration modes (Chivens and Nelson, 1975).

2 The degenerate pairs of natural frequencies in the axisymmetric system split into pairs of distinct frequencies. In rotating disk applications, natural frequency splitting can significantly alter disk response near the critical speeds (Tobias and Arnold, 1957). The modes in which the natural frequencies split are also subject to a subcritical speed instability that does not exist in axisymmetric disks (Yu and Mote, 1987).

In this work we develop an analytical formulation for coupled, *asymmetric* disk-spindle vibration analysis, determine the eigensolutions, identify the asymmetries causing coupled response, and derive simple, general rules predicting coupling of disk-spindle vibration and splitting of degenerate natural frequencies in these nominally axisymmetric systems.

Coupled, axisymmetric disk-spindle systems were treated analytically by Chivens and Nelson (1975). They concluded that disk flexibility significantly affects natural frequencies but not critical speeds. In a discussion of this work, Klompas (1975) addresses the importance of modeling support structure asymmetry because, in the presence of asymmetry, rotation induces traveling waves in the disk that may be of more concern than critical speeds. Wilgen and Schlack (1979) show that for ratios of disk mass to shaft mass greater than those considered by Chivens and Nelson (1975), disk flexibility can dramatically increase or decrease the critical speeds depending on disk placement. Flowers and Ryan (1993) note that disk flexibility can play a significant role in superharmonic vibration that may be excited by rotating system nonlinearities. The above works focus solely on axisymmetric systems where only the one nodal diameter disk vibration modes couple with the spindle modes. Consequently, they cannot explain the aforementioned expanded coupling and natural frequency splitting phenomena. Inclusion of asymmetry in the present coupled model explains these phenomena with simple formulae. The simple forms of the derived eigensolutions are convenient for use in applications. The structure of the presented formulation can be extended to include gyroscopic effects that are not included herein.

Coupled Disk-Spindle Model

The coupled disk-spindle system is shown in Fig. 1. The disk is modeled as a uniform Kirchhoff plate, the spindle as a uniform Euler-Bernoulli beam, and the clamp as rigid. The spindle can deform in two orthogonal planes. The coupled equations of motion for disk displacement $W(R, \theta, T)$ and spindle displacements $U(Z, T)$, $V(Z, T)$ are

Contributed by the Applied Mechanics Division of THE AMERICAN SOCIETY OF MECHANICAL ENGINEERS for publication in the ASME JOURNAL OF APPLIED MECHANICS.

Discussion on this paper should be addressed to the Technical Editor, Professor Lewis T. Wheeler, Department of Mechanical Engineering, University of Houston, Houston, TX 77204-4792, and will be accepted until four months after final publication of the paper itself in the ASME JOURNAL OF APPLIED MECHANICS.

Manuscript received by the ASME Applied Mechanics Division, June 5, 1995; final revision, Mar. 21, 1996. Associate Technical Editor: S. W. Shaw.

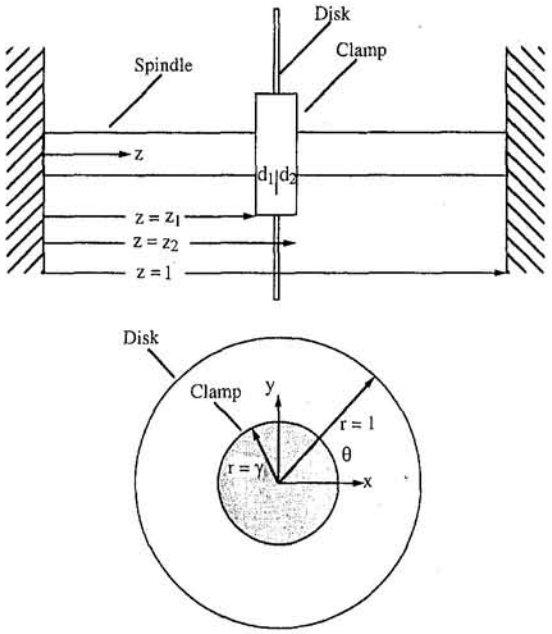

Fig. 1 Coupled flexible spindle-rigid clamp-flexible disk system

$$D\nabla^4 W + \rho_d\left[W_{TT} - R\cos\theta\,\frac{d^2(U_Z|_{z_1})}{dT^2} - R\sin\theta\,\frac{d^2(V_Z|_{z_1})}{dT^2}\right] = 0 \quad \bar{P} \quad (1a)$$

$$EIU_{ZZZZ} + \rho_s U_{TT} = 0 \quad \xi EIV_{ZZZZ} + \rho_s V_{TT} = 0 \quad \bar{S} \quad (1b, c)$$

$$-EIU_{ZZZ}|_{Z_1}^{Z_2} - m\frac{d^2U^m}{dT^2} = 0$$

$$-\xi EIV_{ZZZ}|_{Z_1}^{Z_2} - m\frac{d^2V^m}{dT^2} = 0 \quad (1d, e)$$

$$EI[U_{ZZ}|_{Z_1}^{Z_2} - \bar{d}_2U_{ZZZ}|_{Z_2} - \bar{d}_1U_{ZZZ}|_{Z_1}] - \bar{J}_y\frac{d^2(U_Z|_{z_1})}{dT^2} + \iint_P \rho_d r\cos\theta W_{TT}dA = 0 \quad (1f)$$

$$\xi EI[V_{ZZ}|_{Z_1}^{Z_2} - \bar{d}_2V_{ZZZ}|_{Z_2} - \bar{d}_1V_{ZZZ}|_{Z_1}] - \bar{J}_x\frac{d^2(V_Z|_{z_1})}{dT^2} + \iint_P \rho_d r\sin\theta W_{TT}dA = 0 \quad (1g)$$

$$U^m = U|_{z_1} + \bar{d}_1U_Z|_{z_1} = U|_{z_2} - \bar{d}_2U_Z|_{z_2}$$

$$V^m = V|_{z_1} + \bar{d}_1V_Z|_{z_1} = V|_{z_2} - \bar{d}_2V_Z|_{z_2} \quad (1h, i)$$

$$U_Z|_{z_1} = U_Z|_{z_2} \quad V_Z|_{z_1} = V_Z|_{z_2} \quad (1j, k)$$

where $\bar{P} = a < R < b$, $0 \le \theta < 2\pi$ is the disk domain, $\bar{S} = (0, Z_1) \cup (Z_2, L)$ is the spindle domain, D is the disk flexural rigidity, ρ_d and ρ_s are the disk areal density and spindle density per unit length, EI and ξEI are the spindle bending stiffnesses for the $U(Z, T)$ and $V(Z, T)$ deformations, m is the mass of the clamp plus the mass of the disk, U^m and V^m are the displacements of the clamp center of mass, and $\bar{J}_{x,y}$ are the diametral moments of inertia of the combined clamp/disk about the x and y-axes with respect to point C. We define the dimensionless variables

$$r = \frac{R}{b} \quad z = \frac{Z}{L} \quad t = \left(\frac{D}{\rho_d b^4}\right)^{1/2} T \quad \hat{w} = \frac{W}{b}$$

$$\hat{u} = \frac{U}{L} \quad \hat{v} = \frac{V}{L} \quad \hat{\phi} = \hat{u}_z|_{z_1} \quad \hat{\psi} = \hat{v}_z|_{z_1} \quad (2)$$

$$\gamma = \frac{a}{b} \quad K = \frac{EI/L}{D} \quad \rho = \frac{\rho_s L^3}{\rho_d b^4} \quad \alpha = \frac{mL^2}{\rho_d b^4}$$

$$J_{x,y} = \frac{\bar{J}_{x,y}}{\rho_d b^4} \quad z_{1,2} = \frac{Z_{1,2}}{L} \quad d_{1,2} = \frac{\bar{d}_{1,2}}{L} \quad (3)$$

ϕ and ψ represent the spindle slopes at the spindle/clamp interface and are equivalent to the rotations of the rigid clamp about the y and $-x$-axes, respectively. Assuming the exponential time dependencies

$$\hat{w}(r, \theta, t) = w(r, \theta)e^{i\bar{\lambda}^2 t} \quad \hat{u}(z, t) = u(z)e^{i\bar{\lambda}^2 t}$$

$$\hat{v}(z, t) = v(z)e^{i\bar{\lambda}^2 t}$$

the dimensionless eigenvalue problem is

$$\nabla^4 w - \bar{\lambda}^4[w - r\cos\theta\phi - r\sin\theta\psi] = 0 \quad P \quad (4a)$$

$$B_i[w] + \epsilon C_i[w] + \epsilon^2 D_i[w] = 0 \quad r = \gamma, 1 \quad (4b)$$

$$Ku_{zzzz} - \bar{\lambda}^4\rho u = 0 \quad \xi Kv_{zzzz} - \bar{\lambda}^4\rho v = 0 \quad S \quad (4c, d)$$

$$u = u_z = v = v_z = 0 \quad z = 0, 1 \quad (4e)$$

$$Ku_{zzz}|_{z_1}^{z_2} - \bar{\lambda}^4\alpha u^m = 0 \quad \xi Kv_{zzz}|_{z_1}^{z_2} - \bar{\lambda}^4\alpha v^m = 0 \quad (4f, g)$$

$$-K[u_{zz}|_{z_1}^{z_2} - d_2u_{zzz}|_{z_2} - d_1u_{zzz}|_{z_1}] - \bar{\lambda}^4\left[J_y\phi - \iint_P r\cos\theta w dA\right] = 0 \quad (4h)$$

$$-\xi K[v_{zz}|_{z_1}^{z_2} - d_2v_{zzz}|_{z_2} - d_1v_{zzz}|_{z_1}] - \bar{\lambda}^4\left[J_x\psi - \iint_P r\sin\theta w dA\right] = 0 \quad (4i)$$

$$u^m = u|_{z_1} + d_1u_z|_{z_1} = u|_{z_2} - d_2u_z|_{z_2}$$

$$v^m = v|_{z_1} + d_1v_z|_{z_1} = v|_{z_2} - d_2v_z|_{z_2} \quad (4j, k)$$

$$u_z|_{z_1} = u_z|_{z_2} = \phi \quad v_z|_{z_1} = v_z|_{z_2} = \psi. \quad (4l, m)$$

P is the disk domain $\gamma < r < 1$, $0 \le \theta < 2\pi$; S is the spindle domain $(0, z_1) \cup (z_2, 1)$.

The disk boundary conditions (4b) include small, asymmetric boundary operators ϵC_i, $\epsilon^2 D_i$ superposed on classical, axisymmetric boundary operators B_i. We consider three types of inner boundary asymmetry.

1 Clamped Boundary With Shape Imperfection (Fig. 2).

$$w + \epsilon g w_r + \tfrac{1}{2}\epsilon^2 g^2 w_{rr} = 0$$

$$w_r + \epsilon\left[gw_{rr} - \frac{1}{\gamma^2}\frac{dg}{d\theta}w_\theta\right] + \epsilon^2\left[\frac{2g}{\gamma^3}\frac{dg}{d\theta}w_\theta - \frac{1}{2\gamma^2}\left(\frac{dg}{d\theta}\right)^2 w_r - \frac{g}{\gamma^2}\frac{dg}{d\theta}w_{r\theta} + \frac{1}{2}g^2 w_{rrr}\right] = 0. \quad r = \gamma \quad (5)$$

The asymptotic approximations used to reduce the clamped boundary conditions $w = w_n = 0$ on the irregular boundary to (5) are discussed by Parker and Mote (1996b).

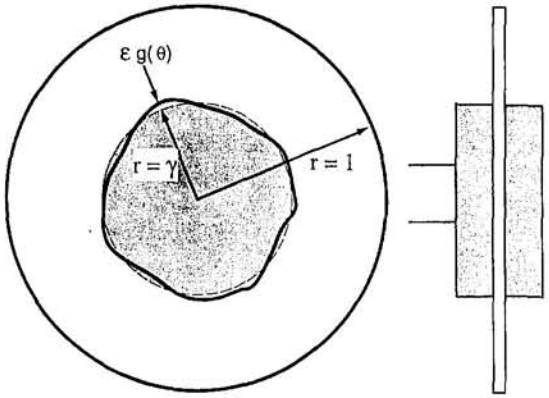

Fig. 2 Inner clamped, outer free annular plate with a geometric shape asymmetry at the inner boundary

2 Circumerentially Varying Linear Spring. The inner boundary displacement is restrained by a spring of stiffness $k = k_0 + \epsilon k(\theta)$

$$w_r = 0$$

$$(\nabla^2 w)_r + \frac{1-\nu}{r^2}\left(w_{r\theta\theta} + \frac{w_{\theta\theta}}{r}\right) + k_0 w + \epsilon k(\theta) w = 0 \quad r = \gamma \quad (6)$$

3 Circumerentially Varying Rotational Spring. The inner boundary rotation is restrained by a spring of stiffness $\kappa = \kappa_0 + \epsilon\kappa(\theta)$

$$w = 0$$

$$w_{rr} - \frac{\nu}{r} w_r + \frac{\nu}{r^2} w_{\theta\theta} - \kappa_0 w_r - \epsilon\kappa(\theta) w_r = 0. \quad r = \gamma \quad (7)$$

Extended Operator Formulation

We cast the coupled system eigenvalue problem in a structured form by defining the extended eigenfunction $\mathbf{a}$ and the extended stiffness ($\mathbf{L}$) and inertia ($\mathbf{M}$) operators

$$\mathbf{a} = \begin{Bmatrix} w(r,\theta) \\ u(z) \\ v(z) \\ u^m \\ v^m \\ \phi \\ \psi \end{Bmatrix} \quad \mathbf{La} = \begin{Bmatrix} \nabla^4 w \\ K u_{zzzz} \\ \xi K v_{zzzz} \\ K u_{zzz}|_{z_1}^{z_2} \\ \xi K v_{zzz}|_{z_1}^{z_2} \\ -K[u_{zz}|_{z_1}^{z_2} - d_2 u_{zzz}|_{z_2} - d_1 u_{zzz}|_{z_1}] \\ -\xi K[v_{zz}|_{z_1}^{z_2} - d_2 v_{zzz}|_{z_2} - d_1 v_{zzz}|_{z_1}] \end{Bmatrix} \quad (8a, b)$$

$$\mathbf{Ma} = \begin{Bmatrix} w - r\cos\theta\phi - r\sin\theta\psi \\ \rho u \\ \rho v \\ \alpha u^m \\ \alpha v^m \\ J_y\phi - \iint_P r\cos\theta w dA \\ J_x\psi - \iint_P r\sin\theta w dA \end{Bmatrix}. \quad (8c)$$

In the sequel, we use $\xi = 1$ and $J_x = J_y = J$. The eigenvalue problem (4) becomes

$$\mathbf{La} - \bar{\lambda}^4 \mathbf{Ma} = 0 \quad (9a)$$

$$B_i[w] + \epsilon C_i[w] + \epsilon^2 D_i[w] = 0 \quad r = \gamma, 1 \quad (9b)$$

$$u = u_z = v = v_z = 0 \quad z = 0, 1. \quad (9c)$$

Equation (9a) is a compact statement of (4a, c, d, f–i). With (4j–m), (8a) is completely defined by w, u, and v. The extended eigenfunctions $\mathbf{a}$ are elements in the Hilbert space H,

$$H = L_2(P) \oplus L_2(S) \oplus L_2(S) \oplus \mathbb{R} \oplus \mathbb{R} \oplus \mathbb{R} \oplus \mathbb{R}. \quad (10)$$

Operators $\mathbf{L}$ and $\mathbf{M}$ are mappings from $H \to H$. The form (10) suggests the inner product for $\mathbf{p}, \mathbf{q} \in H$,

$$\langle \mathbf{p}, \mathbf{q} \rangle = \int \mathbf{p}^T \mathbf{q} = \iint_P p_1 q_1 dA + \int_S p_2 q_2 dz + \int_S p_3 q_3 dz + p_4 q_4 + p_5 q_5 + p_6 q_6 + p_7 q_7. \quad (11)$$

The extended operators $\mathbf{L}$, $\mathbf{M}$ are self-adjoint provided the uncoupled, annular disk eigenvalue problem, (4a, b) with $\phi = \psi = 0$, is self-adjoint. With this specification and proper normalization

$$\langle \mathbf{a}^i, \mathbf{Ma}^j \rangle = \delta_{ij} \quad \langle \mathbf{a}^i, \mathbf{La}^j \rangle = (\bar{\lambda}_i)^4 \delta_{ij} \quad (12)$$

$\mathbf{M}$ is positive definite. The definiteness of $\mathbf{L}$ is the same as the definiteness of the plate bending operator ∇^4 with boundary conditions (9b).

The structure of the coupled disk-spindle eigenvalue problem (9) is identical to that considered by Parker and Mote (1996a), and the perturbation method developed therein applies. This similarity of structure is not evident from (4). The eigensolutions of (9) are represented in asymptotic expansions in the small parameter ϵ

$$\bar{\lambda}^4 = \lambda^4 + \epsilon\mu + \epsilon^2\eta + O(\epsilon^3)$$

$$\mathbf{a} = \mathbf{a}_0 + \epsilon\mathbf{a}_1 + \epsilon^2\mathbf{a}_2 + O(\epsilon^3). \quad (13)$$

Components of $\mathbf{a}_i$, $i = 0, 1, 2$ are denoted w_i, u_i, v_i, u_i^m, v_i^m, ϕ_i, and ψ_i. Substitution of (13a, b) into (9) leads to a sequence of perturbation problems governing $\mathbf{a}_0$, $\mathbf{a}_1$, and $\mathbf{a}_2$

$$\mathbf{La}_0 - \lambda^4 \mathbf{Ma}_0 = \mathbf{0} \quad (14a)$$

$$B_i[w_0] = 0 \quad r = \gamma, 1 \quad (14b)$$

$$u_0 = u_{0_z} = v_0 = v_{0_z} = 0 \quad z = 0, 1 \quad (14c)$$

$$\mathbf{La}_1 - \lambda^4 \mathbf{Ma}_1 = \mu \mathbf{Ma}_0 \quad (15a)$$

$$B_i[w_1] = -C_i[w_0] \quad r = \gamma, 1 \quad (15b)$$

$$u_1 = u_{1_z} = v_1 = v_{1_z} = 0 \quad z = 0, 1 \quad (15c)$$

$$\mathbf{La}_2 - \lambda^4 \mathbf{Ma}_2 = \mu \mathbf{Ma}_1 + \eta \mathbf{Ma}_0 \quad (16a)$$

$$B_i[w_2] = -C_i[w_1] - D_i[w_0] \quad r = \gamma, 1 \quad (16b)$$

$$u_2 = u_{2_z} = v_2 = v_{2_z} = 0 \quad z = 0, 1. \quad (16c)$$

Problem (14) can be solved exactly for the infinite set of unperturbed eigensolutions (λ^4, $\mathbf{a}_0$) of the axisymmetric disk-spindle system. Self-adjointness of (14) ensures orthogonality of the $\mathbf{a}_0$. The normalization $\langle \mathbf{a}, \mathbf{Ma} \rangle = 1$ and (13b) give

$$\langle \mathbf{a}_0, \mathbf{Ma}_0 \rangle = 1 \quad \langle \mathbf{a}_0, \mathbf{Ma}_1 \rangle = 0. \quad (17)$$

Unperturbed Eigensolutions

The unperturbed eigenvalue problem (14) is that of an *axisymmetric,* coupled disk-spindle system. The component equations for w_0, u_0, and v_0 are obtained from (4) with $\epsilon = 0$ and $\bar{\lambda}^4 \to \lambda^4$. The coupled system eigenfunctions are characterized by their numbers of nodal circles m and nodal diameters n in the

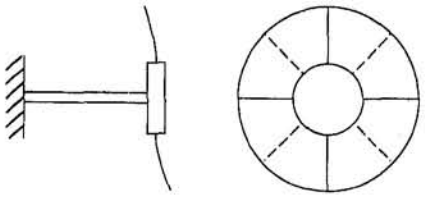

Fig. 3(*a*) Two nodal diameter disk eigenfunction. Solid and dashed lines denote the nodal diameters of the sin 2θ and cos 2θ dependent eigenfunctions, respectively.

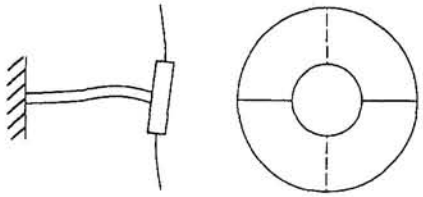

Fig. 3(*b*) One nodal diameter coupled eigenfunction. Solid and dashed lines denote the nodal diameters of the sin θ and cos θ dependent eigenfunctions, respectively.

Fig. 3 Axisymmetric system (unperturbed) eigenfunctions

disk deformation. Two classes of unperturbed, coupled system eigensolutions exist depending on n.

1 Disk Eigensolutions ($n \neq 1$). Disk eigensolutions have eigenvalues λ and disk deformation w_0 determined from the uncoupled, axisymmetric disk eigenvalue problem; the spindle does not deform, $u_0 = v_0 = 0$ (Fig. 3(a)). The one nodal diameter ($n = 1$) disk eigensolutions couple with the spindle and are excluded from this class. For $n = 0$, the eigenvalues are distinct, and the eigenfunction $\mathbf{a}_0$ is defined by

$$w_0 = A_1 J_0(\lambda r) + A_2 I_0(\lambda r) + A_3 Y_0(\lambda r) + A_4 K_0(\lambda r) = R_0(r) \quad u_0 = v_0 = 0. \quad (18)$$

For $n \geq 2$, the eigenvalues are degenerate. The two unperturbed eigenfunctions $\mathbf{a}_{0_1}$ and $\mathbf{a}_{0_2}$ are defined by

$$w_{0_1} = [A_1 J_n(\lambda r) + A_2 I_n(\lambda r) + A_3 Y_n(\lambda r) + A_4 K_n(\lambda r)] \cos n\theta = R_n(r) \cos n\theta \quad n \geq 2$$
$$u_{0_1} = v_{0_1} = 0 \quad (19a)$$

$$w_{0_2} = [A_1 J_n(\lambda r) + A_2 I_n(\lambda r) + A_3 Y_n(\lambda r) + A_4 K_n(\lambda r)] \sin n\theta = R_n(r) \cos n\theta \quad n \geq 2$$
$$u_{0_2} = v_{0_2} = 0 \quad (19b)$$

where $J_n(\lambda r)$, $I_n(\lambda r)$, $Y_n(\lambda r)$, and $K_n(\lambda r)$ are Bessel functions. These solutions satisfy ($4a$). The A_i are fixed by the disk boundary conditions ($4b$) with $\epsilon = 0$. The integrals in ($4h$, i) representing the moments that the disk transmits to the clamp vanish for the solutions (18), (19).

2 Coupled Eigensolutions ($n = 1$). In the coupled eigensolutions, one nodal diameter disk deformation transmits a moment to the clamp and causes spindle deformation (Fig. 3(b)). For an axisymmetric spindle, all eigenvalues are degenerate. The two corresponding eigenfunctions are

$$w_{0_1} = [A_1 J_n(\lambda r) + A_2 I_n(\lambda r) + A_3 Y_n(\lambda r) + A_4 K_n(\lambda r) + r\phi_0] \cos\theta = R_1(r) \cos\theta$$

$$u_{0_1} = \begin{cases} E_1 \sin \beta z + E_2 \sinh \beta z + E_3 \cos \beta z + E_4 \cosh \beta z & 0 < z < z_1 \\ F_1 \sin \beta z + F_2 \sinh \beta z + F_3 \cos \beta z + F_4 \cosh \beta z & z_2 < z < 1 \end{cases}$$

$$v_{0_1} = 0 \quad (20a)$$

$$w_{0_2} = [A_1 J_n(\lambda r) + A_2 I_n(\lambda r) + A_3 Y_n(\lambda r) + A_4 K_n(\lambda r) + r\psi_0] \sin\theta = R_1(r) \sin\theta$$

$$u_{0_2} = 0$$

$$v_{0_2} = \begin{cases} E_1 \sin \beta z + E_2 \sinh \beta z + E_3 \cos \beta z + E_4 \cosh \beta z & 0 < z < z_1 \\ F_1 \sin \beta z + F_2 \sinh \beta z + F_3 \cos \beta z + F_4 \cosh \beta z & z_2 < z < 1 \end{cases}$$

$$\beta^4 = \frac{\rho}{K} \lambda^4. \quad (20b)$$

These satisfy ($4a$, c, d). The characteristic determinant and eigenfunction coefficients A_i, E_i, F_i are readily calculated from ($4b$, e–m) using computer algebra software. Two types of coupled eigenfunctions exist. The first are dominated by spindle deformation with only small disk deformation. The associated eigenvalues are close to those of a spindle with attached rigid mass and inertia. The first and third coupled eigenvalues in Table 1 are of this type; compare these eigenvalues, $\lambda_1 = 2.909$ and $\lambda_2 = 8.575$, to the flexible spindle/*rigid* disk eigenvalues of $\lambda_1 = 2.915$ and $\lambda_2 = 8.204$. The second type of coupled eigenfunction is dominated by disk deformation with small spindle deformation. The associated eigenvalues are close to those of the uncoupled $n = 1$ disk eigenvalues. The second coupled eigenvalue in Table 1, $\lambda_2 = 3.654$, is of this type (the $n = 1$ uncoupled disk eigenvalue is $\lambda_{01} = 3.644$).

The coefficients A_i in (18), (19), and (20) are numerically different. Because of axisymmetry, however, the A_i in ($19a$) and ($19b$) are identical as are the A_i, E_i, and F_i in ($20a$) and ($20b$). Because $\phi_0 = \psi_0$, $R_1(r)$ is the same in ($20a$) and ($20b$).

For the axisymmetric, unperturbed system, coupling occurs in only the one nodal diameter disk eigenfunctions and all but the $n = 0$ eigenvalues are degenerate. This results from axisymmetry of the disk; it is unchanged by (1) the type of axisymmetric, unperturbed disk boundary conditions, (2) spindle asymmetry ($\xi \neq 1$), (3) different spindle stiffnesses in the left and right-hand sections, (4) specified spindle support conditions,

Table 1 Dimensionless (λ) and dimensional unperturbed eigenvalues of an axisymmetric ($\xi = 1$, $J_x = J_y = J$), cantilevered (no right-hand spindle section), coupled disk-spindle system. Disk subscripts refer to the number of nodal circles m and nodal diameters n in the eigenfunction. The coupled subscript m denotes the numerical order of the eigenvalues.

Dimensional Parameters		Dimensionless Parameters
$a = 0.1016\ m$	$EI = 21110.\ N\text{–}m^2$	$\gamma = 0.5$
$b = 0.2032\ m$	$\rho_s = 9.155\ kg/m$	$K = 2815.$
$D = 18.45\ N\text{–}m$	$m = 7.656\ kg$	$\rho = 44.89$
$\rho_d = 8.030\ kg/m^2$	$\bar{J} = 0.02822\ kg\text{–}m^2$	$\alpha = 92.36$
$L = Z_1 = 0.4064\ m$	$\bar{d}_1 = 0.01320\ m$	$J = 2.061$
		$d_1 = 0.0325$

	λ	ω (rad/s)	f (Hz)
Disk, λ_{mn}	$\lambda_{00} = 3.603$	476.7	75.87
	$\lambda_{02} = 3.842$	541.9	86.25
	$\lambda_{03} = 4.325$	686.9	109.3
	$\lambda_{04} = 5.082$	948.2	150.9
	$\lambda_{05} = 6.003$	1323.	210.6
Coupled, λ_m	$\lambda_1 = 2.909$	310.7	49.44
	$\lambda_2 = 3.654$	490.3	78.03
	$\lambda_3 = 8.575$	2700.	429.7

(5) clamp inertia asymmetry ($J_x \neq J_y$), and (6) different clamp thicknesses d_1 and d_2.

Solution of Perturbation Equations

Consider the inner boundary condition perturbations (5–7). The outer boundary conditions are axisymmetric and unperturbed. For each unperturbed eigensolution (λ^4, $\mathbf{a}_0$), (15) and (16) determine the first and second-order eigensolution perturbations.

The boundary conjuncts of the operators $\mathbf{L}$ and $\mathbf{M}$ (Roach, 1982) are

$$J_{\mathbf{L}}(\mathbf{p}, \mathbf{q}) = \langle \mathbf{Lp}, \mathbf{q} \rangle - \langle \mathbf{p}, \mathbf{Lq} \rangle$$

$$J_{\mathbf{M}}(\mathbf{p}, \mathbf{q}) = \langle \mathbf{Mp}, \mathbf{q} \rangle - \langle \mathbf{p}, \mathbf{Mq} \rangle = 0 \tag{21}$$

for $\mathbf{p}, \mathbf{q} \in H$. For elements of H satisfying homogeneous spindle conditions at $z = 0, 1$ (such as $\mathbf{a}_0$, $\mathbf{a}_1$, and $\mathbf{a}_2$ of (13b)), the boundary conjunct $J_{\mathbf{L}}$ reduces to the boundary conjunct J_{∇^4} associated with the plate bending operator ∇^4. For example,

$$J_{\mathbf{L}}(\mathbf{a}_0, \mathbf{a}_1) = J_{\nabla^4}(w_0, w_1) = \langle \nabla^4 w_0, w_1 \rangle - \langle w_0, \nabla^4 w_1 \rangle$$

$$= \int_{\partial P} [\nabla^2 w_1 w_{0_n} - (\nabla^2 w_1)_n w_0 + w_1 (\nabla^2 w_0)_n - w_{1_n} \nabla^2 w_0] d\hat{s} \tag{22}$$

where ∂P denotes the circular plate boundaries and

$$\nabla^2(\bullet) = (\bullet)_{nn} + (1/r)(\bullet)_n + (\bullet)_{ss}.$$

At the outer boundary $r = 1$, $(\bullet)_n = (\bullet)_r$ and $(\bullet)_s = 1/r(\bullet)_\theta$; at the inner boundary $r = \gamma$, $(\bullet)_n = -(\bullet)_r$ and $(\bullet)_s = -1/r(\bullet)_\theta$. Integration is counterclockwise on the outer boundary and clockwise on the inner boundary.

Consider a *distinct* unperturbed eigenvalue λ^4 with eigenfunction $\mathbf{a}_0$. The inner product of each side of (15a) and (16a) with $\mathbf{a}_0$ and use of (21), (17), and (22) give the solvability conditions

$$\mu = -J_{\mathbf{L}}(\mathbf{a}_0, \mathbf{a}_1) = -J_{\nabla^4}(w_0, w_1) \tag{23}$$

$$\eta = -J_{\mathbf{L}}(\mathbf{a}_0, \mathbf{a}_2) = -J_{\nabla^4}(w_0, w_2). \tag{24}$$

Consider a *degenerate* unperturbed eigenvalue λ^4 of multiplicity two having associated orthonormal, unperturbed eigenfunctions $\mathbf{a}_{0_1}$ and $\mathbf{a}_{0_2}$. As a result of the degeneracy, the unperturbed eigenfunction $\mathbf{a}_0$ is initially indeterminate

$$\mathbf{a}_0 = b_1 \mathbf{a}_{0_1} + b_2 \mathbf{a}_{0_2} \tag{25}$$

with b_1 and b_2 determined subsequently. In the degenerate case, two solvability conditions for the problem (15) must be satisfied:

$$b_1 \mu = -J_{\mathbf{L}}(\mathbf{a}_{0_1}, \mathbf{a}_1) = -J_{\nabla^4}(w_{0_1}, w_1)$$

$$b_2 \mu = -J_{\mathbf{L}}(\mathbf{a}_{0_2}, \mathbf{a}_1) = -J_{\nabla^4}(w_{0_2}, w_1). \tag{26}$$

Equations (26) lead to a 2×2, symmetric, algebraic eigenvalue problem (Parker and Mote, 1995a)

$$\mathbf{Db} = \mu \mathbf{b}. \tag{27}$$

The eigenvalues $\mu_{1,2}$ are the first-order perturbations of the degenerate unperturbed eigenvalue. If $\mu_1 = \mu_2$, the eigenvalue λ^4 remains degenerate in a first-order perturbation; the two eigenvectors $\mathbf{b} = (b_1\ b_2)^T$ are arbitrary unit vectors. If $\mu_1 \neq \mu_2$, λ^4 splits into distinct eigenvalues and the eigenvectors $\mathbf{b} = (b_1\ b_2)^T$ fix the two unperturbed eigenfunctions (25).

1 Disk Eigensolutions ($n \neq 1$). Consider the degenerate disk eigenvalues and associated eigenfunctions $\mathbf{a}_{0_{1,2}}$ defined by (19). We represent an arbitrary geometric asymmetry $g(\theta)$ in (5) by its Fourier series

$$g(\theta) = \sum_{j=1}^{\infty} g_j^c \cos j\theta + \sum_{j=1}^{\infty} g_j^s \sin j\theta = \sum_{j=-\infty}^{\infty} g_j e^{ij\theta}$$

$$g_j = \tfrac{1}{2}(g_j^c - i g_j^s). \tag{28}$$

Evaluation of (26) yields

$$\mathbf{D} = \frac{\pi\gamma}{2} \left(\frac{d^2 R_n}{dr^2} \bigg|_{r=\gamma} \right)^2 \begin{bmatrix} g_{2n}^c & g_{2n}^s \\ g_{2n}^s & -g_{2n}^c \end{bmatrix}$$

$$\mu = \pm \pi\gamma \left(\frac{d^2 R_n}{dr^2} \bigg|_{r=\gamma} \right)^2 |g_{2n}|. \tag{29}$$

Eigenvalue splitting in a first-order perturbation is identified immediately from (29b): An n nodal diameter degenerate eigenvalue splits from geometric asymmetry if and only if $g_{2n} \neq 0$. The rate of splitting is proportional to $|g_{2n}|$. The corresponding results for an arbitrary linear stiffness variation $k(\theta)$ in (6) are

$$k(\theta) = \sum_{j=1}^{\infty} k_j^c \cos j\theta + \sum_{j=1}^{\infty} k_j^s \sin j\theta = \sum_{j=-\infty}^{\infty} k_j e^{ij\theta} \tag{30}$$

$$\mathbf{D} = -\frac{\pi\gamma}{2} [R_n(\gamma)]^2 \begin{bmatrix} k_{2n}^c & k_{2n}^s \\ k_{2n}^s & -k_{2n}^c \end{bmatrix}$$

$$\mu = \pm \pi\gamma [R_n(\gamma)]^2 |k_{2n}|. \tag{31}$$

The eigenvalue splitting rule is as follows: An n nodal diameter degenerate eigenvalue splits from linear stiffness asymmetry if and only if $k_{2n} \neq 0$. The rate of splitting is proportional to $|k_{2n}|$. For a general rotational stiffness variation $\kappa(\theta)$ in (7),

$$\kappa(\theta) = \sum_{j=1}^{\infty} \kappa_j^c \cos j\theta + \sum_{j=1}^{\infty} \kappa_j^s \sin j\theta = \sum_{j=-\infty}^{\infty} \kappa_j e^{ij\theta} \tag{32}$$

$$\mathbf{D} = \frac{\pi\gamma}{2} \left(\frac{dR_n}{dr} \bigg|_{r=\gamma} \right)^2 \begin{bmatrix} \kappa_{2n}^c & \kappa_{2n}^s \\ \kappa_{2n}^s & -\kappa_{2n}^c \end{bmatrix}$$

$$\mu = \pm \pi\gamma \left(\frac{dR_n}{dr} \bigg|_{r=\gamma} \right)^2 |\kappa_{2n}|. \tag{33}$$

The eigenvalue splitting rule is as follows: An n nodal diameter degenerate eigenvalue splits from rotational stiffness asymmetry if and only if $\kappa_{2n} \neq 0$. The rate of splitting is proportional to $|\kappa_{2n}|$.

Eigenvalue splitting is independent of the disk outer boundary conditions, provided they are axisymmetric. Outer edge boundary conditions change the eigenvalue perturbations only through their influence on $R_n(r)$ in (29b), (31b), (33b). For geometric or stiffness asymmetries in the disk outer boundary conditions with axisymmetric inner boundary conditions, the splitting rules are identical to the preceding. Rules for simultaneous perturbation of the inner and outer disk boundary conditions are readily derived. For a coupled system with geometric asymmetry at the inner boundary (5) and linear stiffness asymmetry (as in 6) at the outer boundary,

$$\mathbf{D} = \mathbf{D}_{\text{geom}} + \mathbf{D}_{\text{stiff}}$$

$$\mu = \pm \left| \pi [R_n(\gamma)]^2 k_{2n} + \pi\gamma \left(\frac{d^2 R_n}{dr^2} \bigg|_{r=\gamma} \right)^2 g_{2n} \right| \quad n \geq 1 \tag{34}$$

where $\mathbf{D}_{\text{geom}}$ is the matrix from (29a) and $\mathbf{D}_{\text{stiff}}$ is from (31a) with $\gamma = 1$. $k_{2n} = g_{2n} = 0$ implies no first-order splitting. However, $k_{2n} \neq 0$ and $g_{2n} \neq 0$ does not necessarily cause splitting; two asymmetries, either of which would split an n nodal diameter eigenvalue if acting individually, may not split the eigenvalue when present together. Fourier representation of the asymmetry allows the above rules to be applied to arbitrary

continuous or discontinuous asymmetries. Discontinuous asymmetries include radial edge slots or discontinuous boundary supports. All of the above splitting rules are also valid for uncoupled disks and generalize the rules given by Parker and Mote (1996a, b).

Orthogonality and completeness of the unperturbed eigenfunctions $\mathbf{a}_0$ allow expansion of the eigenfunction perturbation $\mathbf{a}_1$ in the infinite series

$$\mathbf{a}_1^k = \sum_{i=1, i\neq k}^{\infty} e_i \mathbf{a}_0^i + \bar{\mathbf{a}} \quad e_i = \frac{J_L(\mathbf{a}_0^i, \bar{\mathbf{a}})}{\lambda_i^4 - \lambda_k^4} \tag{35}$$

where $\mathbf{a}_1^k$ denotes the first-order perturbation of the kth unperturbed eigenfunction $\mathbf{a}_0^k$, i is an index of all eigensolutions, and $\bar{\mathbf{a}}$ is defined by an arbitrary function $\bar{w}$ satisfying the inhomogeneous boundary conditions (15b), $\bar{u}(z) = 0$, and $\bar{v}(z) = 0$. The extended eigenvalue problem formulation and resulting orthogonality make the series solution (35) possible. Though the series (35) converges in the natural metric of (11), its use in calculating the second-order eigenvalue perturbation η may lead to a divergent series (Parker and Mote, 1996b). Additionally, $\mathbf{a}_1^k$ in (35) is approximate, is difficult to use in modal response analyses, may converge slowly, and requires calculation of many unperturbed eigensolutions.

These difficulties do not arise with the *exact* solution for $\mathbf{a}_1$, which is determinable from the decomposition

$$\mathbf{a}_1 = c_1\mathbf{a}_{0_1} + c_2\mathbf{a}_{0_2} + \mathbf{a}_1^h + \mathbf{a}_1^p \rightarrow$$

$$\begin{aligned} w_1 &= c_1 w_{0_1} + c_2 w_{0_2} + w_1^h + w_1^p \\ u_1 &= c_1 u_{0_1} + c_2 u_{0_2} + u_1^h + u_1^p \\ v_1 &= c_1 v_{0_1} + c_2 v_{0_2} + v_1^h + v_1^p. \end{aligned} \tag{36}$$

The components w_1^p, u_1^p, and v_1^p defining $\mathbf{a}_1^p$ are particular solutions of the inhomogeneous component differential equations of (15a); the components w_1^h, u_1^h, and v_1^h defining $\mathbf{a}_1^h$ are general solutions of the homogeneous component differential equations of (15a); the first two terms are indeterminacies required because $\mathbf{a}_{0_{1,2}}$ satisfy the homogeneous form of (15); c_1 and c_2 are constants. For $\mathbf{a}_0$ given by (25) and (19), the critical element $\mathbf{a}_1^p$ of (36) is defined by

$$\begin{aligned} w_1^p = &-\frac{\mu r}{4\lambda^3}[A_1 J_{n+1}(\lambda r) - A_2 I_{n+1}(\lambda r) \\ &+ A_3 Y_{n+1}(\lambda r) + A_4 K_{n+1}(\lambda r)](b_1 \cos n\theta + b_2 \sin n\theta) \\ &+ r\cos\theta\phi_1 + r\sin\theta\psi_1 \end{aligned} \tag{37a}$$

$$u_1^p = v_1^p = 0 \tag{37b}$$

where $\phi_1 = u_{1_z}|_{z_1}$ and $\psi_1 = v_{1_z}|_{z_1}$. Components of the homogeneous solution $\mathbf{a}_1^h$ are

$$\begin{aligned} w_1^h = &\sum_{j=0}^{\infty} [P_j J_j(\lambda r) + Q_j I_j(\lambda r) + \hat{P}_j Y_j(\lambda r) \\ &+ \hat{Q}_j K_j(\lambda r)]\cos j\theta + \sum_{j=1}^{\infty} [R_j J_j(\lambda r) + S_j I_j(\lambda r) \\ &+ \hat{R}_j Y_j(\lambda r) + \hat{S}_j K_j(\lambda r)]\sin j\theta \end{aligned} \tag{38a}$$

$$u_1^h = \begin{cases} \bar{E}_1 \sin\beta z + \bar{E}_2 \sinh\beta z + \bar{E}_3 \cos\beta z \\ \quad + \bar{E}_4 \cosh\beta z \quad 0 < z < z_1 \\ \bar{F}_1 \sin\beta z + \bar{F}_2 \sinh\beta z + \bar{F}_3 \cos\beta z \\ \quad + \bar{F}_4 \cosh\beta z \quad z_2 < z < 1 \end{cases} \tag{38b}$$

$$v_1^h = \begin{cases} \bar{G}_1 \sin\beta z + \bar{G}_2 \sinh\beta z + \bar{G}_3 \cos\beta z \\ \quad + \bar{G}_4 \cosh\beta z \quad 0 < z < z_1 \\ \bar{H}_1 \sin\beta z + \bar{H}_2 \sinh\beta z + \bar{H}_3 \cos\beta z \\ \quad + \bar{H}_4 \cosh\beta z \quad z_2 < z < 1. \end{cases} \tag{38c}$$

With the particular solution (37), the coefficients in (38) are computed from the boundary conditions (15b, c) and the clamp momentum balances of (15a). Exact expressions for the coefficients can be obtained using computer algebra software. Rules to predict when the disk eigenfunctions couple with the spindle emerge from these expressions.

Consider again the examples (5)–(7). For the geometric asymmetry and the general $g(\theta)$ from (28), coefficients $\bar{E}_i$ and $\bar{F}_i$ of (38b) are nonzero if and only if

$$b_1(g_{n+1}^c + g_{n-1}^c) + b_2(g_{n+1}^s + g_{n-1}^s) \neq 0. \tag{39a}$$

$\bar{G}_i$ and $\bar{H}_i$ of (38c) are nonzero if and only if

$$b_1(g_{n+1}^s - g_{n-1}^s) - b_2(g_{n+1}^c - g_{n-1}^c) \neq 0. \tag{39b}$$

Thus, the disk-spindle eigenfunction coupling rule for geometric asymmetry is as follows: If either or both of (39) are satisfied for an n nodal diameter disk eigenfunction, then the perturbed eigenfunction couples the disk and spindle deformations; otherwise the perturbed eigenfunction involves only disk deformation. For linear stiffness asymmetry and $k(\theta)$ from (30), u_1 and v_1 are nonzero if and only if

$$b_1(k_{n+1}^c + k_{n-1}^c) + b_2(k_{n+1}^s + k_{n-1}^s) \neq 0 \tag{40a}$$

$$b_1(k_{n+1}^s - k_{n-1}^s) - b_2(k_{n+1}^c - k_{n-1}^c) \neq 0. \tag{40b}$$

The coupling rule for linear stiffness asymmetry is as follows: If either or both of (40) are satisfied for an n nodal diameter disk eigenfunction, then the perturbed eigenfunction couples disk and spindle deformations; otherwise the perturbed eigenfunction involves only disk deformation. For rotational stiffness asymmetry and $\kappa(\theta)$ from (32), u_1 and v_1 are nonzero if and only if

$$b_1(\kappa_{n+1}^c + \kappa_{n-1}^c) + b_2(\kappa_{n+1}^s + \kappa_{n-1}^s) \neq 0 \tag{41a}$$

$$b_1(\kappa_{n+1}^s - \kappa_{n-1}^s) - b_2(\kappa_{n+1}^c - \kappa_{n-1}^c) \neq 0. \tag{41b}$$

The coupling rule for rotational stiffness asymmetry is as follows: If either or both of (41) are satisfied for an n nodal diameter disk eigenfunction, then the perturbed eigenfunction couples disk and spindle deformations; otherwise the perturbed eigenfunction involves only disk deformation. Satisfaction of the coupling conditions (39)–(41) implies only that $\mathbf{a}_1$ involves spindle deformation ($u_1 \neq 0$ and/or $v_1 \neq 0$). Absence of coupling does not imply $\mathbf{a}_1 = \mathbf{0}$ because $w_1 \neq 0$.

With $\mathbf{a}_1$ known, the normalization condition (17b) and two solvability conditions for (16) generate the matrix equation (Parker and Mote, 1996a)

$$\begin{bmatrix} D_{11} - \mu & D_{12} & -b_1 \\ D_{12} & D_{22} - \mu & -b_2 \\ -b_1 & -b_2 & 0 \end{bmatrix} \begin{Bmatrix} c_1 \\ c_2 \\ \eta \end{Bmatrix}$$

$$= \begin{Bmatrix} \mu\langle \mathbf{a}_{0_1}, \mathbf{M}[\mathbf{a}_1^h + \mathbf{a}_1^p]\rangle + \tilde{J}_L(\mathbf{a}_{0_1}, \mathbf{a}_2) \\ \mu\langle \mathbf{a}_{0_2}, \mathbf{M}[\mathbf{a}_1^h + \mathbf{a}_1^p]\rangle + \tilde{J}_L(\mathbf{a}_{0_2}, \mathbf{a}_2) \\ b_1\langle \mathbf{a}_{0_1}, \mathbf{M}[\mathbf{a}_1^h + \mathbf{a}_1^p]\rangle + b_2\langle \mathbf{a}_{0_2}, \mathbf{M}[\mathbf{a}_1^h + \mathbf{a}_1^p]\rangle \end{Bmatrix} \tag{42}$$

where D_{ij} are components of $\mathbf{D}$ and $\tilde{J}_L(\mathbf{a}_{0_i}, \mathbf{a}_2) = J_L(\mathbf{a}_{0_i}, \mathbf{a}_2)|_{c_1=c_2=0}$. The operator in (42) is invertible if and only if $\mathbf{D}$ has distinct eigenvalues μ. In this case, c_1, c_2, and η are found from (42). Computer algebra software simplifies evaluation of the right-hand side of (42). c_1 and c_2 complete the solution (36) and η gives the exact, second-order eigenvalue perturbation. If

the μ are degenerate, the $\mathbf{b} = (b_1\ b_2)^T$ are indeterminate. b_1, b_2, and η are calculable, however, from the first two equations of (42) and $b_1^2 + b_2^2 = 1$. The exact solution for $\mathbf{a}_2$ utilizes a decomposition analogous to (36) and requires the particular solutions w_2^p, u_2^p, and v_2^p. Though not pursued here, determination of w_2^p, u_2^p, and v_2^p is achievable (Parker and Mote, 1997).

For the zero nodal diameter unperturbed eigenfunctions (18), (23) yields $\mu = 0$ for the three examples. The solution for $\mathbf{a}_1$ is obtained by reduction of the results presented for the degenerate $n \geq 2$ eigensolutions. The perturbed eigenfunction $\mathbf{a}_1$ does not couple with the spindle; this and the result $\mu = 0$ arise because the asymmetries (28), (30), and (32) have zero mean. The exact, second-order eigenvalue perturbation η is calculated from (24) and is nonzero, in general.

2 Coupled Eigensolutions ($n = 1$). For the coupled eigensolutions (20), the matrices $\mathbf{D}$ and eigenvalue perturbations μ for geometric, linear stiffness, and rotational stiffness asymmetry are given by (29), (31), and (33) with $n = 1$. Eigenvalue splitting is predicted by use of $n = 1$ in the appropriate splitting rule. The eigenfunction perturbation $\mathbf{a}_1$ is decomposed as in (36). The particular solution $\mathbf{a}_1^p$ is defined by

$$w_1^p = -\frac{\mu r}{4\lambda^3}\left[A_1 J_2(\lambda r) - A_2 I_2(\lambda r) + A_3 Y_2(\lambda r) + A_4 K_2(\lambda r)\right] \times (b_1 \cos\theta + b_2 \sin\theta) + r\cos\theta\phi_1 + r\sin\theta\psi_1 \quad (43a)$$

$$u_1^p = \frac{\mu\rho z}{4K\beta^3} b_1 \begin{cases} E_1 \cos\beta z + E_2 \cosh\beta z \\ \quad - E_3 \sin\beta z + E_4 \sinh\beta z \quad 0 < z < z_1 \\ F_1 \cos\beta z + F_2 \cosh\beta z \\ \quad - F_3 \sin\beta z + F_4 \sinh\beta z \quad z_2 < z < 1 \end{cases} \quad (43b)$$

$$v_1^p = \frac{\mu\rho z}{4K\beta^3} b_2 \begin{cases} G_1 \cos\beta z + G_2 \cosh\beta z \\ \quad - G_3 \sin\beta z + G_4 \sinh\beta z \quad 0 < z < z_1 \\ H_1 \cos\beta z + H_2 \cosh\beta z \\ \quad - H_3 \sin\beta z + H_4 \sinh\beta z \quad z_2 < z < 1. \end{cases} \quad (43c)$$

$\mathbf{a}_1^h$ is defined by (38), and again its coefficients are calculable exactly. Exact solution for η is given by (42) as for the disk eigenvalues.

Example: Geometric Shape Asymmetry

To illustrate the eigenvalue splitting and eigenfunction coupling phenomena, we consider the cantilevered system of Fig. 2 with the parameters of Table 1. The specific shape asymmetry corresponding to (28) is

$$g(\theta) = \tfrac{1}{9}\cos\theta + \tfrac{1}{5}\sin\theta + \tfrac{1}{4}\cos 2\theta - \tfrac{1}{4}\sin 2\theta - \tfrac{1}{4}\cos 4\theta - \tfrac{1}{3}\cos 6\theta. \quad (44)$$

The splitting and coupling rules (29) and (39) give the following results.

1 Disk Eigensolutions.

$n = 2$: The eigenvalues split at first-order perturbation ($g_4 \neq 0$). The eigenvectors of (29a) are $\mathbf{b}_1 = (1\ \ 0)^T$ and $\mathbf{b}_2 = (0\ \ 1)^T$. Conditions (39) are satisfied for $\mathbf{b}_1$ and $\mathbf{b}_2$, so the perturbed eigenfunctions associated with both eigenfunctions (25) couple with the spindle.

$n = 3$: The eigenvalues split at first-order perturbation ($g_6 \neq 0$). For the eigenvector $\mathbf{b}_1 = (1\ \ 0)^T$, neither of (39) is satisfied and the eigenfunction does not couple with the spindle.

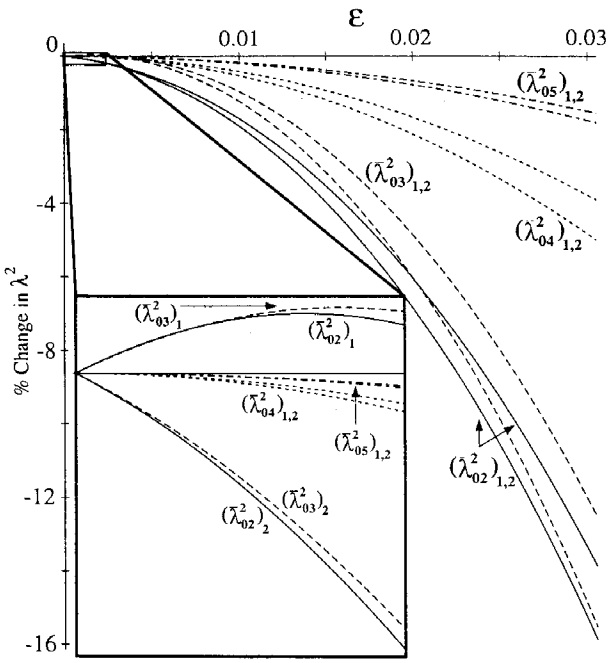

Fig. 4 Percent changes in the disk eigenvalues for the geometric shape asymmetry of (44). Subscripts *mn* denote the number of nodal circles (*m*) and nodal diameters (*n*) in the unperturbed eigenfunction. Subscripts 1, 2 indicate the split eigenvalue loci. The inset is an exploded view for small ϵ.

For the eigenvector $\mathbf{b}_2 = (0\ \ 1)^T$, (39$b$) is satisfied and the asymmetry introduces disk-spindle coupling (with $v(z)$) for this perturbed eigenfunction.

$n = 4$: The eigenvalues do not split at first-order perturbation ($g_8 = 0$). Because $g_3 = g_5 = 0$, neither of (39) is satisfied and the $n = 4$ eigenfunctions do not couple with the spindle.

$n = 5$: The eigenvalues do not split at first-order perturbation ($g_{10} = 0$). $\mathbf{b}_{1,2}$ of (29a) are indeterminate. They are determined with η from the equations of (42). They are such that (39) are satisfied and both eigenfunctions couple with the spindle.

The above results illustrate independent eigenvalue splitting and disk-spindle vibration coupling. The $n = 2$ eigensolution splits and couples. In contrast, the $n = 3$ eigenvalue splits but one eigenfunction does not couple. Conversely, the $n = 5$ eigenfunction couples but the eigenvalue does not split. The $n = 4$ eigensolution neither splits nor couples, showing that eigensolutions can be remarkably insensitive to certain asymmetry distributions.

Eigenvalue changes as a function of asymmetry amplitude are shown in Fig. 4. The $n = 2$, 3 eigenvalues, which split at first order perturbation, are most dramatically affected, with changes around 16 percent occurring for $\epsilon = 0.03$. For $\epsilon = 0.03$, the peak-to-peak amplitude of the shape deviation $\epsilon g(\theta)$ is 8.6 percent of the inner radius $\gamma = 0.5$. Splitting of the $n = 2$, 3 eigenvalues is evident in the inset of Fig. 4. That splitting of the $n = 4$, 5 eigenvalues is a higher order effect is also apparent from the inset. For small ϵ, the loci associated with one of the split eigenvalues increases while the other decreases. For larger ϵ all eigenvalues decrease, a result of the additional flexibility from spindle coupling.

2 Coupled Eigensolutions. The eigenvalues split at first-order perturbation because $g_2 \neq 0$. Changes in the first three coupled disk-spindle eigenvalues are shown in Fig. 5. Coupled eigensolutions whose unperturbed eigenfunctions are dominated by disk deformation are more strongly affected by disk clamp asymmetry than coupled eigensolutions dominated by spindle

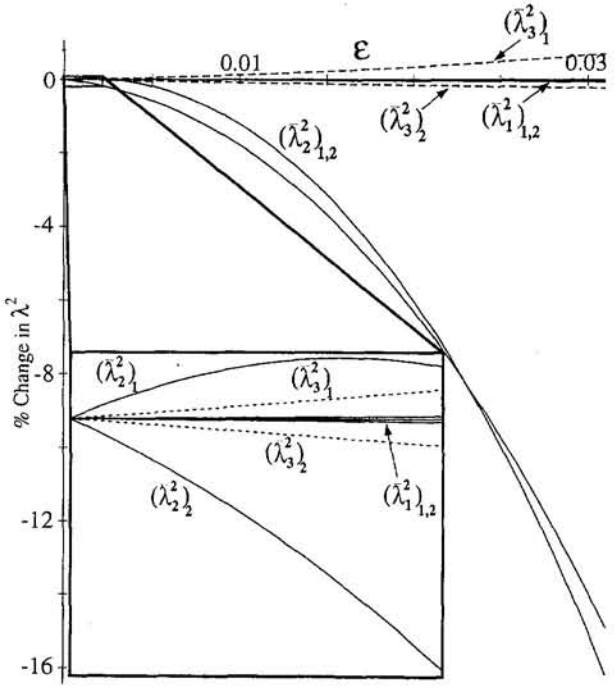

Fig. 5 Percent changes in the coupled eigenvalues for the geometric shape asymmetry of (44). The first subscripts (1, 2, 3) denote the numerical order of the unperturbed eigenvalues. The second subscripts (1, 2) indicate the split eigenvalue loci. The inset is an exploded view for small ϵ.

deformation. The unperturbed $\bar{\lambda}_2$ eigenfunction involves primarily disk deformation with small spindle deformation, and $\bar{\lambda}_2$ is significantly affected by disk asymmetry. The eigenvalues $\bar{\lambda}_1$ and $\bar{\lambda}_3$ are associated with unperturbed eigenfunctions dominated by spindle deformation; they change only slightly with increasing asymmetry.

Eigenvalue Splitting and Eigenfunction Coupling Rules

From the identical form of the eigenvalue splitting and eigenfunction coupling rules for the boundary asymmetries considered, it is evident that splitting and coupling are dictated by the *distribution* and not the *source* of the asymmetry. Though only geometric and stiffness asymmetries were considered, inertia asymmetry will lead to identical forms for the splitting and coupling rules. Furthermore, disk eigenvalue splitting and disk-spindle coupling in other than the one nodal diameter eigenfunctions occur *only* in the presence of disk asymmetry (including disk nonuniformities such as circumferentially varying thickness). These effects are independent of spindle characteristics. For a *uniform* disk, boundary asymmetry is the only asymmetry that splits the degenerate disk eigenvalues and leads to expanded disk-spindle coupling. Other possible asymmetries include different spindle stiffnesses in the $u(z)$, $v(z)$ bending planes ($\xi \neq 1$), different clamp rotational inertia in the two bending planes ($J_x \neq J_y$), different spindle stiffnesses in the left and right-hand spindle sections, nonuniform spindle stiffness $EI(z)$, different left and right clamp thicknesses ($d_1 \neq d_2$), and different spindle boundary conditions. Though these asymmetries alter the eigenvalues and some of them remove the degeneracy in the coupled eigenvalues, they neither split the disk eigenvalues nor induce additional coupling beyond the $n = 1$ eigenfunction.

The utility of the perturbation solution, splitting rules, and coupling rules is enhanced by their simplicity and generality. Because the perturbations are derived for arbitrarily distributed asymmetries, they can be used in design to distribute unavoidable boundary asymmetries so as to minimize vibrational effects. For example, if the bearing excitation spectrum is known (even if only approximately), asymmetries can be chosen to avoid coupling in eigenfunctions with natural frequencies near the excitation frequencies. A similar process could be used to isolate spindle vibration from disk excitation. Additionally, asymmetry can be deliberately introduced so as to tune natural frequencies away from forcing frequencies of disk, spindle, or clamp excitation. The simplicity of the rules allows them to be utilized with minimal calculation for initial design or for troubleshooting existing vibration problems. The explicit parameter dependence further simplifies the process by showing which parameters have maximal influence on the eigensolutions.

Conclusions

1 The eigenvalue problem for coupled disk-spindle-clamp vibration is cast in a self-adjoint form (9) by incorporating the disk, spindle, and clamp displacements into an extended eigenfunction (8*a*). This formulation preserves the orthogonality of the coupled system eigenfunctions and provides a concise framework for coupled disk-spindle vibration analysis.

2 *Exact* eigenvalue and eigenfunction perturbations are derived for coupled disk-spindle systems with geometric shape, stiffness, and combined geometric/stiffness asymmetries in the disk boundary conditions. Eigensolution approximation results only from truncation of the asymptotic series (13). Fourier representation of the asymmetries allows treatment of general continuous or discontinuous asymmetry distributions.

3 The unperturbed, *axisymmetric* system eigenfunctions are exactly calculable and are of two types: disk eigenfunctions with no spindle deformation and coupled disk-spindle eigenfunctions. Only the one nodal diameter disk eigenfunctions couple with the spindle.

4 Splitting of the degenerate, unperturbed eigenvalues and coupling of the uncoupled, unperturbed disk eigenfunctions from disk boundary condition asymmetry are predicted by simple, general rules based on the Fourier distribution of the asymmetry. Both splitting and coupling depend on the distribution of the asymmetry and are independent of the source of asymmetry. Coupling is caused solely by disk asymmetry; spindle asymmetry does not induce coupling.

5 Asymmetry-induced coupling of the unperturbed, disk eigenfunctions with the spindle provides a mechanism for energy transfer from bearing/spindle excitation to disk vibration and vice versa. Coupling also introduces additional flexibility that can significantly reduce the system natural frequencies.

6 The self-adjoint formulation of the coupled system eigenvalue problem and the complete, orthonormalized set of extended eigensolutions are well suited for modal response analyses. Generalized coordinates $p_i(t)$ of the modal representation

$$\mathbf{a}(r, \theta, z, t) = \sum_{i=1}^{\infty} p_i(t)\mathbf{a}^i(r, \theta, z)$$

decouple as a result of orthogonality. Disk, spindle, clamp, and bearing excitations can be incorporated in an extended forcing vector analogous to (8*a*). The coupled system eigenfunctions $\mathbf{a}^i$ are also well suited for use as expansion functions in Ritz-Galerkin discretizations or as basis functions for nonlinear perturbation analyses.

References

Chivens, D. R., and Nelson, H. D., 1975, "The Natural Frequencies and Critical Speeds of a Rotating, Flexible Shaft-Disk System," ASME *Journal of Engineering for Industry*, Vol. 97, pp. 881–886.

Flowers, G. T., and Ryan, S. G., 1993, "Development of a Set of Equations for Incorporating Disk Flexibility Effects in Rotordynamic Analyses," ASME *Journal of Engineering for Gas Turbines and Power,* Vol. 115, pp. 227–233.

Klompas, N., 1975, discussion of "The Natural Frequencies and Critical Speeds of a Rotating, Flexible Shaft-Disk System," ASME *Journal of Engineering for Industry,* Vol. 97, p. 886.

Parker, R. G., and Mote, Jr., C. D., 1996a, "Exact Boundary Condition Perturbation Solutions in Eigenvalue Problems," ASME JOURNAL OF APPLIED MECHANICS, Vol. 63, pp. 128–135.

Parker, R. G., and Mote, Jr., C. D., 1996b, "Exact Perturbation for the Vibration of Almost Annular or Circular Plates," ASME *Journal of Vibration and Acoustics,* Vol. 63, pp. 436–445.

Parker, R. G., and Mote, Jr., C. D., 1997, "Higher-order Perturbation for Asymmetric Disks and Disk-Spindle Systems," ASME JOURNAL OF APPLIED MECHANICS, manuscript in preparation.

Roach, G. F., *Green's Functions,* 1982, Cambridge Univ. Press, Cambridge, UK, p. 156.

Tobias, S. A., and Arnold, R. N., 1957, "The Influence of Dynamical Imperfection on the Vibration of Rotating Disks," *Proc. of the Inst. of Mech. Engineers,* Vol. 171, pp. 669–690.

Wilgen, F. J., and Schlack, Jr., A. L., 1979, "Effects of Disk Flexibility on Shaft Whirl Stability," ASME *Journal of Mechanical Design,* Vol. 101, pp. 298–303.

Yu, R. C., and Mote, Jr., C. D., 1987, "Vibration and Parametric Excitation in Asymmetric Circular Plates Under Moving Loads," ASME *Journal of Sound and Vibration,* Vol. 119, pp. 409–427.

Exact Time-Dependent Plane Stress Solutions for Elastic Beams: A Novel Approach

P. Ladevèze

Laboratoire de Mécanique et Technologie,
ENS Cachan/CNRS/Université Paris 6,
France
Mem. ASME

J. G. Simmonds

Institute of Applied Mathematics
and Mechanics,
University of Virginia,
Thornton Hall,
Charlottesville, VA 22903
Fellow ASME

We consider an elastically isotropic beam of narrow rectangular cross section governed by the dynamic equations of linearized plane stress theory and subject to typical boundary and initial conditions associated with flexure. We use one of the three stress-displacement relations to express the axial stress σ_x in terms of the axial displacement U and the normal stress σ. Assuming this latter stress and the shear stress τ to be given functions of position (x, z) and time t, we write the remaining two stress-displacement equations as a nonhomogeneous hyperbolic system for U and the normal displacement W. This system has a simple, explicit solution in terms of σ, τ, and V, the value of W on the centerline of the beam. Introducing certain body forces f_x and f_z, we obtain explicit formulas for σ, τ, U, and W valid in the interior of the beam and satisfying any imposed tractions on the faces of the beam. We satisfy initial conditions by adding certain explicitly computable increments to the initial displacements and velocities. Satisfaction of end conditions of displacement or traction yields a certain consistency condition along the centerline in edge zones ("boundary layers") of width $\sqrt{\nu}H$, where ν is Poisson's ratio and $2H$ is the depth of the beam. In particular, if V is taken as a solution of the equations of elementary beam theory, then outside these end zones the body forces f_x and f_z and the incremental initial conditions are "small." If V within the edge zones is also identified with the solution of elementary beam theory, then a certain increment of the order of the dominant longitudinal stress σ_x must be added within the edge zones to the prescribed value of τ on the face of the beam. (This is consistent with the neglect of two-dimensional end effects in elementary beam theory.) These results should be of use as analytical benchmarks for checking numerical codes.

Introduction

Our motivation for this paper is the question of how to evaluate the errors in approximate solutions to initial/boundary value problems in the linearized theory of (two or three-dimensional) elasticity, such approximations arising either from numerical solutions or from exact solutions of simplified structural models such as beam, plate, or shell theories. In attempting to assess the accuracy of the stress fields inferred from such models, especially from so-called "higher-order" theories, many authors use as their standard of comparison *very special* benchmarks. Not only are such exact solutions usually *static,* they nearly always satisfy *periodic* boundary conditions (i.e., conditions of simple support) and thus fail to exhibit *edge zones* (boundary layers) where the accuracy of various structural models is apt to be the worst.

As a first (and perhaps novel) step towards obtaining exact, time-dependent, realistic benchmarks, we construct exact plane stress solutions for elastically isotropic rectangular beams, as described in the abstract, in terms of a normal and shear stress, $\sigma(x, z, t)$ and $\tau(x, z, t)$, and a function $V(x, t)$, where x and z are axial and normal distance, respectively, and t is time.

To obtain these exact solutions we must impose certain explicitly computable incremental external loads and initial conditions. In particular, incremental shears must be imposed on the upper and lower faces of the beam, but *only within a distance from the ends of the order of the depth of the beam.*

It is very natural to identify V with a solution of elementary (Euler-Bernoulli) beam theory and σ and τ with the associated two-dimensional stresses inferred from the exact equations of motion. In doing so, we find that the incremental loads and initial conditions are "small" away from the end zones, as expected. Within the end zones, the incremental loads are of the order of magnitude of the (dominant) axial stress, again consistent with known asymptotic solutions of plane stress theory (e.g., Duva and Simmonds, 1992). Thus, our method of constructing exact solutions not only gives us a way to measure the accuracy of beam theory, it also provides standards against which to compare two-dimensional numerical solutions.

The Equations of Plane Stress Theory

To avoid distracting details, we confine attention to an elastically homogeneous isotropic beam, subject to certain body forces and boundary/initial conditions specified below. Thus, in a region $0 < x < L$, $-H < z < H$ of the xz-plane, we have the three displacement-stress relations

$$EU_{,x} = \sigma_x - \nu\sigma,\ G(U_{,z} + W_{,x}) = \tau,\ EW_{,z} = \sigma - \nu\sigma_x \quad (1)$$

plus the two equations of motion

$$\sigma_{x,x} + \tau_{,z} + f_x = \rho U_{,tt},\quad \tau_{,x} + \sigma_{,z} + f_z = \rho W_{,tt}. \quad (2)$$

Here, U and W are displacements in the x and z-directions, respectively, σ_x is the axial stress, τ is the shear stress, and σ is the normal stress. Further, E is Young's modulus, $G = E/2(1 + \nu)$ is the shear modulus, ρ is the constant mass density, f_x and f_z are body forces—destined to be taken as error loads—

Contributed by the Applied Mechanics Division of THE AMERICAN SOCIETY OF MECHANICAL ENGINEERS for publication in the ASME JOURNAL OF APPLIED MECHANICS.

Discussion on this paper should be addressed to the Technical Editor, Professor Lewis T. Wheeler, Department of Mechanical Engineering, University of Houston, Houston, TX 77204-4792, and will be accepted until four months after final publication of the paper itself in the ASME JOURNAL OF APPLIED MECHANICS.

Manuscript received by the ASME Applied Mechanics Division, June 27, 1995; final revision, Oct. 18, 1995. Associate Technical Editor: D. M. Barnett.

and a comma followed by a subscript denotes differentiation with respect to that subscript.

The boundary conditions on the face of the beam are

$$\sigma(x, \pm H, t) = \pm\tfrac{1}{2}p(x, t), \quad \tau(x, \pm H, t) = \tfrac{1}{2}q(x, t), \quad (3)$$

where p is prescribed and q is to be chosen later as a certain error load. The initial conditions are

$$U(x, z, 0) = U^*(x, z), \quad U_{,t}(x, z, 0) = U_t^*(x, z) \quad (4)$$

$$W(x, z, 0) = W^*(x, z), \quad W_{,t}(x, z, 0) = W_t^*(x, z), \quad (5)$$

where U^*, etc., are prescribed.

Using the notation

$$\bar{f} = f/E, \quad \kappa = E/G \quad (6)$$

and following Duva and Simmonds (1992), we rewrite $(1)_1$ as

$$\bar{\sigma}_x = U_{,x} + \nu\bar{\sigma} \quad (7)$$

and henceforth use this relation to eliminate the axial stress in favor of U and $\bar{\sigma}$. The two remaining displacement-stress relations may now be given the form

$$U_{,z} + W_{,x} = \kappa\bar{\tau}, \quad W_{,z} + \nu U_{,x} = (1 - \nu^2)\bar{\sigma}. \quad (8)$$

If we assume that $\bar{\sigma}$ and $\bar{\tau}$ are known, then (8) represents a simple first-order system of partial differential equations for U and W, hyperbolic in the *spatial* variables x and z. As the time t enters the system (8) only as a parameter, we shall often suppress t when writing down the arguments of a function.

To integrate (8) we introduce the characteristic coordinates

$$\xi = x + \sqrt{\nu}z, \quad \zeta = x - \sqrt{\nu}z \quad (9)$$

so that

$$\frac{\partial}{\partial x} = \frac{\partial}{\partial \xi} + \frac{\partial}{\partial \zeta}, \quad \frac{\partial}{\partial z} = \sqrt{\nu}\left(\frac{\partial}{\partial \xi} - \frac{\partial}{\partial \zeta}\right). \quad (10)$$

If we add to or subtract from $(8)_2$ Eq. $(8)_1$ multiplied by $\sqrt{\nu}$ and introduce the notation[1]

$$A^{\pm} = (1 - \nu^2)\bar{\sigma} \pm \sqrt{\nu}\kappa\bar{\tau}, \quad (11)$$

our hyperbolic system takes the form

$$2\sqrt{\nu}(\sqrt{\nu}U + W)_{,\xi} = A^+(\xi, \zeta) \quad (12)$$

$$2\sqrt{\nu}(\sqrt{\nu}U - W)_{,\zeta} = A^-(\xi, \zeta) \quad (13)$$

which may be integrated to yield

$$2\sqrt{\nu}(\sqrt{\nu}U + W) = \int_{\alpha(\zeta)}^{\xi} A^+(\bar{\xi}, \zeta)d\bar{\xi} + \sqrt{\nu}F(\zeta) \quad (14)$$

$$2\sqrt{\nu}(\sqrt{\nu}U - W) = \int_{\alpha(\xi)}^{\zeta} A^-(\xi, \bar{\zeta})d\bar{\zeta} + \sqrt{\nu}G(\xi), \quad (15)$$

where F and G are unknown functions of integration and

$$\alpha(\xi) = \begin{cases} -\xi, & \xi \in [-\sqrt{\nu}H, \sqrt{\nu}H] \\ \xi - 2\sqrt{\nu}H, & \xi \in [\sqrt{\nu}H, \sqrt{\nu}H + L] \end{cases}. \quad (16)$$

(See Fig. 1.)

[1] In (11) and what follows, we take the spatial arguments of $A^{\pm}$ to be (ξ, ζ), but those of $\bar{\sigma}$ and $\bar{\tau}$ to be x and z. If we wish to write $A^{\pm}$ as a function of x and z (with t suppressed), we shall use (9) to write $A^{\pm}(x + \sqrt{\nu}z, x - \sqrt{\nu}z)$, etc.

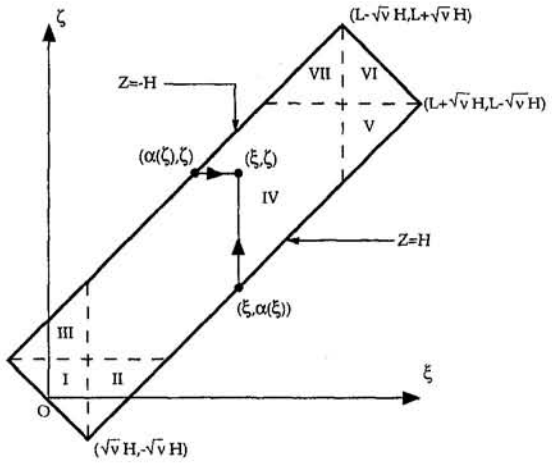

Fig. 1 Geometry and integration paths for a rectangular beam in characteristic coordinates

To proceed further, we henceforth confine attention to the *flexure problem* in which

$$\begin{Bmatrix} W, \bar{\tau} \\ U, \bar{\sigma} \end{Bmatrix} \text{ are } \begin{Bmatrix} \text{even} \\ \text{odd} \end{Bmatrix} \text{ in } z. \quad (17)$$

(The parity is reversed in the complementary *extension problem.*) From (9) we see that replacing z by $-z$ is equivalent to interchanging ξ and ζ. Thus, by (11) and (17),

$$A^+(\xi, \zeta) = -A^-(\zeta, \xi). \quad (18)$$

Substituting (18) into (14) and again using (17), we further conclude that

$$G(\xi) = -F(\xi), \quad -\sqrt{\nu}H \le \xi. \quad (19)$$

Finally, by adding and subtracting (14) and (15) and changing the dummy variable of integration from $\bar{\xi}$ to $\bar{\zeta}$, we obtain the following explicit formulas for the horizontal and vertical displacements in terms of $\bar{\sigma}$, $\bar{\tau}$ (via A^-), and the unknown function F:

$$4\nu U = \int_{\alpha(\xi)}^{\zeta} A^-(\xi, \bar{\zeta})d\bar{\zeta} - \int_{\alpha(\zeta)}^{\xi} A^-(\zeta, \bar{\zeta})d\bar{\zeta} + \sqrt{\nu}[F(\zeta) - F(\xi)] \quad (20)$$

$$4\sqrt{\nu}W = -\int_{\alpha(\xi)}^{\zeta} A^-(\xi, \bar{\zeta})d\bar{\zeta} - \int_{\alpha(\zeta)}^{\xi} A^-(\zeta, \bar{\zeta})d\bar{\zeta} + \sqrt{\nu}[F(\zeta) + F(\xi)]. \quad (21)$$

If $\nu = 0$, (20) and (21) no longer hold (because our hyperbolic system degenerates to a parabolic one). However, returning to (8), we readily obtain by direct integration

$$W = \int_0^z \bar{\sigma}(x, \bar{z})d\bar{z} + F(x) \quad (22)$$

$$U = \int_0^z [(\bar{z} - z)\bar{\sigma}_{,x}(x, \bar{z}) + \kappa\bar{\tau}(x, \bar{z})]d\bar{z} - zF'(x), \quad (23)$$

where $F(x)$ is an arbitrary function of integration and where the argument t has been suppressed. Henceforth, we shall assume that $\nu \neq 0$.

Motion of a Cantilevered Beam

Our aim is to construct, a posteriori, error loads and incremental initial conditions such that (20) and (21) represent *exact solutions* of the dynamic equations of linearized plane stress

theory. This requires that we specify $\bar{\sigma}(x, z, t)$ and $\bar{\tau}(x, z, t)$ (so that we may compute A^-), and that we insure that the displacement and/or traction conditions on the ends of the beam are satisfied exactly. As a first step in this direction we set

$$\bar{\tau} = \tilde{\tau}(x, z, t) + \tfrac{1}{2}\bar{q}(x, t) \tag{24}$$

$$W = \tilde{W}(x, z, t) + \tfrac{1}{2}\kappa \int_0^x \bar{q}(\bar{x}, t)d\bar{x}, \tag{25}$$

where, from $(3)_2$, $\frac{1}{2}\bar{q}$ is the value of $\bar{\tau}$ on the faces of the beam. Under this change of variables, (8) continues to hold with W and $\bar{\tau}$ replaced by $\tilde{W}$ and $\tilde{\tau}$, respectively. This, in turn, implies that (20) and (21) continue to hold with W replaced by $\tilde{W}$ and A^- replaced by

$$A \equiv (1 - \nu^2)\bar{\sigma} - \sqrt{\nu}\kappa\tilde{\tau}. \tag{26}$$

That is,

$$\begin{aligned} 4\nu U &= \int_{\alpha(\xi)}^{\zeta} A(\xi, \bar{\zeta})d\bar{\zeta} - \int_{\alpha(\zeta)}^{\xi} A(\zeta, \bar{\zeta})d\bar{\zeta} \\ &\quad + \sqrt{\nu}[F(\zeta) - F(\xi)] \\ &\equiv \nu\mathcal{U}(x, z, t) \end{aligned} \tag{27}$$

$$\begin{aligned} 4\sqrt{\nu}\tilde{W} &= -\int_{\alpha(\xi)}^{\zeta} A(\xi, \bar{\zeta})d\bar{\zeta} - \int_{\alpha(\zeta)}^{\xi} A(\zeta, \bar{\zeta})d\bar{\zeta} \\ &\quad + \sqrt{\nu}[F(\zeta) + F(\xi)] \\ &\equiv 4\sqrt{\nu}\tilde{\mathcal{W}}(x, z, t), \end{aligned} \tag{28}$$

where, for later use in the initial conditions, we have restored the independent variable t.

For simplicity, we now consider a *cantilevered beam* attached to a rigid wall at $x = 0$ and traction free at $x = L$. If we note (7), (24), and (25) and assume that

$$q(L, t) = 0, \tag{29}$$

we have the boundary conditions

$$U(0, z, t) = 0, \quad \tilde{W}(0, z, t) = 0 \tag{30}$$

$$\tilde{\tau}(L, z, t) = 0, \quad U_{,x}(L, z, t) + \nu\bar{\sigma}(L, z, t) = 0. \tag{31}$$

On the left end of the beam, $-\zeta = \xi \in [-\sqrt{\nu}H, \sqrt{\nu}H]$. Thus, by (16), (27), and (28), the zero displacement condition (30) will be satisfied providing we set

$$F(\xi) = 0, \quad \xi \in [-\sqrt{\nu}H, \sqrt{\nu}H]. \tag{32}$$

On the right end of the beam, $2L - \zeta = \xi \in [L - \sqrt{\nu}H, L + \sqrt{\nu}H]$ and $(31)_2$ leads to a formula for $F'(\xi)$ on the interval $[L, L + \sqrt{\nu}H]$ in terms of $F'(\xi)$ on the interval $[L - \sqrt{\nu}H, L]$ and values and integrals of $\bar{\sigma}$ and $\tilde{\tau}$. The details are as follows.

From $(10)_1$ and (27), we have, using Leibniz' Rule for differentiating integrals with variable limits,

$$\begin{aligned} 4\nu U_{,x} &= 4\nu(U_{,\xi} + U_{,\zeta}) \\ &= -A(\xi, \alpha(\xi))\alpha'(\xi) + \int_{\alpha(\xi)}^{\zeta} A_1(\xi, \bar{\zeta})d\bar{\zeta} \\ &\quad - A(\zeta, \xi) + A(\xi, \zeta) \\ &\quad + A(\zeta, \alpha(\zeta))\alpha'(\zeta) - \int_{\alpha(\zeta)}^{\xi} A_1(\zeta, \bar{\zeta})d\bar{\zeta} \\ &\quad + \sqrt{\nu}[F'(\zeta) - F'(\xi)], \end{aligned} \tag{33}$$

where A_1 means the partial derivative of A with respect to its first argument. If (ξ, ζ) are the characteristic coordinates of a point on the right end of the beam, then from (16),

$$\alpha'(\xi) = \alpha'(\zeta) = 1, \tag{34}$$

and from (3), (26), $(31)_1$, and Fig. 1 (and with the argument t suppressed),

$$A(\xi, \alpha(\xi)) = \tfrac{1}{2}(1 - \nu^2)\bar{p}(\xi - \sqrt{\nu}H) \tag{35}$$

$$A(\xi, \zeta) - A(\zeta, \xi) = 2(1 - \nu^2)\bar{\sigma}(L, \xi/\sqrt{\nu} - L/\sqrt{\nu}), \tag{36}$$

where the last relation follows because $\bar{\sigma}$ is odd and $\tilde{\tau}$ is even in z. Thus, rewriting $(31)_2$ in the form

$$4\nu U_{,x} = -4\nu^2\bar{\sigma} \tag{37}$$

and setting $\zeta = 2L - \xi$, we obtain

$$\begin{aligned} \sqrt{\nu}F'(\xi) &= \sqrt{\nu}F'(2L - \xi) - \tfrac{1}{2}(1 - \nu^2) \\ &\quad \times [\bar{p}(2L - \xi - \sqrt{\nu}H) + \bar{p}(\xi - \sqrt{\nu}H)] \\ &\quad + 2(1 + \nu^2)\bar{\sigma}(L, \xi/\sqrt{\nu} - L/\sqrt{\nu}) \\ &\quad + \int_{\xi - 2\sqrt{\nu}H}^{2L - \xi} A_1(\xi, \bar{\zeta})d\bar{\zeta} - \int_{2L - 2\sqrt{\nu}H - \xi}^{\xi} \\ &\quad A_1(2L - \xi, \bar{\zeta})d\bar{\zeta}, \quad \xi \in [L, L + \sqrt{\nu}H]. \end{aligned} \tag{38}$$

An integration now determined $F(\xi)$ within a constant on the interval $[L, L + \sqrt{\nu}H]$, in terms of $F'(\xi)$ on the interval $[L - \sqrt{\nu}H, L]$, the prescribed value of $\bar{p}$, and the yet-to-be-determined values of $\bar{\sigma}$ and $\tilde{\tau}$.

To obtain a useful formula for $F(\xi)$ on the interval $[\sqrt{\nu}H, L]$, let

$$V = W(x, 0, t) \tag{39}$$

denote the vertical displacement of the centerline of the beam. If we set $z = 0$, i.e., if we set $\zeta = \xi = x$, then, in view of (25) and (39), we obtain from (28), upon setting $\bar{\zeta} = \sqrt{\nu}\eta$ and suppressing the argument t,

$$F(\xi) = 2V(\xi) - \kappa \int_0^{\xi} \bar{q}(\bar{x})d\bar{x} + \int_{\alpha(\xi)/\sqrt{\nu}}^{\xi/\sqrt{\nu}} A(\xi, \sqrt{\nu}\eta)d\eta, \quad \xi \in [\sqrt{\nu}H, L]. \tag{40}$$

This relation, of course, also must hold on the interval $[0, \sqrt{\nu}H]$ in which case it must agree with (32). This yields the *consistency condition*

$$\kappa \int_0^{\xi} \bar{q}(\bar{x})d\bar{x} = 2V(\xi) + \int_{-\xi/\sqrt{\nu}}^{\xi/\sqrt{\nu}} A(\xi, \sqrt{\nu}\eta)d\eta, \quad \xi \in [0, \sqrt{\nu}H], \tag{41}$$

where we have used (16) to set $\alpha(\xi) = -\xi$. Differentiating this relation with respect to ξ and noting that $A(\xi, \xi) = -\sqrt{\nu}\kappa\tilde{\tau}(\xi, 0)$ (because $\bar{\sigma}$ is odd in z), we have the alternative consistency condition

$$\kappa\bar{q}(\xi) = 2V_{,\xi}(\xi) - 2\kappa\tilde{\tau}(\xi, 0) + \int_{-\xi/\sqrt{\nu}}^{\xi/\sqrt{\nu}} A_1(\xi, \sqrt{\nu}\eta)d\eta, \quad \xi \in [0, \sqrt{\nu}H]. \tag{42}$$

Given *any* (sufficiently smooth) choice of $\bar{\sigma}(x, z, t)$, $\tilde{\tau}(x, z, t)$, and $V(x, t)$, we may compute $F(\xi)$ from (32), (38), and (40), and thence $U(x, z, t)$ and $W(x, z, t)$ from (25), (27), and (28). We may then choose $\bar{q}$ according to (42)—the value of $\bar{q}$ in the interval $[\sqrt{\nu}H, L]$ being arbitrary—and choose the body forces f_x and f_z so that the equations of motion (2) are satisfied identically.

To meet the initial conditions (4) and (5), we must add to the given initial data for U, $U_{,t}$, W, and $W_{,t}$, the respective *incremental displacements and velocities*—see (27) and (28)—

$$\Delta U(x, z) \equiv \mathcal{U}(x, z, 0) - U^*(x, z) \tag{43}$$

$$\Delta U_t(x, z) \equiv \mathcal{U}_{,t}(x, z, 0) - U_t^*(x, z) \tag{44}$$

$$\Delta W(x, z) \equiv \tilde{W}(x, z, 0) + \tfrac{1}{2}\kappa \int_0^x \bar{q}(\bar{x}, 0)d\bar{x} - W^*(x, z) \tag{45}$$

$$\Delta W_t(x, z) \equiv \tilde{W}_{,t}(x, z, 0) + \tfrac{1}{2}\kappa \int_0^x \bar{q}_{,t}(\bar{x}, 0)d\bar{x} - W_t^*(x, z). \tag{46}$$

All of the machinery that we have developed permits us to evaluate a posteriori, but explicitly, the errors we make in approximating $\bar{\sigma}$, $\bar{\tau}$, and V, such errors being reflected in the *error loads* $\bar{f}_x$, $\bar{f}_z$, and $\bar{q}$, and in the incremental initial displacements and velocities ΔU, ΔW, ΔU_t, and ΔW_t. We now consider the simplest possible choice of $\bar{\sigma}$, $\bar{\tau}$, and V.

Elementary (Euler-Bernoulli) Beam Theory

Here, the vertical centerline displacement satisfies the well-known equation of motion

$$(\tfrac{2}{3})H^3V_{,xxxx} + 2\bar{p}HV_{,tt} = \bar{p}(x, t), \tag{47}$$

where, from $(3)_1$, $\frac{1}{2}\bar{p}$ is the prescribed value of the normal stress on the faces of the beam, divided by Young's modulus E. Further, we choose $\bar{\sigma}$ and $\bar{\tau}$ to be the associated dimensionless normal and shear stresses—see Duva and Simmonds (1992)—which satisfy

$$-zV_{,xxx} + \bar{\tau}_{,z} = 0, \quad \bar{\tau}_{,x} + \bar{\sigma}_{,z} = \bar{p}V_{,tt} \tag{48}$$

together with the face traction conditions $\bar{\sigma}(x, \pm H, t) = \pm\frac{1}{2}\bar{p}(x, t)$ and $\bar{\tau}(x, \pm H, t) = 0$. That is,

$$\bar{\tau} = \tfrac{1}{2}H^2(\hat{z}^2 - 1)V_{,xxx}(x, t) \tag{49}$$

$$\bar{\sigma} = (\hat{z}/4)[2\bar{p}H(\hat{z}^2 - 1)V_{,tt}(x, t) + (3 - \hat{z}^2)\bar{p}(x, t)], \tag{50}$$

where

$$\hat{z} = z/H. \tag{51}$$

At the built-in end of the beam we impose the classical conditions

$$V(0, t) = V_{,x}(0, t) = 0. \tag{52}$$

The first condition is a necessary consequence of the fact that $V(0, t) = W(0, 0, t)$. The second condition could be conceivably modified, say

$$V_{,x}(0, t) = \kappa\bar{\tau}(0, 0, t) = -\tfrac{1}{2}\kappa H^2V_{,xxx}(0, t), \tag{53}$$

which, by (42), would yield $\bar{q}(0, t) = 0$. However, we shall use (52) for simplicity.

By (24), (29), and (49), the absence of shear stress at the right end of the beam leads to the classical condition

$$V_{,xxx}(L, t) = 0. \tag{54}$$

To satisfy the condition of vanishing normal stress at the free end, we differentiate $(31)_2$ with respect to z and then use $(8)_1$ to write the resulting condition in the form

$$W_{,xx}(L, z, t) = \kappa\bar{\tau}_{,x}(L, z, t) + \nu\bar{\sigma}_{,z}(L, z, t). \tag{55}$$

Setting $z = 0$ and recalling (24), (39), $(48)_2$, and (50), we obtain

$$V_{,xx}(L, t) = \tfrac{1}{2}(3\kappa - \nu)\bar{p}V_{,tt}(L, t) - (\tfrac{3}{4})H^{-1}(\kappa - \nu)\bar{p}(L, t) + \tfrac{1}{2}\kappa\bar{q}_{,x}(L, t). \tag{56}$$

In the classical theory of beams, the right side of (56) is zero. Note that choosing $F'(\xi)$ according to (38) insures that (55) is satisfied for $z \in [-H, H]$ and is automatically consistent with (56).

The initial conditions (5) on W and $W_{,t}$ imposed, in particular, at $z = 0$, require that

$$V(x, 0) = W^*(x, 0), \quad V_{,t}(x, 0) = W_t^*(x, 0). \tag{57}$$

It only remains to satisfy the equations of motion. Dividing (2) by E and substituting (7), (24), and (48), we obtain the error body forces

$$\bar{f}_x = \bar{p}U_{,tt} - (zV_{,x} + U)_{,xx} - \nu\bar{\sigma}_{,x} \tag{58}$$

$$\bar{f}_z = -\tfrac{1}{2}\bar{q}_{,x} + \bar{p}(W - V)_{,tt}. \tag{59}$$

All error loads and incremental initial conditions have now been expressed in terms of the solution of the governing differential equation of elementary beam theory, (47). This solution satisfies the boundary conditions (52), (54), and (56), together with the initial conditions (57). Since the applied face shear $\frac{1}{2}q$ remains arbitrary outside an edge zone at the left end of the beam, we set, for simplicity,

$$\bar{q}(x, t) = 0, \quad x \in [\sqrt{\nu}H, L] \tag{60}$$

so that, in particular, the term $\frac{1}{2}\kappa\bar{q}_{,x}(L, t)$ disappears from the boundary condition (56).

Example

To run through the mechanics of computing the error loads, let us consider the simple static solution for a beam under a constant face traction $p(x, t) = p_0$.

Equation (47) of elementary beam theory—with the slightly modified classical boundary conditions (52), (54), and (56)—has the solution

$$V = (\bar{p}_0L^4/16H^3)\hat{x}^2\{6[1 - (\kappa - \nu)\epsilon^2] - 4\hat{x} + \hat{x}^2\}, \tag{61}$$

where

$$\hat{x} = x/L \quad \text{and} \quad \epsilon = H/L. \tag{62}$$

From (49) and (50), the dimensionless (modified) shear and normal stresses follow as

$$\bar{\tau} = (3\bar{p}_0L/4H)(1 - \hat{x})(1 - \hat{z}^2) \tag{63}$$

$$\bar{\sigma} = (\bar{p}_0/4)\hat{z}(3 - \hat{z}^2). \tag{64}$$

To compute the error load $\bar{q}$, we first need A, which follows from (26), (63), and (64) as

$$A = -(3\sqrt{\nu}\kappa\bar{p}_0L/4H)[(1 - \hat{x})(1 - \hat{z}^2) + O(\epsilon)]. \tag{65}$$

Thus, from (9),

$$A_1 = A_{,\xi} = (\tfrac{1}{2}\sqrt{\nu}H)(\sqrt{\nu}\epsilon A_{,\hat{x}} + A_{,\hat{z}}) = (3\kappa\bar{p}_0L/4H^2)[(1 - \hat{x})\hat{z} + O(\epsilon)]. \tag{66}$$

Inserting (66) into (42) and setting

$$\hat{x} = \frac{\xi + \zeta}{2L}, \quad \hat{z} = \frac{\xi - \zeta}{2\sqrt{\nu}H}, \tag{67}$$

we obtain from (61), (63), and (66)

$$\kappa\bar{q} = (\bar{p}_0 L^3/2H^3)[3\hat{x} - 3\hat{x}^2 + \hat{x}^3 + O(\epsilon^2)] \times \mathcal{H}(\sqrt{\nu}\epsilon - \hat{x}) = O(\bar{p}_0 L^2/H^2), \quad (68)$$

where $\mathcal{H}$ is the Heavyside step function. Thus, in the edge zone where $\hat{x} \in [0, \sqrt{\nu}\epsilon]$, the shear error load on the faces of the beam is of the same order of magnitude as the dominant axial stress in the interior of the beam, consistent with the well-known edge effect at a built-in end. (See, for example, Duva and Simmonds, 1992.)

The error body force $\bar{f}_z$ follows immediately from (59) and (68) as

$$\bar{f}_z = -(3\bar{p}_0 L^2/4\kappa H^3) \times [\mathcal{H}(\sqrt{\nu}\epsilon - \hat{x}) - \sqrt{\nu}\epsilon\delta(\hat{x} - \sqrt{\nu}\epsilon) + O(\epsilon)], \quad (69)$$

where δ is the Dirac delta. Thus, L times the vertical body force is of the order of magnitude of the dominant axial stress within a boundary layer of width $\sqrt{\nu}H$, with a concentrated force at $x = \sqrt{\nu}H$, but is zero elsewhere. The appearance of the delta function in (69) is easily avoided by taking $\bar{q}$ on the interval $[\sqrt{\nu}H, 2\sqrt{\nu}H]$ to be not zero but

$$\bar{q} = \bar{q}(\sqrt{\nu}H, t)\phi(x/\sqrt{\nu}H - 1), \quad (70)$$

where $\phi(\alpha)$ is a function such that $\phi(0) = 1$, $\phi'(0) = \phi(1) = \phi'(1) = 0$, and which smoothly and monotonically decreases as α decreases. With this choice,

$$\bar{f}_z = \begin{cases} O(\bar{p}_0 L^2/H^3), & x \in [0, 2\sqrt{\nu}H) \\ 0, & x \in [2\sqrt{\nu}H, L] \end{cases}. \quad (71)$$

In computing the remaining error load $\bar{f}_x$ from (58), we note, according to (27) and Fig. 1, that the horizontal displacement U has a different representation in each of the regions labeled I to VII. As the major errors in elementary beam theory can be expected to occur at a built-in end, we compute $\bar{f}_x$ for region I only. Thus, by (16) and (32), (27) reduces to

$$4\nu U = \int_{-\xi}^{\zeta} [A(\xi, \eta) - A(\zeta, -\eta)]d\eta, \quad \xi, \zeta \in [-\sqrt{\nu}H, \sqrt{\nu}H]. \quad (72)$$

But in region I, $\hat{x} = O(\sqrt{\nu}\epsilon)$ and $\hat{z} = O(1)$. Hence, from (65), $A = O(\sqrt{\nu}\bar{p}_0 L/H)$. Moreover, because $\xi + \zeta = O(\sqrt{\nu}H)$, (72) yields the estimate

$$U = O(\bar{p}_0 L), \quad \xi, \zeta \in [-\sqrt{\nu}H, \sqrt{\nu}H]. \quad (73)$$

On the other hand, (61) shows that in region I

$$zV = O(\bar{p}_0 L^2). \quad (74)$$

Thus, in region I, (58) takes the form

$$\bar{f}_x = O(\bar{p}_0/L) \quad (75)$$

so, in this region, the horizontal error body force is smaller by a factor of H^3/L^3 than the vertical error body force.

Conclusions

We have presented a scheme whereby, given (dimensionless) fields of normal and shear stress $\bar{\sigma}(x, z, t)$ and $\bar{\tau}(x, z, t)$, and the vertical centerline displacement $V(x, t)$, we may compute exact two-dimensional displacement fields in an elastic beam, provided that certain explicitly computable error loads and incremental initial conditions are imposed. The simple example of a cantilevered beam under a constant normal pressure on its face shows that, if elementary beam theory is used to relate $\bar{\sigma}$ and $\bar{\tau}$ to V, then, as expected, the largest error loads occur within an edge zone of $O(H)$ near the built-in end.

Acknowledgment

The work of J.G.S. was supported, in part, by the Army Research Office under contract ARO-DAAH04-94-G0189.

References

Duva, J. M., and Simmonds, J. G., 1992, "The Influence of Two-Dimensional End Effects on the Natural Frequencies of Cantilevered Beams Weak in Shear," ASME JOURNAL OF APPLIED MECHANICS, Vol. 59, pp. 230–232.

Three-Dimensional Finite Element Analysis of Subsurface Stresses and Shakedown Due to Repeated Sliding on a Layered Medium

E. R. Kral[1]
Graduate Research Assistant,
Assoc. Mem. ASME.

K. Komvopoulos
Associate Professor,
Mem. ASME.

Department of Mechanical Engineering,
University of California,
Berkeley, CA 94720

Results of three-dimensional finite element simulations are presented for the subsurface stress and strain fields in a layered elastic-plastic half-space subjected to repeated sliding contact by a rigid sphere. A single perfectly adhering layer with an elastic modulus and yield strength both two and four times that of the substrate material is modeled. Applied sliding loads are equivalent to 100 and 200 times the initial yield load of the substrate material and sliding is performed to distances of approximately two times the contact radius. The effects of layer material properties and normal load on the loaded and residual stresses occurring from repeated load cycles are examined and compared with stresses produced during the first load cycle. Results for the maximum tensile stresses at the layer/substrate interface and the maximum principal stress in the substrate are presented and their significance for layer decohesion and crack initiation is discussed. Further yielding of substrate material during unloading is discussed, and the possibility of shakedown to an elastic or plastic loading cycle is analyzed for the different material properties and contact loads investigated.

1 Introduction

Sliding contact is an important technical issue since the lifetime of various machine elements is often controlled by the wear resistance of repeatedly contacting solid surfaces. Hard or wear-resistant layers are often used in parts subjected to contact stresses to improve the functional lifetime without necessitating major design or load changes, or in parts where the function of the element requires an unobtrusive means of wear protection, such as in magnetic storage devices. Hence, analysis of the stresses and deformation in layered media resulting from sliding contact is of great practical importance in addition to being of theoretical interest.

Among the earliest studies of elastic-plastic contact is that of Merwin and Johnson (1963), who examined the problem under the assumptions of Hertzian contact pressure and equivalence between the total strain cycle and the elastic strain cycle due to rolling contact loading. In spite of these simplifications, this analysis has provided valuable insight into the plastic flow behavior occurring in rolling contact, particularly the accumulation of residual stresses just below the contact interface and the threshold load for elastic shakedown of the plastically deforming medium. Jiang and Sehitoglu (1994) performed a similar analysis for homogeneous media in which the stress cycle during elastic-plastic rolling contact was assumed to be equivalent to the elastic cycle. Kral et al. (1993) used the finite element method to analyze repeated elastic-plastic indentation of a homogeneous half-space by a rigid sphere. Both isotropic hardening and elastic-perfectly plastic material properties were used, without other simplifying material assumptions. The contacting sphere was modeled with contact elements, thus removing the need for assuming a particular contact pressure distribution. For all the cases investigated, an elastic steady-state cycle was achieved, to within numerical accuracy, after four loading cycles.

Several finite element analyses of elastic-plastic deformation of layered media have been presented in recent years. Komvopoulos (1989) investigated the plane-strain problem of a rigid cylinder indenting an elastic-plastic layered medium with a layer harder and stiffer than the substrate. Significant flattening of the contact pressure profile was found, especially with increasing plastic deformation, and the maximum pressure moved outward toward the contact edge. Tian and Saka (1991a) considered the plane-strain indentation of a multilayered half-space exhibiting linear isotropic strain hardening. Elastic-plastic indentations produced relatively uniform pressure distributions with a slightly higher pressure near the contact edge for sufficiently deep indentations or a sufficiently thin interlayer. Kral et al. (1995a, 1995b) have analyzed repeated elastic-plastic indentation of a half-space with a single harder and stiffer layer. Expressions for an effective modulus and representative flow stress were derived based on layer thickness, material properties, and contact dimensions. A nondimensional strain parameter was formulated which allows comparison with indentation results for a homogeneous half-space. Kral et al. (1996) have also used finite element simulations of three-dimensional elastic-plastic sliding contact to verify scratch hardness models used to interpret the results of scratch tests performed on layered media.

Of particular interest in elastic-plastic contact are the conditions under which the permanent deformation, residual stresses, and conforming contact geometry may result in purely elastic response under repeated loading, known as elastic shakedown.

[1] Present address: IBM Almaden Research Center, San Jose, CA 95120.

Contributed by the Applied Mechanics Division of THE AMERICAN SOCIETY OF MECHANICAL ENGINEERS for publication in the ASME JOURNAL OF APPLIED MECHANICS.

Discussion on this paper should be addressed to the Technical Editor, Professor Lewis T. Wheeler, Department of Mechanical Engineering, University of Houston, Houston, TX 77204-4792, and will be accepted until four months after final publication of the paper itself in the ASME JOURNAL OF APPLIED MECHANICS.

Manuscript received by the ASME Applied Mechanics Division, Sept. 18, 1995; final revision, Mar. 1, 1996. Associate Technical Editor: M. Ortiz.

Applied loads above the shakedown limit will result in either a continuous increase of plastic strain with each load cycle (ratchetting) or a closed cycle of alternating plastic strain (plastic shakedown). Merwin and Johnson (1963) and Johnson (1985) have reported shakedown limits for repeated sliding of line and point contacts, respectively, on homogeneous media. Johnson (1986) and Bower and Johnson (1989) have investigated the shakedown limits of elastic-perfectly plastic and kinematically hardening materials under both line and point rolling contact. The shakedown limit and deformation characteristics were found to depend primarily on the applied load and contact friction. Above the shakedown limit, repeatedly deforming material remained confined to a subsurface region under low friction conditions ($\mu < 0.25$), while a thin surface layer was repeatedly deformed when higher tractive loads were applied ($\mu > 0.25$). Conversely to the condition with line contact, Ponter et al. (1985) have shown that a protective system of residual shear stresses may arise in point contact that will prevent ratchetting. Bhargava et al. (1985) analyzed repeated plane-strain frictionless rolling contact at and above the shakedown limit by the finite element method. In this analysis, a significantly larger peak of incremental shear strain per cycle was found in the steady state than that predicted by Merwin and Johnson (1963). Kulkarni et al. (1990, 1991) have also performed finite element analysis of repeated rolling contact on a homogeneous half-space both at and above the shakedown limit for elastic-perfectly plastic and kinematic hardening materials. Hertzian pressure loads were applied for several passes. At the shakedown limit, the steady state was attained quickly, within one cycle for the perfectly plastic material. For loads above the shakedown limit, plastic strain accumulated in a subsurface region of the hardening material, and up to the surface for the perfectly plastic material. In addition, the hardening material achieved a steady cycle of plastic deformation immediately, while the perfectly plastic material exhibited incremental plastic strain growth.

In the above analyses, only loading on homogeneous materials has been considered; however, the situation for layered media is significantly more complicated due to the stress and strain discontinuities induced by the material interface. Nevertheless, some analyses of elastic-plastic contact on layered media have been amenable to a shakedown analysis. For instance, in the finite element study of Kral et al. (1995b) it was shown that, based on the pattern of reyielding during unloading, certain cases could not reach elastic shakedown under repeated indentation loading and would continue to deform plastically with subsequent load cycles.

The objective of this study, therefore, is to utilize finite element simulation techniques to analyze the effects of the layer material properties and normal load on the subsurface stress and deformation behavior due to repeated sliding contact on an elastic-plastic layered half-space without requiring simplifying assumptions on either the contact pressure or the stress and strain cycles. In the present analysis, the sphere was modeled by contact elements, thus eliminating the simplification of an assumed pressure profile. A single layer thickness was considered, and the effect of layer material properties was assessed by modeling layers two and four times stiffer and stronger than the substrate. In addition, the significance of subsurface stresses on cracking and reyielding upon unloading and the likelihood of shakedown to an elastic or plastic loading cycle will be examined. Finite element results for loaded and residual stresses and deformation at the surface of a layered medium have been reported previously (Kral and Komvopoulos, 1996).

2 Modeling Procedures

2.1 Finite Element Mesh. A detailed description of the finite element mesh and contact and friction formulation has been presented elsewhere (Kral and Komvopoulos, 1996). A brief synopsis will be given here for completeness. The three-dimensional finite element mesh used in the present study is shown in Fig. 1. The figure shows half of the mesh corresponding to the region $x \geq 0$. The mesh consists of 8146 eight-node linear interpolation reduced integration elements comprising a total of 10,347 nodes. The reduced-integration elements use a Gaussian integration scheme one order less than the usual 2×2 linear integration, resulting in one integration point per element. The mesh extends from -1120 to 1120 nm in the x direction, from zero to 960 nm in the y direction, and from zero to 1070 nm in the z direction. A rigid spherical indenter with a radius, R, of 1500 nm was modeled, giving normalized mesh dimensions of $-0.747 \leq x/R \leq 0.747$, $0 \leq y/R \leq 0.640$, and $0 \leq z/R \leq 0.713$. The plane $y = 0$ is a plane of symmetry, and sliding proceeds in the positive x direction. The plane of symmetry and the bounding plane $y/R = 0.640$ are constrained against displacement in the y direction, the bounding planes $x/R = -0.747$ and 0.747 are constrained against displacement in the x direction, and the plane $z/R = 0.713$ is constrained against displacement in the z direction.

The finite element mesh models a single layer with thickness, t, equal to 30 nm, thus yielding a normalized thickness $t/R = 0.02$. The inset of Fig. 1 shows the layer and the finer mesh region at the sliding interface. The dimensions of the smallest cubic elements are 5 nm, which is roughly equivalent to the contact radius at initial yielding of the substrate material. The mesh was refined by using linear constraints for the corner nodes of two elements lying on the edge of a larger element, or bilinear constraints for corner nodes lying on the face center of a larger element. Results for elastic indentation of a homogeneous half-space represented by the mesh shown in Fig. 1 compared favorably with analytical results (Kral and Komvopoulos, 1996), and elastic-plastic indentation results were in good agreement with results from the axisymmetric indentation simulations (Kral et al., 1995a, 1995b).

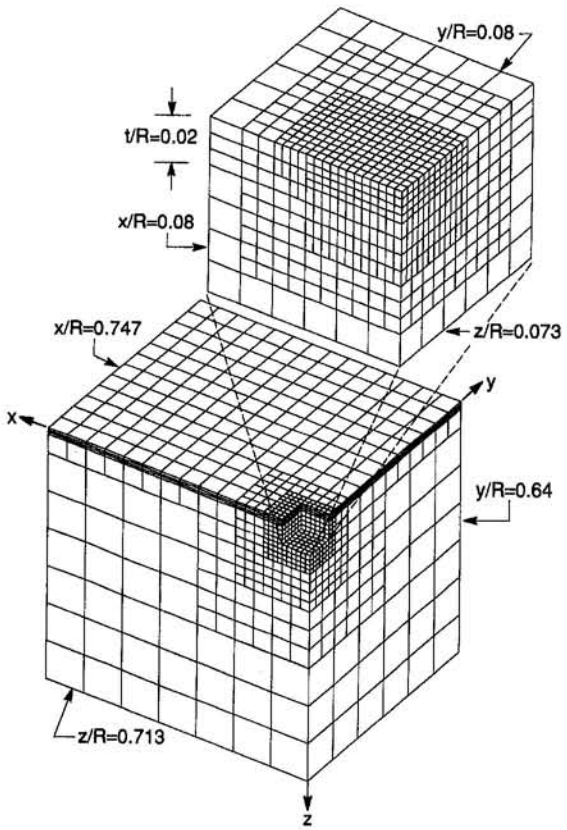

Fig. 1 Three-dimensional finite element discretization of the layered half-space

The indenting and sliding sphere was modeled by 429 two-node rigid surface contact elements. One node of each contact element corresponded to a common master node through which loads and displacements were applied to the sphere. Hard contact was modeled, in which normal traction is applied only when the clearance between a surface node of the deformable layered medium and the rigid sphere surface reaches zero.

2.2 Material Properties and Plasticity Models. According to the von Mises yield criterion, the yield condition is given by

$$\sigma_M = [\tfrac{3}{2} S_{ij} S_{ij}]^{1/2} = \sigma^o,$$

where σ_M is the von Mises equivalent stress, S_{ij} are components of the deviatoric stress tensor, and σ^o is the uniaxial tensile yield stress. The material model for plastic deformation is based on the usual associated flow rule, and the assumption of negligible plastic volume change is maintained. To account for boundary nonlinearities due to the contact elements, an updated Lagrangian formulation is used in the analysis. Elastic-perfectly plastic material behavior is adopted throughout. The equivalent plastic strain, ϵ^p_{eq}, is defined as

$$\epsilon^p_{eq} = \int_S [\tfrac{2}{3} d\epsilon^p_{ij} d\epsilon^p_{ij}]^{1/2},$$

where S is the strain path. The plastic flow rule applies only to yielding material for which $\sigma_M = \sigma^o$. When $\sigma_M < \sigma^o$, the usual elastic constitutive equations apply.

Stresses were normalized by the yield stress of the substrate, σ_y, and loads and distances by the load, P_y, and contact radius, a_y, respectively, corresponding to the initial yield condition of a homogeneous substrate with an elastic modulus equal to 684.6 times σ_y. Results are presented in terms of the parameter β, which is the ratio of both the layer-to-substrate elastic moduli and the layer-to-substrate yield stresses.

2.3 Simulation of Indentation and Sliding. The analysis was performed with the multipurpose finite element code ABAQUS. Simulations were performed for layers both two and four times stiffer and stronger than the substrate (i.e., $\beta = 2$ and 4, respectively). The layer and substrate were modeled as elastic-perfectly plastic. The simulations consisted of an incremental indentation to the specified normal load, P, followed by sliding at a constant normal load and friction coefficient equal to 0.1. Sliding was performed in 2-nm increments to a total distance, Δx, of 60 nm (i.e., $\Delta x/a_y = 12$), which is equivalent to approximately two to three times the initial contact radius. The simulation was completed by incrementally unloading the sphere in the same steps as for the loading. The layered media were then subjected to a second load cycle identical to the first. Table 1 summarizes the material properties and normal loads used in the simulations. Typical CPU times for a 2-nm sliding increment were approximately 36 to 44 hours on an IBM RS/6000 Model 540 workstation and 16 to 18 hours on an IBM RS/6000 Model 580 workstation. The convergence tolerance for most runs was set to $10^{-5}\sigma_y$, although a smaller tolerance was used for some runs.

Table 1 Summary of three-dimensional simulations

	β=2	β=4	
	μ=0.1	μ=0.1	
P/P_y	100	100	200
$\Delta x/a_y$	12	12	12
$(x/a_y)_i$	-8	-8	-8
$(x/a_y)_f$	4	4	4
# load cycles	2	2	2

$(x/a_y)_i$ = initial x coordinate of sphere center
$(x/a_y)_f$ = final x coordinate of sphere center

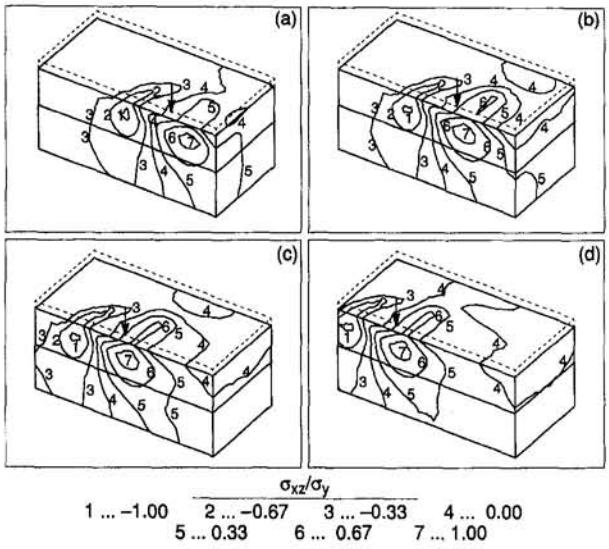

Fig. 2 Contours of σ_{xz} shear stress for $\beta = 2$ and $P/Py = 100$ in the region $-12 \le x/a_y \le 12$, $0 \le y/a_y \le 12$, $1 \le z/a_y \le 12$, at sliding distances $\Delta x/a_y$ equal to (a) 2, (b) 4, (c) 8, and (d) 12

3 Results and Discussion

In the subsequent discussion, it will be understood that either "stiffer" or "harder" refers to the layer with the larger elastic modulus and yield strength (or hardness) ratio (i.e., $\beta = 4$), while "softer" or "more compliant" refers to the layer with the smaller elastic modulus and yield strength ratio (i.e., $\beta = 2$). The effect of increasing the stiffness and hardness of the layer will be shown by comparing results for $\beta = 2$ and 4 with otherwise identical loading conditions (i.e., $P/P_y = 100$ and $\mu = 0.1$), while the effect of normal load will be demonstrated by comparing results for the material cases with $\beta = 4$.

Contours of the σ_{xz} shear stress as a function of sliding distance for the first load cycle are presented in Fig. 2 for the material case with $\beta = 2$ and $P/P_y = 100$. Results are shown in the subsurface region given by $-12 \le x/a_y \le 12$, $0 \le y/a_y$, and $1 \le z/a_y \le 12$ in order to show the distribution of the σ_{xz} stress near the surface as well as on the plane of symmetry. The dotted lines in the figure indicate the contact surface plane ($z/a_y = 0$). The location of the layer interface is shown by a solid line and the sphere center is denoted by an arrow. The shear stress results for this material case and the first load cycle are qualitatively representative of all the material cases and load cycles. The extreme values of the σ_{xz} shear stress occur in elements on the plane of symmetry within the layer at approximately half the layer thickness and exhibit no sensitivity to the sliding distance. A maximum negative shear stress occurs in front of the sphere center, followed by a maximum positive shear stress in the wake. This pattern is commonly seen in plane-strain elastic-plastic analyses of sliding cylinders (Tian and Saka, 1991b; Bhargava et al., 1985), and also occurs in the sliding of a sphere on a layered elastic half-space (O'Sullivan and King, 1988). The reversal of subsurface shear stress coupled with the plastic deformation produces an offset in the stress-strain cycle so that the strain is not completely reversed upon passage of the load (Johnson, 1985). This produces a net forward surface displacement with each load cycle during which the layer is plastically deformed (Kral and Komvopoulos, 1996). In all the present cases, the maximum σ_{xz} shear stress on the plane of symmetry corresponds to the shear yield stress

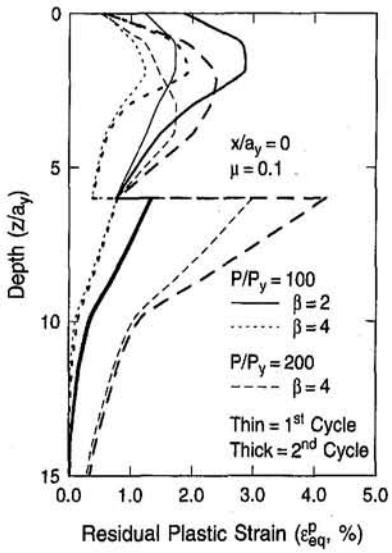

Fig. 3 Residual equivalent plastic strain at $x/a_y = 0$ and $y/a_y = 0$ as a function of depth and load cycle

of the layer, given by $k = \beta\sigma_y/\sqrt{3}$, and is also the only nonzero shear stress. The maximum positive shear stress is slightly closer to the center of contact than is the maximum negative shear stress due to the effect of friction. For frictionless sliding, the locations of the two maxima are approximately evenly spaced about the center of the spherical slider, depending on the amount of residual pile-up material in front of the sphere. A similar shift in the maximum shear stress points due to friction may be seen in the plane-strain finite element simulation of sliding contact on a two-layer half-space by Tian and Saka (1991b).

Results for subsurface plastic strain fields (Kral and Komvopoulos, 1997) indicate that substrate yielding occurs in a region from the interface to some distance into the substrate. Since substrate yielding occurs at the interface, the maximum possible shear stresses at the substrate interface are bounded by the shear yield stress of the substrate. The σ_{xz} interfacial shear stress reaches the substrate shear yield stress on the plane of symmetry since it is the only nonzero shear stress. The σ_{yz} stress never reaches the shear yield stress at the interface, with maximum magnitudes of typically $0.43\sigma_y$ to $0.45\sigma_y$ for $\beta = 4$ and $0.49\sigma_y$ for $\beta = 2$. Therefore the maximum interfacial shear stress in the substrate is the σ_{xz} stress component, which reaches the shear yield stress of the substrate. The largest interfacial shear stress in the layer is the σ_{xy} stress (Kral and Komvopoulos, 1997). These maximum σ_{xz} and σ_{xy} shear stresses would be expected to most greatly influence the adhesion of the layer to the substrate and the likelihood of a shear rupture at the interface during sliding.

A second load cycle was simulated in order to assess the effect of repeated loading on the stresses and plastic strains and the likelihood of shakedown to an elastic loading cycle for the various material combinations and sphere loads investigated. In each case the first load cycle was simply repeated, i.e., the sphere was replaced at the initial indentation location, reloaded to the same normal load with the same load history, translated a distance $\Delta x/a_y = 12$ at a constant normal load as before, and then unloaded by reversing the load steps. In the following graphs, the line types correspond to the material and load case, and the line thickness indicates the load cycle for which the results are given, with the thin and thick lines indicating results from the first and second load cycles, respectively. In addition, all the comparisons with results from the first load cycle are done at a sliding distance $\Delta x/a_y = 8$ to avoid any influence of the residual pile-up material in front of the contact groove on the results for the second load cycle. Thus, the figures compare the stress and strain fields for approximately steady-state sliding with prow formation (first load cycle) with those for sliding in the residual groove in which the frontal material has been removed (second load cycle).

Contours of the equivalent plastic strain, ϵ^p_{eq}, at a sliding distance $\Delta x/a_y = 12$ during the second load cycle for the three repeated cases exhibited identical qualitative features to those occurring during the first load cycle (Kral and Komvopoulos, 1996), though quantitative features differ. Figure 3 shows results for the residual equivalent plastic strain as a function of depth after each load cycle at $x/a_y = 0$ and $y/a_y = 0$. For all cases, the plastic strain in the layer increases significantly during the second load cycle. This incremental increase is related to the phenomenon of forward surface flow that was discussed with reference to the surface displacements in a previous publication (Kral and Komvopoulos, 1996). Forward flow, or a steady increment of permanent forward surface displacement, occurs because the increment of forward shearing due to the subsurface positive shear stress is slightly greater than the increment in backward shearing due to the subsurface negative shear stress, as mentioned previously with reference to Fig. 2. The largest increase of plastic strain in the layer occurs in the region $1 \leq z/a_y \leq 2$, with a much less significant increase below $z/a_y \approx 3$ for $\beta = 4$ at $P/P_y = 100$ or $z/a_y \approx 5$ for the other two cases. The localized accumulation of plastic strain in the layer and the pattern of localized shear stress maxima shown in Fig. 2 indicate that continued plastic deformation under repeated loading may occur in only a portion of the plastically deformed layer. A similar phenomenon was reported by Merwin and Johnson (1963) for repeated line contact on a homogeneous half-space. It was shown that a repeatedly deformed layer exists slightly under the surface extending to a depth of approximately 1.6 times the contact radius, while the depth of the plastic zone produced during the first load cycle is approximately 2.6 times the contact radius. In the present analysis, all the material cases show a decrease in the accumulation of plastic strain in the layer below $z/a_y \approx 4$; this is most pronounced for the case with $\beta = 4$ and $P/P_y = 100$. In the substrate, only the higher load case exhibits a significant accumulation of plastic strain during the second load cycle. The two lower load cases exhibit only very small increases in substrate plastic strain both during and after the second load cycle, indicating that the substrate may be approaching elastic shakedown in these cases. The maximum equivalent plastic strain in the layer and substrate at the end of each loading cycle is given in Table 2 as a function of the layer material properties and normal load. The increase of plastic strain in the layer is significant in all cases, while the growth of the maximum plastic strain in the substrate is very small for the lower load cases but still quite large for the higher load case.

The pattern of accumulation of plastic strain in the layer and substrate raises the question of whether the layer and/or the substrate will shakedown to an elastic deformation cycle under repeated sliding. The ratio of the peak contact pressure to a representative shear yield stress (p_o/k_{eff}) assumes values greater than 6 for all the repetitive loading cases (Kral and Komvopoulos, 1996), which is well above the shakedown limit for point contact on a half-space, given by $p_o/k = 4.7$ (Johnson, 1985). However, since the layer and substrate consist of differ-

Table 2 Maximum equivalent plastic strain versus load cycle

β	P/P$_y$	First Load Cycle (%)		Second Load Cycle (%)	
		layer	substrate	layer	substrate
2	100	2.26	1.34	3.39	1.38
4	100	1.29	0.77	2.01	0.78
	200	1.92	3.02	2.83	4.28

ent materials, it is reasonable to consider that there may be two shakedown loads. Indeed, the patterns of increasing plastic strain shown in Fig. 3 indicate that the layers show no proclivity toward purely elastic deformation, while the substrates under the lower load show a definite tendency toward mitigation of plastic deformation with subsequent load cycles. Since the dimensions of the contact groove do not change significantly after the first load cycle (Kral and Komvopoulos, 1996), the contact pressure distribution during the second load cycle may be assumed to have reached a steady state. According to Melan's theorem (Merwin and Johnson, 1963), if any residual stress state may be found which, when coupled with the stresses due to the repeated load, produces an elastic cycle, the material will shake down to an elastic state. Conversely, if it can be shown that no such system of residual stresses exists, then the material will not shake down to an elastic cycle but will continue to plastically deform during each subsequent load cycle. In such cases, the material may shakedown to a steady cycle of plastic deformation (plastic shakedown) or may continue to accumulate plastic strain on each successive load cycle (ratchetting).

Although the stress state in three-dimensional contact is very complicated, insight into the shakedown state can be obtained by restricting attention to the stress state on the plane of symmetry. As discussed previously, the σ_{xz} stress is the only shear stress present on the plane of symmetry, and thus its maximum values can be expected to control the ability of the material to reach elastic shakedown. The features of the σ_{xz} stress during the second load cycle remain identical to those during the first cycle shown in Fig. 2, i.e., a maximum negative shear stress occurs in front of the sphere center and a maximum positive shear stress arises in the wake. In all the repeated load cases, the maximum and minimum shear stresses in the layer are the positive and negative shear yield stresses. Therefore, since certain layer material points yield at both the negative and positive shear yield stresses as the contact load passes, the load path encompasses the diameter of the yield locus, and hence there is no residual stress state that can be added to these stresses to inhibit further yielding. Thus, the layer will continue to plastically deform on each passage of the load and will not shake down to an elastic stress cycle. If the region of continuing plastic deformation is contained within the subsurface, the eventual steady state must be one of reversed plastic flow, or plastic shakedown, due to the constraint of surrounding elastic material. As discussed by Johnson and Jefferis (1963), a residual σ_{xy} shear stress arises on the surface due to the restraint of the undeformed elastic material on the sides of the contact groove. Equilibrium under residual conditions requires a nonzero subsurface σ_{xz} shear stress component, which resists forward flow. After sufficient load passes to build up these residual σ_{xz} shear stresses, the increment of forward flow would be expected to gradually decrease to zero, resulting in a closed cycle of plastic deformation (plastic shakedown) in the layer subsurface region undergoing repeated plastic deformation. However, if the repeatedly deforming region reaches the free surface, then the mechanism of incremental collapse, or ratchetting, is enabled (Ponter et al., 1985). In the present analysis, the softer layer ($\beta = 2$) exhibits a pronounced increase in plastic strain up to the surface (Fig. 3), indicating that ratchetting is a possibility in this case. The two cases with the harder layer ($\beta = 4$) also show an increase in plastic strain on the surface after the second load cycle, but with a profoundly smaller increase in magnitude (Fig. 3). It is therefore considered likely that these two cases will exhibit plastic shakedown in the layer with further load cycles.

A similar stress state exists in the substrate, with a maximum negative shear stress occurring on the plane of symmetry in front of the sphere center and a positive maximum occurring behind the sphere center, as shown in Fig. 2. For the high load case, the maximum shear stresses attained in the substrate during the second load cycle are equal to the shear yield stress, and hence by the same reasoning as before, the substrate will not exhibit shakedown for this case. However, for both the lower load cases, the maximum σ_{xz} shear stresses on the plane of symmetry in the substrate, although still the only nonzero shear stresses, are well below the shear yield stress. Thus, a residual shear stress which will inhibit yielding in the substrate could be devised, and it is therefore expected that the substrate will attain an elastic steady-state cycle for these cases.

A comparison of the σ_{xx} and σ_{yy} stresses in the layer at the layer/substrate interface for the two load cycles is shown in Fig. 4. For both normal load cases, the σ_{xx} stresses (Fig. 4(a)) at the layer interface are qualitatively similar, but the peak tensile stress (for the $\beta = 4$ cases) decreases during the second load cycle. The σ_{xx} stress for $\beta = 2$ is compressive throughout. The σ_{yy} stresses are also qualitatively similar between the two load cycles (Fig. 4(b)). For this stress component, the magnitude of the local maximum tensile stress in the wake ($x/a_y = -12$ to -16) does not change significantly with the load cycle, while in front of the sphere it exhibits a decrease during the second load cycle. Since these tensile stresses are associated with the hoop stress constraining the plastic zone (Kral and Komvopoulos, 1997), the decrease in magnitude may be associated with the smaller increment of accumulated plastic strain in the layer during the second load cycle.

The effect of load cycle and sliding distance on the maximum value of the maximum principal stress in the substrate, σ_1, is shown in Fig. 5. In all cases, the maximum remains relatively constant with sliding distance during the second cycle, maintaining approximately the magnitude attained after unloading from the first load pass. The maximum principal stress in the second load cycle exhibits a slight decrease in maximum magnitude with distance for $\beta = 4$, and all cases exhibit a final maximum stress slightly below the value reached after the first load cycle. Thus, the propensity for crack initiation in the substrate does not change significantly, at least over the first two load cycles. Stress results (not shown here for brevity) indicate that in all cases, the maximum σ_{xy} interfacial shear stress during the second load cycle is slightly less than or comparable to the maximum attained during the first cycle (Kral and Komvopoulos, 1997). For the lower load cases, the maximum σ_{xz} interfacial shear stress decreases during the second load cycle,

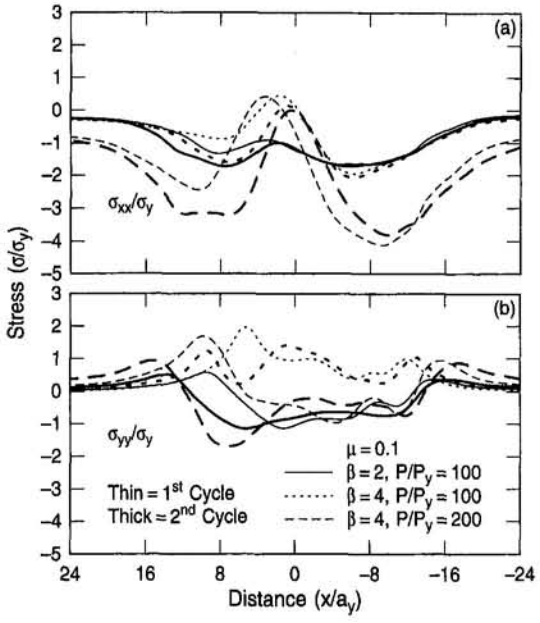

Fig. 4 Stresses at the layer interface ($z/a_y = 6^-$) on the plane of symmetry ($y/a_y = 0$) at a sliding distance $\Delta x/a_y = 8$ as a function of load cycle: (a) σ_{xx} stress and (b) σ_{yy} stress

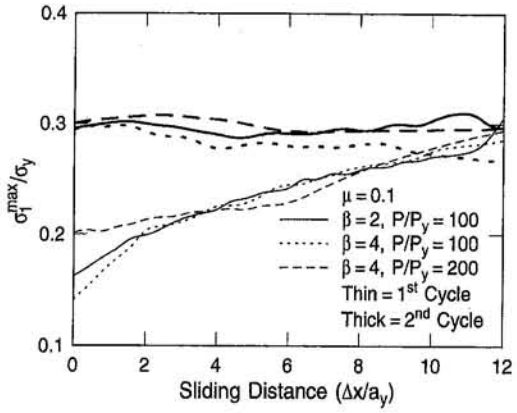

Fig. 5 Maximum value of the maximum principal stress σ_1 in the substrate as a function of sliding distance and load cycle

as evidenced by the general lack of continued substrate yielding. The maximum interfacial σ_{yz} shear stress actually increases by about five to ten percent for these cases, but is still below the shear yield stress of the substrate. For the higher load case, the magnitude of the σ_{xz} interfacial shear stress in the second load cycle is equal to the substrate shear yield stress due to the continued yielding of the substrate, while there is virtually no change in the maximum σ_{yz} interfacial shear stress.

Figure 6 compares the residual σ_{xx} and σ_{yy} stresses at the layer interface as a function of load cycle. The results for the σ_{xx} stress, shown in Fig. 6(a), are very similar for all the load cases, with the residual stress remaining compressive along the entire layer interface. The σ_{yy} component, shown in Fig. 6(b), also exhibits similar characteristics between load cycles, but with a slight increase in the tensile residual stress in front of the contact groove at the end of the second load cycle. However, the maximum tensile residual σ_{yy} stresses are still less than or comparable to those arising during sliding in the same region (Fig. 4(b)). Thus, the tendency for crack initiation at the interface remains greatest during sliding for repeated load cycles. Finally, the tensile residual σ_{zz} stresses at the interface after the second load cycle assume magnitudes comparable to those

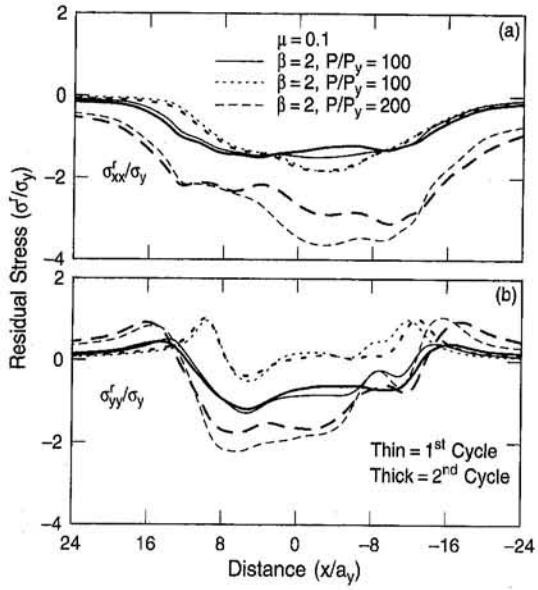

Fig. 6 Residual stresses in the layer at the interface ($z/a_y = 6^-$) on the plane of symmetry ($y/a_y = 0$) as a function of load cycle after unloading at a sliding distance $\Delta x/a_y = 12$: (a) σ_{xx} stress and (b) σ_{yy} stress

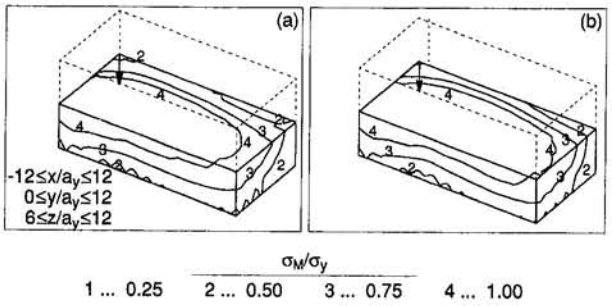

Fig. 7 Contours of residual von Mises equivalent stress σ_M in the substrate after unloading from $P/Py = 200$ for $\beta = 4$: (a) first load cycle and (b) second load cycle

occurring after the first load cycle (Kral and Komvopoulos, 1997) for all the load cases.

Figure 7 shows contours of the residual von Mises equivalent stress, revealing the actively yielding region in the substrate as a function of load cycle for the higher load case. It is shown that unloading after the second load cycle again produces significant reyielding of the substrate material. In addition, the reyielding occurs over a larger region than in the first cycle. However, the layer exhibits no yielding points in the residual state. The case with $\beta = 4$ at $P/P_y = 100$ exhibited no reyielding in either the layer or the substrate after the second load cycle, while the $\beta = 2$ case exhibited reyielding in the substrate at only three integration points after the second cycle, which is not considered significant. It may be inferred that the reyielding of substrate material during unloading from $P/P_y = 200$ will make the achievement of an elastic steady-state cycle less likely for the higher load case.

4 Conclusions

The subsurface stress and strain fields resulting from repeated sliding contact on a layered half-space were examined with the finite element technique. A 30-nm-thick layer was modeled, with stiffness and yield strength both two and four times that of the substrate. Elastic-perfectly plastic material was assumed throughout the simulations. Sliding was simulated for loads 100 and 200 times the yield load of the substrate material in order to determine the effect of normal load on the subsurface stresses and strains.

The σ_{xz} stress in the layer on the plane of symmetry exhibited a region of high negative shear stress in front of the sphere center, followed by a reversal to a high positive shear stress in the wake of the sphere. The σ_{xz} interfacial shear stress reached the maximum possible value, i.e., the shear yield stress of the substrate, for all cases during the first load cycle, but fell below that during the second load cycle for the low load cases. The σ_{yz} stress at the interface was below the shear yield stress of the substrate for all cases. The maximum principal stress in the substrate arising under repetitive loading was similar for all cases considered, indicating that the propensity for crack initiation in the substrate is not greatly affected by the layer material properties or normal load.

All cases exhibited a substantial accumulation of plastic strain in the layer during the second load cycle, but only the higher load case exhibited significant accumulation of plastic strain in the substrate. It was shown based on the shear stresses on the plane of symmetry that the higher load case will not shake down to an elastic cycle, whereas the shear stresses indicate that the lower load cases will shake down only in the substrate. The tensile σ_{xx} and σ_{yy} stresses along the layer interface during the second load cycle were less than those during the first cycle, while the residual σ_{xx} and σ_{yy} stresses were very similar to those occurring after completion of the first load cycle. The σ_{xy} and σ_{xz} interfacial shear stresses were generally less than or compa-

rable to those occurring during the first cycle, while the σ_{yz} interfacial shear stress increased slightly in the second cycle. Reyielding in the substrate after the second load cycle occurred only for the highest contact load, and resulted in a larger plastic zone than that produced in the first load cycle.

Acknowledgments

This work was partially supported by the Surface Engineering and Tribology Program of the National Science Foundation under Grant No. MSS-8996309 and the Computer Mechanics Laboratory at the University of California at Berkeley.

References

Bhargava, V., Hahn, G. T., and Rubin, C. A., 1985, "An Elastic-Plastic Finite Element Model of Rolling Contact Part 2: Analysis of Repeated Contacts," ASME JOURNAL OF APPLIED MECHANICS, Vol. 52, pp. 75–82.

Bower, A. F., and Johnson, K. L., 1989, "The Influence of Strain Hardening on Cumulative Plastic Deformation in Rolling and Sliding Line Contact," *Journal of Mechanics and Physics of Solids,* Vol. 37, pp. 471–493.

Jiang, Y., and Sehitoglu, H., 1994, "An Analytical Approach to Elastic-Plastic Stress Analysis of Rolling Contact," ASME *Journal of Tribology,* Vol. 116, pp. 577–587.

Johnson, K. L., and Jefferis, J. A., 1963, "Plastic Flow and Residual Stresses in Rolling and Sliding Contact," *Proceedings of the Institution of Mechanical Engineers, Symposium on Rolling Contact Fatigue,* London, U. K., pp. 50–61.

Johnson, K. L., 1985, *Contact Mechanics,* Cambridge University Press, Cambridge, U. K., pp. 157–184.

Johnson, K. L., 1986, "Plastic Flow, Residual Stress and Shakedown in Rolling Contact," *Proceedings of the Second International Symposium on Contact Mechanics and Wear of Rail/Wheel Systems,* University of Waterloo Press, Canada, pp. 83–97.

Komvopoulos, K., 1989, "Elastic-Plastic Finite Element Analysis of Indented Layered Media," ASME *Journal of Tribology,* Vol. 111, pp. 430–439.

Kral, E. R., Komvopoulos, K., and Bogy, D. B., 1993, "Elastic-Plastic Finite Element Analysis of Repeated Indentation of a Half-Space by a Rigid Sphere," ASME JOURNAL OF APPLIED MECHANICS, Vol. 60, pp. 829–841.

Kral, E. R., Komvopoulos, K., and Bogy, D. B., 1995a, "Finite Element Analysis of Repeated Indentation of an Elastic-Plastic Layered Medium by a Rigid Sphere: Part I—Surface Results," ASME JOURNAL OF APPLIED MECHANICS, Vol. 62, pp. 20–28.

Kral, E. R., Komvopoulos, K., and Bogy, D. B., 1995b, "Finite Element Analysis of Repeated Indentation of an Elastic-Plastic Layered Medium by a Rigid Sphere: Part II—Subsurface Results," ASME JOURNAL OF APPLIED MECHANICS, Vol. 62, pp. 29–42.

Kral, E. R., Komvopoulos, K., and Bogy, D. B., 1996, "Hardness of Thin-Film Media: Scratch Experiments and Finite Element Simulations," ASME *Journal of Tribology,* Vol. 118, pp. 1–11.

Kral, E. R., and Komvopoulos, K., 1996, "Three-Dimensional Finite Element Analysis of Surface Deformation and Stresses in an Elastic-Plastic Layered Medium Subjected to Indentation and Sliding Contact Loading," ASME JOURNAL OF APPLIED MECHANICS, Vol. 63, pp. 365–375.

Kral, E. R., and Komvopoulos, K., 1997, "Three-Dimensional Finite Element Analysis of Subsurface Stress and Strain Fields Due to Sliding Contact on an Elastic-Plastic Layered Medium," ASME *Journal of Tribology,* Vol. 119, to be published.

Kulkarni, S. M., Hahn, G. T., Rubin, C. A., and Bhargava, V., 1990, "Elastoplastic Finite Element Analysis of Three-Dimensional, Pure Rolling Contact at the Shakedown Limit," ASME JOURNAL OF APPLIED MECHANICS, Vol. 57, pp. 57–65.

Kulkarni, S. M., Hahn, G. T., Rubin, C. A., and Bhargava, V., 1991, "Elasto-Plastic Finite Element Analysis of Three-Dimensional Pure Rolling Contact Above the Shakedown Limit," ASME JOURNAL OF APPLIED MECHANICS, Vol. 58, pp. 347–353.

Merwin, J. E., and Johnson, K. L., 1963, "An Analysis of Plastic Deformation in Rolling Contact," *Proceedings of the Institution of Mechanical Engineers,* Vol. 177, pp. 676–690.

O'Sullivan, T. C., and King, R. B., 1988, "Sliding Contact Stress Field Due to a Spherical Indenter on a Layered Elastic Half-Space," ASME *Journal of Tribology,* Vol. 110, pp. 235–240.

Ponter, A. R. S., Hearle, A. D., and Johnson, K. L., 1985, "Application of the Kinematical Shakedown Theorem to Rolling and Sliding Point Contacts," *Journal of Mechanics and Physics of Solids,* Vol. 33, pp. 339–362.

Tian, H., and Saka, N., 1991a, "Finite Element Analysis of an Elastic-Plastic Two-Layer Half-Space: Normal Contact," *Wear,* Vol. 148, pp. 47–68.

Tian, H., and Saka, N., 1991b, "Finite Element Analysis of an Elastic-Plastic Two-Layer Half-Space: Sliding Contact," *Wear,* Vol. 148, pp. 261–285.

N. Sankar
Department of Computing and Information Science, Queen's University, Kingston, Ontario K7L 3N6, Canada
Assoc. Mem. ASME

V. Kumar
Department of Mechanical Engineering and Applied Mechanics, University of Pennsylvania, Philadelphia, PA 19104
Assoc. Mem. ASME

Xiaoping Yun
Department of Electrical and Computer Engineering, Naval Postgraduate School, Monterey, CA 93943-5121

Velocity and Acceleration Analysis of Contact Between Three-Dimensional Rigid Bodies

During manipulation and locomotion tasks encountered in robotics, it is often necessary to control the relative motion between two contacting rigid bodies. In this paper we obtain the equations relating the motion of the contact points on the pair of contacting bodies to the rigid-body motions of the two bodies. The equations are developed up to the second order. The velocity and acceleration constraints for contact, for rolling, and for pure rolling are derived. These equations depend on the local surface properties of each contacting body. Several examples are presented to illustrate the nature of the equations.

1 Introduction

In robot manipulation tasks, when the robot arm interacts with an object or the environment, it is beneficial to be able to control the contact motion. For example, when exploring the environment by feeling or touching, it is necessary to be able to move the robot arm while in contact with the environment and estimate the geometric properties of the environment (Mason and Salisbury, 1985; Montana, 1988). When grasping an object it may be desirable (Brock, 1988) to roll or to slide the object over one or more fingers in a specified manner. A similar situation also arises in an actively coordinated vehicle traversing uneven terrain where it is efficient to maintain rolling contact with the ground at all contacts (Kumar and Waldron, 1989). In all these examples, it is necessary to control the motion of an actively coordinated system relative to the contacting object or environment in order to achieve a desired motion of the contact point on the surface of the object and on the surface of the robot effector.

While extensive work has been done on contact between planar rigid bodies (see, for example, Beggs, 1966; Paul, 1979; Hall, 1966; Rosenauer and Willis, 1953; Whittaker, 1988), the work on the kinematics of three-dimensional contact is much more recent and much less is known in this area. Pars (1968) describes the configuration space associated with the relative motion between two rigid bodies in point contact. He shows that it is five-dimensional. For the special case of a sphere rolling over a plane he shows that the configuration space is completely accessible. In other words, from any point in the configuration space it is possible to reach any other specified point.

Cai and Roth (1986; 1987) study the relative motion of two contacting bodies in point contact. In Cai and Roth (1987) they derive expressions for the motion of the contact point on each contacting surface in terms of the relative motion and the local geometric properties of each surface. However, their focus is limited to the motion of the contact points and hence their study is restricted to a subspace of the configuration space. In Cai and Roth (1988) they extend their work to line contacts. Montana (1988), like Pars (1968), considers the five-dimensional space but his parameterization is somewhat different than Pars' (see Section 2). He derives the equations relating the velocity of the contact points on the rigid bodies to the relative velocities of the rigid bodies. It is also worth mentioning the work of Kirson and Yang (1978) who developed equations for moving and fixed axodes with a relative rolling and sliding motion.

This paper derives the velocity and acceleration equations relating the rigid-body motions of the contacting bodies and the motions of the contact points on the surfaces of the rigid bodies. The papers by Montana (1988) and Cai and Roth (1987) are most closely related to this work. We use Montana's definition of the configuration space but our approach is quite different. Although Montana does derive the velocity equations, as seen later in the paper, they do not lend themselves to straightforward differentiation. Our approach and results differ from those of Cai and Roth because we do consider the entire five-dimensional configuration space.

2 Preliminaries

2.1 Notation. In Fig. 1, we consider two rigid objects (obj 1 and obj 2) contacting at a point. The contact point is the coincidence of two points, p_1 fixed to obj 1, and p_2 fixed to obj 2 at time t. c_1 and c_2 are a pair of points, which do not belong to either body but move along the surface of obj 1 and obj 2 respectively so that they are instantaneously at the point of contact. We choose reference frames on obj 1 and obj 2 at point o_1 and o_2, respectively. These reference frames are attached to the objects. We attach coordinate systems at points c_1 and c_2 which move with the contact points. Finally, we define object-fixed coordinate frames at points p_1 and p_2 in such a way that they coincide with c_1 and c_2 frames, respectively, at time t. Note that the same symbol is used to denote either a point or a reference frame attached to this point. So far our notation is identical to that in Montana (1988).

r is used for position vectors, V is used for linear velocities and ω, for angular velocities. a and α denotes linear and angular accelerations, respectively. Ω is used to represent the skew symmetric matrix form of ω. R denotes rotation matrices.

A leading superscript is used to denote the reference frame in which the quantity is observed. A vector q with two trailing

Contributed by the Applied Mechanics Division of THE AMERICAN SOCIETY OF MECHANICAL ENGINEERS for publication in the ASME JOURNAL OF APPLIED MECHANICS.

Discussion on this paper should be addressed to the Technical Editor, Professor Lewis T. Wheeler, Department of Mechanical Engineering, University of Houston, Houston, TX 77204-4792, and will be accepted until four months after final publication of the paper itself in the ASME JOURNAL OF APPLIED MECHANICS.

Manuscript received by the ASME Applied Mechanics Division, Mar. 4, 1994; final revision, Mar. 27, 1996. Associate Technical Editor: E. J. Haug, Jr.

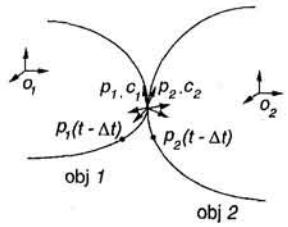

Fig. 1 Two rigid bodies with point contact

subscripts, a and b denotes the difference between q at point a and q at point b. For example, $r_{c_1o_1}$ is the position vector from o_1 to c_1. ${}^{o_1}V_{c_1o_1}$ represents the difference between the velocity of point c_1 and that of point o_1 as observed in reference frame o_1. On the other hand, when there is only one trailing subscript then it denotes the reference frame attached to that point. Thus, ${}^{o_1}\omega_{c_1}$ or ${}^{o_1}\Omega_{c_1}$ denotes the angular velocity of reference frame c_1 when it is observed in the reference frame o_1. Note that, unless otherwise specified, we refer to the vectors themselves and not to their components in a particular coordinate system. When we do refer to components, we denote these with subscripts x, y, and z and explicitly specify the coordinate system. When components are considered, ${}^aR_b$ is a rotation matrix which transforms components of a vector in frame b to components in frame a.

In the case of position vectors, a leading superscript is not used because a position vector does not depend upon the frame in which it is observed. However, any derivative, and therefore any velocity or acceleration, does depend on the reference frame in which the differentiation operation is performed. We follow a notation that is similar to that used in Kane and Levinson (1985). For example, consider the derivative of $r_{c_1o_1}$. Since the point o_1 is fixed to the reference frame o_1,

$$ {}^{o_1}v_{c_1o_1} = \frac{{}^{o_1}d}{dt} r_{c_1o_1} $$

is the velocity of point c_1 in frame o_1. Similarly,

$$ \frac{{}^{o_1}d}{dt} ({}^{o_1}v_{c_1o_1}) = {}^{o_1}a_{c_1o_1} $$

is the acceleration of point c_1 in frame o_1.

Thus, the derivative of $r_{c_1p_1}$ in frame p_2 is not ${}^{p_1}v_{c_1p_1}$. Instead,

$$ \frac{{}^{p_2}d}{dt} r_{c_1p_1} = \frac{{}^{p_1}d}{dt} r_{c_1p_1} + {}^{p_2}\omega_{p_1} \times r_{c_1p_1} $$

$$ = {}^{p_1}v_{c_1p_1} + {}^{p_2}\omega_{p_1} \times r_{c_1p_1} $$

The development here is identical to that presented by Kane and Levinson (1985, p. 23).

2.2 Local Properties of Surfaces in $\Re^3$. Here we briefly discuss a few definitions and concepts that will be used later in the paper to derive the contact kinematic equations. Detailed discussion can be found in any standard differential geometry text (e.g., Millman and Parker, 1977; Stoker, 1969; Lipschutz, 1969).

DEFINITION 1. *Coordinate System: Let S_p be an open and connected subset of the surface S containing the point p. Then the pair (f, U) is called a coordinate system of S_p if there exists an open subset U of $\Re^2$ and an invertible map $f: U \to S_p \in \Re^3$ such that the partial derivatives $(\partial f(\xi)/\partial \xi^1)$ and $(\partial f(\xi)/\partial \xi^2)$ are linearly independent for all $\xi = (\xi^1, \xi^2) \in U$. The open connected subset S_p is called a coordinate patch.*

It may so happen that not all points of S can be represented by a single coordinate patch. In such a case, we can construct a set of coordinate patches which cover all the points of S, that is, $S = \cup_{i=1}^n S_i$, where S_i's are coordinate patches for S. The set $\{S_i\}_{i=1}^n$ is called an *atlas* for S.

In what follows we will need to compute derivatives of f in order to characterize the local properties of S. We will assume that $f(\xi^1, \xi^2)$ is at least of class C^3.

DEFINITION 2. *Natural Basis and Unit Normal: $x_i = (\partial f/\partial \xi^i)$ $(i = 1, 2)$ are linearly independent at a given point and are called the natural basis of the surface. x_1 and x_2 minimally span the tangent plane at that particular point. A unit normal n is a unit vector which is perpendicular to the tangent plane at a given point and is defined by $(x_1 \times x_2)/(\|x_1 \times x_2\|)$.*

If $\langle x_1, x_2 \rangle = 0$ where $\langle , \rangle$ is the symbol for inner product, then (f, U) is called an orthogonal coordinate system. It should be noted that x_i is not necessarily a unit vector.

DEFINITION 3. *Contact Frame: This is a local reference frame at the contact point consisting of the unit vector triad $(x_1/\|x_1\|)$, $(x_2/\|x_2\|)$, and n.*

We choose the coordinate system (f, U) in such a way that n is an outward pointing normal.

DEFINITION 4. *Metric Tensor: A metric tensor G is a 2×2 symmetric, positive definite matrix whose coefficients g_{ij} are defined as*

$$ g_{ij} = \langle x_i, x_j \rangle \quad i, j = 1, 2. $$

The g_{ij} are coefficients of the first fundamental form. G is diagonal for an orthogonal coordinate system.

DEFINITION 5. *Christoffel Symbols: There are two types of Christoffel symbols. Christoffel symbols of the first kind, denoted by $[ij, k]$, are defined as*

$$ [ij, k] = \left\langle \frac{\partial x_i}{\partial \xi^j}, x_k \right\rangle \quad i, j, k = 1, 2. $$

Christoffel symbols of the second kind, Γ_{ij}^k, are defined as

$$ \Gamma_{ij}^k = \sum_{l=1}^{2} \left\langle \frac{\partial x_l}{\partial \xi^j}, x_l \right\rangle g^{lk} = \sum_{l=1}^{2} [ij, l] g^{lk} \quad i, j, k = 1, 2 $$

where g^{lk} are the components of the inverse of the metric tensor G.

It is clear from the definition that both kinds of Christoffel symbols are symmetric in the paired indices ij, that is, $[ij, k] = [ji, k]$ and $\Gamma_{ij}^k = \Gamma_{ji}^k$. Note that all the Christoffel symbols vanish when the coordinate system is Cartesian.

It is useful to note that the derivative of the components of the metric tensor can be expressed in terms of the Christoffel symbols.

$$ \frac{\partial g_{ij}}{\partial \xi^k} = [jk, i] + [ik, j] = g_{il}\Gamma_{jk}^l + g_{jl}\Gamma_{ik}^l \qquad (1) $$

DEFINITION 6. *Gauss's Equations: The derivatives of the basis vectors are given by*

$$ \frac{\partial x_i}{\partial \xi^j} = L_{ij} n + \sum_k \Gamma_{ij}^k x_k. $$

The L_{ij} are related to the coefficients of the second fundamental form only through the metric tensor. They measure the normal component of $(\partial x_i/\partial \xi^j)$ while the Γ_{ij}^k measure the tangential components.

Higher Order Derivatives: If f is at least of class C^3, we can differentiate L_{ij} and Γ_{ij}^k. By straighforward differentiation, it can be shown (Lipschutz, 1969, p. 224) that

$$ \frac{\partial^2 x_i}{\partial \xi^k \partial \xi^j} = \sum_{\alpha,\beta=1}^{2} [\Gamma_{ik,j}^\alpha + \Gamma_{ij}^\beta \Gamma_{\beta k}^\alpha - L_{ij}L_k^\alpha] x_\alpha + [\Gamma_{ij}^\alpha L_{\alpha k} + L_{ij,k}] n $$

where $\Gamma_{ik,j}^\alpha = (\partial \Gamma_{ik}^\alpha/\partial \xi^j)$ and $L_{ij,k} = (\partial L_{ij}/\partial \xi^k)$.

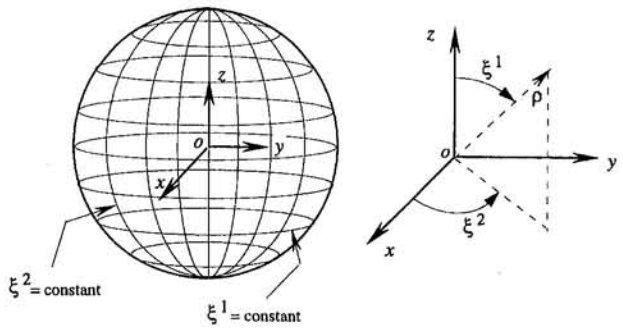

Fig. 2 Coordinate curves for a sphere

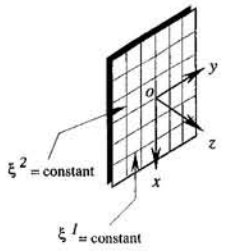

Fig. 3 Coordinate curves for a plane

2.3 Examples.

2.3.1 Geometric Properties of a Sphere. For a sphere with radius ρ, let us define a coordinate system (Fig. 2),

$$f: U \to \Re^3 : (\xi^1, \xi^2) \mapsto$$

$$(\rho \sin \xi^1 \cos \xi^2, \quad \rho \sin \xi^1 \sin \xi^2, \quad \rho \cos \xi^1).$$

The natural basis for this coordinate system and the corresponding unit normal are

$$x_1 = \begin{bmatrix} \rho \cos \xi^1 \cos \xi^2 \\ \rho \cos \xi^1 \sin \xi^2 \\ -\rho \sin \xi^1 \end{bmatrix} \quad x_2 = \begin{bmatrix} -\rho \sin \xi^1 \sin \xi^2 \\ \rho \sin \xi^1 \cos \xi^2 \\ 0 \end{bmatrix}$$

$$n = \begin{bmatrix} \sin \xi^1 \cos \xi^2 \\ \sin \xi^1 \sin \xi^2 \\ \cos \xi^1 \end{bmatrix}.$$

So the contact frame is defined by $[(x_1/\|x_1\|)\ (x_2/\|x_2\|)\ n]$.

The components of the metric tensor G are given by

$$g_{11} = \rho^2 \quad g_{12} = 0$$

$$g_{21} = 0 \quad g_{22} = \rho^2 \sin (\xi^1)^2.$$

G is diagonal because the coordinate system is orthogonal ($\langle x_1, x_2 \rangle = 0$).

The Christoffel symbols and the coefficients L_{ij} are

$$\Gamma^1_{11} = 0 \quad \Gamma^2_{11} = 0$$

$$\Gamma^1_{12} = 0 \quad \Gamma^2_{12} = \cot \xi^1$$

$$\Gamma^1_{21} = 0 \quad \Gamma^2_{21} = \cot \xi^1$$

$$\Gamma^1_{22} = -\sin \xi^1 \cos \xi^1 \quad \Gamma^2_{22} = 0$$

$$L_{11} = -\rho \quad L_{12} = 0$$

$$L_{21} = 0 \quad L_{22} = -\rho \sin (\xi^1)^2.$$

The derivatives of Γ^k_{ij} and L_{ij} that are not zero are

$$\Gamma^2_{12,1} = -\csc^2 \xi^1 \quad \Gamma^2_{21,1} = -\csc^2 \xi^1$$

$$\Gamma^1_{22,1} = -\cos (2\xi^1) \quad L_{22,1} = -2\rho \sin \xi^1 \cos \xi^1$$

Note that although the Gaussian curvature and the mean curvature of a sphere are constant, the coefficients, g_{ij}, Γ^k_{ij} and L_{ij} are not.

2.3.2 Geometric Properties of a Planar Surface. Consider the plane (Fig. 3) with the coordinate system:

$$f: U \subset \Re^2 \to \Re^3 : (\xi^1, \xi^2) \mapsto (\xi^1, \xi^2, 0).$$

The following results are obtained from the definitions in the previous subsection.

$$x_1 = \begin{bmatrix} 1 \\ 0 \\ 0 \end{bmatrix} \quad x_2 = \begin{bmatrix} 0 \\ 1 \\ 0 \end{bmatrix} \quad n = \begin{bmatrix} 0 \\ 0 \\ 1 \end{bmatrix}$$

$$g_{11} = 1 \quad g_{12} = 0$$

$$g_{21} = 0 \quad g_{22} = 1$$

Since the natural basis vectors and the components of the metric tensor are constant for a plane, all other higher order derivatives are zero.

2.4 Contact Coordinates. We now define five *contact coordinates* that characterize the motion of the point of contact. First for obj i, we let $\xi^1 = u_i$ and $\xi^2 = v_i$ as shown in Fig. 4. The point of contact is uniquely defined by the four coordinates u_1, v_1, u_2, and v_2. The fifth parameter is ψ, the angle of contact which is the angle between the u_1 and u_2 curves (Montana, 1988). In Fig. 5, it is the angle between $(x_1)_1$ (tangent to the v_1 = constant curve) and $(x_1)_2$ (tangent to the v_2 = constant curve). The sign of ψ is defined in such a way that a rotation of $(x_1)_1$ about the outward pointing unit normal $(n)_1$ to the surface at point p_1 through $-\psi$ aligns the axes $(x_1)_1$ and $(x_1)_2$.

We use a trailing subscript i to denote obj i. For example, the contact frame for obj i is denoted by $[(x_1/\|x_1\|)_i\ (x_2/\|x_2\|)_i\ (n)_i]$.

3 Closure Equations

In Fig. 1, using the triangle law of vector addition (Paul, 1979), we can write

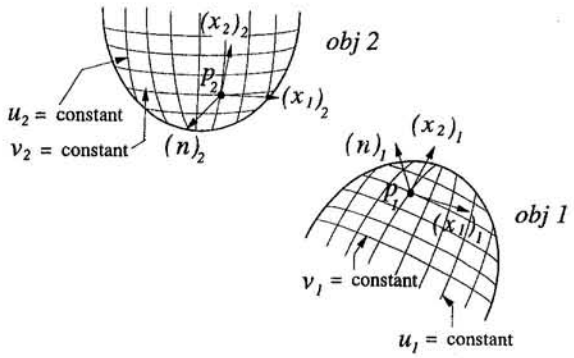

Fig. 4 Coordinate curves and contact frames on two contacting bodies

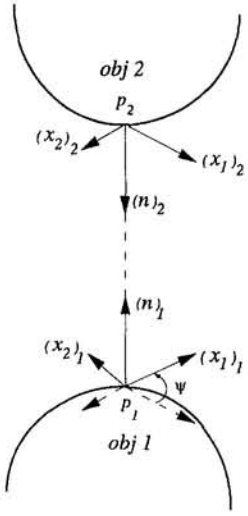

Fig. 5 The definition of angle ψ

$$r_{c_i o_i} = r_{c_i p_i} + r_{p_i o_i}. \tag{2}$$

Note that, in this notation, we implicitly assume that Eq. (2) can be written in component form in any convenient coordinate system. (At this point we are only concerned with vector equations and not their components in a particular coordinate system.) Differentiating each term of Eq. (2) with respect to time t in the reference frame o_i, we get

$$^{o_i}V_{c_i o_i} = {}^{p_i}V_{c_i p_i} + {}^{o_i}\omega_{p_i} \times r_{c_i p_i} + {}^{o_i}V_{p_i o_i}. \tag{3}$$

Differentiating Eq. (3) in the reference frame o_i, we get

$$^{o_i}a_{c_i o_i} = {}^{p_i}a_{c_i p_i} + {}^{o_i}\omega_{p_i} \times {}^{p_i}V_{c_i p_i} + {}^{o_i}\dot{\omega}_{p_i} \times r_{c_i p_i} + {}^{o_i}\omega_{p_i} \times ({}^{p_i}V_{c_i p_i} + {}^{o_i}\omega_{p_i} \times r_{c_i p_i}) + {}^{o_i}a_{p_i o_i}. \tag{4}$$

Applying the addition theorem for angular velocities (Kane and Levinson, 1985, p. 24), we get

$$^{o_i}\omega_{c_i} = {}^{o_i}\omega_{p_i} + {}^{p_i}\omega_{c_i}. \tag{5}$$

Differentiating each term in Eq. (5) in the o_i frame, we get

$$^{o_i}\dot{\omega}_{c_i} = {}^{o_i}\dot{\omega}_{p_i} + {}^{p_i}\dot{\omega}_{c_i} + {}^{o_i}\omega_{p_i} \times {}^{p_i}\omega_{c_i} \tag{6}$$

where ${}^a\dot{\omega}_b$ denotes the time derivative of ${}^a\omega_b$ in frame a.

Since p_i and o_i are fixed in body i,

$$^{o_i}\omega_{p_i} = 0, \quad {}^{o_i}\dot{\omega}_{p_i} = 0, \quad {}^{o_i}V_{p_i o_i} = 0.$$

Substituting these in Eqs. (3)–(6) we get

$$^{o_i}V_{c_i o_i} = {}^{p_i}V_{c_i p_i} \tag{7}$$

$$^{o_i}a_{c_i o_i} = {}^{p_i}a_{c_i p_i} \tag{8}$$

$$^{o_i}\omega_{c_i} = {}^{p_i}\omega_{c_i} \tag{9}$$

$$^{o_i}\dot{\omega}_{c_i} = {}^{p_i}\dot{\omega}_{c_i}. \tag{10}$$

Consider the closed loop: $p_2 \to c_1 \to p_1 \to p_2$. The triangle law of vector addition applied to position vectors yields

$$r_{c_1 p_2} = r_{c_1 p_1} + r_{p_1 p_2}. \tag{11}$$

Differentiating each term of Eq. (11) in the reference frame p_2 two times, we get

$$^{p_2}V_{c_1 p_2} = {}^{p_1}V_{c_1 p_1} + {}^{p_2}\omega_{p_1} \times r_{c_1 p_1} + {}^{p_2}V_{p_1 p_2} \tag{12}$$

$$^{p_2}a_{c_1 p_2} = {}^{p_1}a_{c_1 p_1} + {}^{p_2}\dot{\omega}_{p_1} \times r_{c_1 p_1} + {}^{p_2}\omega_{p_1} \times ({}^{p_2}\omega_{p_1} \times r_{c_1 p_1}) + 2{}^{p_2}\omega_{p_1} \times {}^{p_1}V_{c_1 p_1} + {}^{p_2}a_{p_1 p_2}. \tag{13}$$

Note that $r_{c_i p_i} = 0$ in the above equations. Similarly for angular velocities, we obtain the velocity and acceleration equations:

$$^{p_2}\omega_{c_1} = {}^{p_1}\omega_{c_1} + {}^{p_2}\omega_{p_1} \tag{14}$$

$$^{p_2}\dot{\omega}_{c_1} = {}^{p_1}\dot{\omega}_{c_1} + {}^{p_2}\omega_{p_1} \times {}^{p_1}\omega_{c_1} + {}^{p_2}\dot{\omega}_{p_1}. \tag{15}$$

Now consider the closed loop: $p_2 \to c_1 \to c_2 \to p_2$. The translation closure equations are

$$r_{c_1 p_2} = r_{c_1 c_2} + r_{c_2 p_2} \tag{16}$$

$$^{p_2}V_{c_1 p_2} = {}^{c_2}V_{c_1 c_2} + {}^{p_2}\omega_{c_2} \times r_{c_1 c_2} + {}^{p_2}V_{c_2 p_2} \tag{17}$$

$$^{p_2}a_{c_1 p_2} = {}^{c_2}a_{c_1 c_2} + {}^{p_2}\dot{\omega}_{c_2} \times r_{c_1 c_2} + {}^{p_2}\omega_{c_2} \times ({}^{p_2}\omega_{c_2} \times r_{c_1 c_2}) + 2{}^{p_2}\omega_{c_2} \times {}^{c_1}V_{c_1 c_2} + {}^{p_2}a_{c_2 p_2}. \tag{18}$$

By definition, the vectors $r_{c_1 c_2}$, ${}^{c_2}V_{c_1 c_2}$ and ${}^{c_2}a_{c_1 c_2}$ vanish in the above equations. The loop equations for the angular velocities are

$$^{p_2}\omega_{c_1} = {}^{c_2}\omega_{c_1} + {}^{p_2}\omega_{c_2} \tag{19}$$

$$^{p_2}\dot{\omega}_{c_1} = {}^{c_2}\dot{\omega}_{c_1} + {}^{p_2}\omega_{c_2} \times {}^{c_2}\omega_{c_1} + {}^{p_2}\dot{\omega}_{c_2}. \tag{20}$$

We now manipulate the loop equations to obtain what we call the *contact closure equations.* Equating the right-hand sides of Eqs. (12) and (17) we get after setting $r_{c_1 p_1}$, $r_{c_1 c_2}$ and $V_{c_1 c_2}$ to zero

$$^{p_2}V_{c_2 p_2} = {}^{p_1}V_{c_1 p_1} + {}^{p_2}V_{p_1 p_2}. \tag{21}$$

From Eq. (3), because ${}^{o_i}V_{p_i o_i} = 0$ and ${}^{o_i}\omega_{p_i} = 0$, Eq. (21) can be written as

$$^{o_2}V_{c_2 o_2} = {}^{o_1}V_{c_1 o_1} + {}^{p_2}V_{p_1 p_2}. \tag{22}$$

Equating the right-hand sides of Eqs. (14) and (19) and then substituting from Eq. (9), we get

$$^{o_1}\omega_{c_1} + {}^{p_2}\omega_{p_1} = {}^{c_2}\omega_{c_1} + {}^{o_2}\omega_{c_2}. \tag{23}$$

Next, we equate the right-hand sides of Eqs. (13) and (18) and simplify using Eqs. (7)–(8) to get

$$^{o_2}a_{c_2 o_2} = {}^{o_1}a_{c_1 o_1} + 2{}^{p_2}\omega_{p_1} \times {}^{o_1}V_{c_1 o_1} + {}^{p_2}a_{p_1 p_2}. \tag{24}$$

Finally, equating the right-hand sides of Eqs. (15) and (20) and simplifying using Eqs. (9)–(10), we write

$$^{o_1}\dot{\omega}_{c_1} + {}^{p_2}\omega_{p_1} \times {}^{o_1}\omega_{c_1} + {}^{p_2}\dot{\omega}_{p_1} = {}^{c_2}\dot{\omega}_{c_1} + {}^{o_2}\omega_{c_2} \times {}^{c_2}\omega_{c_1} + {}^{o_2}\dot{\omega}_{c_2}. \tag{25}$$

In summary, the velocity contact closure equations are (22) and (23) and the acceleration contact closure equations are (24) and (25).

4 Contact Equations: Velocity Analysis

Let the components of the relative linear and angular velocities of the contacting rigid bodies in the frame p_2 (also in the frame c_2) be given in vector form by

$$^{p_2}V_{p_1 p_2} = \begin{bmatrix} V_x \\ V_y \\ V_z \end{bmatrix} \quad {}^{p_2}\omega_{p_1} = \begin{bmatrix} \omega_x \\ \omega_y \\ \omega_z \end{bmatrix}.$$

In this section we find expressions for the remaining terms in Eqs. (22) and (23) in terms of the contact coordinates and their

derivatives and thus relate changes in contact coordinates to the relative linear and angular velocities defined above.

The position vector of the contact point c_i of obj i in o_i is

$$r_{c_i o_i} = r_{c_i o_i}(\xi^1, \xi^2) \quad i = 1, 2. \tag{26}$$

Next we consider the transformations between o_i and c_i, and between c_1 and c_2. The rotation matrix ${}^{o_i}R_{c_i}$ is quite simply

$$\begin{aligned} {}^{o_i}R_{c_i} &= \left[\left(\frac{x_1}{\|x_1\|}\right)_i \quad \left(\frac{x_2}{\|x_2\|}\right)_i \quad (n)_i \right] \\ &= [(x_1)_i \quad (x_2)_i \quad (n)_i] \begin{bmatrix} (\sqrt{G_i})^{-1} & 0_{2\times 1} \\ 0_{1\times 2} & 1 \end{bmatrix}. \end{aligned} \tag{27}$$

Note that since the coordinate system is orthogonal, all the elements of the metric tensor, G_i, are positive and the square root operation is a valid one. From the definition of ψ, ${}^{c_2}R_{c_1}$ can be seen to be

$${}^{c_2}R_{c_1} = \begin{bmatrix} \cos\psi & -\sin\psi & 0 \\ -\sin\psi & -\cos\psi & 0 \\ 0 & 0 & -1 \end{bmatrix} = \begin{bmatrix} R_\psi & 0_{2\times 1} \\ 0_{1\times 2} & -1 \end{bmatrix}.$$

We now proceed to obtain expressions for the velocity terms. Differentiating Eq. (26) in the o_i frame, we get the velocity of the contact point c_i in that frame. The resulting equation is

$${}^{o_i}V_{c_i o_i} = \frac{d}{dt}\left[{}^{o_i}r_{c_i o_i}(\xi^1, \xi^2)\right] = \sum_{j=1}^{2} (x_j)_i \dot{\xi}^j \quad i = 1, 2. \tag{28}$$

Therefore,

$${}^{c_2}\Omega_{c_1} = {}^{c_2}\dot{R}_{c_1}\,{}^{c_2}R_{c_1}^T = \begin{bmatrix} 0 & \dot{\psi} & 0 \\ -\dot{\psi} & 0 & 0 \\ 0 & 0 & 0 \end{bmatrix}. \tag{31}$$

Here ${}^{c_2}\Omega_{c_1}$ is the angular velocity expressed in the contact frame c_2 in matrix form. Similarly, ${}^{o_i}\Omega_{c_i}$, in the contact frame c_i, can be simplified to (see Appendix for intermediate steps):

$$\begin{aligned} {}^{o_i}\Omega_{c_i} = {}^{o_i}R_{c_i}^T\,{}^{o_i}\dot{R}_{c_i} &= \begin{bmatrix} (\sqrt{G_i})^{-1} & 0_{2\times 1} \\ 0_{1\times 2} & 1 \end{bmatrix} \begin{bmatrix} (x_1)_i^T \\ (x_2)_i^T \\ (n)_i^T \end{bmatrix} \\ &\times \left\{ [(x_1)_i \quad (x_2)_i \quad (n)_i] \begin{bmatrix} (\dot{(\sqrt{G_i})}^{-1}) & 0_{2\times 1} \\ 0_{1\times 2} & 0 \end{bmatrix} \right. \\ &+ \left[\sum_{j=1}^{2} \left(\frac{\partial x_1}{\partial \xi^j}\right)_i \dot{\xi}^j \quad \sum_{j=1}^{2} \left(\frac{\partial x_2}{\partial \xi^j}\right)_i \dot{\xi}^j \quad \sum_{j=1}^{2} \left(\frac{\partial n}{\partial \xi^j}\right)_i \dot{\xi}^j \right] \\ &\left. \times \begin{bmatrix} (\sqrt{G_i})^{-1} & 0_{2\times 1} \\ 0_{1\times 2} & 1 \end{bmatrix} \right\}. \end{aligned}$$

We introduce Christoffel symbols, $[ij, k]$ and Γ_{jk}^i and the coefficients of the second fundamental form, L_{ij}, and after some algebraic manipulation we get

$$\begin{aligned} {}^{o_1}\Omega_{c_1} = &- \begin{bmatrix} \frac{1}{(g_{11})_1}([11,1]_1\dot{u}_1 + [12,1]_1\dot{v}_1) & 0 & 0 \\ 0 & \frac{1}{(g_{22})_1}([21,1]_1\dot{u}_1 + [22,1]_1\dot{v}_1) & 0 \\ 0 & 0 & 0 \end{bmatrix} \\ &+ \begin{bmatrix} \frac{1}{(g_{11})_1}([11,1]_1\dot{u}_1 + [12,1]_1\dot{v}_1) & -\frac{1}{(g_{11})_1}\frac{1}{(g_{22})_1}([11,2]_1\dot{u}_1 + [12,2]_1\dot{v}_1) & -\frac{1}{(g_{11})_1}\{(L_{11})_1\dot{u}_1 + (L_{12})_1\dot{v}_1\} \\ \frac{1}{(g_{11})_1}\frac{1}{(g_{22})_1}([11,2]_1\dot{u}_1 + [12,2]_1\dot{v}_1) & \frac{1}{(g_{22})_1}([21,1]_1\dot{u}_1 + [22,1]_1\dot{v}_1) & -\frac{1}{(g_{22})_1}\{(L_{21})_1\dot{u}_1 + (L_{22})_1\dot{v}_1\} \\ \frac{1}{(g_{11})_1}\{(L_{11})_1\dot{u}_1 + (L_{12})_1\dot{v}_1\} & \frac{1}{(g_{22})_1}\{(L_{21})_1\dot{u}_1 + (L_{22})_1\dot{v}_1\} & 0 \end{bmatrix} \end{aligned}$$

Expressing the velocities of the contact points in contact frame c_2 (using Eq. (28)):

$${}^{o_1}V_{c_1 o_1} = {}^{c_2}R_{c_1}\,{}^{c_1}R_{o_1}[(x_1)_1\dot{u}_1 + (x_2)_1\dot{v}_1] = \begin{bmatrix} R_\psi\sqrt{G_1}\dot{U}_1 \\ 0 \end{bmatrix} \tag{29}$$

$${}^{o_2}V_{c_2 o_2} = {}^{c_2}R_{o_2}[(x_1)_2\dot{u}_2 + (x_2)_2\dot{v}_2] = \begin{bmatrix} \sqrt{G_2}\dot{U}_2 \\ 0 \end{bmatrix} \tag{30}$$

where $U_1 = [u_1\ v_1]^T$ and $U_2 = [u_2\ v_2]^T$.

The skew symmetric matrix representation of the angular velocity is directly obtained from the rotation matrix (McCarthy, 1990). For any rotation matrix ${}^fR_m$, its derivative in frame f is given by

$${}^f\Omega_m = \dot{R}R^T.$$

which can be simplified to

$${}^{o_1}\Omega_{c_1} = \begin{bmatrix} 0 & (-\sigma_1\Gamma_1\dot{U}_1) & \{-(\sqrt{G_1})^{-1}L_1\dot{U}_1)\}_{2\times 1} \\ (\sigma_1\Gamma_1\dot{U}_1) & 0 & \\ \{(\sqrt{G_1})^{-1}L_1\dot{U}_1\})_{1\times 2}^T & & 0 \end{bmatrix} \tag{32}$$

where $\sigma_i = \{(g_{22})_i/(g_{11})_i\}^{1/2}$ for $i = 1, 2$ are the ratios of the norms of the natural base vectors. For an orthonormal system, $\sigma_i = 1$. Γ_i and L_i are 1×2 and 2×2 matrices consisting of the Christoffel symbols of the second kind and the coefficients of the second fundamental form, respectively, for obj i. Γ and L are defined as follows:

$$\Gamma = [\Gamma_{11}^2 \quad \Gamma_{12}^2]$$

$$L = \begin{bmatrix} L_{11} & L_{12} \\ L_{21} & L_{22} \end{bmatrix}.$$

Similarly,

$$ {}^{o_2}\Omega_{c_2} = \begin{bmatrix} 0 & (-\sigma_2\Gamma_2\dot{U}_2) & \{-(\sqrt{G_2})^{-1}L_2\dot{U}_2)\}_{2\times 1} \\ (\sigma_2\Gamma_2\dot{U}_2) & 0 & \\ \{(\sqrt{G_2})^{-1}L_2\dot{U}_2\})^T_{1\times 2} & & 0 \end{bmatrix} \tag{33} $$

Substituting for ${}^{o_2}V_{c_2o_2}$ and ${}^{o_1}V_{c_1o_1}$ from Eqs. (29)–(30) in Eq. (22), expressing each vector in the c_2 frame, we get

$$ \sqrt{G_2}\dot{U}_2 = R_\psi\sqrt{G_1}\dot{U}_1 + \begin{bmatrix} V_x \\ V_y \end{bmatrix} $$

$$ V_z = 0. $$

In Eq. (23), after substituting for ${}^{o_1}\omega_{c_1}$ from Eq. (32), ${}^{o_2}\omega_{c_2}$ from Eq. (33), and ${}^{c_2}\omega_{c_1}$ from Eq. (31), we get

$$ R_\psi(\sqrt{G_1})^{-1}L_1\dot{U}_1 + \begin{bmatrix} \omega_y \\ -\omega_x \end{bmatrix} = -(\sqrt{G_2})^{-1}L_2\dot{U}_2 $$

$$ -\sigma_1\Gamma_1\dot{U}_1 + \omega_z = -\dot{\psi} + \sigma_2\Gamma_2\dot{U}_2. $$

Simplifying the above equations we obtain the first-order contact kinematics relating the rate of change of contact coordinates to the rigid-body velocities:

$$ \dot{U}_1 = (\sqrt{G_1})^{-1}R_\psi(\tilde{H}_1 + H_2)^{-1}\left[-\begin{pmatrix} \omega_y \\ -\omega_x \end{pmatrix} - H_2\begin{pmatrix} V_x \\ V_y \end{pmatrix} \right] \tag{34} $$

$$ \dot{U}_2 = (\sqrt{G_2})^{-1}(\tilde{H}_1 + H_2)^{-1}\left[-\begin{pmatrix} \omega_y \\ -\omega_x \end{pmatrix} + \tilde{H}_1\begin{pmatrix} V_x \\ V_y \end{pmatrix} \right] \tag{35} $$

$$ \dot{\psi} = \sigma_1\Gamma_1\dot{U}_1 + \sigma_2\Gamma_2\dot{U}_2 - \omega_z \tag{36} $$

$$ V_z = 0 \tag{37} $$

where $H_i = (\sqrt{G_i})^{-1}L_i(\sqrt{G_i})^{-1}$ and $\tilde{H}_1 = R_\psi H_1 R_\psi$.

These equations are the velocity contact equations which were first presented by Montana (1988). However, our notation and derivation are slightly different. First, we use standard differential geometric notation (g_{ij}, Γ^k_{ij}, and L_{ij}) to describe the surface properties. Second, we resolve all vectors in the frame c_2 and not in c_1 like Montana.

5 Contact Equations: Acceleration Analysis

Let the components of the relative linear and angular accelerations of the contacting rigid bodies in the frame c_2 be

$$ {}^{p_2}a_{p_1p_2} = \begin{bmatrix} a_x \\ a_y \\ a_z \end{bmatrix} \quad {}^{p_2}\dot{\omega}_{p_1} = \begin{bmatrix} \alpha_x \\ \alpha_y \\ \alpha_z \end{bmatrix}. $$

In this section we find expressions for the remaining terms in Eqs. (24) and (25) in terms of the contact coordinates and their derivatives in order to relate changes in contact coordinates to the relative linear and angular accelerations defined above.

It is convenient to define other matrix functions of the surface properties (analogous to Γ and L).

$$ \bar{\Gamma} = \begin{bmatrix} \Gamma^1_{11} & 2\Gamma^1_{12} & \Gamma^1_{22} \\ \Gamma^2_{11} & 2\Gamma^2_{12} & \Gamma^2_{22} \end{bmatrix} $$

$$ \bar{L} = [L_{11} \quad 2L_{12} \quad L_{22}] $$

$$ \bar{\bar{\Gamma}} = \begin{bmatrix} (\Gamma^2_{21} - \Gamma^1_{11})\Gamma^2_{11} + \dfrac{\partial\Gamma^2_{11}}{\partial\xi^1} \\ (\Gamma^2_{21} - \Gamma^1_{11})\Gamma^2_{12} + (\Gamma^2_{22} - \Gamma^1_{12})\Gamma^2_{11} + \dfrac{\partial\Gamma^2_{12}}{\partial\xi^1} + \dfrac{\partial\Gamma^2_{11}}{\partial\xi^2} \\ (\Gamma^2_{22} - \Gamma^1_{12})\Gamma^2_{12} + \dfrac{\partial\Gamma^2_{12}}{\partial\xi^2} \end{bmatrix}^T $$

$$ \bar{\bar{L}} = \begin{bmatrix} \begin{pmatrix} \Gamma^1_{11}L_{11} - \dfrac{\partial L_{11}}{\partial\xi^1} \\ \Gamma^1_{11}L_{12} + \Gamma^1_{12}L_{11} - \dfrac{\partial L_{12}}{\partial\xi^1} - \dfrac{\partial L_{11}}{\partial\xi^2} \\ \Gamma^1_{12}L_{12} - \dfrac{\partial L_{12}}{\partial\xi^2} \end{pmatrix}^T \\ \begin{pmatrix} \Gamma^2_{21}L_{21} - \dfrac{\partial L_{21}}{\partial\xi^1} \\ \Gamma^2_{21}L_{22} + \Gamma^2_{22}L_{21} - \dfrac{\partial L_{22}}{\partial\xi^1} - \dfrac{\partial L_{21}}{\partial\xi^2} \\ \Gamma^2_{22}L_{22} - \dfrac{\partial L_{22}}{\partial\xi^2} \end{pmatrix}^T \end{bmatrix} $$

We first consider the linear accelerations of the contact points. In the o_i frame,

$$ {}^{o_i}a_{c_io_i} = \frac{d}{dt}[{}^{o_i}V_{c_io_i}] = \sum_{j=1}^{2}(x_j)_i\ddot{\xi}^j + \sum_{j,k=1}^{2}\left(\frac{\partial x_j}{\partial\xi^k}\right)_i\dot{\xi}^j\dot{\xi}^k. $$

Expressing this in the contact frame c_2,

$$ {}^{o_1}a_{c_1o_1} = {}^{c_2}R_{c_1}{}^{c_1}R_{o_1}\left[(x_1)_1\ddot{u}_1 + (x_2)_1\ddot{v}_1 + \left(\frac{\partial x_1}{\partial u_1}\right)_1(\dot{u}_1)^2 + 2\left(\frac{\partial x_1}{\partial v_1}\right)_1\dot{u}_1\dot{v}_1 + \left(\frac{\partial x_2}{\partial v_1}\right)_1(\dot{v}_1)^2 \right] $$

$$ {}^{o_1}a_{c_1o_1} = \begin{bmatrix} R_\psi\sqrt{G_1}(\dot{U}_1 + \bar{\Gamma}_1W_1) \\ -\bar{L}_1W_1 \end{bmatrix} \tag{38} $$

where $W_i = [(\dot{u}_i)^2 \ (\dot{u}_i\dot{v}_i) \ (\dot{v}_i)^2]^T$ represent the nonlinear velocity terms.

Similarly,

$$ {}^{o_2}a_{c_2o_2} = \begin{bmatrix} \sqrt{G_2}(\dot{U}_2 + \bar{\Gamma}_2W_2) \\ \bar{L}_2W_2 \end{bmatrix}. $$

We next find an expression for ${}^{o_i}\dot{\Omega}_{c_i}$, the skew symmetric matrix for the angular acceleration of the frame c_i relative to the frame o_i which is attached to obj i, in the contact frame c_i.

$$ {}^{o_i}\dot{\Omega}_{c_i} = {}^{o_i}R^T_{c_i}{}^{o_i}\ddot{R}_{c_i} - ({}^{o_i}R^T_{c_i}{}^{o_i}\dot{R}_{c_i})({}^{o_i}R^T_{c_i}{}^{o_i}\dot{R}_{c_i}) $$
$$ = {}^{o_i}R^T_{c_i}{}^{o_i}\ddot{R}_{c_i} - {}^{o_i}\Omega_{c_i}{}^{o_i}\Omega_{c_i} $$

We substitute from (32) for ${}^{o_i}\Omega_{c_i}$ and from (27) for ${}^{o_i}R_{c_i}$, and after considerable simplification (see Appendix) we obtain

$$ {}^{o_i}\dot{\Omega}_{c_i} = \begin{bmatrix} 0 & (-\sigma_i(\Gamma_i\dot{U}_i + \bar{\bar{\Gamma}}_i W_i)) & ((\sqrt{G_i})^{-1}(\bar{\bar{L}}_i W_i - L_i\dot{U}_i))_{2\times 1} \\ (\sigma_i(\Gamma_i\dot{U}_i + \bar{\bar{\Gamma}}_i W_i)) & 0 & \\ ((\sqrt{G_i})^{-1}(\bar{\bar{L}}_i W_i - L_i\dot{U}_i))^T_{1\times 2} & & 0 \end{bmatrix}. $$

Note that the 1×3 matrix $\bar{\bar{\Gamma}}$ and the 2×3 matrix $\bar{\bar{L}}$ representing third-order surface properties enter into the equations.

Other terms in Eqs. (24) and (25) in the c_2 frame are as follows:

$$ {}^{p_2}\omega_{p_1} \times {}^{o_1}V_{c_1o_1} = \begin{bmatrix} \omega_z E_1 R_\psi \sqrt{G_1}\dot{U}_1 \\ \begin{pmatrix} -\omega_y \\ \omega_x \end{pmatrix}^T R_\psi (\sqrt{G_1})^{-1}\dot{U}_1 \end{bmatrix} $$

$$ {}^{p_2}\omega_{p_1} \times {}^{o_1}\omega_{c_1} = \begin{bmatrix} -R_\psi(\sqrt{G_1})^{-1}L_1\dot{U}_1\omega_z + \sigma_1\Gamma_1\dot{U}_1\begin{pmatrix} -\omega_y \\ \omega_x \end{pmatrix} \\ -\begin{pmatrix} -\omega_y \\ \omega_x \end{pmatrix}^T R_\psi E_1(\sqrt{G_1})^{-1}L_1\dot{U}_1 \end{bmatrix} $$

$$ {}^{o_2}\omega_{c_2} \times {}^{c_2}\omega_{c_1} = \begin{bmatrix} (\sqrt{G_2})^{-1}L_2\dot{U}_2\dot{\psi} \\ 0 \end{bmatrix} $$

$$ {}^{c_2}\dot{\omega}_{c_1} = \begin{bmatrix} 0 \\ 0 \\ -\ddot{\psi} \end{bmatrix} $$

where

$$ E_1 = \begin{bmatrix} 0 & -1 \\ 1 & 0 \end{bmatrix}. $$

Substituting the relevant expressions in Eq. (24) we get

$$ \sqrt{G_2}(\dot{U}_2 + \Gamma_2 W_2) = R_\psi\sqrt{G_1}(\dot{U}_1 + \Gamma_1 W_1) + 2\omega_z E_1 R_\psi\sqrt{G_1}\dot{U}_1 + \begin{bmatrix} a_x \\ a_y \end{bmatrix} \quad (39) $$

$$ \bar{L}_2 W_2 = -\bar{L}_1 W_1 + 2\begin{pmatrix} -\omega_y \\ \omega_x \end{pmatrix}^T R_\psi\sqrt{G_1}\dot{U}_1 + a_z. \quad (40) $$

And from Eq. (25), we get

$$ R_\psi E_1(\sqrt{G_1})^{-1}(\bar{\bar{L}}_1 W_1 - L_1\dot{U}_1) - R_\psi(\sqrt{G_1})^{-1}L_1\dot{U}_1\omega_z + \sigma_1\Gamma_1\dot{U}_1\begin{pmatrix} -\omega_y \\ \omega_x \end{pmatrix} + \begin{bmatrix} \alpha_x \\ \alpha_y \end{bmatrix} = (\sqrt{G_2})^{-1}L_2\dot{U}_2\dot{\psi} + E_1(\sqrt{G_2})^{-1}(\bar{\bar{L}}_2 W_2 - L_2\dot{U}_2) \quad (41) $$

$$ -\sigma_1(\Gamma_1\dot{U}_1 + \bar{\bar{\Gamma}}_1 W_1) - \begin{pmatrix} -\omega_y \\ \omega_x \end{pmatrix}^T R_\psi E_1(\sqrt{G_1})^{-1}L_1\dot{U}_1 + \alpha_z = -\ddot{\psi} + \sigma_2(\Gamma_2\dot{U}_2 + \bar{\bar{\Gamma}}_2 W_2). \quad (42) $$

Solving Eqs. (39), (41), and (42), we obtain the five second-order contact kinematic equations relating double derivatives of the contact coordinates to the rigid-body velocities and accelerations:

$$ \begin{bmatrix} \dot{U}_1 \\ \dot{U}_2 \end{bmatrix} = \begin{bmatrix} R_\psi\sqrt{G_1} & -\sqrt{G_2} \\ R_\psi E_1 H_1\sqrt{G_1} & -E_1 H_2\sqrt{G_2} \end{bmatrix}^{-1} \times \left\{ \begin{bmatrix} R_\psi\sqrt{G_1}\Gamma_1 \\ R_\psi E_1(\sqrt{G_1})^{-1}\bar{\bar{L}}_1 \end{bmatrix} W_1 + \begin{bmatrix} \sqrt{G_2}\Gamma_2 \\ E_1(\sqrt{G_2})^{-1}\bar{\bar{L}}_2 \end{bmatrix} W_2 + \begin{bmatrix} -2\omega_z E_1 R_\psi\sqrt{G_1} & 0 \\ -\omega_z R_\psi H_1\sqrt{G_1} & -\dot{\psi}H_2\sqrt{G_2} \end{bmatrix}\begin{bmatrix} \dot{U}_1 \\ \dot{U}_2 \end{bmatrix} - \begin{bmatrix} 0_{2\times 1} \\ \sigma_1\Gamma_1\dot{U}_1\begin{pmatrix} \omega_y \\ -\omega_x \end{pmatrix} \end{bmatrix} + \begin{bmatrix} 0_{2\times 1} & \begin{pmatrix} a_x \\ a_y \end{pmatrix} \\ \begin{pmatrix} \alpha_x \\ \alpha_y \end{pmatrix} & 0_{2\times 1} \end{bmatrix} \right\} \quad (43) $$

$$ \ddot{\psi} = \sigma_1(\Gamma_1\dot{U}_1 + \bar{\bar{\Gamma}}_1 W_1) + \sigma_2(\Gamma_2\dot{U}_2 + \bar{\bar{\Gamma}}_2 W_2) + \begin{pmatrix} \omega_y \\ -\omega_x \end{pmatrix}^T R_\psi E_1(\sqrt{G_1})^{-1}L_1\dot{U}_1 - \alpha_z. \quad (44) $$

Equation (40) is an acceleration constraint equation which can be rearranged in the following manner:

$$ a_z = \bar{L}_1 W_1 + \bar{L}_2 W_2 + 2\begin{pmatrix} \omega_y \\ -\omega_x \end{pmatrix}^T R_\psi\sqrt{G_1}\dot{U}_1. \quad (45) $$

6 Examples

6.1 Two Spheres in Contact. Here we derive the first and second-order contact kinematic equations for two spheres in contact (obj 1 and obj 2). The choice of coordinates and notation is according to Section 2.3. Using Eqs. (34)–(36) we obtain the following first-order contact kinematic equations:

$$ \dot{u}_1 = \frac{\rho_2}{\rho_1 + \rho_2}[\omega_x \sin\psi + \omega_y \cos\psi] + \frac{[V_y \sin\psi - V_x \cos\psi]}{\rho_1 + \rho_2} \quad (46) $$

$$ \dot{v}_1 = \frac{1}{(\rho_1 + \rho_2)\sin u_1}[\rho_2(\omega_x \cos\psi - \omega_y \sin\psi) + (V_x \sin\psi + V_y \cos\psi)] \quad (47) $$

$$ \dot{u}_2 = \frac{\rho_1\omega_y + V_x}{\rho_1 + \rho_2} \quad (48) $$

$$ \dot{v}_2 = \frac{-\rho_1\omega_x + V_y}{(\rho_1 + \rho_2)\sin u_2} \quad (49) $$

$$ \dot{\psi} = -\omega_z + \frac{1}{\tan v_1}\left[\frac{\rho_2}{\rho_1 + \rho_2}(\omega_x \cos\psi - \omega_y \sin\psi) + \frac{V_x \sin\psi + V_y \cos\psi}{\rho_1 + \rho_2}\right]. \quad (50) $$

At the acceleration level, Eq. (43) can be written in the form

$$\begin{bmatrix} \dot{u}_1 \\ \dot{v}_1 \\ \dot{u}_2 \\ \dot{v}_2 \end{bmatrix} = \frac{1}{\Delta} \begin{bmatrix} \rho_2 \sin\psi \sin u_1 \sin u_2 & \rho_2 \cos\psi \sin u_1 \sin u_2 & \cos\psi \sin u_1 \sin u_2 & \sin\psi \sin u_1 \sin u_2 \\ \rho_2 \cos\psi \sin u_2 & \rho_2 \sin\psi \sin u_2 & \sin\psi \sin u_2 & \cos\psi \sin u_2 \\ 0 & \rho_1 \sin u_1 \sin u_2 & \sin u_1 \sin u_2 & 0 \\ \rho_1 \sin u_1 & 0 & 0 & \sin u_1 \end{bmatrix} \left(\begin{pmatrix} \alpha_x \\ \alpha_y \\ a_x \\ a_y \end{pmatrix} + h \right) \quad (51)$$

where h is a nonlinear function of the rigid-body velocities and the rates of change of contact coordinates given by

$$h = \begin{pmatrix} \dot{\psi}\dot{u}_2 + \omega_z \dot{u}_1 \cos\psi - \omega_y \dot{v}_1 \cos u_1 - \dot{u}_1 \dot{v}_1 \cos\psi \cos u_1 + \dot{u}_2 \dot{v}_2 \cos u_2 - \omega_z \dot{v}_1 \sin\psi \sin u_1, \\ \omega_x \dot{v}_1 \cos u_1 - \omega_z \dot{u}_1 \sin\psi + \dot{u}_1 \dot{v}_1 \cos u_1 \sin\psi - \omega_z \dot{v}_1 \cos\psi \sin u_1 + \dot{\psi}\dot{v}_2 \sin u_2, \\ 2\omega_z \rho_1 \dot{u}_1 \sin\psi - 2\rho_1 \dot{u}_1 \dot{v}_1 \cos u_1 \sin\psi + 2\omega_z \rho_1 \dot{v}_1 \cos\psi \sin u_1 - \rho_1 \dot{v}_1^2 \cos\psi \cos u_1 \sin u_1 + \rho_2 \dot{v}_2^2 \cos u_2 \sin u_2, \\ 2\omega_z \rho_1 \dot{u}_1 \cos\psi - 2\rho_1 \dot{u}_1 \dot{v}_1 \cos\psi \cos u_1 - 2\rho_2 \dot{u}_2 \dot{v}_2 \cos u_2 - 2\omega_z \rho_1 \dot{v}_1 \sin\psi \sin u_1 + \rho_1 \dot{v}_1^2 \cos u_1 \sin\psi \sin u_1 \end{pmatrix}$$

and

$$\Delta = (\rho_1 + \rho_2) \sin u_1 \sin u_2.$$

From Eq. (44), we get

$$\begin{aligned} \ddot{\psi} = &-\alpha_z + \dot{v}_1 \cos u_1 + \dot{v}_2 \cos u_2 \\ &- \omega_y(\dot{u}_1 \sin\psi + \dot{v}_1 \sin u_1 \cos\psi) - \dot{u}_1 \dot{v}_1 \sin u_1 \\ &- \dot{u}_2 \dot{v}_2 \sin u_2 + \omega_x(\dot{v}_1 \sin u_1 \sin\psi - \dot{u}_1 \cos\psi) \end{aligned} \quad (52)$$

and the acceleration constraint from Eq. (40) is

$$\begin{aligned} a_z = &-(\rho_1 \dot{u}_1^2 + \rho_1(\dot{v}_1 \sin u_1)^2 + \rho_2 \dot{u}_2^2 \\ &+ \rho_2(\dot{v}_2 \sin u_2)^2 - 2\rho_1 \omega_y \dot{u}_1 + 2\rho_1 \omega_x \dot{v}_1 \sin u_1). \end{aligned} \quad (53)$$

The development in Cai and Roth (1987) deals with the special case in which the coordinate curves on the two surfaces are aligned so that the angle ψ is zero. For this special case, we get the same results by substituting

$$\psi = 0, \quad u_1 = \frac{\pi}{2}, \quad v_1 = 0, \quad u_2 = \frac{\pi}{2}, \quad v_2 = 0$$

in our equations above.

$$\dot{u}_1 = \frac{\rho_2 \omega_y - V_x}{\rho_1 + \rho_2}$$

$$\dot{v}_1 = \frac{\rho_2 \omega_x + V_y}{\rho_1 + \rho_2}$$

$$\dot{u}_2 = \frac{\rho_1 \omega_y + V_x}{\rho_1 + \rho_2}$$

$$\dot{v}_2 = \frac{-\rho_1 \omega_x + V_y}{\rho_1 + \rho_2}$$

$$\ddot{u}_1 = \frac{-a_x + \alpha_y \rho_2 - \omega_x \omega_z \rho_2 - 2\omega_z v_y}{\rho_1 + \rho_2}$$

$$\dot{v}_1 = \frac{a_y + \alpha_x \rho_2 + \omega_y \omega_z \rho_2 - 2\omega_z v_x}{\rho_1 + \rho_2}$$

$$\ddot{u}_2 = \frac{a_x + \alpha_y \rho_1 + \omega_x \omega_z \rho_1}{\rho_1 + \rho_2}$$

$$\dot{v}_2 = \frac{a_y - \alpha_x \rho_1 + \omega_y \omega_z \rho_1}{\rho_1 + \rho_2}$$

The paper (Cai and Roth, 1987) does not deal with the rate of change of ψ which evolves (at $\psi = 0$) according to the equations

$$\dot{\psi} = -\omega_z$$

$$\ddot{\psi} = \frac{\omega_x(\omega_y \rho_1 + v_x)}{\rho_1 + \rho_2}.$$

6.2 A Sphere Contacting a Plane. We consider the example of a plane (obj 1) contacting a sphere (obj 2). The velocity equations are

$$\dot{u}_1 = \rho(\omega_y \cos\psi + \omega_x \sin\psi - V_x \cos\psi + V_y \sin\psi)$$

$$\dot{v}_1 = \rho(-\omega_y \sin\psi + \omega_x \cos\psi + V_x \sin\psi + V_y \cos\psi)$$

$$\dot{u}_2 = \omega_y$$

$$\dot{v}_2 = -\omega_x \csc u_2$$

$$\dot{\psi} = -(\omega_x \cot u_2 + \omega_z).$$

The acceleration equations are

$$\begin{aligned} \ddot{u}_1 = &\rho\dot{\psi}(\dot{u}_2 \sin\psi + \dot{v}_2 \sin u_2 \cos\psi) \\ &- \rho\dot{u}_2\dot{v}_2 \cos u_2 \sin\psi - \rho(\dot{v}_2)^2 \sin u_2 \cos u_2 \cos\psi - 2\omega_z \dot{v}_1 \\ &+ \rho(\alpha_x \sin\psi + \alpha_y \cos\psi) - (a_x \cos\psi - a_y \sin\psi) \end{aligned}$$

$$\begin{aligned} \dot{v}_1 = &\rho\dot{\psi}(\dot{u}_2 \cos\psi - \dot{v}_2 \sin u_2 \sin\psi) \\ &- \rho\dot{u}_2\dot{v}_2 \cos u_2 \cos\psi + \rho(\dot{v}_2)^2 \sin u_2 \cos u_2 \sin\psi + 2\omega_z \dot{u}_1 \\ &+ \rho(\alpha_x \cos\psi - \alpha_y \sin\psi) + (a_x \sin\psi + a_y \cos\psi) \end{aligned}$$

$$\ddot{u}_2 = \dot{v}_2\dot{\psi} \sin u_2 + \alpha_y$$

$$\dot{v}_2 = \dot{u}_2\dot{\psi} \csc u_2 - \dot{u}_2\dot{v}_2 \cot u_2 - \alpha_x \csc u_2$$

$$\ddot{\psi} = \dot{v}_2 \sin u_2 - \dot{u}_2\dot{v}_2 \cos u_2 - \alpha_z.$$

7 Kinematics of Rolling Contact

Two bodies are said to be in a condition of rolling contact if the velocity of the point of contact on one body is equal to the velocity of the point of contact on the other body. In other words, the *sliding velocity* (Cai and Roth, 1986; Cai and Roth, 1987) or the relative velocity between the points of contact is zero. This definition is well known and can be found in standard kinematics texts (see, for example, Paul, 1979). Because this definition imposes a condition on velocities (and not on higher order derivatives), it defines rolling contact up to the first order (Cai and Roth, 1987). We will refer to this as the *first-order condition for rolling.*

However, if the relative velocity between the points of contact, in addition to being zero, stays constant through a small time interval, the two bodies are in a condition of rolling contact up to the second order. In other words, the derivative of the sliding velocity is zero. We will refer to this as the *second-order condition for rolling.*

In Fig. 6, p_i and $\acute{p}_i$ are points attached to obj i. p_i is the point of contact at time t while $\acute{p}_i$ is the contact point at time $\acute{t}$. t and $\acute{t}$ are considered to be time instants that are separated by a small interval Δt.

For the *first-order condition for rolling* we have

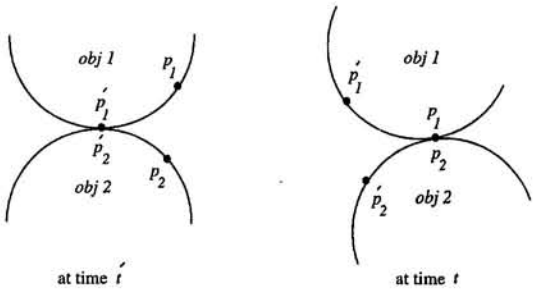

Fig. 6 Rolling motion of two rigid bodies

$$^{p_2}V_{p_1p_2}(t) = 0. \tag{54}$$

In the contact frame c_2 this is

$$\begin{bmatrix} V_x \\ V_y \\ V_z \end{bmatrix} = 0. \tag{55}$$

For the *second-order condition for rolling* we have

$$\begin{bmatrix} a_x \\ a_y \\ a_z \end{bmatrix} = \begin{bmatrix} -(\rho_1\dot{u}_1 \sin\psi + \rho_2\dot{v}_1\cos\psi)\omega_z \\ -(\rho_1\dot{u}_1\cos\psi - \rho_2\dot{v}_1)\omega_z \\ (\rho_1\dot{u}_1\sin\psi + \rho_2\dot{v}_1\cos\psi)\omega_x + (\rho_1\dot{u}_1\cos\psi - \rho_2\dot{v}_1\sin\psi)\omega_y \end{bmatrix} \tag{63}$$

$$\lim_{(t-\hat{t})\to 0} \frac{^{p_2}V_{p_1p_2}(t) - {}^{\hat{p}_2}V_{\hat{p}_1\hat{p}_2}(\hat{t})}{t-\hat{t}} = 0. \tag{56}$$

We rewrite Equation (56) to get

$$\lim_{(t-\hat{t})\to 0} \frac{^{p_2}V_{p_1p_2}(t) - {}^{p_2}V_{p_1p_2}(\hat{t})}{t-\hat{t}} + \lim_{(t-\hat{t})\to 0} \frac{^{p_2}V_{p_1p_2}(\hat{t}) - {}^{\hat{p}_2}V_{\hat{p}_1\hat{p}_2}(\hat{t})}{t-\hat{t}} = 0. \tag{57}$$

The first term of the above equation is nothing but $^{p_2}a_{p_1p_2}(t)$. Recognizing that $^{\hat{p}_2}V_{\hat{p}_1\hat{p}_2} = {}^{p_2}V_{\hat{p}_1p_2}$, the second term can be written as $\lim_{(t-\hat{t})\to 0} (-{}^{p_2}\omega_{p_1} \times {}^{p_1}r_{\hat{p}_1p_1}/t-\hat{t})$. As $\Delta t \to 0$

$$\lim_{(t-\hat{t})\to 0} \frac{^{p_1}r_{\hat{p}_1p_1}}{t-\hat{t}} = -{}^{p_1}V_{c_1p_1}.$$

Thus, we get

$$^{p_2}a_{p_1p_2}(t) + {}^{p_2}\omega_{p_1} \times ({}^{p_1}V_{c_1p_1}) = 0. \tag{58}$$

Because

$$^{p_1}V_{c_1p_1} = {}^{o_1}V_{c_1o_1},$$

Eq. (58) simplifies to

$$^{p_2}a_{p_1p_2}(t) = -{}^{p_2}\omega_{p_1} \times {}^{o_1}V_{c_1o_1}. \tag{59}$$

This is the second-order condition for rolling. In the contact frame c_2, it becomes

$$\begin{bmatrix} a_x \\ a_y \\ a_z \end{bmatrix} = \begin{bmatrix} (-E_1R_\psi\sqrt{G_1}\dot{U}_1)\omega_z \\ \begin{pmatrix} \omega_y \\ -\omega_x \end{pmatrix}^T R_\psi\sqrt{G_1}\dot{U}_1 \end{bmatrix} \tag{60}$$

where we have substituted the expression for $^{o_1}V_{c_1o_1}$ from Eq. (29) and $^{p_2}\omega_{p_1} = [\omega_x\ \omega_y\ \omega_z]^T$.

It can be shown (Sarkar, 1993) that the third scalar equation is actually the same equation as (45), provided the first-order condition for rolling is satisfied.

In addition to the rolling conditions defined previously, if we impose another condition known as the *no-spin* condition, we achieve what is called *pure rolling* (Johnson, 1985, p. 242). The pivoting component of the angular velocity is zero for pure rolling (Neimark and Fufaev, 1972, p. 18). In other words, in the frame c_2,

$$\omega_z = 0. \tag{61}$$

For pure rolling up to the second order, the derivative of the pivoting velocity or the z component of the derivative of the relative angular velocity must vanish (Sarkar, 1993).

$$\alpha_z = 0 \tag{62}$$

7.1 Example: Two Spheres in Contact. In the previous section we considered the example of a sphere contacting another sphere. The conditions for rolling up to the first order are

$$V_x = 0 \quad V_y = 0 \quad V_z = 0$$

For rolling up to the second order, from Eq. (60),

where $\dot{u}_i$ and $\dot{v}_i$ are given by Eqs. (46)–(49). Further, for pure rolling, we have

$$\omega_z = 0 \tag{64}$$

$$\alpha_z = 0. \tag{65}$$

This yields, upon substitution for $\dot{u}_i$ and $\dot{v}_i$ from Eqs. (46)–(49),

$$a_x = 0 \tag{66}$$

$$a_y = 0 \tag{67}$$

$$a_z = \frac{(\omega_x^2 + \omega_y^2)\rho_1\rho_2}{\rho_1 + \rho_2}. \tag{68}$$

8 Discussion

We have derived and presented in this paper the velocity equations (Eqs. (34)–(37)) and the acceleration equations (Eqs. (43)–(44)) for contact between two three-dimensional bodies. This is the first time that the equations have been presented in this general form. The work by Cai and Roth (1986; 1987) comes closest to the work presented here. They derived similar equations that are valid for a Cartesian coordinate system whose origin is coincident with the contact frame. However, because of this assumption, their coordinate covering of the contacting surfaces changes as the contact point moves and as the relative orientation between the two rigid bodies changes. In our approach the surface coordinates are independent of where contact occurs and the relative orientation between the two bodies. Also, our coordinate systems are, in general, curvilinear, and include the special case of a Cartesian coordinate system. Finally, the equations derived by Cai and Roth predict the motion of the contact point over each surface. However, they do not consider the evolution of the fifth contact coordinate ψ.

The special case of pure rolling is particularly interesting in robotic applications. Rolling contact is generally preferred because it is more efficient and also because rolling motion is easier to control. In order to maintain a condition of rolling the

relative motion between the two contacting bodies must be such that the relative acceleration at the contact point is given by Eq. (60). In general, this acceleration includes tangential (a_x and a_y) components as well as a normal component (a_z). This is unlike the planar case in which the tangential acceleration must be zero for rolling. In three dimensions, only in the special case of pure rolling do the tangential components have to be zero. The application of the rolling constraint equations to the derivation of the equations of motion and the controller for a two-arm manipulation system is presented in Sarkar et al. (1993) and Sarkar (1993).

The acceleration level equations depend on first, second, and third-order properties of the contacting surfaces. In other words, we encounter upto the third derivative of the coordinate map, f, for each object in these equations. Similarly, the velocity equations depend on first and second order properties. It is worth noting that while an object such as a sphere can be described by a second-order equation in the Cartesian space, it does not mean that all third-order partial derivatives are zero. In fact, as shown earlier in the example of a sphere, the coefficients, g_{ij}, Γ_{ij}^k, and L_{ij} are not constant and the partial derivatives, $(\partial^2 x_i / \partial \xi^k \partial \xi^j)$, are, in general, nonzero.

Finally a comment about the two examples considered in the paper. At first sight they may appear trivial and may not serve to provide adequate justification for the theoretical development in this paper. But Eqs. (34)–(36) and Eqs. (43)–(45) are completely general, and they work for any contacting surfaces. The only information needed are the local differential geometric surface properties (the coefficients of the first and second fundamental forms and their derivatives). The main motivation for presenting these "simpler examples" is because for these examples, the equations are well known for planar motions, and for spatial motions under the condition of pure rolling. Therefore, for these examples, there is some opportunity for comparing the general contact kinematics equations derived here with these special equations. And in fact, it can be seen from Section 2.3.1 that, even in these "simple" cases, the derivatives of g_{ij}, Γ_{ij}^k and L_{ij} do not vanish and that a spherical surface does not really simplify the second-order equations.

Current work addresses the application of these equations to better understand the stability of multi-contact grasps and the optimization of fixtures for restraining three-dimensional machine components.

Acknowledgment

This work was in part supported by the grants NSF MSS-91-57156, ARPA N0014-88-K-0632 and NATO grant No. 0224/85.

References

Beggs, J. S., 1966, *Advanced Mechanism,* Macmillan, New York.

Brock, D. L., 1988, "Enhancing the Dexterity of a Robot Hand Using Controlled Slip," *Proceedings of the IEEE International Conference on Robotics and Automation,* Philadelphia, PA, pp. 249–251.

Cai, C., and Roth, B., 1986, "On the planar motion of rigid bodies with point contact," *Mechanism and Machine Theory,* Vol. 21, No. 6, pp. 453–466.

Cai, C., and Roth, B., 1987, "On the spatial motion of rigid bodies with point contact," *Proceedings of the IEEE International Conference on Robotics and Automation,* Raleigh, NC, pp. 686–695.

Cai, C., and Roth, B., 1988, "On the spatial motion of rigid bodies with line contact," *Proceedings of IEEE International Conference on Robotics and Automation,* Philadelphia, PA, pp. 1036–1041.

Hall, A. S., 1966, *Kinematics and Linkage Design,* Balt Publishers, West Lafayette, IN.

Johnson, K. L., 1985, *Contact Mechanics,* Cambridge University Press, London.

Kane, T. R., and Levinson, D. A., 1985, *Dynamics, theory and applications,* McGraw-Hill, New York.

Kirson, Y., and Yang, A. T., 1978, "Instantaneous Invariants in Three-Dimensional Kinematics," ASME JOURNAL OF APPLIED MECHANICS, Vol. 45, pp. 409–414.

Kumar, V., and Waldron, K. J., 1989, "Actively coordinated mobility systems," ASME *Journal of Mechanisms, Transmissions, and Automation in Design,* Vol. 111, No. 2 pp. 223–231.

Lipschutz, M. M., 1969, *Differential Geometry,* McGraw-Hill, New York.

Mason, M., and Salisbury, J. K., 1985, *Robot Hands and the Mechanics of Manipulation,* MIT Press, Cambridge, MA.

McCarthy, J. M., 1990, *An Introduction to Theoretical Kinematics,* MIT Press, Cambridge, MA.

Millman, R. S., and Parker, G. D., 1977, *Elements of Differential Geometry,* Prentice-Hall Englewood Cliffs, NJ.

Montana, D. J., 1988, "The kinematics of contact and grasp," *The International Journal of Robotics Research,* Vol. 7, No. 3, pp. 17–32.

Neimark, J. I., and Fufaev, N. A., 1972, *Dynamics of Nonholonomic Systems,* American Mathematical Society, Providence, RI.

Pars, L. A., 1968, *A Treatise on Analytical Dynamics,* John Wiley and Sons, New York.

Paul, B., 1979, *Kinematics and Dynamics of Planar Machinery,* Prentice-Hall, Englewoods Cliffs, NJ.

Rosenauer, N., and Willis, A. H., 1953, *Kinematics of Mechanisms,* Associated General Publications Pty Ltd., Sydney, Australia.

Sarkar, N., 1993, "Control of Mechanical Systems with Rolling Contacts: Applications to Robotics," Ph.D. thesis, Department of Mechanical Engineering and Applied Mechanics, University of Pennsylvania, Philadelphia, PA.

Sarkar, N., Yun, X., and Kumar, V., 1993, "Dynamic control of 3-D rolling in multi-arm manipulation," *Proceedings of the IEEE International Conference on Robotics and Automation,* Atlanta, GA, pp. 978–983.

Stoker, J. J., 1969, *Differential Geometry,* John Wiley and Sons, New York.

Whittaker, E. T., 1988, *A Treatise on the Analytical Dynamics of Particles & Rigid Bodies,* Cambridge University Press, Cambridge, UK.

APPENDIX

A Expressions for ${}^{o_i}\Omega_{c_i}$ and ${}^{o_i}\dot{\Omega}_{c_i}$

For any rotation matrix ${}^fR_m$, its derivatives in frame f is given by

$$ {}^f\Omega_m = \dot{R}R^T $$

$$ {}^f\dot{\Omega}_m = \ddot{R}R^T - \Omega\Omega $$

Thus in contact frame c_i,

$$ {}^{o_i}\Omega_{c_i} = {}^{o_i}R_{c_i}^T {}^{o_i}\dot{R}_{c_i} $$

$$ {}^{o_i}\Omega_{c_i} = {}^{o_i}R_{c_i}^T {}^{o_i}\dot{R}_{c_i} = \begin{bmatrix} (\sqrt{G_i})^{-1} & 0_{2\times 1} \\ 0_{1\times 2} & 1 \end{bmatrix} \begin{bmatrix} (x_1)_i^T \\ (x_2)_i^T \\ (n)_i^T \end{bmatrix} \Bigg\{ [(x_1)_i \quad (x_2)_i \quad (n)_i] \begin{bmatrix} ((\dot{\sqrt{G_i}})^{-1}) & 0_{2\times 1} \\ 0_{1\times 2} & 0 \end{bmatrix} $$

$$ + \left[\sum_{j=1}^{2} \left(\frac{\partial x_1}{\partial \xi^j} \right)_i \dot{\xi}^j \quad \sum_{j=1}^{2} \left(\frac{\partial x_2}{\partial \xi^j} \right)_i \dot{\xi}^j \quad \sum_{j=1}^{2} \left(\frac{\partial n}{\partial \xi^j} \right)_i \dot{\xi}^j \right] \begin{bmatrix} (\sqrt{G_i})^{-1} & 0_{2\times 1} \\ 0_{1\times 2} & 1 \end{bmatrix} \Bigg\}. $$

We introduce Christoffel symbols, $[ij, k]$ and Γ_{jk}^i and the coefficients of the second fundamental form, L_{ij}, and simplify the derivative of the metric tensor through Eq. (1). After some algebraic manipulation we get

$$
{}^{o_1}\Omega_{c_1} = -\begin{bmatrix} \frac{1}{(g_{11})_1}([11,1]_1\dot{u}_1 + [12,1]_1\dot{v}_1) & 0 & 0 \\ 0 & \frac{1}{(g_{22})_1}([21,1]_1\dot{u}_1 + [22,1]_1\dot{v}_1) & 0 \\ 0 & 0 & 0 \end{bmatrix}
$$

$$
+\begin{bmatrix} \frac{1}{(g_{11})_1}([11,1]_1\dot{u}_1 + [12,1]_1\dot{v}_1) & -\frac{1}{(g_{11})_1}\frac{1}{(g_{22})_1}([11,2]_1\dot{u}_1 + [12,2]_1\dot{v}_1) & -\frac{1}{(g_{11})_1}\{(L_{11})_1\dot{u}_1 + (L_{12})_1\dot{v}_1\} \\ \frac{1}{(g_{11})_1}\frac{1}{(g_{22})_1}([11,2]_1\dot{u}_1 + [12,2]_1\dot{v}_1) & \frac{1}{(g_{22})_1}([21,1]_1\dot{u}_1 + [22,1]_1\dot{v}_1) & -\frac{1}{(g_{22})_1}\{(L_{21})_1\dot{u}_1 + (L_{22})_1\dot{v}_1\} \\ \frac{1}{(g_{11})_1}\{(L_{11})_1\dot{u}_1 + (L_{12})_1\dot{v}_1\} & \frac{1}{(g_{22})_1}\{(L_{21})_1\dot{u}_1 + (L_{22})_1\dot{v}_1\} & 0 \end{bmatrix}
$$

which can be simplified to

$$
{}^{o_1}\Omega_{c_1} = \begin{bmatrix} 0 & (-\sigma_1\Gamma_1\dot{U}_1) & \{-(\sqrt{G_1})^{-1}L_1\dot{U}_1)\}_{2\times 1} \\ (\sigma_1\Gamma_1\dot{U}_1) & 0 & \\ \{(\sqrt{G_1})^{-1}L_1\dot{U}_1\})^T_{1\times 2} & & 0 \end{bmatrix} \tag{69}
$$

where $\sigma_i = \{(g_{22})_i/(g_{11})_i\}^{1/2}$ for $i = 1, 2$ are the ratios of the norms of the natural base vectors.

In order to obtain an expression for ${}^{o_i}\dot{\Omega}_{c_i}$ we start with Eq. (69).

$$
{}^{o_i}\dot{\Omega}_{c_i} = \begin{bmatrix} (\sqrt{G_i})^{-1} & 0_{2\times 1} \\ 0_{1\times 2} & 1 \end{bmatrix}\begin{bmatrix} (x_1)_i^T \\ (x_2)_i^T \\ (n)_i^T \end{bmatrix} \times \left\{\begin{bmatrix} \sum_{j=1}^{2}\left(\frac{\partial x_1}{\partial \xi^j}\right)_i\dot{\xi}^j & \sum_{j=1}^{2}\left(\frac{\partial x_2}{\partial \xi^j}\right)_i\dot{\xi}^j & \sum_{j=1}^{2}\left(\frac{\partial n}{\partial \xi^j}\right)_i\dot{\xi}^j \end{bmatrix}\begin{bmatrix} ((\dot{\sqrt{G_i}})^{-1}) & 0_{2\times 1} \\ 0_{1\times 2} & 0 \end{bmatrix}\right.
$$

$$
+\begin{bmatrix} \sum_{j=1}^{2}\left(\frac{\partial x_1}{\partial \xi^j}\right)_i\ddot{\xi}^j + \sum_{j,k=1}^{2}\left(\frac{\partial^2 x_1}{\partial \xi^j\partial \xi^k}\right)_i\dot{\xi}^j\dot{\xi}^k & \sum_{j=1}^{2}\left(\frac{\partial x_2}{\partial \xi^j}\right)_i\ddot{\xi}^j + \sum_{j,k=1}^{2}\left(\frac{\partial^2 x_2}{\partial \xi^j\partial \xi^k}\right)_i\dot{\xi}^j\dot{\xi}^k & \sum_{j=1}^{2}\left(\frac{\partial n}{\partial \xi^j}\right)_i\ddot{\xi}^j \\ + \sum_{j,k=1}^{2}\left(\frac{\partial^2 n}{\partial \xi^j\partial \xi^k}\right)_i\dot{\xi}^j\dot{\xi}^k \end{bmatrix}\begin{bmatrix} (\sqrt{G_i})^{-1} & 0_{2\times 1} \\ 0_{1\times 2} & 1 \end{bmatrix} + [(x_1)_i \quad (x_2)_i \quad (n)_i]\begin{bmatrix} ((\ddot{\sqrt{G_i}})^{-1}) & 0_{2\times 1} \\ 0_{1\times 2} & 0 \end{bmatrix}
$$

$$
\left.+\begin{bmatrix} \sum_{j=1}^{2}\left(\frac{\partial x_1}{\partial \xi^j}\right)_i\dot{\xi}^j & \sum_{j=1}^{2}\left(\frac{\partial x_2}{\partial \xi^j}\right)_i\dot{\xi}^j & \sum_{j=1}^{2}\left(\frac{\partial n}{\partial \xi^j}\right)_i\dot{\xi}^j \end{bmatrix}\begin{bmatrix} (\dot{\sqrt{G_i}})^{-1}) & 0_{2\times 1} \\ 0_{1\times 2} & 0 \end{bmatrix}\right\}
$$

$$
-\begin{bmatrix} 0 & (-\sigma_i\Gamma_i\dot{U}_i) & \{-(\sqrt{G_i})^{-1}L_i\dot{U}_i\}_{2\times 1} \\ (\sigma_i\Gamma_i\dot{U}_i) & 0 & \\ \{(\sqrt{G_i})^{-1}L_i\dot{U}_1\}^T_{1\times 2} & & 0 \end{bmatrix} \times \begin{bmatrix} 0 & (-\sigma_i\Gamma_i\dot{U}_i) & \{-(\sqrt{G_i})^{-1}L_i\dot{U}_i\}_{2\times 1} \\ (\sigma_i\Gamma_i\dot{U}_i) & 0 & \\ \{(\sqrt{G_i})^{-1}L_i\dot{U}_i\}^T_{1\times 2} & & 0 \end{bmatrix}
$$

After simplification, we finally write ${}^{o_i}\dot{\Omega}_{c_i}$ in the following compact form:

$$
{}^{o_i}\dot{\Omega}_{c_i} = \begin{bmatrix} 0 & (-\sigma_i(\Gamma_i\dot{U}_i + \bar{\bar{\Gamma}}_iW_i)) & ((\dot{\sqrt{G_i}})^{-1}(\bar{\bar{L}}_iW_i - L_i\dot{U}_i))_{2\times 1} \\ (\sigma_i(\Gamma_i\dot{U}_i + \bar{\bar{\Gamma}}_iW_i)) & 0 & \\ ((\dot{\sqrt{G_i}})^{-1}(\bar{\bar{L}}_iW_i - L_i\dot{U}_i))^T_{1\times 2} & & 0 \end{bmatrix}.
$$

Curvilinear Coordinates and Physical Components: An Application to the Problem of Viscous Flow and Heat Transfer in Smoothly Curved Ducts

C. J. Bolinder
Division of Fluid Mechanics,
Lund Institute of Technology,
Box 118,
221 00 Lund, Sweden

Expressions are derived for the gradient, divergence, Laplacian, curl, and material time derivative in terms of general curvilinear coordinates using physical components of all vector quantities. The results are conveniently expressed in terms of two new coefficients, involving physical and reciprocal base vectors. An application to the problem of viscous flow and heat transfer in arbitrarily smoothly curved ducts is presented. In particular, helical ducts are considered.

Introduction

When analyzing a flow problem, it is desirable to have a coordinate system that follows the boundaries of the flow domain smoothly, i.e., a boundary-fitted coordinate system. The reason for this is that the boundary conditions then may be applied easily and in an exact manner. In CFD, a boundary-fitted grid is often generated by some numerical technique (see, e.g., Thompson, 1984). This is required to be able to handle arbitrary complex geometries. For particular geometries, however, it might be possible to find a simple analytical expression (according to Eq. (2) below) for a curvilinear coordinate system that fits the boundaries exactly. This is the case for example for smoothly curved ducts, which are considered in this paper. The governing equations may be derived in terms of the curvilinear coordinates in an exact manner, and the equations may then be solved by any convenient analytical or numerical technique. An advantage of this approach, compared to CFD employing numerical grid generation, is that no approximation is introduced in the formulation of the flow problem, which is attractive at least from an academic point of view.

The main motive for writing this paper is to present a method for deriving the governing equations for the flow and heat transfer in helical ducts, even though the obtained results are more generally applicable. A helical duct is characterized by the center-line having a constant curvature and a constant torsion, which, for example, enables the study of fully developed flow conditions. A finite torsion of the center-line implies a finite pitch of the duct, and it also makes the associated coordinate system nonorthogonal.

Among the first to analyze, from a theoretical point of view, the flow in helical ducts with a finite pitch or torsion were Wang (1981) and Germano (1982). They, however, reached different conclusions about the effect of torsion on the secondary flow. While Wang found a first-order effect of torsion, Germano only found a second-order effect. The reason for the discrepancy was that different velocity components were used for the secondary flow. Wang employed so-called contravariant components (to be defined below), and Germano employed physical components, i.e., the velocity vector was expanded in a physical (i.e., an orthonormal) basis. From a conceptual point of view, as argued for below, it is recommended to describe the flow using physical components, even though full consensus about this matter not yet exists. Liu and Masliyah (1993), for example, recommend using contravariant components.

In this paper, a method is presented for deriving the governing equations directly in terms of the desired coordinates and suitable physical velocity components. Previous authors on helical duct flows have used indirect methods to derive the governing equations, in the sense that a transformation is involved, either of the coordinates or of the velocity components. In the first section expressions are derived for some basic vector quantities, e.g., the gradient, divergence, and curl. In the next section, the derived expressions are applied to the problem of incompressible flow of a Newtonian fluid, and in the final section smoothly curved ducts are considered. No solutions of the derived equations are presented in this paper. Applications to laminar flow and heat transfer in helical rectangular ducts may be found in Bolinder (1993, 1995, 1996) and in Bolinder and Sundén (1995, 1996).

Basic Definitions and Relationships

In this section, expressions are derived for the gradient, divergence, Laplacian, curl, and material time derivative in terms of general curvilinear coordinates using physical components of all vector quantities.

The position vector $\mathbf{r}$ expanded in the Cartesian basis ($\mathbf{e}_x$, $\mathbf{e}_y$, $\mathbf{e}_z$) reads

$$\mathbf{r} = x\mathbf{e}_x + y\mathbf{e}_y + z\mathbf{e}_z, \tag{1}$$

where x, y, and z are the Cartesian coordinates. Curvilinear coordinates (χ^1, χ^2, χ^3) are defined as functions of the Cartesian coordinates, i.e.,

$$\chi^i = \chi^i(x, y, z), \quad i = 1, 2, 3, \tag{2}$$

where the functions are assumed to be smooth, reversible, and single-valued in some region of space.

The natural base vectors $\mathbf{a}_i$ and the reciprocal base vectors $\mathbf{a}^i$ of the curvilinear coordinate system (χ^1, χ^2, χ^3) are defined by

$$\mathbf{a}_i = \frac{\partial \mathbf{r}}{\partial \chi^i}, \quad \mathbf{a}^i = \nabla \chi^i. \tag{3}$$

Contributed by the Applied Mechanics Division of THE AMERICAN SOCIETY OF MECHANICAL ENGINEERS for publication in the ASME JOURNAL OF APPLIED MECHANICS.

Discussion on this paper should be addressed to the Technical Editor, Professor Lewis T. Wheeler, Department of Mechanical Engineering, University of Houston, Houston, TX 77204-4792, and will be accepted until four months after final publication of the paper itself in the ASME JOURNAL OF APPLIED MECHANICS.

Manuscript received by the ASME Applied Mechanics Division, Jan. 30, 1995; final revision, Mar. 11, 1996. Associate Technical Editor: S. A. Berger.

Thus, $\mathbf{a}_i$ is tangent to the χ^i-coordinate curve, and $\mathbf{a}^i$ is normal to the coordinate surface χ^i-constant. The components of a vector $\mathbf{v}$ expanded in the natural basis are called contravariant and are denoted by v^i, and the components of $\mathbf{v}$ expanded in the reciprocal basis are called covariant and are denoted by v_i, thus

$$\mathbf{v} = v^i \mathbf{a}_i, \quad \mathbf{v} = v_i \mathbf{a}^i, \tag{4}$$

employing the familiar summation convention.

If the natural basis is nonorthogonal, so is the reciprocal basis, and it is generally not convenient to use either basis to expand, for example, the velocity vector. Instead, it is often preferable to use a physical (i.e., an orthonormal) basis for the velocity. With the terminology of Bowen and Wang (1976), a basis which is not the natural basis is also called an anholonomic basis. For a physical basis $(\mathbf{e}_1, \mathbf{e}_2, \mathbf{e}_3)$ it is required that

$$\mathbf{e}_i \cdot \mathbf{e}_j = \delta_{ij} = \begin{cases} 1, & \text{if} \quad i = j \\ 0, & \text{if} \quad i \neq j \end{cases}. \tag{5}$$

Expanding a vector $\mathbf{v}$ in a physical basis yields

$$\mathbf{v} = v_i \mathbf{e}_i, \tag{6}$$

where v_i are called physical components. Only for a physical basis, the components are obtained as projections of the vector on the respective base vectors, i.e.,

$$v_i = \mathbf{v} \cdot \mathbf{e}_i. \tag{7}$$

This property makes physical bases attractive from a conceptual point of view.

The following relationship is useful (see, e.g., Sokolnikoff, 1964):

$$\Gamma^j_{ji} = \frac{1}{\sqrt{g}} \frac{\partial \sqrt{g}}{\partial \chi^i}, \tag{8}$$

where the Christoffel symbols Γ^k_{ij} (also denoted by $\{^k_{ij}\}$) are defined by

$$\Gamma^k_{ij} = \mathbf{a}^k \cdot \frac{\partial \mathbf{a}_i}{\partial \chi^j}, \tag{9}$$

and where

$$g = \det (g_{ij}) = \det (\mathbf{a}_i \cdot \mathbf{a}_j). \tag{10}$$

g_{ij} are so-called metric coefficients. Two new coefficients, involving the physical base vectors $\mathbf{e}_i$, are defined by

$$E_{ijk} = \mathbf{e}_i \cdot \frac{\partial \mathbf{e}_j}{\partial \chi^k}, \quad \gamma^j_i = \mathbf{e}_i \cdot \mathbf{a}^j. \tag{11}$$

Obviously, for Cartesian velocity components, all the coefficients E_{ijk} would vanish. This approach is often taken in CFD, but for curved duct flows a more convenient choice is made to distinguish the so-called axial flow from the secondary flow, and also to be able to assume fully developed conditions, see further below.

We are now in a position to derive a variety of vector quantities. Many of the basic definitions may be found in the book by Gurtin (1981). In the following a lower index is used to denote a physical component (and not a covariant component).

By use of the chain rule and the definition $(3)_2$, the following expression for the physical components of the gradient of a scalar field f is obtained:

$$(\nabla f)_i = \mathbf{e}_i \cdot \nabla f = \frac{\partial f}{\partial \chi^j} \gamma^j_i. \tag{12}$$

For the gradient of a vector field $\mathbf{v}$ one obtains

$$(\nabla \mathbf{v})_{ij} = \mathbf{e}_i \cdot (\nabla \mathbf{v}) \mathbf{e}_j = \mathbf{e}_i \cdot \left(\frac{\partial \mathbf{v}}{\partial \chi^k} \otimes \nabla \chi^k \right) \mathbf{e}_j = \gamma^k_j \left(\frac{\partial v_i}{\partial \chi^k} - v_l E_{lik} \right), \tag{13}$$

and for the divergence of a vector field $\mathbf{v}$, using Eq. (8),

$$\text{div } \mathbf{v} \equiv \text{tr } (\nabla \mathbf{v}) = \frac{\partial \mathbf{v}}{\partial \chi^i} \cdot \nabla \chi^i = \frac{1}{\sqrt{g}} \frac{\partial}{\partial \chi^i} (\sqrt{g} v_j \gamma^i_j). \tag{14}$$

The divergence of a tensor field $\mathbf{T}$ is a vector field, which for any vector field $\mathbf{v}$ satisfies (Gurtin, 1981)

$$\mathbf{v} \cdot \text{div } \mathbf{T} = \text{div } (\mathbf{T}^T \mathbf{v}) - \text{tr } (\mathbf{T}^T \nabla \mathbf{v}). \tag{15}$$

Using this, the physical components of div $\mathbf{T}$ may be written

$$(\text{div } \mathbf{T})_i = \frac{1}{\sqrt{g}} \frac{\partial}{\partial \chi^k} (\sqrt{g} T_{ij} \gamma^k_j) - T_{kl} E_{kij} \gamma^j_l, \tag{16}$$

where T_{ij} are physical components of $\mathbf{T}$, which satisfy

$$\mathbf{T} = T_{ij} \mathbf{e}_i \otimes \mathbf{e}_j, \quad T_{ij} = \mathbf{e}_i \cdot \mathbf{T} \mathbf{e}_j. \tag{17}$$

Note that Eq. $(17)_2$ requires that Eq. (5) is fulfilled.

For the Laplacian of a scalar field f one obtains

$$\Delta f \equiv \text{div } \nabla f = \frac{1}{\sqrt{g}} \frac{\partial}{\partial \chi^i} \left(\sqrt{g} \frac{\partial f}{\partial \chi^j} \gamma^j_k \gamma^i_k \right). \tag{18}$$

An expression for the physical components of the Laplacian of a vector field $\mathbf{v}$, $\Delta \mathbf{v} \equiv \text{div } \nabla \mathbf{v}$, is easy to obtain using Eqs. (16) and (13).

For the curl of a vector field $\mathbf{v}$ one obtains

$$(\text{curl } \mathbf{v})_i = \epsilon_{ijk} (\nabla \mathbf{v})_{kj} = \epsilon_{ijk} \gamma^l_j \left(\frac{\partial v_k}{\partial \chi^l} - v_m E_{mkl} \right), \tag{19}$$

where ϵ_{ijk} is the usual permutation symbol.

Finally, expressions are given for the material time derivative of scalar and vector fields. For a scalar field f, one obtains

$$\dot{f} = \frac{\partial f}{\partial t} + \mathbf{v} \cdot \nabla f = \frac{\partial f}{\partial t} + v_i \gamma^j_i \frac{\partial f}{\partial \chi^j}, \tag{20}$$

where $\mathbf{v}$ is the velocity field, and for a vector field $\mathbf{u}$,

$$(\dot{\mathbf{u}})_i = \frac{\partial u_i}{\partial t} + (\nabla \mathbf{u})_{ij} v_j = \frac{\partial u_i}{\partial t} + \gamma^k_j \left(\frac{\partial u_i}{\partial \chi^k} - u_l E_{lik} \right) v_j, \tag{21}$$

assuming the physical base vectors $\mathbf{e}_i$ to be time independent.

Governing Equations for an Incompressible Newtonian Fluid

The formulas derived in the preceding section are applicable to any problem involving partial differential equations. In this section, the formulas are applied to the problem of incompressible flow of a Newtonian fluid, which is governed by the continuity, the Navier-Stokes, and the energy equations. In direct vector notation these equations read

$$\text{div } \mathbf{v} = 0, \tag{22}$$

$$\dot{\mathbf{v}} = -\frac{1}{\rho} \nabla p - \nu \text{ curl } (\text{curl } \mathbf{v}), \tag{23}$$

$$\dot{T} = \frac{\nu}{\text{Pr}} \Delta T + \frac{\nu}{C_p} \text{tr } (\nabla \mathbf{v}^T \nabla \mathbf{v} + \nabla \mathbf{v} \nabla \mathbf{v}), \tag{24}$$

where the kinematic viscosity ν is assumed constant and where p is a generalized pressure, which includes conservative body forces. The last term in the energy Eq. (24) is the viscous dissipation. In component notation, according to the previously derived expressions, the governing equations read

$$\frac{\partial}{\partial \chi^i}(\sqrt{g} v_j \gamma_j^i) = 0, \tag{25}$$

$$\frac{\partial v_i}{\partial t} + \gamma_j^k \left(\frac{\partial v_i}{\partial \chi^k} - v_l E_{lik} \right) v_j = -\frac{1}{\rho} \frac{\partial p}{\partial \chi^j} \gamma_i^j - \nu \epsilon_{ijk} \gamma_j^l \left(\frac{\partial (\text{curl } \mathbf{v})_k}{\partial \chi^l} - (\text{curl } \mathbf{v})_m E_{mkl} \right), \tag{26}$$

$$\frac{\partial T}{\partial t} + v_i \gamma_i^j \frac{\partial T}{\partial \chi^j} = \frac{\nu}{\text{Pr}} \frac{1}{\sqrt{g}} \frac{\partial}{\partial \chi^i} \left(\sqrt{g} \frac{\partial T}{\partial \chi^j} \gamma_k^j \gamma_k^i \right) + \frac{\nu}{C_p} \left\{ \left(\frac{\partial v_l}{\partial \chi^i} \frac{\partial v_l}{\partial \chi^j} + 2 v_l \frac{\partial v_m}{\partial \chi^i} E_{mlj} + v_l v_m E_{nli} E_{nmj} \right) \gamma_k^i \gamma_k^j + \left(\frac{\partial v_k}{\partial \chi^i} + v_m E_{kmi} \right) \left(\frac{\partial v_l}{\partial \chi^j} + v_n E_{lnj} \right) \gamma_k^j \gamma_l^i \right\}, \tag{27}$$

where $(\text{curl } \mathbf{v})_i$ in Eq. (26) is given by Eq. (19).

Flow in a Smoothly Curved Duct

In this section, a method is outlined for the derivation of the governing equations in a form suitable for the flow in arbitrarily smoothly curved ducts. The results are then applied to the special case of a helical duct.

Let the center-line or any other convenient line of the duct be described by the space curve $\mathbf{r}_c(s)$, where the parameter s is the arc length. $\mathbf{r}_c$ is assumed to be smooth enough, so that all required derivatives of $\mathbf{r}_c$ are continuous. It is not always possible to parametrize $\mathbf{r}_c$ explicitly in terms of arc length s. If $\mathbf{r}_c$ is parametrized in terms of another parameter θ, then s and θ are related by

$$ds = \sqrt{\frac{d\mathbf{r}_c}{d\theta} \cdot \frac{d\mathbf{r}_c}{d\theta}}\, d\theta. \tag{28}$$

From Eq. (28), one cannot generally obtain an explicit function $\theta = \theta(s)$. However, using Eq. (28) and the chain rule, derivatives with respect to s are possible to obtain.

As an example, consider a circular helix, with the parametric representation

$$\mathbf{r}_c(\theta) = R\mathbf{e}_r(\theta) + K\theta \mathbf{e}_z, \tag{29}$$

where R is the radius of the cylinder to which the helix is coiled, and $2\pi K$ is the pitch (see Fig. 1). R and K are assumed constant. $\mathbf{e}_r$, $\mathbf{e}_\theta$, and $\mathbf{e}_z$ are unit base vectors of the cylindrical coordinate system indicated in Fig. 1. Evaluating Eq. (28), one finds that

$$ds = \sqrt{R^2 + K^2}\, d\theta \quad \text{or} \quad s = \sqrt{R^2 + K^2}\,\theta + \text{constant}. \tag{30}$$

Thus, for a circular helix, $\mathbf{r}_c$ may be explicitly parametrized in terms of s.

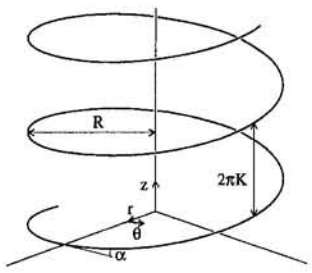

Fig. 1 Circular helix with pitch $2\pi K$

The tangent $\mathbf{t}$, normal $\mathbf{n}$, and binormal $\mathbf{b}$ of a space curve $\mathbf{r}_c$ are defined by

$$\mathbf{t} = \mathbf{r}_c', \quad \mathbf{n} = \frac{1}{\kappa} \mathbf{r}_c'', \quad \mathbf{b} = \mathbf{t} \times \mathbf{n}, \tag{31}$$

where a prime denotes a derivative with respect to arc length s. Note that $\mathbf{t}$, $\mathbf{n}$, and $\mathbf{b}$ constitute a physical basis. The curvature κ and the torsion τ of $\mathbf{r}_c$ are defined by

$$\kappa = |\mathbf{r}_c''|, \quad \tau = \mathbf{n}' \cdot \mathbf{b}. \tag{32}$$

Using Eqs. (31) and (32), the so-called Frenet formulas may be derived, i.e.,

$$\mathbf{t}' = \kappa \mathbf{n}, \quad \mathbf{n}' = \tau \mathbf{b} - \kappa \mathbf{t}, \quad \mathbf{b}' = -\tau \mathbf{n}. \tag{33}$$

For the circular helix described by Eqs. (29) and (30), $\mathbf{t}$, $\mathbf{n}$, and $\mathbf{b}$ are given by

$$\left.\begin{aligned} \mathbf{t}(s) &= \cos\alpha \mathbf{e}_\theta(s) + \sin\alpha \mathbf{e}_z, \\ \mathbf{n}(s) &= -\mathbf{e}_r(s), \\ \mathbf{b}(s) &= -\sin\alpha \mathbf{e}_\theta(s) + \cos\alpha \mathbf{e}_z. \end{aligned}\right\} \tag{34}$$

α is the slope of the helix relative to the plane z = constant (see Fig. 1). One finds that

$$\cos\alpha = \frac{R}{\sqrt{R^2 + K^2}}, \quad \sin\alpha = \frac{K}{\sqrt{R^2 + K^2}}. \tag{35}$$

For a circular helix, κ and τ are constant with the following values:

$$\kappa = \frac{R}{R^2 + K^2}, \quad \tau = \frac{K}{R^2 + K^2}. \tag{36}$$

So far, only the center-line $\mathbf{r}_c$ of the duct has been discussed. To represent points off the center-line, the coordinates x and y are used, where x runs in the direction of $\tilde{\mathbf{n}}$ and y in the direction of $\tilde{\mathbf{b}}$. $\tilde{\mathbf{n}}$ and $\tilde{\mathbf{b}}$ are the orthogonal unit vectors obtained by a rotation of $\mathbf{n}$ and $\mathbf{b}$ the angle $\varphi(s)$ in the $\mathbf{n}$, $\mathbf{b}$-plane, i.e.,

$$\left.\begin{aligned} \tilde{\mathbf{n}} &= \cos\varphi \mathbf{n} - \sin\varphi \mathbf{b}, \\ \tilde{\mathbf{b}} &= \sin\varphi \mathbf{n} + \cos\varphi \mathbf{b}, \end{aligned}\right\} \tag{37}$$

(see also Fig. 2). The position vector $\mathbf{r}$ of points in the duct is thus given by

$$\mathbf{r}(s, x, y) = \mathbf{r}_c(s) + x\tilde{\mathbf{n}}(s) + y\tilde{\mathbf{b}}(s). \tag{38}$$

This representation of $\mathbf{r}$ is especially suitable for ducts of rectangular cross section. The angle $\varphi(s)$ is then chosen such that $\tilde{\mathbf{n}}$ and $\tilde{\mathbf{b}}$ are aligned to the boundaries of the duct. This makes the boundary conditions easy to apply. For a duct of circular cross section, it is more convenient to use polar coordinates in the $\mathbf{n}$, $\mathbf{b}$-plane.

Using the definition $(3)_1$ and the Frenet formulas (33), the following expressions for the natural base vectors $\mathbf{a}_i$ of the coordinate system (s, x, y) may be derived

$$\left.\begin{aligned} \mathbf{a}_s &= \frac{\partial \mathbf{r}}{\partial s} = M\mathbf{t} - (\tau - \varphi')y\tilde{\mathbf{n}} + (\tau - \varphi')x\tilde{\mathbf{b}}, \\ \mathbf{a}_x &= \frac{\partial \mathbf{r}}{\partial x} = \tilde{\mathbf{n}}, \\ \mathbf{a}_y &= \frac{\partial \mathbf{r}}{\partial y} = \tilde{\mathbf{b}}, \end{aligned}\right\} \tag{39}$$

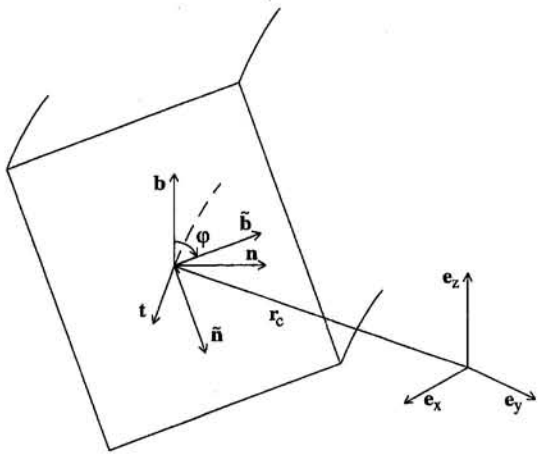

Fig. 2 Various vectors related to the center-line of a duct

where

$$M = 1 - \kappa(x \cos \varphi + y \sin \varphi). \tag{40}$$

Thus, unless $\tau = \varphi'$, the coordinate system is not orthogonal. An orthogonal coordinate system is obtained, for example, if the center-line of the duct lies in a plane, then $\tau = 0$, and also φ is constant, i.e., $\varphi' = 0$.

A suitable physical basis to expand the velocity vector in is obviously $(\mathbf{t}, \tilde{\mathbf{n}}, \tilde{\mathbf{b}})$, which yields

$$\mathbf{v} = w\mathbf{t} + u\tilde{\mathbf{n}} + v\tilde{\mathbf{b}}, \tag{41}$$

where w is called the axial flow component, and u and v are called the secondary flow components. Accordingly, the axial flow is the projection of $\mathbf{v}$ on the tangent $\mathbf{t}$, and the secondary flow is the projection of $\mathbf{v}$ on the $\mathbf{n}$, $\mathbf{b}$-plane.

The following identifications are made

$$\left.\begin{aligned} &\chi^1 = s, \quad \chi^2 = x, \quad \chi^3 = y, \\ &\mathbf{e}_1 = \mathbf{t}, \quad \mathbf{e}_2 = \tilde{\mathbf{n}}, \quad \mathbf{e}_3 = \tilde{\mathbf{b}}, \\ &v_1 = w, \quad v_2 = u, \quad v_3 = v. \end{aligned}\right\} \tag{42}$$

Then, the nonzero coefficients E_{ijk} and γ_i^j, defined by Eq. (11), are found to be

$$\left.\begin{aligned} &E_{211} = -E_{121} = \kappa \cos \varphi, \quad E_{311} = -E_{131} = \kappa \sin \varphi, \\ &E_{321} = -E_{231} = \tau - \varphi', \\ &\gamma_1^1 = 1/M, \quad \gamma_1^2 = (\tau - \varphi')y/M, \\ &\gamma_1^3 = -(\tau - \varphi')x/M, \quad \gamma_2^2 = \gamma_3^3 = 1. \end{aligned}\right\} \tag{43}$$

$\sqrt{g}$ appears in the divergence and the Laplacian. Using the definition (10), one obtains

$$\sqrt{g} = M = 1 - \kappa(x \cos \varphi + y \sin \varphi). \tag{44}$$

The governing Eqs. (25)–(27) may now be expressed in full detail, in a form suitable for arbitrarily smoothly curved ducts. In the following, the analysis is restricted to fully developed flow in helical ducts.

For a helical duct, the center-line is a circular helix, which implies that κ and τ are constant (see Eq. (36)). We also require that φ is constant. A helical duct with a rectangular cross section is depicted in Fig. 3. Helical ducts include two important special cases, namely toroidal ducts, for which τ is zero, and straight twisted ducts, for which κ is instead zero. If κ and τ both are zero, the trivial case of a straight untwisted duct is obtained.

Often a fully developed flow is considered. The flow is fully developed when it does not change in the axial direction, i.e., the velocity $\mathbf{v}$ is independent of the s-coordinate. To be able to find a fully developed flow, the coefficients in Eqs. (43) and (44) must clearly be independent of s, which implies that $\tau - \varphi'$ has to be constant, and that either κ and φ are constant, or if κ is zero, φ may be a function of s, as long as $\tau - \varphi'$ is constant. However, if κ is zero, the duct is a straight twisted one, and φ does always enter in the form $\tau - \varphi'$ in Eqs. (43) and (44). Accordingly, in this case, the degree of twist $\tau - \varphi'$ can be fully described by τ only, and without loss of generality, we may for a fully developed flow assume that κ, τ, and φ all are constant. This, in turn, implies that a fully developed flow is possible to obtain only in a helical duct, or degenerate helical (i.e., toroidal or straight twisted). Further, it is also required that the pressure gradient is independent of s, and that the boundary conditions do not change in the axial direction.

For a fully developed flow in a helical duct with κ, τ, and φ constant, the continuity Eq. (25) assumes the form

$$\frac{\partial}{\partial x}(Mu + \tau yw) + \frac{\partial}{\partial y}(Mv - \tau xw) = 0. \tag{45}$$

Expressions for the Navier-Stokes and the energy equations may be found in previous papers by the author, referred to in the Introduction.

A stream function $\Psi = \Psi(x, y)$, which automatically satisfies the continuity Eq. (45), may be defined according to

$$\left.\begin{aligned} \frac{\partial \Psi}{\partial y} &= Mu + \tau yw, \\ -\frac{\partial \Psi}{\partial x} &= Mv - \tau xw. \end{aligned}\right\} \tag{46}$$

$\Psi(x, y) =$ constant defines a three-dimensional surface, and $\nabla\Psi$ is normal to this surface. For a given s, $\Psi(x, y) =$ constant defines a curve in the $\mathbf{n}$, $\mathbf{b}$-plane, and $\nabla\Psi$ is orthogonal to the tangent of this curve. Using Eq. (12), one finds that

$$\nabla\Psi = \left(\frac{\tau y}{M}\frac{\partial \Psi}{\partial x} - \frac{\tau x}{M}\frac{\partial \Psi}{\partial y}\right)\mathbf{t} + \frac{\partial \Psi}{\partial x}\tilde{\mathbf{n}} + \frac{\partial \Psi}{\partial y}\tilde{\mathbf{b}}. \tag{47}$$

Denote the secondary flow by $\mathbf{v}_{\text{sec}}$, i.e.,

$$\mathbf{v}_{\text{sec}} = u\tilde{\mathbf{n}} + v\tilde{\mathbf{b}}. \tag{48}$$

Then, Eqs. (46)–(48) give

$$\nabla\Psi \cdot \mathbf{v}_{\text{sec}} = u\frac{\partial \Psi}{\partial x} + v\frac{\partial \Psi}{\partial y} = \tau w(xu + yv),$$

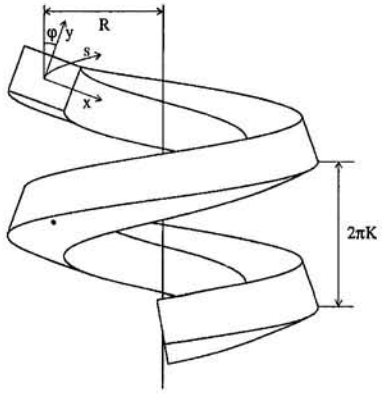

Fig. 3 Helical duct with rectangular cross section

which means that, unless $\tau = 0$, so that the above expression is zero, the curves Ψ = constant do *not* define streamlines for the secondary flow. However, one finds that

$$\nabla\Psi \cdot \mathbf{v} = \nabla\Psi \cdot (w\mathbf{t} + \mathbf{v}_{sec}) = 0,$$

which proves that the velocity is tangent to the *surfaces* Ψ = constant. That is, these surfaces define streamtubes for the velocity field. Note also that similar results concerning the stream function apply, if instead polar coordinates are used in the **n**, **b**-plane.

References

Bolinder, C. J., 1993, "Numerical Visualization of the Flow in a Helical Duct of Rectangular Cross-section," *Experimental and Numerical Flow Visualization,* ASME FED-Vol. 172, pp. 329–338.

Bolinder, C. J., 1995, "The Effect of Torsion on the Bifurcation Structure of Laminar Flow in a Helical Square Duct," ASME *Journal of Fluids Engineering,* Vol. 117, pp. 242–248.

Bolinder, C. J., 1996, "First- and Higher-order Effects of Curvature and Torsion on the Flow in a Helical Rectangular Duct," *Journal of Fluid Mechanics,* Vol. 314, pp. 113–138.

Bolinder, C. J., and Sundén, B., 1995, "Flow Visualization and LDV Measurements of Laminar Flow in a Helical Square Duct with a Finite Pitch," *Experimental Thermal and Fluid Science,* Vol. 11, pp. 348–363.

Bolinder, C. J., and Sundén, B., 1996, "Numerical Prediction of Laminar Flow and Forced Convective Heat Transfer in a Helical Square Duct with a Finite Pitch," *International Journal of Heat and Mass Transfer,* Vol. 39, pp. 3101–3115.

Bowen, R. M., and Wang, C.-C., 1976, *Introduction to Vectors and Tensors,* Vol. 2, Plenum Press.

Germano, M., 1982, "On the Effect of Torsion on a Helical Pipe Flow," *Journal of Fluid Mechanics,* Vol. 125, pp. 1–8.

Gurtin, M. E., 1981, *An Introduction to Continuum Mechanics,* Academic Press.

Liu, S., and Masliyah, J. H., 1993, "Axially Invariant Laminar Flow in Helical Pipes with a Finite Pitch," *Journal of Fluid Mechanics,* Vol. 251, pp. 315–353.

Sokolnikoff, I. S., 1964, *Tensor Analysis,* John Wiley and Sons, New York.

Thompson, J. F., 1984, "Grid Generation Techniques in Computational Fluid Dynamics," *AIAA Journal,* Vol. 22, No. 11, pp. 1505–1523.

Wang, C. Y., 1981, "On the Low-Reynolds-number Flow in a Helical Pipe," *Journal of Fluid Mechanics,* Vol. 108, pp. 185–194.

Hideo Yano
Professor.

Katsuya Hirata
Associate Professor.

Department of Mechanical Engineering,
Doshisha University,
Koyoto 610-03, Japan

Masanori Komori
Appliance System Group,
Sharp Corporation,
Osaka 581, Japan

An Approximate Method for the Drags of Two-Dimensional Obstacles at Low Reynolds Numbers

We propose a new simple method of computing the drag coefficients of two-dimensional obstacles symmetrical to the main-flow axis at Reynolds numbers less than 100. The governing equations employed in this method are the modified Oseen's linearized equation of motion and continuity equation, and the computation is based on a discrete singularity method. As examples, simple obstacles such as circular cylinders, rectangular prisms, and symmetrical Zhukovskii aerofoils are considered. And it was confirmed that the computed drags agree well with experimental values. Besides optimum shapes of these geometries, which minimize the drag coefficients, are also determined at each Reynolds number.

1 Introduction

The modified Oseen method (Lewis and Carrier, 1949) is really an extension of the original Oseen's approximation (Oseen, 1910), in that it employs a proper approximation to linearize the convective terms of governing equations such as the Navier-Stokes equations and the energy equations. The method is featured by the fact that it introduces some empirical modification parameter into the convective terms. Namely, Lewis and Carrier (1949) introduced a modification of the Oseen linearization in which uniform upstream speed of the convective term in the Oseen's approximation is replaced with an appropriate average speed.

This modified Oseen method has been applied to solve several outer-flow problems, such as the flow past a semi-infinite or finite plate (Lewis and Carrier, 1949; Carrier, 1965), the heat transfer to a melting body in a high speed stream (Carrier, 1958), and the flow past a quarter infinite plate and the related heat transfer (Carrier, 1965) where their solutions were obtained analytically, not computationally.

As is clear from these papers, the governing equations can be tackled with comparative easiness owing to its linearity, analytical approaches being taken in some cases. Whereas, this method is not considered so effective where a nonlinearity plays an important role in the flow field. However, the method including the Oseen's approximation is sometimes useful so long as global characters of flow are concerned. For example, the drag coefficient of a sphere at an infinite Reynolds number was successfully obtained using the Oseen's approximation (Weisenborn and Ten Bosh, 1993). This means that such an approximation is expected to provide useful information at Reynolds numbers even much greater than unity.

Combination of singularity methods or boundary element methods, and the modified Oseen method, enables us to compute the flow past various obstacles efficiently and conveniently. In this paper, this type of technique is employed to obtain approximately the drags of two-dimensional obstacles symmetrical to the main-flow axis, with the Reynolds number varied from zero to about 100. The obstacle geometries considered here are circular cylinders, rectangular prisms, and symmetrical Zhukovskii aerofoils. The numerical results are discussed, being compared with experimental ones. Besides, using the present method, we reveal that, at each Reynolds number tested, there are optimum shapes which minimize the drag coefficients of rectangular prisms and aerofoils.

2 Basic Theory

2.1 Modified Oseen's Equation. In this subsection, based on the basic concept of the modified Oseen method, we try, in our way, to linearize the Navier-Stokes equation of motion for two-dimensional flow.

The nonlinear convective term is expressed as

$$\mathbf{f}_C = (\mathbf{u}\cdot\nabla)\mathbf{u}, \tag{1}$$

where $\mathbf{u} = (u, v)$, $\nabla = (\partial/\partial x, \partial/\partial y)$, x and y being the Cartesian coordinates, and u and v the velocity components along x and y, respectively. Velocity $\mathbf{u}$ is a function of space, and can be written as

$$\mathbf{u} = \hat{\mathbf{u}} + \mathbf{u}', \tag{2}$$

where $\hat{\mathbf{u}}$ is the velocity spatially averaged with weight all over the flow field Ω. If we introduce a weighting function $N = N(x, y)$, the space-averaged velocity $\hat{\mathbf{u}}$ can be expressed by

$$\hat{\mathbf{u}} = \frac{1}{\hat{A}}\int_\Omega N\mathbf{u}\,dA/\hat{A}, \tag{3}$$

with

$$\hat{A} = \int_\Omega N dA. \tag{4}$$

Here, in order to simplify the problem, we assume symmetry of both $\mathbf{u}$ and N to the x-axis, viz. the axis parallel to the direction of the main flow. This assumption leads Eq. (3) to

$$\hat{\mathbf{u}} = (\hat{u}, 0). \tag{5}$$

Contributed by the Applied Mechanics Division of THE AMERICAN SOCIETY OF MECHANICAL ENGINEERS for publication in the ASME JOURNAL OF APPLIED MECHANICS.

Discussion on this paper should be addressed to the Technical Editor, Professor Lewis T. Wheeler, Department of Mechanical Engineering, University of Houston, Houston, TX 77204-4792, and will be accepted until four months after final publication of the paper itself in the ASME JOURNAL OF APPLIED MECHANICS.

Manuscript received by the ASME Applied Mechanics Division, Nov. 28, 1994; final revision, July 7, 1996. Associate Technical Editor: S. A. Berger.

Substituting both Eqs. (2) and (5) into Eq. (1), we get

$$\mathbf{f}_C \cong \hat{u}\partial\mathbf{u}/\partial x. \tag{6}$$

Letting $\hat{u} = \beta U_\infty$, the convective term is

$$\mathbf{f}_C \cong \beta U_\infty \partial\mathbf{u}/\partial x, \tag{7}$$

where U_∞ is the velocity at infinity in the direction of the x-axis, and β a modification parameter. Then we arrive at the modified Oseen's equation first suggested by Lewis and Carrier (1949), for two-dimensional incompressible steady flow, namely,

$$\beta U_\infty \partial\mathbf{u}/\partial x = -\nabla p/\rho + \nu\nabla^2\mathbf{u}, \tag{8}$$

where ρ denotes the density of fluid, ν the kinematic viscosity of fluid, and p the pressure. In addition, $\nabla^2\mathbf{u} = \partial^2 u/\partial x^2 + \partial^2 v/\partial y^2$. And the equation of continuity is

$$\partial u/\partial x + \partial v/\partial y = 0. \tag{9}$$

As is well known, with increasing Reynolds number Re, inertia force compared with viscous force increases over most of the flow field. Then, the error in simulations by the Oseen's approximation ($\beta = 1$ in Eq. (8)) increases, particularly near the body surface. In the present case $N(x, y)$, having larger values near the surface, or an appropriate value of β, is expected to provide a more accurate computation. More specifically, the flow details over the whole flow region governed by Eqs. (8) and (9), are not considered to coincide with those by the full Navier-Stokes equations. However, it can be expected that the global flow characters, such as a drag acting on an obstacle, are computed accurately by the present equations, even for Re $\gg$ 1, if β is properly chosen.

As far as the drag is concerned, β is considered to be a function of both Reynolds number and the shape of the cross section. To decide the function, it is necessary to compare computations by Eqs. (8) and (9) with experiments for a variety of geometries. In this context, β is regarded as an empirical parameter. Fortunately, it will be revealed in Section 5.2 that β is almost independent of the geometries tested in this study.

According to the existing drag formulae for the Oseen's flow, we have the corresponding formulae for the modified version. For example, referring to Lamb (1932), the drag coefficient C_D of circular cylinders in uniform flow is given by

$$C_D = 2D/(\rho U_\infty^2 d) = 8\pi/(\mathrm{Re}T), \tag{10}$$

where $T = \frac{1}{2} - \gamma - \log_e(\beta\,\mathrm{Re}/8)$, $\mathrm{Re} = U_\infty d/\nu$ and $\gamma = 0.57721\ldots$ (Euler's constant), D being the drag per unit length and d the diameter of the cylinder. It is found from this formula that C_D is reduced as β decreases. In the next section, we shall present a more general method to obtain the drags of two-dimensional obstacles, including circular cylinders.

2.2 Discrete Singularity Method. It was shown by Yano and Kieda (1980) that a discrete singularity method is expedient to solve the Oseen's equations. According to this method, the complex velocity $W_o = u_o - iv_o$ perturbed by a modified Oseenlet for two-dimensional flow, which is located at the origin of the coordinate system, is given by

$$W_o = \sum_{k=1}^{2} \{a^{(k)} W_e^{(k)}\}, \tag{11}$$

where

$$W_e^{(1)} = \exp(\lambda x)\{K_0(\lambda r) + K_1(\lambda r)\exp(-i\theta)\} - 1/(\lambda z) \tag{12}$$

and

$$W_e^{(2)} = i\exp(\lambda x)\{-K_0(\lambda r) + K_1(\lambda r)\exp(-i\theta)\} - i/(\lambda z) \tag{13}$$

with $\lambda = \beta U_\infty/(2\nu)$, $r = |z|$, $\theta = \arg(z)$, $i = \sqrt{(-1)}$ and $z = x + iy$. In addition, K_0 and K_1 are modified Bessel functions of the second kind.

To realize the flow around an arbitrary obstacle in an unbounded uniform flow field with the velocity U_∞, we can discretely distribute modified Oseenlets of number n on the surface (see Fig. 1). Owing to the linearity of Eq. (8), the complex velocity $W = u - iv$ is assumed as

$$W = \sum_{j=1}^{n}\sum_{k=1}^{2} \{a_j^{(k)} W_j^{(k)}\} + U_\infty, \tag{14}$$

where

$$W_j^{(1)} = \exp(\lambda x_j)\{K_0(\lambda r_j) + K_1(\lambda r_j)\exp(-i\theta_j)\} - 1/(\lambda z_j),$$

$$W_j^{(2)} = i\exp(\lambda x_j)\{-K_0(\lambda r_j) + K_1(\lambda r_j)\exp(-i\theta_j)\} - i/(\lambda z_j),$$

$r_j = |z_j|$, $\theta_j = \arg(z_j)$ and $z_j = z - z_j^\wedge$ ($z_j^\wedge$ denotes the position of a singularity). Letting $W_m^\wedge = W_j^{(k)}$ and $a_m^\wedge = a_j^{(k)}$ with $m = j + (k-1)n$, we get

$$W = \sum_{m=1}^{2n} (a_m^\wedge W_m^\wedge) + U_\infty. \tag{15}$$

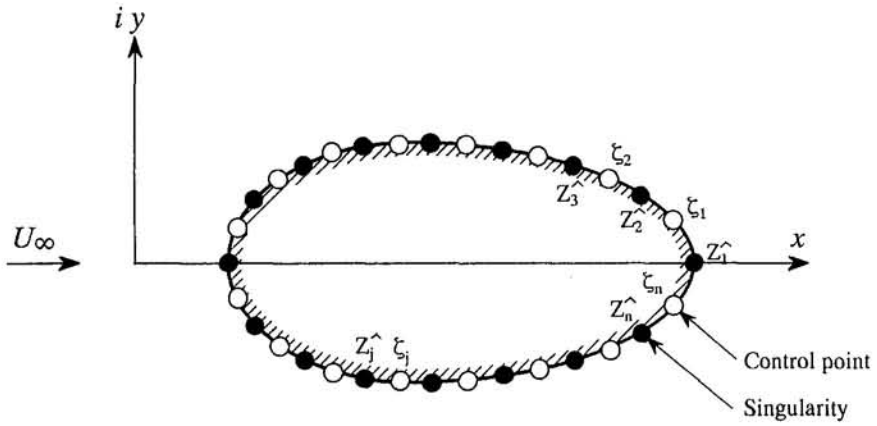

Fig. 1 Flow around an arbitrary symmetrical obstacle in a stream with uniform velocity U_∞: ●, the position of a singularity z_j; ○, the position of a control point ζ_j

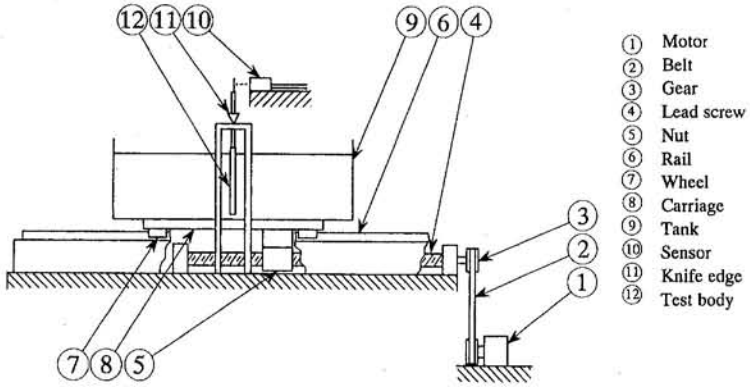

Fig. 2 Side view of experimental apparatus

So as to satisfy the no-slip boundary condition approximately on the surface, the $2n$ unknowns a_m have to be determined numerically from the following system of linear equations:

$$W(\zeta_k)W^*(\zeta_k) = 0, \quad k = 1, 2, \ldots, n, \tag{16}$$

where the asterisk denotes the complex conjugate and ζ_k is the position of a control point (see also Fig. 1).

Considering the Filon's formulae (1926), the drag coefficient of an obstacle is

$$C_D = 2D/(\rho U_\infty^2 L) = -8\pi/(U_\infty \mathrm{Re}) \sum_{m=1}^{n} (a_m), \tag{17}$$

where $\mathrm{Re} = U_\infty L/\nu$, L being the representative length.

3 Experimental Arrangements

To verify the computed drags, experiments were conducted with a water tank moving smoothly with a constant velocity on a horizontal railway. As is shown in Fig. 2, the tank is driven by a variable speed motor by means of a nut engaged on a lead screw. The fluid filled is a glycerol-water solution, so as to vary its kinematic viscosity.

The present technique adopted to measure the drag (exactly the time-averaged drag, because the drag fluctuates at higher values of Re) is primarily identical with what is called "lamp scale and mirror method" by Taneda in 1964. The model is hung vertically in the tank as a pendulum by a knife edge, and the drag can be obtained from the inclination angle of the model. In the original lamp scale and mirror method, the inclination angle is determined from the image on a ruler reflected by a mirror which is attached to the model. But in the present experiment the inclination angle was measured using a laser extensometer.

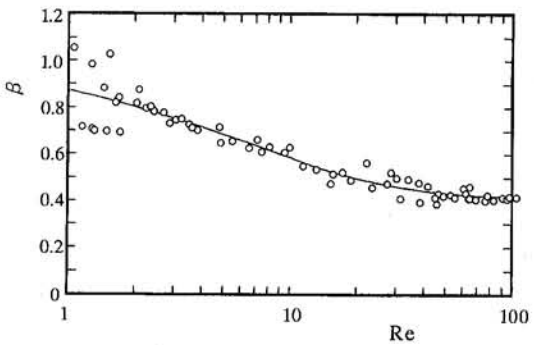

Fig. 3 Relationship between modification parameter β and Reynolds number Re

4 Modification Parameter β for Circular Cylinders

It is obvious from the theory in the preceding sections that the computational C_D of a circular cylinder based on Eqs. (8) and (9) is dependent both on β and Re, as can be also seen from the drag formula (10), whereas the experimental C_D depends only on Re. Therefore, under the condition that they agree with each other, the parameter β is assumed as a function of Re only. More specifically, we determined such a value of β that the computational C_D, obtained by a singularity method with 60 singularities (modified Oseenlets) on the surface of a circular cylinder at regular intervals as shown in Fig. 1, may agree with the Tritton's experimental data (1959) (as will be shown in Fig. 4).

Figure 3 indicates the relation between the modification parameter β and the Reynolds number Re, which is obtained in the range of $0 < \mathrm{Re} \leq 100$. The blank dots show direct computations based on the foregoing theory, and the solid line indicates the empirical formula in the form

$$\beta = -0.162 \log_e (1.23\ \mathrm{Re} + 1) + 1 \quad (0 < \mathrm{Re} \leq 12)$$

and

$$\beta = 0.0310 (\log_e (\mathrm{Re}/12))^2 - 0.130 \log_e (\mathrm{Re}/12) + 0.553 \quad (12 \leq \mathrm{Re} \leq 100). \tag{18}$$

In this figure it is shown that, in $\mathrm{Re} \leq 2$, there is some scatter in β values obtained by direct computations due to a scatter in the original C_D measurements, whereas this formula is reasonable in this range in that $\beta \to$ as $\mathrm{Re} \to 0$.

Figure 4 shows computational and experimental drag coefficients C_D of circular cylinders, plotted against the Reynolds

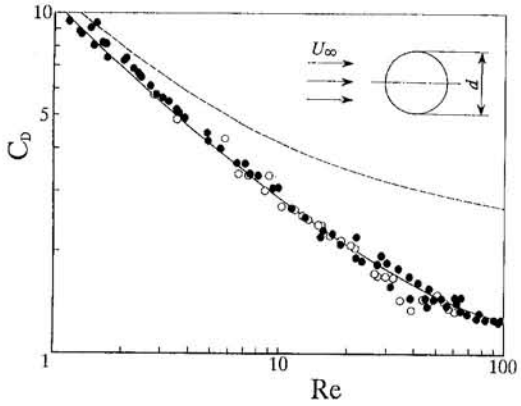

Fig. 4 Drag coefficient C_D versus Reynolds number Re for circular cylinders: ——, modified Oseen's approximation; -----, Oseen's approximation; ○, experimental results (present); ●, experimental results (Tritton, 1959)

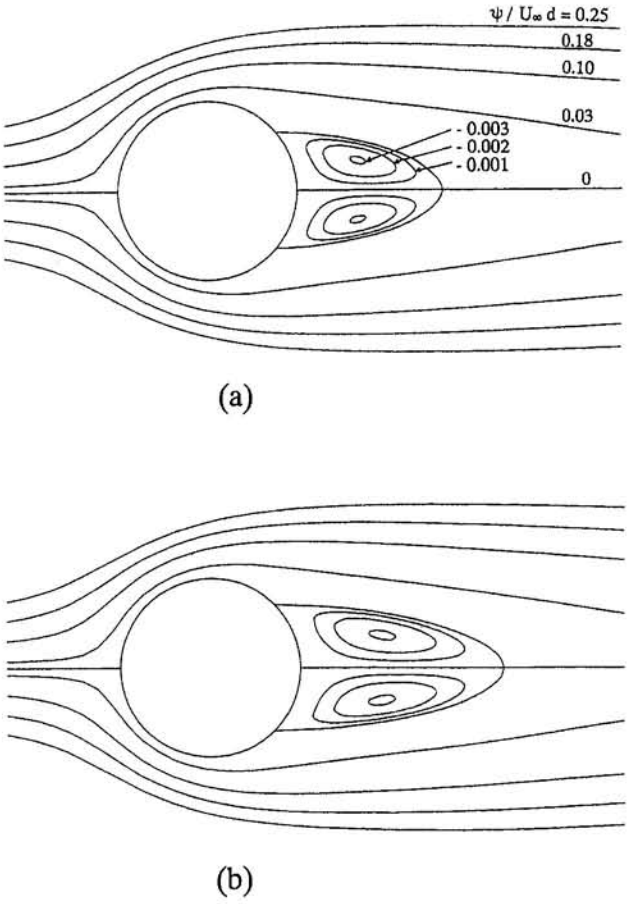

Fig. 5 Streamlines of flow past a circular cylinder at Re = 26: (*a*) Modified Oseen's approximation; (*b*) flow visualization by Taneda (Van Dyke, 1982)

number Re based on the diameter d. Here two computational curves for $\beta = 1$ and for $\beta = \beta$ (Re) given by Eq. (18) are shown. A good fit between the curve for $\beta = \beta(\mathrm{Re})$ and experimental data shows that Eq. (18) is a proper approximation. Additionally, the curve for $\beta = 1$ (Oseen) is not so good over the whole range except in the neighborhood of Re = 1. Moreover, data from the present experiment are also added to check their accuracy.

To check the range of the present approximation with β, we computed the flow field around a circular cylinder at Re = 26. Figure 5 shows streamlines of flow past a cylinder. The computed length of the region of closed streamlines behind a cylinder (Fig. 5(*a*)) is somewhat shorter than that of the observation (Van Dyke, 1982) (Fig. 5(*b*)).

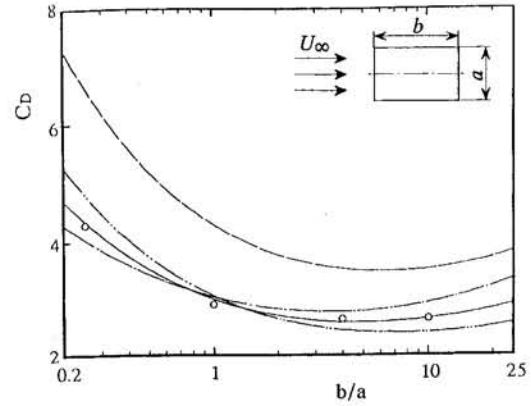

Fig. 7 Drag coefficient C_D versus depth-to-height ratio b/a for rectangular prisms at Re = 10: ——, modified Oseen's approximation; – · –, $\beta = \beta(\mathrm{Re}(a))$; – · · –, $\beta = \beta(\mathrm{Re}(b))$; - - - -, Oseen's approximation; ○, experimental results

5 β Independent of Geometry

In the following sections, it will be shown that the present method is applicable to two-dimensional noncircular cylinders, using the same β as given by Eqs. (18) for circular cylinders. That is, we shall examine two types of obstacles: rectangular prisms and symmetrical Zhukovskii aerofoils. (For these computations n is set such that $n \geq 80$.)

5.1 Equivalent Diameter d_e. To obtain the value of β for geometries other than circular cylinders we introduce a new representative length or equivalent diameter d_e, which enables us to use the relationship between β and Re for circular cylinders in Eqs. (18). The equivalent diameter d_e can be defined as

$$d_e = \sqrt{(4S/\pi)}, \tag{19}$$

where S denotes the area of the cross section. According to this definition $d_e = d$ for circular cylinders. The eligibility of this assumption will be examined in the next section.

5.2 Drags of Rectangular Prisms. Figure 6 shows the drag coefficient C_D plotted against the Reynolds number Re for a rectangular prism with the depth-to-height ratio $b/a = 1.0$ (a square-section prism) where a is the height (cross-streamwise

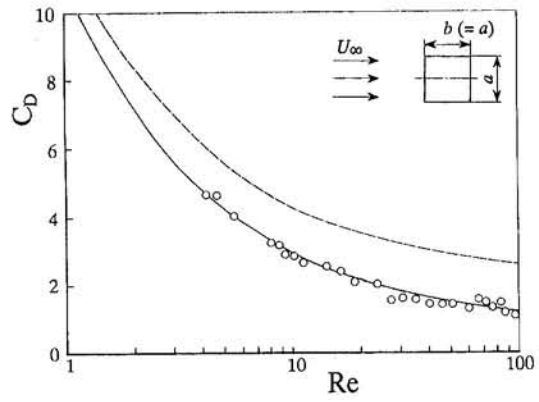

Fig. 6 Drag coefficient C_D versus Reynolds number Re for square-section prisms (b/a = 1.0): ——, modified Oseen's approximation; - - - -, Oseen's approximation; ○, experimental results

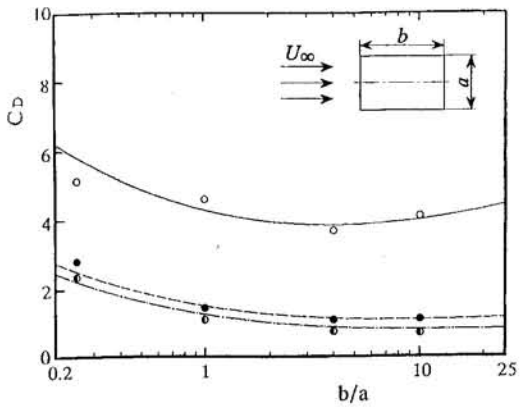

Fig. 8 Drag coefficient C_D versus depth-to-height ratio b/a for rectangular prisms: ○, ——, Re = 5; ●, - - - -, Re = 50; ◐, – · –, Re = 100; ○, ●, ◐, experimental results

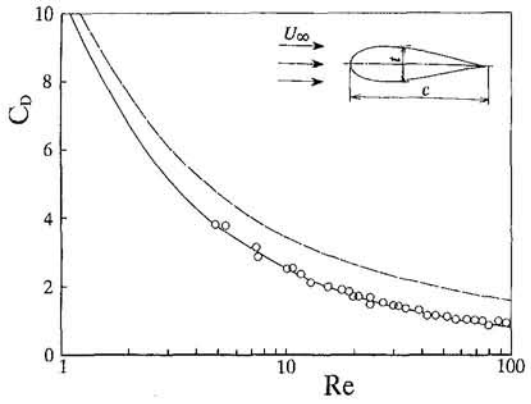

Fig. 9 Drag coefficient C_D versus Reynolds number Re for symmetrical Zhukovskii aerofoils with $t/c = 0.25$: ——, modified Oseen's approximation; -----, Oseen's approximation; ○, experimental results

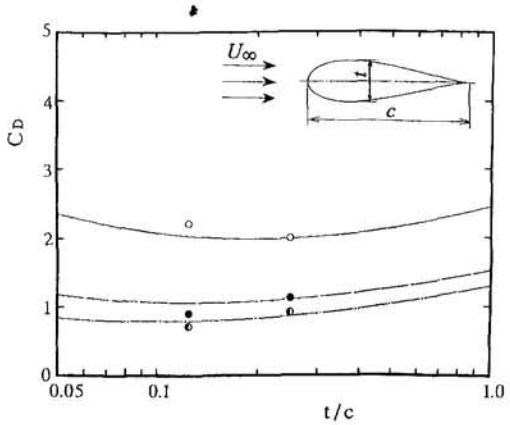

Fig. 11 Drag coefficient C_D versus thickness ratio t/c for symmetrical Zhukovskii aerofoils: ○, ——, Re = 15; ●, -----, Re = 50; ◐, – · –, Re = 100; ○, ●, ◐, experimental results

dimension) and b is the depth (streamwise dimension). Solid and a broken lines represent the numerical results by the modified Oseen's approximation and by the Oseen's approximation, respectively. Blank dots represent the results by the present experiment. Over the wide range of Re from 4 to 100, the computations almost coincide with the experiments. In addition, it is obvious that the drag by the present method is more accurate than that by the Oseen's approximation.

Figure 7 shows C_D plotted against b/a for rectangular prisms at Re = 10. The definitions of lines and dots are the same as in Fig. 6. The modified Oseen's approximation agrees well with the experiment over a wide range of b/a.

Until the preceding paragraph, the equivalent diameter d_e and the corresponding Reynolds number Re have been used for data reduction. Here we try to employ two other definitions of length scales $L = a$ and b and the corresponding Reynolds number Re(a) and Re(b). In Fig. 7, in addition to the drags calculated using Re (solid line), those using Re(a) and Re(b) are shown by a chain line and a two-dot chain line, respectively, where each C_D is based on d_e. It can be seen from a comparison of these lines with blank dots (for the experiment) that a choice of the equivalent diameter d_e as a representative length L enables us to predict most accurately the drag within the confine of $0.2 < b/a < 20$.

Figure 8 shows C_D plotted against b/a for rectangular prisms at Re = 5, 50, and 100. As well as the drag at Re = 10, the calculated drags agree well with the experimental ones, over a wide range of b/a.

5.3 Drags of Symmetrical Zhukovskii Aerofoils. Figure 9 shows C_D plotted against Re for a symmetrical Zhukovskii aerofoil with the thickness ratio $t/c = 0.25$, where c is the chord and t the thickness of the aerofoil. A solid and a broken lines denote the results by the modified Oseen's and the Oseen's approximations, respectively. Blank symbols denote the results by the present experiment. As in the case of rectangular prisms, the modified Oseen's approximation agrees well with the experiment.

Figure 10 shows C_D plotted against t/c for the aerofoils at Re = 10. The definitions of lines and dots are the same as in Fig. 6. We can clearly see that the modified Oseen's approximation agrees well with the experiment.

Figure 11 shows C_D plotted against t/c for the aerofoils at Re = 15, 50, and 100. As can be seen, at each Reynolds number, there is a good agreement between the modified Oseen's approximation and the experiment.

After all, we can confirm that the drags of noncircular prisms, such as rectangular prisms and symmetrical Zhukovskii aerofoils, can be computed accurately by the present method, in spite of β determined for circular cylinders with the use of the equivalent diameter d_e defined in Eqs. (18), so long as the obstacle is symmetrical with respect to the main-flow axis. This β's independency of geometry should be further examined theoretically, computationally, and experimentally for a variety of cross section geometries.

6 Optimum Shapes

Again in Figs. 7 and 8, it can be seen that, at each Reynolds number Re, there is an optimum depth-to-height ratio $(b/a)_{opt}$

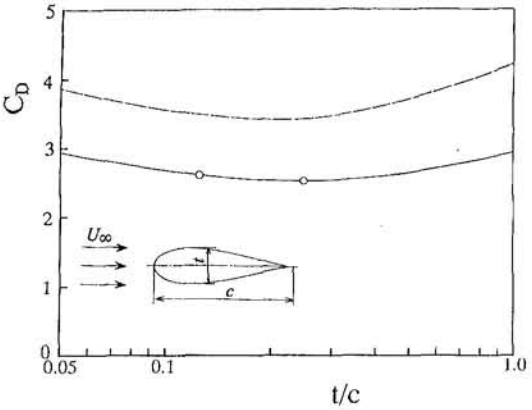

Fig. 10 Drag coefficient C_D versus thickness ratio t/c for symmetrical Zhukovskii aerofoils at Re = 10: ——, modified Oseen's approximation; -----, Oseen's approximation; ○, experimental results

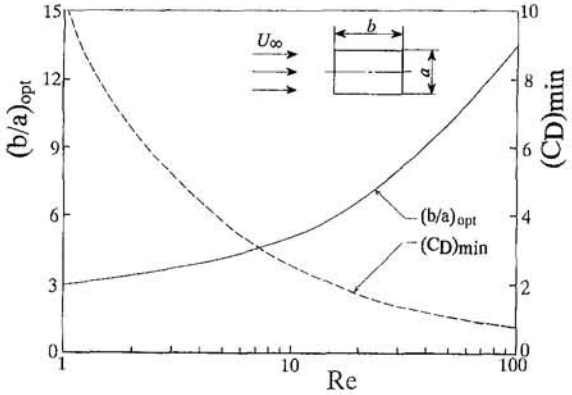

Fig. 12 Optimum depth-to-height ratio $(b/a)_{opt}$ (solid line) and minimum drag coefficient $(C_D)_{min}$ (broken line) of rectangular prisms, against Reynolds number Re

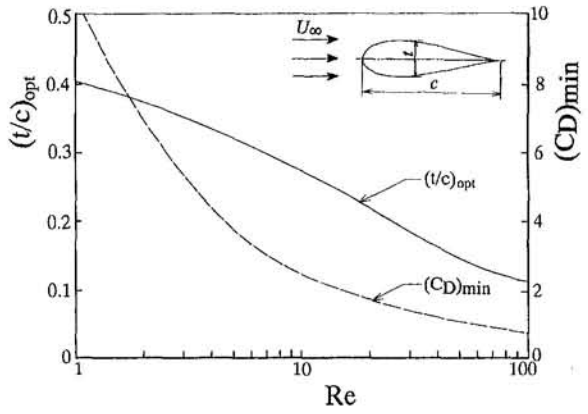

Fig. 13 Optimum thickness ratio $(t/c)_{opt}$ (solid line) and minimum drag coefficient $(C_D)_{min}$ (broken line) of symmetrical Zhukovskii aerofoils, against Reynolds number Re

at which the drag coefficient C_D of the rectangular prism has the least value $(C_D)_{min}$.

Figure 12 shows $(b/a)_{opt}$ (solid line) and the minimum drag coefficient $(C_D)_{min}$ (broken line) plotted against Re for the rectangular prism. As Re increases, $(b/a)_{opt}$ becomes larger, while $(C_D)_{min}$ is reduced.

In Figs. 10 and 11, we can also recognize that, at each Reynolds number, there is an optimum thickness ratio $(t/c)_{opt}$ at which the drag coefficient C_D of the aerofoil has the least value $(C_D)_{min}$.

Figure 13 shows $(t/c)_{opt}$ (solid line) and the minimum drag coefficient $(C_D)_{min}$ (broken line) plotted against Re for the aerofoil. $(t/c)_{opt}$ as well as $(C_D)_{min}$ decreases with increasing Re.

Additionally, Figs. 14 and 15 show examples of optimum shapes for the rectangular prism and the symmetrical Zhukovskii aerofoil at some Reynolds numbers.

7 Conclusions

In order to obtain approximately the drag coefficients of two-dimensional obstacles symmetrical to the main-flow axis, the authors proposed a new simple method of computing the modified Oseen's linearized equations, with an empirical parameter β, on the basis of a discrete singularity method. Namely, the drag coefficients of simple blunt bodies, such as circular cylinders, rectangular prisms and symmetrical Zhukovskii aerofoils,

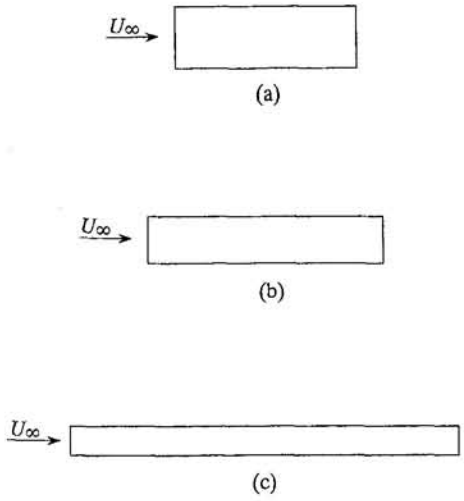

Fig. 14 Optimum shapes of rectangular prisms: (a) Re = 1; (b) Re = 10; (c) Re = 100

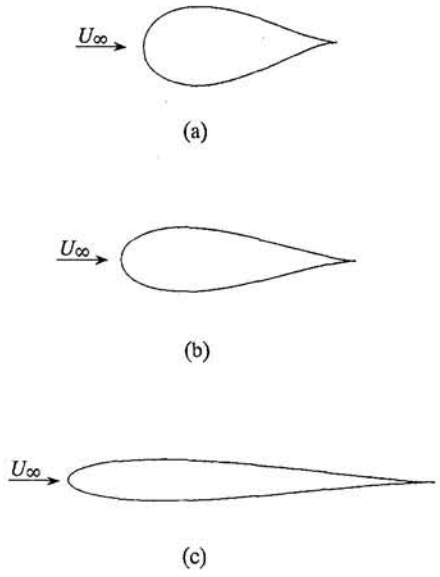

Fig. 15 Optimum shapes of symmetrical Zhukovskii aerofoils: (a) Re = 1; (b) Re = 10; (c) Re = 100

were computed in a Reynolds number range up to about 100. The method has advantages of the simplicity of computational algorithm and of the time saving for computing execution. For example, for the case of 150 singularities, the time for computation was about 1/500–1/1000 times that by a finite difference method.

In the present study, an equivalent diameter d_e was introduced as a representative length, so as to utilize the relationship between β and Re determined for the case of the drag of circular cylinders. Examinations of the computational and experimental data for rectangular prisms and the aerofoils lead to the following confirmation. This approximation with β enables us to compute an accurate drag of an obstacle with an arbitrary shaped cross section symmetrical to the main-flow axis.

Besides, it was revealed using the method that, at each Reynolds number, there is an optimum shape which minimizes the drag coefficient of the rectangular prism or the aerofoil, if the cross-sectional area is given.

Lastly, it should be added that all computations were performed on a HITAC M-680H computer in double precision, and that systems of linear algebraic equations were solved by the Gaussian elimination method.

Acknowledgments

The authors thank Dr. Jiro Funaki (lecturer, Doshisha University), Mr. Katsunori Matsumura (graduate student, Doshisha University), and Mr. Yasushi Ipponghi (student, Doshisha University) for technical assistances in computation and experiment.

References

Carrier, G. F., 1958, "Aerodynamic Heat Transfer to a Melting Body," Space Technology Laboratories Report, GM-TM-0165-00268.

Carrier, G. F., 1965, "Analytic Approximation Techniques in Applied Mathematics," *Journal of the Society for Industrial and Applied Mathematics,* Vol. 13, No. 1, pp. 68–95.

Filon, L. N. G., 1926, "The Forces on a Cylinder in a Stream of Viscous Fluid," *Proceedings of the Royal Society of London,* Vol. A113, pp. 7–27.

Imai, I., 1973, *Fluid Dynamics,* Vol. 1, Syokabo, Tokyo, (in Japanese).

Lamb, H., 1932, *Hydrodynamics,* 6th ed., Cambridge University Press, Cambridge, U.K.

Lewis, J. A., and Carrier, G. F., 1949, "Some Remarks on the Flat Plate Boundary Layer," *Quarterly of Applied Mathematics,* Vol. 7, No. 2, pp. 228–234.

Oseen, C. W., 1910, "Über die Stokes'sche formel und über eine verwandte aufgabe in der hydrodynamik," *Ark. Mat. Astronom. Phys.*, Vol. 6, No. 29, pp. 1–20.

Taneda, S., 1964, "Experimental Investigation of the Wall-Effect on a Cylindrical Obstacle Moving in a Viscous Fluid at Low Reynolds Numbers," *Journal of the Physical Society of Japan*, Vol. 19, pp. 1024–1030.

Tritton, D. J., 1959, "Experiments on the Flow Past a Circular Cylinder at Low Reynolds Numbers," *Journal of Fluid Mechanics*, Vol. 6, pp. 547–567.

Van Dyke, M., ed., 1982, *An Album of Fluid Motion*, Parabolic Press, Stanford, CA.

Weisenborn, A. J., and Ten Bosh, B. I. M., 1993, "Analytical Approach to the Oseen Drag of a Sphere at Infinite Reynolds Number," *SIAM J. Appl. Math.*, pp. 601–620.

Yano, H., and Kieda, A., 1980, "An Approximate Method for Solving Two-Dimensional Low-Reynolds-Number Flow Past Arbitrary Cylindrical Bodies," *Journal of Fluid Mechanics*, Vol. 97, pp. 157–179.

Closed-Form Transient Response of Distributed Damped Systems, Part I: Modal Analysis and Green's Function Formula

Bingen Yang
Associate Professor,
Department of Mechanical Engineering,
University of Southern California,
Los Angeles, CA 90089-1453
Mem. ASME.

An analytical method is developed for closed-form estimation of the transient response of complex distributed parameter systems that are nonproportionally damped, and subject to arbitrary external, initial, and boundary excitations. A new modal analysis leads to the Green's function formula for the distributed system and an eigenfunction expansion of the system Green's function. The legitimacy of the modal expansion is also shown.

1 Introduction

This work is concerned with closed-form evaluation of the transient response of complex distributed damped systems. The distributed system in consideration is an assembly of multiple flexible continua, which are subject to various damping and constraints, are combined with lumped parameter systems, and are under arbitrary external and boundary disturbances. The beam structure in Fig. 1 is one example. The structure, while hypothetic, presents certain commonly used damping models that are developed and justified in a wide range of engineering applications, including machine and engine mounting, damping treatment, vibration isolation, dynamic vibration absorption, passive and active vibration suppression, and smart structure design. Structures like that are often termed as constrained and combined systems.

Constrained and combined distributed systems, because of their important engineering applications, have been of continued research interest for years; for instance, see Bergman and McFarland (1988), Yang (1994a), and the references cited therein. Due to viscous damping constraints and coupling of distributed and lumped elements, constrained and combined systems are typically nonproportionally damped, and mathematically non-self-adjoint in the original equations of motion. For a non-self-adjoint system, conventional modal analysis would lead to an infinite set of coupled second-order differential equations, whose closed-form solution is intractable. In this case, modal truncation and other discretization approaches are often used to estimate the response of the distributed damped system.

Nonproportionally damped systems, mainly lumped damped systems, have been extensively studied in the past several decades. A summary of the developments is given by Bellos and Inman (1989). In predicting the dynamic response of damped systems, modal analysis is one popular technique. The modal analysis procedure in use is either real-valued (Caughey and O'Kelly, 1965), or complex-valued (Foss, 1958). The real-valued method is computationally inexpensive, and thus has found wide application in many engineering problems. The major disadvantage of the real-valued method is that it cannot decouple nonproportionally damped systems. Because of this, approximate real-valued methods using undamped modal data or proportional damping presumption have been developed. While being intuitive, these approximate methods can lead to large errors whose bounds are difficult to estimate, and miss some important dynamic characteristics of nonproportionally damped systems, like nonconstant phase in vibration.

The complex-valued method, on the other hand, can decouple nonproportionally damped systems via bi-orthogonality of eigenfunctions in a state-space formulation. In a broader prospect, state-space formalism is also capable of decoupling other non-self-adjoint systems with gyroscopic and circulatory effects (Huseyin, 1978; Meirovitch, 1980). Nevertheless, the complex-valued modal analysis does have some drawbacks. The method is computationally intensive because both associate and adjoint state-space eigenfunctions have to be calculated. Unlike in the real-valued method, the physical significance of the various elements of the complex-value modal analysis is not well classified. Furthermore, in analyzing distributed systems, the convergence of complex modal superposition depends on the completeness of bi-orthogonal eigenfunctions in an infinite dimensional function space, which may not be true, but is often assumed. These disadvantages have limited the utility of the complex-valued method in engineering analysis.

Besides nonproportional damping, closed-form transient analysis of constrained and combined systems is also complicated by the coupling of distributed and lumped elements, which is mathematically described by a set of hybrid partial/ordinary differential equations along with coupled boundary conditions. In fact, even if damping is ignored, this coupling may render the spatial differential operators of distributed elements non-self-adjoint (Friedman, 1956). Thus, these hybrid partial/ordinary differential equations are often solved by approximate methods. In the literature, no exact and closed-form solution method is available for transient analysis of constrained and combined, distributed damped systems.

The current study is motivated by the need for a solution technique which can efficiently deal with the non-self-adjointnees caused by nonproportional damping, and coupling of distributed and lumped elements. In this two-part paper, a new method is proposed for closed-form transient analysis of complex distributed damped systems. In Part I a modal analysis and a Green's function formula are developed based on a state-space formulation, which predict the transient response of nonproportionally damped systems in infinite series of vibration modes. In Part II (Yang, 1996), the solution method is extended to constrained and combined systems through use of energy func-

Contributed by the Applied Mechanics Division of THE AMERICAN SOCIETY OF MECHANICAL ENGINEERS for publication in the ASME JOURNAL OF APPLIED MECHANICS.

Discussion on this paper should be addressed to the Technical Editor, Professor Lewis T. Wheeler, Department of Mechanical Engineering, University of Houston, Houston, TX 77204-4792, and will be accepted until four months after final publication of the paper itself in the ASME JOURNAL OF APPLIED MECHANICS.

Manuscript received by the ASME Applied Mechanics Division, Nov. 28, 1994; final revision, Aug. 15, 1995. Associate Technical Editor: S. W. Shaw.

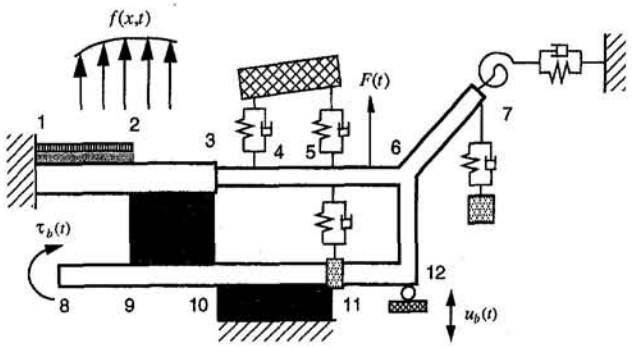

Fig. 1 A complex beam structure: a constrained damping layer in segment 1-2; a rigid body viscoelastically mounted at points 4 and 5; damping constraints at point 7 (spring-dashpot) and in segment 10-11 (e.g., viscoelastic foundation); a lumped mass at point 11; a combined oscillator at point 7; and viscoelastically coupling at points 5 and 11 and in the region 2-3-10-9-2

tionals. Throughout the development, no approximation or discretization has been made; closed-form solution for the coupled partial and ordinary differential equations governing the motion of the complex system is obtained.

The proposed method is different from existing modal analysis techniques in three major aspects. First, a relationship between modes of vibration and adjoint state-space eigenfunctions of distributed damped systems is established, which implies that the calculation of state-space eigenfunctions is unnecessary, and tremendous computation can be saved. Second, the convergence of the modal superposition is proven without the completeness assumption for state-space eigenfunctions. Third, the method systematically treats constraints and distributed-lumped subsystem interaction in an energy form. These features make the new solution method more attractive, reliable, and practical in engineering analysis.

2 Lumped Systems: A Tutorial Example

The main idea behind the proposed method can be obtained from the analysis of nonproportionally damped lumped systems. The response of such a system is described by

$$\mathbf{M}\ddot{\mathbf{x}}(t) + \mathbf{D}\dot{\mathbf{x}}(t) + \mathbf{K}\mathbf{x}(t) = \mathbf{f}(t)$$
$$\mathbf{x}(0) = \mathbf{x}_0, \quad \dot{\mathbf{x}}(0) = \mathbf{v}_0 \tag{1}$$

where the overdot denotes temporal differentiation, $\mathbf{x}(t) \in R^n$ is the vector of generalized coordinates, $\mathbf{f}(t) \in R^n$ is the forcing vector, and $\mathbf{M}$, $\mathbf{D}$, and $\mathbf{K} \in R^{n\times n}$ are the inertia, damping, and stiffness matrices with the properties

$$\mathbf{M}^T = \mathbf{M} > 0, \quad \mathbf{D}^T = \mathbf{D} \geq 0, \quad \mathbf{K}^T = \mathbf{K} > 0.$$

The associate eigenvalue problem is

$$\{\lambda_k^2\mathbf{M} + \lambda_k\mathbf{D} + \mathbf{K}\}\mathbf{v}_k = 0 \tag{2}$$

where $\lambda_k \in C$ is the kth eigenvalue, and $\mathbf{v}_k \in C^n$ is the corresponding eigenvector. Since the system is nonproportionally damped, i.e., $\mathbf{D}\mathbf{M}^{-1}\mathbf{K} \neq \mathbf{K}\mathbf{M}^{-1}\mathbf{D}$ (Caughey and O'Kelly, 1965), the eigenvectors are complex and nonorthogonal. As a result, the classical (real-valued) modal analysis does not decouple the equation of motion.

To derive a modal expansion of the system response, the equivalent state-space form

$$\dot{\mathbf{z}}(t) = \mathbf{A}\mathbf{z}(t) + \mathbf{B}\mathbf{f}(t), \quad \mathbf{z}(0) = \mathbf{z}_0 \tag{3a}$$
$$\mathbf{z} = \begin{pmatrix}\mathbf{x}\\ \dot{\mathbf{x}}\end{pmatrix}, \quad \mathbf{A} = \begin{bmatrix}0 & I\\ -\mathbf{M}^{-1}\mathbf{K} & -\mathbf{M}^{-1}\mathbf{D}\end{bmatrix}$$
$$\mathbf{B} = \begin{pmatrix}0\\ \mathbf{M}^{-1}\end{pmatrix}, \quad \mathbf{z}_0 = \begin{pmatrix}\mathbf{a}_0\\ \mathbf{b}_0\end{pmatrix} \tag{3b}$$

is used. According to Yang (1994b), the solutions of the eigenvalue problems associated with (3)

$$\mathbf{A}\boldsymbol{\phi}_k = \lambda_k\boldsymbol{\phi}_k, \quad \mathbf{A}^T\boldsymbol{\psi}_k = \bar{\lambda}_k\boldsymbol{\psi}_k \tag{4}$$

can be represented by those of the original eigenvalue problem (2):

$$\boldsymbol{\phi}_k = \begin{pmatrix}\mathbf{v}_k\\ \lambda_k\mathbf{v}_k\end{pmatrix} \in C^{2n}, \quad \boldsymbol{\psi}_k = \overline{\frac{1}{\lambda_k^2}\begin{pmatrix}-K\mathbf{v}_k\\ \lambda_k M\mathbf{v}_k\end{pmatrix}} \in C^{2n},$$
$$k = \pm 1, \pm 2, \ldots, \pm n \tag{5a, b}$$

where the overbar represents complex conjugation, $\lambda_{-k} = \bar{\lambda}_k$, and $\mathbf{v}_{-k} = \bar{\mathbf{v}}_k$. The eigenvectors ϕ_k and ψ_k are in the bi-orthogonality relations

$$(\boldsymbol{\psi}_j, \boldsymbol{\phi}_k) = 2\delta_{jk}, \quad (\boldsymbol{\psi}_j, \mathbf{A}\boldsymbol{\phi}_k) = 2\lambda_j\delta_{jk} \tag{6}$$

where δ_{jk} is the Kronecker delta, and the inner product $(\mathbf{a}, \mathbf{b}) = \mathbf{a}^*\mathbf{b}$, $\mathbf{a}^* = \bar{\mathbf{a}}^T$, $\forall \mathbf{a}, \mathbf{b} \in C^{2n}$. By (5) and (6), the normalization condition for the eigenvectors is

$$(\boldsymbol{\psi}_k, \boldsymbol{\phi}_k) = \mathbf{v}_k^T\mathbf{M}\mathbf{v}_k - \frac{1}{\lambda_k^2}\mathbf{v}_k^T\mathbf{K}\mathbf{v}_k = 2. \tag{7}$$

Applying (6) to the state space Eq. (3) yields

$$\mathbf{z}(t) = \mathbf{G}(t)\mathbf{z}_0 + \int_0^t \mathbf{G}(t-\tau)\mathbf{B}\mathbf{f}(\tau)d\tau \tag{8}$$

where

$$\mathbf{G}(t) = \tfrac{1}{2}\sum_{k=\pm 1}^{\pm n} e^{\lambda_k t}\boldsymbol{\phi}_k\boldsymbol{\psi}_k^* \in R^{2n\times 2n}. \tag{9}$$

By (3b) and (5), the solution to Eq. (1) is given by

$$\mathbf{x}(t) = \dot{\mathbf{g}}(t)\mathbf{M}\mathbf{x}_0 + \mathbf{g}(t)(\mathbf{M}\mathbf{v}_0 + \mathbf{D}\mathbf{x}_0) + \int_0^t \mathbf{g}(t-\tau)\mathbf{f}(\tau)d\tau \tag{10}$$

where the Green's function, an n by n real matrix, is of the form

$$\mathbf{g}(t) = \frac{1}{2}\sum_{k=\pm 1}^{\pm n}\frac{1}{\lambda_k}e^{\lambda_k t}\mathbf{v}_k\mathbf{v}_k^T. \tag{11}$$

The relationship (5b) between the vibration modes (λ_k, $\mathbf{v}_k$) and the adjoint state-space eigenvectors $\boldsymbol{\psi}_k$ is an important key to the eigenfunction expansion. With this relationship, the state-space analysis is conveniently converted back to the original physical coordinates, and the calculation of the adjoint state-space eigenvectors is avoided.

3 Modal Analysis of Distributed Systems

The displacement $w(x, t)$ of a distributed damped system is governed by

$$Mw_{,tt}(x,t) + Dw_{,t}(x,t) + Kw(x,t) = f(x,t), \quad x \in \Omega \tag{12a}$$
$$\Gamma w(x,t) = 0, \quad x \in \partial\Omega \tag{12b}$$
$$w(x,0) = a_0(x), \quad w_{,t}(x,0) = b_0(x), \quad x \in \Omega \tag{12c}$$

where $(\ )_{,t} = \partial(\ )/\partial t$, Ω is a bounded open region in R^m with boundary $\partial\Omega$, $1 \leq m \leq 3$, $f(x, t)$ is the external force, $a_0(x)$ and $b_0(x)$ are given functions, M, D, and K are spatial differential operators describing the system inertia, damping,

and stiffness, respectively, and Γ is the spatial boundary operator. The M, D, and K are symmetric; namely,

$$\langle Mu, v\rangle_{H(\Omega)} = \langle u, Mv\rangle_{H(\Omega)},$$

$$\langle Du, v\rangle_{H(\Omega)} = \langle u, Dv\rangle_{H(\Omega)}, \quad \langle Ku, v\rangle_{H(\Omega)} = \langle u, Kv\rangle_{H(\Omega)}$$

where the inner product is defined by $\langle u, v\rangle_{H(\Omega)} = \int_\Omega \bar{u}v dx$, and u and v are comparison functions from a Hilbert space $H(\Omega)$. Also, M and K are positive definite and D is positive semi-definite. The eigenvalue problem associated with (12) is

$$\{\lambda_k^2 M + \lambda_k D + K\} v_k(x) = 0,$$

$$k = \pm 1, \pm 2, \ldots, x \in \Omega \quad (13)$$

where $\lambda_{-k} = \bar{\lambda}_k$, and $v_{-k} = \bar{v}_k$. Without loss of generality, assume that the distributed system has no rigid body motion, i.e., $|\lambda_k| \neq 0$ for all k.

When the distributed system is nonproportionally damped, which is often the case in engineering practice, the eigenfunctions $v_k(x)$ are nonorthogonal, and cannot decouple Eqs. (12). Consequently, conventional modal analysis is not applicable here and new techniques are needed for closed-form solution. In the following, the concepts described in Section 2 are generalized to develop a new modal analysis for the distributed damped system.

Equations (12) are transferred to an equivalent state-space form

$$A_0 z_{,t}(x,t) = A_1 z(x,t) + Bf(x,t), \quad z(x,0) = z_0(x) \quad (14a)$$

where

$$z = \begin{pmatrix} w \\ w_{,t} \end{pmatrix}, \quad A_0 = \begin{bmatrix} 1 & 0 \\ 0 & M \end{bmatrix}, \quad A_1 = \begin{bmatrix} 0 & 1 \\ -K & -D \end{bmatrix},$$

$$B = \begin{pmatrix} 0 \\ 1 \end{pmatrix}, \quad z_0(x) = \begin{pmatrix} a_0(x) \\ b_0(x) \end{pmatrix}. \quad (14b)$$

The associate and adjoint eigenvalue problems are

$$A_1\phi_k(x) = \lambda_k A_0\phi_k(x), \quad A_1^T\psi_k(x) = \bar{\lambda}_k A_0\psi_k(x) \quad (15a, b)$$

where $k = \pm 1, \pm 2, \ldots$, and $\phi_{-k} = \bar{\phi}_k$. The $\phi_k(x)$ of (15a) are related to $v_k(x)$ of (13) by

$$\phi_k(x) = \begin{pmatrix} v_k(x) \\ \lambda_k v_k(x) \end{pmatrix}. \quad (16)$$

It is easy to show that the state-space eigenfunctions are in the bi-orthogonality relations

$$\langle \psi_j, A_0\phi_k\rangle = \langle A_0\psi_j, \phi_k\rangle = 2\delta_{jk}$$

$$\langle \psi_j, A_1\phi_k\rangle = \langle A_1^T\psi_j, \phi_k\rangle = 2\lambda_j\delta_{jk} \quad (17a, b)$$

where the inner product is defined by $\langle a, b\rangle = \langle a_1, a_2\rangle_{H(\Omega)} + \langle b_1, b_2\rangle_{H(\Omega)}$, $a = (a_1, a_2)^T$, $b = (b_1, b_2)^T \in H(\Omega) \oplus H(\Omega)$.

It is well known that the state-space eigenfunctions $\phi_k(x)$ can be expressed by the mode shapes $v_k(x)$, Eq. (16). However, what is not known in the literature is that the adjoint eigenfunctions $\psi_k(x)$ can also be represented by $v_k(x)$, which plays an important role in the proposed transient analysis. To show this, write

$$\psi_k(x) = \begin{pmatrix} \chi_1(x) \\ \chi_2(x) \end{pmatrix}, \quad \chi_1, \chi_2 \in H(\Omega). \quad (18)$$

Substituting the above into (15b) gives

$$\chi_1 = -\frac{1}{\bar{\lambda}_k} K\chi_2, \quad (\lambda_k^2 M + \lambda_k D + K)\bar{\chi}_2 = 0. \quad (19a, b)$$

Comparing (13) and (19b) leads to

$$\chi_1 = -\frac{1}{\bar{\lambda}_k} K\bar{v}_k, \quad \chi_2 = \bar{v}_k. \quad (20)$$

Thus, the adjoint eigenfunctions ψ_k are in the form

$$\psi_k(x) = \frac{1}{\bar{\lambda}_k^2}\begin{pmatrix} -K\bar{v}_k(x) \\ \bar{\lambda}_k\bar{v}_k(x) \end{pmatrix}, \quad k = \pm 1, \pm 2, \ldots. \quad (21)$$

The normalization condition for ϕ_k and ψ_k, by (16) and (21), becomes

$$\langle \psi_k, A_0\phi_k\rangle = \langle \bar{v}_k, Mv_k\rangle_{H(\Omega)} - \frac{1}{\lambda_k^2}\langle \bar{v}_k, Kv_k\rangle_{H(\Omega)}$$

$$= \int_\Omega (v_k M v_k - v_k K v_k/\lambda_k^2) dx = 2. \quad (22)$$

Assume that the ϕ_k and ψ_k are complete in the Hilbert space $H(\Omega) \oplus H(\Omega)$. The state-space vector $z(x, t)$ is expressed as

$$z(x,t) = \sum_{k=\pm 1}^{\pm\infty} q_k(t)\phi_k(x) \quad (23)$$

where q_k are the modal coordinates. (The legitimacy of the modal expansion will be shown in Section 6.) Substitute the modal series (23) into (14) and use the bi-orthogonality relations (17), to obtain

$$q_k(t) = \tfrac{1}{2} e^{\lambda_k t}\langle \psi_k, A_0 z_0\rangle + \tfrac{1}{2}\int_0^t e^{\lambda_k(t-\tau)}\langle \psi_k, Bf(\cdot, \tau)\rangle d\tau. \quad (24)$$

By (23) and (24), the state-space vector is determined as

$$z(x,t) = \int_\Omega G(x, \xi, t) A_0 z_0(\xi) d\xi + \int_0^t \int_\Omega G(x, \xi, t-\tau) Bf(\xi, \tau) d\xi d\tau \quad (25)$$

with the two-by-two real matrix

$$G(x, \xi, t) = \tfrac{1}{2}\sum_{k=\pm 1}^{\pm\infty} e^{\lambda_k t}\phi_k(x)\psi_k^*(\xi) \quad (26)$$

where $\psi_k^* = \bar{\psi}_k^T$. By (14$b$) and (25), the solution to (12) is obtained as

$$w(x,t) = \int_\Omega \{g_{,t}(x, \xi, t) Ma_0(\xi) + g(x, \xi, t)(Mb_0(\xi) + Da_0(\xi))\} d\xi + \int_0^t \int_\Omega g(x, \xi, t-\tau) f(\xi, \tau) d\xi d\tau \quad (27)$$

where the Green's function of the distributed system is given in the eigenfunction expansion

$$g(x, \xi, t) = \tfrac{1}{2}\sum_{k=\pm 1}^{\pm\infty} \frac{1}{\lambda_k} e^{\lambda_k t} v_k(x) v_k(\xi), \quad x, \xi \in \Omega. \quad (28)$$

The Green's function is the impulse response of the distributed damped system that is subject to zero boundary and initial disturbances; i.e.,

$$Mg_{,tt}(x, \xi, t) + Dg_{,t}(x, \xi, t) + Kg(x, \xi, t) = \delta(t)\delta(x - \xi), \quad x, \xi \in \Omega \quad (29a)$$

$$\Gamma g(x, \xi, t) = 0, \quad x, \xi \in \partial\Omega \tag{29b}$$

$$g(x, \xi, 0) = 0, \quad g_{,t}(x, \xi, 0) = 0, \quad x, \xi \in \Omega \tag{29c}$$

where the operators M, D, K, and Γ act on ξ.

If the distributed system has repeated eigenvalues, the associated eigenvalue problem becomes

$$\{\lambda_k^2 M + \lambda_k D + K\} v_{kj}(x) = 0,$$

$$j = 1, 2, \ldots, m_k, \quad k = 1, 2, \ldots$$

where m_k is the multiplicity of the eigenvalue λ_k. In this case, the Green's function formula (27) is still valid, and the Green's function is given by

$$g(x, \xi, t) = \tfrac{1}{2} \sum_{k=\pm 1}^{\pm\infty} \frac{1}{\lambda_k} e^{\lambda_k t} \sum_{j=1}^{m_k} v_{kj}(x) v_{kj}(\xi), \quad x, \xi \in \Omega.$$

The distributed damped system (12) is non-self-adjoint in its original equations of motion. Based on a state-space formulation, the response $w(x, t)$ and the Green's function $g(x, \xi, t)$ are represented by series of complex and nonorthogonal eigenfunctions describing the modes of vibration of the damped system. This new method differs from the existing modal analyses in that it utilizes the relationship between the vibration modes and the adjoint state-space eigenfunctions.

4 Laplace Transform

While the Green's function in (28) is an eigenfunction series, the Green's function formula (27) does not depend on the modal analysis. In this section, we show that the Green's function formula (27) can be obtained by Laplace transform. The purpose here is threefold: (a) to enhance the usefulness and versatility of the proposed method by relating it to a frequency-domain analysis tool; (b) to define distributed transfer functions which have wide application in various dynamics and control problems of distributed damped systems (Butkoviskiy, 1983; Yang and Mote, 1991; Yang and Tan, 1992; Yang, 1994a); and (c) to provide a new way to evaluate transfer function residues, which are needed for transient response by inverse Laplace transform.

Laplace transform of Eqs. (12) with respect to time gives

$$(s^2 M + sD + K)\hat{w}(x, s) = f_{el}(x, s) \equiv \hat{f}(x, s)$$

$$+ M(sa_0(x) + b_0(x)) + Da_0(x), \quad x \in \Omega \tag{30a}$$

$$\Gamma \hat{w}(x, s) = 0, \quad x \in \partial\Omega \tag{30b}$$

where $\hat{w}(x, s)$ and $\hat{f}(x, s)$ are the Laplace transforms of $w(x, t)$ and $f(x, t)$, respectively, and s is the Laplace transform parameter. The solution $\hat{w}(x, s)$ of (30) is of the integral form (Roach, 1982)

$$\hat{w}(x, s) = \int_\Omega \hat{g}(x, \xi, s) f_{el}(\xi, s) d\xi, \quad x \in \Omega \tag{31}$$

where the integral kernel $\hat{g}(x, \xi, s)$ is the distributed transfer function of the damped system (Butkoviskiy, 1983). The transfer function is the Laplace transform of the Green's function, and by (28) is in the modal expansion form

$$\hat{g}(x, \xi, s) = \frac{1}{2} \sum_{k=\pm 1}^{\pm\infty} \frac{1}{\lambda_k (s - \lambda_k)} v_k(x) v_k(\xi), \quad x, \xi \in \Omega. \tag{32}$$

The transfer function is the solution of the equations

$$(s^2 M + sD + K)\hat{g}(x, \xi, s) = \delta(x - \xi), \quad x, \xi \in \Omega \tag{33a}$$

$$\Gamma \hat{g}(x, \xi, s) = 0, \quad x, \xi \in \partial\Omega \tag{33b}$$

which are the Laplace transforms of Eqs. (29).

It is easy to show that inverse Laplace transform of (31) with $\mathcal{L}^{-1}[\hat{g}(x, \xi, s)] = g(x, \xi, t)$ retains (27). Hence, without modal analysis, the Green's function formula for distributed damped systems is derived although one still needs to determine the Green's function to predict the system response. Equation (28) provides one way to determine the Green's function in closed form.

Theoretically, when the distributed transfer function is available, the Green's function can be estimated by residue theorem:

$$g(x, \xi, t) = \mathcal{L}^{-1}[\hat{g}(x, \xi, s)]$$

$$= \sum_{j=\pm 1}^{\pm\infty} e^{\lambda_j t} \operatorname*{Res}_{s=\lambda_j} \{\hat{g}(x, \xi, s)\} \tag{34}$$

where λ_j are the poles of the transfer function, or the eigenvalues of the distributed system. Unfortunately, because the transfer function of a complex distributed system can only be estimated numerically and because the singularities of $\hat{g}(x, \xi, s)$ at its poles can lead to large errors in computation, accurate prediction of the residues of $\hat{g}(x, \xi, s)$ is impractical, if not impossible. The modal analysis proposed herein actually provides a new way to calculate the residues; i.e., by (32), these residues are

$$\operatorname*{Res}_{s=\lambda_j} \{\hat{g}(x, \xi, s)\} = \frac{1}{2\lambda_j} v_k(x) v_j(\xi), \quad j = \pm 1, \pm 2, \ldots. \tag{35}$$

The eigenpairs (λ_j, v_j) of a distributed system can be estimated by many well-developed techniques, and have been obtained in exact and closed form for a large class of complex distributed systems (Yang, 1994a). Thus, the relation (35) warrants accurate prediction of transfer function residues for distributed damped systems.

5 Boundary Disturbances

The distributed damped system studied in the previous sections is under homogeneous boundary conditions. In this section, the effects of boundary disturbances on the system response is investigated. Let $y(x, t)$ be the displacement of the damped system described by

$$My_{,tt}(x, t) + Dy_{,t}(x, t) + Ky(x, t) = f(x, t),$$

$$x \in \Omega \tag{36a}$$

$$\Gamma_j y(x, t) = \gamma_j(x, t), \quad x \in \partial\Omega, \quad j = 1, 2, \ldots, N_{inh} \tag{36b}$$

$$\Gamma_j y(x, t) = 0, \quad x \in \partial\Omega,$$

$$j = N_{inh} + 1, N_{inh} + 2, \ldots, N_b \tag{36c}$$

$$y(x, 0) = a_0(x), \quad y_{,t}(x, 0) = b_0(x), \quad x \in \Omega \tag{36d}$$

where among the total N_b boundary conditions, N_{inh} ($\leq N_b$) are inhomogeneous, with the functions $\gamma_j(x, t)$ representing the boundary disturbances (either external loads or displacement excitations), and Γ_j are the spatial boundary operators. By superposition, the solution to (36) is decomposed into

$$y(x, t) = w(x, t) + u(x, t) \tag{37}$$

where $w(x, t)$ satisfies Eqs. (12), and $u(x, t)$ is the solution of

$$Mu_{,tt}(x, t) + Du_{,t}(x, t) + Ku(x, t) = 0, \quad x \in \Omega \tag{38a}$$

$$\Gamma_j u(x, t) = \gamma_j(x, t), \quad x \in \partial\Omega, \quad j = 1, 2, \ldots, N_{inh} \tag{38b}$$

$$\Gamma_j u(x, t) = 0, \quad x \in \partial\Omega,$$

$$j = N_{inh} + 1, N_{inh} + 2, \ldots, N_b \tag{38c}$$

$$u(x, 0) = 0, \quad u_{,t}(x, 0) = 0, \quad x \in \Omega. \tag{38d}$$

The solution to (12) has been given in (27) and (28). So, only Eqs. (38) are to be solved.

Laplace transform of (38) gives

$$(s^2M + sD + K)\hat{u}(x, s) = 0, \quad x \in \Omega \tag{39a}$$

$$\Gamma_j\hat{u}(x, s) = \hat{\gamma}_j(x, s), \quad x \in \partial\Omega, \quad j = 1, 2, \ldots, N_{inh} \tag{39b}$$

$$\Gamma_j\hat{u}(x, s) = 0, \quad x \in \partial\Omega, \quad j = N_{inh} + 1, N_{inh} + 2, \ldots, N_b. \tag{39c}$$

Recall that the transfer function $\hat{g}(x, \xi, s)$ satisfies (33). Consider the integral

$$0 = \int_\Omega \hat{g}(x, \xi, s)(s^2M + sD + K)\hat{u}(\xi, s)d\xi$$

$$= \int_\Omega \hat{u}(\xi, s)(s^2M + sD + K)\hat{g}(x, \xi, s)d\xi + B(\hat{u}, \hat{g})|_{\partial\Omega} = \hat{u}(x, s) + B(\hat{u}, \hat{g})|_{\partial\Omega}$$

where the boundary conjunct

$$B(\hat{u}, \hat{g})|_{\partial\Omega} = \int_{\partial\Omega} \sum_{j=1}^{N_b} (-E_j[\hat{g}]\Gamma_j\hat{u} + E_j^*[\hat{u}]\Gamma_j^*\hat{g})d\xi.$$

E_j are the boundary operators arising from integral by part, and E_j^* and Γ_j^* are adjoint to E_j and Γ_j. Because the operators M, D, and K are symmetric, $E_j = E_j^*$ and $\Gamma_j = \Gamma_j^*$. It follows that

$$\hat{u}(x, s) = \int_{\partial\Omega} \sum_{j=1}^{N_b} (E_j[\hat{g}]\Gamma_j\hat{u} - E_j[\hat{u}]\Gamma_j\hat{g})d\xi = \int_{\partial\Omega} \sum_{j=1}^{N_{inh}} E_j[\hat{g}(x, \xi, s)]\hat{\gamma}_j(\xi, s)d\xi \tag{40}$$

where the boundary conditions (33b) for $\hat{g}(x, \xi, s)$ and (38b, c) for $\hat{u}(x, s)$ have been used. Finally, inverse Laplace transform of (40) leads to the convolution integral

$$u(x, t) = \int_0^t \int_{\partial\Omega} \sum_{j=1}^{N_{inh}} h_j(x, \xi, t - \tau)\gamma_j(\xi, \tau)d\xi d\tau \tag{41}$$

where the boundary influence functions

$$h_j(x, \xi, t) = \mathcal{L}^{-1}\{E_j[\hat{g}(x, \xi, s)]\}, \quad j = 1, 2, \ldots, N_{inh}. \tag{42}$$

It is seen that the boundary influence functions of a distributed damped system can be represented by the Green's function of the system. Once $u(x, t)$ is known, the complete solution to (36) is obtained by the superposition (37).

As an example, consider a cantilever beam subject to a displacement excitation $w_b(t)$ at its left end, and a torque $\tau_b(t)$ at its right end; see Fig. 2. Assume zero external and initial disturbances. The s-domain response $\hat{w}(x, s)$ of the beam is governed by

$$(s^2\rho + sd_v)\hat{w}(x, s) + ((sd_h + EI)\hat{w}_{,xx}(x, s))_{,xx} = 0, \quad x \in (0, L) \tag{43a}$$

$$\hat{w}(0, s) = \hat{w}_b(s), \quad \hat{w}_x(0, s) = 0$$
$$(sd_h + EI)\hat{w}_{,xx}|_{x=L} = \hat{\tau}_b(s),$$
$$((sd_h + EI)\hat{w}_{,xx})_{,x}|_{x=L} = 0 \tag{43b}$$

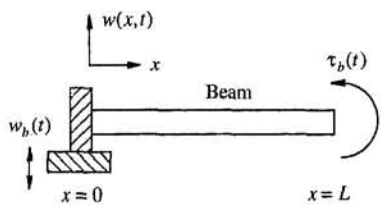

Fig. 2 A cantilever beam under boundary disturbances

where ρ is the linear density, EI is the bending stiffness, d_v and d_h are the viscous and material damping coefficients, and $\hat{w}_b(s)$ and $\hat{\tau}_b(s)$ are the Laplace transforms of $w_b(t)$ and $\tau_b(t)$, respectively. The transfer function of the beam satisfies

$$(s^2\rho + sd_v)\hat{g} + ((sd_h + EI)\hat{g}_{,\xi\xi})_{,\xi\xi} = \delta(x - \xi), \quad x, \xi \in (0, L) \tag{44a}$$

$$\hat{g}(x, 0, s) = 0, \quad \hat{g}_{,\xi}(x, 0, s) = 0, \quad x \in (0, L)$$
$$(sd_h + EI)\hat{g}_{,\xi\xi}|_{\xi=L} = 0, \quad ((sd_h + EI)\hat{g}_{,\xi\xi})_{,\xi}|_{x=L} = 0, \quad x \in (0, L) \tag{44b}$$

where $(\ )_{,\xi} = \partial(\ )/\partial\xi$. By (43) and (44), it is easy to show that

$$0 = \int_\Omega \hat{g}(x, \xi, s)\{(s^2\rho + sd_v)\hat{w}(\xi, s) + ((sd_h + EI)\hat{w}_{,\xi\xi}(\xi, s))_{,\xi\xi}\}d\xi = \hat{w}(x, s) - ((sd_h + EI)\hat{g}_{,\xi\xi})_{,\xi}|_{\xi=0}\hat{w}_b(s) + \hat{g}_{,\xi}|_{\xi=L}\hat{\tau}_b(s).$$

Hence the time-domain response of the beam

$$w(x, t) = \int_0^t (h_1(x, t - \tau)w_b(\tau) + h_2(x, t - \tau)\tau_b(\tau))d\tau \tag{45}$$

where the boundary influence functions are given by

$$h_1(x, t) = ((d_h\partial/\partial t + EI)g_{,\xi\xi})_{,\xi}|_{\xi=0}, \quad h_2(x, t) = -g_{,\xi}|_{\xi=L} \tag{46}$$

and $g(x, \xi, t) = \mathcal{L}^{-1}[\hat{g}(x, \xi, s)]$ is the Green's function of the beam.

The vibration of the distributed system (36) is excited by external, initial, and boundary disturbances. The contribution of the external disturbance is represented by the system Green's function. Equations (27) and (42) show that the influence of the initial and boundary disturbances on the system response can also be described by the Green's function. Knowing this will greatly simplify the solution procedure: The key step in the closed-form transient analysis is to determine the impulse response (Green's function) of the distributed damped system under zero initial and boundary disturbances.

6 Legitimacy of Eigenfunction Expansion

The modal analysis proposed in Section 3 has assumed that ϕ_k and ψ_k are complete so that the eigenfunction expansion of the system system response can be derived. The completeness of the state-space eigenfunctions is difficult to prove for general damped systems. However, as suggested in Roach (1982), it is possible to obtain the eigenfunction series through direct use of the Green's function. In this section, without assuming completeness of the state-space eigenfunctions, we show that the proposed eigenfunction expansion is legitimate.

First, show that the series (34) (residue theorem) is legitimate. Assume that the boundary value problem described by (12) is well posed and has a unique solution. Assume that the damped system has a discrete spectrum, which is always the case for vibrating continua in a finite bounded region. Then, the Green's function of the damped system exists and the system response can be represented by the integral (27) although the modal expansion (28) is not viable yet. Because M and K are positive definite and D is positive semi-definite, the system impulse response is such that $\lim_{t\to\infty} g(x, \xi, t)e^{-\alpha t} = 0$, $\forall\alpha > 0$, which means that the Laplace transform of the Green's function, namely the distributed transfer function $\hat{g}(x, \xi, s)$, exists. Because none of the poles of $\hat{g}(x, \xi, s)$ are located in the open

right-half complex plane and because $\lim_{s\to\infty} s\hat{g}(x, \xi, s) = g(x, \xi, 0) = 0$ by (29c), $\lim_{t\to\infty} \hat{g}(x, \xi, s)e^{st} = 0$ for $\mathrm{Re}(s) < 0$. Thus, inverse Laplace transform of $\hat{g}(x, \xi, s)$ by the Bromwich integral is legal, and gives the Green's function in a convergent series, which is (34).

Second, show that (34) is an eigenfunction series. For s near the kth pole (eigenvalue) λ_k, the transfer function given in (34) can be written as

$$\hat{g}(x, \xi, s) = \sum_{j=\pm 1}^{\pm\infty} \frac{b_j(x, \xi)}{s - \lambda_j} = \frac{b_k(x, \xi)}{s - \lambda_k} + R(x, \xi, s) \quad (47)$$

where $b_k(x, \xi)$ is the residue of the transfer function at λ_k, and $R(x, \xi, s) = \sum_{j\neq k} b_j(x, \xi)/(s - \lambda_j)$ is analytic at λ_k. Substituting (47) into (33) gives

$$\frac{1}{s - \lambda_k} L_s^{\xi}[b_k(x, \xi)] + L_s^{\xi}[R(x, \xi, s)] = \delta(x - \xi)$$

where L_s^{ξ} is the operator $s^2M + sD + K$ acting on ξ. The Cauchy integral

$$\frac{1}{2\pi i}\int_{\Gamma_k} \left(\frac{1}{s - \lambda_k} L_s^{\xi}[b_k(x, \xi)] + L_s^{\xi}[R(x, \xi, s)]\right) ds = \frac{1}{2\pi i}\int_{\Gamma_k} \delta(x - \xi) ds$$

on the contour $\Gamma_k = \{s \in C: |s - \lambda_k| = \epsilon, \epsilon < |\lambda_j - \lambda_k| \text{ for all } \lambda_j \neq \lambda_k\}$ leads to

$$L_{\lambda_k}^{\xi}[b_k(x, \xi)] = (\lambda_k^2 M + \lambda_k D + K)b_k(x, \xi) = 0 \quad (48)$$

which suggests that

$$b_k(x, \xi) = a(x)v_k(\xi). \quad (49)$$

Here $v_k(\xi)$ is the kth eigenfunction of the damped system, and $a(x)$ is a function of x. Because the operator $s^2M + sD + K$ is symmetric, $\hat{g}(x, \xi, s) = \hat{g}(\xi, x, s)$, and therefore

$$L_s^{x}[\hat{g}(x, \xi, s)] = \delta(x - \xi) \quad (50)$$

where L_s^x is the operator $s^2M + sD + K$ acting on x. Plugging (47) and (49) into (50) and conducting the Cauchy integration on Γ_k lead to

$$L_{\lambda_k}^{x}[b_k(x, \xi)] = v_k(\xi)(\lambda_k^2 M + \lambda_k D + K)a(x) = 0$$

which implies $a(x) = \beta_k v_k(x)$, where β_k is a constant. Thus, the residue $b_k(x, \xi) = \beta_k v_k(x)v_k(\xi)$ and the Green's function and transfer function are expressed by the eigenfunction series

$$g(x, \xi, t) = \sum_{k=\pm 1}^{\pm\infty} \beta_k e^{\lambda_k t} v_k(x)v_k(\xi) \quad (51)$$

$$\hat{g}(x, \xi, s) = \sum_{k=\pm 1}^{\pm\infty} \frac{1}{s - \lambda_k} \beta_k v_k(x)v_k(\xi). \quad (52)$$

Third, evaluate the constants β_k. Let the damped system (12) be subject zero initial disturbances. By (27), the displacement and velocity of the damped system are given by

$$w(x, t) = \int_0^t \int_\Omega g(x, \xi, t - \tau)f(\xi, \tau)d\xi d\tau \quad (53a)$$

$$w_{,t}(x, t) = \int_0^t \int_\Omega g_{,t}(x, \xi, t - \tau)f(\xi, \tau)d\xi d\tau \quad (53b)$$

where (29c) has been used. By (51) and (53), the state-space vector $z(x, t)$ in (14a) is

$$z(x, t) = \begin{pmatrix} w(x, t) \\ w_{,t}(x, t) \end{pmatrix} = \sum_{k=\pm 1}^{\pm\infty} \beta_k \phi_k(x) \int_0^t e^{\lambda_k(t-\tau)} f_k(\tau)d\tau \quad (54)$$

where $f_k(t) = \int_\Omega v_k(\xi)f(\xi, t)d\xi$. Substituting the Laplace transform of (54) into that of the state-space Eq. (14a), and applying (15a) leads to

$$\sum_{j=\pm 1}^{\pm\infty} \beta_j \hat{f}_j(s) A_0 \phi_j(x) = \begin{pmatrix} 0 \\ 1 \end{pmatrix} \hat{f}(x, s) \quad (55)$$

where $\hat{f}_j(s)$ and $\hat{f}(x, s)$ are the Laplace transforms of $f_j(t)$ and $f(x, t)$, respectively. Take the inner product $\langle \psi_k, \cdot \rangle$ of both sides of the above equation, and use the bi-orthogonality property (17a) to obtain

$$\beta_k \hat{f}_k \langle \psi_k, A_0\phi_k \rangle = \frac{1}{\lambda_k} \hat{f}_k. \quad (56)$$

The forcing function $f(x, t)$ can always be chosen such that $\hat{f}_k \neq 0$. It follows that

$$\beta_k = \frac{1}{\lambda_k \langle \psi_k, A_0\phi_k \rangle}. \quad (57)$$

Finally, show that the Green's function is uniquely determined by (51). Although β_k can be an arbitrary nonzero constant, depending on how the eigenfunctions ϕ_k and ψ_k are scaled, $\beta_k v_k(x)v_k(\xi)$ is independent of any eigenfunction normalization. In fact it is easy to see that for $\tilde{v}_k(x) = \alpha v_k(x)$, with α being an arbitrary nonzero constant

$$\frac{v_k(x)v_k(\xi)}{\lambda_k \langle \psi_k, A_0\phi_k \rangle} = \frac{\tilde{v}_k(x)\tilde{v}_k(\xi)}{\lambda_k \langle \tilde{\psi}_k, A_0\tilde{\psi}_k \rangle} \quad (58)$$

where $\tilde{\psi}_k$ and $\tilde{\phi}_k$ are the state-space eigenfunctions corresponding to $\tilde{v}_k$. Accordingly, the Green's function given by the modal expansion (51) is uniquely determined. Furthermore, by letting $\langle \psi_k, A_0\phi_k \rangle = 2$, which is just the normalization condition (22), the coefficients $\beta_k = 1/(2\lambda_k)$ and the series (51) is identical to (28). Therefore, the modal analysis presented in Section 3 is indeed legitimate, and does give convergent eigenfunction representation of the system Green's function and system response.

7 Conclusions

The distributed damped system in consideration is non-self-adjoint in its original equations of motion; conventional modal analysis cannot yield closed-form solutions. In this work, by a new modal analysis and a Green's function formula, the response of the distributed system to arbitrary external, initial, and boundary disturbances is given in a closed-form eigenfunction series. The main results presented in this paper are summarized as follows:

(i) A relationship between the modes of vibration and adjoint state-space eigenfunctions of the distributed damped system is established. Because of this, the analysis in the state space can be conveniently converted back into the physical coordinates and the modal space where the physical meaning of eigenfunctions has been well classified. It is based on this relationship that the proposed modal analysis and Green's function formula are derived.

(ii) The legitimacy of modal expansion for general distributed damped systems is proven, without assuming completeness of the system eigenfunctions. Previous modal analyses for non-

self-adjoint systems usually adopt the assumption of complete eigenfunctions, which may not be true, and are difficult to verify. The proof given in Section 6 guarantees the convergence of the new modal analysis for distributed damped systems.

(iii) The proposed method does not necessarily need to calculate state-space eigenfunctions. Although a state-space formulation has been used in the development, the closed-form transient analysis presented only needs to know the eigensolutions (vibration modes) associated with the original equations of motion. This feature indicates potential savings in computation.

The relationship between modes of vibration and adjoint state-space eigenfunctions has two other implications. First, the modal representation of the system Green's function, Eq. (28), provides a physical insight into certain dynamics and control problems of distributed damped systems, such as eigenvalue inclusion phenomena and modal controllability and observability (Yang, 1992, 1994b). These problems are directly related to the mode shapes of vibration of given physical systems, and would be difficult to solve in a state-space formulation if the physical meaning of the adjoint eigenfunctions is not clear. Second, the proposed method can be applied to systems with unidentified damping. Many existing methods require a complete knowledge of damping operators, and would fail to predict the damped response if any damping parameter cannot be identified. The Green's function given in Eq. (28) is a superposition of vibration modes, which does not explicitly relate to damping operators. With modern modal analysis equipment, say structural analyzers, the eigenvalues and mode shapes that are dominant in vibration of an uncertain damped system can be obtained experimentally in many practical applications. Accordingly, the proposed method may provide a new way to study dynamics of uncertain distributed damped systems. These subjects are interesting future research topics.

Acknowledgments

This work was partially supported by the US Army Research Office.

References

Bellos, J., and Inman, D. J., 1989, "A Survey on Nonprotionsl Damping," *The Shock and Vibration Digest,* Vol. 21, No. 10, pp. 7--12.

Bergman, L. A., and McFarland, D. M., 1988, "On the Vibration of a Point-Supported Linear Distributed System," ASME *Journal of Vibration, Acoustics, Stress, and Reliability in Design,* Vol. 110, pp. 485–492.

Butkovskiy, A. G., 1983, *Structural Theory of Distributed Theory,* Ellis Horwood Limited.

Caughey, T. H., and O'Kelly, M. E., 1965, "Classical Normal Modes in Damped Linear Dynamic Systems," ASME JOURNAL OF APPLIED MECHANICS, Vol. 32, pp. 563–588.

Foss, K. A., 1958, "Coordinates Which Uncouple the Equations of Motion of Damped Linear Dynamic Systems," ASME JOURNAL OF APPLIED MECHANICS, Vol. 25, pp. 361–364.

Friedman, B., 1956, *Principles and Techniques of Applied Mathematics,* John Wiley and Sons, New York.

Huseyin, K., 1978, *Vibration and Stability of Multiple Parameter Systems,* Noordholl International Publishing.

Meirovitch, L., 1980, *Computational Methods in Structural Dynamics,* Sijthoff & Noordhoff.

Roach, G. F., 1982, *Green's Functions,* Cambridge University Press, New York.

Yang, B., 1992, "Eigenvalue Inclusion Principles for Distributed Gyroscopic Systems," ASME JOURNAL OF APPLIED MECHANICS, Vol. 59, pp. 650–656.

Yang, B., 1994a, "Distributed Transfer Function Analysis of Complex Distributed Parameter Systems," ASME JOURNAL OF APPLIED MECHANICS, Vol. 61, pp. 84–92.

Yang, B., 1994b, "Modal Controllability and Observability of General Mechanical Systems," *Proceedings of the 1994 ASME Winter Annual Meeting,* DE-Vol. 75, pp. 363–370.

Yang, B., 1996, "Closed-Form Transient Response of Distributed Damped Systems, Part II: Energy Formulation for Constrained and Combined Systems," ASME JOURNAL OF APPLIED MECHANICS, Vol. 63, pp. 1004–1010.

Yang, B., and Mote, C. D., Jr., 1991, "Active Vibration Control of the Axially Moving String in the *s* Domain," ASME JOURNAL OF APPLIED MECHANICS, Vol. 58, pp. 189–196.

Yang, B., and Tan, C. A., 1992, "Transfer Functions of One Dimensional Distributed Parameter Systems," ASME JOURNAL OF APPLIED MECHANICS, Vol. 59, pp. 1009–1014.

Closed-Form Transient Response of Distributed Damped Systems, Part II: Energy Formulation for Constrained and Combined Systems

Bingen Yang
Associate Professor,
Department of Mechanical Engineering,
University of Southern California,
Los Angeles, CA 90089-1453
Mem. ASME.

The transient response analysis presented in Part I is generalized for distributed damped systems which are viscoelastically constrained or combined with lumped parameter systems. An energy formulation is introduced to regain symmetry for the spatial differential operators, which is destroyed in the original equations of motion by the constraints, and the coupling of distributed and lumped elements. As a result, closed-form solution is systematically obtained in eigenfunction series.

1 Introduction

The closed-form solution method given in Part I (Yang, 1996) assumes that the operators D and K are symmetric, which is true for "purely" distributed systems. When a distributed damped system is viscoelastically constrained at discrete points or combined with lumped parameter systems, the operators lose symmetry. Consequently, the closed-form analysis cannot be directly applied to constrained and combined damped systems. Developed in this part is an equivalent augmented formulation in which the generalized or augmented operators retain symmetry in their domain. With this augmented formulation, closed-form solution for the transient response of complex systems is achieved.

It is worth mentioning that generalized or augmented methods for certain *undamped* combined systems have been proposed (Friedman, 1956; Meirovitch, 1967; Ramkrishna and Amundson, 1974; Mote, 1977; Bergman and Nicholson, 1985). In the previous study, orthogonality relations for system eigenfunctions are derived through inclusion of the boundary conjunct that is from the integration of the system governing equations, and as such, closed-form solutions are obtained in modal series. No closed-form solution methods for the transient response of general *damped* constrained and combined systems are available in the literature.

Unlike the existing methods, the augmented formulation proposed in this work is based on the energy functionals of constrained and combined damped systems. These energy functionals are used for three good reasons. First, the functionals serve as guidance for obtaining augmented operators whose symmetry and definiteness are automatically guaranteed by the quadratic form of the functionals. Second, by Hamilton's principle, the functionals conveniently lead to the augmented equations of motion. Third, the functionals naturally give the normalization condition for the augmented eigenfunctions, which is needed for the closed-form transient analysis. These features make the proposed energy formulation systematic and efficient in describing various constraints and coupling of distributed and lumped elements.

Contributed by the Applied Mechanics Division of THE AMERICAN SOCIETY OF MECHANICAL ENGINEERS for publication in the ASME JOURNAL OF APPLIED MECHANICS.

Discussion on this paper should be addressed to the Technical Editor, Professor Lewis T. Wheeler, Department of Mechanical Engineering, University of Houston, Houston, TX 77204-4792, and will be accepted until four months after final publication of the paper itself in the ASME JOURNAL OF APPLIED MECHANICS.

Manuscript received by the ASME Applied Mechanics Division, Nov. 28, 1994; final revision, Aug. 15, 1996. Associate Technical Editor: S. W. Shaw.

2 Energy Formulation and Augmented Operators

A distributed damped system is constrained at point x_c by an attached spring-mass-damper system; see Fig. 1 where the displacement of the lumped mass is identical to $w(x_c, t)$ of the distributed system. The equations of motion of the constrained system are

$$Mw_{,tt}(x, t) + Dw_{,t}(x, t) + Kw(x, t) = f(x, t) - \delta(x - x_c)q_c(t), \quad x \in \Omega \tag{1a}$$

$$\Gamma w(x, t) = 0, \quad x \in \partial\Omega \tag{1b}$$

$$w(x, 0) = a_0(x), \quad w_{,t}(x, t) = b_0(x), \quad x \in \Omega \tag{1c}$$

where $q_c(t)$ is the constraint force, $\delta(x)$ is the Dirac delta, and all other symbols have been defined in Part I (Yang, 1996). The constrained force is described by

$$mw_{,tt}(x_c,t) + d_T w_{,t}(x_c, t) + k_T w(x_c, t) = q_c(t) + q_e(t) \tag{1d}$$

where $q_e(t)$ is the external force applied to the lumped mass (not shown in the figure).

The constraint renders D and K asymmetric; i.e., $\langle Du, v\rangle_{H(\Omega)} \neq \langle u, Dv\rangle_{H(\Omega)}$, and $\langle Ku, v\rangle_{H(\Omega)} \neq \langle u, Kv\rangle_{H(\Omega)}$. As a result, the modal analysis developed in Part I is not directly applicable here. To overcome the difficulty, a new function space whose inner product permits symmetric operators is defined by introducing the following functionals:

$$\Pi_M(u, v) = \langle M^{1/2}u, M^{1/2}v\rangle_{H(\Omega)} + m\bar{u}\cdot v|_{x_c}$$

$$\Pi_D(u, v) = \langle D^{1/2}u, D^{1/2}v\rangle_{H(\Omega)} + d_T\bar{u}\cdot v|_{x_c}$$

$$\Pi_K(u, v) = \langle K^{1/2}u, K^{1/2}v\rangle_{H(\Omega)} + k_T\bar{u}\cdot v|_{x_c} \tag{2}$$

where the inner product $\langle u, v\rangle_{H(\Omega)} = \int_\Omega \bar{u}v dx$ $u, v \in H(\Omega)$, $M^{1/2}M^{1/2} = M$, $D^{1/2}D^{1/2} = D$, and $K^{1/2}K^{1/2} = K$. It is seen that $\Pi_M(w_{,t}, w_{,t})/2$, $\Pi_D(w_{,t}, w_{,t})/2$, and $\Pi_K(w, w)/2$ are the kinetic energy, Rayleigh dissipation function, and potential energy of the constrained system, respectively.

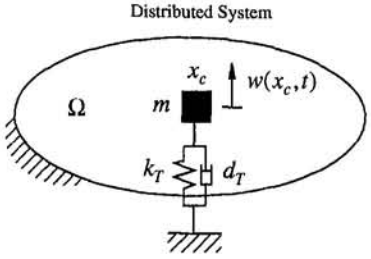

Fig. 1 A distributed damped system subject to a constraint

Integrating the energy functionals by part yields

$$\Pi_M(u, v) = \langle Mu, v\rangle_{H(\Omega)} + m\bar{u}\cdot v|_{x_c}$$

$$\Pi_D(u, v) = \langle Du, v\rangle_{H(\Omega)} + D_T\bar{u}\cdot v|_{x_c} + d_T\bar{u}\cdot v|_{x_c}$$

$$\Pi_K(u, v) = \langle Ku, v\rangle_{H(\Omega)} + K_T\bar{u}\cdot v|_{x_c} + k_T\bar{u}\cdot v|_{x_c} \quad (3)$$

where the operators D_T and K_T describe the jumps of the internal forces at point x_c, and are related to the constraint force by

$$q_c(t) = -D_T w_{,t}(x_c, t) - K_T w(x_c, t). \quad (4)$$

Consider the function space $\mathcal{H} = H(\Omega) \oplus C$, whose element U has the form $U = (u(x) \quad u_1)^T$. The inner product on $\mathcal{H}$ is

$$\langle U, V\rangle_{\mathcal{H}} = \langle u, v\rangle_{H(\Omega)} + \bar{u}_1 v_1, \quad U, V \in \mathcal{H}. \quad (5)$$

Define augmented operators based on (3)

$$\hat{M} = \begin{bmatrix} M & 0 \\ 0 & m \end{bmatrix}, \quad \hat{D} = \begin{bmatrix} D & 0 \\ 0 & D_T + d_T \end{bmatrix},$$

$$\hat{K} = \begin{bmatrix} K & 0 \\ 0 & K_T + k_T \end{bmatrix} \quad (6)$$

with the domain

$$\mathcal{D} \equiv \{U | U = (u(x) \quad u(x_c))^T, u \in H(\Omega)\} \subset \mathcal{H}. \quad (7)$$

It follows that for $\forall U, V \in \mathcal{D}$

$$\Pi_M(u, v) = \langle \hat{M}U, V\rangle_{\mathcal{H}} = \langle U, \hat{M}V\rangle_{\mathcal{H}}$$

$$\Pi_D(u, v) = \langle \hat{D}U, V\rangle_{\mathcal{H}} = \langle U, \hat{D}V\rangle_{\mathcal{H}}$$

$$\Pi_K(u, v) = \langle \hat{K}U, V\rangle_{\mathcal{H}} = \langle U, \hat{K}V\rangle_{\mathcal{H}}. \quad (8)$$

Therefore the augmented operators are symmetric in $\mathcal{D}$ under the inner product defined in (5). Also from (2), $\hat{M}$ and $\hat{K}$ are positive definite, and $\hat{D}$ is positive semi-definite.

With the symmetric augmented operators, the modal analysis developed in Part I is now extended to the constrained system. The system response and external force in the augmented form are $W(x, t) = (w(x, t), w(x_c, t))^T \in \mathcal{D} \times T$, $T = \{t | 0 \le t < \infty\}$, and $F(x, t) = (f(x, t)q_e(t))^T$, respectively. The generalized Hamilton's principle for the constrained system reads

$$\int_{t_1}^{t_2} (\Pi_M(w_{,t}, \delta w_{,t}) - \Pi_K(w, \delta w) - \Pi_D(w_{,t}, \delta w) + \langle F, \delta W\rangle_{\mathcal{H}})dt = 0. \quad (9)$$

By (8), (9), and (1b, c), the augmented equation of motion for the constrained system is

$$\hat{M}W_{,tt}(x, t) + \hat{D}W_{,t}(x, t) + \hat{K}W(x, t) = F(x, t) \quad (10a)$$

with the initial conditions

$$W(x, 0) = U_0(x) = \begin{pmatrix} a_0(x) \\ a_0(x_c) \end{pmatrix},$$

$$W_{,t}(x, 0) = V_0(x) = \begin{pmatrix} b_0(x) \\ b_0(x_c) \end{pmatrix}. \quad (10b)$$

The eigenvalue problem associated with (10a) is

$$\{\lambda_k^2\hat{M} + \lambda_k\hat{D} + \hat{K}\}V_k(x) = 0, \quad V_k \in \mathcal{D}, \quad k = \pm 1, \pm 2, \ldots \quad (11)$$

where $V_k(x) = (v_k(x)v_k(x_c))^T$, and λ_k and $v_k(x)$ are the eigensolutions associated with the original equations of motion, (1) and (4). The normalization condition for V_k, by (22) of Part I, is

$$\langle \bar{V}_k, \hat{M}V_k\rangle_{\mathcal{H}} - \frac{1}{\lambda_k^2}\langle \bar{V}_k, \hat{K}V_k\rangle_{\mathcal{H}} = \Pi_M(\bar{v}_k, v_k) - \frac{1}{\lambda_k^2}\Pi_K(\bar{v}_k, v_k) = 2. \quad (12)$$

Following (27) of Part I, the solution to (10) is

$$W(x, t) = \int_\Omega \{G_{,t}(x, \xi, t)\Xi\hat{M}U_0(\xi) + G(x, \xi, t)\Xi(\hat{M}V_0(\xi) + \hat{D}U_0(\xi))\}d\xi + \int_0^t\int_\Omega G(x, \xi, t - \tau)\Xi F(\xi, \tau)d\xi d\tau \quad (13)$$

where $\Xi = \text{diag}\{1 \quad \delta(x - x_c)\}$, and

$$G(x, \xi, t) = \frac{1}{2}\sum_{k=\pm 1}^{\pm\infty}\frac{1}{\lambda_k}e^{\lambda_k t}V_k(x)V_k^T(\xi) = \frac{1}{2}\sum_{k=\pm 1}^{\pm\infty}\frac{1}{\lambda_k}e^{\lambda_k t}\begin{bmatrix} v_k(x)v_k(\xi) & v_k(x)v_k(x_c) \\ v_k(x_c)v_k(\xi) & v_k(x_c)v_k(x_c) \end{bmatrix}. \quad (14)$$

The legitimacy and convergence of the above eigenfunction expansion can be proven following Section 6 of Part I. Thus, the displacement of the constrained system is given by

$$w(x, t) = \int_\Omega \{g_{,tt}(x, \xi, t)Ma_0(\xi) + g(x, \xi, t)[Mb_0(\xi) + Da_0(\xi)]\}d\xi + g_{,t}(x, x_c, t)ma_0(x_c) + g(x, x_c, t)[mb_0(x_c) + (D_T + d_T)a_0(x_c)] + \int_0^t\int_\Omega g(x, \xi, t - \tau)f(\xi, \tau)d\xi d\tau + \int_0^t g(x, x_c, t - \tau)q_e(\tau)d\tau \quad (15)$$

where the Green's function

$$g(x, \xi, t) = \frac{1}{2}\sum_{k=\pm 1}^{\pm\infty}\frac{1}{\lambda_k}e^{\lambda_k t}v_k(x)v_k(\xi), \quad x, \xi \in \Omega. \quad (16)$$

Equation (16) has the same form as (28) in Part I although the two systems are different. This means that the energy formulation is valid for general distributed systems. In other words, given a damped system, either purely distributed or constrained, one only needs to derive proper operators based on the energy functionals; the eigenfunction normalization, the integral representation of the system response, and the modal expansion of the system Green's function have the same form as (12), (15), and (16).

In summary, the proposed energy formulation takes three major steps: (i) derive the energy functionals Π_M, Π_D, and Π_K; (ii) define symmetric, augmented operators based on the functionals; and (iii) apply the modal analysis developed in Part I to derive the eigenfunction expansion of the system response.

3 Energy Functionals for Other Constrained Systems

The energy formulation is applied to distributed damped systems with other types of constraints. In Fig. 2 is a distributed damped system with a rotational constraint at point x_c, where I_R, d_R, and k_R are the rotational inertia, damping, and spring parameters, respectively, and η is a unit directional vector describing the orientation of the constraint. The energy functionals for such a constrained system are

$$\Pi_M(u, v) = \langle M^{1/2}u, M^{1/2}v\rangle_{H(\Omega)} + I_R \frac{\partial \bar{u}}{\partial \eta}\cdot\frac{\partial v}{\partial \eta}\bigg|_{x_c}$$

$$\Pi_D(u, v) = \langle D^{1/2}u, D^{1/2}v\rangle_{H(\Omega)} + d_R \frac{\partial \bar{u}}{\partial \eta}\cdot\frac{\partial v}{\partial \eta}\bigg|_{x_c}$$

$$\Pi_K(u, v) = \langle K^{1/2}u, K^{1/2}v\rangle_{H(\Omega)} + k_R \frac{\partial \bar{u}}{\partial \eta}\cdot\frac{\partial v}{\partial \eta}\bigg|_{x_c}. \quad (17)$$

where $\partial u/\partial\eta$ is the directional derivative of u in the direction η. For an n-dimensional region Ω, $x = (x_1, \ldots, x_n)$, $\eta = (\eta_1, \ldots, \eta_n)$, and $\partial/\partial\eta = \sum_{j=1}^{n} \eta_j \partial/\partial x_j$. Through integration of (17) by part, the augmented operators are found as

$$\hat{M} = \begin{bmatrix} M & 0 \\ 0 & I_R \end{bmatrix}, \quad \hat{D} = \begin{bmatrix} D & 0 \\ 0 & D_R + d_R \end{bmatrix},$$

$$\hat{K} = \begin{bmatrix} K & 0 \\ 0 & K_R + k_R \end{bmatrix} \quad (18)$$

with the domain $\mathcal{D} \equiv \{U | U = (u(x)\partial u(x_c)/\partial\eta)^T, u \in H(\Omega)\} \subset \mathcal{H} = H(\Omega) \oplus R$. The operators D_R and K_R describe the jumps of the internal forces at x_c, and are in the relation

$$\tau_c(t) = -\frac{\partial}{\partial \eta}(D_R w_{,t}(x_c, t) + K_R w(x_c, t))$$

where $\tau_c(t)$ is the constraint torque at x_c. The Green's function formula for the constrained system can be obtained following the steps in the previous section, and therefore is omitted.

Now consider a distributed system subject to both translational and rotational constraints at n_c points $x_1, x_2, \ldots, x_{n_c}$, with the parameters (m_j, d_{Tj}, k_{Tj}) and $(I_{Rj}, d_{Rj}, k_{Rj}, \eta^{(j)})$, $j = 1, 2, \ldots, n_c$, where $\eta^{(j)}$ is the unit directional vector of the jth rotational constraint. The energy functionals of the constrained system are written as

$$\Pi_M(u, v) = \langle M^{1/2}u, M^{1/2}v\rangle_{H(\Omega)} + \sum_{j=1}^{n_c}\left(m_j \bar{u}\cdot v + I_{Rj}\frac{\partial \bar{u}}{\partial \eta^{(j)}}\cdot\frac{\partial v}{\partial \eta^{(j)}}\right)\bigg|_{x_j}$$

$$\Pi_D(u, v) = \langle D^{1/2}u, D^{1/2}v\rangle_{H(\Omega)} + \sum_{j=1}^{n_c}\left(d_{Tj} \bar{u}\cdot v + d_{Rj}\frac{\partial \bar{u}}{\partial \eta^{(j)}}\cdot\frac{\partial v}{\partial \eta^{(j)}}\right)\bigg|_{x_j}$$

$$\Pi_K(u, v) = \langle K^{1/2}u, K^{1/2}v\rangle_{H(\Omega)} + \sum_{j=1}^{n_c}\left(k_{Tj} \bar{u}\cdot w + k_{Rj}\frac{\partial \bar{u}}{\partial \eta^{(j)}}\cdot\frac{\partial v}{\partial \eta^{(j)}}\right)\bigg|_{x_j}. \quad (19)$$

The function space for the augmented formulism is $\mathcal{H} = H(\Omega) \oplus C^{2n_c}$ with the inner product defined by

$$\langle U, V\rangle_{\mathcal{H}} = \langle u, v\rangle_{H(\Omega)} + \sum_{j=1}^{2n_c} \bar{u}_j v_j, \quad U, V \in \mathcal{H} \quad (20)$$

where any element U of $\mathcal{H}$ has the form $U = (u(x)\ u_1 \ldots u_{2n_c})^T$. The augmented operators are

$$\hat{M} = \text{diag}\{M \quad m_1 \quad I_{R1} \ldots m_{n_c} \quad I_{Rn_c}\}$$

$$\hat{D} = \text{diag}\{D \quad D_{T1} + d_{T1} \quad D_{R1} + d_{R1} \ldots D_{Tn_c} + d_{Tn_c} \quad D_{Rn_c} + d_{Rn_c}\}$$

$$\hat{K} = \text{diag}\{K \quad K_{T1} + k_{T1} \quad K_{R1} + k_{R1} \ldots K_{Tn_c} + k_{Tn_c} \quad K_{Rn_c} + k_{Rn_c}\} \quad (21)$$

with the domain

$$\mathcal{D} \equiv \{U | U = (u(x) \quad u(x_1) \quad \partial u(x_1)/\partial\eta^{(1)} \ldots u(x_{n_c}) \quad \partial u(x_{n_c})/\partial\eta^{(n_c)})^T, u \in H(\Omega)\}.$$

Here the operators D_{Tj}, D_{Rj}, K_{Tj}, and K_{Rj} characterize the jumps of the internal forces at x_j. The symmetry of the augmented operators is automatically guaranteed by the quadratic form of the energy functionals. The Green's function formula can be derived following Eqs. (9) to (16).

The energy formulation is also applicable to distributed systems subject to viscoelastic constraints on a curve or in a subregion. The energy functionals in these cases are

$$\Pi_M(u, v) = \langle M^{1/2}u, M^{1/2}v\rangle_{H(\Omega)}$$

$$\Pi_D(u, v) = \langle D^{1/2}u, D^{1/2}v\rangle_{H(\Omega)} + \int_{\sigma_c} d(x)\bar{u}(x)v(x)dx$$

$$\Pi_K(u, v) = \langle K^{1/2}u, K^{1/2}v\rangle_{H(\Omega)} + \int_{\sigma_c} k(x)\bar{u}(x)v(x)dx$$

where $\sigma_c \subset \Omega$ is either a curve or a subregion, and $d(x)$ and $k(x)$ are the damping and stiffness distributions of the constraint. The Green's function formula can be similarly derived.

The energy formulation is illustrated on an Euler-Bernoulli beam subject to both translational and rotational constraints at

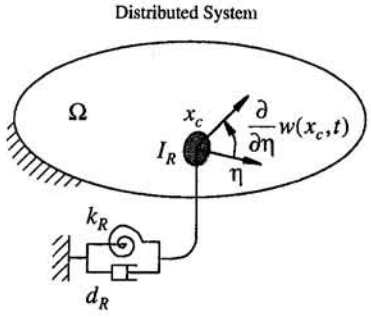

Fig. 2 A distributed damped system subject to a rotational constraint

point x_c; see Fig. 3. The displacement $w(x, t)$ of the constrained beam is governed by

$$\rho w_{,tt} + d_v w_{,t} + (d_h w_{,xxt})_{,xx} + (EIw_{,xx})_{,xx} = f(x, t) - q_c(t)\delta(x - x_c) + \tau_c(t)\frac{\partial}{\partial x}\delta(x - x_c) \quad (22)$$

where d_v and d_h are the viscous and material damping coefficients, respectively, and $q_c(t)$ and $\tau_c(t)$ are the constraint force and torque. The energy functionals for the beam are

$$\Pi_M(u, v) = \int_0^L \rho\bar{u}\bar{v}dx + m\bar{u}\cdot v|_{x_c} + I\bar{u}_{,x}\cdot v_{,x}|_{x_c}$$

$$\Pi_D(u, v) = \int_0^L (d_v\bar{u}\bar{v} + d_h\bar{u}_{,xx}v_{,xx})dx + d_T\bar{u}\cdot v|_{x_c} + d_R\bar{u}_{,x}\cdot v_{,x}|_{x_c}$$

$$\Pi_K(u, v) = \int_0^L EI\bar{u}_{,xx}v_{,xx}dx + k_T\bar{u}\cdot v|_{x_c} + k_R\bar{u}_{,x}\cdot v_{,x}|_{x_c}. \quad (23)$$

Integrating Π_D and Π_K by part gives

$$\Pi_D(u, v) = \int_0^L (d_v\bar{u} + (d_h\bar{u}_{,xx})_{,xx})vdx + (D_T\bar{u} + d_T\bar{u})\cdot v|_{x_c} + (D_R\bar{u}_{,x} + d_R\bar{u}_{,x})\cdot v_{,x}|_{x_c}$$

$$\Pi_K(u, v) = \int_0^L (EI\bar{u}_{,xx})_{,xx}vdx + (K_T\bar{u} + k_T\bar{u})\cdot v|_{x_c} + (K_R\bar{u}_{,x} + k_R\bar{u}_{,x})\cdot v_{,x}|_{x_c} \quad (24)$$

where

$$D_T\bar{u} = [(d_h\bar{u}_{,xx})_{,x}]_{x_c-}^{x_c+}, \quad D_R\bar{u}_{,x} = -[d_h\bar{u}_{,xx}]_{x_c-}^{x_c+}$$

$$K_T\bar{u} = [(EI\bar{u}_{,xx})_{,x}]_{x_c-}^{x_c+}, \quad K_R\bar{u}_{,x} = -[EI\bar{u}_{,xx}]_{x_c-}^{x_c+} \quad (25)$$

with $[\alpha(x)]_{x_c-}^{x_c+} = \alpha(x_c+) - \alpha(x_c-)$ describing the jump of $\alpha(x)$ at x_c. The operators D_T, et al. are related to the constraint force and torque by

$$q_c(t) = -D_T w_{,t}(x_c, t) - K_T w(x_c, t),$$

$$\tau_c(t) = -D_R w_{,xt}(x_c, t) - K_R w_{,x}(x_c, t).$$

The augmented function space is $\mathcal{H} = H([0, L]) \oplus C^2$ with the inner product $\langle U, V\rangle_{\mathcal{H}} = \int_0^L \bar{u}vdx + \bar{u}_1v_1 + \bar{u}_2v_2$. The augmented operators, by (23) and (24), are

$$\hat{M} = \text{diag}\{\rho \quad m \quad I\}$$

$$\hat{D} = \text{diag}\left\{d_v + \frac{\partial^2}{\partial x^2}\left(d_h\frac{\partial^2}{\partial x^2}\right) \quad D_T + d_T \quad D_R + d_R\right\}$$

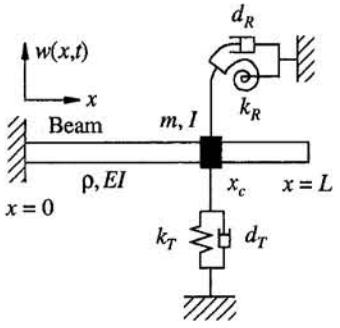

Fig. 3 A constrained Euler-Bernoulli beam

$$\hat{K} = \text{diag}\left\{\frac{\partial^2}{\partial x^2}\left(EI\frac{\partial^2}{\partial x^2}\right) \quad K_T + k_T \quad K_R + k_R\right\} \quad (26)$$

with the domain $\mathcal{D} \equiv \{U | U = (u(x)\ u(x_c)\ u_{,x}(x_c))^T, u \in H([0, L])\}$. The augmented equation of motion takes the form (10a) with $F(x, t) = (f(x, t)\ q_e(t)\ \tau_e(t))^T$. The normalization conditions for the system eigensolutions (λ_k and $v_k(x)$) is

$$\int_0^L \rho v_k^2 dx + (mv_k^2 + Iv_{k,x}^2)|_{x_c} - \frac{1}{\lambda_k^2}\left\{\int_0^L EIv_{k,xx}^2 dx + (k_T v_k^2 + k_R v_{k,x}^2)|_{x_c}\right\} = 2. \quad (27)$$

Following Eqs. (13) to (15), the response of the constrained beam is expressed by

$$\begin{aligned} w(x, t) = \int_0^L & \{g_{,t}(x, \xi, t)\rho a_0(\xi) \\ & + g(x, \xi, t)[\rho b_0(\xi) + d_v a_0(\xi) + (d_h a_{0,\xi\xi}(\xi))_{,\xi\xi}]\}d\xi \\ & + g_{,t}(x, x_c, t)ma_0(x_c) + g(x, x_c, t)[mb_0(x_c) \\ & + (D_T + d_T)a_0(x_c)] + g_{,\xi t}(x, x_c, t)Ia_0(x_c) \\ & + g_{,\xi}(x, x_c, t)[Ib_{0,x}(x_c) + (D_R + d_R)a_{0,x}(x_c)] \\ & + \int_0^t\int_\Omega g(x, \xi, t - \tau)f(\xi, \tau)d\xi d\tau \\ & + \int_0^t g(x, x_c, t - \tau)q_e(\tau)d\tau \\ & + \int_0^t g_{,\xi}(x, x_c, t - \tau)\tau_e(\tau)d\tau \end{aligned} \quad (28)$$

where $(\ )_{,\xi} = \partial(\ )/\partial\xi$, and the Green's function has the form (16).

4 Combined Systems

A Combination of a Distributed System and a Lumped System. Shown in Fig. 4(a) is a schematic of viscoelastic connection of a distributed damped system and a lumped system, where the connecting points of the lumped system are $y_1, \ldots, y_r$, and those of the distributed system are $x_1, \ldots, x_r$. The lumped system also has p other points $z_1, \ldots, z_p$ that are not connected to the distributed system. The displacement $w(x, t)$ of the damped system is described by

$$Mw_{,tt}(x, t) + Dw_{,t}(x, t) + Kw(x, t) = f(x, t) - \sum_{j=1}^{r}\delta(x - x_j)q_{cj}(t), \quad x \in \Omega \quad (29)$$

where $q_{cj}(t)$ are the constraint force at point x_j due to the connection. The equation of motion for the lumped system is

$$\left[\mathbf{M}_L\frac{d^2}{dt^2} + \mathbf{D}_L\frac{d}{dt} + \mathbf{K}_L\right]\begin{pmatrix}\boldsymbol{\alpha}(t)\\ \boldsymbol{\beta}(t)\end{pmatrix} = \begin{pmatrix}\mathbf{q}_c(t) + \mathbf{f}_\alpha(t)\\ \mathbf{f}_\beta(t)\end{pmatrix} \quad (30)$$

where $\boldsymbol{\alpha}(t) \in R^r$ and $\boldsymbol{\beta}(t) \in R^p$ are the vectors of displacements at points $y_1, \ldots, y_r$ and $z_1, \ldots, z_p$, respectively, $\mathbf{f}_\alpha(t)$ and $\mathbf{f}_\beta(t)$ are the external force vectors, and $q_c(t) = (q_{c1}(t) \ldots q_{cr}(t))^T$ is the constraint force vector. Assume that $\mathbf{M}_L = \mathbf{M}_L^T > 0$, $\mathbf{D}_L = \mathbf{D}_L^T \geq 0$, $\mathbf{K}_L = \mathbf{K}_L^T \geq 0$. The lumped system itself may be nonproportionally damped. The constraint forces are in the form

$$\mathbf{q}_c(t) = \mathbf{D}_c(\dot{\mathbf{w}}_c(t) - \dot{\boldsymbol{\alpha}}(t)) + \mathbf{K}_c(\mathbf{w}_c(t) - \boldsymbol{\alpha}(t)) \quad (31)$$

where $\mathbf{w}_c(t) = (w(x_1, t) \ldots w(x_r, t))^T \in R^r$, and $\mathbf{D}_c$ and $\mathbf{K}_c$ are two symmetric, positive semi-definite matrices describing the connection.

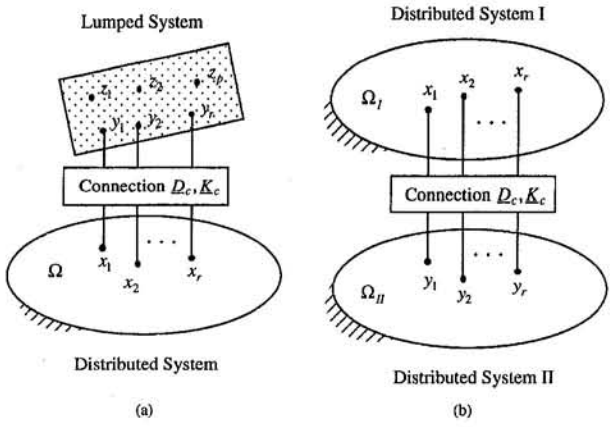

Fig. 4 Multipoint viscoelastic connection of (a) a distributed system and a lumped system; (b) two distributed systems

The energy functionals for the combined system are of the form

$$\Pi_M(u, v; \boldsymbol{\phi}, \boldsymbol{\psi}) = \langle M^{1/2}u, M^{1/2}v\rangle_{H(\Omega)} + \boldsymbol{\phi}^*\mathbf{M}_L\boldsymbol{\psi}$$

$$\Pi_D(u, v; \boldsymbol{\phi}, \boldsymbol{\psi}) = \langle D^{1/2}u, D^{1/2}v\rangle_{H(\Omega)} + \boldsymbol{\phi}^*\mathbf{D}_L\boldsymbol{\psi} + (\mathbf{u}_c - \boldsymbol{\phi}_\alpha)^*\mathbf{D}_c(\mathbf{v}_c - \boldsymbol{\psi}_\alpha)$$

$$\Pi_K(u, v; \boldsymbol{\phi}, \boldsymbol{\psi}) = \langle K^{1/2}u, K^{1/2}\mathbf{v}\rangle_{H(\Omega)} + \boldsymbol{\phi}^*\mathbf{K}_L\boldsymbol{\psi} + (\mathbf{u}_c - \boldsymbol{\phi}_\alpha)^*\mathbf{K}_c(\mathbf{v}_c - \boldsymbol{\psi}_\alpha) \quad (32)$$

where $u, v \in H(\Omega)$, $\mathbf{u}_c = (u(x_1) \ldots u(x_r))^T$, $\mathbf{v}_c = (v(x_1) \ldots v(x_r))^T$, $\boldsymbol{\phi}^* = \bar{\boldsymbol{\phi}}^T$, and

$$\boldsymbol{\phi} = \begin{pmatrix}\boldsymbol{\phi}_\alpha \\ \boldsymbol{\phi}_\beta\end{pmatrix}, \quad \boldsymbol{\psi} = \begin{pmatrix}\boldsymbol{\psi}_\alpha \\ \boldsymbol{\psi}_\beta\end{pmatrix}; \quad \boldsymbol{\phi}_\alpha, \boldsymbol{\psi}_\alpha \in C^r, \quad \boldsymbol{\phi}_\beta, \boldsymbol{\psi}_\beta \in C^p.$$

The kinetic energy, Rayleigh dissipation function, and potential energy of the combined system are represented by $\Pi_M(w_t, w_t; \dot{\boldsymbol{\chi}}, \dot{\boldsymbol{\chi}})/2$, $\Pi_D(w_t, w_t; \dot{\boldsymbol{\chi}}, \dot{\boldsymbol{\chi}})/2$, and $\Pi_K(w, w; \boldsymbol{\chi}, \boldsymbol{\chi})/2$, respectively, where $\boldsymbol{\chi}(t) = (\boldsymbol{\alpha}^T(t) \quad \boldsymbol{\beta}^T(t))^T$.

Integrating of the functionals Π_D and Π_K by part gives

$$\Pi_D(u, v; \boldsymbol{\phi}, \boldsymbol{\psi}) = \langle Du, v\rangle_{H(\Omega)} + (\mathbf{D}_T\mathbf{u}_c)^*\mathbf{v}_c + \boldsymbol{\phi}^*\mathbf{D}_L\boldsymbol{\psi} + (\mathbf{u}_c - \boldsymbol{\phi}_\alpha)^*\mathbf{D}_c(\mathbf{v}_c - \boldsymbol{\psi}_\alpha)$$

$$\Pi_K(u, v; \boldsymbol{\phi}, \boldsymbol{\psi}) = \langle Ku, v\rangle_{H(\Omega)} + (\mathbf{K}_T\mathbf{u}_c)^*\mathbf{v}_c + \boldsymbol{\phi}^*\mathbf{K}_L\boldsymbol{\psi} + (\mathbf{u}_c - \boldsymbol{\phi}_\alpha)^*\mathbf{K}_c(\mathbf{v}_c - \boldsymbol{\psi}_\alpha) \quad (33)$$

where $\mathbf{D}_T$ and $\mathbf{K}_T$ are matrix differential operators presenting the jumps of the internal forces of the distributed system at the connecting points $x_1, \ldots, x_r$, due to the viscoelastic connection. Define the function space

$$\mathcal{H} = \{U | U = (u(x)\mathbf{u}^T)^T, \quad u(x) \in H(\Omega), \quad \mathbf{u} \in C^{2r+p}\} \quad (34)$$

with the inner product $\langle U, V\rangle_{\mathcal{H}} = \langle u, v\rangle_{H(\Omega)} + \mathbf{u}^*v$, $U, V \in \mathcal{H}$. Partition the parameter matrices of the lumped system corresponding to the displacement vectors $\boldsymbol{\alpha}(t)$ and $\boldsymbol{\beta}(t)$:

$$\mathbf{M}_L = \begin{bmatrix}\mathbf{M}_L^{\alpha\alpha} & \mathbf{M}_L^{\alpha\beta} \\ \mathbf{M}_L^{\beta\alpha} & \mathbf{M}_L^{\beta\beta}\end{bmatrix}, \quad \mathbf{D}_L = \begin{bmatrix}\mathbf{D}_L^{\alpha\alpha} & \mathbf{D}_L^{\alpha\beta} \\ \mathbf{D}_L^{\beta\alpha} & \mathbf{D}_L^{\beta\beta}\end{bmatrix},$$

$$\mathbf{K}_L = \begin{bmatrix}\mathbf{K}_L^{\alpha\alpha} & \mathbf{K}_L^{\alpha\beta} \\ \mathbf{K}_L^{\beta\alpha} & \mathbf{K}_L^{\beta\beta}\end{bmatrix}. \quad (35)$$

With (32), (33), and (35), the augmented operators are obtained as

$$\hat{M} = \begin{bmatrix} M & 0 & 0 & 0 \\ 0 & 0 & 0 & 0 \\ 0 & 0 & \mathbf{M}_L^{\alpha\alpha} & \mathbf{M}_L^{\alpha\beta} \\ 0 & 0 & \mathbf{M}_L^{\beta\alpha} & \mathbf{M}_L^{\beta\beta} \end{bmatrix},$$

$$\hat{D} = \begin{bmatrix} D & 0 & 0 & 0 \\ 0 & \mathbf{D}_T + \mathbf{D}_c & -\mathbf{D}_c & 0 \\ 0 & -\mathbf{D}_c & \mathbf{D}_L^{\alpha\alpha} + \mathbf{D}_c & \mathbf{D}_L^{\alpha\beta} \\ 0 & 0 & \mathbf{D}_L^{\beta\alpha} & \mathbf{D}_L^{\beta\beta} \end{bmatrix}$$

$$\hat{K} = \begin{bmatrix} K & 0 & 0 & 0 \\ 0 & \mathbf{K}_T + \mathbf{K}_c & -\mathbf{K}_c & 0 \\ 0 & -\mathbf{K}_c & \mathbf{K}_L^{\alpha\alpha} + \mathbf{K}_c & \mathbf{K}_L^{\alpha\beta} \\ 0 & 0 & \mathbf{K}_L^{\beta\alpha} & \mathbf{K}_L^{\beta\beta} \end{bmatrix}. \quad (36)$$

The domain of the operators is defined by

$$\mathcal{D} = \{U | U = (u(x)u(x_1) \ldots u(x_r)\mathbf{u}^T)^T, \quad u(x) \in H(\Omega), \quad \mathbf{u} \in C^{r+p}\} \subset \mathcal{H}.$$

It is easy to see that the augmented operators are symmetric in $\mathcal{D}$; i.e., for any $U, V \in \mathcal{D}$

$$\Pi_M(u, v; \mathbf{u}, \mathbf{v}) = \langle \hat{M}U, V\rangle_{\mathcal{H}} = \langle U, \hat{M}V\rangle_{\mathcal{H}}$$

$$\Pi_D(u, v; \mathbf{u}, \mathbf{v}) = \langle \hat{D}U, V\rangle_{\mathcal{H}} = \langle U, \hat{D}V\rangle_{\mathcal{H}}$$

$$\Pi_K(u, v; \mathbf{u}, \mathbf{v}) = \langle \hat{K}U, V\rangle_{\mathcal{H}} = \langle U, \hat{K}V\rangle_{\mathcal{H}}. \quad (37)$$

With the energy functionals, the original equations of motion of the combined system are cast into the augmented form (10*a*) with

$$W(x, t) = (w(x, t)\mathbf{w}_c^T(t)\boldsymbol{\alpha}^T(t)\boldsymbol{\beta}^T(t))^T,$$

$$F(x, t) = (f(x, t) \quad \mathbf{0}^T \quad \mathbf{f}_\alpha^T(t) \quad \mathbf{f}_\beta^T(t))^T \quad (38)$$

where $\mathbf{w}_c(t)$ has been given in (31). Let the kth eigenvalue of the combined system be λ_k, and the corresponding mode shape distributions of the distributed and lumped systems be $v_k(x)$ and $\boldsymbol{\chi}_k = (\boldsymbol{\alpha}_k^T\boldsymbol{\beta}_k^T)^T$, respectively. The eigenvalue problem in the augmented form is described by (11) with the augmented eigenfunctions expressed by

$$V_k(x) = (v_k(x) \quad (\mathbf{v}_k^c)^T \quad \boldsymbol{\alpha}_k^T \quad \boldsymbol{\beta}_k^T)^T \quad (39)$$

where the vector $\mathbf{v}_k^c = (v_k(x_1) \ldots v_k(x_r))^T \in C^r$. The eigenfunctions are normalized by

$$\langle M^{1/2}\bar{v}_k, M^{1/2}v_k\rangle_{H(\Omega)} + \boldsymbol{\chi}_k^T\mathbf{M}_L\boldsymbol{\chi}_k - \frac{1}{\lambda_k^2}\{\langle K^{1/2}\bar{v}_k, K^{1/2}v_k\rangle_{H(\Omega)} + \boldsymbol{\chi}_k^T\mathbf{K}_L\boldsymbol{\chi}_k + (\mathbf{v}_k^c - \boldsymbol{\alpha}_k)^T\mathbf{K}_c(\mathbf{v}_k^c - \boldsymbol{\alpha}_k)\} = 2. \quad (40)$$

Let the initial conditions of the combined system be

Distributed system:

$$w(x, 0) = u_0(x), \quad w_{,t}(x, 0) = v_0(x)$$

Lumped system:

$$\boldsymbol{\alpha}(0) = \boldsymbol{\alpha}_0, \quad \dot{\boldsymbol{\alpha}}(0) = \dot{\boldsymbol{\alpha}}_0, \quad \boldsymbol{\beta}(0) = \boldsymbol{\beta}_0, \quad \dot{\boldsymbol{\beta}}(0) = \dot{\boldsymbol{\beta}}_0. \quad (41)$$

Substituting (36), (38), and (39) into (13) yields the response of the combined system

$$\begin{pmatrix} w(x,t) \\ \boldsymbol{\alpha}(t) \\ \boldsymbol{\beta}(t) \end{pmatrix} = \int_0^t \int_\Omega \begin{pmatrix} g^{ww}(x,\xi,t-\tau) \\ g^{\alpha w}(\xi,t-\tau) \\ g^{\beta w}(\xi,t-\tau) \end{pmatrix} f(\xi,\tau)\,d\xi\,d\tau$$

$$+ \int_0^t \begin{bmatrix} g^{w\alpha}(x,t-\tau) & g^{w\beta}(x,t-\tau) \\ g^{\alpha\alpha}(t-\tau) & g^{\alpha\beta}(t-\tau) \\ g^{\beta\alpha}(t-\tau) & g^{\beta\beta}(t-\tau) \end{bmatrix} \begin{pmatrix} \mathbf{f}_\alpha(\tau) \\ \mathbf{f}_\beta(\tau) \end{pmatrix} d\tau$$

$$+ \int_\Omega \left\{ \frac{\partial}{\partial t} \begin{pmatrix} g^{ww}(x,\xi,t) \\ g^{\alpha w}(\xi,t) \\ g^{\beta w}(\xi,t) \end{pmatrix} M u_0(\xi) + \begin{pmatrix} g^{ww}(x,\xi,t) \\ g^{\alpha w}(\xi,t) \\ g^{\beta w}(\xi,t) \end{pmatrix} (M v_0(\xi) + D u_0(\xi)) \right\} d\xi$$

$$+ \frac{\partial}{\partial t} \begin{bmatrix} g^{w\alpha}(x,t) & g^{w\beta}(x,t) \\ g^{\alpha\alpha}(t) & g^{\alpha\beta}(t) \\ g^{\beta\alpha}(t) & g^{\beta\beta}(t) \end{bmatrix} \mathbf{M}_L \begin{pmatrix} \boldsymbol{\alpha}_0 \\ \boldsymbol{\beta}_0 \end{pmatrix}$$

$$+ \begin{bmatrix} g^{w\alpha}(x,t) & g^{w\beta}(x,t) \\ g^{\alpha\alpha}(t) & g^{\alpha\beta}(t) \\ g^{\beta\alpha}(t) & g^{\beta\beta}(t) \end{bmatrix} \left\{ \mathbf{M}_L \begin{pmatrix} \dot{\boldsymbol{\alpha}}_0 \\ \dot{\boldsymbol{\beta}}_0 \end{pmatrix} + \mathbf{D}_L \begin{pmatrix} \boldsymbol{\alpha}_0 \\ \boldsymbol{\beta}_0 \end{pmatrix} \right\}$$

$$+ \begin{bmatrix} g^{wc}(x,t) & g^{w\alpha}(x,t) \\ g^{\alpha c}(t) & g^{\alpha\alpha}(t) \\ g^{\beta c}(t) & g^{\beta\alpha}(t) \end{bmatrix} \begin{bmatrix} \mathbf{D}_T + \mathbf{D}_c & -\mathbf{D}_c \\ -\mathbf{D}_c & \mathbf{D}_c \end{bmatrix} \begin{pmatrix} \mathbf{u}_0^c \\ \boldsymbol{\alpha}_0 \end{pmatrix} \quad (42)$$

where the vector $\mathbf{u}_0^c = (u_0(x_1) \ldots u_0(x_r))^T$, and the Green's functions are given by

$$\begin{bmatrix} g^{ww}(x,\xi,t) & g^{wc}(x,t) & g^{w\alpha}(x,t) & g^{w\beta}(x,t) \\ g^{\alpha w}(\xi,t) & g^{\alpha c}(t) & g^{\alpha\alpha}(t) & g^{\alpha\beta}(t) \\ g^{\beta w}(\xi,t) & g^{\beta c}(t) & g^{\beta\alpha}(t) & g^{\beta\beta}(t) \end{bmatrix}$$

$$= \tfrac{1}{2} \sum_{k\pm1}^{\pm\infty} e^{\lambda_k t} \begin{pmatrix} v_k(x) \\ \boldsymbol{\alpha}_k \\ \boldsymbol{\beta}_k \end{pmatrix} (v_k(\xi) \quad (\mathbf{v}_k^c)^T \quad \boldsymbol{\alpha}_k^T \quad \boldsymbol{\beta}_k^T). \quad (43)$$

On the right-hand side of (42), the first line describes the system response due to the external loads, the second and third lines represent the contributions of the initial disturbances applied to the distributed and lumped systems, and the last line is about the effects of the initial motion at those connecting points on the transient response of the combined system.

B Examples. In employing the above energy formulation, one does not need to know the original equations of motion. By Hamilton's principle, the energy functionals will eventually lead to the augmented form (10*a*). This advantage of the proposed method is shown in the following two examples.

Example 1. For the combined beam-oscillator system shown in Fig. 5(*a*), the energy functionals are

$$\Pi_M(u, v; \phi, \psi) = \int_0^L \rho \bar{u} \bar{v} dx + \phi^* \begin{bmatrix} m_1 & 0 \\ 0 & m_2 \end{bmatrix} \psi$$

$$\Pi_D(u, v; \phi, \psi) = \int_0^L (d_v \bar{u} \bar{v} + d_h \bar{u}_{,xx} v_{,xx}) dx,$$

$$+ \phi^* \begin{bmatrix} d_2 & -d_2 \\ -d_2 & d_2 \end{bmatrix} \psi + d_1(\bar{u}(x_c) - \bar{\phi}_\alpha)(v(x_c) - \psi_\alpha)$$

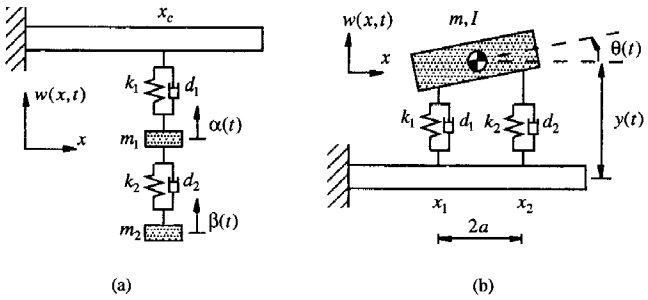

Fig. 5 The Euler-Bernoulli beam combined with (*a*) an oscillator; and (*b*) a rigid body

$$\Pi_K(u, v; \phi, \psi) = \int_0^L EI \bar{u}_{,xx} v_{,xx} dx + \phi^* \begin{bmatrix} k_2 & -k_2 \\ -k_2 & k_2 \end{bmatrix} \psi$$

$$+ k_1(\bar{u}(x_c) - \bar{\phi}_\alpha)(v(x_c) - \psi_\alpha)$$

where d_v and d_h are the viscous and material damping coefficients, and $\phi = (\phi_\alpha \quad \phi_\beta)^T$, $\psi = (\psi_\alpha \quad \psi_\beta)^T \in C^2$. Integrating the functionals by part yields the augmented symmetric operators

$$\hat{M} = \text{diag}\,(\rho \quad 0 \quad m_1 \quad m_2)$$

$$\hat{D} = \begin{bmatrix} d_v + \dfrac{\partial^2}{\partial x^2}\left(d_h \dfrac{\partial^2}{\partial x^2}\right) & 0 & 0 & 0 \\ 0 & D_T + d_1 & -d_1 & 0 \\ 0 & -d_1 & d_1 + d_2 & -d_2 \\ 0 & 0 & -d_2 & d_2 \end{bmatrix},$$

$$\hat{K} = \begin{bmatrix} \dfrac{\partial^2}{\partial x^2}\left(EI \dfrac{\partial^2}{\partial x^2}\right) & 0 & 0 & 0 \\ 0 & K_T + k_1 & -k_1 & 0 \\ 0 & -k_1 & k_1 + k_2 & -k_2 \\ 0 & 0 & -k_2 & k_2 \end{bmatrix}$$

with the domain $\mathcal{D} = \{U | U = (u(x) \quad u(x_c) \quad u^T)^T, u(x) \in H([0, L]), u \in C^2\}$, where D_T and K_T are given in (25). The augmented equation of motion is (10*a*) with $W(x,t) = (w(x,t) \; w(x_c,t) \quad \alpha(t) \quad \beta(t))^T$. The corresponding Green's function formula and the modal expansion of the Green's functions can be obtained based on (42) and (43).

Example 2. In Fig. 5(*b*) a rigid body is viscoelastically mounted on a beam. The energy functionals of the combined system are given by

$$\Pi_M(u, v; \phi, \psi) = \int_0^L \rho \bar{u} \bar{v} dx + \frac{1}{4} m(\bar{\phi}_1 + \bar{\phi}_2)(\psi_1 + \psi_2)$$

$$+ \frac{1}{4a^2} I(\bar{\phi}_1 - \bar{\phi}_2)(\psi_1 - \psi_2)$$

$$\Pi_D(u, v; \phi, \psi) = \int_0^L (d_v \bar{u} \bar{v} + d_h \bar{u}_{,xx} v_{,xx}) dx$$

$$+ d_1(\bar{u}(x_1) - \bar{\phi}_1)(v(x_1) - \psi_1)$$

$$+ d_2(\bar{u}(x_2) - \bar{\phi}_2)(v(x_2) - \psi_2)$$

$$\Pi_K(u, v; \phi, \psi) = \int_0^L EI \bar{u}_{,xx} v_{,xx} dx + k_1(\bar{u}(x_1) - \bar{\phi}_1)$$

$$\times (v(x_1) - \psi_1) + k_2(\bar{u}(x_2) - \bar{\phi}_2)(v(x_2) - \psi_2)$$

where $\phi = (\phi_1 \phi_2)^T$, $(\psi_1 \psi_2)^T \in C^2$. Here ϕ_1 and ψ_1 correspond to the motion of left connecting point of the rigid body, i.e., $y(t) - a\theta(t)$; and ϕ_2 and ψ_2 the motion of the right connecting point, i.e., $y(t) + a\theta(t)$. The augmented operators for this combined system are

$$\hat{M} = \begin{bmatrix} \rho & 0 & 0 & 0 \\ 0 & 0 & 0 & 0 \\ 0 & 0 & (m + I/a^2)/4 & (m - I/a^2)/4 \\ 0 & 0 & (m - I/a^2)/4 & (m + I/a^2)/4 \end{bmatrix}$$

$$\hat{D} = \begin{bmatrix} d_v + \dfrac{\partial^2}{\partial x^2}\left(d_h \dfrac{\partial^2}{\partial x^2}\right) & 0 & 0 & 0 & 0 \\ 0 & D_T + d_1 & 0 & -d_1 & 0 \\ 0 & 0 & D_T + d_2 & 0 & -d_2 \\ 0 & -d_1 & 0 & d_1 & 0 \\ 0 & 0 & -d_2 & 0 & d_2 \end{bmatrix}$$

$$\hat{K} = \begin{bmatrix} \dfrac{\partial^2}{\partial x^2}\left(EI \dfrac{\partial^2}{\partial x^2}\right) & 0 & 0 & 0 & 0 \\ 0 & K_T + k_1 & 0 & -k_1 & 0 \\ 0 & 0 & K_T + k_2 & 0 & -k_2 \\ 0 & -k_1 & 0 & k_1 & 0 \\ 0 & 0 & -k_2 & 0 & k_2 \end{bmatrix}$$

with the domain $\mathcal{D} = \{U | U = (u(x) \quad u(x_1) \quad u(x_2) \quad u^T)^T, u(x) \in H([0, L]), u \in C^2\}$, where D_T and K_T are given in (25). Closed-form solution follows the same steps as discussed before.

C Combination of Two Distributed Systems. The energy formulation is also valid for multipoint connection of two distributed systems as shown in Fig. 4(*b*), where points $x_1, \ldots, x_r$ of body Ω_I and points $y_1, \ldots, y_r$ of body Ω_{II} are connected viscoelastically. Denote the displacements of Ω_I and Ω_{II} by $w_I(x, t)$ and $w_{II}(x, t)$, respectively. Let $\mathbf{q}_I^c(t)$ be the vector of the constraint forces applied at the connecting points $x_1, \ldots, x_r$ of Ω_I, and $\mathbf{q}_{II}^c(t)$ the vector of the constraint forces at $y_1, \ldots, y_r$ of body Ω_{II}. Assume that the constraint forces are determined by

$$\begin{aligned} \mathbf{q}_I^c(t) &= -\mathbf{q}_{II}^c(t) \\ &= \mathbf{D}_c(\dot{\mathbf{w}}_{II}^c(t) - \dot{\mathbf{w}}_I^c(t)) - \mathbf{K}_c(\mathbf{w}_{II}^c(t) - \mathbf{w}_I^c(t)) \end{aligned} \quad (44)$$

where $\mathbf{w}_I^c(t) = (w_I(x_1, t) \ldots w_I(x_r, t))^T \in R^r$, $\mathbf{w}_{II}^c(t) = (w_{II}(y_1, t) \ldots w_{II}(y_r, t))^T \in R^r$, and $\mathbf{D}_c$ and $\mathbf{K}_c$ are given matrices describing the connection. The energy functionals are

$$\begin{aligned} &\Pi_M(u_I, v_I; u_{II}, v_{II}) \\ &\quad = \langle M_I^{1/2} u_I, M_I^{1/2} v_I \rangle_{H(\Omega_I)} + \langle M_{II}^{1/2} u_{II}, M_{II}^{1/2} v_{II} \rangle_{H(\Omega_{II})} \\ &\Pi_D(u_I, v_I; u_{II}, v_{II}) = \langle D_I^{1/2} u_I, D_I^{1/2} v_I \rangle_{H(\Omega_I)} \\ &\quad + \langle D_{II}^{1/2} u_{II}, D_{II}^{1/2} v_{II} \rangle_{H(\Omega_{II})} + (\mathbf{u}_{II}^c - \mathbf{u}_I^c)^* \mathbf{D}_c (\mathbf{v}_{II}^c - v_I^c) \\ &\Pi_K(u_I, v_I; u_{II}, v_{II}) = \langle K_I^{1/2} u_I, K_I^{1/2} v_I \rangle_{H(\Omega_I)} \\ &\quad + \langle K_{II}^{1/2} u_{II}, K_{II}^{1/2} v_{II} \rangle_{H(\Omega_{II})} + (\mathbf{u}_{II}^c - \mathbf{u}_I^c)^* \mathbf{K}_c (\mathbf{v}_{II}^c - v_I^c) \end{aligned} \quad (45)$$

where $\mathbf{u}_I^c = (u_I(x_1) \ldots u_I(x_r))^T$, $\mathbf{v}_I^c = (v_I(x_1) \ldots v_I(x_r))^T$, $\mathbf{u}_{II}^c = (u_{II}(y_1) \ldots u_{II}(y_r))^T$, and $\mathbf{v}_{II}^c = (v_{II}(y_1) \ldots v_{II}(y_r))^T \in C^r$, and M_I, D_I, K_I and M_{II}, D_{II}, K_{II} are the spatial differential operators of Ω_I and Ω_{II}, respectively. The derivation of symmetric augmented operators and subsequent modal analysis are similar to those in the previous cases, and therefore is omitted.

D Multibody Systems. The energy formulation can also be extended to multibody systems. For a system assembled from N distributed subsystems $\Omega_1, \Omega_2, \ldots, \Omega_N$, its energy functionals are defined in the function space $H(\Omega)$, with $\Omega = \Omega_1 \cup \Omega_2 \cup \ldots \cup \Omega_N$. The derivation of augmented operators is similar and the closed-form representation of the system response can be systematically obtained.

5 Conclusions

Through introduction of energy functionals, the closed-form transient response analysis developed in Part I is extended to constrained and combined, distributed damped systems. One advantage of the energy formulation is that it systematically leads to the symmetric augmented operators, the Green's function formula, and the eigenfunction representation of the system Green's function. While the current study is on the construction of analytical solutions, accurate estimation of system eigensolutions, which is needed in the response prediction, is being developed for a variety of distributed systems (Yang, 1992; Yang, 1994; Yang and Fang, 1994; Yang and Zhou, 1995; Zhou and Yang, 1996). Combining with that effort, the closed-form transient analysis proposed herein will find wide applications in modeling, dynamic analysis, and vibration control of complex distributed parameter systems.

Acknowledgments

This work was partially supported by the U.S. Army Research Office.

References

Bergman, L. A., and Nicholson, J. W., 1985, "Forced Vibration of a Damped Combined Linear System," ASME *Journal of Vibration, Acoustics, Stress, and Reliability in Design*, Vol. 107, pp. 275–281.

Friedman, B., 1956, *Principles and Techniques of Applied Mathematics*, John Wiley and Sons, New York.

Meirovitch, L., 1967, *Analytical Methods in Vibrations*, Macmillan Company, London.

Mote, C. D., Jr., 1977, "Moving-Load Stability of a Circular Plate on a Floating Central Collar," *The Journal of the Acoustical Society of American*, Vol. 61, No. 2, pp. 439–447.

Ramkrishna, D., and Amundson, N. R., 1974, "On Vibration Problems with Discretely Distributed Loads: A Rigorous Formalism," ASME JOURNAL OF APPLIED MECHANICS, Vol. 41, pp. 1106–1112.

Yang, B., 1992, "Transfer Functions of Constrained/Combined One-Dimensional Continuous Dynamic Systems," *Journal of Sound and Vibration*, Vol. 156, No. 3, pp. 425–443.

Yang, B., 1994, "Distributed Transfer Function Analysis of Complex Distributed Parameter Systems," ASME JOURNAL OF APPLIED MECHANICS, Vol. 61, pp. 84–92.

Yang, B., 1996, "Closed-Form Transient Response of Distributed Damped Systems, Part I: Modal Analysis and Green's Function Formula," ASME JOURNAL OF APPLIED MECHANICS, Vol. 63, pp. 997–1003.

Yang, B., and Fang, H., 1994, "Transfer Function Formulation of Non-Uniformly Distributed Parameter Systems," ASME *Journal of Vibration and Acoustics*, Vol. 116, No. 4, pp. 426–432.

Yang, B., and Zhou, J., 1995, "Analysis of Ring-Stiffened Cylindrical Shells," ASME JOURNAL OF APPLIED MECHANICS, Vol. 62, pp. 1005–1014.

Zhou, J., and Yang, B., 1996, "Strip Distributed Transfer Function Method for the Analysis of Plates," *International Journal of Numerical Methods in Engineering*, Vol. 39, No. 11, pp. 1915–1932.

Thermomechanical Equations Governing a Material With Prescribed Temperature-Dependent Density With Application to Nonisothermal Plane Poiseuille Flow

D. Cao[1]

S. E. Bechtel
Mem. ASME.

Department of Aerospace Engineering, Applied Mechanics, and Aviation, The Ohio State University, Columbus, OH 43210

M. G. Forest
Department of Mathematics, University of North Carolina, Chapel Hill, NC 25799

The standard practice in the literature for modeling materials processing in which changes in temperature induce significant volume changes is based on the a posteriori substitution of a temperature-dependent expression for density into the governing equations for an incompressible material. In this paper we show this ad hoc approach misses important terms in the equations, and by example show the ad hoc equations fail to capture important physical effects. First we derive the three-dimensional equations which govern the deformation and heat transfer of materials with prescribed temperature-dependent density. Specification of density as a function of temperature translates to a thermomechanical constraint, in contrast to the purely mechanical incompressibility constraint, so that the constraint response function ("pressure") enters into the energy equation as well as the momentum equation. Then we demonstrate the effect of the correct constraint response by comparing solutions of our thermomechanical theory with solutions of the ad hoc theory in plane Poiseuille flow. The differences are significant, both quantitatively and qualitatively. In particular, the observed phenomenon of expansion cooling is captured by the thermomechanically constrained theory, but not by the ad hoc theory.

1 Introduction

In general, material properties depend on both thermal and mechanical state variables. Nonetheless, in some industrial processes such as polymer extrusion and fiber spinning, one can reasonably neglect the pressure dependence of density, specific heat, viscosity, and thermal conductivity. This is because the mechanical dependence of material properties is weak at the low to moderate pressure levels encountered in these processes (Spencer and Gilmore, 1950; Cox and Macosko, 1974; Winter, 1977; Lodge and Ko, 1989). In contrast, the temperatures of these processes are high enough and the temperature changes and gradients are sufficiently large that the thermal dependence of material properties may have a significant effect on process behavior. At a fundamental as well as practical level, models for design or optimization of these processes must incorporate this temperature dependence. The standard practice in the literature for modeling such processes is to a posteriori substitute temperature-dependent expressions for the material properties, in particular density, into the governing equations for an incompressible fluid. We revisit this practice in a practical benchmark flow by comparing solutions of these equations to solutions of our equations of the thermomechanically constrained theory which follows from specified temperature-dependent density.

A general mechanical theory of internal constraints was first developed by Noll (1958). The generalization to thermomechanical constraints was made by Green, Naghdi, and Trapp (1970) and Gurtin and Guidugli (1973). Trapp (1970, 1971) further generalized the form of thermomechanical constraints given by Green et al. (1970), and applied the general theory to the special case of an inextensible material with an additional thermal constraint on the temperature gradient, in the context of small deformations and a linear elastic constitutive assumption. Reddy (1984) constructed a theory of constrained elastic materials which was a slight modification of that proposed by Trapp (1971).

The general form of the thermomechanical constraint adopted by Green et al. (1970) and Trapp (1971) is

$$\mathbf{A}\cdot\mathbf{D} + \mathbf{b}\cdot\operatorname{grad}\Theta + \alpha\dot{\Theta} = 0. \tag{1}$$

In Eq. (1), $\mathbf{D}$ is the symmetric part of the velocity gradient, Θ is absolute temperature, $\mathbf{A}$, $\mathbf{b}$, and α are material-dependent quantities, grad is the Eulerian gradient, and "$\dot{}$" denotes the material derivative with respect to time, e.g.,

$$\dot{\Theta} = \frac{\partial\Theta}{\partial t} + \mathbf{v}\cdot\operatorname{grad}\Theta, \tag{2}$$

where $\partial/\partial t$ is the Eulerian partial derivative with respect to time and $\mathbf{v}$ is velocity.

Prescribed temperature-dependent density was first recognized as a material constraint by Green et al. (1970), but neither they nor any subsequent researchers have studied the flow of a material subject only to this constraint. As we shall see, the

[1] Present address: Department of Biomedical Engineering, The Cleveland Clinic Foundation, Cleveland, OH 44159.

Contributed by the Applied Mechanics Division of THE AMERICAN SOCIETY OF MECHANICAL ENGINEERS for publication in the ASME JOURNAL OF APPLIED MECHANICS.

Discussion on this paper should be addressed to the Technical Editor, Professor Lewis T. Wheeler, Department of Mechanical Engineering, University of Houston, Houston, TX 77204-4792, and will be accepted until four months after final publication of the paper itself in the ASME JOURNAL OF APPLIED MECHANICS.

Manuscript received by the ASME Applied Mechanics Division, Dec. 19, 1994; final revision, June 27, 1995. Associate Technical Editor: S. A. Berger.

constraint demanded by prescribed temperature-dependent density $\rho = \rho(\Theta)$ is the special case of (1) with

$$\mathbf{A} = \mathbf{I}, \quad \mathbf{b} = \mathbf{0}. \quad \alpha = \frac{\rho'}{\rho}, \tag{3}$$

where ρ' denotes the derivative of $\rho(\Theta)$ with respect to Θ.

This paper is the first to develop a self-consistent model for the large-deformation processing of a material with prescribed temperature-dependent density. This thermomechanically constrained theory yields a problem formulation that is simpler to solve than the unconstrained theory, yet predicts temperature-induced volume-change effects that are missed by both the incompressible theory and the ad hoc theory of the incompressible equations with a posteriori substitution of temperature-dependent density. We compare solutions of our thermomechanical theory in plane Poiseuille flow with solutions of the ad hoc theory. This study joins a long list of analyses of nonisothermal flow in capillary and slit dies (Brinkman, 1951; Bird, 1955; Toor, 1956; Gee and Lyon, 1957; Toor, 1957; Kearsley, 1962; Kaganov, 1963; Gerrard et al., 1965; Gerrard et al., 1966; Martin, 1967; Gould, 1971; Sukanek, 1971; Cox and Macosko, 1974; Walters, 1975; Winter, 1975; Hieber, 1977; Winter, 1977; Hulatt and Wilkinson, 1978; Hulatt, 1980; Kamal and Nyun, 1980; Ybarra and Eckert, 1980; Dinh and Armstrong, 1982; Rauwendaal and Fernandez, 1985; Duda et al., 1988; Karagiannis et al., 1989; Langer and Werner, 1989; Lodge and Ko, 1989; Burton, 1990; Ko and Lodge, 1991; Hossain, 1992; Jansen and van Dam, 1992; Vergnes et al., 1993). In particular, we discover that our constrained theory is able to predict thermomechanical flow features that are present in all of the compressible analyses in the above list, but unattainable in the incompressible treatments.

2 The Thermomechanical Constrained Theory for Materials With Temperature-Dependent Density

The governing equations for thermomechanical continua are the conservation laws of mass, linear momentum, angular momentum, and energy:

$$\dot{\rho} + \rho \operatorname{div} \mathbf{v} = 0, \tag{4}$$

$$\rho \dot{\mathbf{v}} = \operatorname{div} \mathbf{T} + \rho \mathbf{g}, \quad \mathbf{T} = \mathbf{T}^T, \tag{5}$$

$$\rho \dot{\epsilon} = \mathbf{T} \cdot \mathbf{D} + \rho \gamma - \operatorname{div} \mathbf{q}, \tag{6}$$

where $\mathbf{T}$, $\mathbf{g}$, ϵ, γ, and $\mathbf{q}$ are the Cauchy stress, body force, internal energy, heat supply per unit mass, and heat flux vector, respectively, and div denotes the Eulerian divergence operator. In a particular application these equations are accompanied by boundary conditions, constitutive equations, and perhaps constraint equations.

For a material with prescribed temperature-dependent density, one specifies $\rho = \rho(\Theta)$. This implies the thermomechanical constraint

$$\frac{\rho'}{\rho} \dot{\Theta} + \mathbf{I} \cdot \mathbf{D} = 0, \tag{7}$$

which is consistent with Eq. (4).

In our derivation of the constraint response necessary to maintain the constraint (7), we replace internal energy ϵ with free energy ψ, defined by a Legendre transformation through

$$\psi = \epsilon - \Theta\eta, \tag{8}$$

where η is entropy per unit mass.

We first assume that there is an additive constraint response to all dependent quantities, i.e., we assume

$$\mathbf{T} = \hat{\mathbf{T}} + \bar{\mathbf{T}}. \quad \mathbf{q} = \hat{\mathbf{q}} + \bar{\mathbf{q}},$$
$$\psi = \hat{\psi} + \bar{\psi}, \quad \eta = \hat{\eta} + \bar{\eta}, \tag{9}$$

where "$\hat{\ }$" denotes a constitutive function of deformation and temperature, and "$\bar{\ }$" denotes the constraint response. The additive constraint response must maintain the constraint while producing no entropy. This demands (Day, 1972; Green and Naghdi, 1977)

$$-\rho\dot{\bar{\psi}} - \rho\bar{\eta}\dot{\Theta} + \bar{\mathbf{T}} \cdot \mathbf{D} - \frac{1}{\Theta} \bar{\mathbf{q}} \cdot \operatorname{grad} \Theta = 0, \tag{10}$$

for all processes satisfying the constraint (7).

In particular (10) must hold for the subset of processes with grad $\Theta \equiv \mathbf{0}$, $\mathbf{D} \equiv \mathbf{0}$ and $\dot{\Theta} \equiv 0$, which necessarily satisfy the constraint (7). For this subset, condition (10) reduces to

$$\dot{\bar{\psi}} = 0, \tag{11}$$

or, without loss of generality,

$$\bar{\psi} = 0. \tag{12}$$

Since the constraint response must be independent of the particular process which satisfies the constraint, Eq. (12) must hold for all processes, not just the above subset. By considering all processes with $\mathbf{D} \equiv \mathbf{0}$, $\dot{\Theta} \equiv 0$, but grad Θ arbitrary, a similar argument enables us to deduce

$$\bar{\mathbf{q}} = \mathbf{0}. \tag{13}$$

Therefore, in a material with temperature-dependent density ψ and $\mathbf{q}$ are determined entirely by constitutive functions of deformation and temperature.

All that remains from condition (10) is

$$-\rho\bar{\eta}\dot{\Theta} + \bar{\mathbf{T}} \cdot \mathbf{D} = 0. \tag{14}$$

The subset of processes with $\mathbf{D} = \mathbf{0}$ but $\dot{\Theta}$ arbitrary is not possible for the thermally constrained material, since $\mathbf{D}$ and $\dot{\Theta}$ are not independent. With $(\dot{\Theta}, \mathbf{D})$ and $(\rho'/\rho, \mathbf{I})$ regarded as vectors in the seven-dimensional inner product space $\mathcal{E}^7$, the constraint (7) demands

$$\left(\frac{\rho'}{\rho}, \mathbf{I}\right) \cdot (\dot{\Theta}, \mathbf{D}) = 0, \tag{15}$$

so that the only admissible vectors $(\dot{\Theta}, \mathbf{D})$ are those perpendicular to $(\rho'/\rho, \mathbf{I})$.

The condition (14), which we rewrite as

$$(-\rho\bar{\eta}, \bar{\mathbf{T}}) \cdot (\dot{\Theta}, \mathbf{D}) = 0, \tag{16}$$

indicates that the response $(-\rho\bar{\eta}, \bar{\mathbf{T}})$ must be perpendicular to all $(\dot{\Theta}, \mathbf{D})$ which are perpendicular to $(\rho'/\rho, \mathbf{I})$. Hence we deduce that $(-\rho\bar{\eta}, \bar{\mathbf{T}})$ is parallel to $(\rho'/\rho, \mathbf{I})$, i.e.,

$$(-\rho\bar{\eta}, \bar{\mathbf{T}}) = -p\left(\frac{\rho'}{\rho}, \mathbf{I}\right), \tag{17}$$

where p is a scalar function of position and time. The total response (constitutive plus constraint) is therefore

$$\mathbf{T} = \hat{\mathbf{T}} - p\mathbf{I}, \quad \mathbf{q} = \hat{\mathbf{q}}, \quad \psi = \hat{\psi}, \quad \eta = \hat{\eta} + p\frac{\rho'}{\rho^2}. \tag{18}$$

Using the relation (8) between ψ, ϵ, and η, we obtain

$$\epsilon = \hat{\epsilon} + p\Theta\frac{\rho'}{\rho^2}. \tag{19}$$

The term $p\Theta(\rho'/\rho^2)$ is needed in the internal energy to offset the entropy created in any volume change by the constraint pressure, so that the net entropy generated by the constraint response is zero.

Combining Eqs. (5), (6), (7), (18), and (19), the field equations for a material with temperature-dependent density are

$$\operatorname{div} \mathbf{v} = -\frac{\rho'}{\rho}\dot{\Theta}, \tag{20}$$

$$\rho\dot{\mathbf{v}} = \operatorname{div}\hat{\mathbf{T}} - \operatorname{grad} p + \rho\mathbf{g}, \quad \hat{\mathbf{T}} = \hat{\mathbf{T}}^T, \tag{21}$$

$$\rho\dot{\hat{e}} + \frac{\rho'}{\rho}\Theta\dot{p} + \frac{p\Theta}{\rho}\dot{\Theta}\left(\rho'' - 2\frac{\rho'^2}{\rho}\right) = \hat{\mathbf{T}}\cdot\mathbf{D} + \rho\gamma - \operatorname{div}\hat{\mathbf{q}}. \tag{22}$$

The complete three-dimensional initial/boundary value problem for a material with temperature-dependent density consists of the field Eqs. (20)–(22), together with initial and boundary conditions and constitutive equations for $\hat{\mathbf{T}}$, $\hat{\mathbf{q}}$, and $\hat{e}$.

3 The a Posteriori Treatment of Temperature-Dependent Density

For the purpose of comparison, we present the straightforward, but inconsistent, extension of incompressibility that is the standard practice in the literature for modeling nonisothermal processes with significant temperature-induced volume changes.

The field equations for an incompressible material are

$$\operatorname{div}\mathbf{v} = 0. \tag{23}$$

$$\rho\dot{\mathbf{v}} = \operatorname{div}\hat{\mathbf{T}} - \operatorname{grad} p + \rho\mathbf{g}, \quad \hat{\mathbf{T}} = \hat{\mathbf{T}}^T \tag{24}$$

$$\rho\dot{\hat{e}} = \hat{\mathbf{T}}\cdot\mathbf{D} + \rho\gamma - \operatorname{div}\hat{\mathbf{q}}. \tag{25}$$

The three-dimensional initial/boundary value problem in the incompressible theory consists of these field equations, constitutive equations for $\hat{\mathbf{T}}$, $\hat{e}$, and $\hat{\mathbf{q}}$, and initial and boundary conditions.

A comparison of Eqs. (23)–(25) with Eqs. (20)–(22) shows that a posteriori substitution of a temperature-dependent function of density into the equations for an incompressible material produces incorrect mass and energy equations. In Hayashi et al. (1992) and Dutta (1987) temperature dependence of density is simply substituted a posteriori into (23)–(25), and terms are missed in both the mass and energy equations. Kase and Matsuo (1965) correctly take into account thermal expansion or shrinkage, i.e., they use (20) instead of (23), but leave out the necessary constraint response terms in the energy equation. Hahn and Kettleborough (1967, 1968) posit a new term in the energy equation, but it is incorrect.

In applications such as the onset of convection in the Rayleigh-Bernard problem, it is standard practice to employ the Boussinesq approximation. In this approximation temperature-dependence of density (assumed small) is included in the buoyancy term $\rho\mathbf{g}$ of the linear momentum Eq. (5) but neglected elsewhere (Rayleigh, 1916). In the context of these approximations our constrained theory offers an alternative, which will be pursued in another place. Here we apply our theory to a problem without an applied temperature gradient.

4 Investigation of Plane Poiseuille Flow

In the following, solutions for the velocity and temperature distributions in steady plane Poiseuille flow are obtained from the constrained theory, Eqs. (20)–(22), and compared to the solutions of the ad hoc extensions of incompressibility, Eqs. (23)–(25) with $\rho = \rho(\Theta)$ or Eqs. (20), (24), (25) with $\rho = \rho(\Theta)$. We show that use of the ad hoc extensions results in considerable error and misses qualitative features of physical response.

4.1 The Boundary Value Problem. To complete the boundary value problem formulation for a material with temperature-dependent density, we must specify the constitutive functions $\hat{\mathbf{T}}$, $\hat{e}$, and $\hat{\mathbf{q}}$ for the determinate parts of stress, internal energy, and heat flux, respectively, the body force $\mathbf{g}$, heat source γ, and density function $\rho(\Theta)$, that appear in the governing Eqs. (20)–(22), and appropriate boundary conditions.

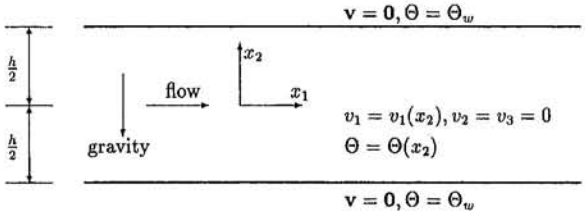

Fig. 1 Nonisothermal plane Poiseuille flow with isothermal walls

Here we model the steady flow between two infinite horizontal planes, depicted in Fig. 1. We assume that the flow is two-dimensional, laminar, and hydrodynamically and thermally fully developed. Hence, the velocity and temperature fields are of the form

$$v_1 = v_1(x_2), \quad v_2 = 0, \quad v_3 = 0, \quad \Theta = \Theta(x_2), \tag{26}$$

subject to the boundary conditions of no slip and isothermal walls:

$$\mathbf{v} = \mathbf{0}, \quad \Theta = \Theta_w, \quad @\, x_2 = \pm\frac{h}{2}, \tag{27}$$

where Θ_w is a specified constant temperature.

For simplicity, we assume constant specific heat and constant thermal conductivity in the constitutive functions for internal energy and heat flux,

$$d\hat{e} = c\,d\Theta, \quad \hat{\mathbf{q}} = -k\operatorname{grad}\Theta, \tag{28}$$

although c and k could just as well be taken as functions of temperature and not change the form of the governing equations. We employ a Newtonian model for the fluid,

$$\hat{\mathbf{T}} = 2\mu(\Theta)\mathbf{D}, \tag{29}$$

where viscosity $\mu(\Theta)$ is a specified function of temperature Θ. Dependence of viscosity on shear rate can be incorporated in a straightforward manner, but this feature is omitted here so as to not complicate the discussion.

The body force is

$$\mathbf{g} = -g\mathbf{e}_2, \tag{30}$$

where g is the acceleration of gravity and $\mathbf{e}_2$ is a unit vector in the x_2 direction. We assume no heat supply, i.e., $\gamma = 0$.

4.2 Solution of the Boundary Value Problem in the Constrained Theory. With assumption (26) on the velocity and temperature fields, the constraint Eq. (20) is identically satisfied for any specified function $\rho(\Theta)$, the x_1, x_2, and x_3 components of the momentum Eq. (21) simplify to

$$\frac{dT_{12}}{dx_2} - \frac{\partial p}{\partial x_1} = 0, \quad -\frac{\partial p}{\partial x_2} - \rho(\Theta)g = 0, \quad 0 = 0, \tag{31}$$

and the energy Eq. (22) becomes

$$\frac{\rho'(\Theta)}{\rho(\Theta)}v_1\Theta\frac{\partial p}{\partial x_1} = T_{12}\frac{dv_1}{dx_2} + k\frac{d^2\Theta}{dx_2^2}. \tag{32}$$

Equations (31) imply

$$p = -\beta x_1 - g\int\rho(\Theta(x_2))dx_2, \tag{33}$$

$$T_{12} = -\beta x_2, \tag{34}$$

where β is the constant rate of pressure drop (positive when the pressure decreases in the flow direction). From Eq. (34)

we see that the absolute value τ_w of shear stress at wall is related to the pressure gradient β by

$$\tau_w = \tfrac{1}{2} h\beta. \tag{35}$$

Eliminating T_{12} from Eqs. (31) and (32), the reduced one-dimensional equations governing the velocity and temperature distribution are

$$\frac{dv_1}{dx_2} = -\frac{\beta}{\mu(\Theta)} x_2, \tag{36}$$

$$\frac{d^2\Theta}{dx_2^2} = -\frac{\beta}{k\mu(\Theta)} x_2^2 - \frac{\beta}{k}\frac{\rho'(\Theta)}{\rho(\Theta)} v_1\Theta. \tag{37}$$

In Eq. (37), the term $-(\beta/k)(\rho'(\Theta)/\rho(\Theta))\, v_1\Theta$ is the effect of constraint response; this term is absent if the temperature-dependent density is inserted a posteriori into the equations for an incompressible material.

To perform specific numerical simulations we must adopt explicit forms for the temperature dependence of density and viscosity. Here we assume a linear dependence of density on temperature,

$$\rho(\Theta) = \rho_0 - \rho_1\Theta, \tag{38}$$

where ρ_0 and ρ_1 are constants, and an Arrhenius form for viscosity,

$$\mu(\Theta) = \mu_w \exp\left[\frac{\mathcal{E}}{R}\left(\frac{1}{\Theta} - \frac{1}{\Theta_w}\right)\right], \tag{39}$$

where the constants, $\mathcal{E}$, R, and μ_w are the activation energy, gas constant, and viscosity at the wall temperature Θ_w, respectively. The constants ρ_0, μ_w, $\mathcal{E}$, R, and Θ_w are positive; ρ_1 will also be positive if the material expands while heated.

To nondimensionalize Eqs. (36) and (37), we scale temperature to the wall temperature Θ_w, lengths to the wall separation h, and velocity to

$$v_0 = \frac{\beta h^2}{8\mu_w} = \frac{\tau_w h}{4\mu_w}, \tag{40}$$

which is the maximum velocity in the isothermal solution of Eq. (36) with the boundary condition of no-slip. The dimensionless transverse coordinate is then

$$\tilde{x}_2 = \frac{x_2}{h}, \tag{41}$$

and dimensionless temperature and velocity are

$$\tilde{\Theta} = \frac{\Theta}{\Theta_w}, \quad \tilde{v}_1 = \frac{v_1}{v_0} = \frac{8\mu_w v_1}{\beta h^2} = \frac{4\mu_w v_1}{\tau_w h}. \tag{42}$$

Using the material density ρ_w at the wall temperature as the characteristic value of density, the dimensionless form of the density function (38) becomes

$$\tilde{\rho}(\tilde{\Theta}) = \frac{\rho(\Theta)}{\rho_w} = \frac{1 - P\tilde{\Theta}}{1 - P}, \tag{43}$$

where the dimensionless thermal expansion number,

$$P = \frac{\rho_1\Theta_w}{\rho_0}, \tag{44}$$

is a characteristic measure of the degree of temperature dependence of the material's density at the processing conditions.

The dimensionless forms of Eqs. (36) and (37) are

$$\frac{d\tilde{v}_1}{d\tilde{x}_2} = -8\tilde{x}_2 \exp\left[-E\left(\frac{1}{\tilde{\Theta}} - 1\right)\right], \tag{45}$$

$$\frac{d^2\tilde{\Theta}}{d\tilde{x}_2^2} = -64\ \mathrm{Br}\ \tilde{x}_2^2 \exp\left[-E\left(\frac{1}{\tilde{\Theta}} - 1\right)\right] + 8\ \mathrm{Br}\ P\frac{\tilde{v}_1\tilde{\Theta}}{1 - P\tilde{\Theta}}, \tag{46}$$

where

$$\mathrm{Br} = \frac{\mu_w v_0^2}{k\Theta_w} = \frac{\beta^2 h^4}{64 k\mu_w\Theta_w} = \frac{\tau_w^2 h^2}{16 k\mu_w\Theta_w}, \quad E = \frac{\mathcal{E}}{R\Theta_w}. \tag{47}$$

Br is the Brinkman number indicating the balance of the competing effects of viscous heating and thermal conductivity, and E is a dimensionless number quantifying the degree of viscosity variation with temperature. The dimensionless boundary conditions are

$$\tilde{v}_1 = 0, \quad \tilde{\Theta} = 1 \quad @\tilde{x}_2 = \pm\tfrac{1}{2}. \tag{48}$$

The two-point coupled boundary value problem (45), (46), and (48), involving the three dimensionless parameters Br, E and P, is solved with a relaxation method, and, as a check, a shooting method.

Because of the constraint response $8\,\mathrm{Br}P(\tilde{v}_1\tilde{\Theta})/(1 - P\tilde{\Theta})$ in the energy equation due to thermal expansion, the governing equations for the fields of velocity and temperature are coupled, and the boundary value problem (45), (46), (48) must be solved simultaneously for the velocity and temperature distributions. Without this term the temperature distribution can be obtained first and then used to determine the velocity profile as done by Burton (1990), but it is precisely this coupling that creates the phenomenon of expansion cooling, as we show below.

4.3 Solution of the Boundary Value Problem in the ad hoc Theory. If we model the same plane Poiseuille flow shown in Fig. 1 with the ad hoc theory, in which a temperature-dependent density is substituted a posteriori into either the incompressible Eqs. (23)–(25) or the incompressible Eqs. (24), (25) accompanied with the thermal expansion constraint (20), the dimensionless governing equations reduce in both cases to

$$\frac{d\tilde{v}_1}{d\tilde{x}_2} = -8\tilde{x}_2 \exp\left[-E\left(\frac{1}{\tilde{\Theta}} - 1\right)\right], \tag{49}$$

$$\frac{d^2\tilde{\Theta}}{d\tilde{x}_2^2} = -64\ \mathrm{Br}\ \tilde{x}_2^2 \exp\left[-E\left(\frac{1}{\tilde{\Theta}} - 1\right)\right], \tag{50}$$

subject to the boundary conditions (48). The parameter P describing the temperature dependence of density does not appear in Eqs. (49) and (50); in fact, the equations are exactly the same as the governing equations derived for an incompressible material in nonisothermal plane Poiseuille flow. Hence, this a posteriori approach leads to a result that, no matter how strong the temperature dependence of density, it has no effect on the velocity, temperature, and stress distributions. The only effect of temperature-dependent density is on the density itself: once $\tilde{\Theta}$ is determined from the boundary value problem (48), (49), and (50), the nondimensional density is obtained from

$$\tilde{\rho}(\tilde{x}_2) = \frac{1 - P\tilde{\Theta}(\tilde{x}_2)}{1 - P}. \tag{51}$$

Also note that Eq. (50) for the temperature distribution decouples from Eq. (49) for the velocity.

4.4 Comparison of the Solutions and Discussion. The effects in the constrained theory of temperature-dependent density on the velocity and temperature fields are shown in Fig.

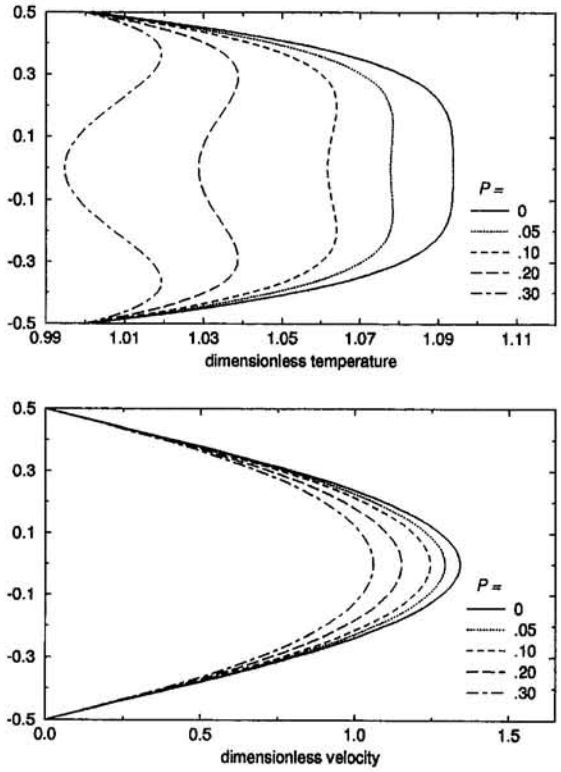

Fig. 2 The transverse velocity and temperature distributions in nonisothermal plane Poiseuille flow with isothermal walls as predicted by the constrained theory, showing the effect of varying the level of temperature dependence of density: $E = 5.0$, Br = 0.2, varying P. The vertical coordinate is the dimensionless transverse coordinate $\tilde{x}_2$. The solution for all values of P from the ad hoc theory (a posteriori substitution of temperature-dependent density into the incompressible theory) is the same as the solution to the constrained theory with $P = 0$.

2. As the temperature dependence of density becomes more pronounced (i.e., as P becomes greater), a depression develops at the center of the temperature profile, and the difference between the wall temperature and mean temperature of the flow decreases. In fact, at $P = 0.3$, the temperature at mid-channel is less than the wall temperature. This behavior is due to the phenomenon of expansion cooling (Toor, 1956; Cox and Macosko, 1974; Winter, 1977): In the plane Poiseuille flow we model, the fluid interior undergoes viscous heating, which tends to increase fluid temperature in the center; however, the viscous heating also tends to expand the fluid when the fluid is heated, and the work done in this expansion leads to loss of temperature. These competing effects lead to the temperature profiles in Fig. 2. The inflection points observed in these temperature profiles from our constrained theory are also predicted in all compressible analyses of fully developed nonisothermal Poiseuille flows in the literature.

The ad hoc theory cannot reflect the competing effects of viscous heating and expansion cooling. Although viscous heating is included, expansion work is missing when the temperature-dependent density is inserted a posteriori in the incompressible equations. The solutions for the velocity and temperature distribution in the ad hoc theory are not affected by the degree of temperature dependence of density: the predicted distributions for temperature-dependent density and constant density are identical, and given by the solutions with $P = 0$ in Fig. 2. When modeling plane Poiseuille flow with the ad hoc theory the temperature dependence of density decouples from the temperature and velocity problem, and only affects the density distribution itself. The ad hoc theory makes both qualitative and quantitative errors: it cannot predict the two inflection points in the temperature distribution, and predicts average and maximum temperatures that are too large. The ad hoc theory overestimates the fluid maximum absolute temperature by 5.3 percent and the velocity at the mid-channel by 16.7 percent for the case with density expansion number $P = 0.2$; polymers are typically processed with P in the range of 0.1 to 0.3 (Toor, 1957).

The density distribution across the channel predicted by the two theories is shown in Fig. 3. In our constrained theory the density has a local maximum in the channel center, reflective of the depressed temperature there due to expansion cooling. In the ad hoc theory, the density minimum is in the center of the channel. Since the ad hoc theory cannot model the lowering of temperature at mid-channel due to expansion cooling, it underestimates fluid density there.

The errors in material density and velocity distributions that result from use of the ad hoc theory have contrary effects on the mass flow rate: the overestimated fluid temperature lowers fluid viscosity and thus leads to higher velocity, as shown in Fig. 2, and therefore too high a volume flow rate; on the other hand, the underestimated density distribution in the ad hoc theory leads to an underpredicted mass flow rate. In the simulation shown in Fig. 4, with $E = 5.0$ and Br = 0.2, the net result of the two competing errors in the ad hoc theory is an overprediction of the mass flow rate. Figure 4 compares the dimensionless mass flow rates $\int_0^1 \tilde{\rho}\tilde{v}_1 d\tilde{x}_2$ resulting from the velocity and density profiles predicted by the two theories, as functions of parameter P. Note that the ad hoc theory overestimates the mass flow rate for any material with temperature-dependent density. The difference is significant even for moderate temperature dependence of density: e.g., when $P = 0.1$, the dimensionless mass flow rate predicted by the ad hoc theory is 5.9 percent higher than the value predicted by the constrained theory.

As an explicit example, when poly(ethylene terephtalate) (PET) is melt processed in a steady nonisothermal plane Poiseuille flow with a wall separation h of 0.2 mm and a wall temperature Θ_w of 558.2 K, the dimensionless numbers E and P are calculated to be 12.18 and 0.1869, respectively (see Table 1). The Brinkman number is in addition a function of the shear stress τ_w at the wall, or equivalently, the imposed pressure gradient $\beta = 2\tau_w/h$. When $\tau_w = 0.82$ MPa ($\beta = 8.2$ MPa/mm), Br = 0.1 and the dimensionless mass flow rate predicted by the constrained theory and the ad hoc theory are 0.7983 and 0.9574, respectively, so the ad hoc theory overestimates the mass flow rate at this wall stress by 19.93 percent.

The relation between volume flow rate and either pressure drop or wall shear stress is important in many process and viscometric measurements. To study this relation, we compute for the process of Table 1 the dimensional volume flow rates per unit channel width as a function of shear stress at wall τ_w predicted by the two theories. For comparison, we also compute the volume flow rate per width given by the exact solution for a flow with "effective" constant values of density and viscosity. The exact solution follows from setting $E = P = 0$ in the boundary value problem (45), (46), and (48). The constant values of density and viscosity in this "effective incompressible flow" model are taken as their values at the wall temperature, i.e., $\rho = \rho_w$, $\eta = \eta_w$.

Figure 5 shows that the ad hoc theory underestimates the wall shear stress τ_w (or pressure gradient β) which is necessary to produce a desired volume flow rate, or, viewed differently, the ad hoc theory overestimates the volume flow rate created by an imposed pressure gradient or wall shear stress. Alternatively, ignoring the temperature dependence of viscosity and density by employing the "effective incompressible flow" model results in errors in the other direction. At the specified volume flow rate per width of 0.15 cm^2/s, the "effective incompressible flow" model produces an error of +4.57 percent in the wall shear stress, and the ad hoc theory produces an error of −2.46 percent. As the flow rate increases, so do the errors: for 0.38 cm^2/s the "effective incompressible flow" model and ad hoc theory give

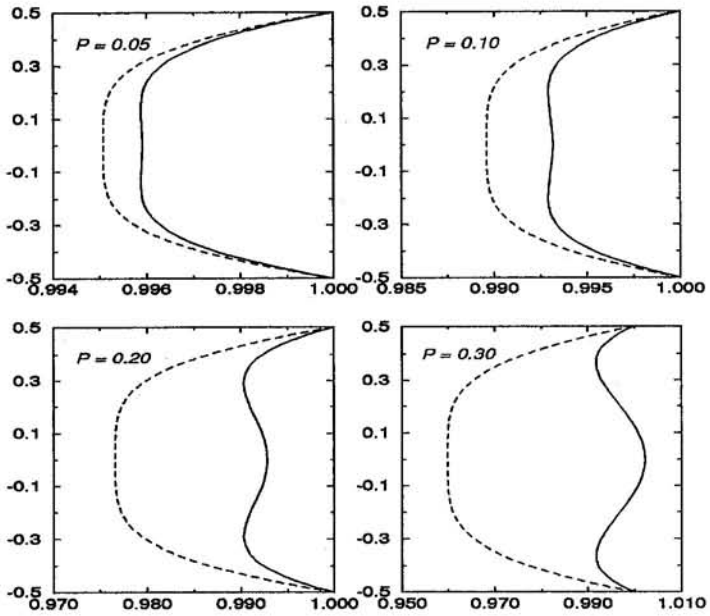

Fig. 3 The density distribution across the channel for different levels of temperature dependence of density: $E = 5.0$, Br = 0.2, varying P. The horizontal coordinate is the dimensionless density, and the vertical coordinate is the dimensionless transverse coordinate $\bar{x}_2$. Solid lines are the predictions from the constrained theory, and dashed lines are the predictions from the ad hoc formulations.

errors of +27.7 and −10.8 percent, respectively. For such flow rates, process modeling based on either the ad hoc theory or the "effective incompressible flow" model can lead to serious design flaws.

The cessation of the curves for both the constrained theory and the ad hoc theory in Fig. 5 indicates that there are no stable solutions to the boundary value problem for fully developed flow in these equations when the pressure gradient exceeds threshold values. This was also noticed in the incompressible theory with temperature-dependent viscosity (equivalent in two-dimensional Poiseuille flow to the ad hoc theory) by Martin (1967) and Sukanek (1971). As can be seen in Fig. 5, this behavior is not captured by the "effective incompressible flow" model.

The effects of temperature dependence of density are augmented by large Br, as shown in Fig. 6. When there is viscous heating in the flow of a fluid with poor thermal conductivity (and hence large Br), the concavity in the temperature distribution at mid-channel deepens, the bulk temperature and mean velocity in the channel increase, and the temperature and velocity gradients at the wall become greater, relative to a fluid with good thermal conductivity.

The effect of temperature dependence of viscosity, or equivalently E, on the temperature distribution is similar to that of Br just described, but less pronounced (see Fig. 7).

Figure 8 illustrates the danger of neglecting temperature dependence of density and viscosity altogether in the modeling of a process. The "effective incompressible flow" solution for temperature-independent viscosity and density differs greatly from the result given by the constrained theory for a process with Br = 0.1, $E = 10$ and $P = 0.2$, and cannot capture the phenomenon of expansion cooling. The maximum dimensionless temperature predicted by the "effective" constant density/constant viscosity theory is 1.033 at the middle of the

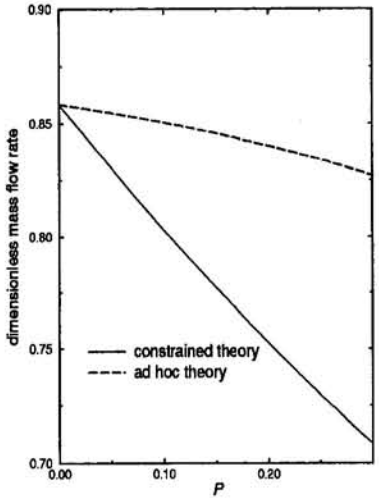

Fig. 4 The dimensionless mass flow rate as a function of the level of temperature dependence of density: $E = 5.0$, Br = 0.2, varying P

Table 1 PET properties and flow conditions used in the simulations of Figs. 5 and 6, and the corresponding dimensionless numbers

Material properties for PET		
Density coefficient ρ_0 =	1493	$kg \cdot m^{-3}$ †
Density coefficient ρ_1 =	0.5	$kg \cdot m^{-3} \cdot K^{-1}$ †
Thermal conductivity k =	0.147	$W \cdot m^{-1} \cdot K^{-1}$ ‡
Intrinsic viscosity $[\eta]$ =	0.6450	$dl \cdot g^{-1}$ ‡
Activation energy $\mathcal{E}$ =	56.54×10^3	$J \cdot mole^{-1}$ †
Flow conditions		
Wall separation h =	0.2	mm
Wall temperature Θ_w =	285	°C = 558.2 K
Viscosity μ_w at wall temperature =	204.6	Pa · s ¶
shear stress at wall τ_w =	variable	
Dimensionless numbers		
Griffith number E =	12.18	
Brinkman number $Br = Br(\tau_w)$ =	$0.1489\tau_w^2$	MPa^{-2}
Dimensionless expansion number P =	0.1869	

†Hayashi *et al* (1992).
‡Polymer Handbook (1989).
¶Calculated by $\mu(\Theta) = [\eta]^{8.18} \exp\{\frac{\mathcal{E}}{R\Theta} - 2.3\}$ poise.

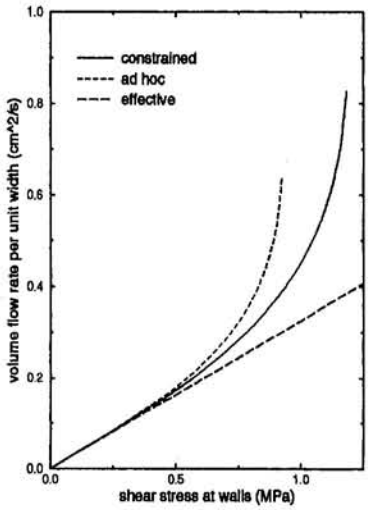

Fig. 5 The relation between volume flow rate per unit width of the channel and wall shear stress τ_w along the flow direction for the PET melt processing of Table 1

channel, and by the constrained theory is 1.020 at dimensionless length scale 0.3. If the material is processed at a wall temperature of 558.2 K, this means the mid-channel temperature predicted by the constant density/constant viscosity solution is 7.1 K higher than the correct temperature given by the constrained theory. For comparision, the mid-channel temperature predicted by the ad hoc theory is 15.3 K too high.

4.5 Conclusion

A theory for the processing of materials with temperature-dependent density is derived in such way that this temperature

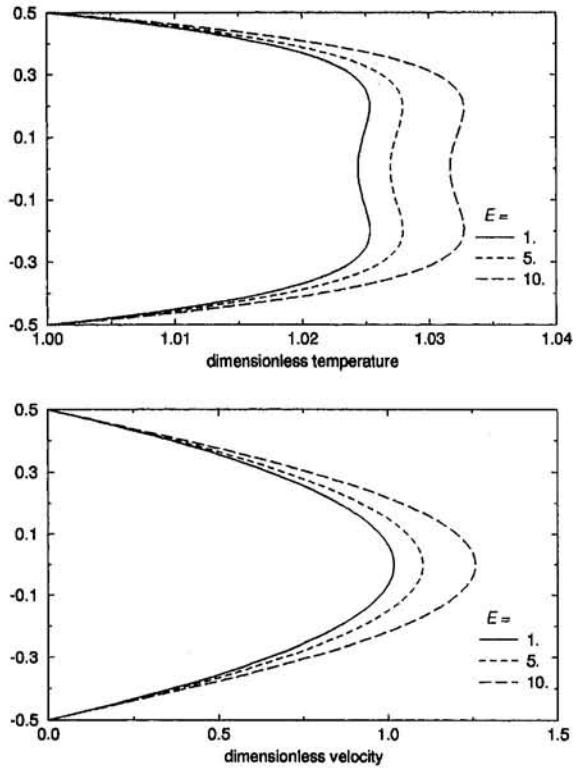

Fig. 7 The transverse velocity and temperature distributions in nonisothermal plane Poiseuille flow with isothermal walls as predicted by the constrained theory, showing the effect of temperature dependence of viscosity: Br = 0.1, P = 0.1, varying E. The vertical coordinate is the dimensionless transverse coordinate $\bar{x}_2$.

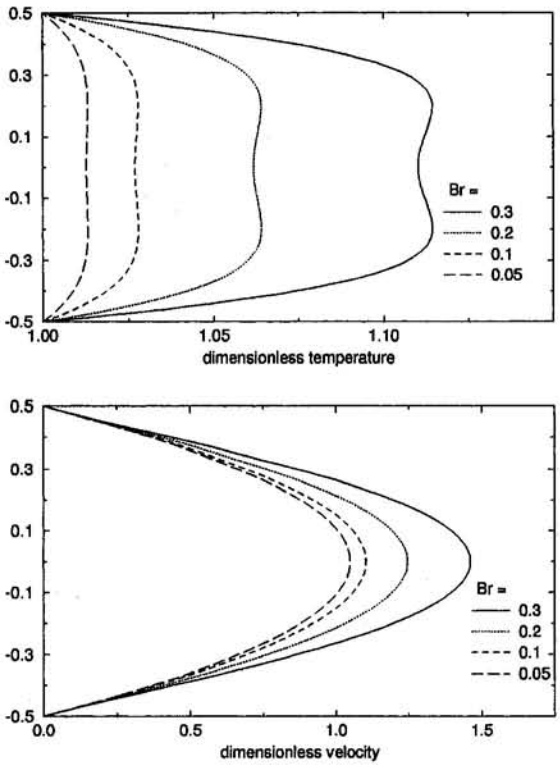

Fig. 6 The transverse velocity and temperature distributions in nonisothermal plane Poiseuille flow with isothermal walls as predicted by the constrained theory, showing the effect of varying the thermal conductivity of the fluid: E = 5.0, P = 0.1, varying Br. The vertical coordinate is the dimensionless transverse coordinate $\bar{x}_2$.

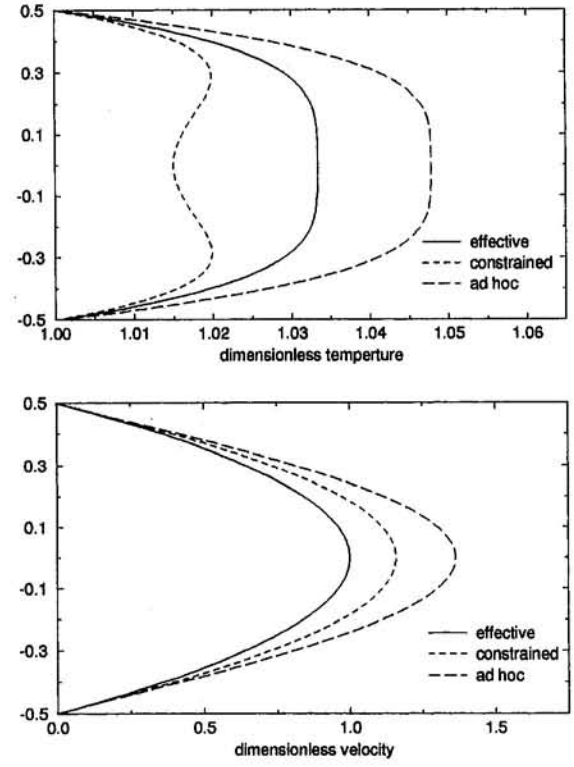

Fig. 8 The transverse velocity and temperature distributions predicted by the constrained theory and the ad hoc theory, which model temperature dependence of density and viscosity: E = 10.0, Br = 0.1, P = 0.2; and by the exact solution for a fluid which replaces density and viscosity with effective constant values: Br = 0.1.

dependence is recognized a priori, and not inserted a posteriori as is often done in the literature. In our a priori treatment, a constraint response appears not only in the momentum balance but also in the energy balance as compression or expansion work. Our theory provides a simpler formulation than the unconstrained compressible theory which retains essential temperature dependence of material properties. We apply our theory to the problem of nonisothermal plane Poiseuille flow to produce the following conclusions: The equations modeling the process from our theory are significantly different for quantitative *and* qualitative predictions than either an ad hoc theory in which temperature-dependent density is inserted a posteriori in the theory for an incompressible fluid, or an "effective" constant density/constant viscosity model. In particular, neither the constant density/constant viscosity theory nor the ad hoc theory can model the phenomenon of expansion cooling in plane Poiseuille flow, and both significantly overestimate the mean temperature and mass flow rate.

Acknowledgment

This research is funded in part by the Air Force Office of Scientific Research under Grant F49620-93-1-0431, the National Science Foundation under Grant CTS-9319128, and by the Hoechst Celanese Corporation.

References

Bird, R. B., 1955, "Viscous Heat Effects in Extrusion of Molten Plastics," *Society of Petroleum Engineers Journal,* Sept., pp. 35–40.

Brandrup, J. and Immergut, E. H., eds., 1989, *Polymer Handbook,* John Wiley and Sons, New York.

Brinkman, H. C., 1951, "Heat Effects in Capillary Flow I," *Applied Scientific Research,* Vol. A2, pp. 121–124.

Burton, R. A., 1990, "Thermally Coupled Reynolds Flows: The Poiseuille Component," *Tribology Transactions,* Vol. 33, No. 4, pp. 493–498.

Cox, H. W., and Macosko, C. W., 1974, "Viscous Dissipation in Die Flows," *AIChE Journal,* Vol. 20, No. 4, pp. 785–795.

Day, W. A., 1972, *The Thermodynamics of Simple Materials with Fading Memory,* Springer-Verlag, New York.

Dinh, S. M. and Armstrong, R. C., 1982, "Non-Isothermal Channel Flow of Non-Newtonian Fluids with Viscous Heating," *AIChE Journal,* Vol. 28, No. 2, pp. 294–301.

Duda, J. L., Klaus, E. E., and Lin, S.-C., 1988, "Capillary Viscometry Study of Non-Newtonian Fluids: Influence of Viscous Heating," *Industrial & Engineering Chemistry Research,* Vol. 27, pp. 352–361.

Dutta, A., 1987, "Role of Quench Air Profiles in Multifilament Melt Spinning of PET Fibers," *Textile Research Journal,* Vol. 57, pp. 13–19.

Gee, R. E., and Lyon, J. B., 1957, "Nonisothermal flow of Viscous Non-Newtonian Fluids," *Industrial and Engineering Chemistry,* Vol. 49, No. 6, pp. 956–960.

Gerrard, J. E., Steidler, F. E., and Appeldoorn, J. K., 1965, "Viscous Heating in Capillaries. The Adiabatic Case," *Industrial & Engineering Chemistry Fundamentals,* Vol. 4, No. 3, pp. 332.

Gerrard, J. E., Steidler, F. E., and Appeldoorn, J. K., 1966, Viscous Heating in Capillaries, *Industrial & Engineering Chemistry Fundamentals,* Vol. 5, No. 2, pp. 260–263.

Gould, P., 1971, "Flow Instability Induced by Viscosity Variation in High Pressure Two-Dimensional Laminar flow Between Parallel Plates," ASME *Journal of Lubrication Technology,* Vol. 93, pp. 465–469.

Green, A. E., and Naghdi, P. M. 1977, "A Note on Thermodynamics of Constrained Materials," ASME JOURNAL OF APPLIED MECHANICS, Vol. 12, pp. 787–788.

Green, A. E., Naghdi, P. M., and Trapp, J. A., 1970, "Thermodynamics of a Continuum with Internal Constraints," *International Journal of Engineering Science,* Vol. 8, pp. 891–908.

Gurtin, M. E., and Guidugli, P. P., 1973, "The Thermodynamics of Constrained Materials," *Archive for Rational Mechanics and Analysis,* Vol. 51, pp. 192–208.

Hahn, E. J., and Kettleborough, C. F., 1967, "Solution for the Pressure and Temperature in an Infinite Slider Bearing of Arbitrary Profile," ASME *Journal of Lubrication Technology,* Vol. 89, pp. 445–452.

Hahn, E. J., and Kettleborough, C. F., 1968, "The Effects of Thermal Expansion in Infinitely Wide Slider Bearings—Free Thermal Expansion," ASME *Journal of Lubrication Technology,* Vol. 90, p. 233.

Hayashi, S., Tani, K., Ishihara, H., and Yasuda, H., 1992, "Fundamental Analysis of Hot Drawing in Spinline and Introduction of Basic Equations for Simulation," *SEN-I GAKKAISHI,* Vol. 48, No. 10, pp. 541–548.

Hieber, C. A., 1977, "Thermal Effects in the Capillary Rheometer," *Rheologica Acta,* Vol. 16, pp. 553–567.

Hossain, M. A., 1992, "Viscous and Joule Heating Effects on MHD-free Convection Flow with Variable Plate Temperature," *International Journal of Heat Mass Transfer,* Vol. 35, No. 12, pp. 3485–3487.

Hulatt, M., 1980, "Heat Transfer to Flowing Polymer Melts," *Journal of Non-Newtonian Fluid Mechanics,* Vol. 7, pp. 345–357.

Hulatt, M., and Wilkinson, W. L., 1978, "Heat Transfer to Molten Polymer Flowing Through Tubes," *Polymer Engineering and Science,* Vol. 18, No. 15, pp. 1148–1154.

Jansen, K. M. B., and van Dam, J., 1992, "An Analytical Solution for the Temperature Profile During Injection Molding including Dissipation Effects," *Rheologica Acta,* Vol. 31, pp. 592–602.

Kaganov, S. A., 1963, "Establishing Laminar Flow for an Incompressible Liquid in a Horizontal Channel and a Curved Cylindrical Tube with Correction for Frictional Heat and the Temperature Dependence of Viscosity," *International Chemical Engineering,* Vol. 3, No. 1, pp. 33–35.

Kamal, M. R., and Nyun, H., 1980, "Capillary Viscometry: A Complete Analysis Including Pressure and Viscous Heating Effects," *Polymer Engineering and Science,* Vol. 20, No. 2, pp. 109–119.

Karagiannis, A., Hrymak, A. W., and Vlachopoulos, J., 1989, "Three-dimensional non-isothermal extrusion flows," *Rheologica Acta,* Vol. 28, pp. 121–133.

Kase, S., and Matsuo, T., 1965, "Studies on Melt Spinning. I. Fundamental Equations on the Dynamics of Melt Spinning," *Journal of Polymer Science: Part A,* Vol. 3, pp. 2541–2554.

Kearsley, E. A., 1962, "The Viscous Heating Correction for Viscometer Flows," *Transactions of the Society of Rheology,* Vol. 6, pp. 253–261.

Ko, Y. S., and Lodge, A. S., 1991, "Viscous Heating Correction for Thermally Developing Flows in Slit Die Viscometry," *Rheologica Acta,* Vol. 30, pp. 357–368.

Langer, G., and Werner, U., 1989, "Non-isothermal flow in a slit viscometer," *Rheologica Acta,* Vol. 14, pp. 935–941.

Lodge, A. S., and Ko, Y.-S., 1989, "Slit Die Viscometry at Shear Rates up to 5×10^6 s^{-1}: An Analytical Correction for Small Viscous Heating Errors," *Rheologica Acta,* Vol. 28, pp. 464–472.

Martin, B., 1967, "Some Analytical Solution for Viscometric Flows of Power-Law Fluids with Heat Generation and Temperature Dependent Viscosity," *International Journal of Non-Linear Mechanics,* Vol. 2, pp. 285–301.

Noll, W., 1958, "A Mathematical Theory of the Mechanical Behavior of Continuous Media," *Archive for Rational Mechanics and Analysis,* Vol. 2, pp. 197–226.

Rauwendaal, C., and Fernandez, F., 1985, "Experimental Study and Analysis of a Slit Die Viscometer," *Polymer Engineering and Science,* Vol. 25, pp. 765–771.

Rayleigh, Lord, 1916, "On Convection Currents in a Horizontal Layer of Fluid, when the Higher Temperature is on the Under Side," *Philosophical Magazine,* Vol. 32, pp. 529–546.

Reddy, B. D., 1984, "The Propagation and Growth of Acceleration Waves in Constrained Thermoelastic Materials," *Journal of Elasticity,* Vol. 14, pp. 387–402.

Spencer, R. S., and Gilmore, G. D., 1950, "Equation of State for High Polymers," *Journal of Applied Physics,* Vol. 21, pp. 523–526.

Sukanek, P. C., 1971, "Poiseuille Flow of a Power-law Fluid with Viscous Heating," *Chemical Engineering Science,* Vol. 26, pp. 1775–1776.

Toor, H. L., 1956, "The Energy Equation for Viscous Flow," *Industrial and Engineering Chemistry,* Vol. 48, pp. 922–926.

Toor, H. L., 1957, "Heat Generation and Conduction in the Flow of a Viscous Compressible Liquid," *Transactions of the Society of Rheology,* Vol. 1, pp. 177–190.

Trapp, J. A., 1970, "Thermomechanical Constraints and Materials Reinforced with Cords," Ph.D. thesis, University of California, Berkeley, CA.

Trapp, J. A., 1971, "Reinforced Materials with Thermo-mechanical Constraints," *International Journal of Engineering Science,* Vol. 9, pp. 757–773.

Vergnes, B., Valle, G. Della, and Tayeb, J., 1993, "A Specific Slit Die Rheometer for Extruded Starchy Products. Design, Validation and Application to Maize Starch," *Rheologica Acta,* Vol. 32, pp. 465–476.

Walters, K., 1975, *Rheometry,* Chapman and Hall, Ltd.

Winter, H. H., 1975, "Temperature Fields in Extruder Dies with Circular, Annular, or Slit Cross-Section," *Polymer Engineering and Science,* Vol. 15, No. 2, pp. 84–89.

Winter, H. H., 1977, "Viscous Dissipation in Shear Flows of Molten Polymers," *Advances in Heat Transfer,* Vol. 13, pp. 205–267.

Ybarra, R. M., and Eckert, R. E., 1980, "Viscous Heat Generation in Slit Flow," *AIChE Journal,* Vol. 26, No. 5, pp. 751–762.

Zhen-qiang Cheng[1]
Associate Professor,
Department of Modern Mechanics,
University of Science and
Technology of China,
Hefei, Anhui 230026, P.R. China

A. K. Jemah
Lecturer.

F. W. Williams
Professor and Head.

Division of Structural Engineering
Cardiff School of Engineering,
University of Wales Cardiff,
Cardiff CF2 1XH, U.K.

Theory for Multilayered Anisotropic Plates With Weakened Interfaces

Rigorous kinematical analysis offers a general representation of displacement variation through thickness of multilayered plates, which allows discontinuous distribution of displacements across each interface of adjacent layers so as to provide the possibility of incorporating effects of interfacial imperfection. A spring-layer model, which has recently been used efficiently in the field of micromechanics of composites, is introduced to model imperfectly bonded interfaces of multilayered plates. A linear theory underlying dynamic response of multilayered anisotropic plates with nonuniformly weakened bonding is presented from Hamilton's principle. This theory has the same advantages as conventional higher-order theories over classical and first-order theories. Moreover, the conditions of imposing traction continuity and displacement jump across each interface are used in modeling interphase properties. In the special case of vanishing interface parameters, this theory reduces to the recently well-developed zigzag theory. As an example, a closed-form solution is presented and some numerical results are plotted to illustrate effects of the interfacial weakness.

1 Introduction

It has long been recognized that the classical two-dimensional laminated plate theory, which is based upon the Kirchhoff hypotheses of straight inextensional normals for the entire plate package, yields inadequate results for analysis of composite plates in many engineering problems. Due to their low ratio of transverse shear modulus to the in-plane modulus, composite laminates often exhibit significant transverse shear deformation, which if neglected as in classical plate theory precludes an accurate prediction of both overall behavior and local failures caused by delamination. From the theoretical viewpoint, one of the central issues of various theories is how to account for the effects of transverse shear flexibility and other nonclassical factors, such as transverse normal strain. Many approaches have been proposed to this end and there are numerous publications in the field of multilayered composite plates and shells; e.g., see the review papers of Bert (1984), Reissner (1985), Noor and Burton (1989) and Reddy and Robbins Jr. (1994), and the references cited in them.

All the different approaches for constructing two-dimensional shear deformation theories of multilayered plates can be categorized as either equivalent single-layer theories or discrete-layer theories. In equivalent single-layer theories a heterogeneous laminated plate or shell is treated as a statistically equivalent single layer, possibly having complex constitutive behavior. Examples are classical and first-order shear deformation theories (e.g., Chia, 1980, 1988) based on linear distribution of the in-plane displacements in the thickness direction, and higher-order theories (e.g., Librescu, 1975; Reddy, 1984) based on a nonlinear distribution of the in-plane displacements in the thickness direction. The advantage of introducing a global displacement approximation in the thickness direction is that only three or five generalized displacement parameters are involved in the resulting equations and the order of the governing equations is independent of the total number of layers. The global response characteristics predicted by higher-order shear deformation theories are fairly accurate. However, the distributions of the stresses and displacements through the thickness obtained by these theories are not so accurate, as transverse stresses do not satisfy continuity at layer interfaces.

In contrast to the equivalent single-layer theories, most displacement-based discrete-layer theories are based on piecewise linear approximation for in-plane displacements in the thickness direction, the transverse shear stresses are constant within each layer and so do not satisfy compatibility conditions on the two bounding surfaces of the plate. On the other hand, although the discrete-layer theories are generally very accurate, they are quite cumbersome in solving practical problems because the number of unknowns and the order of the theories depend upon the number of layers that the plate has.

Because of this, various zigzag theories, alternatively called simplified discrete-layer theories (Noor and Burton, 1989) or refined single-layer theories (Reddy and Robbins Jr., 1994), have recently been proposed for describing the deformation of plates and shells; see Di Sciuva (1986, 1987, 1992), Di Sciuva and Icardi (1993), Savithri and Varadan (1990, 1993), Librescu and Schmidt (1991), Gaudenzi (1992), Cho and Parmerter (1992, 1993, 1994), Xavier et al. (1993), He (1993, 1994), and Schmidt and Librescu (1994). The displacement field assumed is such that the displacements and tractions are continuous at layer interfaces. This continuity can be used to reduce the total number of unknown parameters in the theories. Such approaches formulate a multilayered plate model of the discrete-layer category for which the total number of generalized displacements does not increase with the number of layers. This number is usually five, as in most equivalent single-layer theories such as first-order theory or the third-order theory of Reddy (1984).

Unlike their homogeneous isotropic counterparts, the anisotropic constitution of multilayered composite structures often results in unique phenomena that can occur at vastly different geometric scales, i.e., at the global level, the ply level or the reinforcement-matrix level. The equivalent single-layer theories

[1] Academic Visitor, Division of Structural Engineering, Cardiff School of Engineering, University of Wales Cardiff, Cardiff CF2 1XH, U.K.

Contributed by the Applied Mechanics Division of THE AMERICAN SOCIETY OF MECHANICAL ENGINEERS for publication in the ASME JOURNAL OF APPLIED MECHANICS.

Discussion on this paper should be addressed to the Technical Editor, Professor Lewis T. Wheeler, Department of Mechanical Engineering, University of Houston, Houston, TX 77204-4792, and will be accepted until four months after final publication of the paper itself in the ASME JOURNAL OF APPLIED MECHANICS.

Manuscript received by the ASME Applied Mechanics Division, Feb. 8, 1995; final revision, Oct. 17, 1995. Associate Technical Editor: J. N. Reddy.

are generally capable of accurately describing the global response, whereas at the ply level discrete-layer and zigzag theories are needed to determine the three-dimensional stress field. When equivalent overall elastic properties at the reinforcement-matrix level of random composite materials are required, they can be found by efficient micromechanics theories, e.g., the Mori-Tanaka mean field approach (Mori and Tanaka, 1973; Weng, 1984; Benveniste, 1987), the self-consistent method (Hill, 1965; Budiansky, 1965), the generalized self-consistent method (Christensen and Lo, 1979) and the differential scheme (McLaughlin, 1977; Norris, 1985). The present paper gives a theory which is general in so far as results at the ply level are concerned and only requires that the elasticity constants of each layer have been determined either by experiment or from micromechanics methods. Particular attention is paid to multilayered anisotropic plates with imperfect layer interfaces.

It is well known that properties of composite materials are significantly influenced by the properties of interfaces between the constituents. A perfect interface, which implies continuous displacements and tractions across the interface, is assumed in most analytical and numerical work on composite materials and thus interface properties and structures are eliminated. However, in many cases of interest this perfect interface assumption is not adequate. Examples for multilayered composites are either the presence of a thin layer between adjacent ply layers or of a coating on the surface of the reinforcing constituent. Such an interfacial layer is generally referred to as an interphase. It may be due to chemical interaction between the constituents or it may be deliberately introduced in order to improve the properties of composites. In the limit of vanishing interphase-thickness, displacement jumps occur when crossing the interphase from one side to another while the tractions must remain continuous from simple equilibrium consideration. The simplest approach used to model this is that the jumps in normal and tangential displacements are assumed to be proportional to the tractions, giving a spring-layer model. Such a model has recently been applied in micromechanics-based researches on imperfect interfaces of composites at the reinforcement-matrix level; e.g., see Benveniste (1985), Aboudi (1987), Achenbach and Zhu (1989), Jasiuk and Tong (1989), Benveniste and Dvorak (1990), Hashin (1990, 1991a, b, 1993) and Qu (1993a, b). However, few attempts have been made to evaluate the effects of weak bonding at the ply level of multilayered composites.

A large class of new composite materials, e.g., ARALL (aramid fiber-reinforced aluminium alloy laminates) and CARALL (carbon fiber-reinforced aluminium alloy laminates), has recently been developed for aircraft and civil application. These materials consist of alternating layers of aluminium alloy sheets bonded by an adhesive impregnated with high strength aramid, ramie or carbon fibers; e.g., see Vogelesang and Gunnink (1986), Aboudi and Paley (1992), Mao and Han (1992), Li et al. (1994), and Lin et al. (1994). In addition to their lower density and higher strength than aluminium alloys, excellent fatigue crack growth resistance has been observed for these materials. However, the aluminium alloy has a very different thermal expansion coefficient from that of the adjacent sheet, e.g., of CFRP (carbon fiber-reinforced polymer) sheets for CARALL. Therefore the curing process will certainly produce substantial residual stresses at layer interfaces and these stresses will influence the mechanical properties of such materials, especially their bending behavior. In addition, although the surface of the aluminium sheet is pretreated by chemical or mechanical methods in order to improve adhesion, in practice imperfect bonding still exists to different extents. A recent development (Mao and Han, 1992) is to pre-coat the aluminium alloy and CFRP surfaces of CARALL material with a kind of adhesive called CCVC (copolymer of controllable volume change on curing). CCVC can form a very thin interfacial layer between the aluminium alloy and CFRP sheets, and different ratios of its constituents can lead to different interfacial bonding properties. One purpose of the CCVC coatings is to increase the bonding strength between the aluminium alloy sheet and the CFRP sheet, because the main composition of CCVC is a kind of adhesive, while another purpose is to reduce the residual stresses generated from the curing process so as to prevent premature delamination. These expectations have been confirmed by experiments, including those of Mao and Han (1992).

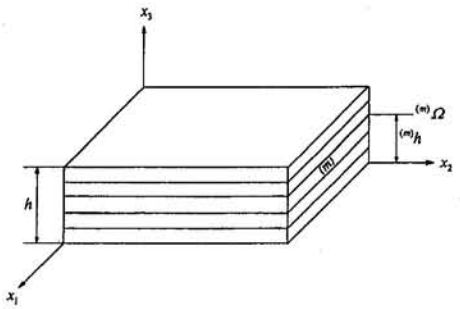

Fig. 1 Geometry of a multilayered plate

The present work incorporates some of the interfacial properties into the theory of multilayered anisotropic plates. Each interface between adjacent layers is characterized by a spring-layer model as employed in micromechanics. An important feature is the introduction of this micromechanics model into macrostructural analysis in order to model interphase properties. As will be shown, the use of this model in the two-dimensional theory of multilayered plates and shells avoids the physically impossible phenomenon of interpenetration at the interfaces. However this model might lead to such interpenetration within the three-dimensional theory of elasticity, as discussed briefly by Achenbach and Zhu (1989), although perhaps more accurate models could be found to overcome this problem. An exact representation of displacement variation through the thickness of a multilayered plate is obtained by rigorous kinematical analysis. This representation can include displacement jumps across each interface and thus can enable interfacial imperfection to be incorporated. However, in the present paper only a small amount of interfacial weakness is allowed because, when deriving the present theory from Hamilton's principle, certain approximations have been made concerning displacement variation. As the displacement model satisfies the compatibility conditions of transverse shear stresses both at layer interfaces and on the two bounding surfaces of the plate, there is no need for the use of shear correction factors, and the number of unknowns is eventually shown to be five irrespective of the number of layers, i.e., the same number as for most first and third-order smeared theories. The governing set of equations has variable coefficients due to the nonuniform bonding strength involved in each interface. Thus in this theory uniform bonding corresponds to governing equations with constant coefficients. In the limit of vanishing interface parameters this theory reduces to exactly the flat-plate limit of the conventional zigzag theory for multilayered anisotropic shells of He (1994). A simple numerical example is presented to give a good understanding of how a small amount of interface weakness affects the overall and local behaviors of multilayered plates.

2 General Representation of Displacement Variation

Figure 1 shows a multilayered plate consisting of k homogeneous anisotropic layers with uniform thickness. For convenience, the undeformed lower surface of the plate is chosen as the reference surface defined by $x_3 = 0$ and the x_3-axis is normal to it, where $\{x_i\}$ $(i = 1, 2, 3)$ is a Cartesian axis system. Let $^{(m)}\Omega$ $(m = 0, \ldots, k)$ denote the lower surface $(m = 0)$, the interface between the mth and $(m + 1)$th layers $(m = 1, \ldots, k - 1)$ and the upper surface $(m = k)$ of the plate. The volume

V of the multilayered plate is thus divided by the $(k-1)$ interfaces ${}^{(m)}\Omega$ $(m = 1, \ldots, k-1)$ into k subspaces ${}^{(m)}V$ $(m = 1, \ldots, k)$ corresponding to the volumes of the k layers. The range of ${}^{(m)}V$ in the x_3-direction is $[{}^{(m-1)}h, {}^{(m)}h]$, where ${}^{(m)}h$ $(m = 0, \ldots, k)$ is the distance between ${}^{(0)}\Omega$ and ${}^{(m)}\Omega$. Obviously, ${}^{(0)}h = 0$ and ${}^{(k)}h = h$, where h is the total thickness of the plate. It is assumed that the displacement vector ${}^{(m)}\mathbf{v}(\mathbf{x}; t)$ at time t of a point in the mth layer after deformation is sufficiently smooth in ${}^{(m)}V$, in the sense that it is differentiable with respect to x_i as many times as necessary. Here $\mathbf{x}$ is the vector (x_1, x_2, x_3) and $\mathbf{v}$ is the corresponding displacement vector.

The displacement vector $\mathbf{v}(\mathbf{x}; t)$ of any point in V can be expressed as

$$\mathbf{v}(\mathbf{x}; t) = \sum_{m=0}^{k-1} [{}^{(m+1)}\mathbf{v}(\mathbf{x}; t) - {}^{(m)}\mathbf{v}(\mathbf{x}; t)] H(x_3 - {}^{(m)}h), \quad (1)$$

where ${}^{(0)}\mathbf{v}(\mathbf{x}; t) \equiv 0$ and $H(x_3 - {}^{(m)}h)$ is the Heaviside step function. Taylor expansion of ${}^{(m)}\mathbf{v}(\mathbf{x}; t)$ $(m = 0, \ldots, k)$ with respect to x_3 gives an alternative form of Eq. (1) as

$$\mathbf{v}(\mathbf{x}; t) = \sum_{m=0}^{k-1} \sum_{n=0}^{\infty} {}^{(m)}\mathbf{u}^{(n)}(x_1, x_2; t) \times (x_3 - {}^{(m)}h)^n H(x_3 - {}^{(m)}h), \quad (2)$$

$${}^{(m)}\mathbf{u}^{(n)}(x_1, x_2; t) = \frac{1}{n!} {}^{(m+1)}\mathbf{v}^{(n)}(x_1, x_2, {}^{(m)}h; t) - \frac{1}{n!} {}^{(m)}\mathbf{v}^{(n)}(x_1, x_2, {}^{(m)}h; t), \quad (3)$$

retaining, unlike He (1994), the term

$${}^{(m)}\mathbf{u}^{(0)}(x_1, x_2; t) = {}^{(m+1)}\mathbf{v}(x_1, x_2, {}^{(m)}h; t) - {}^{(m)}\mathbf{v}(x_1, x_2, {}^{(m)}h; t). \quad (4)$$

This term implies that the displacements at interfaces are allowed to be discontinuous, so as to provide a possible incorporation of imperfect interfaces of multilayered plates, e.g., weakened bonding or even delamination. The case of perfect bonding corresponds to this term being a null vector.

3 Spring-Layer Model of Imperfect Interfaces

To incorporate the properties and structures of interfaces in the evaluation of composite behavior, interfaces must be treated as regions of distinct atomic structure and, possibly, distinct composition. They should have different properties from the bulk properties on either side of the interface. In the context of continuum mechanics, one simple approach is to introduce a thin layer of interphase material which replaces the interface. The limiting case of vanishing interphase-thickness then gives an interface which is a mathematical surface across which material properties change discontinuously, with the interfacial tractions being continuous while the displacements are discontinuous. Although nonlinear relationships may be proposed between the interfacial tractions and displacement jumps, a linear spring-layer model is explored in this paper to characterize the imperfect bonding.

If Ω and $\mathbf{n}$ are used, respectively, to denote the interface and its unit positive normal vector, the interface conditions may be written as

$$\Delta\boldsymbol{\sigma}\cdot\mathbf{n} \equiv [\boldsymbol{\sigma}(\Omega^+) - \boldsymbol{\sigma}(\Omega^-)]\cdot\mathbf{n} = \mathbf{0}, \quad (5)$$

$$\Delta\mathbf{v} \equiv [\mathbf{v}(\Omega^+) - \mathbf{v}(\Omega^-)] = \mathbf{R}\cdot\boldsymbol{\sigma}\cdot\mathbf{n}, \quad (6)$$

where $\boldsymbol{\sigma}(\Omega^+)$ and $\boldsymbol{\sigma}(\Omega^-)$ are the values of stress tensor $\boldsymbol{\sigma}(\mathbf{x})$ as $\mathbf{x}$ approaches the interface from positive and negative directions of the normal to the interface, respectively, and $\mathbf{v}(\Omega^+)$ and $\mathbf{v}(\Omega^-)$ are defined similarly. The second-order tensor $\mathbf{R}$ in Eq. (6) represents the compliance tensor of the spring-layer interface. For simplicity, it is assumed in this paper that $\mathbf{R}$ is symmetrical and positive definite. It is also clear from Eq. (6) that $\mathbf{R} = \mathbf{0}$ corresponds to a perfect interface, while $\mathbf{R}^{-1} = \mathbf{0}$ represents complete debonding, i.e., $\boldsymbol{\sigma}\cdot\mathbf{n} = \mathbf{0}$ on Ω. From this point of view, a slightly weakened interface may be modelled by small values of $\mathbf{R}$. Such an imperfect interface may be due to the presence of an interphase but could also be due to interface bond deterioration caused by, e.g., fatigue damage or environmental and chemical effects.

A special form of $\mathbf{R}$ that has some physical significance is given by

$$\mathbf{R} = R^t\mathbf{I} + (R^n - R^t)\mathbf{n}\otimes\mathbf{n}, \quad (7)$$

where $\mathbf{I}$ denotes a second-order unit tensor and the symbol $\otimes$ is the usual dyad symbol. It can easily be shown that R^t and R^n represent the compliance in the tangential and normal directions of the interface, respectively, i.e.,

$$\Delta\mathbf{v}\cdot(\mathbf{I} - \mathbf{n}\otimes\mathbf{n}) = R^t\mathbf{n}\cdot\boldsymbol{\sigma}\cdot(\mathbf{I} - \mathbf{n}\otimes\mathbf{n}), \quad (8)$$

$$\Delta\mathbf{v}\cdot\mathbf{n} = R^n\mathbf{n}\cdot\boldsymbol{\sigma}\cdot\mathbf{n}. \quad (9)$$

When $R^n = 0$, this constitutive characterization of the interface allows relative sliding between the two surfaces, but no separation. Furthermore, the free-sliding case can be achieved by setting $R^t \to \infty$ with $R^n = 0$. It should be noted that when $R^n \neq 0$ this mathematical model includes solutions which are physically impossible because one constituent would have to penetrate another, as noticed by Achenbach and Zhu (1989) and Qu (1993a, b). This violates the compatibility requirements and therefore the model is apparently unreasonable for such a case. Fortunately, the normal stress σ_{33} for the plate problem under consideration is assumed to be negligibly small compared with other stress components, so that it is ignored in the present theory as in most other theories for plates and shells. This automatically leads to a vanishing displacement jump in the normal direction, see Eq. (9), regardless of the value of the interface parameter R^n. Therefore it seems to be reasonable to adopt this spring-layer model in the theory of plates and shells with imperfect bonding in shear.

4 Approximate Expressions for Displacements

Throughout the following derivations, a comma followed by a subscript denotes a derivative with respect to the corresponding spatial coordinate, and a dot over a quantity refers to a derivative with respect to time, t. The Einsteinian summation convention applies to repeated subscripts of tensor components, with Latin subscripts ranging from 1 to 3 while Greek subscripts are either 1 or 2. The spatial derivative with respect to x_3 is stipulated as the right-hand one so that $H_{,3}(x_3 - {}^{(m)}h) = 0$.

Equation (2) can be rewritten in component form as

$$v_j(x_i; t) = \sum_{m=0}^{k-1} \sum_{n=0}^{\infty} {}^{(m)}u_j^{(n)}(x_\alpha; t) \times (x_3 - {}^{(m)}h)^n H(x_3 - {}^{(m)}h). \quad (10)$$

To develop a practical theory of multilayered plates, which can model weakened interfaces but not debonding, the above series is truncated by using the approximations

$$n = \begin{cases} 0, 1, 2, 3 & \text{for } j = \alpha \text{ and } m = 0 \\ 0, 1 & \text{for } j = \alpha \text{ and } m = 1, \ldots, k-1. \\ 0 & \text{for } j = 3 \text{ and } m = 0, \ldots, k-1 \end{cases} \quad (11)$$

By also using the contact condition of adjacent layers in the normal direction of each interface, i.e.,

$$^{(m+1)}v_3(x_\alpha, {}^{(m)}h^+; t) = {}^{(m)}v_3(x_\alpha, {}^{(m)}h^-; t), \quad (m = 1, \ldots, k-1), \quad (12)$$

the displacements can be expressed as

$$v_\alpha(x_i; t) = u_\alpha + \psi_\alpha x_3 + \varphi_\alpha x_3^2 + \eta_\alpha x_3^3 + \sum_{m=1}^{k-1} [{}^{(m)}\Delta v_\alpha + {}^{(m)}u_\alpha(x_3 - {}^{(m)}h)]H(x_3 - {}^{(m)}h),$$

$$v_3(x_i; t) = u_3, \quad (13)$$

where ${}^{(0)}u_i^{(0)}$, ${}^{(0)}u_\alpha^{(1)}$, ${}^{(0)}u_\alpha^{(2)}$, ${}^{(0)}u_\alpha^{(3)}$, ${}^{(m)}u_\alpha^{(0)}$, and ${}^{(m)}u_\alpha^{(1)}$ in Eq. (10) have been replaced by the quantities u_i, ψ_α, φ_α, η_α, ${}^{(m)}\Delta v_\alpha$ and ${}^{(m)}u_\alpha$, respectively.

For most plate problems transverse normals do not experience significant extensions and therefore it has been assumed, without significant loss of accuracy, that v_3 is independent of the thickness coordinate. Theories higher than third order are not used because the extra accuracy achieved is so small that the effort required to solve the equations is not justified. (Of course, theories developed for calculating delamination need more terms than are retained by Eqs. (13), e.g., see Chattopadhyay and Gu (1994), and so the use of Eqs. (13) in the present theory means that it only applies to multilayered plates with slightly weakened interfaces and no debonding.)

The strain and stress components of the plate can be obtained from

$$e_{ij} = \tfrac{1}{2}(v_{i,j} + v_{j,i}), \quad \sigma_{\alpha\beta} = H_{\alpha\beta\omega\rho}e_{\omega\rho}, \quad \sigma_{\alpha 3} = 2E_{\alpha 3\omega 3}e_{\omega 3}, \quad (14)$$

where e_{ij} and σ_{ij} are components of the strain and stress tensors, E_{ijkl} are components of the elasticity tensor associated with an elastic anisotropic body, and

$$H_{\alpha\beta\omega\rho} = E_{\alpha\beta\omega\rho} - \frac{E_{\alpha\beta 33}E_{33\omega\rho}}{E_{3333}}. \quad (15)$$

Here, as indicated by Librescu (1975), the second and third of Eqs. (14) hold only under the assumptions that each layer possesses a plane of elastic symmetry parallel to the $x_3 = 0$ plane and that σ_{33} is vanishingly small compared with the other components of the stress tensor.

The compatibility conditions of transverse shear stresses on the two bounding surfaces of the plate as well as at the interfaces are now used to reduce the number of unknowns in Eqs. (13). For simplicity, it is assumed that no tangential tractions are exerted on ${}^{(0)}\Omega$ and ${}^{(k)}\Omega$, where Eqs. (13) and the first and third of Eqs. (14) give the tangential tractions. Hence

$$\psi_\alpha = -u_{3,\alpha},$$

$$\eta_\alpha = -\frac{2}{3}\left(\frac{1}{h}\varphi_\alpha + \frac{1}{2h^2}\sum_{m=1}^{k-1} {}^{(m)}u_\alpha\right). \quad (16)$$

The conditions of continuously distributed transverse shear stresses at the interfaces lead to, by using Eqs. (16), (13) and the first and third of Eqs. (14),

$$\frac{1}{2}{}^{(i)}E_{\alpha 3\omega 3}{}^{(i)}u_\omega + ({}^{(i+1)}E_{\alpha 3\omega 3} - {}^{(i)}E_{\alpha 3\omega 3})\left[\left({}^{(i)}h - \frac{1}{h}{}^{(i)}h^2\right)\varphi_\omega + \frac{1}{2}\sum_{m=1}^{i} {}^{(m)}u_\omega - \frac{1}{2h^2}{}^{(i)}h^2\sum_{m=1}^{k-1} {}^{(m)}u_\omega\right] = 0, \quad (i = 1, \ldots, k-1). \quad (17)$$

In fact, Eq. (17) can be regarded as $2(k-1)$ linear algebraic equations involving the $2(k-1)$ unknowns ${}^{(i)}u_\alpha$ $(i = 1, \ldots, k-1)$, which give the following relationship between ${}^{(i)}u_\alpha$ and φ_λ

$${}^{(i)}u_\alpha = {}^{(i)}a_{\alpha\lambda}\varphi_\lambda, \quad (i = 1, \ldots, k-1), \quad (18)$$

in which the ${}^{(i)}a_{\alpha\lambda}$ depend only on the material elasticity properties of each layer and are therefore known constants.

Substitution of Eqs. (16) and (18) into the first of Eqs. (13) yields

$$v_\alpha = u_\alpha - x_3u_{3,\alpha} + f_{\alpha\lambda}\varphi_\lambda + \sum_{m=1}^{k-1} {}^{(m)}\Delta v_\alpha H(x_3 - {}^{(m)}h), \quad (19)$$

in which, using the Kronecker delta,

$$f_{\alpha\lambda} \equiv f_{\alpha\lambda}(x_3) = \delta_{\alpha\lambda}x_3^2 + c_{\alpha\lambda}x_3^3 + \sum_{m=1}^{k-1} {}^{(m)}a_{\alpha\lambda}(x_3 - {}^{(m)}h)H(x_3 - {}^{(m)}h),$$

$$c_{\alpha\lambda} = -\frac{2}{3h}\left(\delta_{\alpha\lambda} + \frac{1}{2h}\sum_{m=1}^{k-1} {}^{(m)}a_{\alpha\lambda}\right). \quad (20)$$

The spring-layer interface model of Eq. (6) for plate problems can be rewritten in the component form

$${}^{(m)}\Delta v_\alpha = {}^{(m)}R_{\alpha\beta}(x_\rho)\sigma_{\beta 3}(x_\alpha, {}^{(m)}h; t), \quad (m = 1, \ldots, k-1). \quad (21)$$

The displacement jump at each interface is obtained, from Eq. (19), the first and third of Eqs. (14) and Eq. (21) as

$${}^{(m)}\Delta v_\alpha = {}^{(m)}R_{\alpha\beta}(x_\rho)({}^{(m+1)}E_{\beta 3\omega 3}f_{\omega\lambda,3}({}^{(m)}h^+)\varphi_\lambda, \quad (22)$$

and then substituting into Eq. (19) gives the approximate displacement expression

$$v_\alpha = u_\alpha - x_3u_{3,\alpha} + h_{\alpha\lambda}\varphi_\lambda, \quad (23)$$

in which

$$h_{\alpha\lambda} \equiv h_{\alpha\lambda}(x_i) = f_{\alpha\lambda}(x_3) + \sum_{m=1}^{k-1} {}^{(m)}R_{\alpha\beta}(x_\rho)({}^{(m+1)}E_{\beta 3\omega 3}f_{\omega\lambda,3}({}^{(m)}h^+)H(x_3 - {}^{(m)}h). \quad (24)$$

The fact that the interface parameter ${}^{(m)}R_{\alpha\beta}$ depends upon x_ρ implies that the bonding strength at the interface ${}^{(m)}\Omega$ $(m = 1, \ldots, k-1)$ may be nonuniform, i.e., general cases of a small amount of interface weakness are included in the present theory.

By using the displacement expressions of Eq. (23) and the second of Eqs. (13), the associated strain and stress components can be obtained from Eqs. (14), but their explicit forms are not given herein.

5 Equations of Motion and Boundary Conditions

It is assumed that the mass density ρ of the plate is independent of time t and that an arbitrarily distributed normal load $q(x_\alpha; t)$ is applied to the surface Ω (${}^{(0)}\Omega$ or ${}^{(k)}\Omega$). From Hamilton's principle

$$\int_0^{t_0}\left(\int_V \sigma_{ij}\delta e_{ij}\,dV - \int_V \dot{v}_i\delta\dot{v}_i\rho dV - \int_\Omega q\delta v_3 d\Omega\right)dt = 0, \quad (25)$$

the dynamic fundamental equations are derived as

$$N_{\alpha\beta,\beta} - I\ddot{u}_\alpha + J\ddot{u}_{3,\alpha} - I_{\alpha\beta}\ddot{\varphi}_\beta = 0,$$

$$M_{\alpha\beta,\alpha\beta} + q - I\ddot{u}_3 - J\ddot{u}_{\alpha,\alpha} + K\ddot{u}_{3,\alpha\alpha} - (J_{\alpha\beta}\ddot{\varphi}_\beta)_{,\alpha} = 0,$$

$$P_{\lambda\beta,\beta} - R_\lambda - I_{\alpha\lambda}\ddot{u}_\alpha + J_{\alpha\lambda}\ddot{u}_{3,\alpha} - K_{\beta\lambda}\ddot{\varphi}_\beta = 0, \quad (26)$$

associated with either one of each of the following pairs of boundary conditions

$$n_\beta N_{\alpha\beta} = 0, \quad \text{or} \quad \delta u_\alpha = 0,$$

$$n_\beta(M_{\alpha\beta,\alpha} - J\ddot{u}_\beta + K\ddot{u}_{3,\beta} - J_{\beta\alpha}\ddot{\varphi}_\alpha) = 0, \quad \text{or} \quad \delta u_3 = 0,$$

$$n_\beta P_{\alpha\beta} = 0, \quad \text{or} \quad \delta\varphi_\alpha = 0,$$
$$n_\beta M_{\alpha\beta} = 0, \quad \text{or} \quad \delta u_{3,\alpha} = 0, \tag{27}$$

where

$$[N_{\alpha\beta}, M_{\alpha\beta}, P_{\lambda\beta}] = \int_0^h \sigma_{\alpha\beta}[1, x_3, h_{\alpha\lambda}]dx_3, \tag{28}$$

$$R_\lambda = \int_0^h \sigma_{\alpha i} h_{\alpha\lambda,i}\, dx_3, \tag{29}$$

$$[I, J, K] = \int_0^h \rho[1, x_3, x_3^2]dx_3, \tag{30}$$

$$[I_{\alpha\beta}, J_{\alpha\beta}, K_{\lambda\beta}] = \int_0^h \rho h_{\alpha\beta}[1, x_3, h_{\alpha\lambda}]dx_3. \tag{31}$$

Furthermore, Eqs. (28) and (29) can be rewritten, by using Eq. (23), the second of Eqs. (13) and Eqs. (14), as

$$\begin{bmatrix} N_{\alpha\beta} \\ M_{\alpha\beta} \\ P_{\lambda\beta} \\ R_\lambda \end{bmatrix} = \begin{bmatrix} C^{(1)}_{\alpha\beta\omega\rho} & -C^{(2)}_{\alpha\beta\omega\rho} & C^{(3)}_{\alpha\beta\nu\rho} & C^{(3)}_{\alpha\beta\nu\rho,\rho} \\ C^{(2)}_{\alpha\beta\omega\rho} & -C^{(4)}_{\alpha\beta\omega\rho} & C^{(5)}_{\alpha\beta\nu\rho} & C^{(5)}_{\alpha\beta\nu\rho,\rho} \\ C^{(3)}_{\omega\rho\lambda\beta} & -C^{(5)}_{\omega\rho\lambda\beta} & C^{(6)}_{\lambda\beta\nu\rho} & C^{(7)}_{\lambda\beta\nu} \\ C^{(3)}_{\omega\rho\lambda\beta,\beta} & -C^{(5)}_{\omega\rho\lambda\beta,\beta} & C^{(7)}_{\nu\rho\lambda} & C^{(8)}_{\lambda\nu} \end{bmatrix} \begin{bmatrix} u_{\omega,\rho} \\ u_{3,\omega\rho} \\ \varphi_{\nu,\rho} \\ \varphi_\nu \end{bmatrix}, \tag{32}$$

where

$$[C^{(1)}_{\alpha\beta\omega\rho}, C^{(2)}_{\alpha\beta\omega\rho}, C^{(3)}_{\alpha\beta\nu\rho}, C^{(4)}_{\alpha\beta\omega\rho}, C^{(5)}_{\alpha\beta\nu\rho}, C^{(6)}_{\lambda\beta\nu\rho}, C^{(7)}_{\lambda\beta\nu}]$$
$$= \int_0^h H_{\alpha\beta\omega\rho}[1, x_3, h_{\omega\nu}, x_3^2, x_3 h_{\omega\nu}, h_{\alpha\lambda}h_{\omega\nu}, h_{\alpha\lambda}h_{\omega\nu,\rho}]dx_3, \tag{33}$$

$$C^{(8)}_{\lambda\nu} = \int_0^h (H_{\alpha\beta\omega\rho}h_{\alpha\lambda,\beta}h_{\omega\nu,\rho} + E_{\alpha 3\omega 3}h_{\alpha\lambda,3}h_{\omega\nu,3})dx_3. \tag{34}$$

Finally, substitution of Eqs. (32) into Eqs. (26) yields

$$C^{(1)}_{\alpha\beta\omega\rho}u_{\omega,\rho\beta} - C^{(2)}_{\alpha\beta\omega\rho}u_{3,\omega\rho\beta} + (C^{(3)}_{\alpha\beta\nu\rho}\varphi_\nu)_{,\rho\beta} - I\ddot{u}_\alpha + J\ddot{u}_{3,\alpha} - I_{\alpha\beta}\ddot{\varphi}_\beta = 0,$$
$$C^{(2)}_{\alpha\beta\omega\rho}u_{\omega,\rho\alpha\beta} - C^{(4)}_{\alpha\beta\omega\rho}u_{3,\omega\rho\alpha\beta} + (C^{(5)}_{\alpha\beta\nu\rho}\varphi_\nu)_{,\rho\alpha\beta} + q - I\ddot{u}_3 - J\ddot{u}_{\alpha,\alpha} + K\ddot{u}_{3,\alpha\alpha} - (J_{\alpha\beta}\ddot{\varphi}_\beta)_{,\alpha} = 0,$$
$$C^{(3)}_{\omega\rho\lambda\beta}u_{\omega,\rho\beta} - C^{(5)}_{\omega\rho\lambda\beta}u_{3,\omega\rho\beta} + C^{(6)}_{\lambda\beta\nu\rho}\varphi_{\nu,\rho\beta} + (C^{(6)}_{\lambda\beta\nu\rho,\beta} + C^{(7)}_{\lambda\rho\nu} - C^{(7)}_{\nu\rho\lambda})\varphi_{\nu,\rho} + (C^{(7)}_{\lambda\beta\nu,\beta} - C^{(8)}_{\lambda\nu})\varphi_\nu - I_{\alpha\lambda}\ddot{u}_\alpha + J_{\alpha\lambda}\ddot{u}_{3,\alpha} - K_{\beta\lambda}\ddot{\varphi}_\beta = 0. \tag{35}$$

These equations need to be solved with the boundary conditions of Eqs. (27) to obtain the unknowns u_α, u_3, and φ_α for any set of plate parameters and the load parameter q. Obviously, Eqs. (35) have variable coefficients simply due to the nonuniform value of interface parameters ${}^{(m)}R_{\alpha\beta}$ at the interfaces ${}^{(m)}\Omega$ ($m = 1, \ldots, k-1$), so that for problems with uniform bonding strength at each interface, Eqs. (35) will have constant coefficients. By setting ${}^{(m)}R_{\alpha\beta} = 0$ ($m = 1, \ldots, k-1$), the corresponding governing equations and boundary conditions become simply those for perfect bonding, being exactly the same as those given by specializing the shell theory of He (1994) to the plate case. They are also very similar to those proposed by Di Sciuva (1992) and by Cho and Parmerter (1992, 1993), but are more general in the sense that layers are anisotropic rather than just orthotropic.

6 Numerical Example

Assessment of the accuracy of the present theory for cases with perfect bonding is unnecessary because of the final sentences of the previous section. However, it is interesting to get an insight into the influence of interfacial weakness on the global and local behaviors of multilayered anisotropic plates. Determination of interface parameters would need either theoretical evaluations of interfacial properties and microstructures or experimental measurements. However, here attention is restricted to investigating the effects of slightly weakened interfaces on the static bending behavior of multilayered plates. Therefore, an infinitely wide three-ply (0 deg/90 deg/0 deg) laminated plate of length l (in the x_1-direction) between simply supported edges at $x_1 = 0$ and $x_1 = l$ was chosen as the example even though it is not so representative as a CARALL plate for analysing interfacial weakness. Another reason for choosing this simple example is that its exact solution was obtained by Pagano (1969) from three-dimensional elasticity analysis of a perfectly bonded plate.

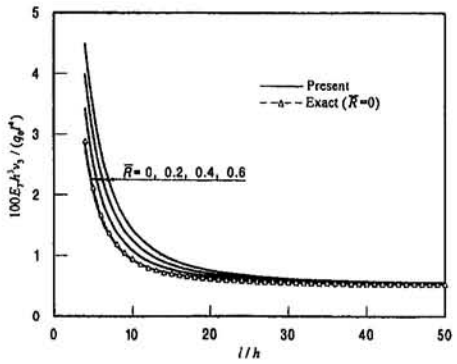

Fig. 2 Effect of span-to-thickness ratio on central deflection

Each layer has identical thickness and the stiffness properties

$$E_L = 172 \text{ GPa } (25 \times 10^6 \text{ psi}), \quad E_T = 6.9 \text{ GPa } (10^6 \text{ psi}),$$
$$G_{LT} = 3.4 \text{ GPa } (0.5 \times 10^6 \text{ psi}),$$
$$G_{TT} = 1.4 \text{ GPa } (0.2 \times 10^6 \text{ psi}), \quad \nu_{LT} = \nu_{TT} = 0.25, \tag{36}$$

where E is the tensile modulus, G is the shear modulus, ν is Poisson's ratio and the subscripts L and T signify parallel and normal to the fibers, respectively. The values are given in English units because the calculations were performed in English units since they were used by Pagano (1969) to obtain the exact results with which we are comparing. It is assumed that the interface parameter ${}^{(m)}R_{\alpha\beta} = \delta_{\alpha\beta}\bar{R}h/E_T$ ($m = 1, 2$), with $\bar{R}$ being a dimensionless quantity. This implies identically uniform bonding of the interfaces. Under the action of $q = q_0 \sin \pi x_1/l$, an exact solution of this problem has the following form

$$[u_1, u_3, \varphi_1] = \left[U_1 \cos\frac{\pi x_1}{l}, U_3 \sin\frac{\pi x_1}{l}, \Phi_1 \cos\frac{\pi x_1}{l}\right]. \tag{37}$$

From these expressions, exact displacements, strains, and stresses can easily be calculated for any point of the plate. Hence some numerical results are plotted in Figs. 2–6 to illustrate the effect of a small amount of interfacial weakness on the overall and local behaviors of the plate.

Figure 2 shows the variation of dimensionless central deflection as the span-to-thickness ratio varies. Figures 3–6 show the variations of dimensionless in-plane displacement, bending stress, and transverse shear stress distributions with position within the plate thickness. Here the transverse shear stress was calculated, respectively, from the constitutive equation to obtain Fig. 5 and from the equilibrium equation $\sigma_{\alpha i,i} = 0$ to obtain Fig. 6. The exact results given by Pagano (1969) for perfect bonding of the plate are also plotted in these figures. It is already well recognized in the literature, e.g. see Di Sciuva (1986, 1992), Cho and Parmerter (1992, 1993) and He (1994), that for the cases of moderately thick

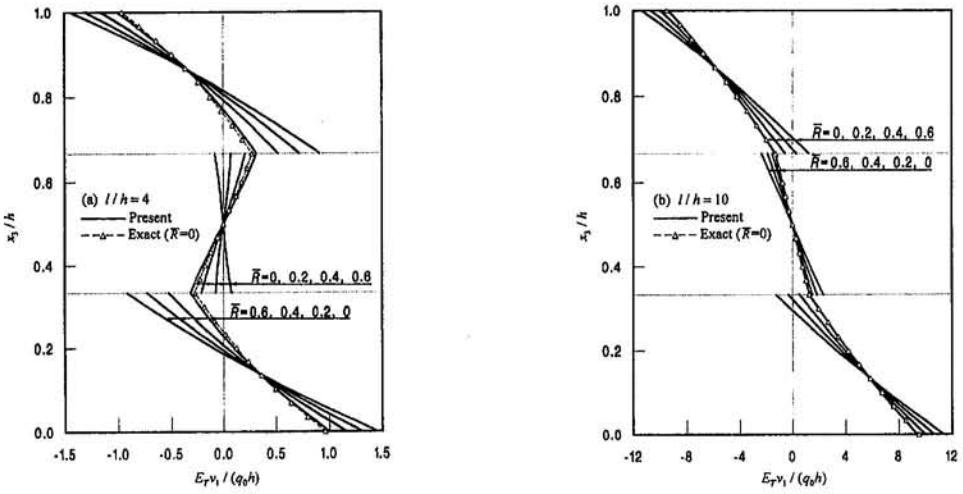

Fig. 3(*a*, *b*) Variation of in-plane displacement through thickness at $x_1 = 0$

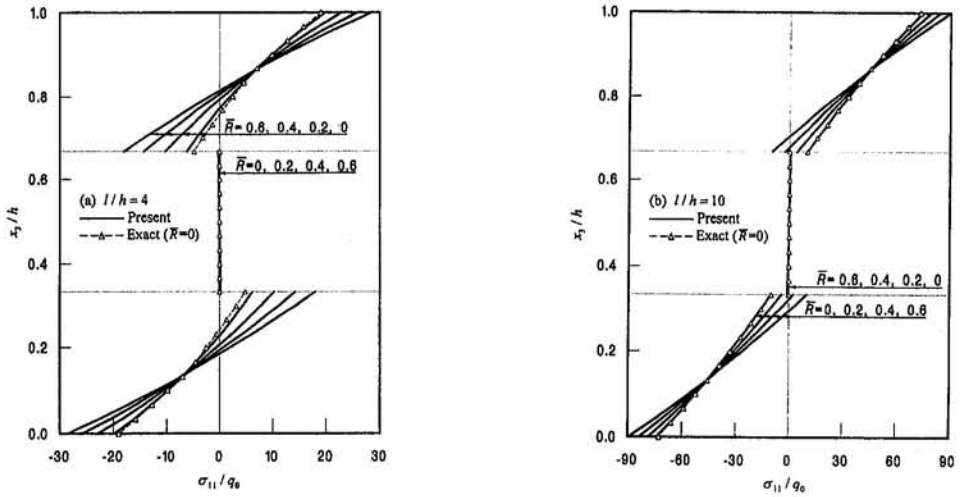

Fig. 4(*a*, *b*) Bending stress distribution through thickness at the midspan, $x_1 = l/2$

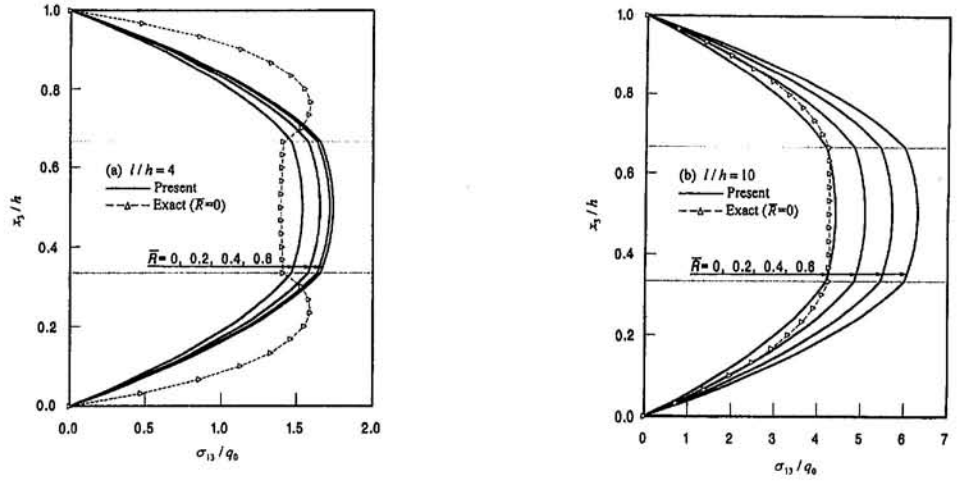

Fig. 5(*a*, *b*) Transverse shear stress through thickness at $x_1 = 0$, using constitutive equation

and very thick plates most plate theories which make an a priori assumption of through-thickness displacement distribution fail to accurately predict transverse shear stresses directly from constitutive equations. This is true for perfect interfaces with continuity conditions of tractions and displacements enforced. Instead, accurate evaluation of transverse shear stresses is obtained by using equilibrium equations. This is confirmed by comparing our results for $\bar{R} = 0$

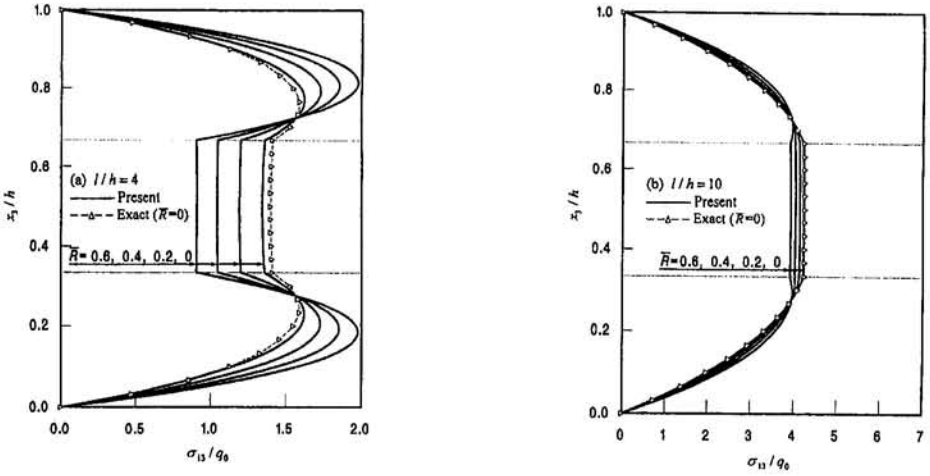

Fig. 6(*a*, *b*) Transverse shear stress through thickness at $x_1 = 0$, using equilibrium equation

on Figs. 5(a, b) and 6(a, b) with the exact results for perfect bonding. It can also be seen clearly that the trend of interface stress in Fig. 5 changes in an unexpected pattern, while the trend of interface stress in Fig. 6 is physically reasonable. Therefore, conclusions concerning transverse shear stress should be drawn from Figs. 6(a, b) rather than Figs. 5(a, b).

Figs. 2–6 show results when the interfacial parameter has the values $\bar{R} = 0$, 0.2, 0.4, 0.6. These values represent a decreasingly stiff interphase, i.e. a progressively weakened bonding, with $\bar{R} = 0$ corresponding to a perfect bond. Therefore increasing $\bar{R}$ means relaxation of the interfacial bonding strength, and hence reduction in the overall rigidity of plates. When curing composite materials, one purpose of weakening the interfacial bonding is to reduce interfacial stresses. Consistently with the foregoing, examination of Figs 2–6 reveals that the dimensionless central deflection increases as the interface parameter increases, while the dimensionless interface stress decreases, especially for small span-to-thickness ratios. Thus, as expected, increasing the parameter $\bar{R}$ causes reductions in interface stresses which are beneficial, but at the expense of increases of the central deflection.

7 Concluding Remarks and Suggestions for Future Work

A spring-layer model has been introduced to simulate interfacial weakness of multilayered anisotropic plates. By invoking rigorous analysis of through thickness displacement variation, the linear dynamic response of the plates has been incorporated in the present theory, which preserves all of the advantages of existing zigzag theories for perfect interfaces. Numerical results indicate that the strength of weakened bonding has significant effects on both the overall and local behaviors of the plates.

Suggestions for further improving the current predictive capability of the response of multilayered composite plates with interfacial imperfection include the following possible extensions of the theory presented:

1 The exact representation of through thickness displacement variation for plates in the present paper makes possible the incorporation of imperfect interfaces, including not only the slightly weakened bonding covered in this paper but also more pronounced weakening and even debonding. This would require retention of more terms than in Eqs. (13) for the displacement expressions.

2 Within the range prior to debonding, interfacial optimization and design could be performed so as to improve overall and local behaviours of the multilayered plates in a controlled manner, especially for interface stresses.

3 Complicating factors such as the microstructures and nonlinear properties of interphases and the residual strains resulting from curing of laminations are expected to be accounted for in due course.

Acknowledgments

The first author is grateful for helpful discussion with Prof. L. H. He and financial support, partly, from the Cardiff Advanced Chinese Engineering Centre and the National Science Foundation of China.

References

Aboudi, J., 1987, "Damage in composites—Modelling of imperfect bonding," *Composites Science and Technology,* Vol. 28, pp. 103–128.

Aboudi, J., and Paley, M., 1992, "Plastic buckling of ARALL plates," *Composite Structures,* Vol. 22, pp. 217–221.

Achenbach, J. D., and Zhu, H., 1989, "Effect of interfacial zone on mechanical behaviour and failure of fibre-reinforced composites," *Journal of the Mechanics and Physics of Solids,* Vol. 37, pp. 381–393.

Benveniste, Y., 1985, "The effective mechanical behaviour of composite materials with imperfect contact between the constituents," *Mechanics of Materials,* Vol. 4, pp. 197–208.

Benveniste, Y., 1987, "A new approach to the application of Mori-Tanaka's theory in composite materials," *Mechanics of Materials,* Vol. 6, pp. 147–157.

Benveniste, Y., and Dvorak, G. J., 1990, "On a correspondence between mechanical and thermal fields with slipping interfaces," *Inelastic Deformation of Composite Materials (IUTAM Symposium),* G. J. Dvorak, ed., Springer-Verlag, New York, pp. 77–98.

Bert, C. W., 1984, "A critical evaluation of new plate theories applied to laminated composite," *Composite Structures,* Vol. 2, pp. 329–347.

Budiansky, B., 1965, "On the elastic moduli of some heterogeneous materials," *Journal of the Mechanics and Physics of Solids,* Vol. 13, pp. 223–227.

Chattopadhyay, A., and Gu, H. Z., 1994, "New higher order plate theory in modelling delamination buckling of composite laminates," *AIAA Journal,* Vol. 32, pp. 1709–1716.

Chia, C. Y., 1980, *Nonlinear Analysis of Plates,* McGraw-Hill, New York.

Chia, C. Y., 1988, "Geometrically nonlinear behaviour of composite plates: a review," ASME *Applied Mechanics Reviews,* Vol. 41, pp. 439–451.

Cho, M., and Parmerter, R. R., 1992, "An efficient higher-order plate theory for laminated composites," *Composite Structures,* Vol. 20, pp. 113–123.

Cho, M., and Parmerter, R. R., 1993, "Efficient higher order composite plate theory for general lamination configurations," *AIAA Journal,* Vol. 31, pp. 1299–1306.

Cho, M., and Parmerter, R. R., 1994, "Finite element for composite plate bending based on efficient higher order theory," *AIAA Journal,* Vol. 32, pp. 2241–2248.

Christensen, R. M., and Lo, K. H., 1979, "Solutions for effective shear properties of three phase sphere and cylinder models," *Journal of the Mechanics and Physics of Solids,* Vol. 27, pp. 315–330.

Di Sciuva, M., 1986, "Bending, vibration and buckling of simply supported thick multilayered orthotropic plates: an evaluation of a new displacement model," *Journal of Sound and Vibration,* Vol. 105, pp. 425–442.

Di Sciuva, M., 1987, "An Improved Shear Deformation Theory for Moderately thick Multilayered Anisotropic Shells and Plates," ASME JOURNAL OF APPLIED MECHANICS, Vol. 54, pp. 589–596.

Di Sciuva, M., 1992, "Multilayered anisotropic plate models with continuous interlaminar stresses," *Composite Structures,* Vol. 22, pp. 149–167.

Di Sciuva, M., and Icardi, U., 1993, "Discrete-layer models for multilayered shells accounting for interlayer continuity," *Meccanica,* Vol. 28, pp. 281–291.

Gaudenzi, P., 1992, "A general formulation of higher-order theories for the analysis of laminated plates," *Composite Structures,* Vol. 20, pp. 103–112.

Hashin, Z., 1990, "Thermoelastic properties of fibre composites with imperfect interface," *Mechanics of Materials,* Vol. 8, pp. 333–348.

Hashin, Z., 1991a, "Thermoelastic properties of particulate composites with imperfect interface," *Journal of the Mechanics and Physics of Solids,* Vol. 39, pp. 745–762.

Hashin, Z., 1991b, "The Spherical Inclusion With Imperfect Interface," ASME JOURNAL OF APPLIED MECHANICS, Vol. 58, pp. 444–449.

Hashin, Z., 1993, "Errata on 'The spherical inclusion with imperfect interface,' " ASME JOURNAL OF APPLIED MECHANICS, Vol. 60, p. 582.

He, L. H., 1993, "A novel Karman-type nonlinear theory of anisotropic laminated plates," *Proceedings of the 2nd International Conference on Nonlinear Mechanics,* W. Z. Chien, ed., Beijing University Press, Beijing, pp. 237–240.

He, L. H., 1994, "A linear theory of laminated shells accounting for continuity of displacements and transverse shear stresses at layer interfaces," *International Journal of Solids and Structures,* Vol. 31, pp. 613–627.

Hill, R., 1965, "A self-consistent mechanics of composite materials," *Journal of the Mechanics and Physics of Solids,* Vol. 13, pp. 213–222.

Jasiuk, I., and Tong, Y., 1989, "The effect of interface on the elastic stiffness of composites," *Mechanics of Composite Materials and Structures (Proceedings of the Third Joint ASCE/ASME Conference),* J. N. Reddy and J. L. Teply, eds., AMD-Vol. 100, ASME, New York, pp. 49–54.

Li, S. H., Zhou, B. L., Zeng, Q. Y., and Bao, X. R., 1994, "A new kind of super-hybrid composite material for civil use-ramie fibre/Al," *Composites,* Vol. 25, pp. 225–228.

Librescu, L., 1975, *Elastostatics and Kinetics of Anisotropic and Heterogeneous Shell-type Structures,* Noordhoff, Leyden, Netherlands.

Librescu, L., and Schmidt, R., 1991, "Substantiation of a shear-deformable theory of anisotropic composite laminated shells accounting for the interlaminae continuity conditions," *International Journal of Engineering Science,* Vol. 29, pp. 669–683.

Lin, C. T., Kao, P. W., and Jen, M. H. R., 1994, "Thermal residual strains in carbon fibre-reinforced aluminium laminates," *Composites,* Vol. 25, pp. 303–307.

Mao, T. X., and Han, J. H., 1992, "Tensile fracture of carbon/epoxy aluminium laminates," *Proceedings of the Second International Symposium on Composite Materials and Structures,* C. T. Sun and T. T. Loo, eds., Beijing University Press, Beijing, pp. 899–904.

McLaughlin, R., 1977, "A study of the differential scheme for composite materials," *International Journal of Engineering Science,* Vol. 15, pp. 237–244.

Mori, T., and Tanaka, K., 1973, "Average stress in matrix and average elastic energy of materials with misfitting inclusions," *Acta Metallurgica,* Vol. 21, pp. 571–574.

Noor, A. K., and Burton, W. S., 1989, "Assessment of shear deformation theories for multilayered composite plates," ASME *Applied Mechanics Reviews,* Vol. 42, pp. 1–13.

Norris, A. N., 1985, "A differential scheme for the effective moduli of composites," *Mechanics of Materials,* Vol. 4, pp. 1–16.

Pagano, N. J., 1969, "Exact solutions for composite laminates in cylindrical bending," *Journal of Composite Materials,* Vol. 3, pp. 398–411.

Qu, J. M., 1993a, "Eshelby Tensor for an Elastic Inclusion With Slightly Weakened Interfaces," ASME JOURNAL OF APPLIED MECHANICS, Vol. 60, pp. 1048–1050.

Qu, J. M., 1993b, "The effect of slightly weakened interfaces on the overall elastic properties of composite materials," *Mechanics of Materials,* Vol. 14, pp. 269–281.

Reddy, J. N., 1984, "A Simple Higher-Order Theory for Laminated Composite Plates," ASME JOURNAL OF APPLIED MECHANICS, Vol. 51, pp. 745–752.

Reddy, J. N., and Robbins, Jr., D. H., 1994, "Theories and computational models for composite laminates," ASME *Applied Mechanics Reviews,* Vol. 47, pp. 147–169.

Reissner, E., 1985, "Reflections on the theory of elastic plates," ASME *Applied Mechanics Reviews,* Vol. 38, pp. 1453–1464.

Savithri, S., and Varadan, T. K., 1990, "Accurate bending analysis of laminated orthotropic plates," *AIAA Journal,* Vol. 28, pp. 1842–1844.

Savithri, S., and Varadan, T. K., 1993, "Large deflection analysis of laminated composite plates," *International Journal of Non-Linear Mechanics,* Vol. 28, pp. 1–12.

Schmidt, R., and Librescu, L., 1994, "Further results concerning the refined theory of anisotropic laminated composite plates," *Journal of Engineering Mathematics,* Vol. 28, pp. 407–425.

Vogelesang, L. B., and Gunnink, J. W., 1986, "ARALL: a materials challenge for the next generation of aircraft," *Materials and Design,* Vol. 7, pp. 287–300.

Weng, G. J., 1984, "Some elastic properties of reinforced solids with special reference to isotropic ones containing spherical inclusions," *International Journal of Engineering Science,* Vol. 22, pp. 845–856.

Xavier, P. B., Lee, K. H., and Chew, C. H., 1993, "An improved zigzag model for the bending of laminated composite shells," *Composite Structures,* Vol. 26, pp. 123–138.

Analytical Study of the Duffing Oscillator Excited by Colored Noise Using a Systematic Adiabatic Expansion

M. M. Wu[1]
Physics Department.

K. Y. R. Billah[2]

M. Shinozuka

Program in Mechanics,
Materials and Structures,
Department of Civil Engineering
and Operations Research.

Princeton University,
Princeton, NJ 08544

Analytical studies of nonlinear systems driven by colored noise are quite involved. If the inertia of the system is included in analysis, the results are physically realistic although the problem becomes more complex. Research along this line is in progress and this paper is an effort to study a nonlinear oscillator excited by correlated noise. The work delves on the Duffing oscillator driven by exponentially correlated noise. The colored Fokker-Planck equation is derived and the method of systematic adiabatic expansion is used to obtain the reduced probability density function from which the second-order moments are evaluated for different values of system parameters. Numerical simulation is carried out by generating colored noise using the spectral method. In the region where perturbation is valid, the results of adiabatic expansion agree very well with that of Monte Carlo simulation.

1 Introduction

Nonlinear oscillators subjected to random excitation occur in many areas of science and technology. In this context, the nonlinear system model that has received much attention in the last few decades is the Duffing oscillator (Lin and Cai, 1995; Roberts and Spanos, 1989). It is one of the simplest nonlinear systems which nonetheless demonstrates a highly complex behavior (Guckenheimer and Holmes, 1983; Scheffczyk et al., 1991). Many problems in engineering ranging from dynamic buckling to flow-induced vibration have been modeled using the white noise excited Duffing oscillator.

Nonlinear systems excited by white Gaussian noise have been studied thoroughly and are quite well understood. Great stride to the understanding of such oscillators has been made through the use of methods like stochastic linearization, moment closure, and perturbation, etc. (Caughey, 1971, 1986). To model physical systems realistically, however, it is imperative to take into account the correlation time of the noise, i.e., use the so-called colored noise (Moss and McClintock, 1989; Lin and Cai, 1995). Over the last decade substantial work has been carried out on nonlinear systems where the excitation is due to colored noise. Again, the method of stochastic linearization (Falsone and Elishikoff, 1992) has been innovatively applied to solve physical problems, and the results are compared to that of white noise in terms of percentage error of mean square. The method of stochastic averaging (Stratonovich, 1963; Lin and Cai, 1995) has also been applied to evaluate response and stability. A particular kind of noise, the so-called *narrow-band excitation* has been applied to the Duffing's oscillator using a combination of stochastic linearization and the method of multiple scales (Iyengar, 1988, 1989; Davis and Nandall, 1987; Rajan and Davis, 1988). The Duffing oscillator under nonwhite noise has also been studied using the Wiener-Hermite functional representation (Roy and Spanos, 1992). Lately, the so-called van Kampen expansion method, which is a method using the cumulant expansion, has been applied for the Duffing oscillator excited by an exponentially correlated noise (Weinstein and Benaroya, 1994).

In all these methods, the time scales are not explicitly discussed and therefore the effect of correlation time of noise is not directly accounted. It is well known that the method of stochastic averaging, introduced by Stratonovich (1963), considers two distinct time scales for nonlinear systems, and has been applied to many problems in engineering. Its use has been justified based on the rigorous proof of the validility of the method given by Khasminiskii (1967). Unfortunately, the method is suitable for systems where damping is nonlinear. In the case of Duffing oscillator, with hardening or softening spring, the method averages out the nonlinear stiffness effect, and reduces the problem to a linear one.

In physics, some work has been carried out on the nonlinear Duffing oscillator driven by colored noise. Much of the work, however, examines the response behavior of the system represented by one relevant variable, obeying an overdamped equation of motion excited by a color noise. This results in a system where the effect of inertia is neglected from the very beginning (van Kampen 1985) and two coupled first-order equations are solved; one for displacement x and the other for noise y. Even in this case, the coupled system is non-Markovian and approximate analysis must be used. Various methods along this line are outlined in Moss and McClintock (1989).

In many physical situations, however, the assumption of overdamped dynamics is not appropriate. Great difficulties are encountered when the inertia of the nonlinear system and the correlation time of the excitation are accounted for in the analysis (Moss and McClintock, 1989; Lindenberg and West, 1990; Hwalisz et al., 1989; Schimonsky-Geier, 1988; Fronzoni et al., 1986; Marchesori et al., 1988). Nevertheless, the work represented by these references have contributed greatly to the understanding of the response of the nonlinear dynamic systems subjected to colored noise.

2 Problem Definition

The problem of a Duffing oscillator driven by colored noise has not been completely solved as yet and therefore is the source

[1] Current address: Xerox Corp., 3400 Hillview Avenue, Palo Alto, Ca 94304.
[2] Permanent address: Department of Environmental and Coastal Engineering, Stevens Institute of Technology, Hoboken, NJ 07030.

Contributed by the Applied Mechanics Division of THE AMERICAN SOCIETY OF MECHANICAL ENGINEERS for publication in the ASME JOURNAL OF APPLIED MECHANICS.

Discussion on this paper should be addressed to the Technical Editor, Professor Lewis T. Wheeler, Department of Mechanical Engineering, University of Houston, Houston, TX 77204-4792, and will be accepted until four months after final publication of the paper itself in the ASME JOURNAL OF APPLIED MECHANICS.

Manuscript received by the ASME Applied Mechanics Division, June 8, 1995; final revision, May 15, 1996. Associate Technical Editor: L. T. Wheeler.

of interest among many researchers. In particular, recently, the van Kampen expansion method (Weinstein and Benaroya, 1994), and modified stochastic linearization technique (Falsone and Elishakoff, 1994) were applied to the Duffing oscillator which evaluated the response of this oscillator under exponentially correlated colored noise. In the present work, the adiabatic expansion technique (van Kampen, 1985), which was previously found useful in stability studies (Graham and Schenzle, 1982; Billah and Shinozuka, 1991), has been utilized for this problem and the result is compared with that of Monte Carlo simulation.

The system considered is described by an equation of the form

$$\frac{1}{\gamma}\ddot{x} + \dot{x} + dx + bx^3 = y(t). \tag{1}$$

A convenient model for the noise is a stationary Ornstein-Uhlenbeck process, described by the equation

$$\dot{y}(t) = -\frac{1}{\tau}y + \frac{\sqrt{Q}}{\tau}\xi(t), \tag{2}$$

where $\xi(t)$ is the Gaussian white noise with $\langle\xi(t)\rangle = 0$ and $\langle\xi(t)\xi(0)\rangle = \delta(t)$. The correlation function of $y(t)$ thus satisfies

$$\langle y(t)y(0)\rangle = \frac{Q}{2\tau}e^{-|t|/\tau}. \tag{3}$$

Note that $y(t)$ becomes a Gaussian white noise as $\tau \to 0$ with Q fixed, in which case $\langle y(t)\rangle = 0$ and $\langle y(t)y(0)\rangle = Q\delta(t)$.

3 Systematic Adiabatic Expansion and Reduced Probability Density

Usually a dynamic system has widely different response times and often the behavior on a very short time scale is not of much interest. In fact, the purpose of the present paper is to consider the long-term behavior of a nonlinear system using the adiabatic expansion method. The method is consistent with the goal of concentrating on the long time scale of the system (Gardiner, 1986; Moss and McClintock, 1989; van Kampen, 1985). To explicate the method, consider as an example the Brownian motion for which the Lagevin equations are

$$\frac{dx}{dt} = v \tag{4}$$

$$m\frac{dv}{dt} = -\beta v + \sqrt{2\beta kT}\xi(t) \tag{5}$$

with the following Fokker-Planck equation for probability density function $p(x, v, t)$

$$\frac{\partial p}{\partial t} = -\frac{\partial}{\partial x}(vp) + \frac{\partial}{\partial v}\left(\frac{vp}{\tau_r}\right) + \frac{kT}{\tau_r^2}\frac{\partial^2 p}{\partial v^2}, \tag{6}$$

where $\tau_r = m/\beta$ is the relaxation time. The limit of large β and small m should result in very rapid relaxation of Eq. (5) to a quasi-stationary state, i.e., when $\tau_r \to 0$, $dv/dt \to 0$, therefore

$$v = \sqrt{\frac{2kT}{\beta}}\xi(t) \tag{7}$$

resulting in

$$\frac{dx}{dt} = \sqrt{\frac{2kT}{\beta}}\xi(t). \tag{8}$$

In this case v has been eliminated; v is called the *fast variable*, which is assumed to relax very rapidly to the value given by Eq. (7). The Fokker-Planck equation corresponding to Eq. (8) is thus

$$\frac{\partial p(x, t)}{\partial t} = \frac{kT}{\beta}\frac{\partial^2 p(x, t)}{\partial x^2} \tag{9}$$

where

$$p(x, t) = \int_{-\infty}^{\infty} p(x, v, t)dv. \tag{10}$$

The above procedure of eliminating the fast variable is somewhat drastic. A more systematic method of deriving the reduced equation (in the form of Eq. (9) from Eq. (6)) in a perturbative manner with higher corrections in powers of a small parameter is called *adiabatic expansion* (Stratonovich, 1963; Wilemski, 1976; Titulaer, 1978). In the present work, Wilemski's systematic analysis is followed for solving a nonlinear oscillator excited by colored noise.

4 Adiabatic Expansion for the Duffing Oscillator

For Eq. (1), the following scaled variables are introduced:

$$x' = x/\sqrt{Q},$$
$$y' = (1/\sqrt{\gamma Q})y,$$
$$k'(x') = k(x)/\sqrt{Q}, \tag{11}$$

where $k(x) = dx + bx^3$ is the force due to potential $V(x)$ associated with the Duffing equation:

$$V(x) = \frac{d}{2}x^2 + \frac{b}{4}x^4. \tag{12}$$

Two more important parameters are also introduced:

$$\lambda = 1/(\gamma\tau),$$
$$\epsilon = \sqrt{1/\gamma}. \tag{13}$$

Rewriting Eq. (1) in terms of the scaled variables and the new parameters, the following system of ordinary differential equations is obtained:

$$\frac{dx'}{dt} = \frac{1}{\epsilon}u,$$
$$\frac{du}{dt} = -\frac{1}{\epsilon}k'(x') - \frac{1}{\epsilon^2}(u - y'),$$
$$\frac{dy'}{dt} = -\frac{1}{\epsilon^2}\lambda y' + \frac{1}{\epsilon}\lambda\xi(t). \tag{14}$$

This system is solved for long-term behavior with large value of γ (fast relaxation) and arbitrary λ, i.e., $\lambda = O(1)$, and $\epsilon \to 0$. From now on, all primes are omitted in the notation for simplicity.

For the probability density function $p(x, y, u, t)$, the Fokker-Planck equation is obtained by the method introduced by Lax (1966) as outlined below. For systems described by equations

$$\dot{x}_i(t) = L_i(\{x_i\}) + G_{ij}(\{x_i\})F_j, \tag{15}$$

where F_j is the Gaussian white noise, the stochastically equivalent equation for $p(\{x_k\}, t)$ is

$$\frac{\partial}{\partial t}p(\{x_k\}, t) = \frac{\partial}{\partial x_i}(k_i^{(1)}(\{x_k\})p(\{x_k\}, t)) + \frac{1}{2}\frac{\partial^2}{\partial x_i \partial x_j}(k_{ij}^{(2)}(\{x_k\})p(\{x_i\}, t)), \tag{16}$$

where the coefficients $k_i^{(1)}(\{x_k\})$ and $k_{ij}^{(2)}(\{x_k\})$ are related to the coefficients of Eq. (15) by the following relations:

$$k_i^{(1)}(\{x_k\}) = L_i(\{x_k\}) + \frac{1}{2}\frac{\partial G_{ij}}{\partial x_l} G_{lj} \tag{17}$$

and

$$k_{ij}^{(2)}(\{x_k\}) = G_{il}(\{x_k\})G_{jl}(\{x_k\}). \tag{18}$$

It is to be noted that in Eqs. (15)–(18), summation over repeated indices is implied.

The Fokker-Planck equation corresponding to Eq. (14) is then

$$\frac{\partial p}{\partial t} = \frac{1}{\epsilon^2}\left[\lambda\frac{\partial}{\partial y}y + \frac{\lambda^2}{2}\frac{\partial^2}{\partial y^2} + \frac{\partial}{\partial u}(u - y)\right]p + \frac{1}{\epsilon}\left[k(x)\frac{\partial}{\partial u} - \frac{\partial}{\partial x}u\right]p, \tag{19}$$

where p represents $p(x, y, u, t)$. The reduced probability density $p(x, t)$ is marginal density defined as

$$p(x, t) = \int_{-\infty}^{\infty}\int_{-\infty}^{\infty} p(x, y, u, t)dudy, \tag{20}$$

and the moments $j_{n,m}$ are defined as

$$j_{n,m}(x, t) = \int u^n y^m p(x, y, u, t)dudy, \tag{21}$$

and in particular,

$$j_{0,0}(x, t) = p(x, t). \tag{22}$$

Integrating the Fokker-Planck equation Eq. (19) for the joint probability $p(x, y, u, t)$, the following equation for $p(x, t)$ is obtained:

$$\frac{\partial}{\partial t}p(x, t) = -\frac{1}{\epsilon}\frac{\partial}{\partial x}j_{1,0}(x, t). \tag{23}$$

By utilizing a method developed by Wilemski (1976), a closed-form expression for $p(x, t)$ can be derived in the form of a perturbation expansion in the parameter ϵ. Multiplying Eq. (19) by $u^n y^m$ and integrating, the following equation is obtained:

$$\frac{\partial}{\partial t}j_{n,m}(x, t) = -\frac{1}{\epsilon^2}(n + \lambda m)j_{n,m} - \frac{1}{\epsilon}\left[nk(x)j_{n-1,m} + \frac{\partial}{\partial x}j_{n+1,m}\right] + \frac{1}{\epsilon^2}\left[nj_{n-1,m+1} + \frac{\lambda^2}{2}m(m-1)j_{n,m-2}\right]. \tag{24}$$

As $\epsilon \to 0$, Eq. (24) describes a rapidly damped time evolution of the moments $j_{n,m}$ for $n, m \neq 0$ in a time scale ϵ^2 as indicated by the diagonal term in Eq. (24). In the asymptotic time regime ($t \gg \epsilon$), Eq. (24) has the approximate solution

$$j_{n,m}(x, t) = \frac{-\epsilon^2}{n + \lambda m}\left\{\frac{1}{\epsilon}\left[nk(x)j_{n-1,m} + \frac{\partial}{\partial x}j_{n+1,m}\right] - \frac{1}{\epsilon^2}\left[nj_{n-1,m+1} + \frac{\lambda^2}{2}m(m-1)j_{n,m-2}\right]\right\}. \tag{25}$$

Substituting Eq. (25) back into Eq. (24), the iterative solution of $j_{n,m}(x, t)$ is then obtained as

$$j_{n,m}(x, t) = \sum_{l=0}^{\infty}\left[\frac{-\epsilon^2}{n + \lambda m}\frac{\partial}{\partial t}\right]^l \times \frac{1}{n + \lambda m}\left\{-\epsilon\left[nk(x)j_{n-1,m} + \frac{\partial}{\partial x}j_{n+1,m}\right] + \left[nj_{n-1,m+1} + \frac{\lambda^2}{2}m(m-1)j_{n,m-2}\right]\right\}. \tag{26}$$

The moment $j_{1,0}$ is evaluated up to a given order in ϵ by expressing it in terms of $j_{0,0}$ and its derivatives. In order to derive expressions to the first order in ϵ from Eq. (27), $j_{2,0}$ is evaluated to the zeroth order of ϵ and $j_{0,1}$ to the first order, which requires the evaluation of $j_{1,1}$ and $j_{0,2}$ to the zeroth order:

$$j_{0,2} = \frac{\lambda}{2}j_{0,0}, \tag{27}$$

$$j_{1,1} = \frac{1}{1 + \lambda}j_{0,2}, \tag{28}$$

$$j_{0,1} = -\frac{\epsilon}{\lambda}\frac{\partial}{\partial x}j_{1,1} = -\frac{\epsilon}{2}\frac{1}{1 + \lambda}\frac{\partial}{\partial x}j_{0,0}, \tag{29}$$

$$j_{2,0} = j_{1,1} = \frac{1}{2}\frac{\lambda}{1 + \lambda}j_{0,0}, \tag{30}$$

Equation (26) is then simplified to

$$j_{1,0}(x, t) = -\epsilon k(x)p(x, t) - \frac{1}{2}\frac{\epsilon}{1 + \lambda}\left[\frac{\partial}{\partial x} + \lambda\frac{\partial}{\partial x}\right]p(x, t) + O(\epsilon^3). \tag{31}$$

Substituting Eq. (31) into Eq. (23) gives the desired equation for the reduced probability density $p(x, t)$:

$$\frac{\partial}{\partial t}p(x, t) = \frac{\partial}{\partial x}\left[k(x) + \frac{1}{2}\frac{\partial}{\partial x}\right]p(x, t). \tag{32}$$

Table 1 The normalization constants *N* for different system parameters

(a) d=1, Q=1 (b) d=1, b=1 (c) b=1, Q=1

b	N
0.000000	0.8862303
0.500000	0.7916504
1.000000	0.7431586
1.500000	0.7097491
2.000000	0.6842151
2.500000	0.6635685
3.000000	0.6462587
3.500000	0.6313795
4.000000	0.6183469
4.500000	0.6067659
5.000000	0.5963565

Table 1(*a*)

Q	N
0.500000	0.5597789
1.000000	0.7431554
1.500000	0.8692590
2.000000	0.9676239
2.500000	1.0491899
3.000000	1.1193506
3.500000	1.1811996
4.000000	1.2366907
4.500000	1.2871428
5.000000	1.3334919

Table 1(*b*)

d	N
0.0000000	1.077907
0.2500000	0.9641283
1.000000	0.7431586
2.250000	0.5583445
4.000000	0.4338767
6.250000	0.3512605
9.000000	0.2940762
12.25000	0.2525835
16.00000	0.2212347
20.25000	0.1967601
25.00000	0.1771393
30.25000	0.1610662
36.00000	0.1476617
42.25000	0.1363139
49.00000	0.1265841

Table 1(*c*)

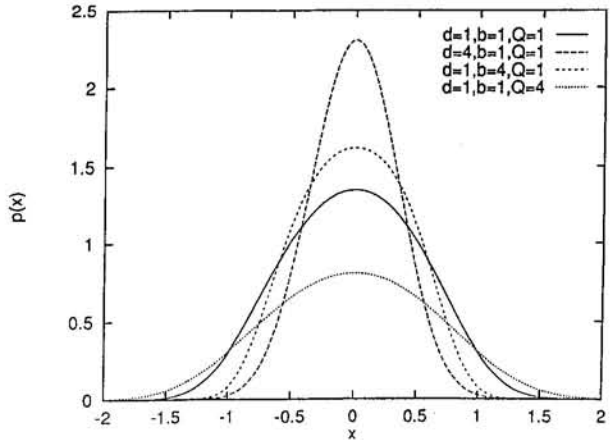

Fig. 1 Stationary probability density distribution $p_0(x)$ with different system parameters d, b and Q

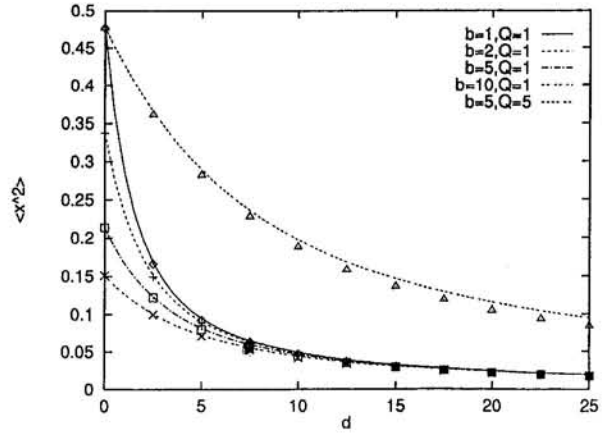

Fig. 3 The comparison of the second-order moments $\langle x^2 \rangle$ from theoretical analysis and Monte Carlo simulation, as functions of b, Q and d, respectively. The lines are from adiabatic expansion, and the points are from numerical simulation.

The corresponding stationary solution is then

$$p_0(x) = N \exp\left\{-\frac{d}{Q}x^2 - \frac{1}{2}\frac{b}{Q}x^4\right\} \tag{33}$$

which is written in terms of the unscaled and unprimed variables with N being the normalization constant. The second-order moment is defined as

$$\langle x^2 \rangle = \int_{-\infty}^{\infty} x^2 p_0(x)\,dx. \tag{34}$$

The normalization constants N are given in Table 1 for different system parameters d, b, and Q.

5 Numerical Simulation

A numerical study is now presented and compared with the above analytical results. To this goal colored noise is generated by a method introduced originally by Shinozuka (Shinozuka, 1972). The method has been revised over the years (Shinozuka and Deodatis, 1991) and has been found to be suitable for the type of nonlinear analysis presented here (Wu et al., 1995; Billah and Shinozuka, 1990, 1991). The one-dimensional Gaussian noise was simulated by the following series with a large N:

$$y(t) = \sqrt{2} \sum_{n=0}^{N-1} (2S(\omega_n)\Delta\omega)^{1/2} \cos(\omega_n t + \Phi_n), \tag{35}$$

where $\omega_n = n\Delta\omega$, $n = 1, 2, \ldots, N$, and $\Delta\omega = \omega_u/N$. ω_u represents an upper cutoff frequency beyond which the power spectral density may be assumed to be zero. The Φ_n appearing in Eq. (35) are independent random phase angles distributed uniformly over the interval $[0, 2\pi]$. The period of the stochastic process is $T_0 = 2\pi/\Delta\omega$.

In the present case the power spectral density $S(\omega)$, corresponding to the exponential correlation function, has the form

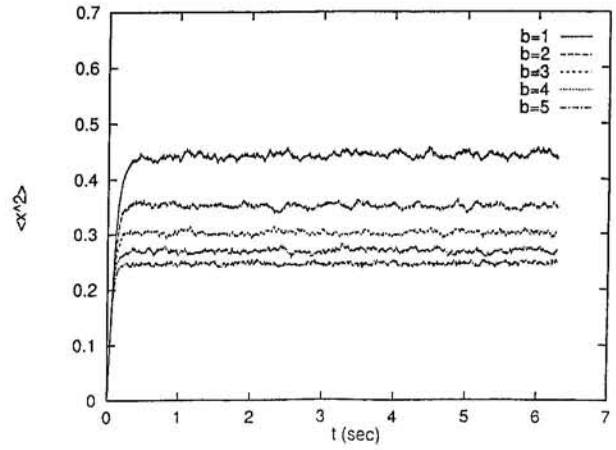

Fig. 2 Time evolution of the second-order moment $\langle x^2 \rangle$ obtained from numerical simulation.

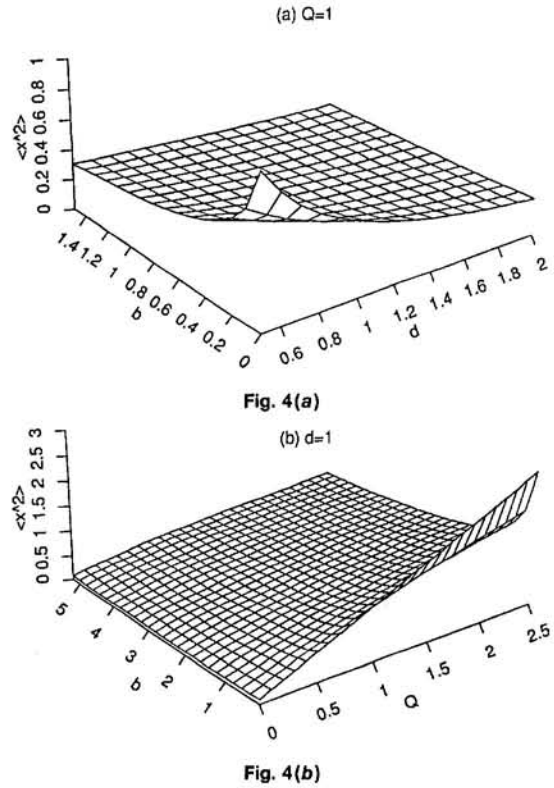

Fig. 4(a)

Fig. 4(b)

Fig. 4 The second-order moments $\langle x^2 \rangle$ as functions of b, d and b, Q by adiabatic expansion

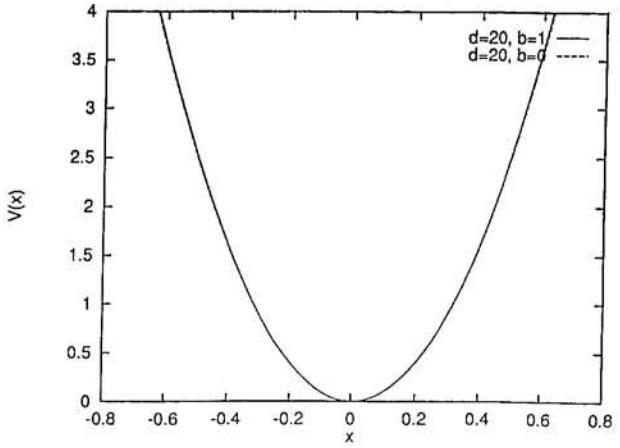

Fig. 5 Potential $V(x) = (d/2)x^2 + (b/4)x^4$ with $d = 20$, $b = 1$ and $d = 20$, $b = 0$

$$S(\omega) = \frac{Q}{2\pi\tau^2}\frac{1}{\omega^2 + (1/\tau)^2}. \quad (36)$$

Using Runge-Kutta method to integrate Eq. (1), the long-term response of the Duffing oscillator excited by colored noise is found, from which statistics such as standard deviation (or the second-order moments) are obtained.

6 Results and Discussion

To satisfy the requirement that γ be large, γ in Eq. (1) is taken as 100. At the same time, τ is chosen as 0.01 to ensure that $\lambda = 1/(\tau\gamma) = O(1)$, thus $\epsilon = \sqrt{1/\gamma} = 0.1$.

Figure 1 shows the stationary probability density distribution $p_0(x)$ with different values of d, b and Q obtained from preceding adiabatic expansion analysis. Figure 2 shows the time evolution of the second-order moment $\langle x^2\rangle$ calculated by means of Monte Carlo simulation. It can be seen that $\langle x^2\rangle$ becomes stable in a short time. Figure 3 shows the comparison of the second-order moment $\langle x^2\rangle$ as functions of b, Q and d, for both theoretical analysis and numerical simulation. It can be seen clearly that the results of theoretical analysis are in very good agreement with those of the numerical simulation. Figure 4 shows the second-order moments $\langle x^2\rangle$ as functions of b, d and b, Q by adiabatic expansion.

For the limiting case $b \to 0$, the oscillator response can be solved exactly and the mean square is obtained as (Stratonovich, 1963; Gardiner, 1985)

$$\langle x^2\rangle = \int_{-\infty}^{+\infty} \frac{Q}{2\pi\tau^2}\frac{1}{\omega^2 + (1/\tau)^2}\frac{1}{(d - \omega^2/\gamma)^2 + \omega^2}d\omega. \quad (37)$$

By using the computer algebra system *Maple*, for $b = 0$, $d = 1$, and $Q = 1$, a value of $\langle x^2\rangle = 0.498$ is obtained. The Monte Carlo simulation (1000 samples) gives $\langle x^2\rangle = 0.496$, which agrees very well with the exact value. The point corresponding $b = 0$ forms an anchor point to verify the accuracy of both theoretical and simulation methods. When d is large compared to b, the system can be approximated by the corresponding linear system. Figure 5 shows the potential $V(x)$ respectively with $d = 20$, $b = 1$ and $d = 20$, $b = 0$. In the range of significance, the potentials are almost identical. The exact mean square for the linear oscillator with $d = 20$ and $Q = 1$ is $\langle x^2\rangle = 0.0227$, while the Monte Carlo simulation gives $\langle x^2\rangle = 0.0226$ for $d = 20$, $Q = 1$ and $b = 1$ (the nonlinear term is included). This agreement again verifies the validity of the Monte Carlo simulation results.

7 Conclusion

The Duffing oscillator excited by colored noise is studied in this paper. The limitations of analytical methods are clearly shown by the restriction on the parameter values of the equation. These limitations are due to the use of colored noise in the analysis which results in extended Fokker-Planck equation. Such an equation is intrinsicaly difficult to solve and therefore, solution of the equation for other parameter values can only be obtained by numerical simulation. Results obtained by using stochastic linearization, stochastic averaging or Van Kampon expansion are difficult to compare with the present results since the former ones do not address the issue of restricted parameter values. The paper emphasizes that such parameter value restrictions are absolutely necessary for obtaining physically valued results.

References

Billah, K. Y. R., and Shinozuka, M., 1990, "Numerical method for colored-noise generation and its application to a bistable system," *Physical Review A*, Vol. 42, R7492–7495.

Billah, K. Y. R., and Shinozuka, M., 1991, "Stabilization of a nonlinear system by multiplicative noise," *Physical Review A*, Vol. 44, R4779–4781.

Caughey, T. K., 1971, "Nonlinear Theory of Random Vibrations," *Advances in Applied Mechanics*, Vol. 11, C. S. Yih, ed., Academic Press, New York, pp. 209–253.

Caughey, T. K., 1986, "On the response of Non-Linear Oscillators to Stochastic Excitation," *Probabilistic Engineering Mechanics*, Vol. 1, No. 1, pp. 2–4.

Davies, H. G., and Nandlall, D., 1986, "Phase Plane for Narrow Band Random Excitation of a Duffing Oscillator," *Journal of Sound and Vibration*, Vol. 104, No. 2, pp. 277–283.

Elishakoff, I., and Zhang, X., 1992, "An Appraisal of Different Stochastic Linearization Techniques," *Journal of Sound and Vibration*, Vol. 153, No. 2, pp. 370–375.

Falsone, G., and Elishakoff, I., 1994, "Modified Stochastic Linearization Technique for Colored Noise Excitation of Duffing Oscillator," *International Journal of Non-linear Mechanics*, Vol. 29, No. 1, pp. 65–69.

Fronzoni, L., Grigolini, P., Hänggi, P., Moss, F., Manella, R., and McClintock, P. V. E., 1986, "Bistable oscillator dynamics driven by nonwhite noise," *Physical Review A*, Vol. 33, pp. 3320–3327.

Gardiner, C. W., 1985, *Handbook of Stochastic Methods for Physics, Chemistry and the Natural Sciences*, 2nd ed., Springer-Verlag, Berlin.

Graham, R., and Schenzle, A., 1982, "Stabilization by Multiplicative Noise," *Physical Review A*, Vol. 26, No. 3, pp. 1676–1685.

Guckenheimer, J., and Holmes, P., 1983, *Nonliear Oscillations, Dynamical Systems, and Bifurcations of Vector Fields*, Springer, Berlin.

H'walisz, L., Jung, P., Hänggi, P., Talkner, P., and Schimansky-Geier, L., 1989, Colored Noise Driven Systems With Inertia," *Zeitschrift für Physik B*, Vol. 77, pp. 471–483.

Iwan, W. D., and Spanos, P.-T., 1978, "Response Envelope Statistics for Nonlinear Oscillators with Random Excitation," ASME JOURNAL OF APPLIED MECHANICS, Vol. 45, pp. 170–174.

Iyengar, R. N., 1988, "Stochastic Response and Stability of the Duffing Oscillator under Narrowband Excitation," *Journal of Sound and Vibration*, Vol. 126, No. 2, pp. 255–263.

Iyengar, R. N., 1989, "Response of Nonlinear Systems to Narrow-band Excitation," *Structural Safety*, Vol. 6, pp. 177–185.

Lax, M., 1966, "Classical noise IV: Langevian Methods," *Reviews of Modern Physics*, Vol. 38, pp. 541–546.

Lin, Y. K., and Cai, 1995, *Probabilistic Structural Dynamics, Advanced Theory and Applications*, McGraw-Hill, New York.

Lindenberg, K., and West, B. J., 1990, *The Nonequilibrium Statistical Mechanics of Open and Closed Systems*, VCH Publisher, New York, 1990.

Marchesori, F., Menichella-Suetta, E., Pochini, M., and Santucci, S., 1988, *Phys. Rev.*, Vol. A37, p. 3059.

Moss, F., and McClintock, P. V. E., 1989, *Noise in Nonlinear Dynamical Systems*, Vol. 1–3, Cambridge University Press, Cambridge, U.K.

Rajan, S., and Davies, H. G., 1988, "Multiple Time Scaling of the Response of a Duffing Oscillator to Narrow-band Random Excitation," *Journal of Sound and Vibration*, Vol. 123, No. 3, pp. 497–506.

Roberts, J. B., and Spanos, P. D., 1990, *Random Vibration and Statistical Linearization*, John Wiley and Sons, New York.

Roy, R. V., and Spanos, P. D., 1989, "Wiener-Hermite Functional Representation of Nonlinear Stochastic Systems," *Structural Safety*, Vol. 6, pp. 187–202.

Schimonsky-Geier, L., 1988, "Effect of Additive Colored Noise on the Motion in an External Field," *Physics Letters A*, Vol. 126, pp. 455–458.

Scheffczk, C., Parlitz, U., Kurz, T., Knop, W., Lauterborn, W., 1991, "Comparison of Bifurcation Structures of Driven Dissipative Nonlinear Oscillators," *Physical Review A*, Vol. 43, pp. 6495–6502.

Shinozuka, M., 1972, "Monte Carlo Solution of Structural Dynamics," *Computers and Structures*, Vol. 2, pp. 855–874.

Shinozuka, M., and Deodatis, G., 1991, "Simulation of Stochastic Processes by Spectral Representation," *Applied Mechanics Reviews*, Vol. 44, No. 4, pp. 191–204.

Spanos, P. D., 1981, "Stochastic Linearization in Structural Dynamics," *Applied Mechanics Reviews*, Vol. 34, No. 1, pp. 1–8.

Stratonovich, R. L., 1963, *Introduction to the Theory of Random Noise,* Gordon and Breach, New York.

Titulaer, U. M., 1978, "A Systematic Solution Precedure for the Fokker-Planck Equation of a Brownian Particle in the High-friction Case," *Physica,* Vol. 91A, pp. 321–344.

Weinstein, E. M., and Benaroya, H., 1994, "The van Kampen Expansion for the Fokker-Planck Equation of a Duffing Oscillator Excited by Colored Noise," *Journal of Statistical Physics,* Vol. 77, Nos. 3/4, pp. 681–690.

Wilemski, G., 1976, "On the Derication of Smoluchowski Equations with corrections in the Classical Theory of Brownian Motion," *Journal of Statistical Physics,* Vol. 14, No. 2, pp. 153–169.

Wu, M., Billah, Y. K. R., and Shinozuka, M., 1995, "Numerical Solution of the Kardar-Parisi-Zhang Equation With Long-range Spatial Correlated Noise," *Physical Review E,* Vol. 51, pp. 995–998.

van Kampen, N. G., 1985, "Elimination of fast variables," *Phys. Rep.,* Vol. 124, pp. 69–160.

Out-of-Plane Displacement Derivative Measurements Using Interferometric Strain/Slope Gage

Keyu Li[1]
Department of Mechanical Engineering,
Oakland University,
Rochester, MI 48309

An optical method originally developed for measuring derivatives of in-plane displacements is redefined to measure derivatives of out-of-plane displacements. The technique is based on interference of laser beams reflected and diffracted from two microindentations closely depressed on a specimen surface. As in-plane and out-of-plane displacements cause the microindentations to move relatively to each other, the two interference fringe patterns change accordingly. Movement of the interference fringes is monitored with linear photodiode arrays and analyzed via a computer-controlled system that allows simultaneous measurements of the in-plane and out-of-plane displacement derivatives. The technique is referred to as the interferometric strain/slope gage (ISSG). Having short gage length (~100 μm), the technique is unique for measurements of high deformation gradients and for applications in complex geometries. Its principle as well as an experimental validation of measuring bending strains/stresses and deflection slopes in a cantilever beam is presented. The experiment shows that both the first-order and second-order derivatives of out-of-plane displacements can be obtained. Measurement sensitivities to in-plane and out-of-plane rigid-body motions are systematically investigated. The technique can be potentially extended to measure large deflection angles. The derived governing equations indicate a coupling effect between the in-plane and out-of-plane components. The associated instrumentation for data acquisition and analysis is described in great detail.

Introduction

Derivative of the in-plane displacement or strain is often measured using a strain gage. Resistance strain gages, extensometers, and capacitor strain gages are examples of conventional strain measurement devices. With the advent of the laser, optical strain gages including diffraction strain gages (Bell, 1956; Pryor and North, 1971) and interferometric strain gages (ISG) (Sharpe, 1968) have been developed. The interferometric strain rosette (ISR) (Li, 1995) is extended from the ISG for measurements of three in-plane strain components, which functions similarly as a strain rosette. Optical strain gages possess advantages over conventional gages in that they are associated with short gage lengths and noncontacting nature. Full-field optical strain measurement techniques such as holographic, speckle, and moiré interferometry methods (Kobayashi, 1987) can be used to measure derivatives of out-of-plane displacements in addition to derivatives of in-plane displacements (Hovanesian and Varner, 1970; Hung et al., 1974; Chiang et al., 1976; Ligtenberg, 1954). However, these interferometry methods require special environmental stability and are not well suited for industrial applications (Klumpp and Schnack, 1990; Sirkis and Lim, 1991; Sullivan, 1991; Schultheisz and Knauss, 1994). The moiré method requires a grating on a flat surface and thus prohibits its application to complex geometries such as notched areas (Parks, 1993; Post, 1993).

In this work, an interferometric strain/slope gage (ISSG) is extended from the ISG to measure derivatives of out-of-plane displacements besides derivatives of in-plane displacements. The principle of the ISG technique for measuring an in-plane strain (Sharpe, 1968) is based on the interference of laser light reflected from two microindentations placed on a specimen surface. The size and separation of the indentations are made small enough for the light diffracted from the two indentations to interfere. Strain causes the spacing between the indentations to change, which generates a phase shift in the interference fringes. Therefore, by measuring the shift in the interference fringes, the strain component in the direction of the indentation separation can be determined. When three indentations are used in an ISR technique (Li, 1995), the system is equivalent to a strain rosette and three strain gages are defined in the directions of the indentation separations. In the previous papers of Sharpe (1968) and Li (1995), measurements of out-of-plane displacements were not considered. The phase shift in the fringe patterns of an ISG or ISR can be caused by not only in-plane but also out-of-plane displacements. Measuring the phase shift in the fringe patterns could allow the simultaneous determination of both in-plane and out-of-plane displacement derivatives. This leads to the development of the ISSG technique. Besides measuring in-plane strains, the ISSG technique can be used to measure deflection slopes in beams, plates, and shells. The measurement principle is presented and the governing equations are derived for a pair of ISG microindentations. Using the same principle, the derivation may be extended to an ISR. An experimental investigation of cantilever beam deformations using a

[1] Keyu Li was formerly an assistant professor at Western Michigan University, Kalamazoo, MI, when part of the research was conducted.

Contributed by the Applied Mechanics Division of THE AMERICAN SOCIETY OF MECHANICAL ENGINEERS for presentation at the International Mechanical Engineering Congress and Exposition, the Winter Annual Meeting of The ASME, Atlanta, GA, Nov. 17–22, 1996.

Discussion on this paper should be addressed to the Technical Editor, Professor Lewis T. Wheeler, Department of Mechanical Engineering, University of Houston, Houston, TX 77204-4792, and will be accepted until four months after final publication of the paper itself in the ASME JOURNAL OF APPLIED MECHANICS.

Manuscript received by the ASME Applied Mechanics Division, June 6, 1995; final revision, Mar. 3, 1996. Associate Technical Editor: J. T. Jenkins.

Paper No. 96-WA/APM-3.

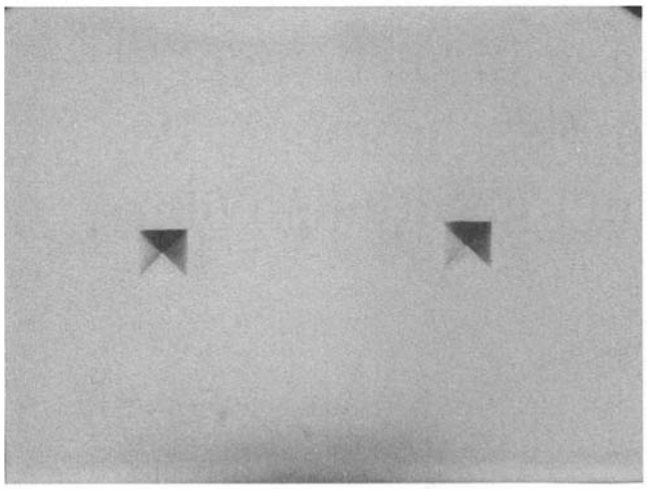

Fig. 1 A photomicrograph of a pair of the ISG indentations spaced 100 μm apart

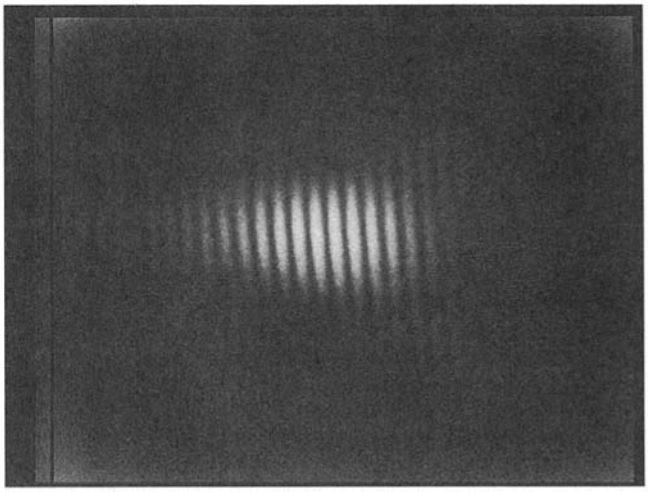

Fig. 3 A photograph of the interference fringe pattern of the two indentations in Fig. 1, taken at a distance of 30 cm from the indentations

pair of the ISG indentations is described. The ISSG technique is validated by comparing the experimental results with the well established analytical solutions. Advantages of the new technique over conventional methods will be discussed.

Principles of Measuring In-Plane and Out-of-Plane Displacement Derivatives

An ISSG consists of two ISG indentations which are pyramidal in shape, Fig. 1. The indentations are depressed on a specimen surface using a microhardness tester (LECO M-400-H). The size of the indentations is approximately 20 μm and the indentation separation is about 100 μm. The angle between the opposite facets in each indentation is 136 deg.

As illustrated in Fig. 2, two ISSG indentations on a deflected specimen surface are illuminated by a laser beam that is perpendicular to the original position of the specimen surface. Two reflective facets in each indentation diffract the incident laser beam in two directions. The diffracted patterns from the two indentations overlap to create two Young's interference fringe patterns. A typical fringe pattern is shown in Fig. 3. Since the fringe patterns are distant from the indentations, it is assumed that the interfering beams are parallel to each other between which the path length difference is formulated. The path length difference between the two incident laser beams upon the two indentations is $\Delta_1 = d \sin \alpha$. The path length difference between the reflected laser beams takes different formula for the two patterns: $\Delta_{1,r} = d \sin (\theta_1 + \alpha)$, for the pattern numbered 1; $\Delta_{2,r} = d \sin (\theta_2 - \alpha)$, for the pattern numbered 2. The total of the path length difference includes both differences between the incident beams and between the reflected beams: $\Delta_1 = [d \sin (\theta_1 + \alpha) + d \sin \alpha]$, for pattern 1; $\Delta_2 = [d \sin (\theta_2 - \alpha) - d \sin \alpha]$, for pattern 2. The interference principle dictates that fringes occur when the path length difference equals one wavelength or an integer multiple of a wavelength, which can be described by

$$\Delta_1 = d[\sin (\theta_1 + \alpha) + \sin \alpha] = \lambda m_1 \quad (1)$$

$$\Delta_2 = d[\sin (\theta_2 - \alpha) - \sin \alpha] = \lambda m_2 \quad (2)$$

where Δ_1 and Δ_2 are the respective path length differences for the fringe pattern numbered 1 on the top and the fringe pattern numbered 2 on the bottom; λ is the wavelength of the laser; m_1 and m_2 are fringe orders in the two fringe patterns; d is the indentation separation; α is the deflection angle of the specimen surface which approximately equals to the out-of-plane slope for small deflection; θ_1 and θ_2 are the respective angles between the incident and reflected laser beams for pattern 1 and pattern 2. For small deformation, the reflective facets in each indentation can be assumed to remain the same reflecting directions, and we have $\theta_1 = \theta_2 = \theta$. Angle θ is twice the inclination angle of the reflective facets in an indentation.

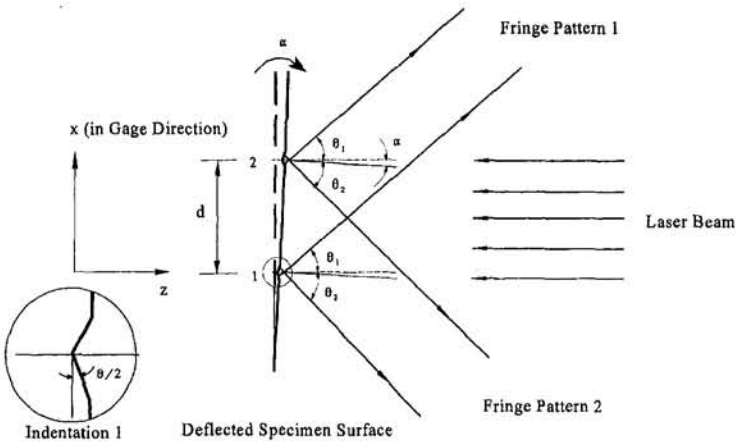

Fig. 2 A schematic diagram showing the interference principle of laser beams reflected from the ISSG indentations closely spaced by d on a specimen surface deflected with a tangent angle of α

Specimen deformation causes a relative displacement between the two indentations. As a result, the path length difference between the interfering beams changes, which induces a phase shift in each fringe pattern. The relative displacement generally consists of both in-plane and out-of-plane displacement components. Consequently, the phase shift is related to a combination of both displacements. Since the separation of the indentations is small, the relative displacement may be considered as a displacement derivative. Differentiating Eqs. (1) and (2) gives two equations relating the two dependent variables of the indentation separation d and deflection angle α to the independent variables of the fringe orders m_1 and m_2, while other parameters such as λ and θ are constants. In the derivation, it is assumed that the deformation and the deflection angle α are small so that the following relations hold: $\theta_1 \approx \theta_2 \approx \theta$; $\cos \alpha \approx 1$, $\tan \alpha \approx \sin \alpha \approx \alpha$ and $\delta\alpha \approx \delta w/d$ where w is the out-of-plane displacement. Simplification of the two differentiated equations gives in-plane and out-of-plane displacement derivatives as follows:

$$\frac{\delta d}{d} = \frac{\lambda}{2d \sin \theta} (\delta m_1 + \delta m_2) \tag{3}$$

$$\frac{\delta w}{d} = \frac{\lambda}{2d(1 + \cos \theta)} (\delta m_1 - \delta m_2) \tag{4}$$

where δd and δw are in-plane and out-of-plane components of the relative displacements between the two indentations; δm_1 and δm_2 are the change of the fringe orders in the two interference fringe patterns. Equations (3) and (4) show that the derivative of the out-of-plane displacement is measured independently from that of the in-plane displacement. Simultaneous determination of the derivatives of in-plane and out-of-plane displacements is accomplished by measuring the phase shift in the two fringe patterns, i.e., δm_1 and δm_2. The effect is additive for determining the in-plane displacement derivative or strain, and subtractive for determining the out-of-plane displacement derivative or deflection slope.

Equations (3) and (4) are valid under the condition that the deflection angle is small. As for a large deflection angle, the previous assumptions regarding a small deflection angle do not hold any more. Considering the case that a rigid-body rotation of the indentations causes the diffraction patterns to turn slightly, the path length difference formulated between the interfering beams is only related to the positions of the indentations to the first order approximation, and thus is not influenced by the change of the reflective directions of the indentation facets. Therefore, the angles θ_1 and θ_2, in Eqs. (1) and (2) can be taken as θ for large deflection angles as well as small deflection angles. The governing equations for measuring the in-plane strain and out-of-plane deflection angle can be derived directly from Eqs. (1) and (2) and shown as follows:

$$\frac{\delta d}{d} - \tan \alpha \delta\alpha = \frac{\lambda}{2d \sin \theta \cos \alpha} (\delta m_1 + \delta m_2) \tag{5}$$

$$\tan \alpha \frac{\delta d}{d} + \delta\alpha = \frac{\lambda}{2d(1 + \cos \theta) \cos \alpha} (\delta m_1 - \delta m_2) \tag{6}$$

The in-plane strain and out-of-plane deflection angle are coupled in the above equations. Since the measurement is in real time, increments are measured with the obtained instantaneous value of the deflection angle. The increments are accumulated to get the next instantaneous value for the next sampling step of increment measurements. As the fringe shift of interference patterns can be measured, the in-plane strain and the deflection angle of bending can be obtained. Experiments on large beam deflection will be conducted in near future.

Computer-Controlled Signal Processing System

A 10-mW He-Ne laser is used as a coherent light source. The wavelength of the laser light is 0.6328 μm. A linear photodiode array (EG & G Retican, RL512S) is mounted on a model RC 1001 satellite board which is installed on a precision stage (Edmund Scientific, G36,347). The position of the satellite board can be adjusted in two orthogonal directions to intercept an interference fringe pattern. Two boards are kept approximately at a distance of 48 cm from the indentations and oriented perpendicular to the reflected laser beams. The satellite boards are connected to mother boards (RC1000). One mother board is used as the master board to slave the other board for scan and trigger control. The mother boards are enclosed in an electronic case as a remote controller to process the optical signals sent from the satellite boards. The linear photodiode array system monitors the light intensities of the fringe patterns and converts them into electrical voltage signals.

A Pentium-based microcomputer (60 MHz) is equipped with a data acquisition board (Data Translation DT2821-F-8DI) for data acquisition and analysis. The computer algorithm used to implement the technique is similar to that of ISG and ISR, and requires two steps of data acquisition. The first step involves scanning the sensors and displaying and storing the fringe signals in the computer. The second step is to analyze fringe signals from the ISSG so that the derivatives of in-plane and out-of-plane displacements in the specimen can be calculated using Eqs. (3) and (4). Phase shift of fringes is measured by determining the position change of the minimum light intensity. The increments of strains and deflection angles are accumulated in real time to get instantaneous measurement results.

Experiments and Discussions

The purpose of the experimental investigation is to verify the capabilities of the ISSG technique in measuring derivatives of in-plane and out-of-plane displacements. A thin cantilever beam is chosen as the test sample because the setup is simple and is well suited for creating a significant deflection angle. However, the in-plane strain is small and represents an extreme case for measurement accuracy. The material is Aluminum 6061-T6 and has a Young's modulus of 70 GPa. The dimensions of the beam are: length = 254.0 mm, width = 25.3 mm, and thickness = 3.0 mm. The beam is clamped at one end, and the free end of the beam is subjected to a lateral load at the middle point of its width. Deflection of the free end is measured using a micrometer gage that has a resolution of 0.0254 mm. A pair of ISSG indentations with a separation of 150 μm is applied to a surface point at 136.5 mm from the fixed end of the beam. The ISSG gage is centered and oriented along the axis of the beam. An incident laser beam upon the indentations creates two symmetrical Young's interference fringe patterns. Therefore, two linear photodiode arrays are needed to monitor the fringe patterns. A schematic diagram of the experimental setup is shown in Fig. 4. Seven tests were conducted. During each test, a lateral force is manually applied to the free end of the beam using the micrometer gage. As the load increases, the bending strain and the beam deflection increase. The computer-controlled system is used to measure and record the bending strain and the deflection angle in real time.

During each measurement, the rigid-body motion takes place at the location of ISSG, which includes in-plane and out-of-plane components. The in-plane rigid-body motion causes the two fringe patterns to move in the same direction. Since the linear photodiode arrays are mounted opposite to each other, the fringe order may be taken as positive in one and negative in the other. Thus the in-plane rigid-body motion is canceled in the additive calculation of the two fringe orders in Eq. (3). The in-plane rigid-body motion does not alter measurement results of in-plane strains. However, its influence on the measurement of the deflection angle is doubled due to subtraction of the fringe orders in Eq. (4). On the other hand, the out-of-plane rigid-body motion causes the fringes to move in opposite directions and the fringe spacing in the two patterns to change

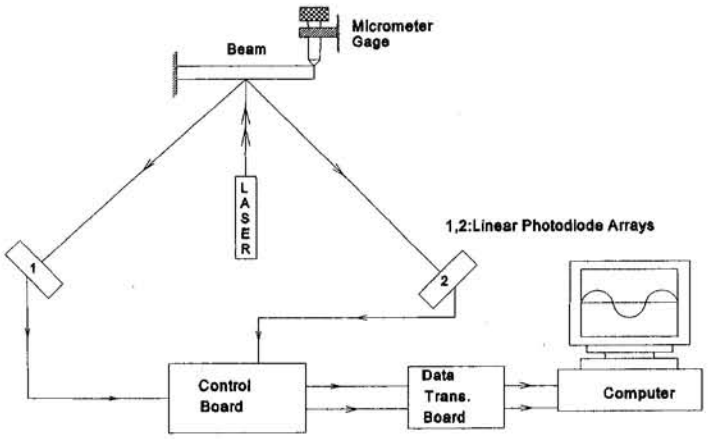

Fig. 4 A schematic diagram of the computer-controlled system for measuring in-plane strains and deflection angles of a cantilever beam

by the same amount, so that the fringe orders have the same sign. The out-of-plane rigid-body motion should not influence the deflection angle measurement but has a doubling effect on the in-plane strain measurement. Due to linear relationship between fringe movements and the change of the path length difference between the interfering laser beams, measurement sensitivities to rigid-body motion are proportional to the amount of rigid-body motion. Therefore, the factor of the measurement sensitivity can be defined as the strain/angle reading caused by one micro of rigid-body motion. In addition, since the fringe spacing increases proportionally with the distance between the ISSG and the photodiode arrays, the influence of the rigid-body motion on the relative change of the fringe orders is inversely proportional to the distance. The measurement sensitivity is inversely proportional to the distance between the ISSG and the photodiode arrays.

An investigation of the measurement sensitivities to rigid-body motion is conducted on a rigid steel plate. The sample is mounted on a x-y translation stage equipped with two micrometer gages. The in-plane and out-of-plane rigid-body motions of the sample are generated and measured using the micrometer gages. A pair of ISSG indentations with a separation of 150 μm is placed on the surface of the sample. Two satellite boards are mounted opposite to each other and are positioned at a distance of 48 cm from the indentations, which duplicates the experimental protocol for the cantilever beam test. For any rigid-body motion of the sample, the computer-controlled system assesses the movement of the fringe patterns to give readings for strains and deflection angles. The test results show that one micron of in-plane rigid-body motion causes a reading of 6.8×10^{-7} radians of the deflection angle, and gives essentially zero reading for the in-plane strain. The maximum in-plane rigid-body motion, which can be detected, is limited by the diameter of the laser beam. Measurements can only be made if the indentations remain within the middle third of the laser beam to insure that the intensity is satisfactory for monitoring with the current measuring facility. On the other hand, one micron of out-of-plane rigid-body motion causes a reading of 1.45 microstrains of in-plane strain, and gives essentially zero reading for the deflection angle. The strain sensitivity to out-of-plane rigid-body motion increases to 1.65 microstrains per micron as the distance between the indentations and the linear photodiode arrays decreases to 43 cm. Because of the strain insensitivity to in-plane rigid-body motion and the deflection angle insensitivity to out-of-plane rigid-body motion, the technique is tolerant to certain vibrations, and does not always require strict environmental stability.

In the cantilever beam experiment, the in-plane rigid-body motion is small and its influence on the measurement of the deflection angle is negligible. The measured results of deflection angles at the location of the ISSG are compared with the analytical results using Eq. (9) in Table 1. However, the out-of-plane rigid-body motion in the beam experiment is significant and compensation must be made for the determination of in-plane strain. The sensitivity factor calibrated in the above rigid-body motion tests is used to estimate the influence of the out-of-plane rigid-body motion on the in-plane strain measurement. Generally, the out-of-plane rigid-body motion may be measured using a dial gage or calculated using beam theory. Here, Eq. (7) is used. The strain correction is calculated by multiplying the sensitivity factor with the amount of the out-of-plane rigid-body motion. Subtraction of the strain correction from the ISSG measurement gives the in-plane strain. The experimental results of in-plane strains after compensation are compared in Table 2 with the analytical solutions given by Eq. (8). The out-of-plane displacement, bending strain, and small deflection angle given in the following equations are taken from the well-established cantilever beam theory:

Table 1 Comparison of the measured and calculated tangent angles of the beam deflections

Test no.	W (mm)	$\alpha_{measured}$ (10^{-3} rad.)	$\alpha_{analytical}$ (10^{-3} rad.)	$\frac{\lvert\alpha_{measured} - \alpha_{analytical}\rvert}{\alpha_{analytical}}$
1	0.127	0.564	0.589	4.2%
2	0.254	1.215	1.179	3.1%
3	0.381	1.783	1.770	0.7%
4	0.635	2.944	2.950	0.2%
5	1.016	4.722	4.716	0.1%
6	1.270	5.906	5.895	0.2%
7	2.540	11.81	11.79	0.2%

Table 2 Comparison of the measured and calculated bending strains

Test no.	W (mm)	$\sigma_{measured}$ (MPa)	$\epsilon_{measured}$ ($\mu\epsilon$)	$\epsilon_{analytical}$ ($\mu\epsilon$)	$\frac{\lvert\epsilon_{measured} - \epsilon_{analytical}\rvert}{\epsilon_{analytical}}$
1	0.127	0.235	3.36	4.098	18%
2	0.254	0.680	9.71	8.196	15%
3	0.381	0.735	10.5	12.29	14%
4	0.635	1.645	23.5	20.49	14%
5	1.016	2.471	35.3	32.78	7.6%
6	1.270	2.702	38.6	40.98	5.8%

$$w = \frac{Wx^2}{2L^3}(3L - x) \tag{7}$$

$$\epsilon = \frac{h}{2}\frac{\delta^2 w}{\delta x^2} = \frac{3Wh}{2L^3}(L - x) \tag{8}$$

$$\alpha = \frac{\delta w}{\delta x} = \frac{3Wx}{2L^3}(2L - x) \tag{9}$$

where h is the thickness of the beam, which equals 3 mm in the test; x is the distance between the ISSG location and the fixed end of the beam, which equals 136.5 mm in the test; W is the deflection at the free end of the beam; and L is the beam length.

Table 1 shows that the difference between the measured and calculated deflection angles is small. The maximum deflection applicable to the free end of the beam is 2.54 mm as found out in the seventh test. The maximum deflection angle measured at the ISSG location is 1.18×10^{-4} radians. After the maximum deflection is reached, the interference fringe patterns move out of the scanning windows of the linear photodiode arrays and measurements can not be made. Therefore, the system requires modification to measure larger deflections. Future research is planned to measure large beam deflections using longer linear photodiode arrays. The measured tangent angles of the beam deflections during a test are plotted versus time in Fig. 5. The waviness of the data shown in the plot is due to fluctuations of the manually loading condition. The measurement is carried out on a real-time basis. This shows that the technique has a potential to be applied to study vibration problems. As real-time measurements are made, the first and second-order time derivatives of vibrational displacements, which are equivalent to velocity and acceleration, may be determined.

As shown in Table 2, bending strains and stresses in the beam are measured using the current ISSG system. Equation (8) elucidates the fact that bending strain is related to the second-order derivative of out-of-plane displacements. Therefore, the ISSG technique can be used to measure both the first and second-order derivatives of out-of-plane displacements. Considering the very small strains which are measured with the compensation of the rigid-body motion, the experimental data agree satisfactorily with the analytical solutions. The measurement difference decreases with increasing strain. Therefore, for measurements at the fixed end of the beam, where maximum bending stresses are expected, the difference between the measurements and analytical solutions should be reduced. Similarly, for stiffer beam structures with stiffer support conditions, for which out-of-plane rigid-body motions are small and bending strains are large, the measurement accuracy is expected to increase. The technique provides a useful means to study bending stress problems in various solid structures where out-of-plane rigid-body motion is negligible.

The interferometric strain rosette technique (Li, 1995) can be extended to measurements of three derivatives of in-plane and three derivatives of out-of-plane displacements. Based on the same principles which have been discussed for the ISSG, the ISR can be also used to measure bending strains and stresses as well as deflection angles. Because the ISR measures derivatives with respect to three gage directions, it can be used to study bending problems in two-dimensional structures in such as plates and shells.

Conclusions

The ISSG method for measuring derivatives of in-plane and out-of-plane displacements has been presented. By means of laser beam interferometry, strain and deflection slope on a surface point can be accurately measured in real time. The optical principle and experimental procedure are described in the paper and easy to follow. A systematical study of the measurement sensitivities to rigid-body motion shows that an application of the ISSG to in-plane strain measurements is not influenced by in-plane rigid-body motion and its application to out-of-plane displacement derivative measurements is not influenced by out-of-plane rigid-body motion. Influences of in-plane rigid-body motion on out-of-plane displacement derivative measurements and out-of-plane rigid-body motion on in-plane strain measurements can be compensated for. Experiments conducted on a cantilever beam have shown that the ISSG is a satisfactory method for measuring the first and second-order derivatives of the out-of-plane displacements as well as bending strains and stresses. A small beam deflection angle approximately equals the first-order derivative of out-of-plane displacements or the slope of the deflection, which can be separately measured from the in-plane strain. The governing equations for measurements of large deflection angles have been derived and indicate a coupling effect between the in-plane and out-of-plane components. The ISSG technique is useful for studying bending problems of beams, plates, and shells, and has a potential to be extended to vibration measurements.

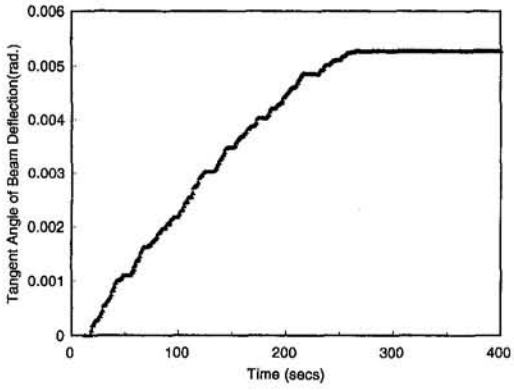

Fig. 5 Real-time measurement result of the tangent angle of the beam deflection plotted versus time

Acknowledgments

The author wishes to acknowledge the partial support of the National Science Foundation, research equipment grant number CMS-9596231, and Alcoa Foundation's science support grant. The reviewers' suggestions are highly appreciated.

References

Bell, J. F., 1956, "Determination of dynamic plastic strain through the use of diffraction grating," *Journal of Applied Physics,* Vol. 27, No. 10, pp. 1109–1113.

Chiang, F. P., and Juang, R. M., 1976, "Laser speckle interferometry for plate bending problems," *Applied Optics,* Vol. 15, No. 9, pp. 2199–2204.

Hovanesian, J., and Varner, J., 1970, "Method for determining the bending moments in normal loaded thin plates by holographic interferometry," *Engineering Uses of Holography,* E. R. Robertson and J. M. Harvey, eds., Cambridge University Press, London, pp. 173–185.

Hung, Y. Y., and Taylor, C. E., 1974, "Measurement of slopes of structural deflections by speckle-shearing interferometry," *Experimental Mechanics,* Vol. 14, No. 7, pp. 281–285.

Klumpp, P. A., and Schnack, E., 1990, "Speckle-interferometric camera for displacement measurement," *Experimental Mechanics,* Vol. 30, No. 4, pp. 411–415.

Kobayashi, A. S., 1987, *Handbook on Experimental Mechanics,* 2nd ed., Prentice-Hall, Englewood Cliffs, NJ.

Li, K., 1995, "Interferometric 45° and 60° strain rosettes," *Journal of Applied Optics,* Vol. 34, No. 28, pp. 6376–6379.

Ligtenberg, F. K., 1954, "The moiré method: A new experimental method for the determination of moments in small slab models," *Proc. SESA,* Vol. 12, No. 2, pp. 83–98.

Parks, V. J., 1993, "Geometric Moiré," *Handbook on Experimental Mechanics,* 2nd ed., A. S. Kobayashi, ed., Prentice-Hall, Englewood Cliffs, NJ, pp. 267–296.

Post, D., 1993, "Moiré interferometry," *Handbook on Experimental Mechanics,* 2nd ed., A. S. Kobayashi, ed., Prentice-Hall, Englewood Cliffs, NJ, pp. 297–364.

Pryor, T. R., and North, W. P. T., 1971, "The diffractographic strain gage," *Experimental Mechanics,* Vol. 11, No. 12, pp. 565–568.

Schultheisz, C. R., and Knauss, W. G., 1994, "Governing equations of moiré interferometry I. The effect of out-of-plane displacement gradients for application to crack-tip field," *Optics and Lasers in Engineering,* Vol. 20, No. 4, pp. 259–282.

Sharpe, W. N., Jr., 1968, "The interferometric strain gage," *Experimental Mechanics,* Vol. 8, No. 4, pp. 164–170.

Sirkis, J. S., and Lim, T. J., 1991, "Displacement and strain measurement with automated Grid methods," *Experimental Mechanics,* Vol. 31, No. 4, pp. 382–388.

Sullivan, J. L., 1991, "Phase-stepped fractional moiré," *Experimental Mechanics,* Vol. 31, No. 4, pp. 373–381.

Journal of Applied Mechanics

Brief Notes

A Brief Note is a short paper that presents a specific solution of technical interest in mechanics but which does not necessarily contain new general methods or results. A Brief Note should not exceed 1500 words *or equivalent* (a typical one-column figure or table is equivalent to 250 words; a one line equation to 30 words). Brief Notes will be subject to the usual review procedures prior to publication. After approval such Notes will be published as soon as possible. The Notes should be submitted to the Technical Editor of the JOURNAL OF APPLIED MECHANICS. Discussions on the Brief Notes should be addressed to the Editorial Department, ASME, United Engineering Center, 345 East 47th Street, New York, N. Y. 10017, or to the Technical Editor of the JOURNAL OF APPLIED MECHANICS. Discussions on Brief Notes appearing in this issue will be accepted until two months after publication. Readers who need more time to prepare a Discussion should request an extension of the deadline from the Editorial Department.

On the Oblique Compression of Two Elastic Spheres

D. Elata[1]

In this note Walton's (1987) force-displacement relations for a contact between two identical elastic spheres are discussed. The relations are based on the solution for the oblique compression of two elastic spheres (Walton, 1978) which is rederived here in a simple fashion that relates it to Mindlin's (1949) solution for contact stress. Specific limitations of these relations are reviewed and it is demonstrated that misusing the relations leads to thermodynamic inconsistencies.

Introduction

An exact solution for the contact traction between two elastic spheres can assist in developing models for the mechanical behavior of granular materials. One problem of particular interest is the oblique compression of two identical elastic spheres. This problem was solved by Walton (1978) who used laborious symmetry and energy flux considerations. Walton's solution is different from the one obtained by Mindlin (1949) in that the latter predicts a singular shear traction on the contact area contour, which may cause slip, whereas the former predicts a bounded shear traction that either causes slip on the entire contact area or does not cause slip at all.

Based on his solution of the oblique compression of two identical elastic spheres, Walton (1987) calculates the effective elastic moduli of a random packing of identical spheres. In this work it is assumed that the centers of the spheres and their mutual contacts are displaced in accordance with a uniform displacement field (pointwise displacement affinity). Endres (1990) further developed this model by considering the effect of generation and elimination of contacts as the granular material deforms.

The solution proposed by Walton (1978) is rederived in a simple and straightforward way that trivially relates it to the work of Mindlin (1949). The derivation is the same as in Johnson (1985) (Section 7.3), but Johnson did not relate it to Walton's solution. Next, based on this solution, contact force-displacement relations are derived, and their limitations are discussed. Specifically, it is shown that misuse of these relations leads to violation of the second law of thermodynamics.

Contact Traction

Mindlin (1949) has shown that when two identical elastic spheres of radius R are pressed together the stress distribution on the contact surface is

$$N = \frac{2}{\pi^2 RB}(a^2 - r^2)^{1/2}, \tag{1a}$$

$$P = \frac{2u}{\pi^2(2B + C)}(a^2 - r^2)^{-1/2}, \tag{1b}$$

where

$$a^2 = Rw, \tag{1c}$$

$$B = \frac{1}{4\pi}\left(\frac{1}{\mu} + \frac{1}{\lambda + \mu}\right), \tag{1d}$$

$$C = \frac{1}{4\pi}\left(\frac{1}{\mu} - \frac{1}{\lambda + \mu}\right). \tag{1e}$$

In the equations above, N is the normal traction, P is the tangential traction, a is the radius of the contact area, r is the radial distance from the center of the circular contact area, w and u are, respectively, the values of the normal and tangential displacements of the center of the contact relative to the center of the spheres, and λ and μ are Lamé's constants. This solution is based on the assumption that the two spheres are initially pressed together along the normal to their mutual contact area and only then a relative displacement parallel to the contact area is applied. The tangential traction (1*b*) is clearly singular on the contour of the contact area whereas the normal traction is bounded. This means that the possibility of slip must be addressed (Mindlin, 1949).

By using lengthy symmetry and energy flux considerations, Walton (1978) has shown that when the relative displacements w and u increase from zero to their final value with a fixed

[1] Earth Sciences Division, Lawrence Livermore National Laboratory, P.O. Box 808, Livermore, CA 94551.

Contributed by the Applied Mechanics Division of THE AMERICAN SOCIETY OF MECHANICAL ENGINEERS for publication in the ASME JOURNAL OF APPLIED MECHANICS. Manuscript received by the ASME Applied Mechanics Division, May 1995; final revision, Mar. 1996. Associate Technical Editor: J. T. Jenkins.

proportionality, the traction distribution on the contact surface is

$$N = \frac{2}{\pi^2 RB}(a^2 - r^2)^{1/2}, \tag{2a}$$

$$P = \frac{4u}{\pi^2(2B + C)Rw}(a^2 - r^2)^{1/2}. \tag{2b}$$

In contrast to (1*b*) the tangential traction (2*b*) is bounded. Moreover, there is a fixed ratio between N and P which means that slip occurs over the entire contact area or does not occur at all (Walton, 1978).

In the following, Eq. (2*b*) is rederived in a simple and straightforward fashion. It is assumed that the displacements w and u increase with a variable proportionality so that

$$\frac{\delta u}{\delta w} = c(w), \tag{3}$$

where c is a scalar valued parametric function of w. Since Mindlin's solution assumes that the tangential displacement is applied only after the normal displacement has been applied, the variation in contact traction is related to variations in contact displacement by

$$\delta N = \frac{1}{\pi^2 B}(Rw - r^2)^{-1/2}\delta w, \tag{4a}$$

$$\delta P = \frac{2\delta u}{\pi^2(2B + C)}(Rw - r^2)^{-1/2} = \frac{2c(w)\delta w}{\pi^2(2B + C)}(Rw - r^2)^{-1/2}, \tag{4b}$$

where δP results from an applied δu while keeping w fixed. Notice that although δP and δN are singular on the circumference of the contact area, their ratio is a (bounded) linear function of $c(w)$. This means that the normal displacement variation either causes slip around the contour of the contact area or does not cause slip at all. At any given radius r in the final contact area, assuming that no slip occurs, the integrated tangential traction is

$$P(w, r) = \int_{\hat{w}=r^2/R}^{\hat{w}=w} \frac{2c(\hat{w})}{\pi^2(2B + C)}(R\hat{w} - r^2)^{-1/2}d\hat{w}, \tag{5}$$

where the lower boundary of the integration is due to the fact that while $w < r^2/R$, all points at radius r are subjected to no traction. In the specific case where $c(w)$ is a constant, the tangential traction is

$$P(w, r) = \frac{4c}{\pi^2(2B + C)R}(Rw - r^2)^{1/2} = \frac{4u}{\pi^2(2B + C)Rw}(a^2 - r^2)^{1/2}, \tag{6}$$

which is identical to Walton's (1978) solution.

In addition to eliminating the lengthy derivation and complicated theoretical considerations in Walton (1978), the present derivation clarifies the relation of Walton's solution to Mindlin's solution. It is noted here that for any nonproportional strain path the tangential traction must be calculated by (5) while continuously considering the possibility of slip (Mindlin and Deresiewicz, 1953; Chang et al., 1992).

Contact Force-Displacement Relations

By integrating Eqs. (2*a*, *b*) over the contact area, Walton (1987) has calculated the resultant forces:

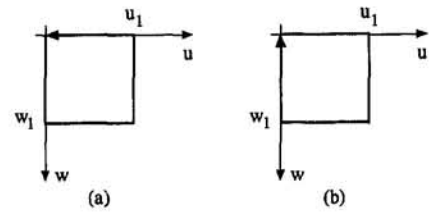

Fig. 1 Two possible contact displacement cycles for which misuse of Eqs. (7*a*, *b*) results in (*a*) dissipation of energy, (*b*) "generation" of energy

$$\bar{N} = \int_{r=0}^{r=\sqrt{Rw}} \frac{2}{\pi^2 RB}(Rw - r^2)^{1/2}2\pi r dr = \frac{4R^{1/2}}{3\pi B}w^{3/2}, \tag{7a}$$

$$\bar{P} = \int_{r=0}^{r=\sqrt{Rw}} \frac{4u}{\pi^2(2B + C)Rw}(Rw - r^2)^{1/2}2\pi r dr = \frac{8R^{1/2}}{3\pi(2B + C)}\left(\frac{u}{w}\right)w^{3/2}. \tag{7b}$$

These contact force-displacement relations are relatively simple and it is enticing to use them in modeling the mechanical response of granular material. In this respect it is important to emphasize that these force-displacement relations are path-dependent and they are derived assuming a fixed ratio between the normal and tangential displacements of the contact. Considering the intergaranular contacts in a general (unordered) granular material, this specific displacement trajectory is unlikely even when the overall material is subjected to boundary displacements of a fixed arbitrary proportionality.

Another deterring consideration is the thermodynamic implication of misusing these contact force-displacement relations by regarding them as path-independent. If Eqs. (7) are used to calculate the work W done by the contact forces in a displacement cycle described in Fig. 1(*a*) it may be shown that

$$W = \frac{8R^{1/2}}{6\pi(2B + C)}u_1^2 w_1^{1/2}. \tag{8}$$

The forces vanish at the beginning and end of the displacement cycle and therefore the elastic strain at these points vanishes. Consequently, all the work done by the forces has dissipated. The fact that a cyclic displacement of a contact is mechanically dissipative is well known (Mindlin and Deresiewicz, 1953). The physical reason for this dissipation is energy loss due to friction. In contrast, the dissipation quantified in (8) is solely due to the misuse of the contact force-displacement relations (7) to described nonproportional contact displacements. In particular, consideration of the reverse displacement cycle described in Fig. 1(*b*) shows that a net energy equal to W may be generated (without any work being done), which clearly violates the second law of thermodynamics.

Acknowledgment

The author would like to acknowledge helpful discussions with James G. Berryman from LLNL and Lawrence M. Schwartz from Schlumberger-Doll Research. This work was performed under the auspices of the United States Department of Energy at Lawrence Livermore National Laboratory under Contract No. W-7405-ENG-48 and supported specifically by the Geosciences Research Program of the Department of Energy Office of Energy Research within the Office of Basic Energy Sciences, Division of Engineering and Geosciences.

References

Chang, C. S., Chang, Y., and Kabir, M. G., 1992, "Micromechanics Modeling for Stress-Strain Behavior of Granular Soils. I: Theory," *ASCE Journal of Geotechnical Engineering*, Vol. 118, pp. 1959–1974.

Endres, A. L., 1990, "The Effect of Contact Generation on the Elastic Properties of a Granular Medium," ASME JOURNAL OF APPLIED MECHANICS, Vol. 57, pp. 330–336.

Johnson, K. L., 1985, *Contact Mechanics,* Cambridge University Press, Cambridge, UK.

Mindlin, R. D., 1949, "Compliance of Elastic Bodies in Contact," ASME JOURNAL OF APPLIED MECHANICS, Vol. 16, pp. 259–268.

Mindlin, R. D., and Deresiewicz, H., 1953, "Elastic Spheres in Contact Under Varying Oblique Forces," ASME JOURNAL OF APPLIED MECHANICS, Vol. 20, pp. 327–344.

Walton, K., 1978, "The Oblique Compression of Two Elastic Spheres," *Journal of the Mechanics and Physics of Solids,* Vol. 26, pp. 139–150.

Walton, K., 1987, "The Effective Elastic Moduli of a Random Packing of Spheres," *Journal of the Mechanics and Physics of Solids,* Vol. 35, pp. 213–226.

Extremum Problem Formulations of Mixed-Form Models for Elastostatics

J. E. Taylor[2]

The material of this note is related to variational models for the analysis of elastostatic structural response. Established and familiar *mixed stress and deformation* models for such analysis, e.g., the Hu-Washizu, Hellinger-Reissner, and the various models summarized in Oden and Reddy (1976) and elsewhere in the literature, have the form of saddlepoint problems. As an alternative to dealing with the functional associated with the saddlepoint form, expression is given here to the general elastostatics problem in the (stronger) form of convex constrained extremum problems. The alternate formulations make use of a decomposition of the measure of stress or strain into two variationally independent components. This provides for the interpretation of the results as *mixed models,* as is to be demonstrated in what follows. Two examples are described below; they are complementary formulations, parallel in sense to the basic minimum potential energy and minimum complementary energy principles.

The developments to follow are expressed for linear elastostatics of general continua. As a first step in each description, the symbolic expression of a constrained minimization problem, supposed to represent the elastostatics analysis, is simply stated. That the model does in fact comprise a valid statement for the mechanics analysis is then confirmed through an interpretation of the variational problem. For the first example formulation, which amounts to an extension of the classical minimum potential energy characterization, the problem is expressed symbolically in the form

$$\left.\begin{aligned} &\min_{\sigma_{ij},\epsilon_{ij},u_l} \left\{ \int_\Omega \left[\tfrac{1}{2} E_{ijkl}\epsilon_{ij}\epsilon_{kl} + \tfrac{1}{2} C_{ijkl}\sigma_{ij}\sigma_{kl} - f_l u_l \right] dV - \int_{\Gamma_t} t_l u_l dS \right\} \\ &\text{subject to} \\ &\tfrac{1}{2}(u_{i,j} + u_{j,i}) - (\epsilon_{ij} + C_{ijkl}\sigma_{kl}) = 0 \quad x \in \Omega \end{aligned}\right\} [P].$$

The notation here is to reflect that the minimum point in $[P]$ is identified with independent variation with respect to (w.r.t.) the arguments σ_{ij}, ϵ_{ij}, and u_l. Symmetric, positive definite tensors fields E_{ijkl} and C_{ijkl} (to be interpreted later) and (load) vector fields f_l and t_l are prescribed. u_l symbolizes elements of the set of vectors defined (in the usual way) to be kinematically admissible, σ_{ij} are differentiable in Ω, and σ_{ij} and ϵ_{ij} are further defined jointly in relation to u_l according to the constraint in $[P]$.

Symbol λ_{kl} is introduced to represent the Lagrange multiplier associated with this constraint. The necessary conditions for a minimum in problem $[P]$, stated in order w.r.t. variation of σ_{ij}, ϵ_{ij}, and u_l, are

$$\left.\begin{aligned} C_{ijkl}\sigma_{ij} - C_{ijkl}\lambda_{kl} &= 0 \quad (1) \\ E_{ijkl}\epsilon_{ij} - \lambda_{kl} &= 0 \quad (2) \\ \lambda_{kl,k} + f_l &= 0 \quad (3) \end{aligned}\right\} \quad x \in \Omega$$

$$\lambda_{kl}n_k - t_l = 0 \qquad x \text{ on } \Gamma_t. \qquad (3a)$$

Using the result (1) that $\lambda_{kl} \equiv \sigma_{kl}$, (2) and (3) are restated as

$$\left.\begin{aligned} E_{ijkl}\epsilon_{ij} - \sigma_{kl} &= 0 \quad (2') \\ \sigma_{kl,k} + f_l &= 0 \quad (3') \end{aligned}\right\} \quad x \in \Omega$$

$$\sigma_{kl}n_k - t_l = 0 \qquad x \text{ on } \Gamma_t. \qquad (3a')$$

With the standard model for linear elastostatics in mind, in view of (3′) and (3a′) the σ_{ij}, up to this point undesignated, is identified as representing a stress field that equilibrates the external forces f_l and t_l.

According to the constraint equation of $[P]$, an interpretation of the quantity $(\epsilon_{ij} + C_{ijkl}\sigma_{kl})$ as total strain is consistent with convention for the linear model, and of course this measure of strain is then compatible. In order to complete the confirmation that the system comprises a full statement of the elastostatics boundary value problem, it remains only to identify the constitutive relation. With the introduction of $\tilde{C}_{ijkl}$ to represent the effective compliance tensor, and making use of the interpretations for stress and strain already described, the net stress-strain relation is expressed as

$$\tilde{C}_{ijkl}\sigma_{ij} = (\epsilon_{ij} + C_{ijkl}\sigma_{kl}). \qquad (4)$$

With the substitution for ϵ_{ij} in (4) from (2′), the effective property $\tilde{C}_{ijkl}$ is evaluated in terms of the original, undesignated tensors as

$$\tilde{C}_{ijkl} = (E_{ij}^{-1} + C_{ijkl}). \qquad (5)$$

Thus the demonstration is complete, i.e., it has been shown that the system of necessary conditions associated with problem $[P]$ comprise a complete statement of the classical linear elasticity problem, with σ_{ij} and $(\epsilon_{ij} + C_{ijkl}\sigma_{kl})$ representing stress and strain, and $\tilde{C}_{ijkl}$ providing the relation between them. The relative value of E_{ijkl} and C_{ijkl} is still open, and may be set for convenience (perhaps to achieve proper scaling). For example, for equal values of E_{ijkl} and C_{ijkl} the net compliance $\tilde{C}_{ijkl}$ has twice the value of compliance for each constituent within the expression for total strain. In summary, note that

1 the problem represented in $[P]$ is a constrained, convex programming problem, and so the solution is generally a *unique minimizer* of the objective, and

2 relative to the purpose in using a mixed model, namely to provide for *independence with respect to variation* of the field variables, characterization of elastostatics in the form of variational problem $[P]$ reflects independent variation among σ_{ij}, ϵ_{ij}, and u_l.

As noted in the introductory statement, a second mixed formulation for elastostatics is available in the form of a relaxed version of the classical, single field statement of the "minimum complementary potential energy" model in mechanics. Following an approach similar to the one used above, the exposition

[2] University of Michigan, Ann Arbor, MI 48109.

Contributed by the Applied Mechanics Division of THE AMERICAN SOCIETY OF MECHANICAL ENGINEERS for publication in the ASME JOURNAL OF APPLIED MECHANICS. Manuscript received by the ASME Applied Mechanics Division, Apr. 1995; final revision, Sept. 1995. Associate Technical Editor: W. K. Liu.

Endres, A. L., 1990, "The Effect of Contact Generation on the Elastic Properties of a Granular Medium," ASME JOURNAL OF APPLIED MECHANICS, Vol. 57, pp. 330–336.

Johnson, K. L., 1985, *Contact Mechanics,* Cambridge University Press, Cambridge, UK.

Mindlin, R. D., 1949, "Compliance of Elastic Bodies in Contact," ASME JOURNAL OF APPLIED MECHANICS, Vol. 16, pp. 259–268.

Mindlin, R. D., and Deresiewicz, H., 1953, "Elastic Spheres in Contact Under Varying Oblique Forces," ASME JOURNAL OF APPLIED MECHANICS, Vol. 20, pp. 327–344.

Walton, K., 1978, "The Oblique Compression of Two Elastic Spheres," *Journal of the Mechanics and Physics of Solids,* Vol. 26, pp. 139–150.

Walton, K., 1987, "The Effective Elastic Moduli of a Random Packing of Spheres," *Journal of the Mechanics and Physics of Solids,* Vol. 35, pp. 213–226.

Extremum Problem Formulations of Mixed-Form Models for Elastostatics

J. E. Taylor[2]

The material of this note is related to variational models for the analysis of elastostatic structural response. Established and familiar *mixed stress and deformation* models for such analysis, e.g., the Hu-Washizu, Hellinger-Reissner, and the various models summarized in Oden and Reddy (1976) and elsewhere in the literature, have the form of saddlepoint problems. As an alternative to dealing with the functional associated with the saddlepoint form, expression is given here to the general elastostatics problem in the (stronger) form of convex constrained extremum problems. The alternate formulations make use of a decomposition of the measure of stress or strain into two variationally independent components. This provides for the interpretation of the results as *mixed models,* as is to be demonstrated in what follows. Two examples are described below; they are complementary formulations, parallel in sense to the basic minimum potential energy and minimum complementary energy principles.

The developments to follow are expressed for linear elastostatics of general continua. As a first step in each description, the symbolic expression of a constrained minimization problem, supposed to represent the elastostatics analysis, is simply stated. That the model does in fact comprise a valid statement for the mechanics analysis is then confirmed through an interpretation of the variational problem. For the first example formulation, which amounts to an extension of the classical minimum potential energy characterization, the problem is expressed symbolically in the form

$$\left.\begin{aligned} &\min_{\sigma_{ij},\epsilon_{ij},u_l} \left\{ \int_\Omega \left[\tfrac{1}{2} E_{ijkl}\epsilon_{ij}\epsilon_{kl} + \tfrac{1}{2} C_{ijkl}\sigma_{ij}\sigma_{kl} - f_l u_l \right] dV - \int_{\Gamma_t} t_l u_l dS \right\} \\ &\text{subject to} \\ &\tfrac{1}{2}(u_{i,j} + u_{j,i}) - (\epsilon_{ij} + C_{ijkl}\sigma_{kl}) = 0 \quad x \in \Omega \end{aligned}\right\} [P].$$

The notation here is to reflect that the minimum point in $[P]$ is identified with independent variation with respect to (w.r.t.) the arguments σ_{ij}, ϵ_{ij}, and u_l. Symmetric, positive definite tensors fields E_{ijkl} and C_{ijkl} (to be interpreted later) and (load) vector fields f_l and t_l are prescribed. u_l symbolizes elements of the set of vectors defined (in the usual way) to be kinematically admissible, σ_{ij} are differentiable in Ω, and σ_{ij} and ϵ_{ij} are further defined jointly in relation to u_l according to the constraint in $[P]$.

Symbol λ_{kl} is introduced to represent the Lagrange multiplier associated with this constraint. The necessary conditions for a minimum in problem $[P]$, stated in order w.r.t. variation of σ_{ij}, ϵ_{ij}, and u_l, are

$$\left.\begin{aligned} C_{ijkl}\sigma_{ij} - C_{ijkl}\lambda_{kl} &= 0 \quad (1) \\ E_{ijkl}\epsilon_{ij} - \lambda_{kl} &= 0 \quad (2) \\ \lambda_{kl,k} + f_l &= 0 \quad (3) \end{aligned}\right\} \quad x \in \Omega$$

$$\lambda_{kl} n_k - t_l = 0 \qquad x \text{ on } \Gamma_t. \qquad (3a)$$

Using the result (1) that $\lambda_{kl} \equiv \sigma_{kl}$, (2) and (3) are restated as

$$\left.\begin{aligned} E_{ijkl}\epsilon_{ij} - \sigma_{kl} &= 0 \quad (2') \\ \sigma_{kl,k} + f_l &= 0 \quad (3') \end{aligned}\right\} \quad x \in \Omega$$

$$\sigma_{kl} n_k - t_l = 0 \qquad x \text{ on } \Gamma_t. \qquad (3a')$$

With the standard model for linear elastostatics in mind, in view of (3′) and (3a′) the σ_{ij}, up to this point undesignated, is identified as representing a stress field that equilibrates the external forces f_l and t_l.

According to the constraint equation of $[P]$, an interpretation of the quantity $(\epsilon_{ij} + C_{ijkl}\sigma_{kl})$ as total strain is consistent with convention for the linear model, and of course this measure of strain is then compatible. In order to complete the confirmation that the system comprises a full statement of the elastostatics boundary value problem, it remains only to identify the constitutive relation. With the introduction of $\tilde{C}_{ijkl}$ to represent the effective compliance tensor, and making use of the interpretations for stress and strain already described, the net stress-strain relation is expressed as

$$\tilde{C}_{ijkl}\sigma_{ij} = (\epsilon_{ij} + C_{ijkl}\sigma_{kl}). \qquad (4)$$

With the substitution for ϵ_{ij} in (4) from (2′), the effective property $\tilde{C}_{ijkl}$ is evaluated in terms of the original, undesignated tensors as

$$\tilde{C}_{ijkl} = (E_{ij}^{-1} + C_{ijkl}). \qquad (5)$$

Thus the demonstration is complete, i.e., it has been shown that the system of necessary conditions associated with problem $[P]$ comprise a complete statement of the classical linear elasticity problem, with σ_{ij} and $(\epsilon_{ij} + C_{ijkl}\sigma_{kl})$ representing stress and strain, and $\tilde{C}_{ijkl}$ providing the relation between them. The relative value of E_{ijkl} and C_{ijkl} is still open, and may be set for convenience (perhaps to achieve proper scaling). For example, for equal values of E_{ijkl} and C_{ijkl} the net compliance $\tilde{C}_{ijkl}$ has twice the value of compliance for each constituent within the expression for total strain. In summary, note that

1 the problem represented in $[P]$ is a constrained, convex programming problem, and so the solution is generally a *unique minimizer* of the objective, and

2 relative to the purpose in using a mixed model, namely to provide for *independence with respect to variation* of the field variables, characterization of elastostatics in the form of variational problem $[P]$ reflects independent variation among σ_{ij}, ϵ_{ij}, and u_l.

As noted in the introductory statement, a second mixed formulation for elastostatics is available in the form of a relaxed version of the classical, single field statement of the "minimum complementary potential energy" model in mechanics. Following an approach similar to the one used above, the exposition

[2] University of Michigan, Ann Arbor, MI 48109.

Contributed by the Applied Mechanics Division of THE AMERICAN SOCIETY OF MECHANICAL ENGINEERS for publication in the ASME JOURNAL OF APPLIED MECHANICS. Manuscript received by the ASME Applied Mechanics Division, Apr. 1995; final revision, Sept. 1995. Associate Technical Editor: W. K. Liu.

of this second model starts with an unqualified, symbolic statement of a constrained minimization problem. The problem so represented also is convex. Here too, the identification of the problem statement with the mechanics of elastostatics is accomplished through an interpretation of the "necessary conditions." The form for this characterization, stated here for simplicity as though boundary displacement where prescribed has value zero, is given as

$$\left.\begin{aligned} &\min_{\sigma_{ij},u_k}\left\{\int_\Omega\left[\tfrac{1}{2}E_{ijkl}u_{i,j}u_{k,l}+\tfrac{1}{2}C_{ijkl}\sigma_{ij}\sigma_{kl}dV\right]\right\}\\ &\text{subject to:}\\ &(\sigma_{ij}+E_{ijkl}u_{k,l})_{,j}+f_i=0 \quad \text{in} \quad \Omega\\ &(\sigma_{ij}+E_{ijkl}u_{k,l})n_j-t_i=0 \quad \text{on} \quad \Gamma_t \end{aligned}\right\}[Q].$$

The problem statement reflects minimization (of the sum of quadratic measures) independently w.r.t. admissible fields σ_{ij} and u_l, where admissibility requirements correspond to those of model $[P]$. According to the constraints of $[Q]$, these fields jointly equilibrate (loads) f_i and t_i. As in the prior formulation, here E_{ijkl} and C_{ijkl} represent differentiable, positive definite, symmetric tensors. Also as before, E_{ijkl}, C_{ijkl}, f_i, and t_i symbolize data. λ_i and β_i are introduced as multipliers associated with the field equation and boundary condition constraints of $[Q]$. Stationarity w.r.t. σ_{ij} and u_l, respectively, requires

$$C_{ijkl}\sigma_{kl}-\lambda_{i,j}=0 \quad \text{in} \quad \Omega \tag{6}$$

$$\beta_i+\lambda_i=0 \quad \text{on} \quad \Gamma_t \tag{6a}$$

$$[-E_{klij}u_{i,j}+E_{ijkl}\lambda_{i,j}]_{,l}=0 \quad \text{in} \quad \Omega. \tag{7}$$

This system is satisfied with $\lambda_i = u_i$, and making use of the linear strain-displacement relation $\epsilon_{ij} = (u_{i,j} + u_{j,i})/2$ and the symmetries in the stress and material properties tensors, (6) is interpreted as

$$C_{ijkl}\sigma_{kl}=\epsilon_{ij}. \tag{8}$$

It is clear from the equilibrium equation constraint that $\sigma_{ij} + E_{ijkl}\epsilon_{kl}$ represents total stress, and so with the introduction of $\tilde{E}$ to symbolize the net modulus, the total stress-strain relation is expressed as

$$\sigma_{ij}+E_{ijkl}\epsilon_{kl}=\tilde{E}_{ijkl}\epsilon_{kl}. \tag{9}$$

Accordingly, in view of (8) the effective modulus for this model has the value

$$\tilde{E}_{ijkl}=E_{ijkl}+C^{-1}_{ijkl}. \tag{10}$$

For example, if $E_{ijkl} = C^{-1}_{ijkl}$ then $\tilde{E}_{ijkl} = 2E_{ijkl}$. This completes a verification that the formulation $[Q]$ comprises an authentic portrayal of linear elastostatics. The earlier comments given in relation to version $[P]$ of the problem apply here as well, i.e., the solution to $[Q]$ is generally a unique minimizer.

Summary

Formulations $[P]$ and $[Q]$ have the relatively simple form (among constrained nonlinear programming problems) of "quadratic objective with linear constraints," which is convenient. Creation of these formulations for continuum mechanics relies on the feature of the models that has total stress or total strain interpreted via a *decomposition* into variationally independent components which are coupled through the constraints. In each of the two problem statements the decomposition is expressed in a form that provides for both static and kinematic field measures to be present, and so the results appear as mixed models. Where the goal in using such models is to achieve a desirable balance in precision between the computational evaluation of stresses and deformations, the relative value of E_{ijkl} and C_{ijkl} may be adjusted to control this balance. More generally, compared to familiar forms for mixed principles the extremum problem formulations presented in this note may be more convenient in the treatment of applications, e.g., the development of computational models, performance of analysis toward the establishment of bounds, or the treatment of structural optimization problems, to name a few.

Notwithstanding the simplicity of problem formulations $[P]$ and $[Q]$, these two features i.e., the interpretation of the dual field variables in terms of a set of (independent) constituents, and the interpretation for analysis that follows standard form for the mathematical modeling of constrained nonlinear programming models, can be exploited to obtain other useful extensions to the energetic formulations in solid mechanics. For example, extended versions of the classical complementary statements of "energy principles" are available in forms that comprise constructive formulations for the elastostatics of *constitutively nonlinear* systems (see, e.g., Taylor, 1993, 1994; Plaxton and Taylor, 1994). Also, the same approach can be used to model the more general problem of finite strain elastostatics with nonlinear materials (Hollister et al., 1995).

References

Hollister, S. J., Taylor, J. E., and Washabaugh, P. D., 1995, "A General Finite Strain Model for Elastostatics With Stiffening Materials," ASME JOURNAL OF APPLIED MECHANICS, to appear.

Oden, J. T., and Reddy, J. N., 1976, *Variational Methods in Theoretical Mechanics,* Springer-Verlag, Heidelberg, Germany.

Plaxton, S., Taylor, J. E., 1994, "Applications of a Generalized Complementary Energy Principle for the Equilibrium Analysis of Softening Material," *Comp. Meth. Appl. Mech. Engng.,* Vol. 117, pp. 91–103.

Taylor, J. E., 1993, "A Global Extremum Principle for the Analysis of Solids Composed of Softening Material," *Int. J. Solids Struct.,* Vol. 30, pp. 2057–2069.

Taylor, J. E., 1994, "A Global Extremum Principle in Mixed Form for Equilibrium Analysis with Elastic/Stiffening Materials: A Generalized Minimum Potential Energy Principle," ASME JOURNAL OF APPLIED MECHANICS, Vol. 61, pp. 914–918.

Elastic Force on a Point Defect in or Near a Surface Layer

H. Yu[3], S. C. Sanday[3], and D. J. Bacon[4]

The elastic force on a point defect within or near a surface layer is determined by the image method. There is no stable equilibrium position for the point defect in the surface layer, it is attracted either to the free surface or to the interface. When the point defect is in the substrate it is attracted to the interface when the surface layer is softer than the substrate and to an equilibrium position in the substrate when the surface layer is stiffer than the substrate, the equilibrium position being a function of the elastic constants and the layer thickness.

1 Introduction

The interaction between a point defect and the free surface of a material have been studied extensively for many years, mainly because it plays an important role in material behavior

[3] Naval Research Laboratory, Washington, DC 20375-5343. Mem. ASME.

[4] University of Liverpool, Liverpool, U.K.

Contributed by the Applied Mechanics Division of THE AMERICAN SOCIETY OF MECHANICAL ENGINEERS for publication in the ASME JOURNAL OF APPLIED MECHANICS. Manuscript received by the ASME Applied Mechanics Division, Jan. 4, 1995; final revision, Mar. 1, 1996. Associate Technical Editor: X. Markenscoff.

of this second model starts with an unqualified, symbolic statement of a constrained minimization problem. The problem so represented also is convex. Here too, the identification of the problem statement with the mechanics of elastostatics is accomplished through an interpretation of the "necessary conditions." The form for this characterization, stated here for simplicity as though boundary displacement where prescribed has value zero, is given as

$$\left.\begin{aligned} &\min_{\sigma_{ij},u_k}\left\{\int_\Omega\left[\tfrac{1}{2}E_{ijkl}u_{i,j}u_{k,l}+\tfrac{1}{2}C_{ijkl}\sigma_{ij}\sigma_{kl}dV\right]\right\}\\ &\text{subject to:}\\ &(\sigma_{ij}+E_{ijkl}u_{k,l})_{,j}+f_i=0 \quad \text{in} \quad \Omega\\ &(\sigma_{ij}+E_{ijkl}u_{k,l})n_j-t_i=0 \quad \text{on} \quad \Gamma_t \end{aligned}\right\}[Q].$$

The problem statement reflects minimization (of the sum of quadratic measures) independently w.r.t. admissible fields σ_{ij} and u_l, where admissibility requirements correspond to those of model $[P]$. According to the constraints of $[Q]$, these fields jointly equilibrate (loads) f_i and t_i. As in the prior formulation, here E_{ijkl} and C_{ijkl} represent differentiable, positive definite, symmetric tensors. Also as before, E_{ijkl}, C_{ijkl}, f_i, and t_i symbolize data. λ_i and β_i are introduced as multipliers associated with the field equation and boundary condition constraints of $[Q]$. Stationarity w.r.t. σ_{ij} and u_l, respectively, requires

$$C_{ijkl}\sigma_{kl}-\lambda_{i,j}=0 \quad \text{in} \quad \Omega \tag{6}$$

$$\beta_i+\lambda_i=0 \quad \text{on} \quad \Gamma_t \tag{6a}$$

$$[-E_{klij}u_{i,j}+E_{ijkl}\lambda_{i,j}]_{,l}=0 \quad \text{in} \quad \Omega. \tag{7}$$

This system is satisfied with $\lambda_i = u_i$, and making use of the linear strain-displacement relation $\epsilon_{ij} = (u_{i,j} + u_{j,i})/2$ and the symmetries in the stress and material properties tensors, (6) is interpreted as

$$C_{ijkl}\sigma_{kl}=\epsilon_{ij}. \tag{8}$$

It is clear from the equilibrium equation constraint that $\sigma_{ij} + E_{ijkl}\epsilon_{kl}$ represents total stress, and so with the introduction of $\tilde{E}$ to symbolize the net modulus, the total stress-strain relation is expressed as

$$\sigma_{ij}+E_{ijkl}\epsilon_{kl}=\tilde{E}_{ijkl}\epsilon_{kl}. \tag{9}$$

Accordingly, in view of (8) the effective modulus for this model has the value

$$\tilde{E}_{ijkl}=E_{ijkl}+C^{-1}_{ijkl}. \tag{10}$$

For example, if $E_{ijkl} = C^{-1}_{ijkl}$ then $\tilde{E}_{ijkl} = 2E_{ijkl}$. This completes a verification that the formulation $[Q]$ comprises an authentic portrayal of linear elastostatics. The earlier comments given in relation to version $[P]$ of the problem apply here as well, i.e., the solution to $[Q]$ is generally a unique minimizer.

Summary

Formulations $[P]$ and $[Q]$ have the relatively simple form (among constrained nonlinear programming problems) of "quadratic objective with linear constraints," which is convenient. Creation of these formulations for continuum mechanics relies on the feature of the models that has total stress or total strain interpreted via a *decomposition* into variationally independent components which are coupled through the constraints. In each of the two problem statements the decomposition is expressed in a form that provides for both static and kinematic field measures to be present, and so the results appear as mixed models. Where the goal in using such models is to achieve a desirable balance in precision between the computational evaluation of stresses and deformations, the relative value of E_{ijkl} and C_{ijkl} may be adjusted to control this balance. More generally, compared to familiar forms for mixed principles the extremum problem formulations presented in this note may be more convenient in the treatment of applications, e.g., the development of computational models, performance of analysis toward the establishment of bounds, or the treatment of structural optimization problems, to name a few.

Notwithstanding the simplicity of problem formulations $[P]$ and $[Q]$, these two features i.e., the interpretation of the dual field variables in terms of a set of (independent) constituents, and the interpretation for analysis that follows standard form for the mathematical modeling of constrained nonlinear programming models, can be exploited to obtain other useful extensions to the energetic formulations in solid mechanics. For example, extended versions of the classical complementary statements of "energy principles" are available in forms that comprise constructive formulations for the elastostatics of *constitutively nonlinear* systems (see, e.g., Taylor, 1993, 1994; Plaxton and Taylor, 1994). Also, the same approach can be used to model the more general problem of finite strain elastostatics with nonlinear materials (Hollister et al., 1995).

References

Hollister, S. J., Taylor, J. E., and Washabaugh, P. D., 1995, "A General Finite Strain Model for Elastostatics With Stiffening Materials," ASME JOURNAL OF APPLIED MECHANICS, to appear.

Oden, J. T., and Reddy, J. N., 1976, *Variational Methods in Theoretical Mechanics,* Springer-Verlag, Heidelberg, Germany.

Plaxton, S., Taylor, J. E., 1994, "Applications of a Generalized Complementary Energy Principle for the Equilibrium Analysis of Softening Material," *Comp. Meth. Appl. Mech. Engng.,* Vol. 117, pp. 91–103.

Taylor, J. E., 1993, "A Global Extremum Principle for the Analysis of Solids Composed of Softening Material," *Int. J. Solids Struct.,* Vol. 30, pp. 2057–2069.

Taylor, J. E., 1994, "A Global Extremum Principle in Mixed Form for Equilibrium Analysis with Elastic/Stiffening Materials: A Generalized Minimum Potential Energy Principle," ASME JOURNAL OF APPLIED MECHANICS, Vol. 61, pp. 914–918.

Elastic Force on a Point Defect in or Near a Surface Layer

H. Yu[3], S. C. Sanday[3], and D. J. Bacon[4]

The elastic force on a point defect within or near a surface layer is determined by the image method. There is no stable equilibrium position for the point defect in the surface layer, it is attracted either to the free surface or to the interface. When the point defect is in the substrate it is attracted to the interface when the surface layer is softer than the substrate and to an equilibrium position in the substrate when the surface layer is stiffer than the substrate, the equilibrium position being a function of the elastic constants and the layer thickness.

1 Introduction

The interaction between a point defect and the free surface of a material have been studied extensively for many years, mainly because it plays an important role in material behavior

[3] Naval Research Laboratory, Washington, DC 20375-5343. Mem. ASME.

[4] University of Liverpool, Liverpool, U.K.

Contributed by the Applied Mechanics Division of THE AMERICAN SOCIETY OF MECHANICAL ENGINEERS for publication in the ASME JOURNAL OF APPLIED MECHANICS. Manuscript received by the ASME Applied Mechanics Division, Jan. 4, 1995; final revision, Mar. 1, 1996. Associate Technical Editor: X. Markenscoff.

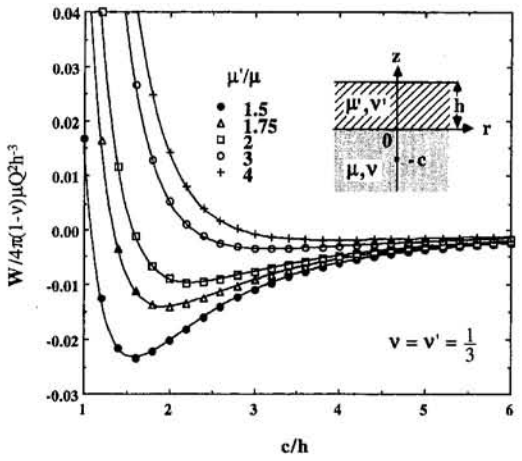

Fig. 1 Variation of interaction energy W with c/h for the point defect in the substrate for $\nu = \nu' = \frac{1}{3}$ and different μ'/μ ratios

related to diffusion, oxidation, corrosion, spinoidal decomposition, etc. When a planar, uniform elastic layer is bonded to an elastic semi-infinite solid of different elastic properties and the materials are isotropic and homogeneous, the problem of finding the elastic force on a point defect which is approximated as a center of dilation is an axisymmetric one and the theory of Hankel transforms given by Sneddon (1951) is a powerful tool for solving it. For example, the force on a point defect in a semi-infinite solid near a surface layer was studied by using Hankel transformations (Dundurs and Stippes, 1966; Bacon 1972). Equally important is the case when the point defect, such as a solute atom, a vacancy, or an interstitial, is in the surface layer of a semi-infinite solid, as might be produced, for example, by deposition or the formation of oxides which, in general, will have different elastic properties from the semi-infinite solid. The aim of this paper is to investigate the elastic interaction between a point defect, the free surface, and the interface in a plane layered material using the image method (Yu and Sanday, 1993).

2 Elastic Solution

The coated semi-infinite solid consists of an infinite plate (surface layer), of thickness h, shear modulus μ', and Poisson's ratio ν', which is perfectly bonded to a homogeneous, isotropic, elastic solid (substrate) with shear modulus μ and Poisson's ratio ν, at the interface $z = 0$ (see insert in Fig. 1). The point defect, which is approximated as a center of dilatation, is at point $(0, 0, \pm c)$. This problem has cylindrical symmetry and the axes of the cylindrical coordinates (r, θ, z) have been chosen with the origin in the interface. The boundary conditions at the interface, $z = 0$, are continuity of displacements u_r and u_z and stresses σ_z and σ_{rz}. The boundary conditions at the free surface, $z = h$, are the vanishing of the normal stress σ_z and shear stress σ_{rz}.

It has been shown that if σ_{ij}^{∞} is the stress due to a center of dilatation in the homogeneous infinite solid, and $\sigma_{ij}^{\infty} + \sigma_{ij}^{*}$ is that in the body under consideration, the interaction energy W (Bacon, 1972) and the nonzero component of the force on the center of dilatation F_z are

$$W = -\frac{2\pi(1-\nu)}{1+\nu} Q\sigma_{kk}^{*} \quad \text{and} \quad F_z = -\frac{\partial W}{\partial z}, \qquad (1)$$

where Q is the strength of the center of dilatation and σ_{ij}^{*} is the image stress. It should be noted that the force given in Eq. (1) differs from that given by Dundurs and Stippes (1966) by a factor of $\frac{1}{2}$. This is because, as pointed out by Bacon (1972) and Moon and Pao (1967), the image interaction energy W differs by a factor of $\frac{1}{2}$ from the interaction energy produced by an independent source other than the center of dilatation itself, and the results given by Dundurs and Stippes were obtained using Eshelby's expression (1951) for the force exerted on the point defect by an external surface traction.

The elastic solution for a center of dilatation in tri-materials, as given by Yu and Sanday (1993), is obtained using the image method and the Green's functions in a bi-material for the double force, doublet, center of dilatation, and their derivatives. The solutions are expressed in terms of the Galerkin stress function Z which is the z-component of the Galerkin stress vector. From the results given by Yu and Sanday (1993) and by setting the elastic constants of one of the semi-infinite solids in the tri-material equal to zero, the dilatational stress due to the center of dilatation at point $(0, 0, -c)$ is

$$\sigma_{kk}^{*} = 4(1+\nu)\mu Q \frac{\partial^2}{\partial z^2}\chi(r, z), \qquad (2)$$

for points in the substrate $(z \le 0)$ and that due to the center of dilatation at point $(0, 0, c)$ is

$$\sigma_{kk}'^{*} = 8(1+\nu')\mu' Q \frac{\partial^2}{\partial z^2}\chi'(r, z), \qquad (3)$$

for points in the surface layer $(0 \le z \le h)$, where

$$\chi(r, z) = A_1\varphi_0' + A_2\varphi_2' + A_2\sum_{n=1}^{\infty}\left[A_3^n + \sum_{j=0}^{n-1} G_{nj}D_z^{2(j+1)}\right]\varphi_{2(n+1)}', \qquad (4)$$

$$\chi'(r, z) = \varphi_1' + A_4\varphi_1 + \sum_{n=1}^{\infty}(A_3^n\varphi_{2n+1}' + A_4^{n+1}\varphi_{2n+1}) + \sum_{n=1}^{\infty}\sum_{j=0}^{n-1}(H_{nj}D_z^{2j+1}\varphi_{2n} - H_{nj}'D_z^{2j+1}\varphi_{2n}' + G_{nj}D_z^{2(j+1)}\varphi_{2n+1}' + G_{nj}'D_z^{2(j+1)}\varphi_{2n+1}), \qquad (5)$$

$$D_z^k = \frac{\partial^k}{\partial z^k}, \quad (k = 0, 1, 2, \ldots),$$

$$A_1 = 2(\mu - \mu')\beta, \quad A_2 = 32(1-\nu)(1-\nu')\mu\mu'\beta^2,$$

$$A_3 = [(3-4\nu)\mu' - (3-4\nu')\mu]\beta, \quad A_4 = (\mu' - \mu)\beta',$$

$$\beta = \frac{1}{\mu + (3-4\nu)\mu'}, \quad \beta' = \frac{1}{\mu' + (3-4\nu')\mu},$$

$$G_{nj} = (2h)^{2(j+1)}\sum_{k=1}^{n-j}\frac{(n-k)!}{(n-j-k)!j!} \times \frac{(j+k)!}{(k-1)!(j+1)!}A_3^{k-1}A_4^{n-k+1},$$

$$G_{nj}' = (2h)^{2(j+1)}\sum_{k=1}^{n-j}\frac{(n-k)!}{(n-j-k)!j!} \times \frac{(j+k)!}{(k-1)!(j+1)!}A_3^{n-j-k}A_4^{j+k+1},$$

$$H_{nj} = (2h)^{2j+1}\sum_{k=1}^{n-j}\frac{(n-k)!}{(n-j-k)!j!}\frac{(j+k-1)!}{(k-1)!j!}A_3^{k-1}A_4^{n-k+1},$$

$$H_{nj}' = (2h)^{2j+1}\sum_{k=1}^{n-j}\frac{(n-k)!}{(n-j-k)!j!}\frac{(j+k-1)!}{(k-1)!j!}A_3^{n-j-k}A_4^{j+k}.$$

$$\varphi_{2n} = [r^2 + (z - c + 2nh)^2]^{-1/2},$$

$$\varphi_{2n+1} = [r^2 + (z + c + 2nh)^2]^{-1/2},$$

and

$$\varphi'_{2n} = [r^2 + (z - c - 2nh)^2]^{-1/2}, \quad (6)$$

$$\varphi'_{2n+1} = \{r^2 + [z + c - 2(n+1)h]^2\}^{-1/2}.$$

The interaction energy and the forces on the point defect in the substrate and in the surface layer are obtained, respectively, by substituting Eqs. (2), (4) and Eqs. (3), (5) into Eq. (1). When the point defect is in the substrate the results obtained by the image method are the same as those obtained by the method of Hankel transforms (Dundurs and Stippes, 1966) (except for a factor of 2 as pointed out previously).

3 Numerical Results

The convergence of the infinite series given in Section 2 has already been demonstrated (Yu and Sanday, 1993). The force on the point defect in the substrate calculated for $\mu'/\mu = 2$, $\nu = \frac{1}{3}$ and $\nu' = \frac{1}{4}$ and the sum of the first four terms, together with the values obtained by Dundurs and Stippes (1966) of the sum of the first four terms are shown in Table 1. The values in the last two columns are those given by Dundurs and Stippes and the values in the second column are those obtained in the present study. The convergence when using the image method is faster than when using the integral obtained by Hankel transformations as indicated by comparing the sum of the first four terms in each solution with the exact values given in column four.

In the following numerical calculations, the results are the sum of the first 12 and 24 terms for the point defect in the substrate and in the surface layer, respectively. Let us first consider the point defect located in the substrate. The numerical results showed that when the surface layer is softer than the substrate ($\mu'/\mu \leq 1$), the layer attracts the point defect. When the surface layer is stiffer than the substrate ($\mu'/\mu > 1$), the defect is repelled from the interface. The effect of the layer on the defect when the layer is stiffer than the substrate is analyzed in Fig. 1 which shows the variation of W for $\nu = \nu' = \frac{1}{3}$ and $\mu'/\mu = 1.5$, 1.75, 2, 3, and 4. The point defect has a stable equilibrium position, i.e., W is minimum and F_z equals zero, and this equilibrium exists because the stiff layer masks the attraction of the free surface, and its position increases in depth from the interface with increasing layer stiffness. The existence of this effect has implications for the segregation of point defects in coated crystals. When the point defect is in the surface layer, the results for W are given in Fig. 2 for $\nu = \nu' = \frac{1}{3}$ and $\mu/\mu' = 0$, 0.1, 0.5, 1, 2, 10, and ∞. Figure 2 shows that when the surface layer is softer than the substrate, the energy decreases with increasing distance c, and the point defect is attracted to the free surface. However, when the surface layer is stiffer than the substrate, the energy has a maximum where $F_z = 0$ at position c_{max}, i.e., the position of unstable equilibrium. The c_{max} value increases with decreasing μ/μ' ratio and equals $0.5h$ for a plate, i.e., $\mu = 0$.

Table 1 Comparison of the values for the force on the point defect in the substrate for $\mu'/\mu = 2$, $\nu = 1/3$ and $\nu' = 1/4$ with results obtained by Dundurs and Stippes (1966)

c/h	This study*	Dundurs and Stippes†	Exact
0.125	−944.63	−944.64	−944.63
0.5	−3.4953	−3.4998	−3.4941
1	−0.6212	−0.6241	−0.6204
2	−0.0014	−0.0018	−0.0012
3	0.0013	0.0012	0.0014

* in units of $12\pi(1-\nu)\mu Q^2h^{-4}$
† in units of $6\pi(1-\nu)\mu Q^2h^{-4}$

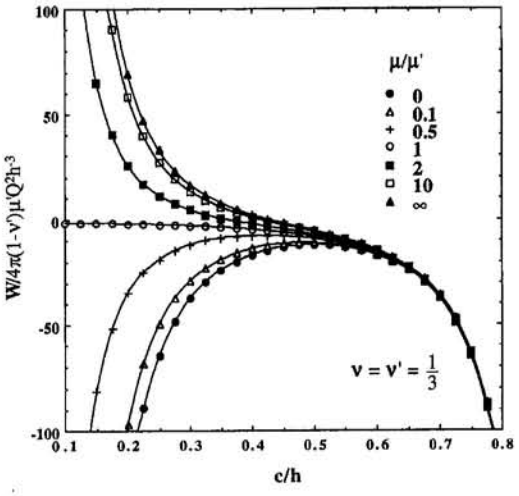

Fig. 2 Variation of interaction energy W with c/h for the point defect in the surface layer for $\nu = \nu' = \frac{1}{3}$ and different μ/μ' ratios

4 Summary

The elastic interaction of a point defect with a surface layer has been discussed in terms of the induced interaction energy and the force acting on the defect. The point defect is treated as a center of dilatation. The surface layer is perfectly bonded to a semi-infinite substrate, and both are isotropic elastic solids but with different elastic constants. The energy and force are obtained by the image method and the results are expressed in terms of convergent infinite series. The comparison of the results obtained by the present method with those obtained by the method of Hankel transforms has been made for the case when the point defect is in the substrate. Numerical examples have been presented and discussed for the point defect in the surface layer and in the substrate. When the point defect is in the substrate and the surface layer is stiffer than the substrate, an equilibrium position exists and the point defect is attracted to this position, which is closer to the surface layer with decreasing stiffness of the layer or decreasing layer thickness. When the point defect is in the surface layer, no stable equilibrium position exists. The point defect is either attracted to the free surface or to the interface, depending on the ratio of the shear moduli of the two materials. These results should be prove of value for researchers concerned with point defect behavior in coated solids.

Acknowledgment

The support of AFSOR and ONR for this investigation is gratefully acknowledged.

References

Bacon, D. J., 1972, "The Mechanical Interaction of a Point Defect with a Surface Layer," *Physica Status Solidi(b)*, Vol. 50, pp. 607–617.

Dundurs, J., and Stippes, M., 1966, "Elastic Interaction of a Point Defect with a Surface Layer," *Recent Advances in Engr. Sci.*, Vol. 3, A. C. Eringen, ed., Gordon and Breach, New York, pp. 323–336.

Eshelby, J. D., 1951, "The Force on an Elastic Singularity," *Philosophical Transactions, of the Royal Society of London*, Vol. A244, pp. 87–112.

Moon, F. C., and Pao, Y. H., 1967, "Interactions of Point Defects and Elastic Inclusions," *Journal of Applied Physics*, Vol. 38, pp. 595–601.

Sneddon, I. N., 1951, *Fourier Transformations*, McGraw-Hill, New York, p. 450.

Yu, H. Y., and Sanday, S. C., 1993, "Elastic Fields Due to Centers of Dilatation and Thermal Inhomogeneities in Plane-Layered Solids," *Journal of Mechanics and Physics of Solids*, Vol. 41, pp. 267–296.

APPENDIX

Some errors made in transposing equations for publication in an earlier study (Bacon, 1972) will be corrected here. All

notation and equation numbers used here are the same as those used in the reference (Bacon, 1972). Equation (16) should be

$$G(k, z) = (A + Bz)e^{-kz} + (C + Dz)e^{kz}, \quad \text{for} \quad z \geq 0$$

and

$$G(k, z) = (A' + B'z)e^{kz} + (C' + D'z)e^{-kz}, \quad \text{for} \quad -t \leq z \leq 0.$$

For a center of dilatation in the surface layer at point $(0, 0, -c)$, which corresponds to point $(0, 0, c)$ in our text, the correct expressions for Eqs. (17e) and (17f) in the reference are

$$ke^{-kt}A' + (2\nu' - kt)e^{-kt}B' + ke^{kt}C' - (2\nu' + kt)e^{kt}D' = Fe^{kt},$$

$$-ke^{-kt}A' + (1 - 2\nu' + kt)e^{-kt}B' + ke^{kt}C' + (1 - 2\nu' - kt)e^{kt}D' = Fe^{kt},$$

respectively. Solving the six simultaneous Eqs. (17a) to (17f) yields

$$A = B = A' = B' = D' = 0, \quad \text{and} \quad C' = \frac{F}{k}. \qquad (a)$$

The elastic field obtained by using Eq. (a) is

$$u_r^0 = -u_r^\infty, \quad \text{and} \quad u_z^0 = -u_z^\infty.$$

The displacements in the layer given by Eqs. (22a) and (22b) are zero, which means that the method given by Bacon (1972) only gives a trivial solution for the elastic interaction of a point defect and a surface layer when the defect is in the surface layer.

Yield Locus in Deep, Single-Face-Cracked Specimens Under Combined Bending and Tension

Yun-Jae Kim,[5,6] F. A. McClintock,[5] and D. M. Parks[5,7]

Introduction

For plates with deep, single face cracks, slip line fields are known under pure tension and under opening bending with compression or small tension (Shiratori and Miyoshi, 1980; Shiratori and Dodd, 1980). For such plates under opening bending and large tension, Rice (1972) gave an analytical-graphical formulation for sliding along the circular arc giving the least upper bound to the limit load. He also proposed an approximate elliptical yield locus for all ranges of positive tensions and net-section moments, which has been widely used (e.g., Hu and Albrecht, 1991).

[5] Department of Mechanical Engineering, Massachusetts Institute of Technology, Cambridge, MA 02139.

[6] Currently at Institute of Materials Research, GKSS Research Center, Geesthact D-21502, Germany.

[7] Mem. ASME.

Contributed by the Applied Mechanics Division of THE AMERICAN SOCIETY OF MECHANICAL ENGINEERS for publication in the ASME JOURNAL OF APPLIED MECHANICS. Manuscript received by the ASME Applied Mechanics Division, Mar. 15, 1993; final revision, July 7, 1993. Associate Technical Editor: L. H. Wheeler.

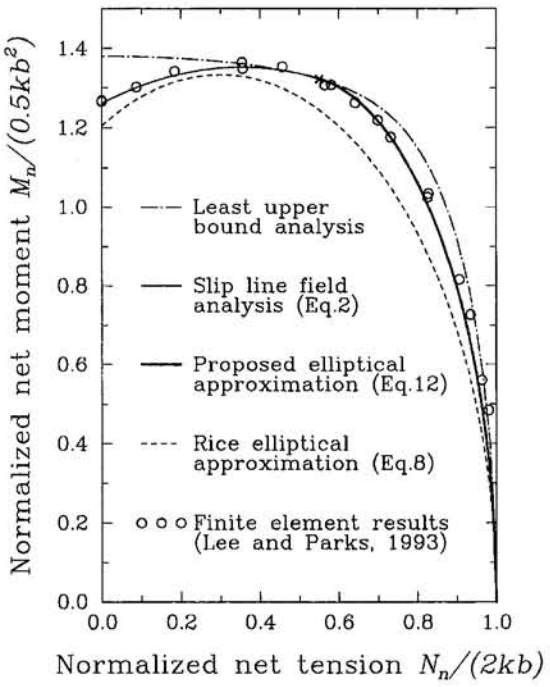

Fig. 1 Yield loci for deep, single-face-cracked specimens under combined bending and tension. Equation 2 holds to the left of the point x.

After a brief review of existing slip line and upper bound fields, we provide a completely analytical formulation for Rice's least upper bound. Then we propose an improved approximate elliptical yield locus and compare it with finite element limit analyses of Lee and Parks (1993).

Opening Bending with Compression or Small Tension

For pure opening bending, Green and Hundy (1956) found the slip line field. For sufficiently small tensile forces, slip line fields can be obtained by "shaving off" some of the constant stress region. When the constant stress sector just vanishes, force and moment equilibrium lead to the following net section tension and bending moment, normalized in terms of an unnotched plate with the shear strength k and remaining ligament b:

$$\hat{N}_n \equiv N_n/(2kb) = 0.5512 \quad \text{and}$$

$$\hat{M}_n \equiv M_n/(2kb^2/4) = 1.3232. \qquad (1)$$

Note that the limiting field of (1) is likely to be only an upper bound: in complete solutions for shallow cracks in pure bending, Ewing (1968) found constant-state triangles at the ends of curved slip lines approaching a free surface. Slip line fields for $\hat{N}_n \leq 0$ with $\hat{M}_n \geq 0$ can be obtained by reducing the circular hinge radius and increasing the constant stress regions. The resulting yield locus from these slip line fields is

$$\Phi_S = \hat{M}_n + 0.7394\hat{N}_n^2 - 0.5212\hat{N}_n - 1.2606 = 0 \quad \text{for} \quad -1 \leq \hat{N}_n < 0.5512, \quad (2)$$

as shown in Fig. 1, with the point ($\hat{N}_n = 0.5512$, $\hat{M}_n = 1.3232$) denoted by "X". See Shiratori and Miyoshi (1980), and Shiratori and Dodd (1980) for closed-form analytical expressions for the numerical coefficients in (1) and (2).

Opening Bending with Large Tension

Slip line fields are not known for large tension ($0.5512 \leq \hat{N}_n < 1$). A possible slip line field, motivated by the field for transverse shear of grooved plates (Mode II) (McClintock and

notation and equation numbers used here are the same as those used in the reference (Bacon, 1972). Equation (16) should be

$$G(k, z) = (A + Bz)e^{-kz} + (C + Dz)e^{kz}, \quad \text{for} \quad z \geq 0$$

and

$$G(k, z) = (A' + B'z)e^{kz} + (C' + D'z)e^{-kz}, \quad \text{for} \quad -t \leq z \leq 0.$$

For a center of dilatation in the surface layer at point $(0, 0, -c)$, which corresponds to point $(0, 0, c)$ in our text, the correct expressions for Eqs. (17e) and (17f) in the reference are

$$ke^{-kt}A' + (2\nu' - kt)e^{-kt}B' + ke^{kt}C' - (2\nu' + kt)e^{kt}D' = Fe^{kt},$$

$$-ke^{-kt}A' + (1 - 2\nu' + kt)e^{-kt}B' + ke^{kt}C' + (1 - 2\nu' - kt)e^{kt}D' = Fe^{kt},$$

respectively. Solving the six simultaneous Eqs. (17a) to (17f) yields

$$A = B = A' = B' = D' = 0, \quad \text{and} \quad C' = \frac{F}{k}. \qquad (a)$$

The elastic field obtained by using Eq. (a) is

$$u_r^0 = -u_r^\infty, \quad \text{and} \quad u_z^0 = -u_z^\infty.$$

The displacements in the layer given by Eqs. (22a) and (22b) are zero, which means that the method given by Bacon (1972) only gives a trivial solution for the elastic interaction of a point defect and a surface layer when the defect is in the surface layer.

Yield Locus in Deep, Single-Face-Cracked Specimens Under Combined Bending and Tension

Yun-Jae Kim,[5,6] F. A. McClintock,[5] and D. M. Parks[5,7]

Introduction

For plates with deep, single face cracks, slip line fields are known under pure tension and under opening bending with compression or small tension (Shiratori and Miyoshi, 1980; Shiratori and Dodd, 1980). For such plates under opening bending and large tension, Rice (1972) gave an analytical-graphical formulation for sliding along the circular arc giving the least upper bound to the limit load. He also proposed an approximate elliptical yield locus for all ranges of positive tensions and net-section moments, which has been widely used (e.g., Hu and Albrecht, 1991).

[5] Department of Mechanical Engineering, Massachusetts Institute of Technology, Cambridge, MA 02139.
[6] Currently at Institute of Materials Research, GKSS Research Center, Geesthact D-21502, Germany.
[7] Mem. ASME.
Contributed by the Applied Mechanics Division of THE AMERICAN SOCIETY OF MECHANICAL ENGINEERS for publication in the ASME JOURNAL OF APPLIED MECHANICS. Manuscript received by the ASME Applied Mechanics Division, Mar. 15, 1993; final revision, July 7, 1993. Associate Technical Editor: L. H. Wheeler.

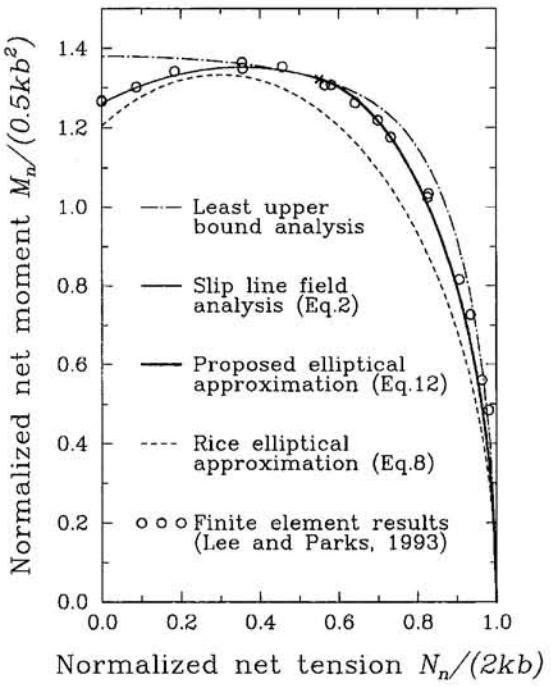

Fig. 1 Yield loci for deep, single-face-cracked specimens under combined bending and tension. Equation 2 holds to the left of the point x.

After a brief review of existing slip line and upper bound fields, we provide a completely analytical formulation for Rice's least upper bound. Then we propose an improved approximate elliptical yield locus and compare it with finite element limit analyses of Lee and Parks (1993).

Opening Bending with Compression or Small Tension

For pure opening bending, Green and Hundy (1956) found the slip line field. For sufficiently small tensile forces, slip line fields can be obtained by "shaving off" some of the constant stress region. When the constant stress sector just vanishes, force and moment equilibrium lead to the following net section tension and bending moment, normalized in terms of an unnotched plate with the shear strength k and remaining ligament b:

$$\hat{N}_n \equiv N_n/(2kb) = 0.5512 \quad \text{and}$$
$$\hat{M}_n \equiv M_n/(2kb^2/4) = 1.3232. \qquad (1)$$

Note that the limiting field of (1) is likely to be only an upper bound: in complete solutions for shallow cracks in pure bending, Ewing (1968) found constant-state triangles at the ends of curved slip lines approaching a free surface. Slip line fields for $\hat{N}_n \leq 0$ with $\hat{M}_n \geq 0$ can be obtained by reducing the circular hinge radius and increasing the constant stress regions. The resulting yield locus from these slip line fields is

$$\Phi_S = \hat{M}_n + 0.7394\hat{N}_n^2 - 0.5212\hat{N}_n - 1.2606 = 0 \quad \text{for} \quad -1 \leq \hat{N}_n < 0.5512, \qquad (2)$$

as shown in Fig. 1, with the point ($\hat{N}_n = 0.5512$, $\hat{M}_n = 1.3232$) denoted by "X". See Shiratori and Miyoshi (1980), and Shiratori and Dodd (1980) for closed-form analytical expressions for the numerical coefficients in (1) and (2).

Opening Bending with Large Tension

Slip line fields are not known for large tension ($0.5512 \leq \hat{N}_n < 1$). A possible slip line field, motivated by the field for transverse shear of grooved plates (Mode II) (McClintock and

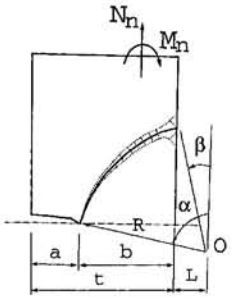

Fig. 2 Possible slip line field for combined bending with large tension (light dotted lines) and kinematically admissible upper bound fields (dark solid line).

Clerico, 1980), is suggested in Fig. 2. They showed that the bound to the limit load in shear is only two percent higher if their slip line field, with fan, arc, and constant stress sectors, is replaced by a single straight line. In Fig. 2, the suggested slip line field is replaced by a single arc of radius R and angular extent $(\alpha - \beta)$, as proposed by Rice (1972). As L and R tend to ∞, both α and β approach $\pi/4$, and the field approaches that for pure tension.

From relative sliding along the circular arc, equilibrium about the point O gives

$$\hat{M}_n = 2\left(\frac{R}{b}\right)^2(\alpha - \beta) - 4\hat{N}_n\left(\frac{L}{b} + \frac{1}{2}\right). \quad (3)$$

For a given $\hat{N}_n$, the least upper bound for $\hat{M}_n$ can be determined by minimizing the right hand side of (3), subject to the two geometric relations from Fig. 2:

$$\frac{L}{b} = \frac{R}{b}\sin\beta, \quad \frac{L}{b} + 1 = \frac{R}{b}\sin\alpha. \quad (4)$$

Eliminating L/b and R/b from (3) using (4) and minimizing the right hand side of (3) with respect to α and β results in two equations in the two unknowns, α and β:

$$(\alpha - \beta)\cos\alpha - (\sin\alpha - \sin\beta)\left(\tfrac{1}{2} + \hat{N}_n \sin\beta\cos\alpha\right) = 0. \quad (5)$$

$$(\alpha - \beta)\cos\beta - (\sin\alpha - \sin\beta)\left(\tfrac{1}{2} + \hat{N}_n \sin\alpha\cos\beta\right) = 0. \quad (6)$$

For a given $\hat{N}_n$, α and β can be determined numerically from (5) and (6). Then $\hat{M}_n$ is determined from (3) with (4) for R/b and L/b. The resulting upper bound to the yield locus is shown in Fig. 1.

Rice (1972) assumed that L is given and minimized the right hand side of (3) with respect to β, which leads to

$$2(\alpha - \beta) = \tan\alpha - \tan\beta. \quad (7)$$

(Note that eliminating $\hat{N}_n$ from (5) and (6) also gives (7).) With (7) he performed a graphical minimization of $\hat{M}_n$ to obtain the same least upper bound as from (5) and (6).

Approximate elliptical yield loci

For the full range of positive tension $(0 \le \hat{N}_n \le 1)$, Rice (1972) approximated the yield locus with an ellipse matched to the slip line solution for pure tension:

$$\Phi_R = \tfrac{1}{0.49}(\hat{N}_n - 0.3)^2 + \tfrac{9}{16}\hat{M}_n^2 - 1 = 0 \quad \text{for} \quad 0 \le \hat{N}_n \le 1. \quad (8)$$

As shown in Fig. 1, this approximate locus falls within the least upper bound locus by up to 9% radially.

We here propose a better elliptical yield locus than (8), for $0.5512 \le \hat{N}_n \le 1$:

$$\Phi_A = A(\hat{M}_n - B)^2 + C(\hat{N}_n - D)^2 - 1 = 0 \quad \text{for} \quad 0.5512 \le \hat{N}_n \le 1. \quad (9)$$

The four unknown coefficients A, B, C, and D are determined such that the ellipse smoothly matches the yield loci of the adjacent slip line solutions at the respective end points:

$$\hat{M}_n = 0 \quad \text{and} \quad \frac{\partial\hat{N}_n}{\partial\hat{M}_n} = 0 \quad \text{at} \quad \hat{N}_n = 1. \quad (10)$$

$$\hat{M}_n = 1.3232 \quad \text{and} \quad \frac{\partial\hat{N}_n}{\partial\hat{M}_n} = \frac{-1}{0.2939} \quad \text{at} \quad \hat{N}_n = 0.5512. \quad (11)$$

The resulting approximate yield locus, shown in Fig. 1, is

$$\Phi_A = 0.56415\hat{M}_n^2 + 3.9258(\hat{N}_n - 0.4953)^2 - 1 = 0 \quad \text{for} \quad 0.5512 \le \hat{N}_n \le 1. \quad (12)$$

The locus (12) lies within that of the least upper bound analysis by at most 4%. No appreciably better fit could be found with a rotated ellipse satisfying the same end conditions.

Lee and Parks (1993) studied yield loci for various crack depths using finite elements. For a given crack depth and tension-to-bending ratio, they found the limit tension and the limit moment. By comparing yield loci for various crack depths, they suggest that relative crack depths of a/t greater than about 0.35 would be "deep enough" to prevent shoulder deformation for all tension-to-bending ratios. (For pure extension, any crack depth is sufficient.) As shown with circles in Fig. 1, their results for relative crack depths of $a/t = 0.5$ and 0.6 are consistent with the modified Green and Hundy solutions. Their results suggest that, for $0.6 \le \hat{N}_n \le 0.9$, the least upper bound locus overestimates by up to 3%, and the Rice ellipse underestimates by up to 6%. Surprisingly, the ellipse (12) fits the finite element results within 1%, as shown in Fig. 1. For $\hat{N}_n > 0.9$, the agreement is still within 2%, the order of the self-consistency of the FEM calculations.

Therefore for opening bending and compression or tension (2) and (12) provide complete plane strain general yield loci for plates with deep enough cracks and small flank angles.

Acknowledgments

This work was supported in part by the Office of Basic Energy Sciences, Department of Energy, under Grant DE-FG02-85ER13331 to M.I.T. and Contract DE-AS07-76ID01670 with the Idaho National Energy Laboratory. This sponsorship is deeply appreciated.

References

Ewing, D. J. F., 1968, "Calculations on the Bending of Rigid/Plastic Notched Bars," *Journal of the Mechanics and Physics of Solids,* Vol. 16, pp. 205–213.

Green, A. P. and Hundy, B. B., 1956, "Initial Plastic Yielding in Notch Bend Tests," *Journal of the Mechanics and Physics of Solids,* Vol. 4, pp. 128–144.

Hu, J. M. and Albrecht, P., 1991, "Limit Load Solution and Loading Behavior of C(T) Fracture Specimen," *International Journal of Fracture,* Vol. 52, pp. 619–645.

Lee, H. and Parks, D. M., 1993, "Fully Plastic Analyses of Plane Strain Single Edge Cracked Specimens Subject to Combined Tension and Bending," *International Journal of Fracture,* Vol. 63, pp. 329–349.

McClintock, F. A., 1971, "Plasticity Aspects of Fracture," *Fracture,* Vol. 3, Liebowitz, H., ed., Academic Press, New York, pp. 47–225. See pp. 155–162.

McClintock, F. A. and Clerico, M., 1980, "The Transverse Shearing of Singly-Grooved Specimens," *Journal of the Mechanics and Physics of Solids,* Vol. 28, pp. 1–16.

Rice, J. R., 1972, "The Line Spring Model for Surface Flaws," *The Surface Crack: Physical Problems and Computational Solutions,* Swedlow, J. L., ed., American Society of Mechanical Engineers, New York, pp. 171–185.

Shiratori, M. and Dodd, B., 1980, "Effect of Deep Wedge-Shaped Notches of Small Flank Angle on Plastic Failure," *International Journal of Mechanical Sciences,* Vol. 22, pp. 127–131.

Shiratori, M. and Miyoshi, T., 1980, "Evaluation of Constraint Factor and J-integral for Single-Edge Notched Specimen", *Proceedings of the Third International Conference on the Mechanical Behavior of Materials*, Vol. 3, Miller, K. J. and Smith, R. F., eds., Pergamon Press, New York, pp. 425–434.

Non-Newtonian Creep Into a Two-Dimensional Cavity of Near-Rectangular Shape

A. Bogobowicz[8]

The plane-strain formulation for the steady-state closure of a near-rectangular, single isolated opening in an indefinite viscoelastic medium is presented. A power creep law describes the creep behavior of the viscous medium. Because of the highly nonlinear nature of the creep, an analytic solution is not possible for the proposed opening geometry, hence an approximation method based upon the minimum principle for velocities is used. The analytic function is used to describe the shape of opening (circular, elliptical, and rectangular with rounded corners).

1 Introduction

The derivations in this paper result from saltrock creep research, but the solution is general enough to be used for any problem of steady-state viscous flow into a single isolated opening. The constraints are a power law creep formulation, an infinite isotropic viscous medium model, and hydrostatic loading at infinity. The formulation is strictly for steady-state creep, which implies constant creep rates due to uniform stress distribution in the viscous medium. Creep generally occurs in two stages: a transient stage, where creep rates are initially high and decrease monotonically with time as stresses are redistributed within the medium and steady-state creep where a dynamic stress equilibrium is established and creep rates become constant. Transient creep response in saltrock is a result of many factors, changes in stress, temperature, moisture content, but primarily is a result of changes in the microstructure of the material itself (Senseny et al., 1992). A true steady-state condition is never attained because of the slow relaxation of stresses as the opening closes. However, determining steady-state creep rates for the intermediate term (years to tens of years) is important for salt mining and storage applications. As the change in creep rate is small the constant creep rates can be assumed. Also, the assumption of a hydrostatic virgin stress state is reasonable because the highly viscous nature of the material will not allow high stress differences to be maintained.

It is generally accepted that steady-state creep at low stresses typical of mined structures is best described by a power law. Because of the highly nonlinear nature of creep, analytic solutions are only possible for two-dimensional problems such as the axisymmetric circular case. For steady-state power law creep, an analytical solution for circular openings (Hardy et al., 1983) and a semi-analytical solution for elliptical openings (Bogobowicz et al., 1991) exist. The focus of this paper is to extend the work done by Bogobowicz et al. for elliptical openings to rectangular openings with rounded corners.

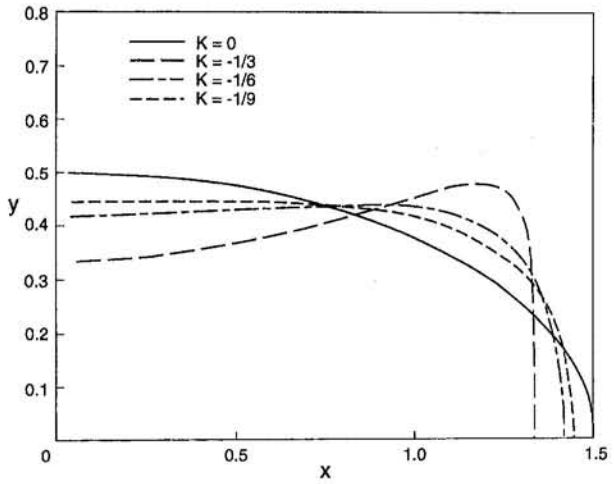

Fig. 1 Shape of the effective opening as a function of constant K for $m = 0.5$

2 Shape Function for the Opening

Excavated openings in saltrock are usually rectangular. Following excavation there is a rock around the opening that fails in a brittle manner because of the high stresses that accompany excavation. Further strain-rate dependent brittle failure can occur over some period (generally several months) because of high creep rates. In deep mines (high stress conditions) an elliptical effective opening is formed. Shallow excavations (low stress conditions) exhibit a rectangular effective opening with rounded corners (Mraz and Dusseault, 1986). A general shape function representing a wide range of realistic effective opening shapes bounded by the described cases is now introduced.

For the problem considered, an infinite saltrock medium, S, is bounded by one simple contour, L, the shape of the effective opening. The region S is transformed onto the infinite plane with a circular hole ($|\xi| > 1$) by the function (Muskhelishvili, 1954):

$$z = \omega(\xi)\left(\xi + \frac{m}{\xi} + \frac{k_1(1-m)}{\xi^2} + \frac{k_2(1-m)}{\xi^3} + \ldots\right) \quad (1)$$

where m is the eccentricity.

The first two terms of Eq. (1) correspond to an ellipse with center at the origin (Muskhelishvili, 1954), and the fourth term forces a rounded corner onto the ellipse. A realistic effective opening geometry for the problem considered is

$$x = \left(\rho + \frac{m}{\rho}\right)\cos\theta + \frac{K}{\rho^3}(1-m)\cos 3\theta$$

$$y = \left(\rho - \frac{m}{\rho}\right)\sin\theta - \frac{K}{\rho^3}(1-m)\sin 3\theta, \quad (2)$$

i.e.,

$$z = \xi + \frac{m}{\xi} + \frac{K(1-m)}{\xi^3}. \quad (3)$$

Because the third term is dependent on 3θ, we must make $|K|$ sufficiently small to prevent looping of the surface contour at the corner. Figure 1 illustrates that to prevent inward curvature of the contour the minimum value of K is approximately $-\frac{1}{9}$; as $K \to 0$, an elliptical shape is reached.

[8] Department of Systems Design Engineering, University of Waterloo, Waterloo, ON N2L 3G1, Canada.

Contributed by the Applied Mechanics Division of THE AMERICAN SOCIETY OF MECHANICAL ENGINEERS for publication in the ASME JOURNAL OF APPLIED MECHANICS. Manuscript received by the ASME Applied Mechanics Division, Oct. 4, 1994; final revision, July 7, 1996. Associate Technical Editor: S. A. Berger.

Shiratori, M. and Miyoshi, T., 1980, "Evaluation of Constraint Factor and J-integral for Single-Edge Notched Specimen", *Proceedings of the Third International Conference on the Mechanical Behavior of Materials*, Vol. 3, Miller, K. J. and Smith, R. F., eds., Pergamon Press, New York, pp. 425–434.

Non-Newtonian Creep Into a Two-Dimensional Cavity of Near-Rectangular Shape

A. Bogobowicz[8]

The plane-strain formulation for the steady-state closure of a near-rectangular, single isolated opening in an indefinite viscoelastic medium is presented. A power creep law describes the creep behavior of the viscous medium. Because of the highly nonlinear nature of the creep, an analytic solution is not possible for the proposed opening geometry, hence an approximation method based upon the minimum principle for velocities is used. The analytic function is used to describe the shape of opening (circular, elliptical, and rectangular with rounded corners).

1 Introduction

The derivations in this paper result from saltrock creep research, but the solution is general enough to be used for any problem of steady-state viscous flow into a single isolated opening. The constraints are a power law creep formulation, an infinite isotropic viscous medium model, and hydrostatic loading at infinity. The formulation is strictly for steady-state creep, which implies constant creep rates due to uniform stress distribution in the viscous medium. Creep generally occurs in two stages: a transient stage, where creep rates are initially high and decrease monotonically with time as stresses are redistributed within the medium and steady-state creep where a dynamic stress equilibrium is established and creep rates become constant. Transient creep response in saltrock is a result of many factors, changes in stress, temperature, moisture content, but primarily is a result of changes in the microstructure of the material itself (Senseny et al., 1992). A true steady-state condition is never attained because of the slow relaxation of stresses as the opening closes. However, determining steady-state creep rates for the intermediate term (years to tens of years) is important for salt mining and storage applications. As the change in creep rate is small the constant creep rates can be assumed. Also, the assumption of a hydrostatic virgin stress state is reasonable because the highly viscous nature of the material will not allow high stress differences to be maintained.

It is generally accepted that steady-state creep at low stresses typical of mined structures is best described by a power law. Because of the highly nonlinear nature of creep, analytic solutions are only possible for two-dimensional problems such as the axisymmetric circular case. For steady-state power law creep, an analytical solution for circular openings (Hardy et al., 1983) and a semi-analytical solution for elliptical openings (Bogobowicz et al., 1991) exist. The focus of this paper is to extend the work done by Bogobowicz et al. for elliptical openings to rectangular openings with rounded corners.

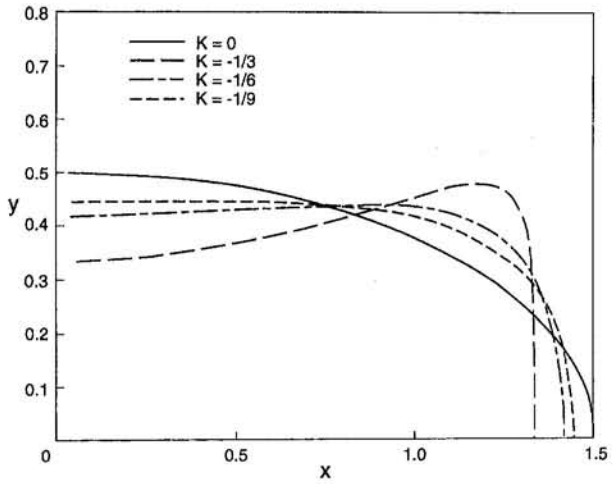

Fig. 1 Shape of the effective opening as a function of constant K for $m = 0.5$

2 Shape Function for the Opening

Excavated openings in saltrock are usually rectangular. Following excavation there is a rock around the opening that fails in a brittle manner because of the high stresses that accompany excavation. Further strain-rate dependent brittle failure can occur over some period (generally several months) because of high creep rates. In deep mines (high stress conditions) an elliptical effective opening is formed. Shallow excavations (low stress conditions) exhibit a rectangular effective opening with rounded corners (Mraz and Dusseault, 1986). A general shape function representing a wide range of realistic effective opening shapes bounded by the described cases is now introduced.

For the problem considered, an infinite saltrock medium, S, is bounded by one simple contour, L, the shape of the effective opening. The region S is transformed onto the infinite plane with a circular hole ($|\xi| > 1$) by the function (Muskhelishvili, 1954):

$$z = \omega(\xi)\left(\xi + \frac{m}{\xi} + \frac{k_1(1-m)}{\xi^2} + \frac{k_2(1-m)}{\xi^3} + \ldots\right) \quad (1)$$

where m is the eccentricity.

The first two terms of Eq. (1) correspond to an ellipse with center at the origin (Muskhelishvili, 1954), and the fourth term forces a rounded corner onto the ellipse. A realistic effective opening geometry for the problem considered is

$$x = \left(\rho + \frac{m}{\rho}\right)\cos\theta + \frac{K}{\rho^3}(1-m)\cos 3\theta$$

$$y = \left(\rho - \frac{m}{\rho}\right)\sin\theta - \frac{K}{\rho^3}(1-m)\sin 3\theta, \quad (2)$$

i.e.,

$$z = \xi + \frac{m}{\xi} + \frac{K(1-m)}{\xi^3}. \quad (3)$$

Because the third term is dependent on 3θ, we must make $|K|$ sufficiently small to prevent looping of the surface contour at the corner. Figure 1 illustrates that to prevent inward curvature of the contour the minimum value of K is approximately $-\frac{1}{9}$; as $K \to 0$, an elliptical shape is reached.

[8] Department of Systems Design Engineering, University of Waterloo, Waterloo, ON N2L 3G1, Canada.

Contributed by the Applied Mechanics Division of THE AMERICAN SOCIETY OF MECHANICAL ENGINEERS for publication in the ASME JOURNAL OF APPLIED MECHANICS. Manuscript received by the ASME Applied Mechanics Division, Oct. 4, 1994; final revision, July 7, 1996. Associate Technical Editor: S. A. Berger.

3 Curvilinear Orthogonal Coordinates

It is more convenient to use a system of curvilinear coordinates by considering the transformation (3). The curvilinear orthogonal system for the problem at hand can be derived from the general strain equations for elastic problems:

$$\dot{\epsilon}_{\rho\rho} = \frac{1}{g}\frac{\delta V_\zeta}{\delta\rho} + \frac{V_\theta}{\rho g^2}\frac{\delta g}{\delta\theta} \tag{4}$$

$$\dot{\epsilon}_{\theta\theta} = \frac{1}{\rho g}\frac{\delta V_\theta}{\delta\theta} + \frac{V_\zeta}{\rho g^2}\frac{\delta(\rho g)}{\delta\rho} \tag{5}$$

$$2\dot{\epsilon}_{\rho\theta} = \rho\frac{\delta}{\delta\rho}\left(\frac{V_\theta}{\rho g}\right) + \frac{1}{\rho}\frac{\delta}{\delta\theta}\left(\frac{V_\zeta}{g}\right) \tag{6}$$

where $g(\rho, \theta)$ is the function of length transformation between the effective opening and a unit circle:

$$g = \left[1 - \frac{2m}{\rho^2}\cos 2\theta + \frac{m^2}{\rho^4} + \frac{6K}{\rho^4}(1-m)\left(\frac{m}{\rho^2}\cos 2\theta - \cos 4\theta\right) + 9K^2\frac{(1-m)^2}{\rho^8}\right]^{1/2}.$$

4 Nonlinear Viscoelastic Problem

The kinematics of the general problem (Eqs. (4) to (6)) are solved in terms of the flow velocity fields; ν_ρ and ν_θ. Additionally, the kinematic constraint of incompressibility

$$\dot{\epsilon}_{\rho\rho} + \dot{\epsilon}_{\theta\theta} + \dot{\epsilon}_{zz} = 0, \quad \dot{\epsilon}_{ii} = 0 \tag{8}$$

and steady-state equilibrium state are assumed:

$$\frac{\delta\sigma_{ij}}{\delta x_j} = 0. \tag{9}$$

Using the notion of stress deviator,

$$\acute{\sigma}_{ij} = \sigma_{ij} - \tfrac{1}{3}\sigma\delta_{ij}, \tag{10}$$

where σ is the sum of principal stresses, we define the constitutive power-law creep equation in the form

$$\dot{\epsilon}_{ij} = \frac{3}{2}\dot{\epsilon}_0\frac{\acute{\sigma}_{ij}}{\sigma_{ef}}\left(\frac{\sigma_{ef}}{\sigma_0}\right)^N. \tag{11}$$

where N is the power-law exponent, σ_0, $\dot{\epsilon}_0$ are material constants and

$$\sigma_{ef} = \sqrt{3}J_2 \tag{12}$$

where

$$J_2 = \tfrac{1}{2}\acute{\sigma}_{ij}\acute{\sigma}_{ij}. \tag{13}$$

The inverted form of the power creep law has the following form (Bogobowicz et al., 1991):

$$\acute{\sigma}_{ij} = \frac{2}{3}\sigma_0\frac{\dot{\epsilon}_{ij}}{\dot{\epsilon}_{ef}}\left(\frac{\dot{\epsilon}_{ef}}{\dot{\epsilon}_0}\right)^{1/N}, \tag{14}$$

where

$$\dot{\epsilon}_{ef} = \frac{\sqrt{2}}{3}\dot{\epsilon}_{ij}\dot{\epsilon}_{ij}. \tag{15}$$

5 Variational Approach to Steady-State Solution

Gilormini and Montheillet (1986) and Bogobowicz et al. (1991) applied the minimum principle for velocities proposed by Hill (1956) to non-Newtonian flow problems in elliptical coordinates. The former deal with the deformation of an elliptical inclusion in a viscous matrix, while the latter present the approximate solution for closure of an elliptical opening in a viscous medium.

The velocity field for a nonlinear flow problem which results in an equilibrium stress field minimizes the rate of energy dissipation on a set of all possible incompressible fields:

$$D(\dot{\epsilon}_{ij}) = \int_V\left(\int_0^{\dot{\epsilon}_{ij}}\sigma_{ij}d\dot{\epsilon}_{ij}\right)dV - \int_B\sigma_{ij}n_j v_i\,dB. \tag{16}$$

The first term represents the rate of energy dissipation in an element of the volume, V, of the medium, and the second term is the power input of boundary tractions, $\sigma_{ij}n_j$, where n is the outward normal to the boundary B surrounding V. The form of the dissipation equation for the nonlinear power law viscous case can be written as (Gilormini and Montheillet, 1986; Bogobowicz et al., 1991):

$$D(\dot{\epsilon}_{ef}) = \frac{N\sigma_0\dot{\epsilon}_0}{N+1}\int_V\left(\frac{\dot{\epsilon}_{ef}}{\dot{\epsilon}_0}\right)^{1/N+1}dV - \int_B\sigma_{ij}n_j v_i\,dB. \tag{17}$$

Application of the minimum potential energy principle results in the following steps of computing:

(1) Assume an incompressible velocity field.
(2) Calculate the effective strain rate.
(3) Calculate stress from Eq. (14).
(4) Calculate D by integration over the volume.
(5) Try all possible fields until a minimum is found.

Many authors utilize a sufficiently wide set of physically admissible velocity fields to solve the specific problems (Gilormini and Montheillet, 1986; Budiansky et al., 1982). Bogobowicz et al. (1991) approached the problem of creep into an elliptical opening in a similar manner. The authors found that fields of linear and nonlinear problems are substantially different for high exponents of power-law viscosity. Both analytical study and finite element method extensive computations suggest the following form of the radial velocity field for non-Newtonian flow:

$$v_\rho(\rho, \theta) = -v_0\left(\frac{1}{\rho g} + \frac{f_1\cos 2\theta}{\rho g} + \frac{f_2\cos 2\theta}{\rho^2 g} + \frac{f_3\cos 2\theta}{\rho^3 g} + \ldots\right). \tag{18}$$

Recognizing the incompressibility constraint and that the velocity functions must be single-valued functions of θ (Bogobowicz et al., 1991), the form of the velocity fields used to describe flow into an elliptical opening are

$$v_\rho = -v_0\left[\frac{1}{\rho g} + \cos 2\theta\left(\frac{c_1}{\rho g} + \frac{c_2}{\rho^2 g} + \frac{c_3}{\rho^3 g}\right)\right]; \tag{19}$$

$$v_\theta = -v_0\left[\frac{1}{2}\sin 2\theta\left(\frac{c_2}{\rho^2 g} + \frac{2c_3}{\rho^3 g}\right)\right]. \tag{20}$$

These trial velocity functions are used for the closure problem for the near-rectangular opening.

6 Minimization Procedure

The minimization of the energy dissipation function (17) is performed subject to hydrostatic stress at infinity ($\sigma_{ij} = p_\infty\delta_{ij}$). In this case the boundary tractions become

$$p_\infty\int_B v_\rho dB = 2\pi p_\infty v_0. \tag{21}$$

For $1/N = n$, the function can be written as

$$D = \frac{\sigma_0 \dot{\epsilon}_0}{n+1} \int_V \left(\frac{\dot{\epsilon}_{ef}}{\dot{\epsilon}_0} \right)^{(n+1)} dV - 2\pi p_\infty v_0, \tag{22}$$

where

$$\dot{\epsilon}_{ef} = \sqrt{\tfrac{4}{3}(\dot{\epsilon}_{\rho\rho}^2 + \dot{\epsilon}_{\rho\theta}^2)}. \tag{23}$$

The radial and shear strain rates are obtained by solving the strain-rate partial differential equations, Eqs. (4), (5), and (6) in terms of the conformal mapping function (Eq. (7)) and the trial velocity fields (Eqs. (19) and (20)). The resulting radial strain rate is

$$\begin{aligned}
\dot{\epsilon}_{\rho\rho} = \frac{V_0}{\rho^2 g^4} \Bigg[& 1 - \frac{m^2}{\rho^4} - \frac{6K}{\rho^4}(1-m)\left(\frac{2m}{\rho^2}\cos 2\theta - \cos 4\theta\right) \\
& - \frac{27K^2}{\rho^8}(1-m)^2 \Bigg] + \frac{v_0 c_1}{\rho^2 g^4} \cos 2\theta \Bigg[1 - \frac{m^2}{\rho^4} \\
& - \frac{6K}{\rho^4}(1-m)\left(\frac{2m}{\rho^2}\cos 2\theta - \cos 4\theta\right) \\
& - \frac{27K^2}{\rho^8}(1-m)^2 \Bigg] + \frac{v_0 c_2}{\rho^3 g^4} \left\{ \left(2 - \frac{18k^2}{\rho^8}(1-m)^2 \right) \right. \\
& \left. \times \cos 2\theta - \frac{m}{2\rho^2}(3 + \cos 4\theta) \right\} \\
& - \frac{v_0 c_2}{\rho^3 g^4} \left\{ \frac{3K}{\rho^4}(1-m) \left[\frac{m}{2\rho^2}(1 + 3\cos 4\theta) \right. \right. \\
& \left. \left. + (\cos 2\theta - \cos 6\theta) \right] \right\} + \frac{v_0 c_3}{\rho^4 g^4} \\
& \times \left\{ \left(3 + m^2\rho^4 - \frac{9K^2}{\rho^8}(1-m)^2 \right) \cos 2\theta \right. \\
& \left. - \frac{m}{\rho^2}(3 + \cos 4\theta) \right\} + \frac{v^0 c^3}{\rho^4 g^4} \left\{ \frac{3K}{\rho^4}(1-m) \right. \\
& \left. \times \left[\frac{m}{\rho^2}(1 - \cos 4\theta) - (3\cos 2\theta - \cos 6\theta) \right] \right\}.
\end{aligned}$$

The shear strain rate is

$$\begin{aligned}
2\dot{\epsilon}_{\rho\theta} = \frac{4v_0}{\rho^2 g^4} \sin 2\theta & \left[\frac{m}{\rho^2} + \frac{3K}{\rho^4}(1-m)\left(4\cos 2\theta - \frac{m}{\rho^2}\right) \right] \\
& + \frac{2v_0 c_1}{\rho^2 g^4} \sin 2\theta \left[1 + \frac{m^2}{\rho^4} + \frac{6K}{\rho^4}(2 + \cos 4\theta) \right. \\
& \left. + \frac{9K^2}{\rho^8}(1-m)^2 \right] + \frac{v_0 c_2}{2\rho^3 g^4} \sin 2\theta \left\{ 7 - \frac{2m}{\rho^2}\cos 2\theta \right. \\
& \left. + \frac{3m^2}{\rho^4} - \frac{9K^2}{\rho^8}(1-m)^2 \right\} + \frac{v_0 c_2}{2\rho^3 g^4} \sin 2\theta \\
& \times \left\{ \frac{6K}{\rho^4}(1-m)\left(8 - \frac{3m}{\rho^2}\cos 2\theta + 5\cos 4\theta\right) \right\} \\
& + \frac{2v_0 c_3}{\rho^4 g^4} \sin 2\theta \left\{ 3 - \frac{2m}{\rho^2}\cos 2\theta + \frac{m^2}{\rho^4} \right. \\
& \left. - \frac{9K^2}{\rho^8}(1-m)^2 \right\} + \frac{2v_0 c_3}{\rho^4 g^4} \sin 2\theta \\
& \times \left\{ \frac{6K}{\rho^4}(1-m)\left(2 - \frac{m}{\rho^2}\cos 2\theta + \cos 4\theta\right) \right\}.
\end{aligned} \tag{25}$$

Thus Eq. (23) can be written as

$$\dot{\epsilon}_{ef} = v_0 \sqrt{\tfrac{4}{3}[(\dot{\epsilon}_{\rho\rho})^2 + (\dot{\epsilon}_{\rho\theta})^2]} = v_0 \dot{\epsilon}_{ef} \tag{26}$$

and the rate of energy dissipation becomes

$$D = \frac{\sigma_0 \dot{\epsilon}_0}{n+1} \int_0^{2K} \int_0^\infty \left(\frac{v_0 \overline{\epsilon_{ef}}}{\dot{\epsilon}_0} \right)^{n+1} \rho g^2 d\rho d\theta - 2\pi p_\infty v_0. \tag{27}$$

This equation is further simplified to

$$D = 2\pi \sigma_0 \dot{\epsilon}_0 \left[\frac{I}{n+1} \left(\frac{v_0}{\dot{\epsilon}_0} \right)^{n+1} - \frac{p_\infty}{\sigma_0} \left(\frac{v_0}{\dot{\epsilon}_0} \right) \right] \tag{28}$$

where the integral I is defined by

$$I = \frac{1}{2\pi} \int_0^{2\pi} \int_0^\infty (\overline{\epsilon_{ef}})^{n+1} \rho g^2 d\rho d\theta. \tag{29}$$

Note that in Bogobowicz et al. (1991) this equation contains a typographical error; the g term must be g^2 as above.

Finding the minimum of Eq. (28) with respect to v_0 yields the mean closure velocity over the whole opening surface:

$$v_0 = \dot{\epsilon}_0 \left(\frac{1}{I} \frac{p_\infty}{\sigma_0} \right)^N. \tag{30}$$

Finally, the integral I is minimized with respect to constants c_1, c_2, and c_3 defining the trial velocity fields. Evaluation of the infinite integral is simplified by performing the following substitution:

$$\zeta = \frac{1}{\rho^2}; \quad \rho d\rho = -\frac{1}{2\zeta^2} d\zeta. \tag{31}$$

Therefore the integral can be written as

$$I = \frac{1}{4\pi} \int_0^{2\pi} \int_0^1 \left[\frac{4}{3\zeta^2} (\overline{\dot{\epsilon}_{\zeta\zeta}^2} + \overline{\dot{\epsilon}_{\zeta\theta}^2}) \right]^{(n+1)/2} \zeta^{n-1} \cdot g^2 d\zeta d\theta. \tag{32}$$

For a circular opening ($m = 0$, $c_1 = c_2 = c_3 = 0$), I can be calculated analytically:

$$I = \frac{N}{\sqrt{3}} \left(\frac{2}{\sqrt{3}} \right)^n \tag{33}$$

If I is normalized by this constant, and new I_0 introduced, then the solution becomes

$$v_0 = \frac{\sqrt{3}}{2} \dot{\epsilon}_0 \left(\frac{\sqrt{3}}{N I_0} \frac{\rho_\infty}{\sigma_0} \right)^N. \tag{34}$$

Now I_0, in its simplest form, is as follows:

$$I_0 = \frac{1}{2\pi N} \int_0^{2\pi} \int_0^1 \left[\frac{1}{\zeta^2} (\overline{\dot{\epsilon}_{\zeta\zeta}^2} + \overline{\dot{\epsilon}_{\zeta\theta}^2}) \right]^{(n+1)/2} \zeta^{n-1} g^2 d\zeta d\theta \tag{35}$$

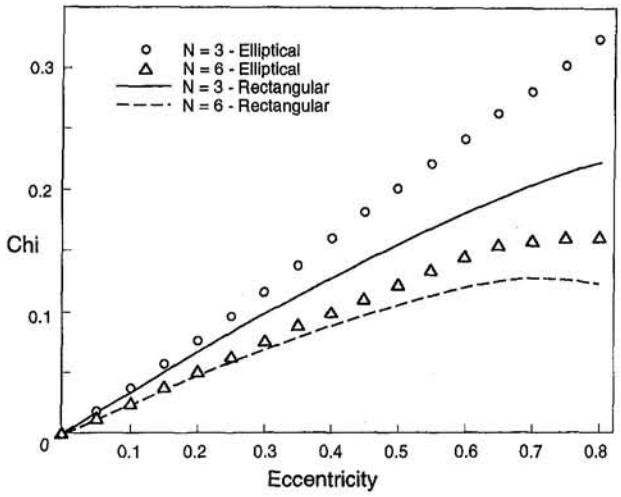

Fig. 2 Comparison of χ between elliptical and near-rectangle solution

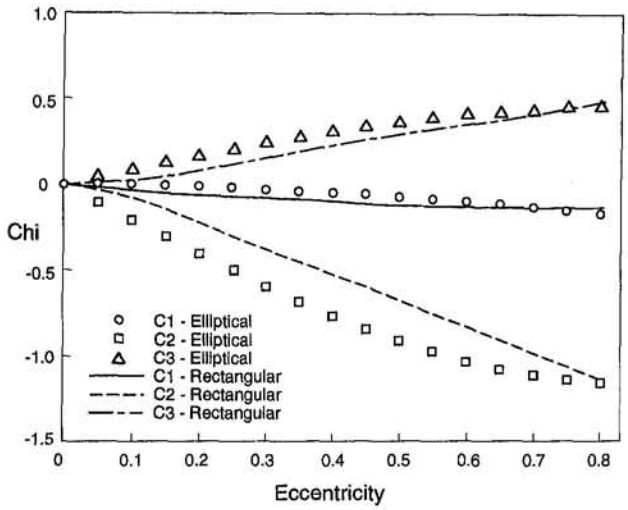

Fig. 4 Minimization results for an elliptical opening and near-rectangle opening, $N = 3$

where the strain rates are given by Eqs. (24) and (25) with v_0 set to unity and the variable substitution from Eq. (31) is performed.

The integral is evaluated numerically using 15-point Gauss-Legendre quadrature. Once minimum $I_0(N, m, c_1, c_2, c_3)$ is found for each power exponent and eccentricity, the steady-state closure solution for the rectangular opening with rounded corner is solved in terms of variables v_0, v_ρ, v_θ and χ using the appropriate equations. Note that the eccentricity m in the shape formula is replaced in the computations by a "dynamic eccentricity" $\chi = (v_h - v_v)/(v_h + v_v)$, where v_h—horizontal velocity, v_v = vertical velocity.

Results

Bogobowicz et al. (1991) use the conjugate gradient method with linear search based on parabolic approximation combined with logarithmic golden-ratio search which utilizes a special concept of dividing an interval $c = a + b$ into two intervals, a and b. Golden-ratio of the division is given by the formula: $(\log a/\log b) = (\log b/\log (a-b))$ (Gottfried, 1983). Skew testing was applied in a minimization procedure. However, it was recently found that for the elliptical opening, by using a shrinking molecule method, identical results to those presented by Bogobowicz et al. (1991) are obtained. The minimization procedure applied in this paper uses a seven-node shrinking molecule which moves through c_1, c_2, c_3 space until a minimum is reached. Comparison of the results obtained for an elliptical and a near-rectangular opening is presented in Fig. 2–4. Compare to the elliptical results, the coefficient c_1 associated with the linear term is about double for the near-rectangular case, whereas the coefficients associated with the quadratic and cubic terms, i.e., c_2, c_3 have a slightly smaller contribution to the velocity fields (Fig. 4). The correlation exists between the semi-analytical solution and the FEM solution for eccentricity less than 0.6 (Fig. 3). Poor correlation thereafter is associated with finite boundary assumed in the FEM solution, as the computations with different extension of the domain indicated.

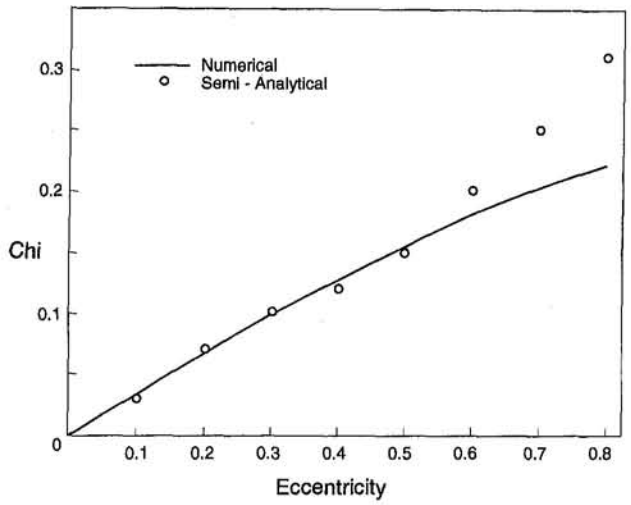

Fig. 3 Comparison of χ between numerical and semi-analytical solution for near-rectangle opening

Conclusions

Although it is difficult to assert with certainty that the trial velocity fields are ideal for the general case, from the computations performed for elliptical and near-rectangular opening it appears that they are adequate. Some interesting properties were observed for the relative closure χ introduced in the paper as "dynamic eccentricity." It was found that for all eccentricities and power exponents (both in elliptical and near-rectangular openings) the relative closure rates become constant after about three months, while the steady state is reached after about six years. It indicates that the rapid stress redistribution occurs early in the transient creep stage. We noted that the velocity field obtained from numerical calculations (FEM) along different lines bisecting the opening were linearly related. It is suggested (and it is a subject of further analysis) that it results from general properties of ellipses (Auerbach et al., 1935).

Acknowledgment

The author would like to thank Prof. Maurice B. Dusseault for his financial support and the MSc student, Pavel Vasak for his computations. The author is grateful to the referees for very careful reading of the manuscript and their suggestions. This manuscript has been submitted as a Brief Note but the author would like to inform that she considers finite boundary as an integral part of the computations in her research on boundary conditions influence and identification.

References

Aurebach, H., Mazur, S., Ulam, S., 1935, "Sur une propriete caracteristique de l'ellipsoide," *Monatshefte fur Mathematik*, Vol. 42, pp. 45–48.

Baar, C. A., 1977, *Applied Salt Rock Mechanics*, Elsevier, Amsterdam.

Bogobowicz, A. D., Rothenburg, L., Dusseault, M. B., 1991, "Solution For Non-Newtonian Flow Into Elliptical Opening," ASME JOURNAL OF APPLIED MECHANICS, Vol. 58, pp. 820–824.

Budiansky, B., Hutchinson, J. W., and Slutsky, S., 1982, "Void Growth and Collapse in Viscous Solids," *Mechanics of Solids*, The Rodney Hill 60th Anniversary Volume, H. G. Hopkins and M. J. Sewell, eds., Pergamon Press, Oxford, U.K., pp. 13–45.

Gilormini, P., and Montheillet, F., 1986, "Deformation of an inclusion in a viscous matrix and induced stress concentration," *Journal of Mechanics and Physics of Solids*, Vol. 34, No. 1, pp. 97–122.

Gottfried, B. S., and Weisman, J., 1973, *Introduction to Optimization Theory*, Prentice-Hall, Englewood Cliffs, NJ, pp. 80–83.

Hardy, H. R., et al., 1983, "Laboratory and Theoretical studies relative to the design of salt caverns for the storage of natural gas," *VI Int. Symp. on Salt*, Vol. 1, Alexandria, VA, pp. 385–416.

Mraz, D. Z., and Dusseault, M. B., 1986, "Effects of geometry on the bearing capacity of pillars in saltrock," CIM RMSCC Workshop, Saskatoon, Canada.

Muskhelishvili, N. I., 1954, *Some Basic problems of the Mathematical Theory of Elasticity*, 4th ed., Noordhoff (1975), pp. 334–443.

Senseny, P. E., Hansen, F. D., Russell, J. E., Carter, N. L., and Handin, J. W., 1992, "Mechanical Behavior of Rock Salt: Phenomenology and Micromechanisms," *International Journal of Rock Mechanics and Mining Sciences & Geomechanics Abstracts*, Vol. 29, No. 4, pp. 363–378.

Critical Angle of Shear Wave Instability in a Film[9]

D. R. Woods[10,12] and S. P. Lin[11,12]

The onset of instability in a liquid film flowing down an inclined plane may manifest itself as long surface waves (soft mode) (Benjamin, 1957; Yih, 1963) or short shear waves (hard mode) (Lin, 1967; DeBruin, 1974; Chin et al., 1986; Floryan et al., 1987), depending on the angle of inclination θ. Floryan, Davis, and Kelly (1987) showed that the change in the critical Reynolds number of the hard mode may not be monotonic as the angles of inclination θ is reduced, or as the surface tension is increased. On the other hand the critical Reynolds number of the soft mode increases monotonically with reduction in θ for all surface tension. Hence, there exists a critical angle depending on the surface tension below which the film becomes unstable with respect to shear waves, and above which the film becomes unstable with respect to surface waves. Here, we confirm the finding of Floryan et al. by use of the Chebychev spectral method (Woods and Lin, 1995). Moreover, we obtain the upper bounds of the critical angle of inclination and the lower bound of the critical Reynolds number for all finite surface tension.

Consider a uniform layer of liquid flowing down an inclined plane under the action of gravity. The basic flow which satisfies exactly the Navier-Stokes equations has a parabolic distribution of velocity $\bar{u}(y)$ parallel to the incline (Benjamin, 1957; Yih, 1963), where y is the distance measured perpendicularly to the flow direction from the middepth of the liquid layer in the unit of the half-layer thickness D. When such a parallel flow is perturbed by an arbitrary Fourier component of the two-dimensional disturbance, the amplitude of the velocity disturbance must satisfy the Orr-Sommerfeld equation (Benjamin, 1957; Yih, 1963).

$$\phi'''' - 2\alpha^2\phi'' + \alpha^4\phi - i\alpha\,\mathrm{Re}[(\bar{u} - c)(\phi'' - \alpha^2\phi) - \bar{u}''\phi] = 0, \quad (1)$$

where ϕ is the normal mode amplitude of the perturbation stream function

$$\psi = \phi(y)\exp[i\alpha(x - ct)]. \quad (2)$$

α is the wave number; x is the dimensionless distance measured in the flow direction; c is the complex wave speed; t is time; primes on ϕ and $\bar{u}$ denote differentiation with respect to y; and Re ≡ Reynolds number = U_aD/ν, U_a and ν being, respectively, the average velocity and the fluid kinematic viscosity. Upon substituting the Chebyshev series expansion of $\phi(y)$

$$\phi(y) = \sum_{n=0}^{N} a_nT_n(y) \quad (3)$$

into the Orr-Sommerfeld equation and its boundary conditions, and demanding the coefficient of the nth order Chebychev polynomial $T_n(y)$ of the resulting equation to be zero (Woods and Lin, 1995), we have

$$\begin{aligned}
&-\tfrac{1}{24}\sum_{\substack{p=n+4\\ n+p\text{even}}}^{N}[p^3(p^2-4)^2 - 3n^2p^5 + 3n^4p^3 - n^2(n^2-4)^2p]a_p + i\alpha Q\sum_{\substack{p=n+3\\ n+p\text{odd}}}^{N} p(p^2 - n^2 - 1)a_p \\
&+ \sum_{\substack{p=n+2\\ n+p\text{even}}}^{N}[2\alpha^2p(p^2-n^2) - \tfrac{1}{2}i\alpha Qp(p^2-n^2-2) + \tfrac{3}{2}i\alpha Qp(p^2-n^2)]a_p + \Big[-\alpha^4 + \tfrac{1}{8}i\alpha^3Q(c_n + c_{n-1}) \\
&- i\alpha^3\tfrac{3}{2}Q + i\alpha Q - \frac{1}{2c_n}i\alpha Qn(n-1)\Big]c_na_n \\
&+ \tfrac{1}{8}i\alpha^3Qc_{n-2}c_na_{n-2} - \tfrac{1}{2}i\alpha^3Qc_nc_{n-1}a_{n-1} \\
&+ i\alpha Q[2n(n+1) - \tfrac{1}{2}\alpha^2c_n]a_{n+1} + \tfrac{1}{8}i\alpha^3Qc_na_{n+2} \\
&+ i\alpha c\,\mathrm{Re}[\sum_{\substack{p=n+2\\ n+p\text{even}}}^{N} p(p^2-n^2)a_p - \alpha^2c_na_n] = 0, \qquad (n = 0, \text{to } N-4), \quad (4)
\end{aligned}$$

$$\sum_{n=0}^{N}(-1)^na_n = 0, \quad \sum_{n=0}^{N}(-1)^{n-1}n^2a_n = 0, \quad (5)$$

$$\sum_{n=0}^{N} a_n + [u(1) - c]h = 0, \quad (6)$$

$$\sum_{n=0}^{N}[n^2(n^2-1)/3 + \alpha^2]a_n + \bar{u}''(1)h = 0, \quad (7)$$

$$\sum_{n=0}^{N}[n^2(n^2-1)(n^2-4)/15 - 3\alpha^2n^2 - i\alpha\,\mathrm{Re}(3/2 - c)n^2]a_n - i\alpha[(3\cot\theta)/4 + \alpha^2\,\mathrm{ReWe}]h = 0, \quad (8)$$

where $Q = 3\,\mathrm{Re}/4$, Re being the Reynolds number defined by $\mathrm{Re} = U_aD/\nu$, $c_o = 2$, $c_n = 1$ $(n > 0)$, We is the Weber number defined by $\mathrm{We} = S/\rho U_a^2D$, S being the surface tension, and h is the displacement of the free surface from its unperturbed position. Equation (4) corresponds to the Orr-Sommerfeld

[9] This work was supported in part by grant no. DAAH04-93-G0395 and no. NAG3-1402 of NASA.

[10] Graduate Research Assistant.

[11] Professor, Mem. ASME.

[12] Department of Mechanical and Aeronautical Engineering, Clarkson University, Potsdam, NY 13699.

Contributed by the Applied Mechanics Division of THE AMERICAN SOCIETY OF MECHANICAL ENGINEERS for publication in the ASME JOURNAL OF APPLIED MECHANICS. Manuscript received by the ASME Applied Mechanics Division, June 23, 1995; final revision, Aug. 6, 1996. Associate Technical Editor: T. R. Akylas.

Bogobowicz, A. D., Rothenburg, L., Dusseault, M. B., 1991, "Solution For Non-Newtonian Flow Into Elliptical Opening," ASME JOURNAL OF APPLIED MECHANICS, Vol. 58, pp. 820–824.

Budiansky, B., Hutchinson, J. W., and Slutsky, S., 1982, "Void Growth and Collapse in Viscous Solids," *Mechanics of Solids,* The Rodney Hill 60th Anniversary Volume, H. G. Hopkins and M. J. Sewell, eds., Pergamon Press, Oxford, U.K., pp. 13–45.

Gilormini, P., and Montheillet, F., 1986, "Deformation of an inclusion in a viscous matrix and induced stress concentration," *Journal of Mechanics and Physics of Solids,* Vol. 34, No. 1, pp. 97–122.

Gottfried, B. S., and Weisman, J., 1973, *Introduction to Optimization Theory,* Prentice-Hall, Englewood Cliffs, NJ, pp. 80–83.

Hardy, H. R., et al., 1983, "Laboratory and Theoretical studies relative to the design of salt caverns for the storage of natural gas," *VI Int. Symp. on Salt,* Vol. 1, Alexandria, VA, pp. 385–416.

Mraz, D. Z., and Dusseault, M. B., 1986, "Effects of geometry on the bearing capacity of pillars in saltrock," CIM RMSCC Workshop, Saskatoon, Canada.

Muskhelishvili, N. I., 1954, *Some Basic problems of the Mathematical Theory of Elasticity,* 4th ed., Noordhoff (1975), pp. 334–443.

Senseny, P. E., Hansen, F. D., Russell, J. E., Carter, N. L., and Handin, J. W., 1992, "Mechanical Behavior of Rock Salt: Phenomenology and Micromechanisms," *International Journal of Rock Mechanics and Mining Sciences & Geomechanics Abstracts,* Vol. 29, No. 4, pp. 363–378.

Critical Angle of Shear Wave Instability in a Film[9]

D. R. Woods[10,12] and S. P. Lin[11,12]

The onset of instability in a liquid film flowing down an inclined plane may manifest itself as long surface waves (soft mode) (Benjamin, 1957; Yih, 1963) or short shear waves (hard mode) (Lin, 1967; DeBruin, 1974; Chin et al., 1986; Floryan et al., 1987), depending on the angle of inclination θ. Floryan, Davis, and Kelly (1987) showed that the change in the critical Reynolds number of the hard mode may not be monotonic as the angles of inclination θ is reduced, or as the surface tension is increased. On the other hand the critical Reynolds number of the soft mode increases monotonically with reduction in θ for all surface tension. Hence, there exists a critical angle depending on the surface tension below which the film becomes unstable with respect to shear waves, and above which the film becomes unstable with respect to surface waves. Here, we confirm the finding of Floryan et al. by use of the Chebychev spectral method (Woods and Lin, 1995). Moreover, we obtain the upper bounds of the critical angle of inclination and the lower bound of the critical Reynolds number for all finite surface tension.

Consider a uniform layer of liquid flowing down an inclined plane under the action of gravity. The basic flow which satisfies exactly the Navier-Stokes equations has a parabolic distribution of velocity $\bar{u}(y)$ parallel to the incline (Benjamin, 1957; Yih, 1963), where y is the distance measured perpendicularly to the flow direction from the middepth of the liquid layer in the unit of the half-layer thickness D. When such a parallel flow is perturbed by an arbitrary Fourier component of the two-dimensional disturbance, the amplitude of the velocity disturbance must satisfy the Orr-Sommerfeld equation (Benjamin, 1957; Yih, 1963).

$$\phi'''' - 2\alpha^2\phi'' + \alpha^4\phi - i\alpha\,\mathrm{Re}[(\bar{u} - c)(\phi'' - \alpha^2\phi) - \bar{u}''\phi] = 0, \quad (1)$$

where ϕ is the normal mode amplitude of the perturbation stream function

$$\psi = \phi(y)\exp[i\alpha(x - ct)]. \quad (2)$$

α is the wave number; x is the dimensionless distance measured in the flow direction; c is the complex wave speed; t is time; primes on ϕ and $\bar{u}$ denote differentiation with respect to y; and Re ≡ Reynolds number = U_aD/ν, U_a and ν being, respectively, the average velocity and the fluid kinematic viscosity. Upon substituting the Chebyshev series expansion of $\phi(y)$

$$\phi(y) = \sum_{n=0}^{N} a_nT_n(y) \quad (3)$$

into the Orr-Sommerfeld equation and its boundary conditions, and demanding the coefficient of the nth order Chebychev polynomial $T_n(y)$ of the resulting equation to be zero (Woods and Lin, 1995), we have

$$\begin{aligned}
&-\tfrac{1}{24}\sum_{\substack{p=n+4\\ n+p\text{even}}}^{N}[p^3(p^2-4)^2 - 3n^2p^5 + 3n^4p^3 - n^2(n^2-4)^2p]a_p + i\alpha Q\sum_{\substack{p=n+3\\ n+p\text{odd}}}^{N} p(p^2 - n^2 - 1)a_p \\
&+ \sum_{\substack{p=n+2\\ n+p\text{even}}}^{N}[2\alpha^2p(p^2-n^2) - \tfrac{1}{2}i\alpha Qp(p^2-n^2-2) + \tfrac{3}{2}i\alpha Qp(p^2-n^2)]a_p + \Big[-\alpha^4 + \tfrac{1}{8}i\alpha^3Q(c_n + c_{n-1}) \\
&- i\alpha^3\tfrac{3}{2}Q + i\alpha Q - \frac{1}{2c_n}i\alpha Qn(n-1)\Big]c_na_n \\
&+ \tfrac{1}{8}i\alpha^3Qc_{n-2}c_na_{n-2} - \tfrac{1}{2}i\alpha^3Qc_nc_{n-1}a_{n-1} \\
&+ i\alpha Q[2n(n+1) - \tfrac{1}{2}\alpha^2c_n]a_{n+1} + \tfrac{1}{8}i\alpha^3Qc_na_{n+2} \\
&+ i\alpha c\,\mathrm{Re}[\sum_{\substack{p=n+2\\ n+p\text{even}}}^{N} p(p^2-n^2)a_p - \alpha^2c_na_n] = 0, \qquad (n = 0, \text{to } N-4), \quad (4)
\end{aligned}$$

$$\sum_{n=0}^{N}(-1)^na_n = 0, \quad \sum_{n=0}^{N}(-1)^{n-1}n^2a_n = 0, \quad (5)$$

$$\sum_{n=0}^{N} a_n + [u(1) - c]h = 0, \quad (6)$$

$$\sum_{n=0}^{N}[n^2(n^2-1)/3 + \alpha^2]a_n + \bar{u}''(1)h = 0, \quad (7)$$

$$\sum_{n=0}^{N}[n^2(n^2-1)(n^2-4)/15 - 3\alpha^2n^2 - i\alpha\,\mathrm{Re}(3/2 - c)n^2]a_n - i\alpha[(3\cot\theta)/4 + \alpha^2\,\mathrm{ReWe}]h = 0, \quad (8)$$

where $Q = 3\,\mathrm{Re}/4$, Re being the Reynolds number defined by $\mathrm{Re} = U_aD/\nu$, $c_o = 2$, $c_n = 1$ $(n > 0)$, We is the Weber number defined by $\mathrm{We} = S/\rho U_a^2D$, S being the surface tension, and h is the displacement of the free surface from its unperturbed position. Equation (4) corresponds to the Orr-Sommerfeld

[9] This work was supported in part by grant no. DAAH04-93-G0395 and no. NAG3-1402 of NASA.

[10] Graduate Research Assistant.

[11] Professor, Mem. ASME.

[12] Department of Mechanical and Aeronautical Engineering, Clarkson University, Potsdam, NY 13699.

Contributed by the Applied Mechanics Division of THE AMERICAN SOCIETY OF MECHANICAL ENGINEERS for publication in the ASME JOURNAL OF APPLIED MECHANICS. Manuscript received by the ASME Applied Mechanics Division, June 23, 1995; final revision, Aug. 6, 1996. Associate Technical Editor: T. R. Akylas.

equation. Equations (5), (6), (7), and (8) arise, respectively, from the no-slip condition at the incline, the kinematic condition at the free surface, the tangential force balance at the free surface, and the normal force balance at the free surface. Equations (4) to (8) can be obtained from the related work of Woods and Lin (1995) by putting the amplitude of vibration of the incline to zero in their corresponding equations, i.e., from their Eqs. (27) – (32). The derivation is lengthy and will not be repeated here. However, the typographical errors in the coefficients of a_n and d in their Eqs. (29) and (32) are corrected here. It should be pointed out that Q in their Eqs. (27) is equal to $\mathrm{Re}^2\,\mathrm{Fr}\sin\theta$, except that the reference velocity used there is different from here.

For a given set of parameters (Re, We, α, θ), the homogeneous system of Eqs. (4) to (8) constitute a Lanczos' (Orszag, 1971) eigenvalue problem. IMSL subroutine DGVCCG is used to obtain the eigenvalue c. c_r gives the wave speed, and c_i gives the temporal growth rate of disturbances, if it is positive. The flow is stable if $c_i < 0$. The flow is neutral if $c_i = 0$. The possible numerical inaccuracy, programing and syntax errors are tested according to the method described in the work of Woods and Lin (1995). The results to be presented are accurate up to the third decimal point.

Figure 1 gives the neutral stability curves $c_i = 0$ for the soft as well as hard modes for several small angles of inclination, and We = 0. The soft mode neutral curves for $\theta = 0.6'$ and $0.5'$ are not included because they are too close to the Re-axis to make the comparison of two modes sufficiently clear with the same length scale. However, the critical Reynolds numbers corresponding to these two cases are given in Table 1. In this table the critical Reynolds numbers for the hard modes are listed together with that given by DeBruin and Floryan et al. DeBruin's results are given in the first, and that of Floryan are given in the second parantheses. For the soft mode our results agree with that of Floryan et al., and DeBruin's results are given

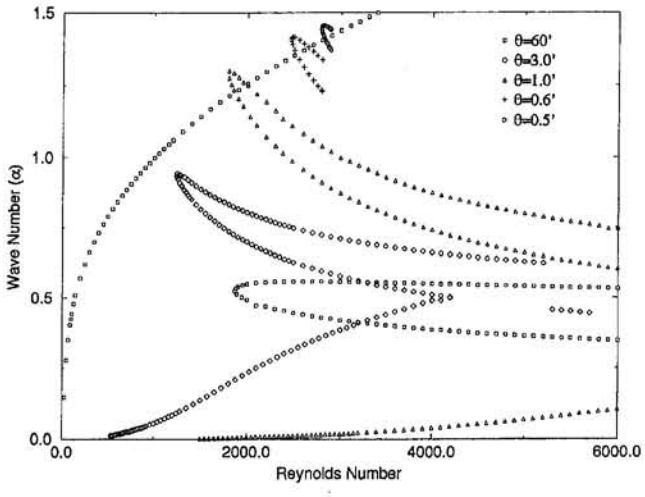

Fig. 1 Effect of plane inclination on neutral curves

Table 1 Critical Reynolds numbers

θ	Soft	Rc present	Hard (DeBruin)	Hard (Floryan et al.)
60′	72 (72)	5602	(5600)	(5602)
3′	1432 (1430)	3711	(3700)	(3711)
1′	4297 (4300)	5391	(5400)	(5363)
0.6′	7162 (—)	7392	(—)	(—)
0.56′	7673 (—)	7981	(—)	(—)
0.5′	8594 (8600)	8373	(8500)	(8369)

in parantheses. It should be pointed out that while the length and velocity are scaled, respectively, with D and U_a in this work, they are scaled with $2D$ and $3U_a/2$ in the works of DeBruin and Floryan et al. Therefore the critical Reynolds numbers, Rc, including those indicated in Fig. 1 are multiplied by three before entering in Table 1. The Rc for $\theta = 60'$ and $3'$ agree with that of Floryan et al. For $\theta = 1'$ and $0.5'$ our Rc are slightly larger than that of theirs. Our results are much closer to that of Floyan et al. than that of DeBruin. Indeed, the critical Reynolds number of the hard mode first decreases with decreasing θ but increases when θ is further decreased below $3'$. The critical Reynolds number for the soft mode increases monotonically with the decreasing θ. The critical Reynolds number for the soft mode remains smaller than that for the hard mode until $0.56'$. Below this angle the hard mode becomes more unstable than the soft mode. Thus, in a deep open channel flow along a gentle slope, one may observe the growth of short shear waves under a relatively quiescent surface. At this critical angle both the hard and soft modes become unstable simultaneously at Rc = 7673. We found numerically, as Floryan et al. did, that the surface tension slightly stabilizes the hard mode at $\theta < 4'$. Therefore, the critical angle we found for zero surface tension provides the upper bound for the angle of inclination below which the hard mode is more unstable in a film with finite surface tension. Moreover, Rc = 7673 for the zero surface tension case offers the lower bound of Rc for the case of finite surface tension.

References

Benjamin, T. B., 1957, "Wave Formation in Laminar Flow Down an Inclined Plane," *Journal of Fluid Mechanics,* Vol. 554, p. 505.

Chin, R. W., Abernathy, F. H., and Bertschy, J. R., 1986, "Gravity and Shear Wave Instability of Free Surface Flows, Part I: Numerical Calculations," *Journal of Fluid Mechanics,* Vol. 168, Vol. 168, p. 501.

DeBruin, G. J., 1974, "Stability of a Layer of Liquid Flowing Down an Inclined Plane," *Journal of Engineering Mathematics,* Vol. 8, p. 259.

Floryan, J. M., Davis, S. H., and Kelly, R. E., 1987, "Instability of a liquid Film Flowing Down a Slightly Inclined Plane," *Physics of Fluids,* Vol. 30, p. 983.

Lin, S. P., 1967, "Instability of a Liquid Film Flowing Down an Inclined Plane," *Physics of Fluids,* Vol. 60, p. 308.

Orszag, S. A., 1971, "Accurate Solution of the Orr-Sommerfeld Equation," *Journal of Fluid Mechanics,* Vol. 50, p. 689.

Woods, D. R., and Lin, S. P., 1995, "Instability of a Liquid Flow Over a Vibrating Inclined Plane," *Journal of Fluid Mechanics,* Vol. 294, p. 391.

Yih, C. S., 1963, "Stability of Liquid Flow Down an Inclined Plane," *Physics of Fluids,* Vol. 6, p. 321.

Journal of Applied Mechanics

Discussion

A General Formulation of the Theory of Wire Ropes[1]

C. Jolicoeur.[2] This paper presents an elegant way to extend a strand model into a wire rope model. The present writer has appreciated very much the basic principle of this work which consists in the replacement of the individual wires by structures that have a more complex behavior than wires and that need an increased number of parameters to describe this behavior in the rope. This is an approach that is related to the homogenization methods.

The author used Costello's model (1990) as a starting point, and has extended it to incorporate the added parameters. He could probably have used another model, but this choice is a reasonable one since Costello's model has proven very reliable for strand modeling (Jolicoeur and Cardou, 1991). The equations provided in the paper for the case of a linear strand should then give identical results with Costello's model. This was not demonstrated in the paper and the present writer has attempted to verify this. In so doing, some flaws have appeared in the formulation of the equations, hence the present discussion.

The main problem identified is in the use of the term $\sqrt{1 + k^2}$ (where $k = \tan \alpha$) in Eqs. (39) and (53). As formulated, when doing the summation for a_s, for example, the terms corresponding to layers that have a left-hand lay (i.e., $\alpha > 90$) take a negative value, leading to an incorrect result for a_s. In other models, use is rather made of sin α and cos α and, in fact, the following identity

$$\cos \alpha = \frac{1}{\sqrt{1 + \tan^2 \alpha}}$$

is valid for $\alpha < 90$ deg. When $\alpha > 90$ deg, a sign error occurs, leading to the aforementioned problem. To correct the error, it is recommended to replace $\sqrt{1 + k_i^2}$ by $1/\cos \alpha_i$ in Eqs. (39) and (53). For the case of a linear strand, Eqs. (53) would be rewritten as

$$a_s = \pi E_0 R_0^2 + \sum_{i=1}^{n} \frac{\pi}{4} m_i E_i R_i^4 \tau_i \kappa_i \cos \alpha_i \times \left[\frac{1}{1 + \nu_i} + k_i^2 - \left(\frac{1 - \nu_i}{1 + \nu_i} + k_i^2 - \frac{4}{R_i^2 \kappa_i^2} \right) \lambda_i \right]$$

$$b_s = -\sum_{i=1}^{n} \frac{\pi}{4} m_i E_i R_i^4 \tau_i \kappa_i \cos \alpha_i \times \left[\frac{\nu_i}{1 + \nu_i} k_i r_i + \left(\frac{1 - \nu_i}{1 + \nu_i} + k_i^2 - \frac{4}{R_i^2 \kappa_i^2} \right) \mu_i \right]$$

$$c_s = -\sum_{i=1}^{n} \frac{\pi}{4} m_i E_i R_i^4 \kappa_i \cos^3 \alpha_i \left[\left(1 + \frac{1 + 2\nu_i}{1 + \nu_i} k_i^2 \right) k_i^2 + \left(1 + k_i^2 - \frac{2\nu_i}{1 + \nu_i} k_i^4 - \frac{4}{R_i^2 \kappa_i^2} \right) \lambda_i \right]$$

$$d_s = \frac{\pi E_0 R_0^4}{4(1 + \nu_0)} + \sum_{i=1}^{n} \frac{\pi}{4} m_i E_i R_i^4 \kappa_i \cos^3 \alpha_i \left[\left(1 + 2k_i^2 + \frac{1}{1 + \nu_i} k_i^4 \right) k_i r_i - \left(1 + k_i^2 - \frac{2\nu_i}{1 + \nu_i} k_i^4 - \frac{4}{R_i^2 \kappa_i^2} \right) \mu_i \right].$$

In addition to this, a typing error has been found in the second of Eqs. (57) where the term λ_{i-1} should be replaced by μ_{i-1}.

Results obtained with the modified equations have proven identical (to the fifth significative digit or better) with results obtained using Costello's (1990) model for two selected multilayered strands, namely the Drake 26/7 ACSR and the Rail 45/7 ACSR, which are referenced to in Jolicoeur and Cardou (1991, 1996).

References

Costello, G. A., 1990, *Theory of Wire Ropes*, Springer-Verlag, New York.

Jolicoeur, C., and Cardou, A., 1991, "A Numerical Comparison of Current Mathematical Models of Twisted Wire Cables under Axisymmetric Loads," ASME *Journal of Energy Resources Technology*, Vol. 113, pp. 241–249.

Jolicoeur, C., and Cardou, A., 1996, "A Semi-continuous Mathematical Model for Bending of Multilayered Wire Strands," *ASCE Journal of Engineering Mechanics*, in press.

A General Formulation of the Theory of Wire Ropes[3]

S. Sathikh[4]**, Jayakumar**[4]**, and C. Jebaraj**[5]**.** The author deserves congratulations for his significant contribution to the rope mechanics through this general formulation. The writers have two points for discussion. First, the question of symmetry of the response of a linear elastic strand or rope structure is not ensured in Eqs. (38) and (52) since $b \neq c$ in Eqs. (39) and (53). Jolicoeur and Cardou (1991) have dealt with this subject of lack of symmetry in several earlier formulations, including the five references of Costello's team in this paper. They showed that the lack of symmetry does not significantly affect the responses. The work of Kumar and Cochran (1987) is worth

[1] By W. Jiang and published in the Sept. 1995 issue of the ASME JOURNAL OF APPLIED MECHANICS, Vol. 62, pp. 747–755.

[2] Department of Mechanical Engineering, Universite Laval, Quebec G1K 7P4, Canada.

[3] By W. Jiang and published in the Sept. 1995 issue of the ASME Journal of Applied Mechanics, Vol. 62, pp. 747–755.

[4] Department of Mechanical Engineering, Crescent Engineering College, Madras 600 048, India.

[5] Department of Mechanical Engineering, Anna University, Madras 600 025, India.

mention since the formulation of the linearized problem is almost similar to that of the present paper, though lacking symmetry. Only the symmetry of the problem and response would guarantee the correctness of the theory and the soundness of the method used. Incidently, in a complex rope structure symmetry could help simplify the computation, since $b = c$. Recently the team of the senior writer (Sathikh et al., 1996a) has identified the origin of the lack of symmetry and formulated the symmetric problem and its solution.

This could be achieved only if the formulation follows Wempner (1973) and Ramsey (1990) by considering the wire stretch ξ as an independent parameter in the definition of the constitutive equations for H and G. Though the author has improved the formulation by considering ξ, but only for H, this partial treatment does not guarantee symmetry and correctness. Hence, Eq. (8) for G also should include a term with ξ as Eq. (7) for H so that

$$H_i = c_i\xi_i + d_i\Delta\tau_i \tag{7}$$

$$G_i = A_i\Delta\kappa_i + B_i\xi_i. \tag{D1}$$

In order to explain this, the simplest example of a resting-lay strand with a rigid core and single layer of m helical wires and its linearized responses are considered neglecting the Poisson's effect. For this case it can be shown that

$$\xi = \epsilon \sin^2\alpha + r \tan\alpha\, \phi \cos^2\alpha \tag{D2}$$

$$d\alpha = \sin\alpha \cos\alpha(\epsilon - r \tan\alpha\phi) \tag{D3}$$

$$\Delta\kappa = -\sin 2\alpha d\alpha$$

$$= -\sin 2\alpha \sin\alpha \cos\alpha(\epsilon - r \tan\alpha\phi) \tag{D4}$$

$$\Delta\tau = \cos 2\alpha d\alpha = \cos 2\alpha \sin\alpha \cos\alpha(\epsilon - r \tan\alpha\phi) \tag{D5}$$

$$H = GJ(\Delta\tau + \tau\xi) \tag{D6}$$

$$G = EI(\Delta\kappa + \kappa\xi) \tag{D7}$$

where

$$GJ/EI = 1/(1 + \nu) \text{ and } I = \pi R^4/4. \tag{D8}$$

It can be noted that from Eqs. (7), (D1), (D6), and (D7) that the stiffness coefficients are

$$A_i = EI; \left(\frac{B_i}{EI}\right) = \kappa; \left(\frac{c_i}{GJ}\right) = \tau; d_i = GJ. \tag{D9}$$

Substituting ξ, $\Delta\tau$, and $\Delta\kappa$ in terms of ϵ and ϕ, G and H in Eq. (1) for N, and in turn in Eq. (15) for F and M, it can be shown that in Eq. (52) $b = c$, and the new values are

$$\bar{a} = a_0 + m\{EA \sin^3\alpha + [GJ \cos^2\alpha + EI \sin^2\alpha] \cos^4\alpha \sin\alpha/r^2\} \tag{D10}$$

$$\bar{b} = \bar{c} = m\{EAr \sin^2\alpha \cos\alpha + [GJ \sin^2\alpha - EI(1 + \sin^2\alpha)] \sin^2\alpha \cos^3\alpha/r\} \tag{D11}$$

$$d = d_0 + m\{EAr^2 \sin\alpha \cos^2\alpha + GJ \sin^7\alpha + EI \sin\alpha \cos^2\alpha (1 + \sin^2\alpha)^2\} \tag{D12}$$

whereas the corresponding values of the paper from Eq. (53) are

$$a = \bar{a} \tag{D13}$$

$$b = m\{EAr \sin^2\alpha \cos\alpha - [EI \sin^2\alpha + GJ \cos^2\alpha] \sin^2\alpha \cos^3\alpha/r\} \tag{D14}$$

$$c = m\{EAr \sin^2\alpha \cos\alpha - [2EI \cos^2\alpha + GJ \sin^2\alpha] \sin^2\alpha \cos\alpha/r\} \tag{D15}$$

$$d = d_0 + m\{EAr^2 \sin\alpha \cos^2\alpha + 2EI \sin^3\alpha \cos^2\alpha + GJ \sin^5\alpha\}. \tag{D16}$$

For the general formulation of the paper, this concept could be readily extended to both resting-lay and closed-pack cases.

Secondly, it is about the limitations of the use of Eqs. (43) and (59). This expression was originally derived by Timoshenko (1956). This is for a case of uncored spring, though this fact is not explicitly visible. In fact, for a strand with no core-wire friction for the resting-lay case, what is derived by LeClair and Costello (1988) for a case with friction is appropriate. However, the factor $2k\sqrt{(1 + k^2)}/(2 + \nu + 2k^2) = 2 \sin\alpha/(2 + \nu \cos^2\alpha)$ in Eqs. (43) and (59), for the practical range of $\alpha = 90$ deg to 70 deg, is nearly unity and hence does not affect the results very much for frictionless contacts. A numerical comparison shows that the bending stiffness for a low friction typical ($\frac{1}{8}$) strand has a factor 1.026 (LeClair Costello Model 5 in Sathikh et al., 1996b) and 0.927 for a frictionless cored spring-like ($\frac{1}{8}$) strand (Model 5 in Sathikh et al., 1996b) against 0.9234 for the uncored spring-like ($\frac{1}{8}$) strand of the paper (Eqs. (43) and (59)).

In fact, in a cored strand $X \neq 0$ and this warrants wire radial force to be nonzero, whereas Eqs. (43) and (59) assume $X = 0$, as for an uncored spring. An elaborate study of the bending of a strand has been recently carried out by the senior writer's team (Sathikh et al., 1996b) which explains the importance of $X \neq 0$.

References

Jolicoeur, C., and Cardou, A. 1991, "A Numerical Comparison of Current Mathematical Models of Twisted Wire Cables Under Axisymmetric Loads," ASME *Journal of Energy Resources Technology*, Vol. 113, pp. 241–249.

Kumar, K., and Cochran, Jr., J. E., 1987, "Closed Form Analysis for Elastic Deformations of Multilayered Strands," ASME JOURNAL OF APPLIED MECHANICS, Vol. 54, pp. 898–903.

LeClair, R. A., and Costello, G. A., 1988, "Axial, Bending and Torsional Loading of a Strand with Friction," ASME *Journal of Offshore Mechanics and Arctic Engineering*, Vol. 110, pp. 38–42.

Ramsey, H., 1990, "Analysis of Interwire Friction in Multilayer Cables under Uniform Extension and Twisting," *International Journal of Mechanical Sciences*, Vol. 32, No. 9, pp. 707–716.

Sathikh, S., Moorthy, M. B. K., and Krishnan, M., 1996a, "A Symmetric Linear Elastic Model for Helical Wire Strand under Axisymmetric Loads," communicated to *Journal of Strain Analysis* and under review.

Sathikh, S., Rajesekaran, S., Krishnan, M., and Jayakumar, 1996b, "Some Alternative Discrete Thin Rod Models for Helical Wire Strand Bending with Friction," communicated to *Journal of Strain Analysis*.

Timoshenko, S., 1956, *Strength of Materials, Part II: Advanced Theory and Problems*, D. Van Nostrand, New York.

Wempner, G., 1973, *Mechanics of solids with Applications to Thin Bodies*, McGraw-Hill New York, Chapter 8.

Author's Closure[6]

Dr. Jolicoeur correctly points out that the use of the expression, $\sqrt{1 + k^2}$, will cause a sign error in the case of a left-hand lay and suggests to replace it by $1/\cos\alpha$. Alternatively, the author suggests to use the negative value of the $\sqrt{1 + k^2}$ in such a case to avoid altering the published expressions. From the mathematic point of view, a square root does have two signs. Dr. Jolicoeur also correctly points out that there is a typing error in Eq. (57). The author then notices a similar typing error in the second of Eq. (55), where λ_{i-1} should also be replaced by μ_{i-1}.

Dr. Sathikh et al. emphasize the importance of the symmetry of the linear force-strain relationships, Eqs. (38) and (52), and suggest to include a term with ξ into the G expression. The lack

[6] Mechanical Engineering Department, Florida International University, University Park, Miami, FL 33199.

of symmetry is very common in cable-wirerope analysis. The difference between b and c, however, is insignificant, as is already well known. It should be noted that while the satisfaction of the Maxwell-Betti reciprocal theorem does make the solution sound and consistent, a slight deviation from that theorem does not make the solution incorrect, because the Maxwell-Betti theorem was established on the linear theory, which is an approximation of the nonlinear theory with small terms being neglected. A fact is that the nonlinear solution is much more accurate, where there is no place for the Maxwell-Betti theorem. Of course, the symmetry of the problem and response would make the theory and method more ideal. The problem is thus whether any modifications are reasonable and can actually improve the accuracy.

The author would like to suggest that Dr. Sathikh et al. further substantiate their modifications. First of all, the correctness of their Eqs. (D6) and (D7) needs to be proved, and how the axial strain ξ can induce moments H and G in a wire should be explained. Note that Eq. (7) is justified in the wire rope analysis because of the well-known coupled extensional-torsional behavior of the cable structure. Note also that in the case of a wire such a coupled behavior is not considered in the paper ($c = 0$). Secondly, the use of Eqs. (D6) and (D7) only results in a slight change of Eq. (53),

$$\begin{cases} a_s = \pi E_0 R_0^2 + \sum_{i=1}^{n} \dfrac{m_i \pi E_i R_i^4 \tau_i \kappa_i}{4\sqrt{1 + k_i^2}} \times \left[\left(\dfrac{1}{1+\nu_i} + k_i^2 \right) - \left(\dfrac{1}{1+\nu_i} + k_i^2 - \dfrac{4}{R_i^2 \kappa_i^2} \right) \lambda_i \right] \\ b_s = -\sum_{i=1}^{n} \dfrac{m_i \pi E_i R_i^4 \tau_i \kappa_i}{4\sqrt{1 + k_i^2}} \times \left[\dfrac{\nu_i}{1+\nu_i} k_i r_i + \left(\dfrac{1}{1+\nu_i} + k_i^2 - \dfrac{4}{R_i^2 \kappa_i^2} \right) \mu_i \right] \\ c_s = -\sum_{i=1}^{n} \dfrac{m_i \pi E_i R_i^4 \kappa_i}{4(1 + k_i^2)^{3/2}} \times \left[\left(1 + \dfrac{1 + 2\nu_i}{1+\nu_i} k_i^2 \right) k_i^2 - \left(k_i^2 + \dfrac{1+2\nu_i}{1+\nu_i} k_i^4 + \dfrac{4}{R_i^2 \kappa_i^2} \right) \lambda_i \right] \\ d_s = \dfrac{\pi E_0 R_0^4}{4(1+\nu_0)} + \sum_{i=1}^{n} \dfrac{m_i \pi E_i R_i^4 \kappa_i}{4(1+k_i^2)^{3/2}} \left[\left(1 + 2k_i^2 + \dfrac{1}{1+\nu_i} k_i^4 \right) k_i r_i + \left(k_i^2 + \dfrac{1+2\nu_i}{1+\nu_i} k_i^4 + \dfrac{4}{R_i^2 \kappa_i^2} \right) \mu_i \right] \end{cases} \quad (53)'$$

and the symmetry can only be reached, as Dr. Sathikh et al. demonstrate, for a very special case of a single resting lay with a rigid core with no Poisson's effect, because at that time λ_1 and μ_1 assume very special values,

$$\begin{cases} \lambda_1 = \dfrac{k_1^2}{1 + k_1^2} \\ \mu_1 = \dfrac{k_1 r_1}{1 + k_1^2}. \end{cases}$$

In general, λ_i, and μ_i are much more complex as are shown in the paper, and the symmetry still cannot be achieved. Note also that the difference between Eqs. (D10)–(D12) and Eqs. (D13)–(D16) is insignificant (of the order of R^2/r^2).

Dr. Sathikh et al. then discuss the limitation of Eqs. (43) and (59), and indicate that "an elaborate study of the bending of a strand has been recently carried out." The details, however, are not given. The author would like to congratulate them on such an accomplishment.

Discussion

P. R. Heyliger[7]. Two papers have recently appeared on the free vibration of elastic solids with traction-free faces (Liew, Hung and Lim, 1995; Young and Dickinson 1995). Several important related studies were not cited in either paper. These include the work of Demarest (1971), Ohno (1976), and Mindlin (1986), who studied the rectangular parallelepiped, and Visscher and co-workers (1991), who examined a wide variety of shapes including spheres, cylinders, parallelepipeds, ellipsoids, pyramids, and cones.

References

Demarest, H. H., 1971, "Cube-resonance method to determine the elastic constants of solids," *Journal of the Acoustical Society of America,* Vol. 49, pp. 768–775.

Liew, K. M., Hung, K. C., and Lim, M. K., 1995, "Free Vibration Studies on Stress-Free Three-Dimensional Elastic Solids," ASME JOURNAL OF APPLIED MECHANICS, Vol. 62, pp. 159–165.

Mindlin, R. D., 1986, "On vibrations of rectangular parallelepipeds," *International Journal of Solids and Structures,* Vol. 22, pp. 1423–1430.

Ohno, I., 1976, "Free vibration of a rectangular parallelepiped crystal and its application to determination of elastic constants of orthorhombic crystals," *Journal of the Physics of the Earth,* Vol. 24, pp. 355–379.

Visscher, W. M., Migliori, A., Bell, T. M., and Reinert, R. A., 1991, "On the normal modes of free vibration of inhomogeneous and anisotropic elastic objects," *Journal of the Acoustical Society of America,* Vol. 90, pp. 2154–2162.

Young, P. G., and Dickinson, S. M., 1995, "Free Vibration of a Class of Homogeneous Isotropic Solids," ASME JOURNAL OF APPLIED MECHANICS, Vol. 62, pp. 706–708.

Authors' Closure[8]

The authors are indebted to Dr. Heyliger for his comment concerning their paper "Free Vibration of a Class of Homogeneous Isotropic Solids" (Young and Dickinson, 1995) and for listing some additional important works on elastic solids with traction-free faces which were not cited in the paper. Particularly of interest is the comprehensive work by Visscher, Migliori, Bell, and Reinert (1991), of which the present writers were not aware, having overlooked it in the literature! It may be noted that two approaches are essentially the same since both seek solutions for which the Lagrangian is stationary and employ the same simple polynomial basis functions.

References

Visscher, W. M., Migliori, A., Bell, T. M., and Reinert, R. A., 1991, "On the normal modes of free vibration of inhomogeneous and anisotropic elastic objects," *The Journal of the Acoustical Society of America,* Vol. 90, pp. 2154–2162.

Young, P. G., and Dickinson, S. M., 1995, "Free Vibration of a Class of Homogeneous Isotropic Solids," ASME JOURNAL OF APPLIED MECHANICS, Vol. 62, pp. 706–708.

[7] Department of Civil Engineering, Colorado State University, Fort Collins, CO 80523.

[8] P. G. Young and S. M. Dickinson, Department of Mechanical Engineering, Faculty & Engineering Science, The University of Western Ontario, London, Ontario N6A 5B9, Canada.

of symmetry is very common in cable-wirerope analysis. The difference between b and c, however, is insignificant, as is already well known. It should be noted that while the satisfaction of the Maxwell-Betti reciprocal theorem does make the solution sound and consistent, a slight deviation from that theorem does not make the solution incorrect, because the Maxwell-Betti theorem was established on the linear theory, which is an approximation of the nonlinear theory with small terms being neglected. A fact is that the nonlinear solution is much more accurate, where there is no place for the Maxwell-Betti theorem. Of course, the symmetry of the problem and response would make the theory and method more ideal. The problem is thus whether any modifications are reasonable and can actually improve the accuracy.

The author would like to suggest that Dr. Sathikh et al. further substantiate their modifications. First of all, the correctness of their Eqs. (D6) and (D7) needs to be proved, and how the axial strain ξ can induce moments H and G in a wire should be explained. Note that Eq. (7) is justified in the wire rope analysis because of the well-known coupled extensional-torsional behavior of the cable structure. Note also that in the case of a wire such a coupled behavior is not considered in the paper ($c = 0$). Secondly, the use of Eqs. (D6) and (D7) only results in a slight change of Eq. (53),

$$\begin{cases} a_s = \pi E_0 R_0^2 + \sum_{i=1}^{n} \dfrac{m_i \pi E_i R_i^4 \tau_i \kappa_i}{4\sqrt{1 + k_i^2}} \times \left[\left(\dfrac{1}{1+\nu_i} + k_i^2 \right) - \left(\dfrac{1}{1+\nu_i} + k_i^2 - \dfrac{4}{R_i^2 \kappa_i^2} \right) \lambda_i \right] \\ b_s = -\sum_{i=1}^{n} \dfrac{m_i \pi E_i R_i^4 \tau_i \kappa_i}{4\sqrt{1 + k_i^2}} \times \left[\dfrac{\nu_i}{1+\nu_i} k_i r_i + \left(\dfrac{1}{1+\nu_i} + k_i^2 - \dfrac{4}{R_i^2 \kappa_i^2} \right) \mu_i \right] \\ c_s = -\sum_{i=1}^{n} \dfrac{m_i \pi E_i R_i^4 \kappa_i}{4(1 + k_i^2)^{3/2}} \times \left[\left(1 + \dfrac{1 + 2\nu_i}{1+\nu_i} k_i^2 \right) k_i^2 - \left(k_i^2 + \dfrac{1+2\nu_i}{1+\nu_i} k_i^4 + \dfrac{4}{R_i^2 \kappa_i^2} \right) \lambda_i \right] \\ d_s = \dfrac{\pi E_0 R_0^4}{4(1+\nu_0)} + \sum_{i=1}^{n} \dfrac{m_i \pi E_i R_i^4 \kappa_i}{4(1+k_i^2)^{3/2}} \left[\left(1 + 2k_i^2 + \dfrac{1}{1+\nu_i} k_i^4 \right) k_i r_i + \left(k_i^2 + \dfrac{1+2\nu_i}{1+\nu_i} k_i^4 + \dfrac{4}{R_i^2 \kappa_i^2} \right) \mu_i \right] \end{cases} \quad (53)'$$

and the symmetry can only be reached, as Dr. Sathikh et al. demonstrate, for a very special case of a single resting lay with a rigid core with no Poisson's effect, because at that time λ_1 and μ_1 assume very special values,

$$\begin{cases} \lambda_1 = \dfrac{k_1^2}{1 + k_1^2} \\ \mu_1 = \dfrac{k_1 r_1}{1 + k_1^2}. \end{cases}$$

In general, λ_i, and μ_i are much more complex as are shown in the paper, and the symmetry still cannot be achieved. Note also that the difference between Eqs. (D10)–(D12) and Eqs. (D13)–(D16) is insignificant (of the order of R^2/r^2).

Dr. Sathikh et al. then discuss the limitation of Eqs. (43) and (59), and indicate that "an elaborate study of the bending of a strand has been recently carried out." The details, however, are not given. The author would like to congratulate them on such an accomplishment.

Discussion

P. R. Heyliger[7]. Two papers have recently appeared on the free vibration of elastic solids with traction-free faces (Liew, Hung and Lim, 1995; Young and Dickinson 1995). Several important related studies were not cited in either paper. These include the work of Demarest (1971), Ohno (1976), and Mindlin (1986), who studied the rectangular parallelepiped, and Visscher and co-workers (1991), who examined a wide variety of shapes including spheres, cylinders, parallelepipeds, ellipsoids, pyramids, and cones.

References

Demarest, H. H., 1971, "Cube-resonance method to determine the elastic constants of solids," *Journal of the Acoustical Society of America,* Vol. 49, pp. 768–775.

Liew, K. M., Hung, K. C., and Lim, M. K., 1995, "Free Vibration Studies on Stress-Free Three-Dimensional Elastic Solids," ASME JOURNAL OF APPLIED MECHANICS, Vol. 62, pp. 159–165.

Mindlin, R. D., 1986, "On vibrations of rectangular parallelepipeds," *International Journal of Solids and Structures,* Vol. 22, pp. 1423–1430.

Ohno, I., 1976, "Free vibration of a rectangular parallelepiped crystal and its application to determination of elastic constants of orthorhombic crystals," *Journal of the Physics of the Earth,* Vol. 24, pp. 355–379.

Visscher, W. M., Migliori, A., Bell, T. M., and Reinert, R. A., 1991, "On the normal modes of free vibration of inhomogeneous and anisotropic elastic objects," *Journal of the Acoustical Society of America,* Vol. 90, pp. 2154–2162.

Young, P. G., and Dickinson, S. M., 1995, "Free Vibration of a Class of Homogeneous Isotropic Solids," ASME JOURNAL OF APPLIED MECHANICS, Vol. 62, pp. 706–708.

Authors' Closure[8]

The authors are indebted to Dr. Heyliger for his comment concerning their paper "Free Vibration of a Class of Homogeneous Isotropic Solids" (Young and Dickinson, 1995) and for listing some additional important works on elastic solids with traction-free faces which were not cited in the paper. Particularly of interest is the comprehensive work by Visscher, Migliori, Bell, and Reinert (1991), of which the present writers were not aware, having overlooked it in the literature! It may be noted that two approaches are essentially the same since both seek solutions for which the Lagrangian is stationary and employ the same simple polynomial basis functions.

References

Visscher, W. M., Migliori, A., Bell, T. M., and Reinert, R. A., 1991, "On the normal modes of free vibration of inhomogeneous and anisotropic elastic objects," *The Journal of the Acoustical Society of America,* Vol. 90, pp. 2154–2162.

Young, P. G., and Dickinson, S. M., 1995, "Free Vibration of a Class of Homogeneous Isotropic Solids," ASME JOURNAL OF APPLIED MECHANICS, Vol. 62, pp. 706–708.

[7] Department of Civil Engineering, Colorado State University, Fort Collins, CO 80523.

[8] P. G. Young and S. M. Dickinson, Department of Mechanical Engineering, Faculty & Engineering Science, The University of Western Ontario, London, Ontario N6A 5B9, Canada.

Journal of Applied Mechanics

Book Reviews

Anisotropic Elasticity: Theory and Applications (Oxford Engineering Science Series, Vol. 45), by T. C. T. Ting. Oxford University Press, New York, NY 1996. 570 pages. Price: $85.00.[1]

REVIEWED BY C. O. HORGAN[2]

The author states in the preface to this book that, in the early 1980s, motivated by the upsurge in research on composite materials, he embarked on anisotropic elasticity research "with little background on isotropic elasticity" and "reluctant and apprehensive in venturing into anisotropic elasticity." He need not have worried. The book under review is a masterly account of the fundamental theory of linear anisotropic elasticity and its applications, with emphasis on the two-dimensional theory.

The book consists of 15 chapters. Following a brief 30-page introductory chapter on a summary of relevant results from Matrix Algebra, Chapter 2 presents the basic stress-strain laws for general anisotropic elastic materials, including classification of materials according to the number of symmetry planes. Chapter 3 is concerned with the basic theory and applications of anti-plane shear deformations. It is refreshing to see this topic treated in a linear elasticity book *before* embarking on the considerably more-complicated plane problems. Chapter 3 discusses some very recent developments from the research literature on the anti-plane shear theory. The remainder of the book, except for the final Chapter 15, is concerned with the two-dimensional plane theory of elasticity. The well-known Lekhniskii formulation, involving a fourth-order partial differential equation for an Airy stress function, is briefly summarized in Chapter 4 (15 pp).

The remaining chapters form the core of this book. The author is one of the pioneers in the use of the Stroh formalism as an alternative to the Lekhnitskii approach, and this method is described in detail in Chapters 5–7 (108 pp). As the author points out in the preface, this algebraic method was first developed by A. N. Stroh in 1958 and 1962; it has been widely used by the physics, materials science, and applied mathematics communities. The present account is the first to appear in book form, and the author clearly hopes to persuade solid mechanics researchers of its utility. A nice personal touch is provided at the end of Chapter 5, where a brief historical account, including a biography of Stroh (1926–1962), is given.

Applications of the Stroh formalism to special subjects are presented in Chapters 8–12, whose contents may be surmised from the chapter headings. Topics covered include Green's functions for infinite space, half-space, and composite space; particular solutions, stress singularities, and stress decay; anisotropic materials with an elliptic boundary; anisotropic media with a crack or a rigid line inclusion; and steady state motion and surface waves. The concluding three chapters are entitled "Degenerate or near degenerate materials," of which the isotropic materials are a special case; "Generalization of the Stroh formalism," which treats more general boundary conditions and extension to thermoelasticity and piezoelectric materials; and "Three-dimensional deformations." An extensive reference list, together with an author and subject index completes the book.

In the preface, the author express the hope "that this book will be useful for the beginners as well as the more advanced researchers who are interested in anisotropic elasticity." This reviewer believes that this will certainly be the case. This is a carefully written account of the fundamental mathematics and mechanics of anisotropic linearly elastic solids by a leading researcher in the field. While the Stroh formalism dominates the treatment in the book (and is clearly the author's preference over the methods of Lekhnitskii), *Anisotropic Elasticity: Theory and Applications* is a self-contained exposition of anisotropic linear elasticity that will undoubtedly become one of the classic reference books on the subject.

The Stone Skeleton: Structural Engineering of Masonry Architecture, by Jacques Heyman. Cambridge University Press, New York, 1995. 160 pages. Price: $59.59.

REVIEWED BY J. H. LIENHARD[3]

Jacques Heyman looks at ancient buildings in his book, *The Stone Skeleton.* Then he tells how the nature of structural design changed 400 years ago. The change began right after 1638 when Galileo wrote a crude theory for calculating stresses in a cantilever beam in his *Two New Sciences.* Ever since then, structural engineers have focused on stress analysis. They have asked, in greater and greater detail, what loads cause beams to crack or arches to collapse. Ever since Galileo, new kinds of mathematics have steadily given us better means for answering those questions.

Ancient and medieval design was another matter entirely. The old masons did not study the theorems and proofs of Euclid. Rather, they used their squares and compasses to form marvelous geometric shapes in stone. Masons found natural shapes that would remain in static equilibrium—even when they were disturbed. As long as you do not subject stone to tension or shear forces that have the effect of sliding one stone on another, masonry stands up. The old cathedrals have repeatedly survived earthquakes and bombing raids that have leveled the cities around them.

In 1675, a generation after Galileo, Robert Hooke made a point that dramatizes the way the old masons built with stone.

[1] Originally published in the October 1996 issue of ASME *Applied Mechanics Reviews,* Vol. 49, No. 10, p. B110 (Review number 10R16).

[2] Wills Johnson Professor of Applied Mathematics and Mechanics, University of Virginia, Charlottesville, VA 22903.

[3] M. D. Anderson Professor of Mechanical Engieering and History, University of Houston, Houston, TX 77204.